Department of Applied Geology

Large Igneous Provinces of the Southern Hemisphere: Isotopic Geochemistry and Plagioclase and Pyroxene $^{40}Ar/^{39}Ar$ Geochronology of the Kalkarindji, Karoo and Ferrar Provinces

Bryant Douglas Ware

This thesis is presented for the Degree of
Doctor of Philosophy
of
Curtin University

April 2017

DECLARATION

To the best of my knowledge and belief this thesis contains no material previously published by any other person except where due acknowledgement has been made. This thesis contains no material which has been accepted for the award of any other degree or diploma in any university.

The author acknowledges that copyright of published works contained within this thesis resides with the copyright holder(s) of those works. I warrant that I have obtained, where necessary, permission from the copyright owners to use any third-party copyright material reproduced in the thesis (e.g. questionnaires, artwork, unpublished letters), or to use any of my own published work (e.g. journal articles) in which the copyright is held by another party (e.g. publisher, co-author).

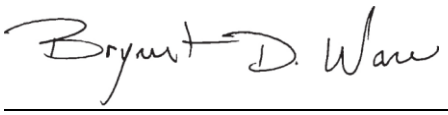

Bryant Douglas Ware

April 27th, 2017

Date

ABSTRACT

To develop a comprehensive understanding of geological processes a multidisciplinary approach must be utilized. This PhD research contributes to the understanding of Large Igneous Provinces (LIPs) petrogenesis through an integrated geochemical and high precision geochronological approach. To provide insights on the origin and duration models of LIPs generation, this research focus' on three Continental Flood Basalts (CFB) located throughout the Southern Hemisphere; the ca. 511 Ma Kalkarindji CFB Province located in the northwest of Australia; the Karoo CFB Province located in southern Africa and parts of Antarctica; and the Tasmanian Dolerite portion of the Ferrar CFB Province outcropped in Antarctica and Tasmania.

An extensive geochemical database of the Kalkarindji igneous constituents display one of the most geochemically homogeneous CFBs currently known. Interpretations from the geochemical data preclude the involvement of the assimilation of crustal material during the emplacement of the Kalkarindji magmas. Instead the geochemistry indicate the enriched characteristics are native to the mantle source. Calculations utilizing the high $^{207}Pb/^{204}Pb$ and elevated $^{208}Pb/^{204}Pb$ for moderate $^{206}Pb/^{204}Pb$ conclude the enriched geochemical characteristics can be reproduced from an ancient enrichment to the sub-continental lithospheric mantle ca. 2.5 Ga into the source region of the Kalkarindji magmas. Using the geochemical data a model of mantle warming for ca. 700 Ma coupled with decompression melting of the anciently fertilized SCLM that was triggered during a large scale rotation of Gondwana ca. 500 Ma is presented for generation of the magmas of the Kalkarindji Province.

High-precision geochronology of the Tasmanian Dolerites reveal a protracted duration of continuous magmatism over ca. 1.6 Ma. The precision of the results distinguishes older generation intrusions ca. 184 Ma from younger generations of intrusions ca. 182 with the latter displaying evidence of inherited plagioclase crystals apparent from the age spectra. The 184 Ma magmatism for the Tasmanian Dolerites is the oldest magmatic activity recorded for the Ferrar CFB province. Coupling the geochemical results with the geochemistry displays a minor geochemical difference between the dolerites emplaced around 184 Ma and those emplaced around 182 Ma suggesting a possible geochemical control of the lack of zircons older than 182 Ma in the Ferrar province.

Furthering the integration of $^{40}Ar/^{39}Ar$ geochronology with geochemical analyses, the Western Cape intrusions (dolerites) display the first direct evidence of a hydrated source for the Karoo CFB province. $^{40}Ar/^{39}Ar$ plagioclase geochronology indicate these Western Cape intrusions are some of the first magmatic expressions of the Karoo CFB province at ca 183.5 Ma. Precluding any evidence of a considerable amount of crustal contamination, the primary hydrated minerals (biotite and hornblende) are representative of a hydrated source. Furthermore, the geochemical and geographic location of the Western Cape intrusions with other low-Ti rocks of the Karoo LIP indicate subduction during the Kibaran Orogeny provided hydrated material to the base of the lithosphere preferentially proximal to the subduction zone. The direct evidence of H_2O in the source region of tholeiitic CFBs provides evidence needed to suggest the SCLM could contribute notably in the generation of CFBs.

The advent of multi-collector noble gas mass spectrometers provides the ability to continue to push various geochronological techniques to new horizons. The *first* geologically meaningful $^{40}Ar/^{39}Ar$ plateau ages for terrestrial pyroxene has been accomplished on dolerites from the Kalkarindji and Ferrar CFBs. Pyroxene is typically more resistant than plagioclase to hydrothermal alteration. Furthermore, pyroxene is an essential phase in ultramafic rocks, which currently lack datable material. A thorough comparison of the $^{40}Ar/^{39}Ar$ pyroxene plateau ages with previously published results from a multitude of geochronological methods indicate these results represent a true geological event. Irradiation induced recoil resulting from extensive exsolution in some of the samples can be mitigated through a thorough petrographic investigation when selecting samples for $^{40}Ar/^{39}Ar$ geochronology. However, the ability to utilize the $^{40}Ar/^{39}Ar$ technique with the mineral pyroxene establishes unprecedented geochronological opportunities for the study of LIPs, metamorphic, and thermochronological applications.

ACKNOWLEDGMENTS

First off, I would like to thank my supervisor Associate Professor Fred Jourdan for all of the support and guidance throughout this PhD dissertation and the many, many drafts that came across his desk. I would also like to thank collaborative researcher Dr. Renaud Merle for the many in person and over email geochemical discussion over the last three years, these were invaluable to the research. I extend an immeasurable thanks to the technical staff of the Western Australian Argon Isotope Facility; Celia Mayer, Adam Frew, and Zdenka Martelli, this PhD would not be completed if it had not been for all of y'alls help, support, and company through the incomprehensible amount of hours picking grains. To the staff and researchers of the Department of Applied Geology and John de Laeter Centre, I am thankfully to have had the opportunity to get to know each and every one of y'all. Lastly the collaborative researchers I had the opportunity to work with throughout these research projects; Dr. Massimo Chiaradia in the Department of Earth Sciences, University of Geneva, for the excellent Sr, Nd, and Pb isotope analyses, Dr. Eric Tohver at the University of Western Australia for the rocks and help with the primary hydrated minerals project, and Brent McInnes at the John de Laeter Centre for all of the advice and opportunities over these last few years here at Curtin.

Finally, I would like to thank all of my many wonderful friends, new and old, spread to all reaches of this wonderful planet of ours; every single one of y'all have made this journey outstanding and unforgettable. I would like to extend my love and thanks to my Australian family who welcomed me to this new country with open arms, instantly making me feel like I was home. Now to my family, all of the love, encouragement,

advice, and help throughout the move to the other side of the world and the long, long hours of PhD research; I would not have got far at all without it. Love love.

LIST OF ADDITIONAL PUBLICATIONS

The following titles are references to conference abstracts where part of the research outlined in this thesis was presented.

Ware, B. and Jourdan, F. (2017) *$^{40}Ar/^{39}Ar$ Geochronology of Terrestrial Pyroxene.* Abstracts with Programs – Goldschmidt 2017

Ware, B. and Jourdan, F. (2016) *$^{40}Ar/^{39}Ar$ Geochronology of Pyroxene.* In Thermochronology and Noble Gas Geochemistry and Geochronology Organization Workshop 2016: TANG^{3}O (eds. M. Danišík, F. Jourdan, C. Talavera, and B. I. A. McInnes).

Ware, B., Fernandes, K. Jourdan, F., and Tohver, E. (2016) *New $^{40}Ar/^{39}Ar$ Geochronology of Primary Hydrous Minerals from the Karoo LIP Magmas: Evidence for a Hydrated Source.* Abstracts with Programs – Goldschmidt 2016

Ware, B., Jourdan, F., and Vinnicomb, K. (2015) *High Precision $^{40}Ar/^{39}Ar$ Geochronology of Large Igneous Provinces: The Tasmanian Dolerites of the Ferrar LIP.* Abstracts with Programs – Goldschmidt 2015

Ware, B., Jourdan, F., Hodges, K., Tessalina, S., Chiaradia, M., Evins, L., and Gole, M. (2014) *Geochemistry of the Kalkarindji Magmas: Insights into the Source of the Oldest Phanerozoic Large Igneous Province.* Abstracts with Programs – American Geophysical Union Conference 2014

TABLE OF CONTENTS

LIST OF FIGURES

LIST OF TABLES

Chapter 1: Introduction

Large Igneous Provinces (LIPs) span almost the entirety of the Earth's history. These geologically significant events have been linked to climate changes, mass extinctions, and even large scale tectonic shifts such as continental breakup. However, the role LIPs play in these important moments across Earth's lifespan is still widely debated. The contribution or consequence LIPs have on the Earth can be answered by an understanding of the origin, duration, and geochemistry of the magmas that comprise these huge igneous events.

The origin and full duration of LIPs is still a widely controversial subject, with many competing models currently available. This study strives to make significant contributions to the understanding of LIPs with high precision geochemical and geochronological data sets. With the advent of multi-collector mass spectrometers, great strides have been made in the study of LIPs as more detailed questions can be asked now more than ever before. In the case of $^{40}Ar/^{39}Ar$ geochronology, these new generation multi-collector mass spectrometers, such as the Thermofisher^{TM} ARGUS VI, provide a stepwise advancement in sensitivity and precision on smaller sample volumes than previous single-collector generations. These recent advancements allow age data obtained using the $^{40}Ar/^{39}Ar$ technique to rival the precision obtained by U/Pb zircon chemical abrasion thermal ionization mass spectrometry - the current "gold" standard for high precision geologic ages. Though volcanic flows constitute the bulk of LIPs, they are naturally devoid of zircon and thus historically have been inaccessible to high precision geochronology. The $^{40}Ar/^{39}Ar$ technique provides greater precision for dating volcanic

flows, which is particularly useful for the study of LIPs. These advances will allow for both methods to be used in tandem to determine the most precise duration of the LIPs. These high precision geochronological results can then be used to place a better context on the geochemically diverse constituents of these magmas. The level of results and spread of techniques is incredibly important in obtaining the most comprehensive understanding of the generation of LIPs.

This study utilizes the availability of the multi-collector ARGUS VI mass spectrometer coupled with major, trace, and isotope geochemistry of three LIPs from the super continent Gondwana. The multi-disciplined results of these three distinct LIPs provide: the first geochemically comprehensive and petrogenetic interpretations of the oldest and most geochemically homogeneous Phanerozoic LIPs; further evidence for a more pronounced magmatic event than the classical idea of a punctuated duration; the first evidence for primary hydrous minerals from Continental Flood Basalts providing the first direct indication of water within these mantle sources; present the first ever geologically meaningful ages on terrestrial pyroxene.

1.1. Geologic Background

Large Igneous Provinces (LIPs) are massive accumulations of igneous rocks emplaced over a geologically short period of time. These large volumes of magmatic rocks occur in both continental and oceanic crust throughout Earth's history. This study focuses particularly on a selection of Continental Flood Basalt (CFB) provinces from the southern hemisphere; the Kalkarindji CFB province, the Ferrar CFB province, and the Karoo CFB province. Within this chapter, a focus on the broader discussion of the current understanding and importance of LIPs is described in detail, while each individual CFB

province is introduced in a global context. A more detailed geologic description and review for each CFB is presented in Chapter 2 (Kalkarindji; Section 2.3), Chapter 3 (Ferrar and the Tasmanian Dolerites; Section 3.3), and Chapter 4 (Karoo; Section 4.3).

1.1.1. Large Igneous Provinces

Large Igneous Provinces are defined by large volumes (greater than 10^6 km^3) of mafic magma emplaced primarily through a series of short igneous pulses over a few million years (Coffin & Eldholm, 1994; Courtillot & Renne, 2003; Bryan & Ernst, 2008; Ernst, 2014). Key events during Earth's history from continental break ups and large scale mantle geodynamic fluxes, to environmental changes that caused mass extinctions or smaller scale biotic turnovers have been linked to LIPs events (Courtillot & Renne, 2003; Bryan & Ernst, 2008; Sobolev *et al.*, 2011; Jones *et al.*, 2016; Ernst & Youbi, 2017). Throughout the Phanerozoic, these large magmatic fluxes represent prominent features across the Earth's surface (*Figure 1.1*) primarily located along previous or present suture/continental margins. Many models have been proposed to explain the generation and origin of LIPs, but regardless of the model chosen, LIPs represent anomalous melting rates. These high melting rates can be attributed primarily to the presence of water content, large scale decompression melting, and high mantle temperatures (Campbell, 2001). With this in mind, various hypotheses for the generations of LIPs can be split into two broad groups; active and passive.

1.1.1.1. Active Large Igneous Province Generation Models

One of the most common dynamic models for the generation of LIPs is impingement of a mantle plume head at the base of the Earth's lithosphere (e.g. White & McKenzie, 1989a; Campbell & Griffiths, 1990; Courtillot *et al.*, 2003; Ernst, 2014). Deep

rooted mantle plume models suggest LIPs are the result of a rising mantle plume from a primitive reservoir near the core-mantle boundary (Duncan & Richards, 1991; Courtillot *et al.*, 2003). The plume models hypothesize that the deep plume generates the "required" anomalously hot material to cause temperature dependent buoyancy fluxes of material through the mantle (Campbell & Griffiths, 1990; Courtillot *et al.*, 2003). For the anomalously hot material to overcome viscosity issues and rise within the lower mantle, the plume produces a head structure to obtain the needed buoyancy (Richards & Duncan, 1988; Campbell & Griffiths, 1990; Campbell, 2001; Courtillot *et al.*, 2003). This head structure in turn produces the large scale melting and volumes apparent in LIPs as it impinges on the base of the lithosphere (Figure 1.2a). After the initial large scale emplacement and volcanism of the LIP, the plume tail should continue causing melts that form volcanic chains as the overriding plate continues to move above the "stationary" plume (Campbell & Griffiths, 1990; Duncan & Richards, 1991; Campbell, 2001; Courtillot *et al.*, 2003) (Figure 1.2a). Another end member to the mantle plume model is the buildup of plume material at the base of the lithosphere (White & McKenzie, 1989a). Within these models, the buildup of material as the plume rises causes the volumes of material of a LIP, rather than a need for a plume head. As with the deep mantle plume models, the plume will continue to produce melts as continental breakup advances, resulting in a volcanic chain along the overriding plate. Regardless of which variety of plume model is used to describe the generation of LIPs, certain physical and geochemical characteristics are typically attributed to LIPs resulting from a mantle plume; (1) regional uplift prior to emplacement; (2) large dyke swarms evidenced by a high abundance of orientated dykes that feed the volcanism; (3) age progression along volcanic chains; (4)

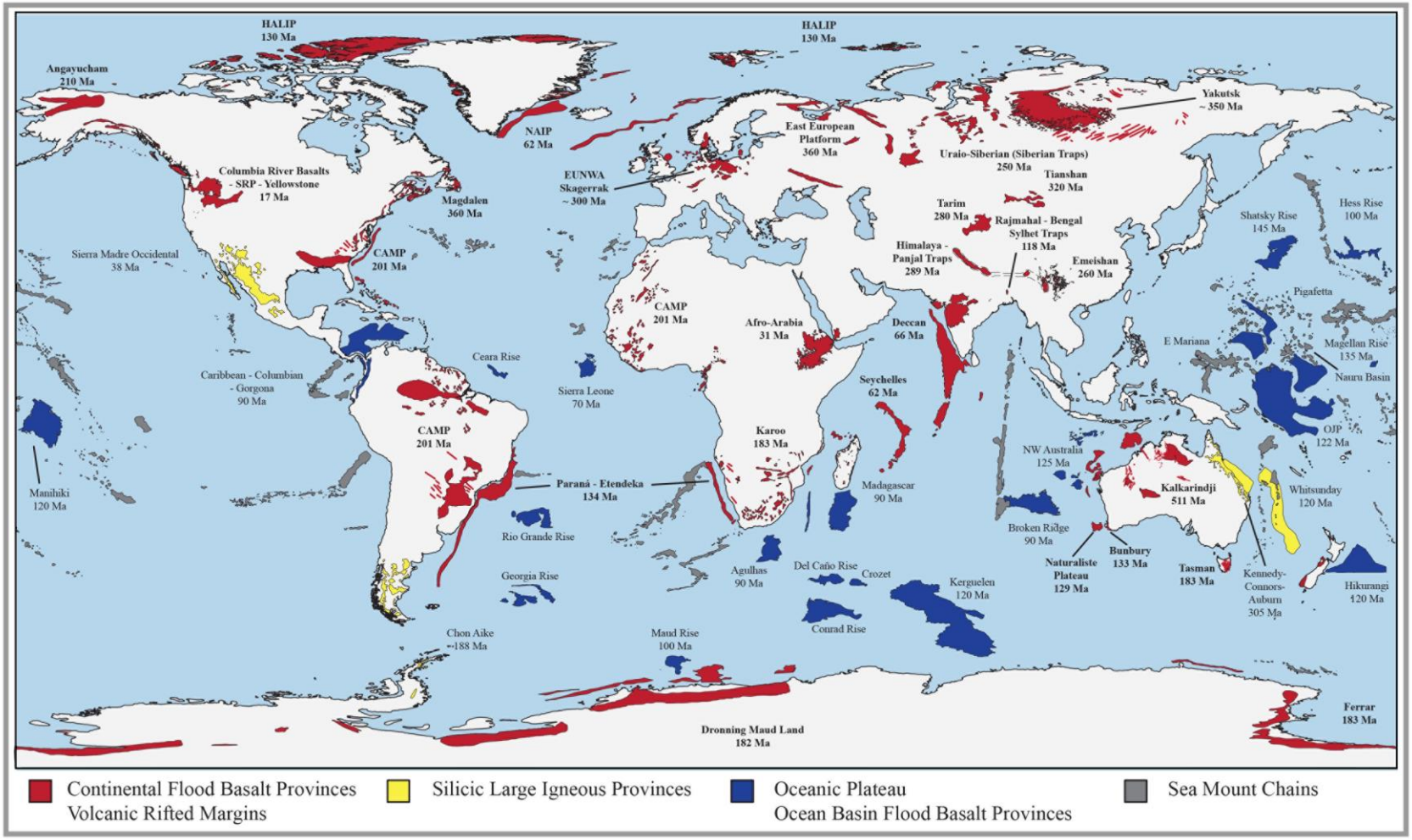

Figure 1.1: Global distribution of Phanerozoic Large Igneous Provinces (LIPs). Quoted ages indicate the onset of activity and are all from Bryan and Ernst (2008) except: Kalkarindji (Jourdan *et al.*, 2014); Bunbury (Olierook *et al.*, 2016); NW Australia (Olierook *et al.*, 2015). Abbreviations: CAMP, Central Atlantic Magmatic Province; HALIP, High Arctic Large Igneous Province; NAIP, North Atlantic Igneous Province; RBS, Rajmahal – Bengal Sylhet; HP, Himalaya – Panjal; OJP, Ontong Java Plateau. Redrafted and modified from Bryan and Ernst (2008).

distinct geochemical characteristics, primarily tholeiitic basalts with minor occurrences of alkali basalts and picrites (Campbell, 2001).

Inherent in these active models, mantle plume and emergence of LIPs drive/aid in tectonic shifts within the lithospheric regime of the Earth (Morgan, 1983; Hill, 1991; Hill, 1993; Courtillot *et al.*, 1999). The most convincing example of this hypothesis is the three plumes associated with the opening of the Atlantic Ocean; the Fernando de Noronha plume resulting in the Central Atlantic magmatic province (CAMP) ~ 200 Ma, the Tristan da Cunha plume causing the Paraná-Etendeka province ~ 130 Ma, and the Icelandic plume opening the north Atlantic ~ 60 Ma (*Figure 1.1*) (Courtillot *et al.*, 1999 and references

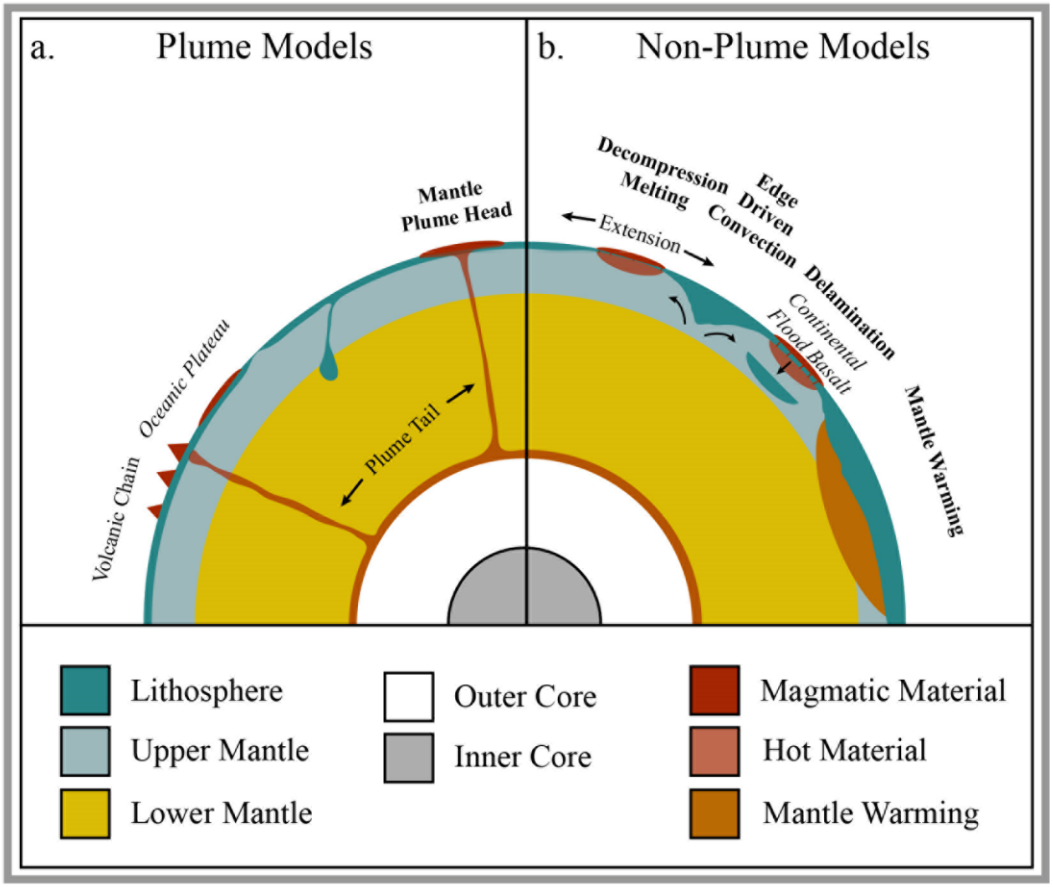

Figure 1.2: Simplified representation of the various models for the large igneous province generation. Created and modified after Anderson (2005).

therein). Debate remains for many LIPs on the involvement of mantle plumes; however, mantle plumes have been linked to the generation of many LIPs throughout Earth's history such as Deccan, Columbia River Basalts, Ethiopian, Kerguelen, and Paraná and Etendeka (*Figure 1.1*) (Hooper, 1982; Duncan & Pyle, 1988; Richards & Duncan, 1988; Storey *et al.*, 1989; Hofmann *et al.*, 1997; Takahahshi *et al.*, 1998; Ewart *et al.*, 2004; Doucet *et al.*, 2005; Ray, 2005; Doucet *et al.*, 2006; Hooper *et al.*, 2007; Rao & Lehmann, 2011).

1.1.1.2. Passive Large Igneous Province Generation Models

Along with active models proposed for the generation of LIPs, many passive models have also been hypothesized. These models are primarily driven from the observation that many LIPs occur along plate boundaries and do not display recognizable evidence for a plume tail after the emplacement of the LIP. As opposed to active/dynamic models for the generation of LIPs, these passive models find the large volumes of melt associated with plate boundaries to be a result of tectonic shifts rather than the cause or aid in initiating the shifts. However, the large scale magmatism can further effect and aid in the tectonic shift after initiation. These models are primarily represented by (1) lithospheric mantle decompression melting through lithospheric thinning by extensional forces (Bond *et al.*, 1984; Li *et al.*, 1996; Coltice *et al.*, 2007; Coltice *et al.*, 2009; Olierook *et al.*, 2016) or slab delamination (Ringwood & Green, 1966; Houseman & Molnar, 2001); (2) physical differences in the lithosphere between craton and non-craton cause edge driven convection along these boundaries which provide hot asthenospheric mantle to thin regions of the lithosphere where melting can occur (Anderson *et al.*, 1992; Anderson, 1994; King & Anderson, 1995; Oostingh *et al.*, 2016); (3) during times of supercontinents, magma and heat are built up underneath large continental bodies with no easy way to

thermodynamically equilibrate, ultimately breaking through the continental crust (Gurnis, 1988; Coltice *et al.*, 2007; Coltice *et al.*, 2009) (Figure 1.2b). These LIP origin models are discussed in greater detail in Chapter 2 in respect to interpretations for the generation of the Kalkarindji CFB province; therefore, the models will just be introduced here in regards to the central differences with mantle plume hypotheses.

Decompression melting occurs when the lithosphere has been thinned enough to begin melting with no net change in temperature (Figure 1.2b). Decompression melting is involved in nearly all of the models for LIP formation in some way or another. However, when considered as a driving mechanism for forming LIPs the models typically involve extensional tectonic regimes that significantly thin the continental lithosphere. In many aspect this model is similar to the mantle plume models relating to/driving continental breakup (White & McKenzie, 1989a; White & McKenzie, 1989b). However, in this passive LIP generation model, the extensional tectonism causes the melting of the lithosphere and mantle. Slab delamination is much like lithospheric mantle decompression, however, instead of large scale decompression melting related to rifting, the magmatic activity is a result of a delamination of a considerable portion to the lithosphere beneath supercontinents, which allows warmer asthenospheric mantle to rise. Delamination can be caused by tectonic stresses, such as continental convergence or large scale plate rotation leading to gravitational instabilities (Ringwood & Green, 1966; Houseman & Molnar, 2001). The catastrophic failure of thick sections of the lithosphere bringing hot asthenosphere to shallow depths. Large scale decompression melting then occurs within these shallow regimes previously occupied by thick lithosphere, providing the magmatic material to create LIPs.

Edge driven convection models originated from observations of LIPs frequency to occur around the margins of continental lithosphere (Figure 1.2b) (Anderson, 1994; King & Anderson, 1995). The plume model does not explain this apparent restriction of the common location for continental LIPs. Although it is conceivable that if a plume head came in contact with a thick cratonic lithosphere it could be deflected or diverted to these thinner, weaker zones of continental lithosphere, or show any evidence of uplift or stretching prior to eruptions, as would be expected during the impingement of a buoyant plume head. Furthermore, many CFBs do not display a hotspot track from the continued eruptions of the plume tail after the main voluminous events of the plume head. The asymmetry across these lithospheric boundaries causes small-scale convection that moves mantle from the deep cratonic lithosphere to shallower, thinner, and younger areas of the lithosphere, enabling a large amount of hot mantle through the 'melting-zone' (Mutter *et al.*, 1988; King & Anderson, 1995). These younger and thinners areas of the lithosphere are typically associated or present as suture zones between older, thicker craton blocks indicating regions of previous subduction, which can explain the enriched nature of the mantle in these areas (King and Anderson, 1995).

Lastly, the supercontinent cycles of the Earth can greatly affect the mantle temperature field and regulation. The movement of plates is largely driven by a combination of slab pull and cold downwelling in the mantle as well as slab push and hot upwellings. When supercontinents have formed, the large areas of continental lithosphere can insulate the sub-lithosphere, forcing mantle flow and convection to longer wavelengths (Coltice *et al.*, 2007; Coltice *et al.*, 2009). During supercontinent cycles, this period of insulation can cause an increase of lithospheric mantle temperature upwards of

70 °C after 100 Ma (Coltice *et al.*, 2007; Coltice *et al.*, 2009). This buildup of hot material below supercontinents provides the magmatic source of LIPs from decompression melting as the lithosphere thins during continental break up (Figure 1.2b). Within these mantle warming models, the continental breakup can be the result of the warming of the lithosphere below these supercontinents.

1.1.2. Geochemical constraints on LIPs

The focus of much of this thesis is on the petrogenesis of CFBs. Therefore, models are proposed or corroborated from a thorough investigation into major, trace, and isotope geochemistry data, and in some cases used in tandem with high precision geochronology data, for these CFBs. For this investigation, not only is a thorough understanding of the various models attributed to LIP generation needed, but also the geochemical characteristics and how they inform each of these models is incredibly important. These observations and interpretations made from the geochemical data will ultimately inform the chosen model. Relating the geochemical observations of LIPs to a respective model is not straight forward, as the natural processes are much more complex than the simplified models discussed above. For instance, the deep-seated mantle plume model hypothesizes that the magmatic material that generates LIPs is derived from the core-mantle boundary; however, the geochemical characteristics of resulting LIPs is rarely of depleted mantle signatures suggesting these mantle plumes entrain material of the lower mantle or recycled material either during the ascent through the mantle and crust or at the core-mantle boundary (Compston *et al.*, 1968; Storey *et al.*, 1988; Hergt *et al.*, 1989b; Ellam *et al.*, 1992; Molzahn *et al.*, 1996; Brauns *et al.*, 2000; Hergt & Brauns, 2001; Deckart *et al.*, 2005; Doucet *et al.*, 2005; Hooper *et al.*, 2007; Jourdan *et al.*, 2007a; McClintock *et al.*,

2007; Dessai & Viegas, 2009; Kinman *et al.*, 2009; Heinonen *et al.*, 2010; Merle *et al.*, 2013; Heinonen *et al.*, 2014; Luttinen *et al.*, 2015; Olierook *et al.*, 2017). Therefore, complexities have been introduced into the various models for LIP generations primarily through two main avenues; (1) contamination of the parental "primitive" magmas by crustal or lithospheric material after leaving the source region; and/or (2) the enrichment of the source region by the introduction of crustal material into the mantle or through a mixing of primitive mantle material with the lithosphere. The complexity of these processes that can act independently or together imbue great difficulty to unravelling the observed geochemical characteristics into a desired origin model for LIPs. The role of continental contamination and source enrichment is discussed extensively during the interpretation of the data in Chapters 2 and 3, and therefore only a brief introduction will be made here to each concept.

1.1.2.1. Continental Contamination

One of the difficulties in explaining the geochemical signatures of LIPs - and in particular CFBs - when considering the various generation hypothesis is remedying the negative Nb and Ta signatures and the enriched isotopic compositions of the magmas. When considering a deep mantle plume or a high degree of asthenospheric melt as the source region from which the LIPs magmatic material originated, a mantle geochemical signature should characterize these provinces. However, observations of CFBs display a negative Nb and Ta anomaly in primitive mantle normalized trace element plots, which is a characteristic indicative of the continental crust. Coupling these trace element observations with that of enriched isotopic signatures in many LIPs, assimilation of lithospheric material into the mantle derived magmas must occur during the petrogenesis

of LIPs (Carlson *et al.*, 1981; Arndt & Christensen, 1992; Arndt *et al.*, 1993; Chiaradia *et al.*, 2011; Bezard *et al.*, 2014). Arguments and models have been made that implicate crustal contamination in various amounts and processes can account for the crustal signatures evident in CFB provinces (Arndt *et al.*, 1993). LIPs such as Deccan, Ethiopian, and Paraná and Etendeka are strongly linked to mantle plume magmatism with varying degrees of crustal contamination (Baker et al. 1996; Hofmann et al. 1997; Duncan & Pyle 1988; Courtillot et al. 1986; Ewart 2004). In many CFBs, a negative Nb and Ta characteristic can be realistically attributed to assimilation of crustal material into the magma during ascent [Siberian Traps: Arndt *et al.* (1993); Karoo Low-Ti basalts: Jourdan *et al.* (2007a); CAMP: Merle *et al.* (2013)] (Figure 1.1). Despite evidence towards crustal contamination, many discussions occur about whether all LIPs can be explained through crustal contamination after the separation of the primary magmas from the source alone, or if the geochemical characteristics observed for some LIPs - CFBs in particular due to intracontinental crust emplacement - is rather the signature of a heterogeneous source such as the sub-continental lithospheric mantle (SCLM).

1.1.2.2. Source Enrichment

With the recognition of enriched geochemical characteristics, particularly in regards to CFBs, some hypotheses have been presented of source enrichment in conjunction with or instead of the crustal contamination processes. Within these models, the mantle source area has been enriched prior to LIP magmatism (Hergt *et al.*, 1989b; Anderson, 1994; Turner & Hawkesworth, 1995; Molzahn *et al.*, 1996; Merle *et al.*, 2013; Heinonen *et al.*, 2014). The means of enriching the source take many shapes and forms that all typically involve an enriched/fertilized SCLM; mantle metasomatism by fluids

(e.g. O'Reilly & Griffin, 2013), enrichment of the SCLM by sediments and/or fluids from subduction (e.g. Hergt *et al.*, 1989b; Gallagher & Hawkesworth, 1992), entrainment and incorporation of enriched material into the plume head during ascent (e.g. Campbell & Griffiths, 1990). Therefore, the heart of these source enrichment hypotheses is where the majority of the material for the LIPs is being sourced from; i.e. the asthenosphere (e.g. mantle plumes) or the SCLM. Broadly, these enriched source processes can be discussed in two main hypotheses: (1) the mixing of asthenospheric mantle/plume with the lithosphere and (2) source exclusively from the lithospheric mantle. These themes of how source areas can be enriched and where the magmatic material for CFBs is sourced beneath the Earth's surface are major discussion points within the chapters below, therefore these processes will only be introduced here.

To remedy the enriched geochemical compositions of the majority of CFBs with the mantle plume models, there have been mantle plume-lithosphere mixing models (Saunders *et al.*, 1992; Chung & Jahn, 1995; Class & Goldstein, 1997; Lassiter & DePaolo, 1997; Gibson *et al.*, 2006). In these hypotheses, a mantle plume mixes with the lithospheric mantle (Ellam *et al.*, 1992; Chung & Jahn, 1995; Gibson *et al.*, 1995), or is indirectly involved in the generation of LIPs by causing heating and subsequent melting of the continental lithosphere (McKenzie & Bickle, 1988; Turner *et al.*, 1996). An ascending plume may be capable of providing enough heat to melt the SCLM, allowing for large scale assimilation of continental crust or mixing between a mantle plume and the SCLM (e.g. plume-lithosphere mixing in the Karoo LIP; Ellam *et al.*, 1992; Jourdan *et al.*, 2007a). In these hypotheses, a deep-seated mantle plume induces melting at the base of the lithosphere, mixing with an enriched SCLM.

Another option for the source of LIPs is a heterogeneous fertilized SCLM. An important stipulation for this model (as well as the plume/lithosphere mixing model presented above); however, is the ability and plausibility of the ascending mantle plume to melt the SCLM. Thermomechanical modelling of the interactions between a plume and a dry lithosphere and decompression melting of a dry lithosphere conclude the lithosphere to be too cold to provide any significant contribution to LIP magmas (Arndt & Christensen, 1992). However, models of hydrating or fertilizing the lithospheric mantle indicate the sub-lithospheric mantle could melt and contribute to the genesis of LIPs as a major magma source (e.g. Hergt *et al.*, 1989b; Gallagher & Hawkesworth, 1992). Therefore, processes of hydrating and/or fertilizing the lithospheric mantle are crucial to the viability of these models. Metasomatic processes can hydrate generally dry regions of the mantle and lithosphere effective at creating a heterogeneous mantle (Menzies *et al.*, 1987). Study of mantle xenoliths have provided, for some authors, direct evidence of metasomatic processes occurring in the SCLM (Menzies *et al.*, 1987). Diamonds found within peridotites provide some inferences to the presence of metasomatism. Depletion events of the SCLM should remove C from the system thus making it difficult to form diamonds or graphite (O'Reilly & Griffin, 2013). Therefore, if diamonds are present in these types of xenoliths, C must have been reintroduced into the system most likely through mantle fluids (O'Reilly and Griffiths, 2013). The other primary process of fertilizing the SCLM is through the introduction of sediment directly into the lithospheric mantle (e.g. Hergt *et al.*, 1989b). Regarding again the negative Nb and Ta anomalies (when normalized to primitive mantle) apparent in CFBs, the lithospheric mantle contains negligible to positive anomalies and therefore is not able to produce the observed geochemical signatures of CFBs. As discussed above these signatures can also be obtained

through assimilation of crustal material after leaving the mantle source as the magmatic material emplaces through the continental crust. This model of introducing sediment material directly into the source was first proposed for the Tasmanian Dolerites to explain not just the Nb and Ta characteristics of the Ferrar province but also the homogeneity of the geochemistry of this province (Hergt *et al.*, 1989a; Hergt *et al.*, 1989b; Brauns *et al.*, 2000; Hergt & Brauns, 2001). The hypothesis of introducing sediment directly into the source explains the lack of variability that would be expected if crustal contamination occurred once the magma had left the source as well as how these magmas obtained the sediment like trace element trends if crustal contamination had not occurred. The low concentrations of the trace elements in MORB melts would allow for the trace elements of the introduced continental material to dominate the signature, while the major elements would retain the more MORB like characteristics. The isotopic characteristics would then be a mix between the two components with the continental material providing the most influence. Ultimately these characteristics would then be inherited by the ensuing magma during a partial melting event, resulting in a homogeneous enriched signature across the province.

1.1.4. Global Consideration of the Southern Hemisphere LIPs of this Study.

The geochemically diverse and temporally different CFBs chosen for this study are located across three (present day) continents (Figure 1.3). The Kalkarindji CFB province is emplaced entirely into the western portion of the Australian continent. The Ferrar CFBs and Tasmanian Dolerites are located across much of Antarctica along with minor outcrops found in the Australian island state of Tasmania, Victoria, as well as parts of New Zealand. The Karoo CFB province is primarily found in the southern region of

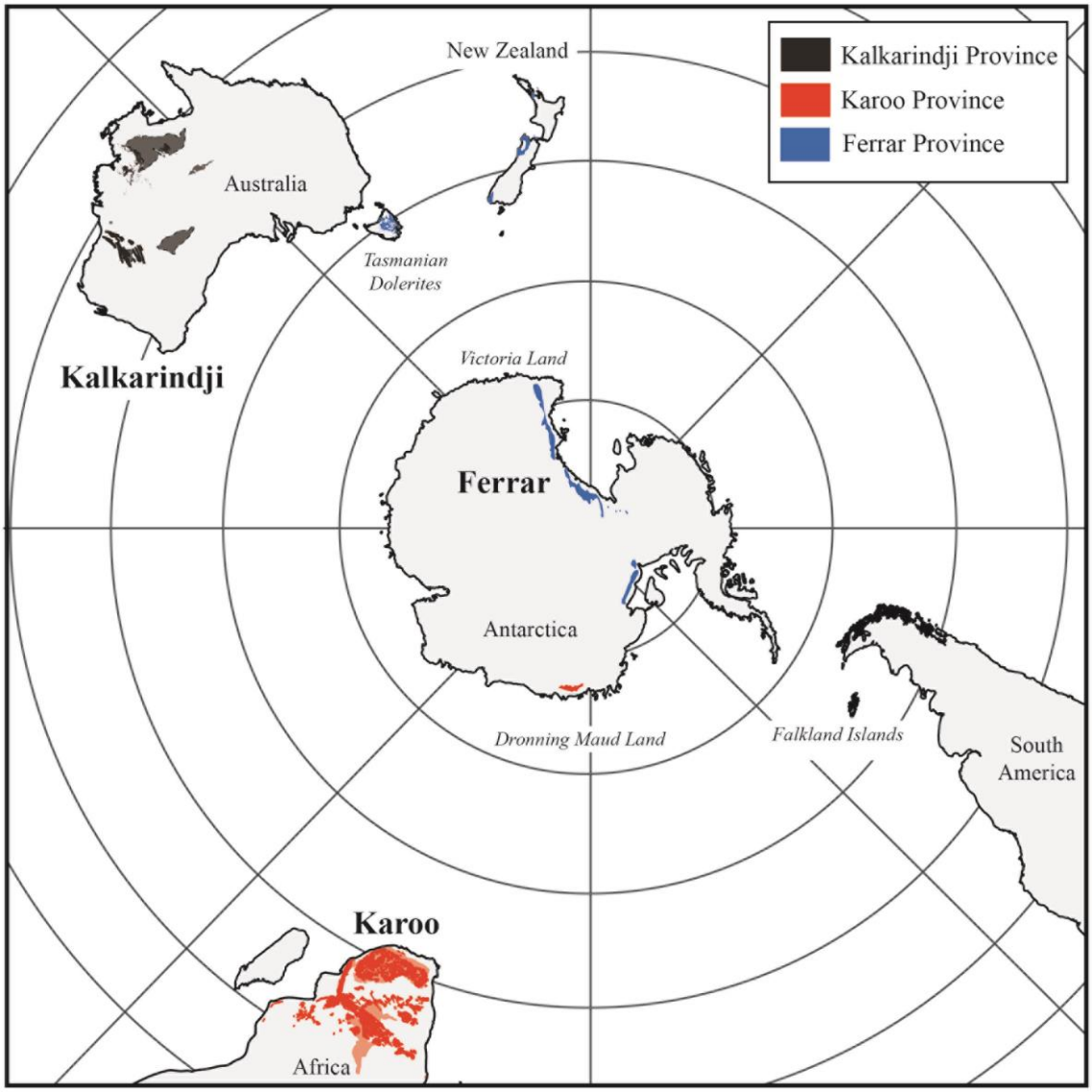

Figure 1.3: Present day location of the Gondwana plates indicating the locations of Karroo, Ferrar, and Kalkarindji large igneous provinces. Province locations after or modified from Bryan and Ernst (2008).

Africa however, minor outcroppings are present in parts of Antarctica as well as the Falkland Islands located off the Southeast coast of South America. These three CFB provinces represent the largest Phanerozoic CFB provinces of Gondwana and now the Southern Hemisphere (Figure 1.1).

The assembly of the Gondwana supercontinent has been estimated to have been concluding around the Early Cambrian (520 Ma) (Powell *et al.*, 1993; Zhao *et al.*, 1996;

Veevers, 2004). The southern portion of the Gondwana supercontinent remained tectonically stable from this final amalgamation in the Middle Cambrian to the initial beginning of breakup around 183 breakup of Africa and Antarctica (Dietz & Holden, 1970; Encarnacion *et al.*, 1996; Veevers, 2004) to a final separation of Antarctica and Australia around ~ 86 Ma (Royer & Sandwell, 1989; Sayers *et al.*, 2001; Veevers, 2004; Veevers, 2006; Gibbons *et al.*, 2013). Therefore, the Kalkarindji, Ferrar, and Karoo CFBs

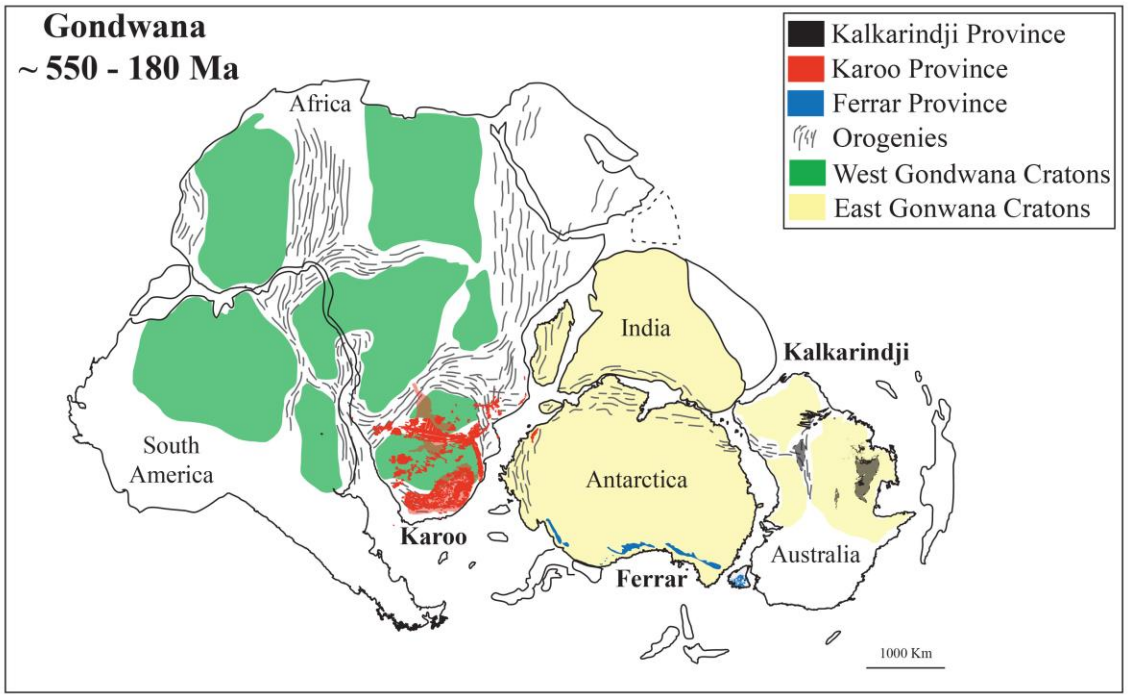

Figure 1.4: Schematic plate reconstruction of Gondwana from roughly 550 – 183 Ma, indicating locations of Karoo, Ferrar, and Kalkarindji large igneous provinces. Reconstructed elements schematically positioned after (Gray *et al.*, 2008).

were emplaced into a relatively tectonically stable history of the Gondwana supercontinent (Veevers, 2001; Veevers, 2004; Veevers, 2006; Gray *et al.*, 2008; Veevers, 2012) (Figure 1.4). The Kalkarindji CFB province was emplaced into the western region of Australia at ca. 511 Ma, shortly after initial amalgamation of Gondwana. The Ferrar (~ 182 – 184 Ma) and Karoo (~184 – 179 Ma) provinces are particularly interesting in that these two CFBs appear to have been emplaced synchronously, however, display

drastically different geochemical signatures. The provinces provide an excellent opportunity to examine the geochemistry similarities and differences of three contrasting provinces to better understand the processes that allow the generation of magma at such large scales. Thus, a more detailed and better understanding of these LIPs can ultimately provide an insight into the geodynamic fluxes of the mantle during periods of supercontinents.

1.2. Aims and Objectives

The aim of this project is to better quantify the petrogenesis and duration of igneous activity related to the emergence of CFBs. This overarching, broad aim will be addressed through the tandem use of geochemistry and geochronology of selected dolerite and volcanic expressions in the following sub-objective from three different CFBs from the southern hemisphere.

1) Using major, trace, and isotope geochemistry to hypothesize about the possible mechanisms to generate the large volumes of magma during LIP events (Chapter 2).

2) New generation multi-collector noble gas mass spectrometer (ARGUS VI) provide a step-wise advancement in the sensitivity, precision, and sample volume requirements than previous generations. With this new technology the use of the $^{40}Ar/^{39}Ar$ technique can provide unprecedented precision to mafic and ultramafic rocks geochronology as well as geologically meaningful ages for the first time ever to the mineral pyroxene. These advances will allow for the most precise duration of these LIPs providing the ability to better understand the magmatic activity in more detail than ever before (Chapters 3 – 5).

3) Utilizing this multi-technique geochronology and geochemistry campaign of high precision $^{40}Ar/^{39}Ar$ geochronology with major, trace, and isotope geochemistry provides evidence for better understanding the source and origin of these LIPs; such as the life span of CFB activity from the crystallization of plagioclase to zircon and why a chronological dichotomy can exist between these two phases (Chapter3); as well as CFB source hydration through the geochronological evidence of primary hydrous minerals (Chapter 4).

1.3. Dissertation Structure

The PhD dissertation begins with an Introduction chapter about the importance of the study of LIPs as well as how new generation machines allow for a more detailed and in depth understanding of these important events that can shape the environment, climate, Earth's surface, and the geodynamics of the mantle. Along with an in depth discussion into the current understanding of the petrogenetic models for the formation of LIPs the Introduction provides a brief geological context of the study locations. A more detailed focus and discussion on each regional geological setting is presented within the relevant chapters. The main body text of this dissertation is comprises chapters 2 – 5. Chapter 2 is currently accepted for publication in Journal of Petrology. The rest of the chapters have been written to be submitted as follows: Chapter 3 has been written in preparation to submit for publication, however, which journal this research will fit best is currently being considered; Chapter 4 will be submitted to Earth and Planetary Science Letters; Chapter 5 is to be submitted to Geochimica et Cosmochimica Acta. Co-author approvals of all submitted and soon to be submitted manuscripts can be found in Appendix A.

Chapter 2: The Kalkarindji Large Igneous Province, Australia: Petrogenesis of the oldest and most compositionally homogenous province of the Phanerozoic. This chapter provides a large geochemical data set for the oldest and most homogeneous province of the Phanerozoic. A thorough investigation into the generation of this LIP has never been published before. The novelty of this research combines a large amount of major and trace element geochemical data with Sr, Nd, and Pb isotope to presents a petrogenetic model for the composition of the magma source for the Kalkarindji CFBs. This detailed and regional discussion of the magma source of the Kalkarindji CFBs provides key insights to understanding the genesis of highly "enriched" CFBs worldwide.

Chapter 3: High Precision $^{40}Ar/^{39}Ar$ Geochronology of Large Igneous Provinces: The Tasmanian Dolerites of the Ferrar Continental Flood Basalt. This Chapter presents high precision $^{40}Ar/^{39}Ar$ geochronology of plagioclase crystals with uncertainties up to 0.1 %. These uncertainties on $^{40}Ar/^{39}Ar$ results for CFBs is unprecedented. Such precise information is extremely important to correctly interpret spatial and temporal trends in magmatism allowing for a more detailed and minute investigation into magmatic activity within the Tasmanian Dolerites than previously able to address. This new $^{40}Ar/^{39}Ar$ geochronology results are then coupled with the geochemistry of the Tasmanian Dolerites to comment and speculate on the differences (geologic or systematic?) in ages obtained between plagioclase with the $^{40}Ar/^{39}Ar$ technique and U/Pb data utilizing the chemical abrasion thermal ionization mass spectrometry method.

Chapter 4. Primary Hydrous Minerals from the Karoo LIP magmas: Evidence for a Hydrated Source component. This chapter provides the first evidence of primary hydrous minerals within the igneous rocks of the Karoo CFB province. Five dolerite sills

intruded into the Karoo Basin have statistically indistinguishable $^{40}Ar/^{39}Ar$ plateau ages between plagioclase and biotite/hornblende crystals. A detailed major, trace and Sr, Nd, and Pb isotope geochemical analysis of these dolerites coupled with the primary nature of these hydrous minerals demonstrate that source of these magmas must have been hydrated. These results have important implications for the genesis of the large magmatic volumes of LIPs, as a hydrated/fertilized source can greatly affect the geodynamics of the magmatic source regions of these province.

Chapter 5. $^{40}Ar/^{39}Ar$ Geochronology of Terrestrial Pyroxene. This chapter showcases the analytical capabilities that can be obtained with the ARGUS VI mass spectrometer. The added sensitivity of the ARGUS VI allowed through the multi-collection capability has provided the ability to obtain geological significant ages to terrestrial pyroxene. The methodology of utilizing the $^{40}Ar/^{39}Ar$ technique for the mineral pyroxene is discussed from ages derived from two different CFBs; the ~ 183 Ma Tasmanian Dolerites that are relatively fresh; and the mildly altered ~ 511 Ma Kalkarindji CFB province. As this chapter presents a novel use of the $^{40}Ar/^{39}Ar$ technique, a detailed theoretical background of previous attempts of $^{40}Ar/^{39}Ar$ pyroxene dating of extraterrestrial and terrestrial material, a detailed methodological approach to processing samples for pyroxene, and a detailed discussion of all the variables and unknowns present when selecting samples and age calculation.

1.4. References

Anderson, D. L. (1994). The sublithospheric mantle as the source of continental flood basalts; the case against the continental lithosphere and plume head reservoirs. *Earth and Planetary Science Letters* **123**, 269-280.

Anderson, D. L., Zhang, Y.-S. & Tanimoto, T. (1992). Plume heads, continental lithosphere, flood basalts and tomography. *Geological Society, London, Special Publications* **68**, 99-124.

Arndt, N. T. & Christensen, U. (1992). The role of lithospheric mantle in continental flood volcanism: Thermal and geochemical constraints. *Journal of Geophysical Research* **97**, 10967.

Arndt, N. T., Czamanske, G. K., Wooden, J. L. & Fedorenko, V. A. (1993). Mantle and crustal contributions to continental flood volcanism. *Tectonophysics* **223**, 39-52.

Bezard, R., Davidson, J. P., Turner, S., Macpherson, C. G., Lindsay, J. M. & Boyce, A. J. (2014). Assimilation of sediments embedded in the oceanic arc crust: myth or reality? *Earth and Planetary Science Letters* **395**, 51-60.

Bond, G. C., Nickeson, P. A. & Kominz, M. A. (1984). Breakup of a supercontinent between 625 Ma and 555 Ma: new evidence and implications for continental histories. *Earth and Planetary Science Letters* **70**, 325-345.

Brauns, C. M., Hergt, J. M., Woodhead, J. D. & Maas, R. (2000). Os Isotopes and the Origin of the Tasmanian Dolerites. *Journal of Petrology* **41**, 905-918.

Bryan, S. E. & Ernst, R. E. (2008). Revised definition of Large Igneous Provinces (LIPs). *Earth-Science Reviews* **86**, 175-202.

Campbell, I. H. (2001). Identification of ancient mantle plumes. *Special Papers-Geological Society of America*, 5-22.

Campbell, I. H. & Griffiths, R. W. (1990). Implications of mantle plume structure for the evolution of flood basalts. *Earth and Planetary Science Letters* **99**, 79-93.

Carlson, R., Lugmair, G. & Macdougall, J. (1981). Crustal influence in the generation of continental flood basalts. *Nature* **289**, 160-162.

Chiaradia, M., Müntener, O. & Beate, B. (2011). Enriched basaltic andesites from mid-crustal fractional crystallization, recharge, and assimilation (Pilavo Volcano, Western Cordillera of Ecuador). *Journal of Petrology* **52**, 1107-1141.

Chung, S.-L. & Jahn, B.-m. (1995). Plume-lithosphere interaction in generation of the Emeishan flood basalts at the Permian-Triassic boundary. *Geology* **23**, 889-892.

Class, C. & Goldstein, S. L. (1997). Plume-lithosphere interactions in the ocean basins: constraints from the source mineralogy. *Earth and Planetary Science Letters* **150**, 245-260.

Coffin, M. F. & Eldholm, O. (1994). Large igneous provinces: Crustal structure, dimensions, and external consequences. *Reviews of Geophysics* **32**, 1-36.

Coltice, N., Bertrand, H., Rey, P., Jourdan, F., Phillips, B. R. & Ricard, Y. (2009). Global warming of the mantle beneath continents back to the Archaean. *Gondwana Research* **15**, 254-266.

Coltice, N., Phillips, B. R., Bertrand, H., Ricard, Y. & Rey, P. (2007). Global warming of the mantle at the origin of flood basalts over supercontinents. *Geology* **35**, 391.

Compston, W., McDougall, I. & Heier, K. S. (1968). Geochemical comparison of the mesozoic basaltic rocks of Antarctica, South Africa, South America and Tasmania. *Geochimica et Cosmochimica Acta* **32**, 129-149.

Courtillot, V., Davaille, A., Besse, J. & Stock, J. (2003). Three distinct types of hotspots in the Earth's mantle. *Earth and Planetary Science Letters* **205**, 295-308.

Courtillot, V., Jaupart, C., Manighetti, I., Tapponnier, P. & Besse, J. (1999). On causal links between flood basalts and continental breakup. *Earth and Planetary Science Letters* **166**, 177-195.

Courtillot, V. E. & Renne, P. R. (2003). On the ages of flood basalt events. *Comptes Rendus Geoscience* **335**, 113-140.

Deckart, K., Bertrand, H. & Liégeois, J.-P. (2005). Geochemistry and Sr, Nd, Pb isotopic composition of the Central Atlantic Magmatic Province (CAMP) in Guyana and Guinea. *Lithos* **82**, 289-314.

Dessai, A. G. & Viegas, A. (2009). Petrogenesis of alkaline rocks from Murud-Janjira, in the Deccan Traps, Western India. *Mineralogy and Petrology* **98**, 297-311.

Dietz, R. S. & Holden, J. C. (1970). Reconstruction of Pangaea: Breakup and dispersion of continents, Permian to Present. *Journal of Geophysical Research* **75**, 4939-4956.

Doucet, S., Moreira, M., Weis, D., Scoates, J. S., Giret, A. & Allègre, C. (2006). Primitive neon and helium isotopic compositions of high-MgO basalts from the Kerguelen Archipelago, Indian Ocean. *Earth and Planetary Science Letters* **241**, 65-79.

Doucet, S., Scoates, J. S., Weis, D. & Giret, A. (2005). Constraining the components of the Kerguelen mantle plume: A Hf-Pb-Sr-Nd isotopic study of picrites and high-MgO basalts from the Kerguelen Archipelago. *Geochemistry, Geophysics, Geosystems* **6**, n/a-n/a.

Duncan, R. & Pyle, D. (1988). Rapid eruption of the Deccan flood basalts at the Cretaceous/Tertiary boundary. *Nature* **333**, 841-843.

Duncan, R. A. & Richards, M. (1991). Hotspots, mantle plumes, flood basalts, and true polar wander. *Reviews of Geophysics* **29**, 31-50.

Ellam, R., Carlson, R. & Shirey, S. (1992). Evidence from Re–Os isotopes for plume–lithosphere mixing in Karoo flood basalt genesis. *Nature* **359**, 718-721.

Encarnacion, J., Fleming, T. H., Elliot, D. H. & Eales, H. V. (1996). Synchronous emplacement of Ferrar and Karoo dolerites and the early breakup of Gondwana. *Geology (Boulder)* **24**, 535-538.

Ernst, R. E. (2014). *Large igneous provinces*: Cambridge University Press.

Ernst, R. E. & Youbi, N. (2017). How Large Igneous Provinces affect global climate, sometimes cause mass extinctions, and represent natural markers in the geological record. *Palaeogeography, Palaeoclimatology, Palaeoecology*.

Ewart, A., Marsh, J., Milner, S., Duncan, A., Kamber, B. S. & Armstrong, R. (2004). Petrology and geochemistry of Early Cretaceous bimodal continental flood volcanism of the NW Etendeka, Namibia. Part 2: Characteristics and petrogenesis of the high-Ti latite and high-Ti and low-Ti voluminous quartz latite eruptives. *Journal of Petrology* **45**, 107-138.

Gallagher, K. & Hawkesworth, C. (1992). Dehydration melting and the generation of continental flood basalts. *Nature* **358**, 57-59.

Gibbons, A. D., Whittaker, J. M. & Müller, R. D. (2013). The breakup of East Gondwana: assimilating constraints from Cretaceous ocean basins around India into a best-fit tectonic model. *Journal of Geophysical Research: Solid Earth* **118**, 808-822.

Gibson, S., Thompson, R., Dickin, A. P. & Leonardos, O. (1995). High-Ti and low-Ti mafic potassic magmas: Key to plume-lithosphere interactions and continental flood-basalt genesis. *Earth and Planetary Science Letters* **136**, 149-165.

Gibson, S. A., Thompson, R. N. & Day, J. A. (2006). Timescales and mechanisms of plume–lithosphere interactions: 40Ar/39Ar geochronology and geochemistry of alkaline igneous rocks from the Paraná–Etendeka large igneous province. *Earth and Planetary Science Letters* **251**, 1-17.

Gurnis, M. (1988). Large-scale mantle convection and the aggregation and dispersal of supercontinents. *Nature* 332, 695-699.

Heinonen, J. S., Carlson, R. W. & Luttinen, A. V. (2010). Isotopic (Sr, Nd, Pb, and Os) composition of highly magnesian dikes of Vestfjella, western Dronning Maud Land, Antarctica: A key to the origins of the Jurassic Karoo large igneous province? *Chemical Geology* **277**, 227-244.

Heinonen, J. S., Carlson, R. W., Riley, T. R., Luttinen, A. V. & Horan, M. F. (2014). Subduction-modified oceanic crust mixed with a depleted mantle reservoir in the sources of the Karoo continental flood basalt province. *Earth and Planetary Science Letters* **394**, 229-241.

Hergt, J. M. & Brauns, C. M. (2001). On the origin of Tasmanian dolerites. *Australian Journal of Earth Sciences* **48**, 543-549.

Hergt, J. M., Chappell, B. W., Faure, G. & Mensing, T. M. (1989a). The geochemistry of Jurassic dolerites from Portal Peak, Antarctica. *Contributions to Mineralogy and Petrology* **102**, 298-305.

Hergt, J. M., Chappell, B. W., McCulloch, M. T., McDougall, I. & Chivas, A. R. (1989b). Geochemical and isotopic constraints on the origin of the Jurassic dolerites of Tasmania. *Journal of Petrology* **30**, 841-883.

Hill, R. I. (1991). Starting plumes and continental break-up. *Earth and Planetary Science Letters* **104**, 398-416.

Hill, R. I. (1993). Mantle plumes and continental tectonics. *Lithos* **30**, 193-206.

Hofmann, C., Courtillot, V., Feraud, G., Rochette, P., Yirgu, G., Ketefo, E. & Pik, R. (1997). Timing of the Ethiopian flood basalt event and implications for plume birth and global change. *Nature* **389**, 838-841.

Hooper, P. R. (1982). The Columbia river basalts. *Science* **215**, 1463-1468.

Hooper, P. R., Camp, V. E., Reidel, S. P. & Ross, M. E. (2007). The origin of the Columbia River flood basalt province: Plume versus nonplume models. *Geological Society of America Special Papers* **430**, 635-668.

Houseman, G. & Molnar, P. (2001). Mechanisms of lithospheric rejuvenation associated with continental orogeny. *Geological Society, London, Special Publications* **184**, 13-38.

Jones, M. T., Jerram, D. A., Svensen, H. H. & Grove, C. (2016). The effects of large igneous provinces on the global carbon and sulphur cycles. *Palaeogeography, Palaeoclimatology, Palaeoecology* **441, Part 1**, 4-21.

Jourdan, F., Bertrand, H., Scharer, U., Blichert-Toft, J., Feraud, G. & Kampunzu, A. B. (2007). Major and Trace Element and Sr, Nd, Hf, and Pb Isotope Compositions of the Karoo Large Igneous Province, Botswana-Zimbabwe: Lithosphere vs Mantle Plume Contribution. *Journal of Petrology* **48**, 1043-1077.

King, S. D. & Anderson, D. L. (1995). An alternative mechanism of flood basalt formation. *Earth and Planetary Science Letters* **136**, 269-279.

Kinman, W. S., Neal, C. R., Davidson, J. P. & Font, L. (2009). The dynamics of Kerguelen Plateau magma evolution: New insights from major element, trace element and Sr isotope microanalysis of plagioclase hosted in Elan Bank basalts. *Chemical Geology* **264**, 247-265.

Lassiter, J. C. & DePaolo, D. J. (1997). Plume/lithosphere interaction in the generation of continental and oceanic flood basalts: chemical and isotopic constraints. *Large igneous provinces: Continental, oceanic, and planetary flood volcanism*, 335-355.

Li, Z. X., Zhang, L. & Powell, C. M. (1996). Positions of the East Asian cratons in the Neoproterozoic supercontinent Rodinia. *Australian Journal of Earth Sciences* **43**, 593-604.

Luttinen, A. V., Heinonen, J. S., Kurhila, M., Jourdan, F., Manttari, I., Vuori, S. K. & Huhma, H. (2015). Depleted Mantle-sourced CFB Magmatism in the Jurassic Africa-Antarctica Rift: Petrology and 40Ar/39Ar and U/Pb Chronology of the Vestfjella Dyke Swarm, Dronning Maud Land, Antarctica. *Journal of Petrology* **56**, 919-952.

McClintock, M., Marsh, J. S. & White, J. D. L. (2007). Compositionally diverse magmas erupted close together in space and time within a Karoo flood basalt crater complex. *Bulletin of Volcanology* **70**, 923-946.

McKenzie, D. & Bickle, M. (1988). The volume and composition of melt generated by extension of the lithosphere. *Journal of Petrology* **29**, 625-679.

Merle, R., Marzoli, A., Reisberg, L., Bertrand, H., Nemchin, A., Chiaradia, M., Callegaro, S., Jourdan, F., Bellieni, G., Kontak, D., Puffer, J. & McHone, J. G. (2013). Sr, Nd, Pb and Os Isotope Systematics of CAMP Tholeiites from Eastern North America (ENA): Evidence of a Subduction-enriched Mantle Source. *Journal of Petrology* **55**, 133-180.

Molzahn, M., Reisberg, L. & Wörner, G. (1996). Os, Sr, Nd, Pb, O isotope and trace element data from the Ferrar flood basalts, antarctica: evidence for an enriched subcontinental lithospheric source. *Earth and Planetary Science Letters* **144**, 529-545.

Morgan, W. J. (1983). Hotspot tracks and the early rifting of the Atlantic. *Tectonophysics* **94**, 123-139.

Mutter, J. C., Buck, W. R. & Zehnder, C. M. (1988). Convective partial melting: 1. A model for the formation of thick basaltic sequences during the initiation of spreading. *Journal of Geophysical Research* **93**, 1031.

O'Reilly, S. Y. & Griffin, W. (2013). Mantle Metasomatism. In: Harlov, D. E. & Austrheim, H. (eds.) *Metasomatism and the chemical transformation of rock*: Springer, 471-533.

Olierook, H. K., Merle, R. E. & Jourdan, F. (2017). Toward a Greater Kerguelen Large Igneous Province: Evolving mantle source contributions in and around the Indian Ocean. *Lithos*.

Olierook, H. K. H., Jourdan, F., Merle, R. E., Timms, N. E., Kusznir, N. & Muhling, J. R. (2016). Bunbury Basalt: Gondwana breakup products or earliest vestiges of the Kerguelen mantle plume? *Earth and Planetary Science Letters* **440**, 20-32.

Oostingh, K. F., Jourdan, F., Merle, R. & Chiaradia, M. (2016). Spatio-temporal Geochemical Evolution of the SE Australian Upper Mantle Deciphered from the Sr, Nd and Pb Isotope Compositions of Cenozoic Intraplate Volcanic Rocks. *Journal of Petrology* **57**, 1509-1530.

Powell, C. M., Li, Z. X., McElhinny, M. W., Meert, J. G. & Park, J. K. (1993). Paleomagnetic constraints on timing of the Neoproterozoic breakup of Rodinia and the Cambrian formation of Gondwana. *Geology*. **21**, 889.

Rao, N. V. C. & Lehmann, B. (2011). Kimberlites, flood basalts and mantle plumes: New insights from the Deccan Large Igneous Province. *Earth-Science Reviews* **107**, 315-324.

Ray, J. S. (2005). Rapid emplacement of the Kerguelen plume–related Sylhet Traps, eastern India: Evidence from40Ar-39Ar geochronology. *Geophysical Research Letters* **32**.

Richards, M. A. & Duncan, R. A. (1988). Flood basalts and hotspot tracks plume heads and tails. Washington, DC: Washington, DC, United States: American Geophysical Union, 1421.

Ringwood, A. & Green, D. (1966). An experimental investigation of the gabbro-eclogite transformation and some geophysical implications. *Tectonophysics* **3**, 383-427.

Royer, J.-Y. & Sandwell, D. T. (1989). Evolution of the eastern Indian Ocean since the Late Cretaceous: Constraints from Geosat altimetry. *Journal of Geophysical Research: Solid Earth* 94, 13755-13782.

Saunders, A. D., Storey, M., Kent, R. & Norry, M. (1992). Consequences of plume-lithosphere interactions. *Geological Society, London, Special Publications* **68**, 41-60.

Sayers, J., Symonds, P. A., Direen, N. G. & Bernardel, G. (2001). Nature of the continent-ocean transition on the non-volcanic rifted margin of the central Great Australian Bight. *Geological Society, London, Special Publications* 187, 51-76.

Sobolev, S. V., Sobolev, A. V., Kuzmin, D. V., Krivolutskaya, N. A., Petrunin, A. G., Arndt, N. T., Radko, V. A. & Vasiliev, Y. R. (2011). Linking mantle plumes, large igneous provinces and environmental catastrophes. *Nature* **477**, 312-316.

Storey, M., Saunders, A., Tarney, J., Gibson, I., Norry, M., Thirlwall, M., Leat, P., Thompson, R. & Menzies, M. (1989). Contamination of Indian Ocean asthenosphere by the Kerguelen–Heard mantle plume. *Nature* **338**, 574-576.

Storey, M., Saunders, A., Tarney, J., Leat, P., Thirlwall, M., Thompson, R., Menzies, M. & Marriner, G. (1988). Geochemical evidence for plume—mantle interactions beneath Kerguelen and Heard Islands, Indian Ocean. *Nature* **336**, 371-374.

Takahahshi, E., Nakajima, K. & Wright, T. L. (1998). Origin of the Columbia River basalts: melting model of a heterogeneous plume head. *Earth and Planetary Science Letters* **162**, 63-80.

Turner, S. & Hawkesworth, C. (1995). The nature of the sub-continental mantle: constraints from the major-element composition of continental flood basalts. *Chemical Geology* **120**, 295-314.

Turner, S., Hawkesworth, C., Gallagher, K., Stewart, K., Peate, D. & Mantovani, M. (1996). Mantle plumes, flood basalts, and thermal models for melt generation beneath continents: assessment of a conductive heating model and application to the Parana. *Journal of Geophysical Research: Solid Earth* **101**, 11503-11518.

Veevers, J. (2001). Atlas of billion-year earth history of Australia and neighbours in Gondwanaland.

Veevers, J. J. (2004). Gondwanaland from 650–500 Ma assembly through 320 Ma merger in Pangea to 185–100 Ma breakup: supercontinental tectonics via stratigraphy and radiometric dating. *Earth-Science Reviews* **68**, 1-132.

Veevers, J. J. (2006). Updated Gondwana (Permian–Cretaceous) earth history of Australia. *Gondwana Research* **9**, 231-260.

Veevers, J. J. (2012). Reconstructions before rifting and drifting reveal the geological connections between Antarctica and its conjugates in Gondwanaland. *Earth-Science Reviews* **111**, 249-318.

White, R. & McKenzie, D. (1989a). Magmatism at rift zones: The generation of volcanic continental margins and flood basalts. *Journal of Geophysical Research: Solid Earth (1978–2012)* **94**, 7685-7729.

White, R. S. & McKenzie, D. P. (1989b). Volcanism at Rifts. *Scientific American* **261**, 62-71.

Zhao, X., Coe, R. S., Gilder, S. A. & Frost, G. M. (1996). Palaeomagnetic constraints on the palaeogeography of China: Implications for Gondwanaland∗. *Australian Journal of Earth Sciences* **43**, 643-672.

1.5. Figure Captions

Figure 1.1: Global distribution of Phanerozoic Large Igneous Provinces (LIPs). Quoted ages indicate the onset of activity and are all from Bryan and Ernst (2008) except: Kalkarindji (Jourdan *et al.*, 2014); Bunbury (Olierook *et al.*, 2016); NW Australia (Olierook *et al.*, 2015). Abbreviations: CAMP, Central Atlantic Magmatic Province; HALIP, High Arctic Large Igneous Province; NAIP, North Atlantic Igneous Province; RBS, Rajmahal – Bengal Sylhet; HP, Himalaya – Panjal; OJP, Ontong Java Plateau. Redrafted and modified from Bryan and Ernst (2008).

Figure 1.2: Simplified representation of the various models for the large igneous province generation. Created and modified after Anderson (2005).

Figure 1.3: Present day location of the Gondwana plates indicating the locations of Karroo, Ferrar, and Kalkarindji large igneous provinces. Province locations after or modified from Bryan and Ernst (2008).

Figure 1.4: Schematic plate reconstruction of Gondwana from roughly 550 – 183 Ma, indicating locations of Karoo, Ferrar, and Kalkarindji large igneous provinces. Reconstructed elements schematically positioned after (Gray *et al.*, 2008).

Chapter 2: The Kalkarindji Large Igneous Province, Australia: Petrogenesis of the oldest and most compositionally homogenous province of the Phanerozoic

Bryant D. Ware[1], Fred Jourdan[1], Renaud Merle[2], Massimo Chiaradia[3], Kyle Hodges[1, 4]

[1]*Western Australian Argon Isotope Facility, Department of Applied Geology and JdL-CMS, Curtin University, Perth, WA 6845, Australia.*

[2] *Research School of Earth Sciences, The Australian National University, Canberra, 0200 Australia.*

[3] *Department of Earth Sciences, University of Geneva, 13 Rue de Maraîchers, 1205, Geneva, Switzerland*

[4] *Sirius Resources, 5 Mumford Place, Balcatta, WA 6021, Australia.*

2.1. Abstract

The Kalkarindji Large Igneous Province (LIP) is a Middle Cambrian Continental Flood Basalt (CFB) province located in northern and central-west Australia that has been linked to an extinction event at the Early-Middle Cambrian boundary. The extent of this LIP has been estimated at about 2.1 x 10^6 km^2 with exposures in Western Australia, Northern Territory, Queensland, and South Australia. Major and trace element datasets reveal geochemical characteristics typical for Continental Flood Basalts (CFBs) including: tholeiitic affinity; an enrichment in

incompatible elements; in particular large-ion lithophile elements (LILEs); enrichment of light rare earth elements (LREEs) compared to heavy rare earth elements (HREEs); and negative Nb and Ta anomalies in normalized extended element patterns.

This study is the first comprehensive geochemical investigation of the Kalkarindji CFB province. The Kalkarindji CFBs are geochemically homogeneous low-Ti basaltic andesites, with a nearly complete lack of basaltic rocks as defined by a total-alkalis vs silica (TAS) diagram. All of the rocks analyzed for Sr-Nd-Pb display enriched initial (t = 511 Ma) isotopic compositions ($^{143}Nd/^{144}N_i$ = 0.51177 – 0.51187; $^{87}Sr/^{86}Sr_i$ = 0.7092 – 0.7103; $^{206}Pb/^{204}Pb_i$ = 18.177 – 18.846; $^{207}Pb/^{204}Pb_i$ = 15.672 – 15.810; $^{208}Pb/^{204}Pb_i$ = 38.201 – 38.890). Crustal assimilation modeling is used to suggest that the geochemical characteristics as well as the homogenous composition across the entire province cannot be explained by crustal contamination. Therefore, the enriched isotopic ratios (particularly the extremely high $^{207}Pb/^{204}Pb_i$ and elevated $^{208}Pb/^{204}Pb_i$ for moderate $^{206}Pb/^{204}Pb_i$), coupled with relative depletions in Nb and Ta concentrations, indicate the involvement of an ancient enriched lithospheric-like component in the genesis of the Kalkarindji CFBs. A model is proposed in which the source region for the Kalkarindji CFB province was affected by an enrichment event around 2.5 Ga (possibly through the addition of subducted sediments). Decompression melting and mantle warming (perhaps accompanied by edge driven convection) allowed melting of the fertile mantle to generate the Kalkarindji CFB province at ca. 511 Ma.

2.2. Introduction

Large igneous provinces (LIPs) are voluminous accumulations of magma emplaced during relatively short periods of time (Hofmann *et al.*, 1997; Courtillot & Renne, 2003; Bryan & Ernst, 2008; Ernst, 2014). The formation of these provinces

involves geodynamic mass fluxes that differ significantly from those inferred to occur at mid-ocean ridges (Courtillot & Renne, 2003). These magmatic provinces typically cover areas greater than 10^6 km^2, with igneous volumes greater than 10^6 km^3, and they are mainly characterized by mafic magmatism. The emplacement of these provinces takes place in short igneous pulses (Courtillot & Renne, 2003; Pirajno & Hoatson, 2012; Ernst, 2014) with about 75 – 80 % of the total volume emplaced in about 1 Ma or less (Courtillot & Renne, 2003; Bryan & Ernst, 2008; Ernst, 2014).

The origin of LIPs is controversial, with many different models proposed to account for the generation of these large accumulations of igneous material. Some hypotheses involve dynamic processes dominated by the upwelling of a deep-seated plume (Campbell & Griffiths, 1990; Hill, 1991). In these models, Continental Flood Basalts (CFBs) originate from the melting of a mantle plume head as it travels towards the surface. Active models propose that tectonic shifts such as rifting and continental breakup are due to the upwelling of these mantle plumes. However, the observation that many CFBs are located around plate boundaries has provided the basis for alternative models with more passive mechanisms being proposed for the formation of CFBs. Shallow processes related to plate tectonics (Foulger, 2007) in extensional environments such as continental rifting (White & McKenzie, 1989b); mantle upwelling due to lateral thermal gradients around the edges of cratons known as edge-driven convection (Anderson *et al.*, 1992; Anderson, 1994; King & Anderson, 1995); and plate delamination or thermal incubation occurring below supercontinents, which allows for the generation of LIPs ultimately leading to breakup (Gurnis, 1988; Coltice *et al.*, 2007; Coltice *et al.*, 2009). More recently a model involving slab-triggered upwelling of wet mantle from a hydrous mantle transition zone has been proposed to account for the lack of pre-magmatic tectonic bulging of the lithosphere, the absence

of ocean island basalt (OIB) geochemical signatures and the geochemical diversity found in many CFBs (Wang *et al.*, 2016).

A number of tholeiitic CFB suites has been recognized in much of the north and west-central parts of Australia (Glass & Phillips, 2006; Evins *et al.*, 2009; Pirajno & Hoatson, 2012). The Kalkarindji province is composed of a large number of lithostratigraphic units; the Antrim Plateau Volcanics, Milliwindi Dolerite, Nutwood Downs, Helen Springs, Peaker Piker, and Colless Volcanics (Glass & Phillips, 2006; Evins *et al.*, 2009; Pirajno & Hoatson, 2012) (Figure 2.1a). These scattered suites are exposed over about 425,000 km^2 (Bultitude, 1976; Veevers, 2001; Glass & Phillips, 2006; Evins *et al.*, 2009; Marshall *et al.*, 2016), distributed across northern and central portions of Western Australia, much of the Northern Territory, western Queensland, and western South Australia. The original extent of the Kalkarindji CFB province has been estimated to be at least 2.1 x 10^6 km^2 making it one of the largest LIPs in the Phanerozoic (Evins *et al.*, 2009). The Kalkarindji CFB province is recognized as the oldest Phanerozoic LIP, with an age of ca. 511 Ma, and has been linked with the first significant extinction event of the Phanerozoic (Jourdan *et al.*, 2014b).

Despite the considerable size of this province, the study of the geochemistry and origin of the Kalkarindji CFB province is limited with very little discussion of the possible sources of this LIP and only and handful of data presented in published papers and survey reports (Bultitude, 1976; Mory & Beere, 1988; Grey *et al.*, 2005; Glass & Phillips, 2006; Evins *et al.*, 2009; Marshall *et al.*, 2016). This study provides the first in depth look at the geochemical characteristics of the Kalkarindji CFB province based on a large data set including 182 new major and trace element analyses and 10 Sr, Nd, and Pb isotopic analyses of the various constituents of the Kalkarindji CFB province.

This comprehensive data set enables detailed comparison between the related basaltic suites and is used to understand the possible magma source(s) and origin of this province.

2.3. Geologic Setting and Previous Results

The Antrim Plateau Volcanics (Figure 2.1a) comprise the largest areal exposures of the Kalkarindji CFB province. With a maximum thickness of about 1500 m west of Halls Creek, the Antrim Plateau Volcanics make up the thickest section and they provide an indication of a possible location for the primary vent from which the Kalkarindji volcanics were erupted (Bultitude, 1976; Mory & Beere, 1988; Grey *et al.*, 2005; Glass & Phillips, 2006; Evins *et al.*, 2009; Marshall *et al.*, 2016). The Antrim Plateau Volcanics are exposed along the eastern edge of the Kimberley Block and form the boundary between the eastern edges of the Victoria River Basin and the western Wiso Basin (Figure 2.1b). These volcanics are made up primarily of basaltic lava flows, although they also contain minor breccias and agglomerates. Discontinuous quartz sandstones, siltstones, chert, sedimentary breccia, and limestones are intercalated with the lavas and breccias (Bultitude, 1976; Marshall *et al.*, 2016). Exposures of the Peaker Piker Volcanics, Colless Volcanics, and Helen Springs Volcanics are found on the eastern and northern margins of the Georgina Basin (Figure 2.1b). The Nutwood Downs Volcanics are exposed along the margins of the Daly River Basin (Figure 2.1b). These areas of the Kalkarindji CFB are exposed as small outcrops interbedded with or separated from the Antrim Plateau Volcanics by younger basin fill sediments (Bultitude, 1976; Grey *et al.*, 2005; Glass & Phillips, 2006; Evins *et al.*, 2009; Marshall *et al.*, 2016). The maximum thicknesses of these outliers is significantly less than that found in the Antrim Plateau Volcanics; 122 m for the

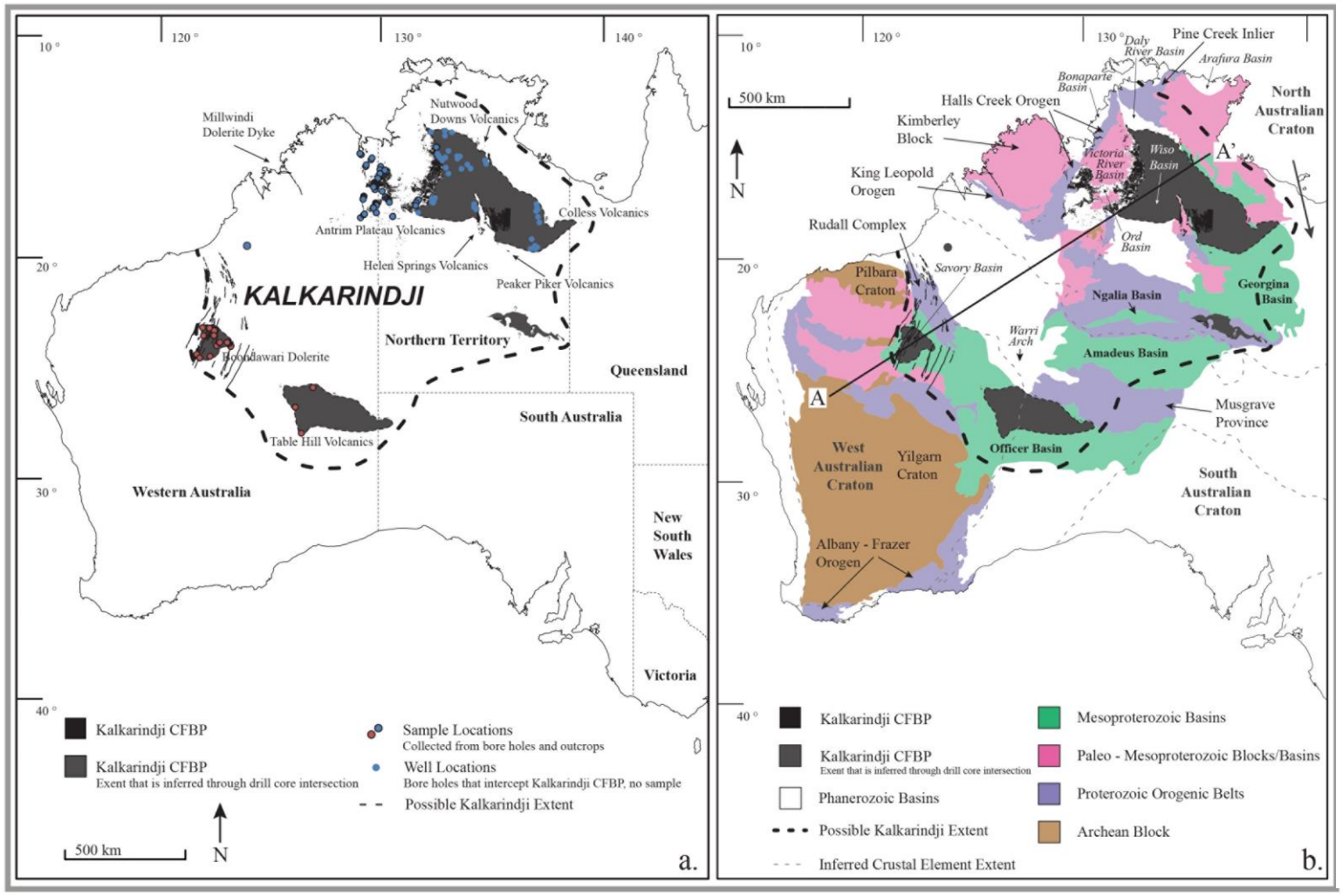

Figure 2.1: (a) Sketch map showing the distribution and constituent suites of the Kalkarindji Continental Flood Basalt (CFB) province. Blue colors represent samples or well locations from the Antrim Plateau Volcanics; red colors represent samples or well locations from the Table Hill Volcanics. (b) Sketch map of the Kalkarindji CFB province. Proterozoic basins and orogens locally associated with the Kalkarindji CFB province are also displayed. Paleozoic basins labeled in italics. Modified and created after (Glass & Phillips, 2006; Hoatson *et al.*, *2008*; Jourdan *et al.*, 2014b)**.** Australian crustal elements from (Shaw *et al.*, 1995; Pirajno & Bagas, 2008). Figure 2.15 schematic cross section locations marked with line A – A'.

Nutwood Downs Volcanics, 37 m for the Helen Springs Volcanics and the Peaker Piker Volcanics, and 61 m for the Colless Volcanics (Bultitude, 1976 and references therein). Data from borehole samples have been interpreted to show that the volcanics extend below the younger sediments of the Daly River, Georgina, and Wiso Basins giving a stratigraphic connection between many of the outcrops in the north, east, and west (Bultitude, 1976). Due to this stratigraphic connection, and for simplicity in the discussion, all of these various suites will be referred to as the Antrim Plateau Volcanics.

The Table Hill Volcanics Suite (herein referred to as the Table Hill Volcanics) is a series of tholeiitic basalt outcrops exposed along the northern borders of the Officer Basin. Note however that, despite its volcanics denotation, it includes several dykes and sills that extend underneath much of the basin (Bultitude, 1976; Stevens & Apak, 1999; Grey *et al.*, 2005; Glass & Phillips, 2006; Evins *et al.*, 2009). On the basis of similar geochemical composition and ages, the Table Hill Volcanics within the Officer Basin have been linked to the Antrim Plateau Volcanics as part of the Kalkarindji province (Evins *et al.*, 2009).

A map of drill-holes that intersected Kalkarindji CFB province throughout northern Australia was presented by Bultitude (1976). The intersections indicate that the volcanics become more fragmented and thin to the east and south away from the thick outcrops of the Antrim Plateau Volcanics (Figure 2.1a). Based on several exploration well completion reports, there is no evidence for the presence of any Kalkarindji CFB related rocks within the Ngalia and Amadeus Basins of central Australia. This could be the result of a lack of geochronological data for intersected volcanics or structural barriers that prevented the province from extending into this

region. The distribution of the Table Hill Volcanics also appear to be highly influenced by structural domains surrounding the basin as Kalkarindji CFBs are commonly discontinuous in spatially close drill-holes. The highest concentration of sills and dykes occur within the Savory Basin with the exposures and intersections lessening toward the eastern boundaries of the Officer Basin and no known drill-hole intersections in South Australia (Figure 2.1).

The geochemistry (including isotopic data) of lamproite and kimberlite pipes (and associated xenoliths) found all through the Kimberley Block and Halls Creek Orogen, S-wave tomography of the surrounding regional lithosphere/asthenosphere, and diamond occurrences indicate that the upper crust below the Kalkarindji province is underlain by an old thick lithospheric root (Jaques *et al.*, 1990; Shaw *et al.*, 1995; Myers *et al.*, 1996; Graham *et al.*, 1999; Sheppard *et al.*, 1999; Betts *et al.*, 2002; Luguet *et al.*, 2009); in particular diamondiferous Archean peridotite xenoliths have been found (Jaques *et al.*, 1990; Graham *et al.*, 1999; Luguet *et al.*, 2009) within the Kimberley Block. The Antrim Plateau Volcanics were emplaced entirely within the North Australian Craton whereas the Table Hill Volcanics occur primarily within the West Australian Craton, with exposures extending into the Musgrave Province between the West Australian and South Australian Cratons. It has been proposed that tectonic activity along the Halls Creek Orogen was associated with a plate boundary between the Kimberley Block and the rest of the North Australian Craton (Jaques *et al.*, 1990; Shaw *et al.*, 1995; Myers *et al.*, 1996; Graham *et al.*, 1999; Sheppard *et al.*, 1999; Betts *et al.*, 2002; Luguet *et al.*, 2009) indicating that the final joining of the Kimberley Block and the North Australian Craton occurred around 1.85 Ga. The last major tectonic activity to occur in the western portion of the Australian continent

before the Kalkarindji CFB event was orogenic activity within the Musgrave province before 1.2 Ga (Wade *et al.*, 2008; Aitken & Betts, 2009; Smithies *et al.*, 2015).

$^{40}Ar/^{39}Ar$ plateau ages range from of 509.0 ± 2.6 Ma to 511.9 ± 1.9 Ma for the Helen Springs Volcanics, Antrim Plateau Volcanics, and the Table Hill Volcanics (data from Glass and Phillips, 2006; and Evins *et al.*, 2009 recalculated to the decay constant of Renne *et al.*, 2011). An $^{40}Ar/^{39}Ar$ analysis on a plagioclase separate from a Kalkarindji CFB dolerite of the Officer Basin gave a plateau age of 510 ± 4 Ma, twenty-eight baddeleyite crystals from mafic enclaves found in the Munro well produced a statistically concordant upper intercept of 511 ± 5 Ma, and CA-TIMS analyses on zircons from the coarse-grained Milliwindi dolerite dike provide a weighted $^{238}U/^{206}Pb$ age of 510.7 ± 0.6 Ma (Jourdan *et al.*, 2014b). All of this new geochronological information constrains the age of the main emplacement pulse for the Kalkarindji CFB province to ca. 511 Ma (Middle-Lower Cambrian boundary), although the duration of the emplacement is still not well constrained (Jourdan *et al.*, 2014b).

2.4. Sample Selection

Nine samples from the Antrim Plateau Volcanics selected for analysis include a range in basaltic rock textures from porphyritic basalts to fine grained massive basalts collected from outcrops throughout the Antrim Plateau Volcanics region as well as a number of cores drilled within the main Antrim Plateau Volcanics found on the boarder of Western Australia and the Northern Territory. Twenty-three dolerite samples from sills and dykes of the Table Hill Volcanics were selected from the Geological Society of Western Australia (GSWA) core library. These 32 samples were combined with geochemical analyses from another 150 rock chip and drill core

samples from northern Australia and the Officer Basin region provided as an Excel database by AusQuest Limited.

Thin section of the 32 samples and cores collected from the Antrim Plateau Volcanics and Table Hill Volcanics were examined for any evidence of alteration as well as to identify magmatic phases. A sub-set of ten of the freshest samples were selected for Sr, Nd, and Pb isotope analysis. In order to obtain a representative rock selection from the whole province, five samples from the Antrim Plateau Volcanics and five samples from the Table Hill Volcanics were selected for isotopic analysis. The five samples selected from the Antrim Plateau Volcanics are all outcrop samples from fine-grained basalt flows. The five samples selected from the Table Hill Volcanics are from dolerite sills believed to be feeders to the province; they are from separate drill-holes and were provided by the GSWA core library in Carlisle, Perth. Complete list of samples, locations, and rock types can be found with the major and trace element data (Appendix B).

2.5. Analytical Procedures

The 32 samples collected for this study were analyzed for major and trace elements at Genalysis Laboratory Services Pty Ltd in Perth (Australia). Major and trace element geochemistry from the 150 rock chip and drill core samples from northern Australia and the Officer Basin region have been previously analyzed following the same procedure within the same laboratory and instruments, thus avoiding any laboratory bias. These data were provided as an Excel database by AusQuest Limited.

Major element geochemical analysis was conducted using X-ray fluorescence (XRF) on fused discs produced using a lithium borate fusion technique in platinum crucibles (Genalysis Laboratory Services Pty Ltd method code FB1/XRF20). Trace element analyses were conducted using the inductively coupled plasma mass

spectrometry (ICP-MS) method on samples dissolved using a lithium metaborate/tetraborate fusion (Genalysis Laboratory Services Pty Ltd method code FB6/MS). Utilizing the same lithium borate fusion, Sc and V underwent analysis by inductively coupled plasma optical (atomic) emission spectrometry (ICP-OES). A four acid digestion (Hydrofluoric, Nitric, Perchloric and Hydrochloric acids in Teflon Tubes) was implemented with ICP-MS (for elements Ag, As, Be, Bi, Cd, Co, Ge, In, Li, Mo, Pb, Re, Sb, Se, Te, Tl: method code 4A/MS) and ICP-OES (for elements Cu, Ni, Zn: method code 4A/OE) analyses. To obtain reproducibility, analyses of samples THD001B and THD002 were duplicated. Overall the 67 elements sampled show extremely good reproducibility with only elements whose concentration was close to the detection limit displaying any significance of inconsistencies. Three procedural blank analyses were also performed: one control blank for every major and trace element analysis and two other control blanks for trace element analyses. Acid blanks analyses were also performed for the trace element measurements. Internal standards (SARM1, SARM4, and SY-4 for the major element analyses and SY-4, WPR-1, OREAS45a, OREAS45b, 40100, GenFe-3, GenFe-5, MA-1b, CD-1, WGB-1 and AMIS0076 for the trace element analyses) were used to monitor the accuracy of the instruments (analytical results for the 32 samples and standards analyzed can be found in Appendix B).

The selected ten samples for Sr, Nd, and Pb isotope analyses were crushed into small chips using a cleaned hydraulic press. Once rinsed with distilled H_2O the chips were carefully selected under a microscope to avoid any saw marks or weathered surfaces. The clean chips were then powdered by hand using an agate mortar and pestle. Approximately 150 mg of powder were dissolved during 7 days in Savillex® Teflon vials using 4 ml of concentrated HF and 1 ml of HNO_3 15 M, at 140 °C. The

vials were placed in ultrasonic bath for 30 min twice a day (Chiaradia *et al.*, 2011). Subsequently, samples were dried down and re-dissolved for 3 days (also with 30 min ultrasonication twice a day) in 3 ml of HNO_3 15 M and dried down again. Sr, Nd and Pb were purified from the sample matrix by cascade column chromatography with Sr-Spec, TRU-Spec and Ln-Spec ion exchange resins according to a protocol modified after Pin *et al.* (1994). Lead was further purified with an AG-MP1-M anion exchange resin in hydrobromic medium. Lead, Sr and Nd isotope ratios were measured on a Thermo TRITON TIMS (thermal ionization mass spectrometer) using Faraday cups in static mode, at the Department of Earth Sciences, University of Geneva (Switzerland). Lead and Sr were loaded on Re single filaments using silica gel (Gerstenberger & Haase, 1997) and Ta oxide solution respectively. Neodymium was loaded on double Re filaments using1M HNO_3. Strontium and Nd were analyzed using the virtual amplifier design to cancel out biases in gain calibration among amplifiers. All samples and standards were measured at a pyrometer-controlled temperature. Lead isotope ratios were corrected for instrumental fractionation by a factor of 0.07 % per a.m.u. based on more than 90 measurements of the SRM981 standard and using the values of Todt *et al.* (1996). External reproducibility of the standard ratios is 0.08 % for $^{206}Pb/^{204}Pb$, 0.12 % for $^{207}Pb/^{204}Pb$ and 0.16 % for $^{208}Pb/^{204}Pb$. $^{87}Sr/^{86}Sr$ values were internally corrected for instrumental fractionation using a $^{88}Sr/^{86}Sr$ value of 8.375209. Raw values were further corrected for external fractionation by a value of + 0.03 ‰, determined by repeated measurements of the SRM987 standard; $^{87}Sr/^{86}Sr = 0.710248$ (McArthur *et al.*, 2001). The long-term external reproducibility of the $^{87}Sr/^{86}Sr$ ratio for the SRM987 standard is 7 ppm (1σ). $^{143}Nd/^{144}Nd$ values were internally corrected for instrumental fractionation using a $^{146}Nd/^{144}Nd$ value of 0.7219 and the ^{144}Sm interference on ^{144}Nd was monitored on the mass ^{147}Sm and corrected by using a

$^{144}Sm/^{147}Sm$ value of 0.206700. These values were further corrected for external fractionation by a value of + 0.03 ‰, determined by repeated measurements of the JNdi-1 standard; $^{143}Nd/^{144}Nd$ 1⁄4 0.512115 (Tanaka *et al.*, 2000). Long-term external reproducibility of the JNdi-1 standard is < 5 ppm. Total procedural blanks were < 500 pg for Pb and < 100 pg for Sr and Nd which are insignificant compared to the amounts of these elements purified from the whole rock samples investigated.

2.6. Results

2.6.1. Mineralogy

The mineralogy of the Kalkarindji CFBs displays little variation across the province. The dominant minerals found within the rocks of the Antrim Plateau Volcanics include plagioclase, augite, pigeonite, ilmenite, titano-magnetite and minor amounts of orthopyroxene (enstatite) (Sweet *et al.*, 1974; Bultitude, 1976). Plagioclase is the most prominent phenocrysts, on average ranging from 1 – 4 mm, throughout the Antrim Plateau Volcanics. However, clinopyroxene and titano-magnetite can also form larger, subhedral to euhedral phenocrysts. These phenocrysts lie in a typically fine-grained groundmass composed of glass, cryptocrystalline plagioclase, clinopyroxene and titano-magnetite. Most of this suite of rocks displays pervasive alteration affecting both the groundmass and phenocrysts. Much of the alteration is apparent as chlorite and sericite alteration; however, this alteration type varies across the province considerably from sample to sample. A small handful of the plagioclase phenocrysts do exhibit characteristic polysynthetic twinning, however, twinning is more common in the groundmass crystals. The Antrim Plateau Volcanics exhibits an aphanitic to porphyritic and on occasion glomeroporphyritic texture. In some samples amygdaloidal and brecciated textures are apparent. Samples with amygdaloidal and

brecciated textures were discarded from geochemical analyses due to the possibility of hydrothermal alteration.

The Table Hill Volcanics consist primarily of medium to coarse-grained dolerite with subophitic textures, but granophyre and gabbro also occur. Basalt flows also occur within the Officer Basin as small isolated outcrops. The data from this study focus on samples from the intrusive sills and dykes found throughout the Officer Basin. A slight mineralogical difference between these intrusive rocks of the Officer Basin and Antrim Plateau Volcanics is apparent, with the former being dominated by plagioclase (labradorite), clinopyroxene (augite), ilmenite, and titano-magnetite (Grey *et al.*, 2005). Some secondary minerals have also been observed within the rocks of the Table Hill Volcanics such as minor hornblende (after clinopyroxene), actinolite, and sulfides. As with the Antrim Plateau Volcanics, the degree of alteration is variable. Sericite is apparent in cloudy plagioclase grains and pervasive chlorite alteration gives a slight green tinge to the appearance of many of the sills. Some of the sills display a visible differentiation toward the core that is characterized by a more granophyric texture and some hand specimen samples display a strong pink color (Jourdan *et al.*, 2014b). The mineralogy of these granophyric cores is different to the surrounding dolerite/gabbro with the presence of quartz-feldspar intergrowths (Grey *et al.*, 2005) as well as hornblende, chlorite and acicular apatite that have been petrographically recognized as secondary by Grey *et al.* (2005) and Jourdan *et al.* (2014b).

2.6.2. Major and trace elements

To avoid samples that may have been affected by alteration, geochemical analyses were filtered rigorously using several criteria. Since the majority of the major and trace element results have been provided as an Excel data sheet from AusQuest Limited, filtering is based on geochemical indicators. Loss on ignition (LOI) was the

primary means used to evaluate the freshness of the samples. Out of all 182 samples 137 displayed low LOI values of less than 2 weight percent (wt. %). A plot of $Na_2O + K_2O/MgO$ vs CaO/MgO provides an indication of feldspar alteration; altered samples have low CaO values and high alkalis (Simpson, 1954). Furthermore, a few altered

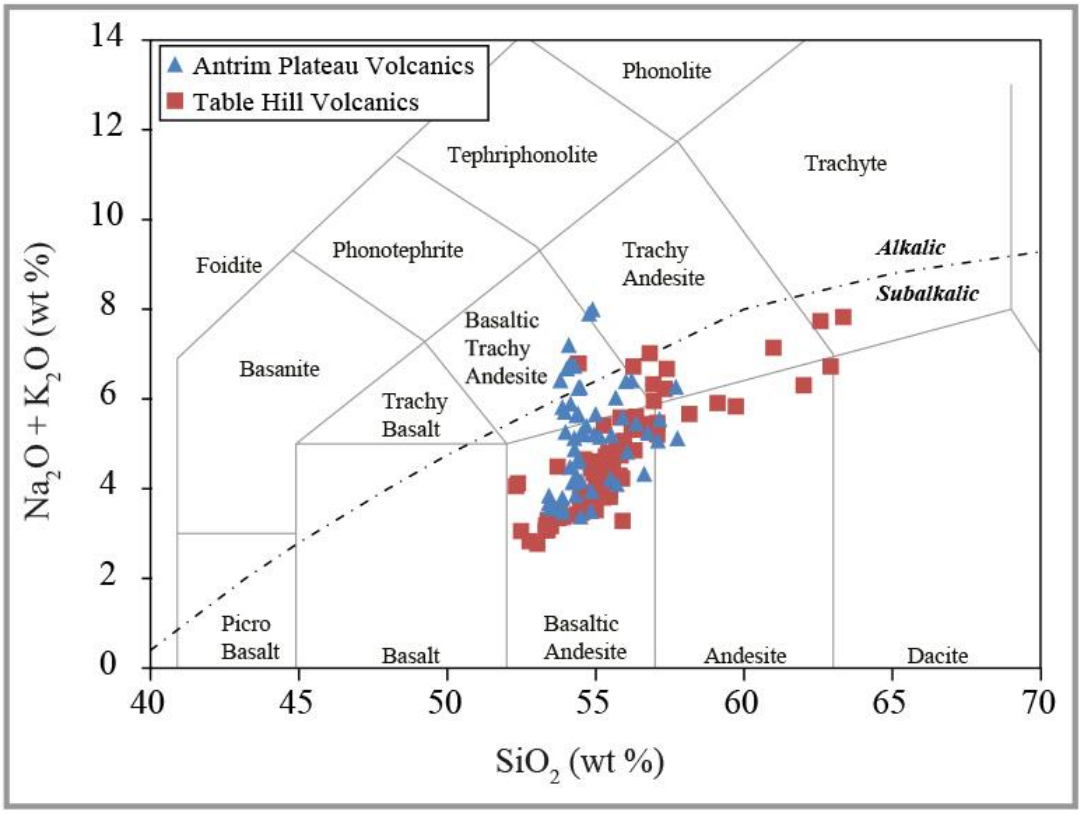

Figure 2.2: Total alkalis-silica (TAS) diagram (Bas *et al.*, 1986) for basalts of the Kalkarindji CFB province. Alkalic-subalkalic line (Irvine & Baragar, 1971).

samples were identified by anomalously high concentrations of MnO (e.g. ≥ 6 wt. %). A subset of samples was selected for isotope analysis based on petrographic analysis, in addition to all the criteria mentioned above.

Bulk rock compositions of relatively unaltered samples are subalkalic (tholeiitic) with the majority of the samples plotting into the basaltic andesite field in the total alkali-silica diagram (Bas *et al.*, 1986) (Figure 2.2). A few samples plot in the fields of basaltic trachyandesite as well as along the trachyandesite/andesite boundary, toward more evolved compositions. Four samples from the Table Hill Volcanics plot near or at the boundary between the trachyandesite/andesite and trachyte/dacite fields

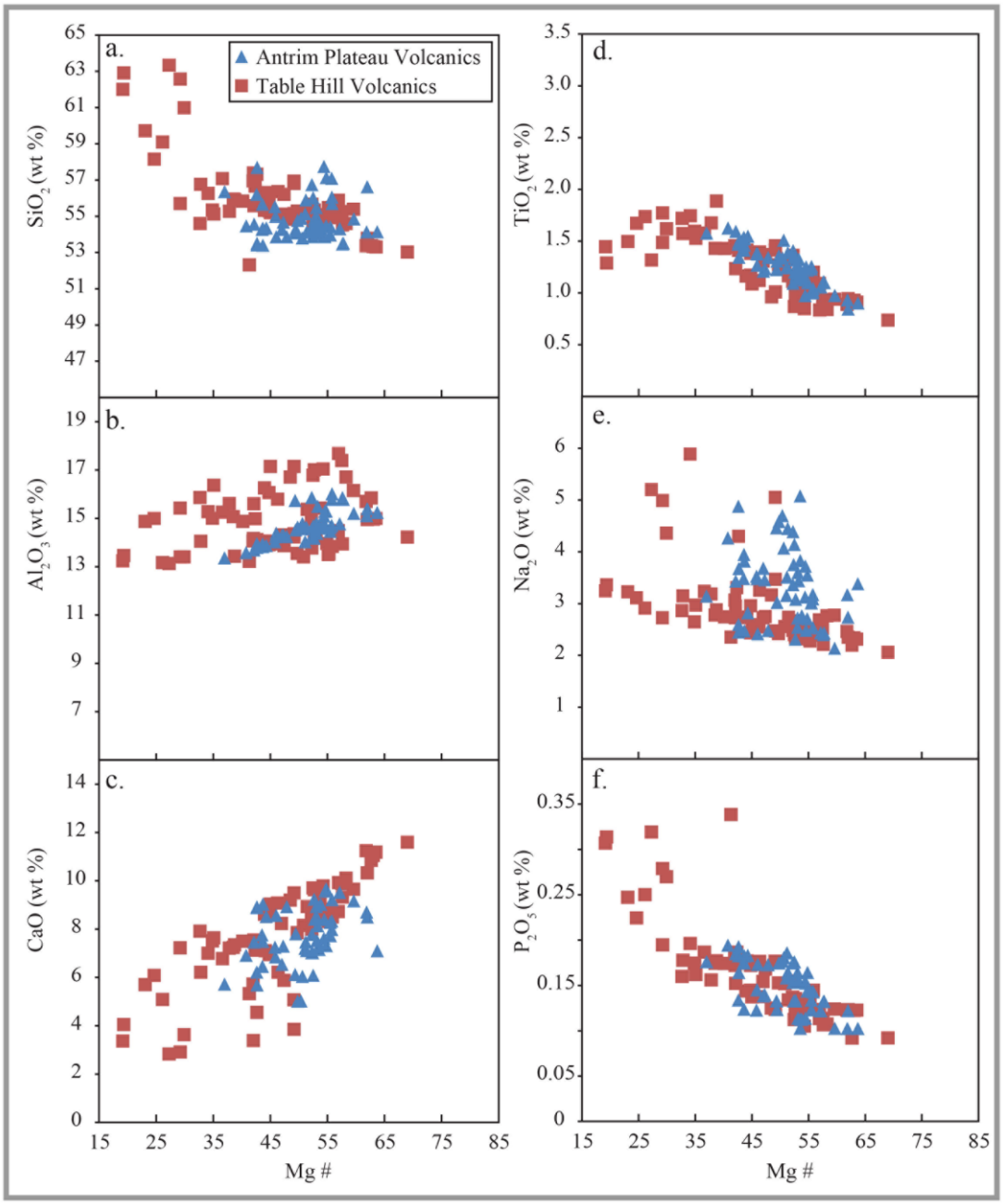

Figure 2.3: Major element (wt. %) vs Mg-number [100 x atomic ratio of Mg/ (Mg + Fe_2^+) with Fe_2O_3/FeO normalized to 0.15] diagrams for basalts of the Kalkarindji CFB province.

(Figure 2.2). The majority of these samples are relatively evolved with MgO contents less than 8 wt. % and Mg # [100 * mol. MgO/(MgO + FeO)] ranging from 75 to 15. Mg # shows various negative and positive covariations when plotted against most major oxide weight percent (Figure 2.3a, c, d, and f). All samples can be classified as low-Ti with TiO_2 content < 2 wt. %. A notable difference between the Antrim Plateau Volcanics and the Table Hill Volcanics is that they define slightly different trends on

major element versus Mg # variation diagrams (Figure 2.3). No Antrim Plateau Volcanics sample has an MgO weight percent less than 3.5 (Mg # of 37). In contrast, the more evolved sample group within the Table Hill Volcanics displays relatively high SiO_2 values and low MgO (Mg #) values forming a sharp shift from the linear trends apparent on major element variation diagrams for samples from the rest of the province.

The chondrite-normalized rare earth element (REE) patterns of the Kalkarindji CFBs show a modest enrichment of light over middle REEs with $(La/Sm)_n$ varying between 1.83 and 3.64 (Figure 2.4) and, in some cases, a small negative Eu anomaly. However, the Kalkarindji basalts display a higher range in of light over heavy REEs with $(La/Yb)_n$ ratios between 2.98 and 8.06 (Figure 2.4). The primitive mantle

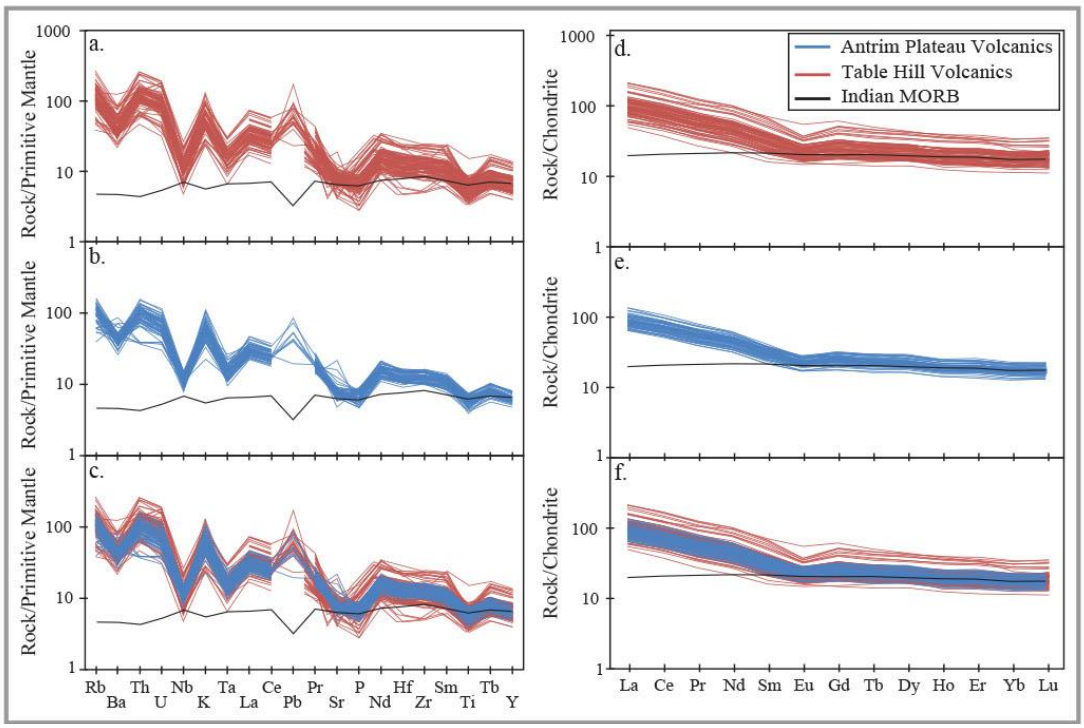

Figure 2.4: (a – c) Primitive mantle normalized incompatible trace elements patterns for the Kalkarindji Continental Flood Basalt (CFB) province. (d – f) Chondrite – normalized REE patterns for the Kalkarindji CFB Province. Diagrams c and f are the Table Hill Volcanics and the Antrim Plateau Volcanics plotted together. Normalization parameters from (Sun & McDonough, 1989). Average Indian MORB compositions from PetDB (www.earthchem.org/petdb).

normalized trace element patterns of the Kalkarindji province basalts display a pronounced negative Nb and Ta anomaly and a positive Pb anomaly (Figure 2.4a – c).

One sample of a coarse grained dolerite from the Boondawari Dolerite (AOB – 09), located in the western Officer Basin (Figure 2.1, Table 2.1) and correlated to the Table Hill Volcanics, deserves particular attention as it has an MgO content greater than 8 wt. % (Mg # of 69, Figure 2.3) and is the most primitive sample identified in this study. The Ni content (91 ppm) of this sample is higher than the Ni content of the rest of the sample suite (0 ppm to 75 ppm); however, is still well below typical values expected of primary mantle-derived basalts (Allègre *et al.*, 1977) (Figure 2.5a). The Cr value for this high MgO sample is also well below values typical of primitive compositions and it is not the highest value from the province (Figure 2.5b). Therefore, these observed Ni and Cr values for AOB – 09 are not high enough to be consistent with a primitive liquid in equilibrium with mantle compositions. On the basis of the geochemistry, the sample AOB – 09 is interpreted to be a cumulate.

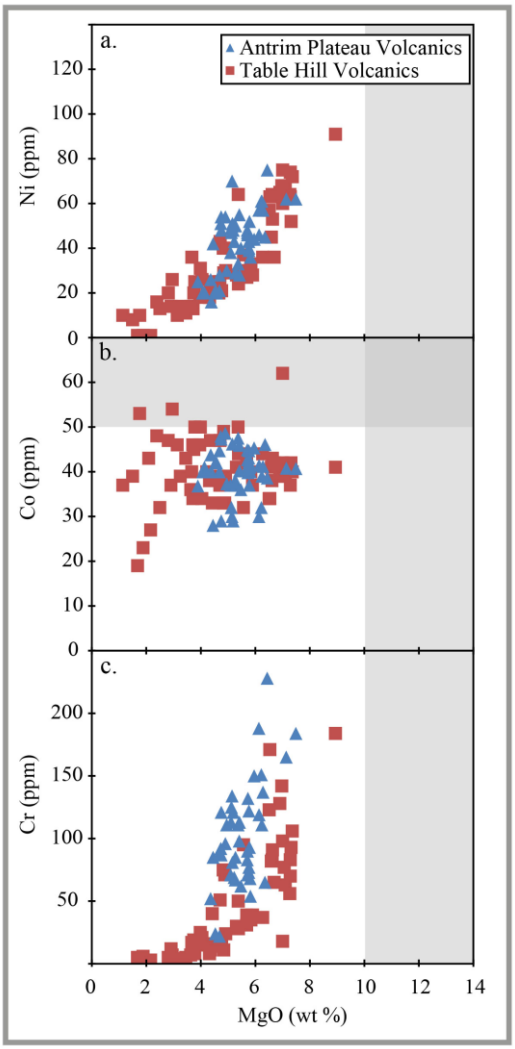

Figure 2.5: **(**a) Ni (ppm) vs MgO (wt. %), (b) Co (ppm) vs MgO (wt. %), (c) Cr (ppm) vs MgO (wt. %) diagrams for basalts of the Kalkarindji CFB province. Gray band represents typical range of primitive basalts. Range expected for magmas in equilibrium with their mantle source: Ni range of 200 – 500 ppm from Allègre *et al.* (1977).

2.6.3. Sr-Nd-Pb isotopes

This study provides the first isotopic data to be published on the Kalkarindji CFB province. Although the Nd isotopic

compositions display a narrow range in values, the Sr and Pb isotope compositions have a variable range (Figure 2.6). The elements Rb, Sr, U, Th, and Pb are generally more mobile than Sm and Nd, particularly in hydrothermal conditions. Therefore, these geochemical trends could be interpreted as an effect of alteration. Although this could always be a possibility, rigorous measures were taken to select unaltered samples (see discussion above) as well as petrographic observations. The measured isotopic ratios were corrected for the in-situ decay of the parental radiogenic isotopes using an age of 511 Ma; $^{40}Ar/^{39}Ar$ plagioclase age and U-Pb zircon ages determined by Jourdan *et al.,* (2014b) and parent/daughter ratios derived from the elemental concentrations measured by ICP-MS (Table 2.1). Although the use of concentrations determined by the ICP-MS method does lead to larger error propagation then if they were measured using the TIMS method, because the measured isotopic ratios are precise enough, this increased error does not affect the values enough to change the interpretations being made from these calculated initial values. Only a slight variation of isotopic values is observed for the Kalkarindji CFB in the analyzed sample suite ($^{143}Nd/^{144}N_i$ = 0.51177 – 0.51187; $^{87}Sr/^{86}Sr_i$ = 0.7092 – 0.7103; $^{206}Pb/^{204}Pb_i$ = 18.178 – 18.85; $^{207}Pb/^{204}Pb_i$ = 15.67 – 15.81; $^{208}Pb/^{204}Pb_i$ = 38.20 – 38.89) (Table 2.2), spanning the entire area of the province (Figure 2.1a).

The $^{87}Sr/^{86}Sr_i$ and $^{143}Nd/^{144}Nd_i$ ratios do not display any correlation with the Mg # (Figure 2.7d). A striking observation in the $^{143}Nd/^{144}Nd_i$ isotopic ratios compared to the trend observed from other CFBs is the restricted range of values, which consequently cause the $^{143}Nd/^{144}Nd_i$ ratios to line up in a near horizontal line when plotted against the slightly, more variable $^{87}Sr/^{86}Sr_i$ and $^{206}Pb/^{204}Pb_i$ ratios (Figure 2.6c and e). This is in stark contrast to many other CFB provinces that show a negative

slope correlation between the $^{143}Nd/^{144}Nd_i$ and $^{87}Sr/^{86}Sr_i$ isotopic ratios (Figure 2.6c). There are no discernable differences in Pb isotope composition between the Antrim Plateau Volcanics and Table Hill Volcanics. All of the data plot above the Northern Hemisphere Reference Line (NHRL) (Figure 2.6a, d). The $^{207}Pb/^{204}Pb_i$ compositions for the Antrim Plateau Volcanics exhibit a wider range in values compared to other isotopic systems. The Kalkarindji CFBs display a positive correlation on a $^{206}Pb/^{204}Pb_i$ and $^{208}Pb/^{204}Pb_i$ graph. In contrast, $^{87}Sr/^{86}Sr_i$ vs $^{206}Pb/^{204}Pb_i$ and $^{207}Pb/^{204}Pb_i$ vs $^{206}Pb/^{204}Pb_i$ plots for the Kalkarindji CFB data define a cluster with no discernable

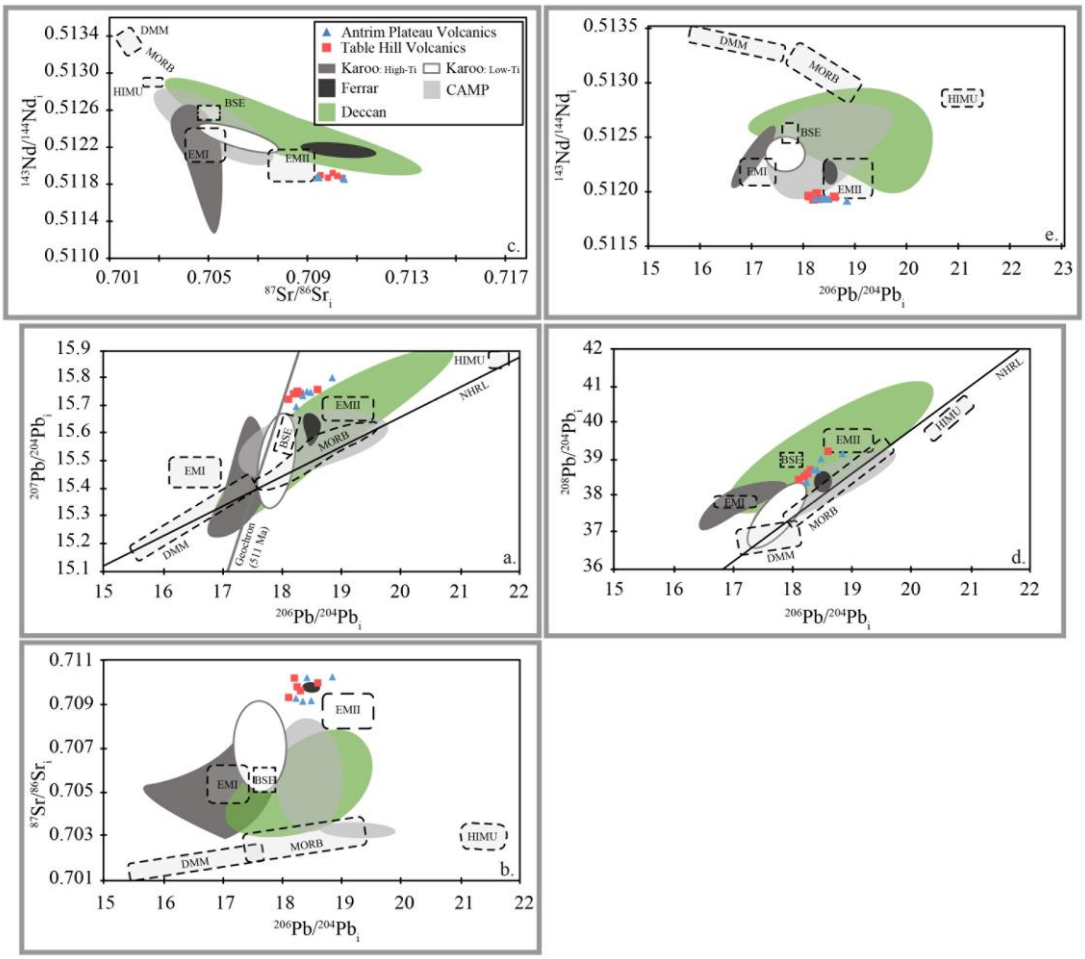

Figure 2.6: Initial (511 Ma) Sr, Nd, and Pb isotopic compositions of the Kalkarindji Continental Flood Basalt (CFB) province. In the two Pb vs Pb isotope diagrams, the Northern Hemisphere Reference Line (NHRL); (Hart, 1984) is shown. Approximate locations of mantle end – members age-corrected to 511 Ma (Zindler & Hart, 1986) are indicated for reference. Also shown are the fields of selected CFBs Karoo, Central Atlantic Magmatic Province (CAMP), Deccan, and Ferrar. All data for these CFBs are from the GEOROC database, Pb isotopic data for Ferrar are from Hergt *et al.* (1989b). The ellipsoids represent where roughly 90 % of the data clusters. Referenced CFBs age-corrected to respective time of emplacement: Karoo (183 Ma), CAMP (201 Ma), Deccan (66.5 Ma), and Ferrar (183 Ma). BSE = Bulk Silicate Earth, EMI = Enriched Mantle I, EMII = Enriched Mantle II, MORB = Mid-Ocean Ridge Basalt, DMM = Depleted MORB Mantle.

trend. The $^{87}Sr/^{86}Sr_i$ isotopes for the Kalkarindji CFBs also appear to be very radiogenic for a given $^{206}Pb/^{204}Pb_i$ (Figure 2.6b), especially when considering other CFBs. This distinguishes the province from most other CFBs except Ferrar, which displays similar $^{87}Sr/^{86}Sr_i$ isotopes for a given $^{206}Pb/^{204}Pb_i$ (see discussion). For all isotopic systems, except $^{207}Pb/^{204}Pb$, the Kalkarindji CFBs plot in close proximity to the field of the enriched mantle II (EMII) mantle end-member.

2.7. Discussion

2.7.1. Petrogenesis

2.7.1.1. Fractional crystallization

The major element contents of the Kalkarindji CFBs indicate relatively evolved compositions (all samples except one have less than 8 wt. % MgO [Mg # < 69]). The petrographic observations coupled with the major element behavior are consistent with patterns and trends for typical gabbroic suites that are commonly interpreted in terms of fractional crystallization involving clinopyroxenes and feldspars with a minor amount of oxide minerals (primarily ilmenite). The rhyolite-MELTS program and code (Ghiorso & Sack, 1995; Gualda *et al.*, 2012) was used to calculate and test the fractionation trend observed in the Kalkarindji CFB rocks as well as to provide an estimate for the composition of the residual liquid (Figure 2.8). Isenthalpic calculations were made using several different initial parameters to model the possible fractionation trends of the Kalkarindji CFB magmas [P = 1 – 3 kbar, H_2O = 0 – 1 %, fO_2 = QFM +1 (quartz-fayalite-magnetite)]. For the starting composition sample AOB07 from the Table Hill Volcanics was chosen because this sample has the highest MgO and the lowest SiO_2 contents. The MELTS calculations as to provide an estimate for the composition of the residual liquid (Figure 2.8). Isenthalpic calculations

were made using several different initial parameters to model the possible fractionation trends of the Kalkarindji CFB magmas [P = 1 – 3 kbar, H_2O = 0 – 1 %, fO_2 = QFM +1 (quartz-fayalite-magnetite)]. For the starting composition sample AOB07 from the Table Hill Volcanics was chosen because this sample has the highest MgO and the lowest SiO_2 contents. The MELTS calculations indicate that the Kalkarindji CFB rocks can be represented by up to 81 % anhydrous fractional crystallization at moderate pressure (3 kbar) (Figure 2.8) with the solid extract comprising plagioclase (47 wt. %), augite (30 wt. %), pigeonite (17 wt. %) and magnetite (5 wt. %). MELTS modeling predicts a crystallization sequence of augite + plagioclase → augite + pigeonite + plagioclase → augite + pigeonite + plagioclase + titano-magnetite.

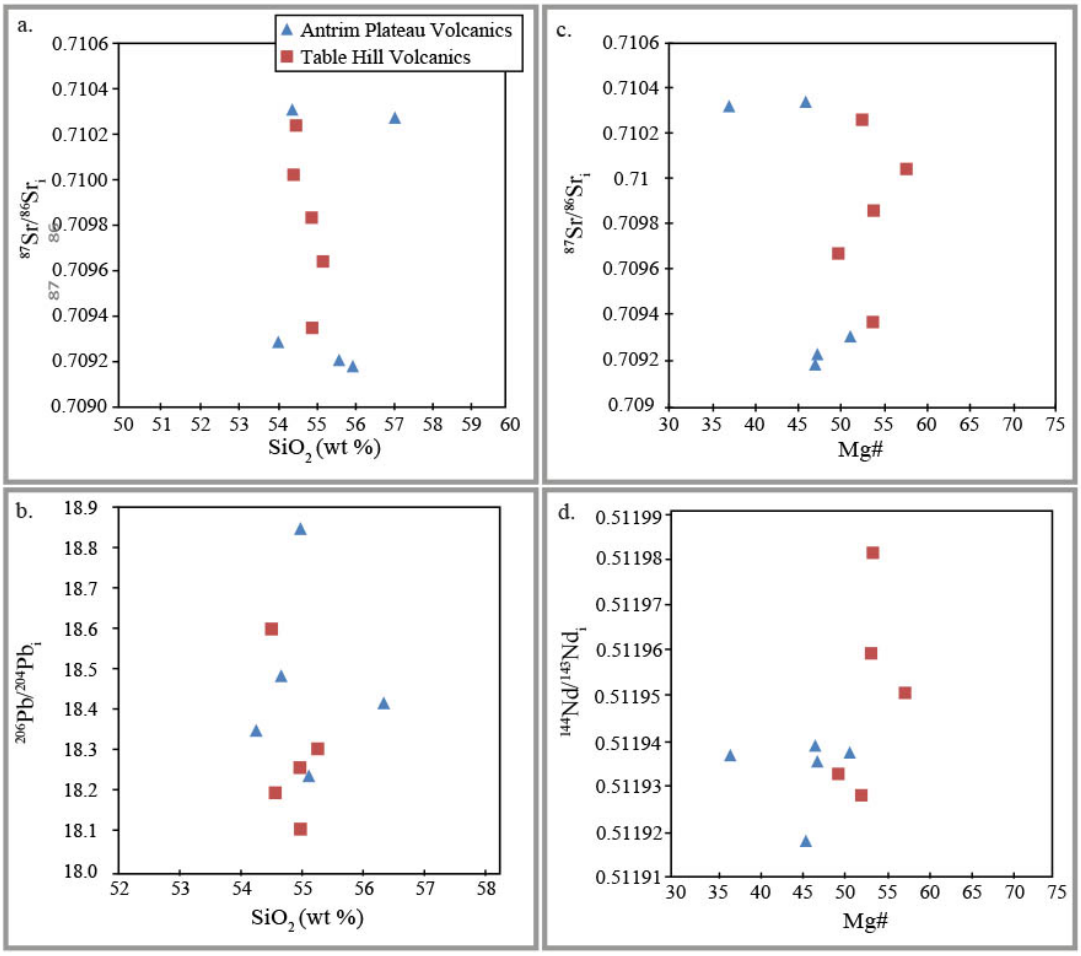

Figure 2.7: Plots of isotopic data for basalts of the Kalkarindji CFB province. (a) $^{87}Sr/^{86}Sr$ initial isotopic composition vs SiO_2 wt. %, (b) $^{206}Pb/^{204}Pb$ initial isotopic composition vs SiO_2 wt. %, (c) $^{143}Nd/^{144}Nd$ initial isotopic composition vs Sm/Nd ratio and, (d) $^{143}Nd/^{144}Nd$ initial isotopic composition vs Mg – number. All isotopic data have been age-corrected to 511 Ma.

Table 2.1a: A selection of major and trace element analyses from the Kalkarindji CFB province.

Major and trace element analyses from the Kalkarindji CFB province, samples analyzed for Sr, Nd, and Pb isotopes

	Type: Antrim Plateau Volcanics Suite					Type: Table Hill Volcanics Suite				
Sample	**052** (28)	**109** (29)	**111** (30)	**112** (31)	**P04** (32)	**07THD-001B_3**	**THD-008_8**	**09THD-029_12**	**09THD-028_16**	**07THD-002_19**
Rock Type	Basalt	Basalt	Basalt	Basalt	Basalt	Dolerite	Dolerite	Dolerite	Dolerite	Dolerite
Locations	Kirrikimbie	Spring Creek	Spring Creek	Spring Creek	Bungle Bungle	MN1	MN1	MN5	MN5	Boondawari
Zone	52	52	52	52	52	51	51	51	51	51
Easting	543159	480282	481086	481266	427461	340154	340828	366034	367563	342847
Northing	8069121	8143676	8142640	8142424	8080318	7367674	7367809	7332952	733542	7392547
Major Elements (wt. %):										
SiO2	53.37	52.91	55.02	53.56	53.62	53.76	53.7	54.06	53.91	53.40
Al2O3	13.82	13.93	13.05	14.02	13.65	15.08	13.73	14.39	13.21	16.42
Fe2O3	12.77	12.63	14.37	12.77	12.20	10.92	11.62	11.46	13.09	9.88
MgO	4.65	4.81	3.62	4.91	5.47	5.44	6.78	5.73	5.55	4.68
CaO	6.65	6.38	5.59	7.15	7.01	8.97	9.18	8.66	7.66	9.49
Na2O	3.38	3.59	3.07	3.39	3.07	2.27	2.18	2.41	2.36	2.35
K2O	2.12	2.98	2.26	1.9	1.95	1.17	1.23	1.4	1.45	1.46
TiO2	1.23	1.18	1.54	1.21	1.21	0.94	0.92	1.03	1.24	0.85
P2O5	0.141	0.135	0.172	0.137	0.154	0.114	0.105	0.126	0.15	0.11
MnO	0.18	0.2	0.36	0.17	0.13	0.170	0.200	0.180	0.20	0.17
H2O+/LOI	1.34	1.08	0.72	0.66	1.31	1.12	0.81	0.6	0.63	0.82
H2O-										
Total	99.65	99.83	99.77	99.88	99.77	99.95	100.46	100.05	99.45	99.63
Trace Elements (ppm):										
La	21.3	20.4	29.6	21.1	19.2	19.7	18.5	21.8	21.20	19.40
Ce	45	42.4	60.9	42.9	39.8	40.4	37.5	44.4	44.10	38.90
Pr	5.26	4.94	7.01	4.91	4.83	4.68	4.3	5.22	5.10	4.50
Nd	21.9	20.4	28.7	20.8	20.2	19	18.1	21.3	20.80	18.40
Sm	4.99	4.54	6.29	4.58	4.36	3.98	3.86	4.38	4.41	4.00
Eu	1.33	1.23	1.56	1.27	1.3	1.1	1.08	1.19	1.24	1.06
Gd	5.24	5.03	6.45	5.2	4.6	4.46	4.2	4.85	4.87	4.28
Tb	0.85	0.82	1.08	0.85	0.83	0.75	0.72	0.8	0.79	0.72
Dy	5.67	5.13	6.59	5.4	5.24	4.64	4.51	5.03	5.21	4.38
Ho	1.16	1.09	1.34	1.09	1.09	0.93	0.9	1.04	1.04	0.90
Er	3.46	3.2	4.02	3.29	3.07	2.7	2.52	3.03	3.00	2.56
Yb	3.19	3.04	3.72	2.99	2.89	2.62	2.45	2.72	2.85	2.46
Lu	0.51	0.47	0.57	0.44	0.45	0.39	0.4	0.39	0.45	0.43
Rb	69.5	63.1	89.3	62.9	61.1	49.9	54.1	60.8	56.70	66.40
Ba	276	303.6	266	202.8	277.2	243.6	216.4	241.8	231.30	259.30

Table 2.1a: Continued.

Major and trace element analyses from the Kalkarindji CFB province, samples analyzed for Sr, Nd, and Pb isotopes

	Type: Antrim Plateau Volcanics Suite					Type: Table Hill Volcanics Suite				
Sample	**052** (28)	**109** (29)	**111** (30)	**112** (31)	**P04** (32)	**07THD-001B_3**	**THD-008_8**	**09THD-029_12**	**09THD-028_16**	**07THD-002_19**
Rock Type	Basalt	Basalt	Basalt	Basalt	Basalt	Dolerite	Dolerite	Dolerite	Dolerite	Dolerite
Locations	Kirrikimbie	Spring Creek	Spring Creek	Spring Creek	Bungle Bungle	MN1	MN1	MN5	MN5	Boondawari
Zone	52	52	52	52	52	51	51	51	51	51
Easting	543159	480282	481086	481266	427461	340154	340828	366034	367563	342847
Northing	8069121	8143676	8142640	8142424	8080318	7367674	7367809	7332952	733542	7392547
Trace Element (ppm): Continued										
Th	9.28	8.22	13.32	8.51	7.05	8.25	7.37	8.9	8.55	8.00
U	1.55	1.33	2.28	1.4	1.17	1.67	1.42	1.7	1.66	1.61
Nb	8.1	7.3	10.1	7.4	6.8	6.9	6.2	7.3	7.30	6.40
K	18104.8	25320.6	19178.1	16077.2	16619.3	9916.8	10345.1	11799.3	12317	12348
Ta	0.6	0.6	0.8	0.6	0.5	0.5	0.5	0.6	0.60	0.50
Pb	9.9	8	13.5	7.4	9.7	7.3	12.2	11.5	11.00	10.80
Sr	123.5	337.1	126	174.7	170.2	147.2	138.4	150.3	133.10	163.60
P	633.0	603.0	767.2	609.4	689.9	507.9	464.2	558.2	665.33	489.03
Hf	3.7	3.2	4.6	3.4	3.3	2.9	2.8	3.1	3.10	2.80
Zr	148	140	182	141	138	125	112	129	135.00	112.00
Ti	7585.3	7240.1	9436.8	7393.5	7446.8	5753.4	5587.6	6268.6	7606	5191
Tb	0.85	0.82	1.08	0.85	0.83	0.75	0.72	0.8	0.79	0.72
Y	31.2	30.4	36.8	30.6	28.4	26.4	25	28.2	29.00	24.50
Co	-	-	-	-	-	-	-	-	-	-
Cr	-	-	-	-	-	-	-	-	-	-
Cu	-	-	-	-	-	-	-	-	-	-
Ni	-	-	-	-	-	-	-	-	-	-
V	-	-	-	-	-	-	-	-	-	-
Zn	-	-	-	-	-	-	-	-	-	-

Table 2.1b: Continued

Representative major and trace element analyses from the Kalkarindji CFB province

	Type: Antrim Plateau Volcanics Suite					Type: Table Hill Volcanics Suite						
Sample	**A001-104.3**	**A001-432.7**	**A002-157.8**	**ANT024**	**ANT005**	**AOB06**	**TH1**	**122601**	**AOB010**	**AOB09**	**389057**	**TH9**
Rock Type	Basalt	Basalt	Basalt	Basalt	Basalt	Basalt	Gabbro	Gabbro	Basalt	Baggro	Basalt	Gabbro
Location	ANTD001	ANTD001	ANTD002	Outcrop	Outcrop	Boondawari 1	Nyianinya RH	M. Jilyili Sill	Empress 1A	Boondawari 1	MD-1A	Trainor Hills
Zone	52	52	52	52	52	51	51	51	51	51	51	51
Easting	7978167	7978167	7995173	8031315	8222530	7398348	7406548	7265369	7005943	7398348	7404962	7312085
Northing	572022	572022	564818	487875	509015	349097	287374	262834	714042	349097	319217	419452
Major Elements (wt. %):												
SiO2	52.71	53.23	55.48	52.66	52.78	52.41	52.22	53.79	52.17	51.79	52.7	53.64
Al2O3	14.99	13.27	15.51	13.98	14.12	14.57	15.5	15.97	14.84	13.89	15	13.38
Fe2O3	10.42	13.68	9.26	12.33	12.44	9.83	9.47	12.41	9.56	9.14	9.36	11.17
MgO	5.1	4.04	4.35	5.82	5.22	6.88	6.82	2.88	7.13	8.73	6.96	6.06
CaO	7.88	6.76	7.61	6.87	7.59	10.06	10.61	7.45	9.71	11.33	9.51	8.22
Na2O	3.33	4.17	3.29	3.67	2.94	2.29	2.15	2.9	2.13	2.01	2.12	2.38
K2O	1.72	1.95	1.84	2.02	1.81	1.16	0.86	1.6	0.96	0.7	1.16	1.45
TiO2	1.28	1.59	1.07	1.32	1.27	0.92	0.9	1.49	0.82	0.72	0.95	1.16
P2O5	0.15	0.19	0.15	0.13	0.12	0.120	0.090	0.158	0.070	0.090	0.130	0.140
MnO	0.19	0.2	0.13	0.17	0.17	0.170	0.160	0.160	0.140	0.170	0.160	0.190
LOI	1.65	1.39	1.62	1.07	1.12	0.56	0.37	1.08	1.41	0.28	1.01	0.92
H2O-												
Total	99.42	100.47	100.31	100.04	99.58	98.97	99.15	99.89	98.94	98.85	99.06	98.71
Trace Elements (ppm):												
La	20.5	24.94	23.9	17.66	20.46	18.58	14.04	25.93	13.84	12.9	18.39	22.64
Ce	44.11	54.07	50.04	36.5	42.02	38.86	29.18	52.92	29.92	27.22	36.93	45.91
Pr	5.272	6.472	5.861	4.409	5.014	4.234	3.446	6.132	3.268	3.191	4.304	5.429
Nd	20.85	26.24	23.44	17.83	19.77	16.87	13.28	24.82	12.91	12.52	15.54	20.6
Sm	4.82	5.97	5.15	4.18	4.46	3.76	3.26	5.59	3.15	2.75	3.61	4.67
Eu	1.38	1.6	1.3	1.27	1.22	1.16	1.01	1.45	0.93	0.91	1.15	1.33
Gd	5.18	6.63	5.43	4.74	4.84	4.06	3.67	6	3.61	3.02	3.8	5.14
Tb	0.917	1.109	0.906	0.802	0.804	0.704	0.682	0.988	0.674	0.525	0.614	0.881
Dy	6.03	7.5	6.01	5.41	5.49	4.46	4.53	6.29	4.51	3.58	4.32	6.15
Ho	1.17	1.43	1.17	1.06	1.04	0.86	0.86	1.28	0.88	0.7	0.88	1.11
Er	3.33	4.29	3.34	3.12	3.01	2.37	2.49	3.71	2.42	1.92	2.42	3.24
Yb	3.18	3.88	3.24	2.83	2.88	2.31	2.34	3.38	2.47	1.93	2.35	3.05
Lu	0.452	0.569	0.469	0.421	0.412	0.342	0.371	0.511	0.363	0.283	0.4	0.477
Rb	65.45	84.98	82.04	59.01	70.84	56.24	37.03	77.03	37.57	29.89	34.33	68.45
Ba	311.4	262	322.2	260	243	236.6	167	343.8	174.8	185.2	246.1	261.8

Table 2.1b: Continued

Representative major and trace element analyses from the Kalkarindji CFB province

	Type: Antrim Plateau Volcanics Suite					Type: Table Hill Volcanics Suite						
Sample	**A001-104.3**	**A001-432.7**	**A002-157.8**	**ANT024**	**ANT005**	**AOB06**	**TH1**	**122601**	**AOB010**	**AOB017**	**389057**	**TH9**
Rock Type	Basalt	Basalt	Basalt	Basalt	Basalt	Basalt	Gabbro	Gabbro	Basalt	Basalt	Basalt	Gabbro
Location	ANTD001	ANTD001	ANTD002	Outcrop	Outcrop	Boondawari 1	Nyianinya RH	M. Jilyili Sill	Empress 1A	Yowalga 2	MD-1A	Trainor Hills
Zone	52	52	52	52	52	51	51	51	51	51	51	51
Easting	7978167	7978167	7995173	8031315	8222530	7398348	7406548	7265369	7005943	7102250	7404962	7312085
Northing	572022	572022	564818	487875	509015	349097	287374	262834	714042	796690	319217	419452
Trace Element (ppm): Continued												
Th	7.85	9.99	10.64	6.33	8.49	5.73	5.43	10.87	7.58	3.98	5.86	9.65
U	1.23	1.67	1.89	1.13	1.53	1.05	0.96	1.78	1.26	0.67	1.31	1.73
Nb	9.45	10.86	8.86	6.32	7.19	5.13	5.08	9.93	4.28	3.43	6.41	7.68
K	14762	16568	15625	17158	15456	9785	7222	13614	8171	5895	9822	12310
Ta	0.92	0.75	0.71	0.51	0.54	0.41	0.5		0.43	0.27	0.49	0.64
Pb												
Sr	160	101	162	156	148	210	144	203.93	101	179	208	145
P	676.7	848.6	669.6	580.5	538.7	532.1	397.6	707.1	313.2	398.4	578.6	624.8
Hf	4.45	5.05	4.55	3.57	3.51	2.95	2.55		2.54	1.45	3.03	3.59
Zr	160.9	177.8	165	123	119	98.7	97.3	148	85.2	56.2	107.2	137
Ti	7933	9755	6561	8096	7831	5604	5462	9155	5040	4378	5808	7111
Tb	0.917	1.109	0.906	0.802	0.804	0.704	0.682	0.988	0.674	0.525	0.614	0.881
Y	29.1	36.76	29.69	29.98	27.25	22.53	22.63	34.77	23.22	18.15	23.24	29.57
Co	37	41	28	45.3	47.5	41	39	54	42	41	39	44
Cr	85	20	85	150	111	77	142	7	93	184	63	37
Cu	49	57	22	29	16	98	68	53	67	91	106	46
Ni	50	20	42	44	33	62	68	26	52	91	68	36
V	262	316	180	333	359	248	235	395	242	216	255	276
Zn	87	128	72	99	96	73	66	148	73	69	72	89

Table 2.1: A selection of major and trace element analyses from the Kalkarindji CFB province. Table 2.1a represented samples are those selected for Sr, Nd, and Pb isotope geochemical analyses. Table 2.1b displays a representative selection of major and trace elements of the province. Analysis details can be obtained in Appendix B. Samples with trace element data indicated with (-) were not analyzed for those particular trace elements. LOI, loss on ignition. GPS Datum: AGD84 unless otherwise noted.

Sample	Sr (ppm)	Rb (ppm)	$^{87}Rb/^{86}Sr$	$^{87}Sr/^{86}Sr_{meas}$	± 1σ	$(^{87}Sr/^{86}Sr)_{i.}$	Nd (ppm)	Sm (ppm)	$^{147}Sm/^{144}Nd$	$^{143}Nd/^{144}Nd_{meas}$	± 1σ	$(^{143}Nd/^{144}Nd)_{i.}$	$\varepsilon Nd_{(0)}$	$\varepsilon Nd_{(511\ Ma)}$
Table Hill volcanics														
07THD-001B_3(A)	49.9	147.2	0.98074	0.71648	0.0000035	0.70934	19.0	4.0	0.111226	0.512249	0.0000019	0.511959	-7.60	-13.2
THD-008_8	54.1	138.4	1.13109	0.71825	0.0000024	0.71001	18.1	3.9	0.113236	0.512257	0.0000017	0.511950	-7.42	-13.4
09THD-029_12(A)	60.8	150.3	1.17053	0.71835	0.0000017	0.70983	21.3	4.4	0.109187	0.512253	0.0000014	0.511981	-7.50	-12.8
09THD-028_16(B)	56.7	133.1	1.23269	0.71861	0.0000081	0.70964	20.8	4.4	0.112577	0.512259	0.0000015	0.511933	-7.40	-13.8
07THD-002_19	66.4	163.6	1.17447	0.71878	0.0000056	0.71023	18.4	4.0	0.115430	0.512234	0.0000021	0.511928	-7.87	-13.8
Antrim Plateau Volcanics														
052 (28)	69.5	123.5	1.62899	0.72216	0.0000020	0.71029	21.9	5.0	0.120985	0.512248	0.0000026	0.511918	-7.60	-14.0
109 (29)	63.1	337.1	0.54136	0.71311	0.0000033	0.70917	20.4	4.5	0.118168	0.512251	0.0000013	0.511938	-7.55	-13.7
111 (30)	89.3	126.0	2.05216	0.72520	0.0000030	0.71026	28.7	6.3	0.116371	0.512210	0.0000030	0.511936	-8.35	-13.7
112 (31)	62.9	174.7	1.04167	0.71678	0.0000041	0.70920	20.8	4.6	0.116917	0.512251	0.0000010	0.511935	-7.55	-13.7
P04 (32)	61.1	170.2	1.03862	0.71684	0.0000090	0.70928	20.2	4.4	0.114607	0.512308	0.0000017	0.511937	-6.44	-13.7

Sample	Pb (ppm)	U (ppm)	Th (ppm)	$^{206}Pb/^{204}Pb_{meas}$	± 1σ	$^{206}Pb/^{204}Pb_{i}$	$^{207}Pb/^{204}Pb_{meas}$	± 1σ	$^{207}Pb/^{204}Pb_{i}$	$^{208}Pb/^{204}Pb_{meas}$	± 1σ	$^{208}Pb/^{204}Pb_{i}$
Table Hill Volcanics												
07THD-001B_3(A)	7.3	1.7	8.3	19.334	0.000866	18.105	15.798	0.000730	15.726	40.392	0.001903	38.445
THD-008_8	12.2	1.4	7.4	19.221	0.000291	18.598	15.797	0.000291	15.761	40.244	0.000917	39.208
09THD-029_12(A)	11.5	1.7	8.9	19.044	0.000261	18.258	15.800	0.000288	15.755	39.922	0.000950	38.602
09THD-028_16(B)	11.0	1.7	8.6	19.108	0.000222	18.304	15.793	0.000202	15.747	40.038	0.000508	38.710
07THD-002_19	10.8	1.6	8.0	18.987	0.000310	18.196	15.792	0.000303	15.746	39.786	0.000904	38.526
Antrim Plateau Volcanics												
052 (28)	9.9	1.6	9.3	19.693	0.000398	18.843	15.854	0.000351	15.805	40.777	0.001088	39.146
109 (29)	8.0	1.3	8.2	19.241	0.000280	18.349	15.792	0.000299	15.740	40.481	0.000873	38.711
111 (30)	13.5	2.3	13.3	19.323	0.000342	18.416	15.808	0.000406	15.755	40.413	0.001377	38.713
112 (31)	7.4	1.4	8.5	19.509	0.000423	18.482	15.811	0.000384	15.752	41.017	0.001102	39.015
P04 (32)	9.7	1.2	7.1	18.875	0.000685	18.238	15.736	0.000619	15.699	39.604	0.001605	38.374

Table 2.2: Sr-Nd-Pb isotope data for the Kalkarindji CFB province. Initial calculations are age-calculated to 511 Ma. Uncertainties on initial ratios include in-run errors and uncertainties on blank corrections. Sample locations can be found in Table 2.1. εNd calculated for a present-day CHUR value of $^{143}Nd/^{144}Nd = 0.512638$ (Jacobsen & Wasserburg, 1980).

The MELTS models and mineral assemblages are consistent with petrographic observations and the geochemical data indicating a realistic possibility for the

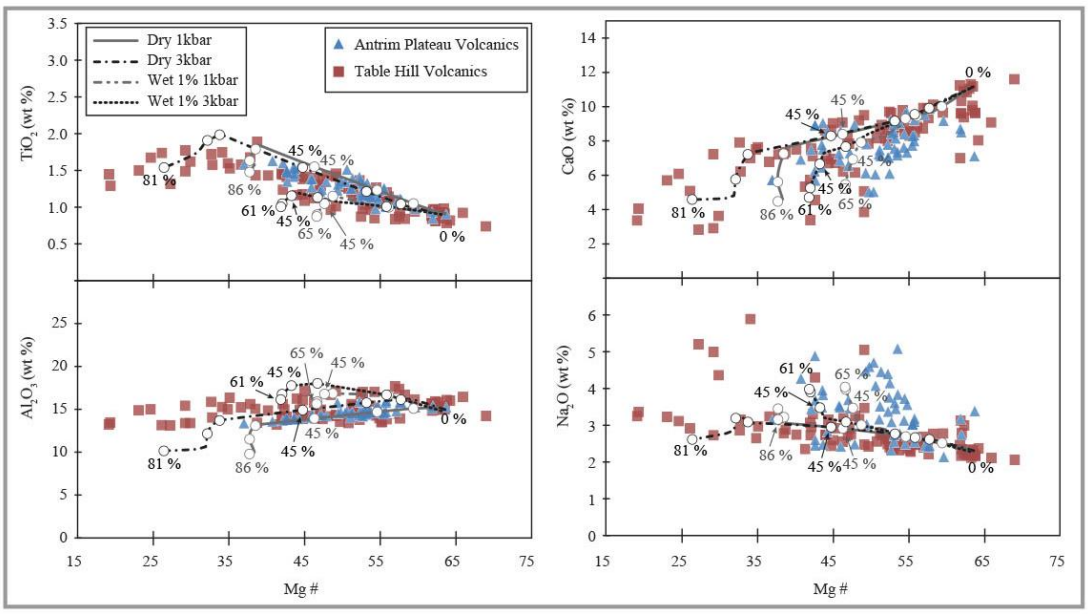

Figure 2.8: MELTS fractional crystallization modeling curves for selected major element trends for the Kalkarindji Continental Flood Basalt. Low pressure (1kbar) anhydrous; moderate pressure (3 kbar) anhydrous; low pressure (1 kbar) hydrous (1 % H_2O); and moderate pressure (3 kbar) hydrous (1 % H_2O) calculations are displayed. A QFM+1 (Quartz – Fayalite – Magnetite) buffer was used for fO_2 (Ghiorso and Sack, 1995). [Circles represent % of fractionation at 15 % intervals]. Model completion percentages: Dry – kbar - 86 %, Dry – kbar - 81 %, Wet 1 % – kbar - 65 %, Wet 1 % – kbar - 61 %.

petrogenesis of the magmas represented by the samples from the Kalkarindji CFB province. The MELTS models also properly reproduce the shift in the trend visible in the TiO_2 vs. Mg # plot (which is due to the crystallization of Ti-magnetite) in the more evolved sub-set found in the dykes of the Officer Basin. The estimated 81 % of fractionation coupled with the acceptable fit of this model occurring in nearly all major oxide vs Mg # plots (a trend to be expected by the covariance observed in all plots) is interpreted to indicate that fractional crystallization was the dominant process controlling the evolution of the Kalkarindji CFBs. Although this model provides the best fit for these chemical trends, the starting composition used is not a primary magma. Thus, these calculations give minimum values for the extent of

which fractional crystallization has occurred; they do not take into account any evolution or fractionation that may have occurred earlier or at a deeper level.

Due to no hand samples available for the AusQuest Limited geochemistry data a mafic vs. felsic index diagram (after McDougall, 1962) was used to determine the nature of high SiO_2 low Mg # subset of data from the Savory Basin. The geochemical trend apparent in the more evolved subset of the Table Hill Volcanics from the Savory Basin samples has been observed and described in other Large Igneous Provinces such as sills and dykes from the Tasmanian Dolerite (such as the Red Hill dolerite) of the Ferrar LIP (Figure 2.9) (McDougall, 1962) and thick dolerites (such as the Hangnest and Blaauwkrans dolerite sills) from Karoo (Walker & Poldervaart, 1949; Roex & Reid, 1978). The Antrim Plateau Volcanics do not display a similarly trend in a mafic vs. felsic index diagram, compared to the Table Hill Volcanics, but rather the data define a more near-horizontal ellipsoid shape (Figure 2.9). Variation observed between the differentiation trends of the Antrim Plateau Volcanics and the Table Hill Volcanics is thus likely to be due to the extrusive nature of the lava flows of the Antrim Plateau Volcanics compared with the relatively thick intrusive sills and dykes of the Table Hill Volcanics (Figure 2.9). Collectively, these observations indicate that this highly evolved subset is likely to

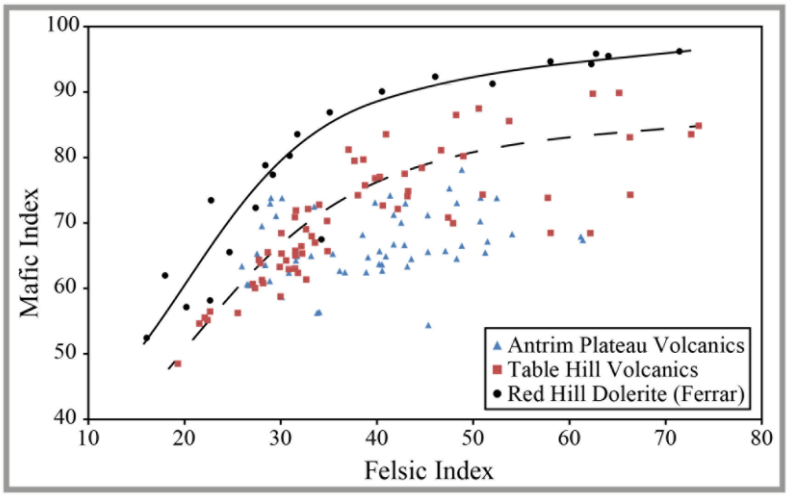

Figure 2.9: Diagram of mafic vs felsic index for basalts of the Kalkarindji CFB province and comparisons with the Ferrar CFB province. Mafic index calculation: [(FeO + Fe_2O_3) x 100 / (FeO + Fe_2O_3 + MgO)]; felsic index calculation: [(Na_2O + K_2O) x 100 / (Na_2O + K_2O + CaO)], after Simpson (1954). Data for the Red Hill Dolerite (part of the Tasmanian Dolerite of the larger Ferrar CFB province) from McDougall (1962).

have formed by the differentiation of thick sills, represented by the coarse-grained found in some cores and recognized petrographically in previous studies of some of the dykes found within the Savory Basin (Grey *et al.*, 2005; Jourdan *et al.*, 2014b).

2.7.1.2. Open system assimilation

In the $^{87}Sr/^{86}Sr_i$ vs. $^{143}Nd/^{144}Nd_i$ diagram (Figure 2.6c), the Kalkarindji CFB samples plot near but off the mantle array with significant variations of Sr isotopic ratios for very limited variations of Nd isotopic ratios displaying highly radiogenic $^{87}Sr/^{86}Sr_i$ ratios (0.7092 – 0.7104) and low, non-radiogenic, $^{143}Nd/^{144}Nd_i$ ratios (0.51177 – 0.51187). Compared to other CFBs, the Kalkarindji CFBs have more radiogenic isotopic ratios (Figure 2.6). Such an enriched signature has been interpreted by some authors to reflect shallow contamination by the continental crust of mantle-derived magmas (Arndt & Christensen, 1992). Therefore, before discussing the nature of the mantle source of the Kalkarindji basalts, an assessment will be made of the involvement of shallow crustal contamination.

Along with no covariation in the $^{87}Sr/^{86}Sr_i$ or $^{143}Nd/^{144}Nd_i$ vs. Mg # plots (Figure 2.7), the Kalkarindji CFB sample suite does not display an obvious negative correlation between Sr and lower Nd isotope ratios that is typical of other CFBs (Figure 2.6c) and is generally attributed to crustal contamination. A lack of covariance is also apparent when isotopes compositions are plotted against SiO_2 content; the variation of isotopic value is not commensurate with changes in SiO_2 abundance (Figure 2.7a). This suggests that crustal contamination has no or very limited influence on the chemical characteristics of these rocks. Furthermore, if assimilation had an important role in the petrogenesis of the Kalkarindji basalts, a Sr and Nd isotopic ratios should be more variable, as is commonly observed for other CFBs. For example, the $^{87}Sr/^{86}Sr_i$

of crustal-contaminated low-Ti magmas in Karoo range from 0.7053 to 0.7073 (Jourdan *et al.*, 2007a).

To further test if crustal contamination affected the composition of the Kalkarindji CFB magmas, the energy-constrained assimilation and fractional crystallization (EC-AFC) model (Bohrson & Spera, 2001) was applied to the isotopic data of the Kalkarindji CFB province. The thermal parameters for a standard upper crust were used (Spera & Bohrson, 2001). For the contaminant the isotopic data are those of the granodioritic Shaw Batholith in the Pilbara Craton. This was chosen because Sr, Nd, and Pb isotopic data are available for this old cratonic crustal material. The Kalkarindji CFB has not directly intruded through the Shaw Batholith, it is still geographically close to the western occurrences of the Table Hill Volcanics and is therefore considered to be a valid representation of at least one of many potential contaminants for the Kalkarindji CFB magmas. Two different assimilation models were considered (compositions and model parameters given in Table 2.3).

Kalkarindji parental magmas assimilation models. The first model involves the introduction of a crustal contaminant into a more MORB-like melt (Figure 2.10). In this scenario, the EC-AFC curves intercept the Sr isotopic compositions of the Kalkarindji CFB samples with the lowest concentration of Sr (ppm). However, the overlap occurs at a minute percentage of assimilation of 0.00002 % (essentially 0 within uncertainties of this model). The Kalkarindji CFB data displays a wide range in Sr concentrations for nearly no change in $^{87}Sr/^{86}Sr_i$ isotopic ratios, which is in stark contrast to the trend predicted by the EC-AFC model curve (Figure 2.10a, MORB initial). More depleted MORB initial compositions were modeled as well, but the models were unable to reproduce the trends observed for the Kalkarindji province in all isotopic systems. Kalkarindji CFB data Nd and Pb form clusters rather than trends

on isotope diagrams and the chemical trends predicted in the models are not matched once assimilation of the crustal material begins. Even when considering the vectors calculated with a MORB initial, the geochemical trends in the Kalkarindji data do not follow the modeled trends indicating no continental crust input for the MORB initial component.

Within suite isotopic variability: assimilation models. A second model was used to test if the variability within each suite can be explained by distinct local crustal components. For this model the samples chosen for initial parameters from the Kalkarindji CFBs were THD-008_8 (the sample from the Table Hill Volcanic suite with the most 'primitive' isotopic composition) and 031 (most 'primitive' sample from the Antrim Plateau Volcanic). The EC-AFC models predict an initial increase in Pb and Nd (ppm) concentrations and a decrease in Sr (ppm) concentrations with no change in the isotopic values for any of the systems (Figure 2.10b – e). This flat trajectory in the models is caused by the lack of any production of anatectic melt due to the time taken for the country rock to reach the solidus temperature. Therefore, this portion of the model displays the fractional crystallization process that characterizes the system (Bohrson & Spera, 2001). These results agree with the MELTS models that indicate a dominant role for fractional crystallization in explaining the variation of the major elements. Once assimilation begins, there is a dramatic increase in the $^{206}Pb/^{204}Pb_i$, $^{207}Pb/^{204}Pb_i$, $^{208}Pb/^{204}Pb_i$ and $^{87}Sr/^{86}Sr_i$ isotopic ratios and a decrease in $^{143}Nd/^{144}Nd_i$ ratios for all modeled assimilation paths (Figure 2.10). Such sharp isotopic variations, even for a small variation in the amount of assimilant, contrasts with the limited amount of isotopic variably observed in the Kalkarindji suite. These models indicate that contamination by the continental crust during the ascent of the magma to the surface is unlikely to have been a major factor controlling chemical

variation. Furthermore, the Antrim Plateau Volcanics and the Table Hill Volcanics are separated by more than 1000 km of variable crustal element types; yet, the major and trace element contents as well as the Sr-Nd-Pb isotopic ratios directly overlap for each suite. This homogeneity is at odds from expected variation assimilation of crustal components would impart onto the geochemical compositions of the province. The isotopic data provided by this study represent a comprehensive areal coverage of the Kalkarindji CFB province. Overall, the available data indicate that large scale crustal

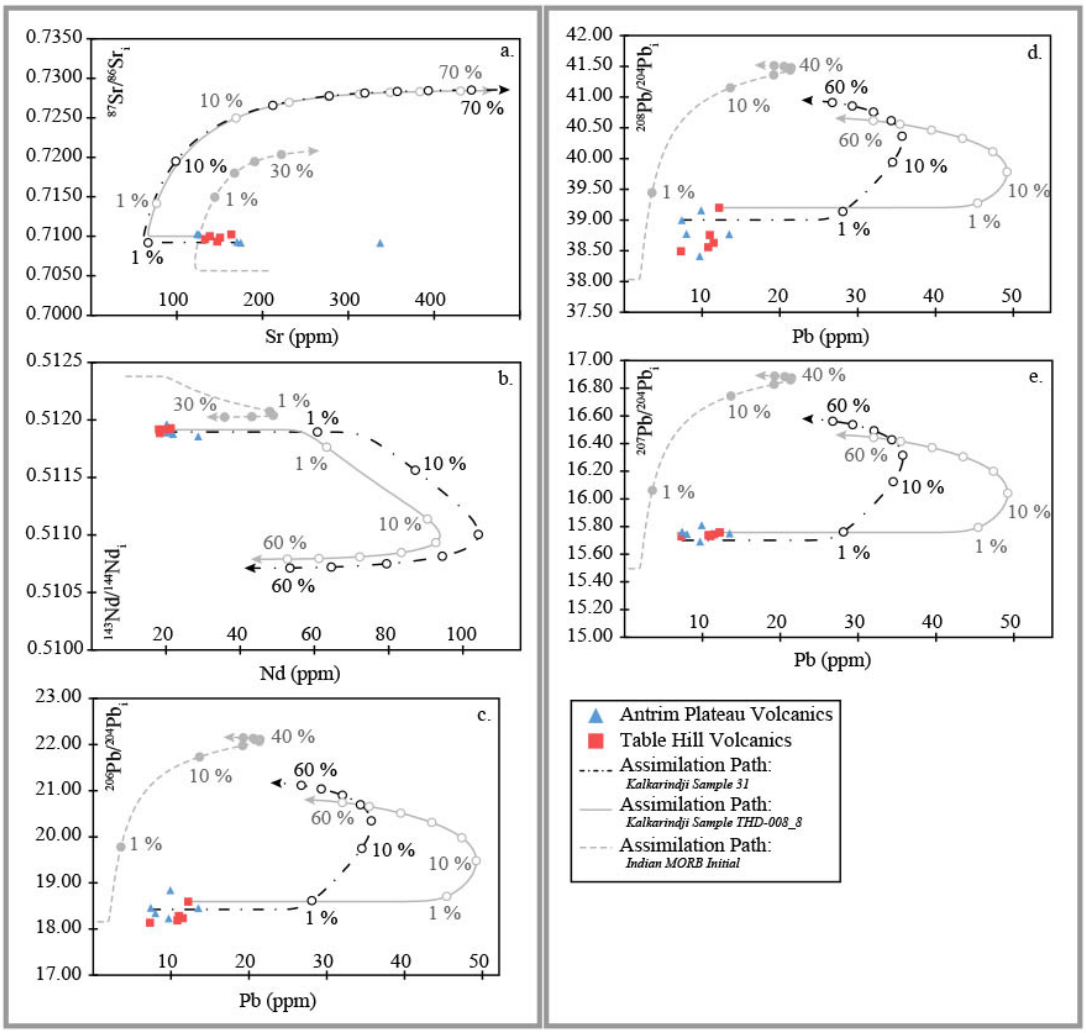

Figure 2.10: Model isotopic ratios and trace element data for basalts of the Kalkarindji CFB province (a) Initial $^{87}Sr/^{86}Sr$ vs Sr (ppm), (b) initial $^{143}Nd/^{144}Nd$ vs Nd (ppm), (c) initial $^{206}Pb/^{204}Pb$ vs Pb (ppm), (d) initial $^{208}Pb/^{204}Pb$ vs Pb (ppm), and (e) initial $^{207}Pb/^{204}Pb$ vs Pb (ppm) diagrams with energy constrained assimilation and fractional crystallization (EC-AFC) model curves for three possible initial calculations (compositions given in Table 2.3) calculated using the code of Spera and Bohrson (2001). Small circles on curves indicate percentage of assimilated contaminant. All isotopic data has been back-calculated to 511 Ma.

Sample	T (°C) NAFC			NAFC
Magma liquidus temperature	1280		Equilibration temperature	949
Magma initial temperature	1280		Crystallization enthalpy (J/kg)	396000
Assimilant liquidus temperature	950		Isobaric specific heat of magma (J/kg per K)	1484
Assimilant initial temperature	300		Fusion enthalpy (J/kg)	270000
Solidus temperature	900		Isobaric specific heat of assimilant (J/kg per K)	1370

Composition parameters	Sr	Nd	$^{206}Pb/^{204}Pb$	$^{207}Pb/^{204}Pb$	$^{208}Pb/^{204}Pb$
Kalkarindji CFB Sample – THD-008_8					
Magma initial concentration (ppm)	138.4	18.1	12.2	12.2	12.2
Magma isotope ratio	0.71001	0.511825	18.598	15.761	39.208
Magma trace element distribution coefficient	1.5	0.25	0.17	0.17	0.17
Kalkarindji CFB Sample – 031					
Magma initial concentration (ppm)	174.7	20.8	7.40	7.40	7.40
Magma isotope ratio	0.70919	0.511805	18.482	15.752	39.015
Magma trace element distribution coefficient	1.5	0.25	0.17	0.17	0.17
Indian MORB					
Magma initial concentration (ppm)	206	9.3	0.60	0.60	0.60
Magma isotope ratio	0.70563	0.512289	18.1577	15.4950	38.0321
Magma trace element distribution coefficient	1.5	0.25	0.17	0.17	0.17
Australian Crust Assimilant					
Assimilant initial concentration (ppm)	574.8	31.8	8.95	8.95	8.95
Assimilant isotope ratio	0.72868	0.510185	22.2909	16.9377	41.6347
Assimilant trace element distribution coefficient	1.5	0.25	0.56	0.56	0.56

Table 2.3: EC-AFC parameters for the Kalkarindji CFB and potential contaminants. Thermodynamic parameters and Sr and Nd distribution coefficients from Bohrson and Spera (2001). Pb distribution coefficients from Jourdan *et al.* (2007) calculated using values reported in the GERM database (http://earthref.org/GERM/). For in-suite composition comparisons initial compositional parameters from samples THD-008_8 (Table Hill Volcanics) and sample 031 (Antrim Plateau Volcanics). Sr and Nd isotopic and element concentrations for assimilant from a 15% trimmed mean of north Australia felsic crust (NAFC) from the GEOROC database. Pb isotopic and element concentration for the assimilant are from the Shaw Batholith located in the Pilbara Craton from the GEOROC database. Average Indian MORB compositions from PetDB (www.earthchem.org/petdb)

contamination is unlikely to account for the enriched nature of the magmas represented by the analyzed samples.

2.7.2.3. Partial melting

As with the major element abundance patterns and isotopic compositions of the Kalkarindji CFBs, the REE and trace element patterns of both the Antrim Plateau Volcanic and the Table Hill Volcanic suites are very similar. Variation between the abundances of the light rare earth elements (LREEs), middle rare earth elements (MREE), and heavy rare earth elements (HREEs) have been controlled by crystal fractionation but they are also an indication of processes controlling the composition of the original primary melts. These include: (i) the degree of partial melting at the source; (ii) source composition in terms of enrichment of LREE relative to HREE and; (iii) variation in source mineralogy with residual garnet or spinel controlling REE behavior. If the degree of melting was constant then elevated La/Yb ratios of primary magmas could indicate source enrichment prior to melting. For the Kalkarindji basalts, the La/Sm_{cn} values are in the range 1.83 to 3.64 and the Dy/Yb ratios are close to 1 (1.03 – 1.82). These LREE/HREE ratios, coupled with the relatively low La/Yb ratios and modest relative enrichments in incompatible trace element abundances are indications that garnet was not a residual phase during mantle melting; melting occurred in the shallow spinel field.

To test the melting conditions for the Kalkarindji CFBs and match the observations made from the LREE/HREE ratios (e.g. La/Sm_{cn} 1.83 – 3.64; Dy/Yb 1.03 – 1.82), the equations from Shaw (1970) were used to model the REE distribution during partial melting. Mantle xenoliths have not been found in the Kalkarindji CFBs so non-modal batch melting calculations were made assuming two theoretical, slightly

LREE-enriched peridotites: a spinel-bearing lherzolite and a garnet-bearing lherzolite; these two mineral assemblages are appropriate for the mantle source of CFBs (e.g. Jourdan *et al.*, 2007a) (Figure 2.11). The partition coefficients used in the calculations are from McKenzie and O'Nions (1983). The spinel-lherzolite source used in the calculations was assumed to have a modal composition of 55 wt. % olivine, 15 wt. %

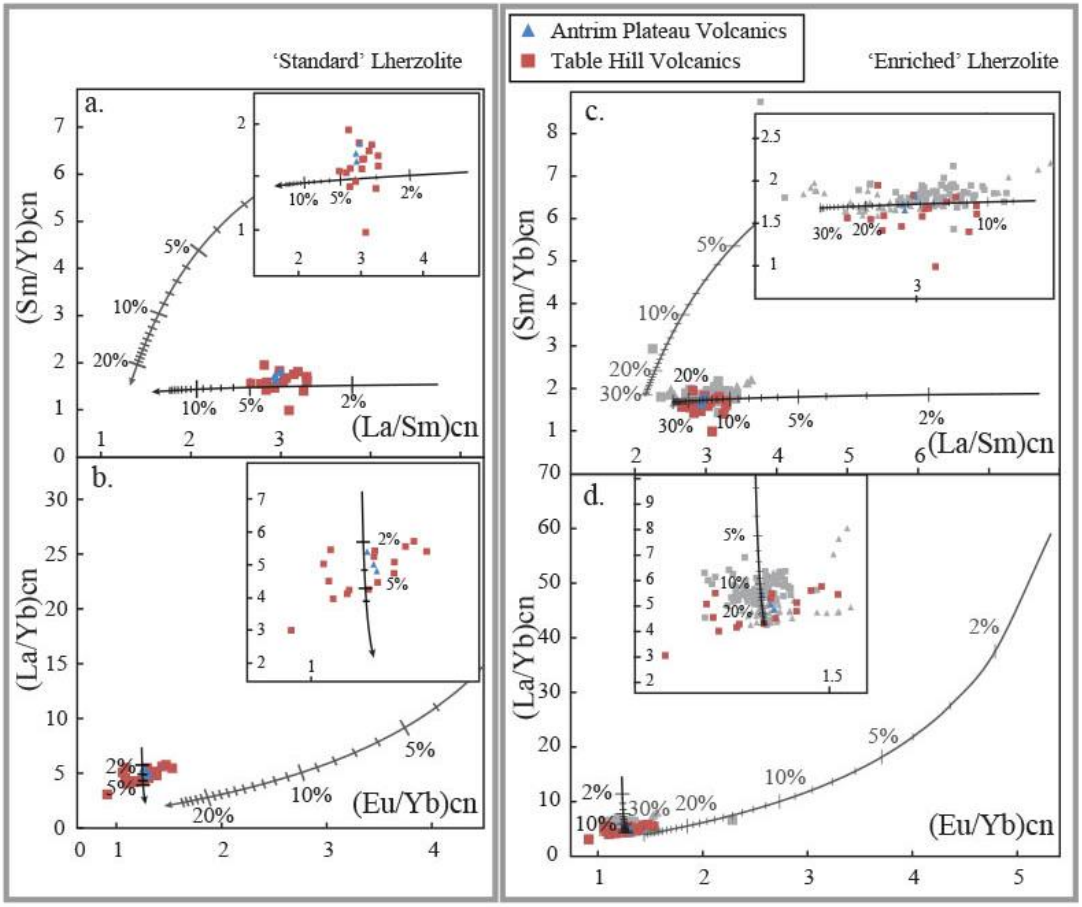

Figure 2.11: Partial melting model diagrams for basalts of the Kalkarindji CFB province. Graphs (a) $(Sm/Yb)_n$ vs $(La/Sm)_n$ and (b) $(La/Yb)_n$ vs $(Eu/Yb)_n$ are non-modal partial melting model results using a garnet lherzolite (grey curve) and a spinel lherzolite (black curve) mantle source, inset graphs are zoom plots of the spinel modeled curves. Calculations made are from equations of Shaw (1970). Compositions are chondrite-normalized after Sun and McDonough (1989). Partition coefficients used in the calculations are from McKenzie and O'Nions (1983). Modal compositions, spinel lherzolite source: 55 wt. % olivine, 15 wt. % orthopyroxene, 28 wt. % clinopyroxene, and 2 wt. % spinel. Melting mode: 20 wt. % olivine, 20 wt. % orthopyroxene, 55 wt. % clinopyroxene, and 5 wt. % spinel. Modal compositions, garnet lherzolite source: 52 wt. % olivine, 33 wt. % orthopyroxene, 10 wt. % clinopyroxene, and 5 wt. % garnet. Melting mode: 16 wt. % olivine, -12 wt. % orthopyroxene, 81 wt. % clinopyroxene, and 15 wt. % garnet Jourdan *et al.* (2007a).

orthopyroxene, 28 wt. % clinopyroxene, and 2 wt. % spinel with a melting mode of 20 wt. % olivine, 20 wt. % orthopyroxene, 55 wt. % clinopyroxene, and 5 wt. % spinel. The modal composition assumed for the garnet-lherzolite source was 52 wt. % olivine,

33 wt. % orthopyroxene, 10 wt. % clinopyroxene, and 5 wt. % garnet with a melting mode of 16 wt. % olivine, -12 wt. % orthopyroxene, 81 wt. % clinopyroxene, and 15 wt. % garnet (Jourdan *et al.*, 2007a and references therein). Due to the compositional homogeneity of the province, the same LREE composition was utilized for calculating melting of both spinel and garnet-lherzolites. The samples that display less than 5 % fractional crystallization (as calculated using the MELTS models) were first considered as representative compositions because these should have compositions closest to those of primitive melts. However, it must also be noted that the degree of fractional crystallization should not noticeably affect the light versus heavy REE ratios (Figure 2.11). Only the spinel-lherzolite melting curve intersects with the data from both the Table Hill Volcanics and Antrim Plateau Volcanics and interpreted to indicate that the primary melts were generated by 3 – 5 % melting, in the field of spinel; i.e. 80 – 100 km (Robinson & Wood, 1998) (Figure 2.11a and b). These modeled results fall within the low range of those found for the central Atlantic magmatic province (CAMP); during initial stages the degree of melting is around 4 % rising to 7 – 15 % in later stages and the low-Ti units (Deckart *et al.*, 2005; Verati *et al.*, 2005). This result implies an unusually low degree of partial melting for tholeiitic rocks; models for tholeiites more typically give melt fractions in the range of 15 – 20 % melting (Green & Ringwood, 1967). Therefore, when these models are compared to those for the low-Ti rocks of CAMP, the inference is that the tholeiites of the Kalkarindji CFB province must have been extracted from a lherzolite with a slightly more enriched composition with a $(La/Sm)_{cn}$ ratio of 3.64 (Figure 2.11a and d). The model melts derived from this "enriched" lherzolite composition provides a better match displaying a more acceptable (or at least upper range) partial melting percentage for quartz normative tholeiites than the slightly LREE-enriched lherzolite compositions used in

the models described above. The modeled melting curve of the "enriched" lherzolite composition reproduces the data in the $(Sm/Yb)_{cn}$ vs. $(La/Sm)_{cn}$ plots, however, the $(La/Yb)_{cn}$ vs. $(Eu/Yb)_{cn}$ plots show more of a cluster rather than a trend along the modeled curve (inset plot Figure 2.11c and d). The Eu variation observed in the data is, however, likely a consequence of fractionation of Eu by plagioclase. As the La/Yb ratio can reflect the effects of partial melting or source enrichment, the low La/Yb ratios of the Kalkarindji CFB are an indication that spinel rather than garnet is a residual phase during melting in the source.

2.7.2. The mantle sources of Kalkarindji

2.7.2.1. Evidence for an enriched component in the mantle source

The absence of correlation between SiO_2 or MgO abundances and Sr and Nd initial isotopic ratios, the EC-AFC results, and the lack of isotopic variation across the province are indications that the enriched signatures measured in the Kalkarindji samples are not the result of the contamination of mantle-derived melts by the assimilation of crustal material. They are more consistent with a model whereby the peridotitic mantle source was enriched prior to the Kalkarindji melting event. In a study of two different dyke swarms within the 1070 Ma Warakurna LIP in Western Australia (Wingate *et al.*, 2004); Zhao and McCulloch (1993) came to the same conclusion, noting that, although the two swarms were emplaced into two different crustal elements, they had similar isotopic compositions. They suggested the involvement of an enriched sub-continental lithospheric mantle (SCLM).

The covariance observed in major element plots (Figure 2.3) and the similar trace elements patterns (Figure 2.4) for both the Antrim Plateau Volcanics and the Table Hill Volcanics are indications that there was not a drastic change of source

composition during the eruption of all the basalts of the Kalkarindji province. The LILE enrichment relative to the HFSE and the negative Nb anomaly in normalized extended element plots are typical chemical characteristics for CFBs (Arndt *et al.*, 1993; Molzahn *et al.*, 1996; Puffer, 2001; Ewart *et al.*, 2004; Jourdan *et al.*, 2007a; Merle *et al.*, 2013) and they are generally attributed to an enriched, continental crust-like component in a mantle source.

The $^{143}Nd/^{144}Nd_i$ isotopic values are much lower than would be expected in the asthenospheric (depleted) mantle and are consistent with a continental crustal input at source (Figure 2.6). Similarly, whereas $^{206}Pb/^{204}Pb_i$ is consistent with MORB values, the $^{207}Pb/^{204}Pb_i$ ratio is significantly higher than typical MORB values for a given $^{206}Pb/^{204}Pb_i$ ratio, plotting well above the NHRL (Figure 2.6a). As shown by the REE patterns, the Kalkarindji basalts display MREE to HREE patterns similar to those of the Indian MORBs (average Indian MORB compositions from PetDB; Figure 2.4). This observation can be explained if an asthenospheric-like mantle was enriched by the input of continental crust-like material. Such a hypothesis has been put forward to explain the enriched signature of the CAMP and the Karoo basalts; in both cases shallow crustal contamination can be ruled out (Jourdan *et al.*, 2007a; Merle *et al.*, 2011; Merle *et al.*, 2013). In addition, two possible processes have been suggested to account for the enriched, continental crust-like, trace element and isotopic signatures of CFBs: (i) shallow metasomatism of the mantle by percolation of silicate or hydrous fluids during an ancient subduction event (Duncan *et al.*, 1984; Puffer, 2001; Ewart *et al.*, 2004); or (ii) the introduction of a small amount of enriched material (e.g. sediment from a subduction event) directly into the source region (Hergt *et al.*, 1989b). The melting models are consistent with a shallow mantle source with residual spinel

(asthenospheric or SCLM) and enrichment by ancient subduction is a realistic hypothesis for the mantle source of the Kalkarindji basalts.

2.7.2.2. A sub-continental lithospheric mantle (SCLM) component

Metasomatized SCLM from the percolation of fluids: Metasomatic processes have been shown to be effective processes in creating a heterogeneous mantle, geochemically and mineralogically (Menzies *et al.*, 1987). Diamonds found within peridotites provide evidence of metasomatism (O'Reilly & Griffin, 2013). Percolation of the lithospheric mantle by fluids and melts can lead to refertilized domains due to melt or fluid infiltration and fluid-rock interactions (Müntener *et al.*, 2010). Such refertilized domains can contain clinopyroxenite veins (from the introduction of fluids) that are more fusible than the average peridotite and this can lead to large-scale melting of the SCLM, which is required to produce the large volumes of magmas within the Kalkarindji CFB province. Small-scale melting of enriched domains in the SCLM and not an asthenospheric mantle has been suggested from the presence of diamonds in the lamproites, lamprophyres, and kimberlites of the Kimberley Block; e.g. Ellendale and Argyle (Gibson *et al.*, 2006) (Figure 2.1b). However, the presence of diamonds is only evident within the Kimberley Block and has yet to be recognized in the North Australian or West Australian Cratons.

SCLM enrichment by subducted sediments: Another possibility is the introduction of a small percentage of continental material into a shallow mantle through the process of subduction. This has been inferred for the EMII mantle component (Zindler & Hart, 1986): deep recycling of continental sediments has been proposed as a mechanism for generating this mantle component. The similarity of the Kalkarindji CFBs to the EMII mantle end member, in terms of isotopic compositions, could indicate the introduction of sediment into the source region. Hergt *et al.* (1989b)

argue that sediment input at source is a plausible process for explaining the geochemistry of the Tasmanian dolerites (Ferrar CFB province), which have signatures very similar to the Kalkarindji CFBs (Figure 2.6). Hergt *et al.* (1989b) and Merle *et al.* (2013) found that only a small amount of sediment (< 3 wt. %) is needed to produce the enriched "crustal" like characteristics of the Tasmanian dolerites and Eastern North America CAMP. Ben Othman *et al.* (1989) postulated that ancient sediment has high $^{232}Th/^{238}U$, which would lead to high present day $^{208}Pb/^{204}Pb$ ratios. Due to the systematics of the decay of ^{238}U and ^{235}U coupled with the high $^{232}Th/^{238}U$ ratios, ancient recycled sediments should be characterized by high $^{207}Pb/^{204}Pb$ and $^{208}Pb/^{204}Pb$ for low $^{206}Pb/^{204}Pb$ ratios compared to asthenospheric mantle values. The Kalkarindji basalts display similar isotopic characteristics as described above as well as high Th/Yb ratios (Figure 2.12b), therefore, the involvement of ancient sediment in the source of these basalts is a possibility. The low concentrations of the trace elements in depleted MORB mantle-like peridotites would allow for the trace elements from the sediments, in particular the LILE which are very abundant in continental crust, to dominate the trace element

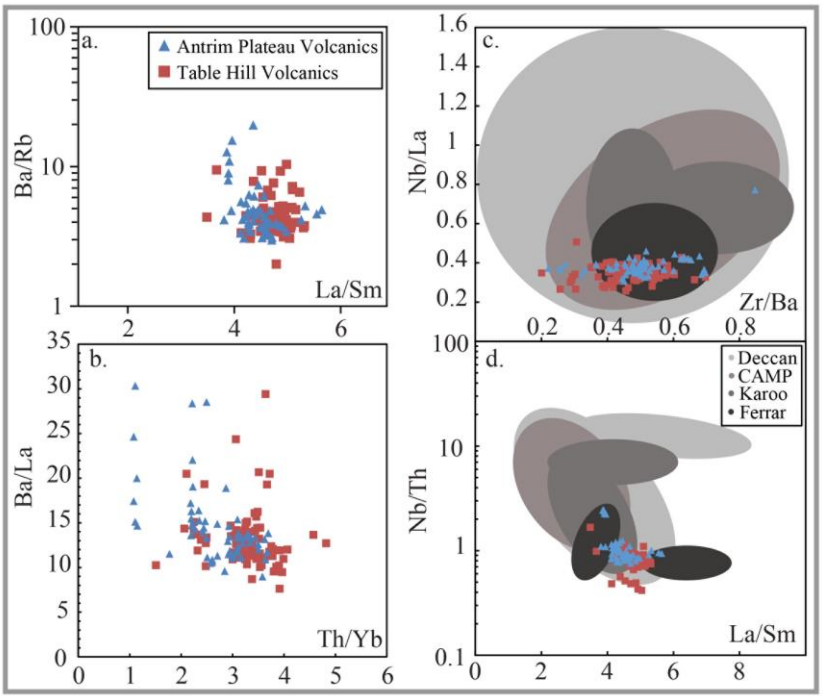

Figure 2.12: Selected trace ratio vs trace ratio graphs for basalts of the Kalkarindji CFB province. Plots a and b display trace element mixing calculation curves after Faure (1986). Each point along calculated curve represents 10 % mixing intervals. Abbreviations: CAMP, Central Atlantic Magmatic Province. Deccan, CAMP, Karoo, and Ferrar compositions from the GEOROC database.

signatures of the magmas, while the major elements would retain basaltic characteristics. In addition, the subducted sediment input could also explain the negative Nb and Ta anomalies in normalized extended element plots; a prominent geochemical feature of subduction-related magmas (Pearce, 1982; Briqueu *et al.*, 1984; Baier *et al.*, 2008) and the enriched isotopic compositions of the magmas. The high $^{207}Pb/^{204}Pb$ and high $^{87}Sr/^{86}Sr$ for given low Nd values of the Kalkarindji basalts when compared to MORBs are consistent with enrichment of the SCLM by ancient subduction.

2.7.2.3. Age of the enrichment

The elevated $^{207}Pb/^{204}Pb$ isotopic values with moderate $^{206}Pb/^{204}Pb$ values can only be explained if source enrichment occurred a long time before the Kalkarindji CFB event (when ^{235}U was still abundant) and the enriched source must have been relatively stable for a long enough period of time for the decay of these two systems to decouple. This has been suggested for several CFBs (e.g. Jourdan *et al.*, 2007a; Merle *et al.*, 2013). Mantle end member analogue isotopic compositions, back calculated to 511 Ma, are not able to reproduce the observed Pb isotopic signatures from the Kalkarindji CFB province, thus necessitating an ancient U enrichment of the SCLM. In order to calculate the age of the lithospheric enrichment, the growth curve calculations of Stacey and Kramers (1975) were used. This approach is taken as there is no evidence within the major and trace element data that Pb has been mobilized. The Pb isotopes were evolved from different ages of enrichment in attempts to determine the most probable minimum age of enrichment that can reproduce the measured isotopic ratios of the Kalkarindji CFB province. The Stacey and Kramers (1975) lead growth curve evolves initially from 4.57 Ga with a $^{238}U/^{204}Pb$ ratio of 7.19 and a $^{232}Th/^{238}U$ of 4.62 (Table 2.4; Figure 2.13) from which a second stage curve with a

higher μ ($^{238}U/^{204}Pb$ = 9.74 and $^{232}Th/^{238}U$ = 3.78) beginning at 3.7 Ga. The isotopic Pb starting composition for the Kalkarindji CFB source area falls on the second stage

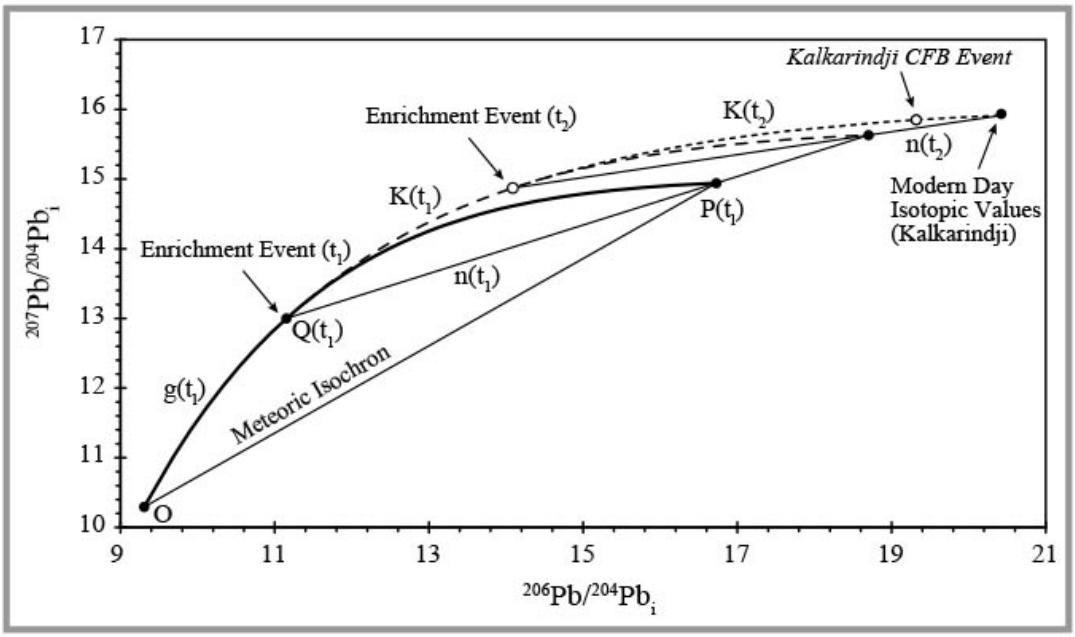

Figure 2.13: Kalkarindji Continental Flood Basalt (CFB) province initial lead isotope calculation model. Calculations and figure modelled after Stacey and Kramers (1975): O = troilite lead, 4.57 Ga; $n(t_i)$: new zero cord, age t_1 (3.7 Ga), t_2 (2.5 Ga); $P(t_1)$: intercept of $n(t_1)$ and the meteoric isochron; $g(t_l)$: Stacey and Kramers (1975) single - stage growth curve; $Q(t_1)$: composition of terrestrial lead at the enrichment event, t_l (3.7 b.y. ago); $Q(t_2)$: composition of Kalkarindji source lead at the enrichment event t_2 (2.5 b.y. ago); $K(t_1)$: growth curve for second stage for average modern lead. $K(t_2)$: growth curve of the source area for the Kalkarindji CFB province after the enrichment event.

curve of Stacey and Kramers (1975) lead model. The enrichment event assumed to have a $^{238}U/^{204}Pb$ value typical of upper continental crust (UCC) of 12.72 (Zartman & Haines, 1988). The UCC $^{232}Th/^{238}U$ ratio (3.78) of Zartman and Haines (1988), however, is identical to that of the postulated second stage of Stacey and Kramers (1975). The high $^{208}Pb/^{204}Pb$ isotopic ratios of the Kalkarindji province basalts require a higher $^{232}Th/^{238}U$ ratio during the enrichment event than would be derived from the curve of Stacey and Kramers (1975). Therefore, a slight modification of the Th content from 14.8 to 16 ppm was introduced to the model to provide a $^{232}Th/^{238}U$ ratio greater than 4 ($^{232}Th/^{238}U$ = 4.06). This is in agreement with Ben Othman *et al.* (1989) who suggested that the $^{232}Th/^{238}U$ is difficult to constrain but, from mass balance considerations, they inferred that the value is likely to be greater than 4. These UCC

$^{238}U/^{204}Pb$ and $^{232}Th/^{238}U$ ratios were affected by various enrichment events at difference times prior to the emplacement of the Kalkarindji CFB province. As a consequence of these enrichments, the isotopic composition of the SCLM source area evolved away from the Pb evolution curve (Stacey & Kramers, 1975) to the present day values. These calculations were made until a particular enrichment time successfully reproduced the measured Pb isotopic values of the Kalkarindji CFB province. The models indicate that an enrichment event has to have occurred at around 2.5 Ga to adequately reproduce the observed Pb isotopic ratios of the Kalkarindji CFB province (Figure 2.14).

Model isotopic compositions were also calculated using different crustal compositions; upper continental crust composition (Taylor & McLennan, 1985); bulk

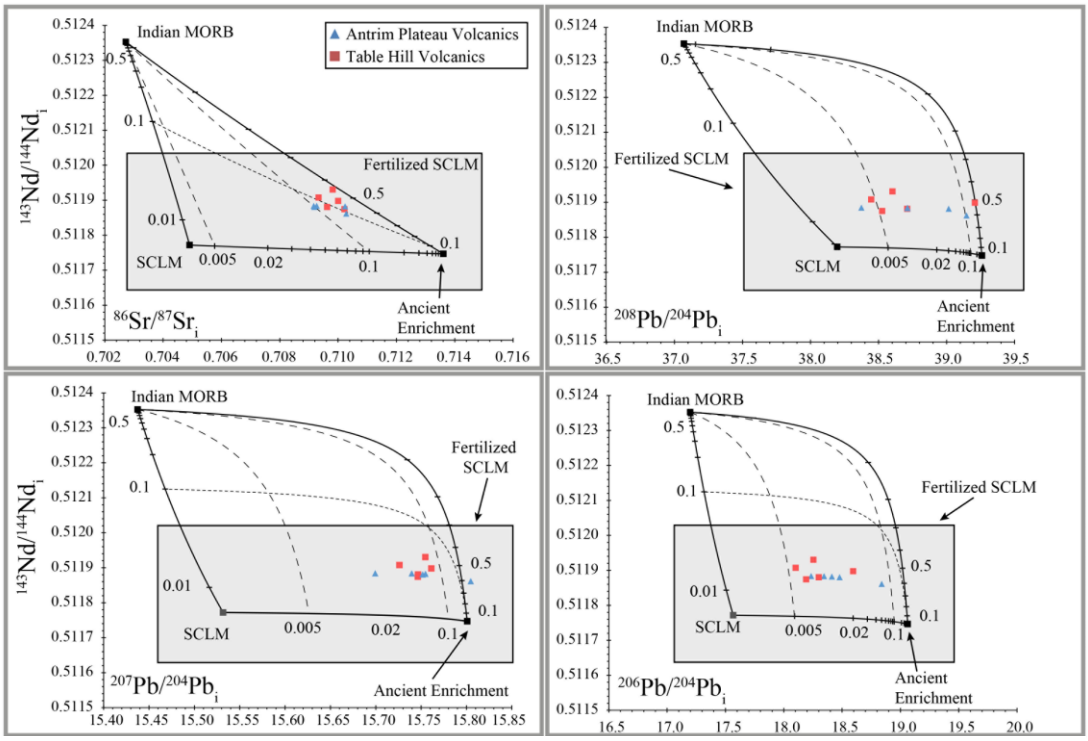

Figure 2.14: Three component-mixing models for basalts of the Kalkarindji CFB province showing Indian MORB melts swamped by SCLM that was contaminated by an ancient, subducted, enriched component. Average Indian MORB compositions from PetDB (www.earthchem.org/petdb), SCLM composition is the BSE estimated average, isotopes from Rollinson (1993) and trace element information from the mantle estimates of Zartman and Haines (1988), enriched component are calculated isotopic data from an enrichment event at 2.5 Ga with elemental compositions taken from upper continental crust estimates of Zartman and Haines (1988). All isotope data age-corrected to 511 Ma.

continental crust composition of (Rudnick & Fountain, 1995); and GLOSS values of (Plank & Langmuir, 1998); to test validity of the sediment composition used to estimate the separation age of the Kalkarindji CFB enriched reservoir. None of these alternative crustal compositions have μ values that can produce viable results for the Kalkarindji CFBs at any time of enrichment; none of them generate isotopic ratios enriched to the levels of the Kalkarindji province because they all have $^{238}U/^{204}Pb$ and $^{232}Th/^{238}U$ ratios too low. Slight changes in the $^{238}U/^{204}Pb$ and $^{232}Th/^{238}U$ ratios can affect the estimated enrichment age; however, to some extent these ratios can be constrained by comparing the results from all three Pb isotopic systems as well as the tectonic history of the area. The calculated age of enrichment of 2.5 Ga is consistent with estimates for the amalgamation of the North Australian Craton, which occurred around this time (Cawood & Korsch, 2008; Drüppel *et al.*, 2009).

Utilizing the estimated enrichment age of 2.5 Ga calculated from the Pb isotopic system, the $^{143}Nd/^{144}Nd$ and $^{87}Sr/^{86}Sr$ isotope compositions that would be required to produce the Kalkarindji magmas were calculated by inputting the measured values from the Kalkarindji CFB province and running the calculation for each sample for time = 2.5 Ga. The final variables in the equation ($^{147}Sm/^{144}Nd$ and $^{87}Rb/^{86}Sr$ ratios) were calculated using the average of the ratios from the Kalkarindji present day measurement results. Using this method the average Nd isotopic ratio at the time of the enrichment of the SCLM was 0.510096 and the average Sr isotopic ratio was 0.675081.

2.7.2.4. Involvement of a MORB-like component: a tri-component source?

The geochemical characteristics of the Kalkarindji basalts are compatible with the involvement of SCLM enriched by an ancient sediment input. However, the incompatible elements and HREE patterns of the Kalkarindji basalts show similarities

with the incompatible and HREE patterns of Indian MORB (Figure 2.4d – f). In addition, some isotopic compositions are close to the mantle array in the $^{143}Nd/^{144}Nd$ vs $^{87}Sr/^{86}Sr$ diagram. These observations are compatible with the involvement of an asthenospheric component. Alternative models of wholesale melting of the SCLM suggest contamination of melts from the sub-lithospheric convective mantle (asthenosphere) by fluids or melts originating from the SCLM (Arndt & Christensen, 1992; Gibson *et al.*, 2006; Heinonen *et al.*, 2010). Therefore, the source for the Kalkarindji basalts could have evolved by an interplay of processes that include mixing between liquids from the SCLM, an enriched, continental-like component, and MORB melts.

Such a tri-component mixture has been suggested for other CFBs sources; e.g. Parana/Etendeka: Ewart *et al.* (2004); CAMP: Merle *et al.* (2013). A tri-component mixing model was tested for the Kalkarindji basalts using realistic geochemical parameters to assess the contribution of each component in the chemical characteristics of the basalts. The three component mixing models were calculated using: (i) the Indian MORB melt composition to represent the primitive component in the system; and a SCLM consisting of a mixture between, (ii) a pre-enriched SCLM component with estimated isotopic composition close to the average of bulk silicate earth (BSE) (Rollinson, 1993) with trace element compositions from the mantle reservoir estimates of Zartman and Haines (1988) and (iii) a 2.5 Ga sediment enriched component calculated from the isotopic ratios utilizing trace element ratios of a standard upper crustal composition of Zartman and Haines (1988). Note that the SCLM component is assumed to have trace element contents of a peridotite. Therefore, this approach models the composition of the primitive melt through a process involving

asthenospheric MORB-like melt swamping an enriched peridotite created by the solid mixing of components (ii) and (iii) described above.

Prior to the proposed enrichment event, the composition of the SCLM would not have produced a low enough $^{143}Nd/^{144}Nd$ isotope ratio to account for the extremely low radiogenic values of the Kalkarindji CFB province. To encompass the Nd isotopic results from the Kalkarindji CFB province requires a slightly higher $^{147}Sm/^{144}Nd$ ratio than the BSE mantle values of Zartman and Haines (1988). Therefore, the pre-enriched SCLM component for the model was calculated using a $^{147}Sm/^{144}Nd$ of 0.259 rather than a value of 0.222. The adjustment is minor considering that a worldwide average value is unlikely to represent a particular mantle end-member and as such, it is considered appropriate for the modeling of the Kalkarindji CFB province isotopic compositions. Differences to consider when interpreting these results are slight variations of sediment composition and/or preferential leaching of elements by fluids or melts that would result in changes in incompatible elements compositions that could modify the shape of the mixing curves.

The mixing field defined by the three components adequately encompasses the observed Kalkarindji CFBs values (Figure 2.14). The isotopic composition of the Kalkarindji CFB can be best modeled by an SCLM enriched by no more than 10 % of sediment melt mixing with less than 10 % Indian MORB melt in the Pb isotopic ratios and between 10 and 20 % Indian MORB melt for the Sr-Nd isotopic ratios (Figure 2.14). This model shows that the chemical signature of the enriched part of the SCLM (SCLM plus the ancient enrichment) dominates the geochemical composition of the Kalkarindji magmas. The array defined by the Pb isotope data for the Kalkarindji CFBs parallels the modeled mixing curves between the SCLM and the ancient sediment end member components. This apparent smear of the Pb isotope data could be due to; (i)

slight variations of U/Pb and Th/U values from the enriched material introduced into the source area that are related to variations of either these ratios in the sediments or degree of sediment melting; or (ii) a continuous input over time, possibly hundreds of million years, into the SCLM source(s) causing a variation in the isotopic ratios within the source (Merle *et al.*, 2013). In addition, the slight difference in the $^{147}Sm/^{144}Nd$ ratio needed to model the Kalkarindji CFBs from the BSE elemental composition of Zartman and Haines (1988) could be due to the level of variation possible when using an average as discussed above; or alternatively it could indicate that there was a second enrichment event into the system, which introduced a slightly higher $^{147}Sm/^{144}Nd$ ratio. Such an event, however, would be required to have U/Pb and Th/U values similar to those prevailing during the initial enrichment event. This later scenario is unlikely, however, as it brings unnecessary complication to an otherwise simple, yet successful model (Figure 2.14).

2.7.3. Geodynamics

2.7.3.1. Cause for the Kalkarindji CFB Magmatism

Mantle Plume involvement: In terms of chemical characteristics, the data and model results do not require an active role for a mantle plume in the genesis of the Kalkarindji magmas. Also the Kalkarindji province does not display convincing evidence for a dyke swarm that could indicate an impingement of a plume during the generation of this LIP. Although the Milliwindi dyke is a major feature in the province, even when considering the several isolated dykes observed in the western Officer Basin, a dyke swarm is not apparent by any definition. A simplified direct and unique link between dyke swarms and LIPs has also been called into question in recent studies such as is the case with Karoo (Jourdan *et al.*, 2006). Therefore, if present, a mantle plume could only be indirectly involved in the genesis of the Kalkarindji CFB province

by providing additional heating and subsequent melting of the enriched Archean SCLM. Such a scenario would account for the size, volume, production timescale of the Kalkarindji CFB province, and the province-wide homogeneity.

Heat flux differences in the SCLM at Craton Boundaries: King and Anderson (1995) suggested that at least the initial control of CFBs volcanism could be attributed to the physical differences in the craton and non-craton lithosphere observed near boundary areas. Small-scale convection (or edge driven convection) develops at cratonic-non cratonic discontinuities that are usually associated with orogenic sutures. The Kalkarindji CFB is located along the margin of the Kimberley Block and North Australian Craton as well as near the margin of the West Australian Craton and the orogenic material between the North and West Australian Cratons (Figure 2.1b). This particular location between thick crustal blocks could facilitate the development of a large amount of melt in these areas through the edge driven convection mechanism. A key requirement of these numerical models is the asymmetry between the craton and non-craton boundary which they recognize requires extensional tectonics to focus the flow at these suture zones (King & Anderson, 1995). One consideration to be addressed if the edge driven convection model is solely responsible for the Kalkarindji CFB province is the timing of the upwelling of material associated with edge driven convection. Once a lithospheric step change is established the upwelling of asthenosphere is likely to happen immediately, causing the formation of the Kalkarindji CFB province much earlier than 511 Ma. Edge driven convection could, however, simply be a trigger when the conditions are right, such as when the crust has thinned enough to let the magma ascend and/or if enough heat had accumulated below the continent. Although many of the orogenic events amalgamating these areas together occurred on the order of 1.5 to 2.0 Ga, tectonic activity and reorganization

continued in these zones throughout the construction of Gondwana into the Phanerozoic, i.e. the Cambrian rotation of Gondwana suggested by Veevers (2001). The rotation that occurred on the Australian continent throughout the Cambrian caused significant changes in the stress regime of the continent leading to regional extension; there is evidence for this in formation of the Ord, Bonaparte, Arafura, Daly River, and Wiso Basins (Figure 2.1b). The Antrim Plateau Volcanics floor many of these basins and the Table Hill Volcanics intrude into and floor the lower sediments of the Officer Basin indicating that emplacement occurred during the formation of these basins. Ongoing tectonic activity would provide the tensional stress to focus the flow of the mantle melts into the thinner suture zones. Therefore, if this model were to be considered into the genesis of the Kalkarindji province it would most likely need to happen in conjunction with decompression melting or mantle warming.

Decompression Melting of the SCLM: Decompression melting can occur in three conceivable ways for this province: (i) delamination of the lithosphere possibly by a catastrophic lithosphere failure or collapse of transformed basaltic crust to dense eclogite at the crust-mantle boundary (Ringwood & Green, 1966; Houseman & Molnar, 2001); (ii) thinning of the lithosphere due to continental rifting (Bond *et al.*, 1984; Li *et al.*, 1996; Olierook *et al.*, 2016); (iii) thinning of the lithosphere over areas of global mantle warming during the period of supercontinents (Coltice *et al.*, 2007).

It has been proposed that catastrophic delamination models occur when tectonic stresses, such as continental convergence, lead to gravitational instabilities causing large scale delamination of a considerable portion of the lithosphere (Ringwood & Green, 1966; Houseman & Molnar, 2001). The catastrophic collapse allows for the upwelling of hot asthenosphere to replace the delaminated lithosphere providing a means for decompression melting to occur at relatively shallow depths.

Torsional stress from roughly 540 – 470 Ma caused a ~ 90° rotation of Gondwana (Veevers, 2001), destabilizing dense lithospheric mantle beneath northern Australia and this could have resulted in a catastrophic delamination of the SCLM. This would allow for a large melting event such as the Kalkarindji magmatic event. However, if the hot rising asthenosphere were to be the main source of the basalts, it would be inconsistent with the enrichment event around 2.5 Ga; this period of isolation is required before the Kalkarindji magmatism. Furthermore, the evidence provided by young diamond pipes sourced in the lower SCLM indicates that the asthenosphere melt did not create the diamonds or replaced the SCLM in the process. Decompression melting due to the thinning of the continental lithosphere below the Kalkarindji CFB province by the initiation of rifting has also been proposed to explain aspects of the tectonic history of the breakup of the China and Australia continents (Bond *et al.*, 1984; Li *et al.*, 1996). Studies by Bond *et al.* (1984) and Li *et al.* (1996) have suggested that the Kimberley Block of Australia and the Tarim Block of southern China were connected in the past. These studies propose that the Antrim Plateau Volcanics are evidence of a failed arm of a triple junction that resulted from the separation of the Tarim Block and the Australian continent. However, this interpretation was made before the Table Hill Volcanics of the Officer Basin were confirmed as being related and included in the Kalkarindji CFB province. Therefore, with the addition of the Kalkarindji CFB province as far south as the Officer Basin and the lack of any current evidence of a dyke swarm, this is unlikely to be the geologic process that formed the Kalkarindji CFB province.

Thinning of the continental lithosphere is evidenced by the large-scale coeval basin formation across the western portion of the Australian continent around the emplacement of the Kalkarindji CFB province; further suggesting decompression

melting in the genesis of the province. These extensional stresses that were present to form these basins may have induced decompression melting of the enriched SCLM (± a minor amount of asthenosphere along the lower SCLM) as a result of crustal thinning. Olierook *et al.* (2016) argue that the melting of a shallow enriched patch of mantle located within a larger, subducted, enriched SCLM could have produced the enriched geochemical signatures observed for the Bunbury Basalts, on the margin of Western Australia, without the need for involvement of the Kerguelen mantle plume. This model could very well apply for the genesis of the Kalkarindji CFB province, at a much larger scale.

Preferred Model for Kalkarindji Magmatism: In a long and relatively stable continental environment, decompression melting following tectonic extension is likely to operate in conjunction with the global mantle warming scenario that has been suggested to occur underneath large continents (Coltice *et al.*, 2007). Coltice *et al.* (2007) propose that an increase in sub-continental lithosphere temperature of up to 100 °C can be obtained on a timescale of about 300 m.y. after continental assembly. The tectonic history for the western portion of Australia provides a stable period for the Australian continent on the order of nearly 700 Ma; the last major tectonic activity to occur in the western portion of the Australian continent before the Kalkarindji CFB event was the orogenic activity of the Musgrave province, which occurred 1.2 Ga (Wade *et al.*, 2008; Aitken & Betts, 2009; Smithies *et al.*, 2015) before the Kalkarindji CFB magmatic event, providing more than enough time for the mantle below this portion of Gondwana to accumulate the heat needed to form the Kalkarindji CFB province. The presence of the Kalkarindji CFB province within and flooring basins throughout Australia indicates that thinning of the lithosphere was occurring contemporaneously with the emplacement of the Kalkarindji CFBs.

Sample	Time (b.y.)	$^{206}Pb/^{204}Pb$	$^{207}Pb/^{204}Pb$	$^{208}Pb/^{204}Pb$	$^{238}U/^{204}Pb$	$^{232}Th/^{204}Pb$	$^{232}Th/^{238}U$	$^{147}Sm/^{144}Nd$
Start of 1st Stage	4.57	9.307	10.294	29.487	7.19	33.21	4.62	-
Start of 2nd Stage	3.70	11.152	12.998	31.230	9.74	36.84	3.78	-
Enrichment Event	2.50	14.089	14.871	33.780	13.37	54.30	4.06	0.1818

Table 2.4: Enrichment model parameters for the Kalkarindji CFB province Calculations from Stacey and Kramers (1975). Elemental compositions resulting in elemental ratios modified from Zartman and Haines (1989).

Therefore, our preferred model for the Kalkarindji CFB province involves decompression melting of the enriched source region from thinning of the lithosphere that has been warmed below the Gondwana continent starting from at least 1.2 Ga, but most likely initiating in the north at ~ 1.85 Ga in the north. In this decompression melting scenario, melts generated during the genesis of the Kalkarindji CFB province would be produced mostly within the SCLM, with perhaps a small contribution from the depleted MORB-like asthenosphere (less than 10 %; Figure 2.14) immediately below the enriched part of the SCLM (Figure 2.15).

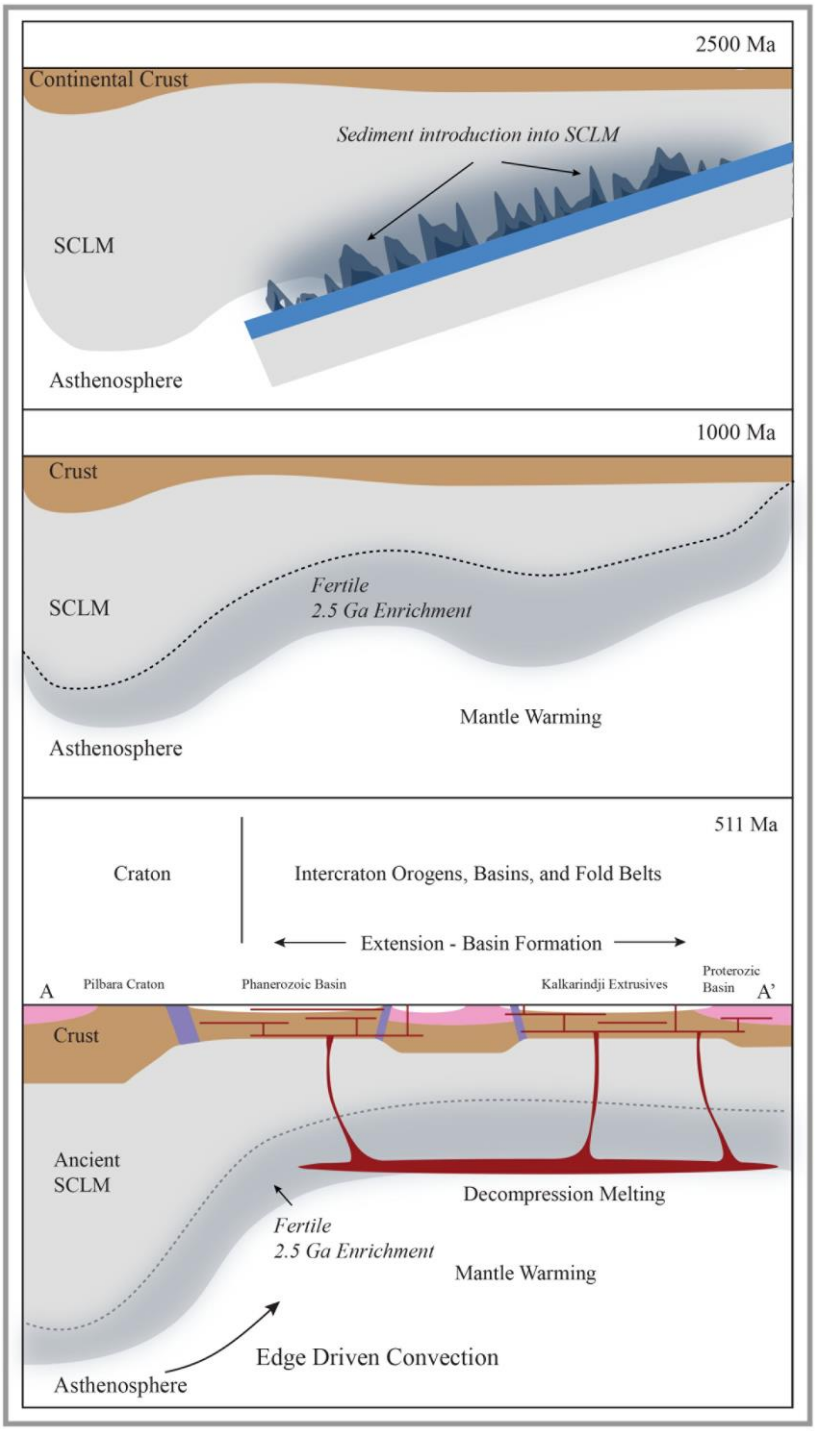

Figure 2.15: Schematic presentation of the internal mantle heating geodynamic model for the generation of the Kalkarindji Continental Flood Basalt province.

2.7.4. Comparison with the Ferrar province

The Ferrar and the Kalkarindji provinces are most chemically similar compared to other LIPs (Figure 2.6). These two provinces share many similar geochemical signatures such as the absence of a high-Ti suite as well as high SiO_2 and low MgO values. These similar geochemical signatures suggest these two provinces might have a similar origin. With this study, both provinces have now been linked to an old lithospheric enrichment process. Only slight differences in some of the trace element ratios are apparent between the Ferrar and Kalkarindji such as the Nb/La ratios of Kalkarindji (0.2 – 0.4) lie on the lower range of the Ferrar Nb/La ratios (0.2 – 0.7) (Figure 2.12c).

The Kalkarindji CFB samples have noticeably higher $^{87}Sr/^{86}Sr_i$ and $^{143}Nd/^{144}Nd_i$ than most other CFBs (Figure 2.6c). The $^{87}Sr/^{86}Sr_i$ isotopes of Kalkarindji overlap completely with those measured for the Ferrar LIP (Figure 2.6b and c) but $^{143}Nd/^{144}Nd_i$ isotopic ratios are significantly lower. The Kalkarindji CFB province has similar isotopic compositions to other CFBs (Figure 2.6d) with moderate $^{208}Pb/^{204}Pb_i$ and $^{206}Pb/^{204}Pb_i$ ratios. However, a marked difference is apparent in the $^{207}Pb/^{204}Pb$ ratios, (Figure 2.6a) which are significantly higher and plot well above the NHRL ($^{207}Pb/^{204}Pb$ = 15.7 – 15.8) and are significantly higher than the average $^{207}Pb/^{204}Pb_i$ isotopic ratios of the Ferrar CFBs.

The Kalkarindji CFB shows similarities with the Ferrar province for $^{206}Pb/^{204}Pb_i$, $^{208}Pb/^{204}Pb_i$, and $^{87}Sr/^{86}Sr_i$ isotopic ratios that could indicate the enrichment process resulted from a similar process. However, the age of the enrichment event of the mantle source of the Kalkarindji CFBs calculated in this study is much older than proposed ages for Ferrar (490 to 300 Ma; Hergt *et al.*, 1989b), which fits well with the discontinuity of the $^{207}Pb/^{204}Pb$ values of the two provinces.

Hergt *et al.* (1989b) found that simple contamination through the processes of bulk assimilation or partial melts of contaminants or even assimilation and fractional crystallization mixing models could not account for both the trace element and isotopic signatures observed for Ferrar. In addition, Molzahn *et al.* (1996) showed that the $^{187}Os/^{188}Os$, $^{87}Sr/^{86}Sr$, and the δO^{18} systematics are within the mantle ranges thereby excluding assimilation of upper and/or lower crust as the cause of the observed trace element and isotopic enrichments of the Ferrar CFB province. Brauns *et al.* (2000) suggest that the observed geochemical trends are better explained by the introduction of an enriched component into the SCLM source region prior to melting (Hergt *et al.*, 1989b; Molzahn *et al.*, 1996; Brauns *et al.*, 2000). The geochemical parallels between Kalkarindji and Ferrar CFB provinces reinforce the scenario proposed for the genesis of the Kalkarindji CFB province. The model of a SCLM enriched by subducted crustal material model proposed here for the Kalkarindji CFB province is similar to that proposed for Ferrar (Hergt *et al.*, 1989b; Molzahn *et al.*, 1996), except that enrichment was much earlier than was the case for the Ferrar province. This could indicate that the Antarctic and Australian cratons were not connected at 2.5 Ga during the age of enrichment suggested here for the Kalkarindji CFB province.

2.8. Conclusions

New geochemical and Sr, Nd, Pb isotopic data for the Kalkarindji CFB province provides novel insights into the petrogenesis of the oldest Large Igneous Province of the Phanerozoic. The continental-like geochemical characteristics of the Kalkarindji CFB province are unlikely to be the product of crustal assimilation, but rather they are the signature of an enriched mantle source for this LIP. The decoupling of the ^{238}U and ^{235}U decay systems indicates that an ancient enrichment component must be involved in the genesis of the Kalkarindji CFB province. The proposed model

here involves enrichment by an ancient subducted sediments component, which was introduced into the mantle source around 2.5 Ga. Such a scenario accounts for the lithospheric incompatible trace element signatures as well as the enriched Sr, Nd, and Pb initial isotopic values of the province. Numerical modeling provides the basis for an interpretive model source comprising a mix of < 10 % of a MORB like component and a dominant SCLM component that was enriched at 2.5 Ga. This model is able to reproduce the observed geochemical and isotopic characteristics of the Kalkarindji CFB province. The mantle source of the Kalkarindji magmas then experienced mantle warming under the stable Australian continent (as part of Gondwana) from ca. 1.2 Ga to 511 Ma. The warming was boosted and focused by the edge driven convection around the old cratonic structures of the West Australian and North Australian Cratons. Magmatism occurred by the decompression melting of the hot warm upper mantle and fertilized SCLM during extension tectonism and basin formation ca. 500 Ma, possibly the result of a large scale rotation of the continent.

2.9. References

Aitken, A. R. A. & Betts, P. G. (2009). Constraints on the Proterozoic supercontinent cycle from the structural evolution of the south-central Musgrave Province, central Australia. *Precambrian Research* **168**, 284-300.

Allègre, C. J., Treuil, M., Minster, J.-F., Minster, B. & Albarède, F. (1977). Systematic use of trace element in igneous process. *Contributions to Mineralogy and Petrology* **60**, 57-75.

Anderson, D. L. (1994). The sublithospheric mantle as the source of Continental Flood Basalts; the case against the continental lithosphere and plume head reservoirs. *Earth and Planetary Science Letters* **123**, 269-280.

Anderson, D. L., Zhang, Y.-S. & Tanimoto, T. (1992). Plume heads, continental lithosphere, flood basalts and tomography. *Geological Society, London, Special Publications* **68**, 99-124.

Arndt, N. T. & Christensen, U. (1992). The role of lithospheric mantle in continental flood volcanism: Thermal and geochemical constraints. *Journal of Geophysical Research* **97**, 10967.

Arndt, N. T., Czamanske, G. K., Wooden, J. L. & Fedorenko, V. A. (1993). Mantle and crustal contributions to continental flood volcanism. *Tectonophysics* **223**, 39-52.

Baier, J., Audétat, A. & Keppler, H. (2008). The origin of the negative niobium tantalum anomaly in subduction zone magmas. *Earth and Planetary Science Letters* **267**, 290-300.

Bas, M. J. L., Maitre, R. W. L., Streckeisen, A. & Zanettin, B. (1986). A Chemical Classification of Volcanic Rocks Based on the Total Alkali-Silica Diagram. *Journal of Petrology* **27**, 745-750.

Betts, P. G., Giles, D., Lister, G. S. & Frick, L. R. (2002). Evolution of the Australian lithosphere. *Australian Journal of Earth Sciences* **49**, 661-695.

Bohrson, W. A. & Spera, F. J. (2001). Energy-constrained open-system magmatic processes II: application of energy-constrained assimilation–fractional crystallization (EC-AFC) model to magmatic systems. *Journal of Petrology* **42**, 1019-1041.

Bond, G. C., Nickeson, P. A. & Kominz, M. A. (1984). Breakup of a supercontinent between 625 Ma and 555 Ma: new evidence and implications for continental histories. *Earth and Planetary Science Letters* **70**, 325-345.

Brauns, C. M., Hergt, J. M., Woodhead, J. D. & Maas, R. (2000). Os Isotopes and the Origin of the Tasmanian Dolerites. *Journal of Petrology* **41**, 905-918.

Briqueu, L., Bougault, H. & Joron, J. L. (1984). Quantification of Nb, Ta, Ti and V anomalies in magmas associated with subduction zones: petrogenetic implications. *Earth and Planetary Science Letters* **68**, 297-308.

Bryan, S. E. & Ernst, R. E. (2008). Revised definition of Large Igneous Provinces (LIPs). *Earth-Science Reviews* **86**, 175-202.

Bultitude, R. (1976). Flood basalts of probable early Cambrian age in northern Australia. *Volcanism in Australasia*, 1-20.

Campbell, I. H. & Griffiths, R. W. (1990). Implications of mantle plume structure for the evolution of flood basalts. *Earth and Planetary Science Letters* **99**, 79-93.

Cawood, P. A. & Korsch, R. J. (2008). Assembling Australia: Proterozoic building of a continent. *Precambrian Research* **166**, 1-35.

Chiaradia, M., Müntener, O. & Beate, B. (2011). Enriched basaltic andesites from mid-crustal fractional crystallization, recharge, and assimilation (Pilavo Volcano, Western Cordillera of Ecuador). *Journal of Petrology* **52**, 1107-1141.

Coltice, N., Bertrand, H., Rey, P., Jourdan, F., Phillips, B. R. & Ricard, Y. (2009). Global warming of the mantle beneath continents back to the Archaean. *Gondwana Research* **15**, 254-266.

Coltice, N., Phillips, B. R., Bertrand, H., Ricard, Y. & Rey, P. (2007). Global warming of the mantle at the origin of flood basalts over supercontinents. *Geology* **35**, 391.

Courtillot, V. E. & Renne, P. R. (2003). On the ages of flood basalt events. *Comptes Rendus Geoscience* **335**, 113-140.

Deckart, K., Bertrand, H. & Liégeois, J.-P. (2005). Geochemistry and Sr, Nd, Pb isotopic composition of the Central Atlantic Magmatic Province (CAMP) in Guyana and Guinea. *Lithos* **82**, 289-314.

Drüppel, K., McCready, A. J. & Stumpfl, E. F. (2009). High-K granites of the Rum Jungle Complex, N-Australia: Insights into the Late Archean crustal evolution of the North Australian Craton. *Lithos* **111**, 203-219.

Duncan, A., Erlank, A. & Marsh, J. (1984). Regional geochemistry of the Karoo igneous province. In: Erlank, A. (ed.) *Duncan, A. R., Erlank, A. J. & Marsh, J. S. (1984). Regional Geochemistry of the Karoo igneous province. In: Erlank, A. J. (ed.) Petrogenesis of the Volcanic Rocks of the Karoo Province. Special Publication of the Geological Society of South Africa, 355–388.*: Special Publication of the Geological Society of South Africa, 355–388.

Ernst, R. E. (2014). *Large igneous provinces*: Cambridge University Press.

Evins, L. Z., Jourdan, F. & Phillips, D. (2009). The Cambrian Kalkarindji Large Igneous Province: Extent and characteristics based on new 40Ar/39Ar and geochemical data. *Lithos* **110**, 294-304.

Ewart, A., Marsh, J., Milner, S., Duncan, A., Kamber, B. S. & Armstrong, R. (2004). Petrology and geochemistry of Early Cretaceous bimodal continental flood volcanism of the NW Etendeka, Namibia. Part 2: Characteristics and petrogenesis of the high-Ti latite and high-Ti and low-Ti voluminous quartz latite eruptives. *Journal of Petrology* **45**, 107-138.

Foulger, G. R. (2007). The "plate" model for the genesis of melting anomalies. *Geological Society of America Special Papers* **430**, 1-28.

Gerstenberger, H. & Haase, G. (1997). A highly effective emitter substance for mass spectrometric Pb isotope ratio determinations. *Chemical Geology* **136**, 309-312.

Ghiorso, M. S. & Sack, R. O. (1995). Chemical mass transfer in magmatic processes IV. A revised and internally consistent thermodynamic model for the interpolation and extrapolation of liquid-solid equilibria in magmatic systems at elevated temperatures and pressures. *Contributions to Mineralogy and Petrology* **119**, 197-212.

Gibson, S. A., Thompson, R. N. & Day, J. A. (2006). Timescales and mechanisms of plume–lithosphere interactions: 40Ar/39Ar geochronology and geochemistry of alkaline igneous rocks from the Paraná–Etendeka Large Igneous Province. *Earth and Planetary Science Letters* **251**, 1-17.

Glass, L. M. & Phillips, D. (2006). The Kalkarindji Continental Flood Basalt province: A new Cambrian Large Igneous Province in Australia with possible links to faunal extinctions. *Geology* **34**, 461.

Graham, S., Lambert, D. D., Shee, S. R., Smith, C. B. & Reeves, S. (1999). Re-Os isotopic evidence for Archean lithospheric mantle beneath the Kimberley block, Western Australia. *Geology* **27**, 431-434.

Green, D. & Ringwood, A. (1967). The genesis of basaltic magmas. *Contributions to Mineralogy and Petrology* **15**, 103-190.

Grey, K., Hocking, R., Stevens, M., Bagas, L., Carlsen, G., Irimies, F., Pirajno, F., Haines, P. & Apak, S. (2005). Lithostratigraphic nomenclature of the Officer Basin and correlative parts of the Paterson Orogen, Western Australia. *Geological Survey of Western Australia Report* **93**, 89.

Gurnis, M. (1988). Large-scale mantle convection and the aggregation and dispersal of supercontinents. *Nature* **332**, 695-699.

Hart, S. R. (1984). A large-scale isotope anomaly in the Southern Hemisphere mantle. *Nature* **309**, 753-757.

Heinonen, J. S., Carlson, R. W. & Luttinen, A. V. (2010). Isotopic (Sr, Nd, Pb, and Os) composition of highly magnesian dikes of Vestfjella, western Dronning Maud Land, Antarctica: A key to the origins of the Jurassic Karoo Large Igneous Province? *Chemical Geology* **277**, 227-244.

Hergt, J. M., Chappell, B. W., McCulloch, M. T., McDougall, I. & Chivas, A. R. (1989). Geochemical and isotopic constraints on the origin of the Jurassic dolerites of Tasmania. *Journal of Petrology* **30**, 841-883.

Hill, R. I. (1991). Starting plumes and continental break-up. *Earth and Planetary Science Letters* **104**, 398-416.

Hoatson, D. M., Jaireth, S. & Claoue-Long, J. (2008). *Guide to using the 1: 5 000 000 map of Australian proterozoic mafic-ultramafic magmatic events*: Geoscience Australia.

Hofmann, C., Courtillot, V., Feraud, G., Rochette, P., Yirgu, G., Ketefo, E. & Pik, R. (1997). Timing of the Ethiopian flood basalt event and implications for plume birth and global change. *Nature* **389**, 838-841.

Houseman, G. & Molnar, P. (2001). Mechanisms of lithospheric rejuvenation associated with continental orogeny. *Geological Society, London, Special Publications* **184**, 13-38.

Irvine, T. & Baragar, W. (1971). A guide to the chemical classification of the common volcanic rocks. *Canadian Journal of Earth Sciences* **8**, 523-548.

Jaques, A., O'Neill, H. S. C., Smith, C., Moon, J. & Chappell, B. (1990). Diamondiferous peridotite xenoliths from the Argyle (AK1) lamproite pipe, Western Australia. *Contributions to Mineralogy and Petrology* **104**, 255-276.

Jourdan, F., Bertrand, H., Scharer, U., Blichert-Toft, J., Feraud, G. & Kampunzu, A. B. (2007). Major and Trace Element and Sr, Nd, Hf, and Pb Isotope Compositions of the Karoo Large Igneous Province, Botswana-Zimbabwe: Lithosphere vs Mantle Plume Contribution. *Journal of Petrology* **48**, 1043-1077.

Jourdan, F., Féraud, G., Bertrand, H., Watkeys, M., Kampunzu, A. & Le Gall, B. (2006). Basement control on dyke distribution in Large Igneous Provinces: case study of the Karoo triple junction. *Earth and Planetary Science Letters* **241**, 307-322.

Jourdan, F., Hodges, K., Sell, B., Schaltegger, U., Wingate, M. T. D., Evins, L. Z., Soderlund, U., Haines, P. W., Phillips, D. & Blenkinsop, T. (2014). High-precision dating of the Kalkarindji Large Igneous Province, Australia, and synchrony with the Early-Middle Cambrian (Stage 4-5) extinction. *Geology* **42**, 543-546.

King, S. D. & Anderson, D. L. (1995). An alternative mechanism of flood basalt formation. *Earth and Planetary Science Letters* **136**, 269-279.

Li, Z. X., Zhang, L. & Powell, C. M. (1996). Positions of the East Asian cratons in the Neoproterozoic supercontinent Rodinia. *Australian Journal of Earth Sciences* **43**, 593-604.

Luguet, A., Jaques, A. L., Pearson, D. G., Smith, C. B., Bulanova, G. P., Roffey, S. L., Rayner, M. J. & Lorand, J. P. (2009). An integrated petrological, geochemical and Re–Os isotope study of peridotite xenoliths from the Argyle lamproite, Western Australia and implications for cratonic diamond occurrences. *Lithos* **112**, 1096-1108.

Marshall, P. E., Widdowson, M. & Murphy, D. T. (2016). The Giant Lavas of Kalkarindji: rubbly pāhoehoe lava in an ancient Continental Flood Basalt province. *Palaeogeography, Palaeoclimatology, Palaeoecology* **441**, 22-37.

McArthur, J. M., Howarth, R. J. & Bailey, T. R. (2001). Strontium Isotope Stratigraphy: LOWESS Version 3: Best Fit to the Marine Sr-Isotope Curve for 0–509 Ma and Accompanying Look-up Table for Deriving Numerical Age. *The Journal of Geology* **109**, 155-170.

McKenzie, D. & O'nions, R. (1983). Mantle reservoirs and ocean island basalts. *Nature* **301**, 229-231.

Menzies, M., Rogers, N., Tindle, A. & Hawkesworth, C. (1987). Metasomatic and enrichment processes in lithospheric peridotites, an effect of asthenosphere-lithosphere interaction. In: Menzies, M. & Hawkesworth, C. (eds.) *Mantle Metasomatism*: Academic Press, 313-364.

Merle, R., Marzoli, A., Bertrand, H., Reisberg, L., Verati, C., Zimmermann, C., Chiaradia, M., Bellieni, G. & Ernesto, M. (2011). 40Ar/39Ar ages and Sr–Nd–Pb–Os geochemistry of CAMP tholeiites from Western Maranhão basin (NE Brazil). *Lithos* **122**, 137-151.

Merle, R., Marzoli, A., Reisberg, L., Bertrand, H., Nemchin, A., Chiaradia, M., Callegaro, S., Jourdan, F., Bellieni, G., Kontak, D., Puffer, J. & McHone, J. G. (2013). Sr, Nd, Pb and Os Isotope Systematics of CAMP Tholeiites from Eastern North America (ENA): Evidence of a Subduction-enriched Mantle Source. *Journal of Petrology* **55**, 133-180.

Molzahn, M., Reisberg, L. & Wörner, G. (1996). Os, Sr, Nd, Pb, O isotope and trace element data from the Ferrar flood basalts, antarctica: evidence for an enriched subcontinental lithospheric source. *Earth and Planetary Science Letters* **144**, 529-545.

Mory, A. J. & Beere, G. M. (1988). *Geology of the onshore Bonaparte and Ord basins in Western Australia*: State Print. Division.

Müntener, O., Manatschal, G., Desmurs, L. & Pettke, T. (2010). Plagioclase peridotites in ocean–continent transitions: refertilized mantle domains generated by melt stagnation in the shallow mantle lithosphere. *Journal of Petrology* **51**, 255-294.

Myers, J. S., Shaw, R. D. & Tyler, I. M. (1996). Tectonic evolution of proterozoic Australia. *Tectonics* **15**, 1431-1446.

O'Reilly, S. Y. & Griffin, W. (2013). Mantle Metasomatism. In: Harlov, D. E. & Austrheim, H. (eds.) *Metasomatism and the chemical transformation of rock*: Springer, 471-533.

Olierook, H. K., Merle, R. E., Jourdan, F., Sircombe, K., Fraser, G., Timms, N. E., Nelson, G., Dadd, K. A., Kellerson, L. & Borissova, I. (2015). Age and geochemistry of magmatism on the oceanic Wallaby Plateau and implications for the opening of the Indian Ocean. *Geology* **43**, 971-974.

Olierook, H. K. H., Jourdan, F., Merle, R. E., Timms, N. E., Kusznir, N. & Muhling, J. R. (2016). Bunbury Basalt: Gondwana breakup products or earliest vestiges of the Kerguelen mantle plume? *Earth and Planetary Science Letters* **440**, 20-32.

Pearce, J. A. (1982). Trace element characteristics of lavas from destructive plate boundaries. *Andesites* **8**, 525-548.

Pin, C., Briot, D., Bassin, C. & Poitrasson, F. (1994). Concomitant separation of strontium and samarium-neodymium for isotopic analysis in silicate samples, based on specific extraction chromatography. *Analytica Chimica Acta* **298**, 209-217.

Pirajno, F. & Bagas, L. (2008). A review of Australia's Proterozoic mineral systems and genetic models. *Precambrian Research* **166**, 54-80.

Pirajno, F. & Hoatson, D. M. (2012). A review of Australia's Large Igneous Provinces and associated mineral systems: Implications for mantle dynamics through geological time. *Ore Geology Reviews* **48**, 2-54.

Plank & Langmuir. (1998). The chemical composition of subducting sediment and its consequences for the crust and mantle. *Chemical Geology* **145**.

Puffer, J. (2001). Contrasting high field strength element contents of Continental Flood Basalts from plume versus reactivated-arc sources. *Geology* **29**, 675-678.

Ringwood, A. & Green, D. (1966). An experimental investigation of the gabbro-eclogite transformation and some geophysical implications. *Tectonophysics* **3**, 383-427.

Robinson, J. A. C. & Wood, B. J. (1998). The depth of the spinel to garnet transition at the peridotite solidus. *Earth and Planetary Science Letters* **164**, 277-284.

Roex, A. P. & Reid, D. L. (1978). Geochemistry of Karroo dolerite sills in the Calvinia district, western Cape Province, South Africa. *Contributions to Mineralogy and Petrology* **66**, 351-360.

Rollinson, H. R. (1993). *Using geochemical data : evaluation, presentation, interpretation / Hugh R. Rollinson*. Harlow, Essex, England : New York: Longman Scientific & Technical ; Copublished in the U.S. with J. Wiley & Sons.

Rudnick, R. L. & Fountain, D. M. (1995). Nature and composition of the continental crust: a lower crustal perspective. *Reviews of Geophysics* **33**, 267-309.

Shaw, D. M. (1970). Trace element fractionation during anatexis. *Geochimica et Cosmochimica Acta* **34**, 237-243.

Shaw, R., Wellman, P., Gunn, P., Whitaker, A., Tarlowski, C. & Morse, M. (1995). Australian crustal elements map. *AGSO Res. Newslett* **23**, 1-3.

Sheppard, S., Tyler, I. M., Griffin, T. J. & Taylor, W. R. (1999). Palaeoproterozoic subduction-related and passive margin basalts in the Halls Creek Orogen, northwest Australia. *Australian Journal of Earth Sciences* **46**, 679-690.

Simpson, E. (1954). On the graphical representation of differentiation trends in igneous rocks. *Geological Magazine* **91**, 238-244.

Smithies, R. H., Kirkland, C. L., Korhonen, F. J., Aitken, A. R. A., Howard, H. M., Maier, W. D., Wingate, M. T. D., Quentin de Gromard, R. & Gessner, K. (2015). The Mesoproterozoic thermal evolution of the Musgrave Province in central Australia — Plume vs. the geological record. *Gondwana Research* **27**, 1419-1429.

Spera, F. J. & Bohrson, W. A. (2001). Energy-constrained open-system magmatic processes I: General model and energy-constrained assimilation and fractional crystallization (EC-AFC) formulation. *Journal of Petrology* **42**, 999-1018.

Stacey, J. t. & Kramers, J. (1975). Approximation of terrestrial lead isotope evolution by a two-stage model. *Earth and Planetary Science Letters* **26**, 207-221.

Stevens, M. & Apak, S. (1999). Empress 1 and 1A well completion report, Savory Sub-basin, Western Australia, with notes on petroleum and mineral potential. *Geological Survey of Western Australia Record* **4**.

Sun, S. s. & McDonough, W. F. (1989). Chemical and isotopic systematics of oceanic basalts: implications for mantle composition and processes. *Geological Society, London, Special Publications* **42**, 313-345.

Sweet, I., Mendum, J., Bultitude, R. & Morgan, C. (1974). The geology of the southern Victoria River region, Northern Territory. *Bur. Miner. Resour. Aust. Rep* **167**.

Tanaka, T., Togashi, S., Kamioka, H., Amakawa, H., Kagami, H., Hamamoto, T., Yuhara, M., Orihashi, Y., Yoneda, S., Shimizu, H., Kunimaru, T., Takahashi, K., Yanagi, T., Nakano, T., Fujimaki, H., Shinjo, R., Asahara, Y., Tanimizu, M. & Dragusanu, C. (2000). JNdi-1: a neodymium isotopic reference in consistency with LaJolla neodymium. *Chemical Geology* **168**, 279-281.

Taylor, S. R. & McLennan, S. M. (1985). *The continental crust: its composition and evolution*. Palo Alto, CA: Blackwell Scientific Publisher.

Todt, W., Cliff, R. A., Hanser, A. & Hofmann, A. (1996). Evaluation of a 202Pb–205Pb Double Spike for High-Precision Lead Isotope Analysis. *Earth processes: reading the isotopic code*, 429-437.

Veevers, J. (2001). Atlas of billion-year earth history of Australia and neighbours in Gondwanaland.

Verati, C., Bertrand, H. & Feraud, G. (2005). The farthest record of the Central Atlantic Magmatic Province into West Africa craton: Precise Ar/Ar dating and geochemistry of Taoudenni basin intrusives (northern Mali). *Earth and Planetary Science Letters* **235**, 391-407.

Wade, B. P., Kelsey, D. E., Hand, M. & Barovich, K. M. (2008). The Musgrave Province: Stitching north, west and south Australia. *Precambrian Research* **166**, 370-386.

Walker, F. & Poldervaart, A. (1949). Karroo dolerites of the Union of South Africa. *Geological Society of America Bulletin* **60**, 591-706.

Wang, X.-C., Wilde, S. A., Xu, B. & Pang, C.-J. (2016). Origin of arc-like continental basalts: Implications for deep-Earth fluid cycling and tectonic discrimination. *Lithos* **261**, 5-45.

White, R. S. & McKenzie, D. P. (1989). Volcanism at Rifts. *Scientific American* **261**, 62-71.

Wingate, M. T. D., Pirajno, F. & Morris, P. A. (2004). Warakurna Large Igneous Province: A new Mesoproterozoic Large Igneous Province in west-central Australia. *Geology* **32**, 105.

Zartman, R. E. & Haines, S. M. (1988). The plumbotectonic model for Pb isotopic systematics among major terrestrial reservoirs. A case for bi-directional transport. . *Geochimica et Cosmochimica Acta* **52**, 1327-1339.

Zhao, J.-x. & McCulloch, M. T. (1993). Melting of a subduction-modified continental lithospheric, mantle: Evidence from Late Proterozoic mafic dike swarms, in central Australia. *Geology* **21**, 463-466.

Zindler, A. & Hart, S. (1986). Chemical geodynamics. *Annual review of earth and planetary sciences* **14**, 493-571.

2.10. Figure Captions

Figure 2.1: (a) Sketch map showing the distribution and constituent suites of the Kalkarindji Continental Flood Basalt (CFB) province. Blue colors represent samples or well locations from the Antrim Plateau Volcanics; red colors represent samples or well locations from the Table Hill Volcanics. (b) Sketch map of the Kalkarindji CFB province. Proterozoic basins and orogens locally associated with the Kalkarindji CFB province are also displayed. Paleozoic basins labeled in italics. Modified and created after (Glass & Phillips, 2006; Hoatson *et al.*, 2008; Jourdan *et al.*, 2014b)**.** Australian crustal elements from (Shaw *et al.*, 1995; Pirajno & Bagas, 2008). Figure 2.15 schematic cross section locations marked with line A – A'.

Figure 2.2: Total alkalis-silica (TAS) diagram (Bas *et al.*, 1986) for basalts of the Kalkarindji CFB province. Alkalic-subalkalic line (Irvine & Baragar, 1971).

Figure 2.3: Major element (wt. %) vs Mg-number [100 x atomic ratio of Mg/ (Mg + Fe_2^+) with Fe_2O_3/FeO normalized to 0.15] diagrams for basalts of the Kalkarindji CFB province.

Figure 2.4: (a – c) Primitive mantle normalized incompatible trace elements patterns for the Kalkarindji Continental Flood Basalt (CFB) province. (d – f) Chondrite – normalized REE patterns for the Kalkarindji CFB Province. Diagrams c and f are the Table Hill Volcanics and the Antrim Plateau Volcanics plotted together. Normalization parameters from (Sun & McDonough, 1989). Average Indian MORB compositions from PetDB (www.earthchem.org/petdb).

Figure 2.5: **(**a) Ni (ppm) vs MgO (wt. %), (b) Co (ppm) vs MgO (wt. %), (c) Cr (ppm) vs MgO (wt. %) diagrams for basalts of the Kalkarindji CFB province. Gray band represents typical range of primitive basalts. Range expected for magmas in equilibrium with their mantle source: Ni range of 200 – 500 ppm from Allègre *et al.* (1977).

Figure 2.6: Initial (511 Ma) Sr, Nd, and Pb isotopic compositions of the Kalkarindji Continental Flood Basalt (CFB) province. In the two Pb vs Pb isotope diagrams, the Northern Hemisphere Reference Line (NHRL); (Hart, 1984) is shown. Approximate locations of mantle end – members age-corrected to 511 Ma (Zindler & Hart, 1986) are indicated for reference. Also shown are the fields of selected CFBs Karoo, Central Atlantic Magmatic Province (CAMP), Deccan, and Ferrar. All data for these CFBs are from the GEOROC database, Pb isotopic data for Ferrar are from Hergt *et al.* (1989b). The ellipsoids represent where roughly 90 % of the data clusters. Referenced CFBs age-corrected to respective time of emplacement: Karoo (183 Ma), CAMP (201 Ma), Deccan (66.5 Ma), and Ferrar (183 Ma). BSE = Bulk Silicate Earth, EMI = Enriched Mantle I, EMII = Enriched Mantle II, MORB = Mid-Ocean Ridge Basalt, DMM = Depleted MORB Mantle.

Figure 2.7: Plots of isotopic data for basalts of the Kalkarindji CFB province. (a) $^{87}Sr/^{86}Sr$ initial isotopic composition vs SiO_2 wt. %, (b) $^{206}Pb/^{204}Pb$ initial isotopic composition vs SiO_2 wt. %, (c) $^{143}Nd/^{144}Nd$ initial isotopic composition vs Sm/Nd ratio and, (d) $^{143}Nd/^{144}Nd$ initial isotopic composition vs Mg – number. All isotopic data have been age-corrected to 511 Ma.

Figure 2.8: MELTS fractional crystallization modeling curves for selected major element trends for the Kalkarindji Continental Flood Basalt. Low pressure (1kbar) anhydrous; moderate pressure (3 kbar) anhydrous; low pressure (1 kbar) hydrous (1 % H_2O); and moderate pressure (3 kbar) hydrous (1 % H_2O) calculations are displayed. A QFM+1 (Quartz – Fayalite – Magnetite) buffer was used for fO_2 (Ghiorso and Sack, 1995). [Circles represent % of fractionation at 15 % intervals]. Model completion percentages: Dry – kbar - 86 %, Dry – kbar - 81 %, Wet 1 % – kbar - 65 %, Wet 1 % – kbar - 61 %.

Figure 2.9: Diagram of mafic vs felsic index for basalts of the Kalkarindji CFB province and comparisons with the Ferrar CFB province. Mafic index calculation: [(FeO + Fe_2O_3) x 100 / (FeO + Fe_2O_3 + MgO)]; felsic index calculation: [(Na_2O + K_2O) x 100 / (Na_2O + K_2O + CaO)], after Simpson (1954). Data for the Red Hill Dolerite (part of the Tasmanian Dolerite of the larger Ferrar CFB province) from McDougall (1962).

Figure 2.10: Model isotopic ratios and trace element data for basalts of the Kalkarindji CFB province (a) Initial $^{87}Sr/^{86}Sr$ vs Sr (ppm), (b) initial $^{143}Nd/^{144}Nd$ vs Nd (ppm), (c) initial $^{206}Pb/^{204}Pb$ vs Pb (ppm), (d) initial $^{208}Pb/^{204}Pb$ vs Pb (ppm), and (e) initial $^{207}Pb/^{204}Pb$ vs Pb (ppm) diagrams with energy constrained assimilation and fractional crystallization (EC-AFC) model curves for three possible initial calculations (compositions given in Table 2.3) calculated using the code of Spera and Bohrson (2001). Small circles on curves indicate percentage of assimilated contaminant. All isotopic data has been back-calculated to 511 Ma.

Figure 2.11: Partial melting model diagrams for basalts of the Kalkarindji CFB province. Graphs (a) $(Sm/Yb)_n$ vs $(La/Sm)_n$ and (b) $(La/Yb)_n$ vs $(Eu/Yb)_n$ are non-modal partial melting model results using a garnet lherzolite (grey curve) and a spinel lherzolite (black curve) mantle source, inset graphs are zoom plots of the spinel modeled curves. Calculations made are from equations of Shaw (1970). Compositions are chondrite-normalized after Sun and McDonough (1989). Partition coefficients used in the calculations are from McKenzie and O'Nions (1983). Modal compositions, spinel lherzolite source: 55 wt. % olivine, 15 wt. % orthopyroxene, 28 wt. % clinopyroxene, and 2 wt. % spinel. Melting mode: 20 wt. % olivine, 20 wt. % orthopyroxene, 55 wt. % clinopyroxene, and 5 wt. % spinel. Modal compositions, garnet lherzolite source: 52 wt. % olivine, 33 wt. % orthopyroxene, 10 wt. % clinopyroxene, and 5 wt. % garnet. Melting mode: 16 wt. % olivine, -12 wt. % orthopyroxene, 81 wt. % clinopyroxene, and 15 wt. % garnet Jourdan *et al.* (2007a).

Figure 2.12: Selected trace ratio vs trace ratio graphs for basalts of the Kalkarindji CFB province. Plots a and b display trace element mixing calculation curves after Faure (1986). Each point along calculated curve represents 10 % mixing intervals. Abbreviations: CAMP, Central Atlantic Magmatic Province. Deccan, CAMP, Karoo, and Ferrar compositions from the GEOROC database.

Figure 2.13: Kalkarindji Continental Flood Basalt (CFB) province initial lead isotope calculation model. Calculations and figure modelled after Stacey and Kramers (1975): O = troilite lead, 4.57 Ga; $n(t_i)$: new zero cord, age t_1 (3.7 Ga), t_2 (2.5 Ga); $P(t_1)$: intercept of $n(t_1)$ and the meteoric isochron; $g(t_i)$: Stacey and Kramers (1975) single - stage growth curve; $Q(t_1)$: composition of terrestrial lead at the enrichment event, t_1 (3.7 b.y. ago); $Q(t_2)$: composition of Kalkarindji source lead at the enrichment event t_2 (2.5 b.y. ago); $K(t_1)$: growth curve for second stage for average modern lead. $K(t_2)$: growth curve of the source area for the Kalkarindji CFB province after the enrichment event.

Figure 2.14: Three component-mixing models for basalts of the Kalkarindji CFB province showing Indian MORB melts swamped by SCLM that was contaminated by an ancient, subducted, enriched component. Average Indian MORB compositions from PetDB (www.earthchem.org/petdb), SCLM composition is the BSE estimated average, isotopes from Rollinson (1993) and trace element information from the mantle estimates of Zartman and Haines (1988), enriched component are calculated isotopic data from an enrichment event at 2.5 Ga with elemental compositions taken from upper continental crust estimates of Zartman and Haines (1988). All isotope data age-corrected to 511 Ma.

Figure 2.15: Schematic presentation of the internal mantle heating geodynamic model for the generation of the Kalkarindji Continental Flood Basalt province.

Chapter 3: High Precision $^{40}Ar/^{39}Ar$ Geochronology of Large Igneous Provinces: The Tasmanian Dolerites of the Ferrar Continental Flood Basalt.

Bryant D. Ware[1], Fred Jourdan[1], Massimo Chiaradia[2]

[1]Western Australian Argon Isotope Facility, Department of Applied Geology and JdL-CMS, Curtin University, Perth, WA 6845, Australia.

[2] Section des Sciences de la Terre, University of Geneva, 13 Rue de Maraîchers, 12011, Geneva, Switzerland

3.1. Abstract

A continuing debate within the study of Large Igneous Provinces (LIPs) is just how prolonged the duration of these large scale magmatic events are. To affectively consider the capability of LIPs to induce climate changes or tectonic shifts, a solid and tight understanding of magma intrusion rate is crucial. High-precision geochronology is the means by which Continental Flood Basalt emplacement rate is constrained, and ultimately is used to unravel the role these enormous magmatic events have throughout Earths history.

With the dawn of U/Pb inductively coupled thermal ionization mass spectrometry (ID-TIMS) the duration of magmatic events are able to be constrained better than ever. However, U/Pb bearing minerals, such as zircon, are required to utilize the ID-TIMS method. Large Igneous Provinces contain primarily mafic rock types, dominated by plagioclase and pyroxene and are nearly devoid of zircon, particularly in fine grained mafic rocks. Therefore, the study of LIPs requires a method

that can utilize the abundance of minerals, such as plagioclase, and provide the precision of zircon.

This study provides the first high-precision plagioclase plateau ages for the Ferrar Province, generated using an ARGUS VI multi-collector mass spectrometer. These results provide unprecedented precision for plagioclase dating that begins to rival the precision obtained by U/Pb zircon chemical abrasion ID-TIMS data. As a comparison to single collector machines previously used for $^{40}Ar/^{39}Ar$ geochronological analyses on larger aliquots of plagioclase with a similar Ca/K ratio of ~ 30; results typically yield a precision of ± 1.5 to ± 2 Ma.

The great exposure of dykes and sills at differing stratigraphic levels throughout the Australian island state of Tasmania allow for an ideal natural laboratory to sample and conduct an intensive study of the Ferrar province, an area that had not previously been adequately utilized for geochronology. New high-precision $^{40}Ar/^{39}Ar$ plagioclase plateau ages for Tasmanian Dolerites indicate ~ 1.5 Ma of continuous magmatic activity from 184.27 ± 0.24 to 182.69 ± 0.54 Ma. The level of precision now available in plagioclase $^{40}Ar/^{39}Ar$ analyses allows high-precision results of mafic material, previously beyond the reach of zircon U/Pb, into the study of LIPs. The increased precision of results provide evidence of slightly older age spectra in the highest heating steps from the younger sills of Tasmanian Dolerites (~ 182 Ma). These older ages may indicate inheritance of plagioclase crystals from slightly older magmatism entrained into younger magmatic pulses by exploiting pre-existing conduits.

Numerical diffusion models, calculated for a theoretical age spectrum resulting from two slightly different plagioclase ages, provide an excellent match for measured data. The new results presented in this study from Tasmanian Dolerites demonstrate

the capability of and importance in employing different high-precision methods to achieve a complete understanding of LIP magmatic systems.

3.2. Introduction

Large Igneous Provinces (LIPs) are voluminous accumulations of magma thought to be emplaced during a relatively short period of time, indicating significant geodynamic mass fluxes (Hofmann *et al.*, 1997; Courtillot & Renne, 2003). Due to their immense size and geologically short emplacement, scientists have suggested these provinces constitute key events during Earth's history, such as linking the emplacement of LIPs to continental break ups and the cause of biotic turnovers (e.g. Courtillot & Renne, 2003; White & Saunders, 2005; Schoene *et al.*, 2010; Burgess *et al.*, 2015; Schoene *et al.*, 2015; Ernst & Youbi, 2017). To adequately evaluate and address the role of LIPs throughout Earth's history a thorough understanding of the onset, peak, and waning stages of LIP magmatism is vital. Therefore, the importance of pushing the boundary in precision for geochronological analyses becomes most important to meticulously unravel the complex evolution of these magmatic systems.

In this study, plagioclase $^{40}Ar/^{39}Ar$ was conducted on samples from thick dolerite sills and dykes of Tasmania, Australia. The Tasmanian Dolerites have been geographically and geochemically linked to the Ferrar Continental Flood Basalt (CFB) province in Antarctica. Tasmania makes up the eastern most extremity of the Ferrar CFB Province. Excellent exposure throughout Tasmania allows for a comprehensive regional collection of samples for high precision geochronological and geochemical analyses. The accessibility of high precision geochronology beyond the use of zircon provides unprecedented insights into the duration and internal plumbing of extensive dyke and sill networks.

3.3. Geologic Setting and Previous Results

3.3.1. The Tasmanian Dolerites and the Ferrar CFB province

In the Australian state of Tasmania extensive intrusions of Ferrar type tholeiitic magma, into Permian and Triassic rocks of the Parmeener Supergroup, are exposed over approximately 30,000 km² of the island (Figure 3.1) (Edwards, 1942a; Edwards, 1942b; McDougall, 1962; Hergt *et al.*, 1989b). The Parmeener Supergroup is tilted in some places by as much as 10° typically caused by faulting or the intrusion of dolerite (Edwards, 1942a; Edwards, 1942b). Dolerite took the form of dykes when intruded into the folded basement rock (small volume of the total dolerite expressions), and the form of sills (often times of great volumes) when intruded along bedding planes and unconformities of the relatively unfolded Parmeener Supergroup (Edwards, 1942a; Edwards, 1942b; McDougall, 1962). The dolerites display a sharp contact with sedimentary rocks. Chilled margins, containing only a few percent of microphenocrysts, are developed along the contacts with sediments (Edwards, 1942a; Edwards, 1942b; McDougall, 1962). Grain size steadily increases inward away from the dense extremely fine grained contact zones to a coarse ophitic texture and in some cases to a granophyre zone in the center of dykes (McDougall, 1962).

The Tasmanian Dolerites are linked to the Ferrar CFB province that is exposed over 3000 km along the Transantarctic Mountains in Antarctica (Figure 3.2). Exposures of Ferrar, although primarily occur in Antarctica and Tasmania, potentially are apparent in portions of New Zealand and the Australian state of Victoria (Hergt *et al.*, 1989a; Hergt *et al.*, 1989b; Molzahn *et al.*, 1996; Hergt & Brauns, 2001; Elliot & Fleming, 2004; Elliot & Fleming, 2008; Burgess *et al.*, 2015). Magmas erupted as basalts (Kirkpatrick Basalt in South Victoria Land), emplaced as shallow intrusive rocks (Ferrar Dolerites in the Central Antarctic Mountains and the Tasmanian

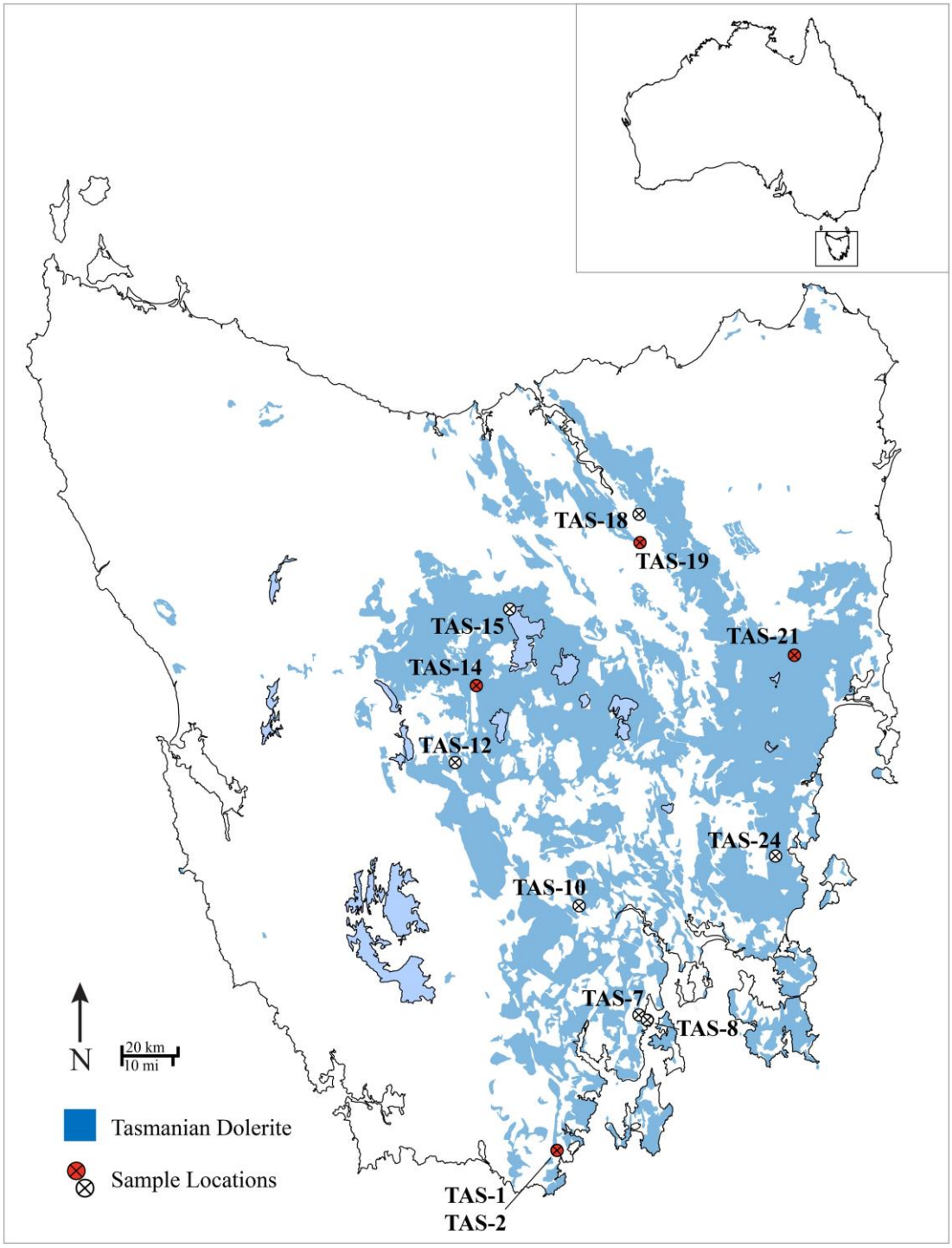

Figure 3.1: Outcrop map of the Tasmanian Dolerites. Sample locations are represented in white dots while the samples chosen for $^{40}Ar/^{39}Ar$ geochronology analyses are represented in red.

Dolerites) as dykes and sills, and as a large layered mafic intrusion (Dufek layered mafic intrusion) (Figure 3.2) (Compston *et al.*, 1968; Hergt *et al.*, 1989a; Hergt *et al.*, 1989b; Heimann *et al.*, 1994; Minor & Mukasa, 1997; Elliot & Fleming, 2004; McClintock & White, 2005; Faure & Mensing, 2011).

3.3.2. Ferrar Geochemistry

Geochemically, Ferrar Province tholeiitic dolerite is characterized by high SiO_2, CaO, and Al_2O_3 and low FeO, TiO_2, Na_2O, K_2O and P_2O_5 content with relatively low MgO (Edwards, 1942a; Edwards, 1942b; McDougall, 1962; Hergt *et al.*, 1989a; Hergt *et al.*, 1989b; Molzahn *et al.*, 1996; Hergt & Brauns, 2001; Elliot & Fleming, 2004). Although the major element compositions are similar to other fractionated tholeiitic basalts, minor, trace, and isotope chemical characteristics are much more analogous to continental signatures, particularly $^{87}Sr/^{86}Sr$ (Hergt *et al.*, 1989b; Molzahn *et al.*, 1996). These unique characteristics led to the discovery of the relationship between the dolerites of Tasmania and the Antarctica extent of the Ferrar CFB province (Edwards, 1942a; Edwards, 1942b; McDougall, 1962; Compston *et al.*, 1968; Hergt *et al.*, 1989b).

Previous results of the K/Pb, Th/K, U/K ratios, low-Ti, and isotope compositions of the Tasmanian Dolerites have suggested a preservation of a mantle/crustal component interaction (Hergt *et al.*, 1989b; Hergt & Brauns, 2001). However, Os signatures indicate there has been no contamination of the continental crust. A strikingly homogeneous geochemical signature is displayed across the whole Ferrar province.

3.3.3. Ferrar Geochronology

The geochronological library of reliable high precision data for the Ferrar Province is largely lacking, with no comprehensive geochronological investigation into the Tasmanian Dolerite portion. Ferrar dolerites from Antarctica have yielded only three $^{40}Ar/^{39}Ar$ plagioclase plateau ages ranging from 180.3 ± 1.0 Ma to 182.5 ± 1.0 Ma (recalculated from Fleming et al., 1997 using the constants and standard age from Renne et al., 2011). However, these previous argon geochronological investigations

were measured using the heterogeneous MMhb hornblende standards (Lee *et al.*, 1991; Onstott *et al.*, 1991; Baksi *et al.*, 1996; Villa *et al.*, 1996; Renne *et al.*, 1998; Spell & McDougall, 2003). The first high precision ages for the Ferrar Province come from U/Pb analyses of zircon and baddeleyite crystals from the Dufek layered mafic

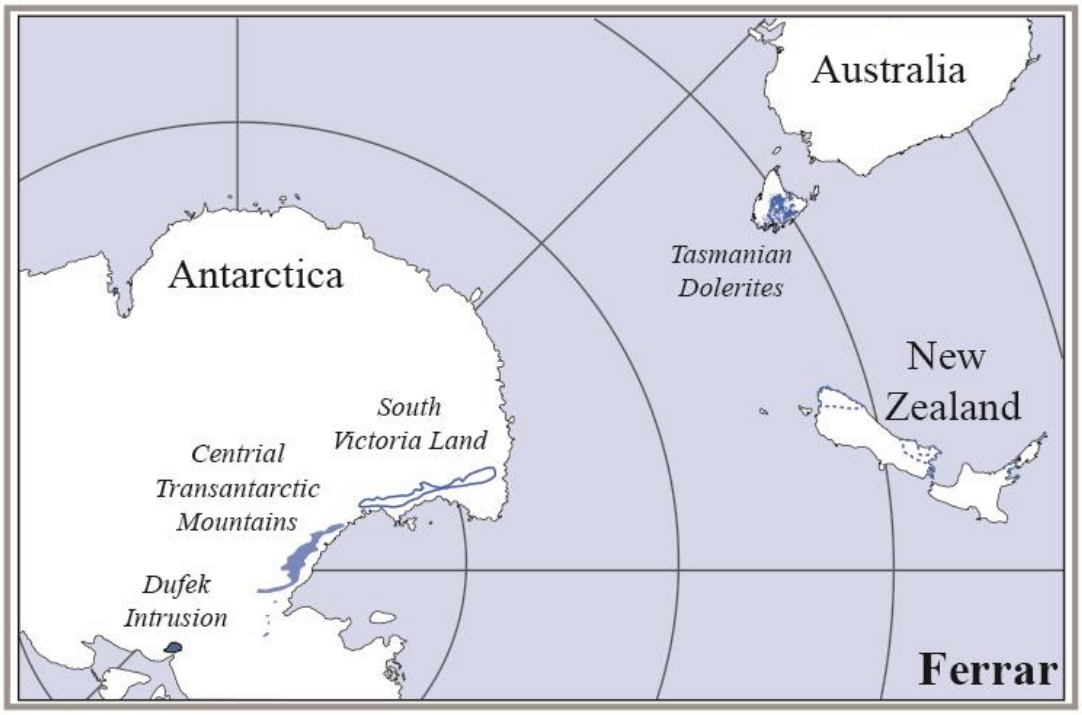

Figure 3.2: Present day location of the constituents of the Ferrar Continental Flood Basalt Province. Locations created and modified from Bryan and Ernst (2008) and Burgess *et al.* (2015).

intrusion (183.9 ± 0.3 Ma; Minor and Mukasa, 1997) and two dolerite sills (183.6 ± 1.0 Ma; Encarnación *et al.*, 1996). Only two Tasmanian Dolerite studies have been undertaken and published thus far, providing 177 ± 5 Ma from a Re/Os isochron of 7 samples from across Tasmania (Brauns *et al.*, 2000) and a K/Ar rough estimate of 174 ± 4 Ma (Schmidt & McDougall, 1977). Recently the geochronological library of reliable isotopic ages from Ferrar was greatly increased by the addition of U/Pb CA-TIMS ages from 20 thick lavas and dolerite/granophyric sills with ages ranging from 182.85 ± 0.40 to 182.43 ± 0.20 Ma (Burgess *et al.*, 2015).

3.4. Sample Selection and Analytical Methods

In this study, the Tasmanian sample suite is entirely comprised of dolerites collected from dykes and sills exposed extensively across the island state Tasmania (Figure 3.1). Twenty-four samples were collected in total of which 10 were selected for major, trace, and isotope geochemistry analyses. Eleven samples were processed and picked for plagioclase $^{39}Ar/^{40}Ar$ geochronology analyses form which four samples returned plateau ages.

3.4.1. $^{40}Ar/^{39}Ar$ Geochronology

Plagioclase was separated from the 150 to 215 μm size fraction using a Frantz isodynamic magnetic separator. The non-magnetic fraction was handpicked grain-by-grain under a binocular stereomicroscope. Once picked the plagioclase crystals were leached using diluted HF (2N) for 5 minutes and thoroughly rinsed in distilled water. The samples were then loaded into separated discs and irradiated for 40 hours across two irradiations (TAS-14 in one irradiation and TAS-01, TAS-19, and TAS-21 together in another). The irradiation discs included a series of fully intercalibrated FCs (Jourdan & Renne, 2007) (TAS-14) and GA1550 (Renne *et al.*, 1998) (TAS-01, TAS-19, and TAS-21) standards, for which ages of 28.294 Ma (± 0.13 %) and 99.74 Ma (± 0.10 %) (Renne *et al.*, 2011a) were used. Samples were irradiated in the central position of Cadmium-Lined In-Core Irradiation Tubes (Cd shielded to minimize undesirable nuclear interference reactions) at the TRIGA Reactor at Oregon State University (USA).

$^{40}Ar/^{39}Ar$ geochronological analyses were conducted at Curtin University within the Western Australian Argon Isotope Facility. The mineral populations were analyzed using a Thermofisher© low volume (600 cc) ARGUS VI mass spectrometer (Phillips & Matchan, 2013). The plagioclase crystals were analyzed as populations

step-heated by a continuous 100 W PhotonMachine© CO_2 (IR, 10.4 μm) laser that was fired and rastered onto the sample populations for 60 seconds. Analyses of the standards were fused in a single step. Sample TAS-14 was in irradiation 21 with a mean J-value computed as 0.010502 ± 0.055 % (1σ). Samples TAS-01, TAS-19, and TAS-21 were irradiated in irradiation 22 with average J-values computed to be 0.010589 ± 0.06 % (1σ) (TAS-01 and TAS-21) and 0.0106317 ± 0.06 % (1σ) (TAS-19). Mass discrimination was monitored regularly through the analysis using an automated air pipette and provided mean values of 0.992279 ± 0.08 % (TAS-14), 0.992802 ± 0.06 % (TAS-01 and TAS-21), and 0.992804 ± 0.05 % (TAS-19) per dalton (atomic mass unit) relative to an air ratio of 298.56 ± 0.31 (Lee *et al.*, 2006b; Mark *et al.*, 2011).

During analyses the gas was purified through an extra low-volume stainless steel extraction line of 240cc, using two SAES AP10 and one GP50 getter. The multi-collection Ar isotope measurements were made with four faraday cups (three 10^{12} ohm resistors for masses ^{40}Ar, ^{38}Ar, ^{37}Ar and a 10^{13} ohm resistor for mass ^{39}Ar, thus providing a less noise/signal ratio) as well as a low background compact discrete dynode ion counter to measure ^{36}Ar. The relative abundance of each mass was measured simultaneously using 10 cycles of peak hopping with 33 seconds of integration time for each mass. Detectors were calibrated to each other electronically followed by air shot beam signal calibrations. Raw data were processed using the ArArCALC software (Koppers, 2002). For all analyses the interfering isotopes were corrected, with 1 sigma errors, with ($^{39}Ar/^{37}Ar$) Ca = 6.95×10^{-4} (± 1.3 %), ($^{36}Ar/^{37}Ar$) Ca = 2.65×10^{-4} (± 0.84 %) and ($^{40}Ar/^{39}Ar$) K = 7.30×10^{-4} (± 12.4 %) correction factors (Renne, 2014). Ages were calculated using the decay constants recommended by Koppers (2002) (Table 3.1). Results were also calculated using a value of

0.00082636 ± 0.11 % (Renne & Norman, 2001) to correct for ^{37}Ar (Ca) produced in the reactor with a half-life of 35 days (these results are only presented in Appendix E) for comparison. Blanks were monitored every 3 to 4 steps.

Plateau ages were determined from at least 70 % of the ^{39}Ar released, distributed over a minimum of 3 consecutive steps agreeing at 95 % confidence level, where results must satisfy a minimum probability of fit (P) of 0.05. Plateau ages are calculated using the mean of all plateau steps, each weighted by the inverse variance of their individual analytical error and then listed at the 2σ level. Uncertainties quoted do not include analytical and J-value errors.

3.4.2. Major and trace element compositions

For this study, all major and trace element analyses were conducted by Genalysis Laboratory Services Pty Ltd in Perth (Australia). Ten samples were crushed with a rigorously cleaned steel hydraulic press. Rock chips for further processing were hand chosen based on how fresh they appeared, avoiding weathered and saw cut surfaces. These chips were then crushed into a powder using an agate mortar and pestle. Major element analyses were performed by X-ray fluorescence (XRF) on fused discs produced by a lithium borate fusion technique in platinum crucibles. Trace element analyses underwent a lithium metaborate/tetraborate fusion and were analyzed by the inductively coupled plasma mass spectrometry (ICP-MS) method. Inductively Coupled Plasma Optical (Atomic) Emission Spectrometry (ICP-OES) was utilized to analyze Sc and V. These two methods, ICP-MS and ICP-OES, were also utilized for the remainder of elements; however, a four acid digestion was implemented. To track and check the accuracy and reproducibility of the instruments two internal standards (SARM1 and SY-4) were used for the major element analyses and four internal standards (SY-4, OREAS25a, OREAS25b and GBW07105) were utilized for the trace

element analyses (standard analytical results can be found in Appendix C; Table C2). In major and trace element analyses the precision was better than 5 %, at the 95 % confidence level, for all elements except V and Zr, which proved to have a precision greater than 5 % for the respective standards. One analysis was duplicated (TAS-12) as a check and three control blanks along with two acid blanks were performed for each sample undergoing full trace element analysis.

3.4.3. Sr-Nd-Pb isotope compositions

Sr, Nd, and Pb isotope analyses were conducted at the Department of Earth Sciences, University of Geneva (Switzerland). As with major and trace element analyses, the ten samples chosen for Sr, Nd, and Pb isotope analyses were crushed into small chips using a rigorously cleaned hydraulic press. Once the chips were rinsed with distilled H_2O a selection of clean non-weathered rock chips with no saw marked surfaces were carefully picked under a binocular microscope. An agate mortar and pestle was used to powder 500 mg of material from the selected clean chips. To dissolve the sample for analyses, ca. 150 mg of powder were attacked during 7 days in Savillex® Teflon vials using 4 ml of concentrated HF and 1 ml of HNO3 15 M, at a temperature of 140 °C and with the help of ultrasonication for 30 min twice a day (see also Béguelin *et al.*, 2015). Subsequently, samples were dried and re-dissolved for 3 days (also with 30 min ultrasonication twice a day) in 3 ml of HNO3 15 M and dried again. Sr, Nd and Pb were purified from the sample matrix using cascade columns with Sr-Spec, TRU-Spec and Ln-Spec resins according to a protocol modified after Pin *et al.* (1994). Finally, the separates were re-dissolved in 2 % HNO_3 solutions and ratios were measured using a Thermofisher© Neptune PLUS Multi-Collector ICP-MS on Faraday cups in static mode using the virtual amplifier mode following methods described by Chiaradia *et al.* (2011). Internal fractionation was corrected using an

$^{88}Sr/^{86}Sr$ value of 8.375209 with an external fractionation correction applied by normalizing the measured SRM987 values to an accepted value of 0.710248 (McArthur *et al.*, 2001). The long-term external reproducibility of the SRM987 standard was 10 ppm. Nd was corrected for internal fractionation using a $^{146}Nd/^{144}Nd$ value of 0.7219. External fractionation was corrected by normalizing to a nominal JNdi-1 value of 0.512115 (Tanaka *et al.*, 2000) with a reproducibility of 10 ppm. Pb isotope ratios were corrected for mass fractionation using a $^{203}T1/^{205}T1$ ratio of 0.418922 (the samples were spiked with a T1 standard solution) for the three Pb isotope systems. The long-term external reproducibility on the measurements of the SRM981 standard for Pb are: 0.0048 % for $^{206}Pb/^{204}Pb$, 0.0049 % for $^{207}Pb/^{204}Pb$, 0.0062 % for $^{208}Pb/^{204}Pb$. Due to a systematic discrepancy between the measured values with the proposed standard values for all of the above standards, further corrections for external fractionation were conducted using a value of - 0.039 ‰ ($^{206}Pb/^{204}Pb$), + 0.047 ‰ ($^{207}Pb/^{204}Pb$), and + 0.5 ‰ ($^{208}Pb/^{204}Pb$) atomic mass units. ^{144}Sm interference on ^{144}Nd was monitored with mass ^{147}Sm and then corrected using a $^{144}Sm/^{147}Sm$ value of 0.206700. The ^{204}Hg interference on ^{204}Pb was corrected for with the monitoring of ^{202}Hg.

3.5. Petrography

Mineralogy for all Tasmanian Dolerite samples is remarkably similar. Plagioclase and clinopyroxene (augite and pigeonite) dominate the mineralogy with varying amounts of Fe-Ti oxide minerals (primarily ilmenite) and minor degrees of secondary biotite and hornblende alteration (Figure 3.3). Dolerite sills and dykes are characterized by a seriate and ophitic texture with crystals ranging from less than a millimeter to up to 4 millimeters long, with only plagioclase and clinopyroxene crystals obtaining the maximum length recorded. Plagioclase are typically euhedral

Sample	Coordinates Zone 55 (UTM)	Mineral	Integrated Age (Ma)	Plateau (Ma)	Total ^{39}Ar Released (%,n)	MSWD	P	Isochron Age (Ma)	Spreading Factor (%)	^{40}Ar/^{36}Ar Intercept	MSWD	P
TAS-01	5183731.9 N 490325.5 E	Plagioclase	183.50 ± 0.38	**183.52 ± 0.37 [0.45]**	100.00 (26)	0.91	0.59	183.56 ± 0.56	134.9	297.7 ± 12.6	0.95	0.53
TAS-14	5345402.7 N 461359.1 E	Plagioclase	183.15 ± 0.48	**182.91 ± 0.52 [0.59]**	79.75 (13)	1.03	0.42	183.12 ± 1.03	26.0	283.5 ± 7.0	1.41	0.16
TAS-19	5397933.9 N 519877.5 E	Plagioclase	184.98 ± 0.24	**184.27 ± 0.24 [0.33]**	72.16 (17)	0.91	0.56	183.91 ± 0.87	33.0	312.0 ± 30.0	0.91	0.55
TAS-21	5355722.9 N 572504.9 E	Plagioclase	183.82 ± 0.30	**183.98 ± 0.33 [0.39]**	84.49 (16)	1.45	0.11	177.17 ± 4.87	2.5	424.1 ± 95.4	0.74	0.74

Table 3.1: ^{40}Ar/^{39}Ar Geochronology of Plagioclase Crystals from the Tasmanian Dolerites, Ferrar CFB Province. Ages in bold indicate preferred ages for interpretation. The calculated J values relative to an age of FCs of 28.294 ± 0.13 % Ma (Turner et al., 1971) [TAS-01, TAS-19, TAS-21] and relative to an age of GA1550 of 99.74 ± 0.10 % Ma [TAS-14]. MSWD and probability (P), percentage of ^{39}Ar degassed used in the plateau calculation, number of analyses included in the isochron, and ^{40}Ar/^{36}Ar intercept are indicated. Analytical uncertainties on the ages are quoted at 2 sigma (2σ) confidence levels and at 1σ for the ^{40}Ar/^{36}Ar intercept. Brackets include all sources of uncertainty that is required when comparing different systems.

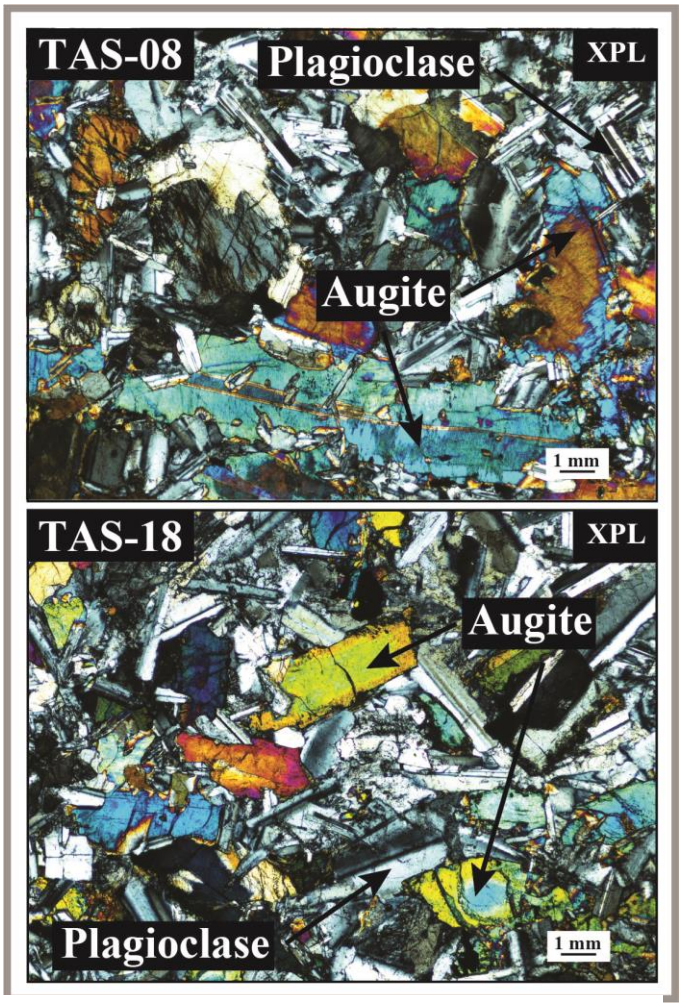

Figure 3.3: Photomicrographs of select samples from the Tasmanian Dolerite.

columnar to prismatic in crystals, displaying well-developed multiple and Carlsbad twinning. Sericite alteration affects all samples to a varying degree (e.g. roughly 40 % of crystals affected in sample TAS-21, although minor; whereas around 70 % of plagioclase crystals affected in sample TAS-07, primarily in cracks) (Figure 3.3). Clinopyroxene is predominantly augite (~ 70 % on average in all samples) with some pigeonite (approximately 30 %). The clinopyroxene crystals display a vast range of habit from anhedral to euhedral depending on the sample. Simple twinning is apparent in clinopyroxene, with some samples displaying a slight zoning from core to rim, evident by differing degree of birefringence. Pyroxene grains are primarily unaltered fresh crystals, minor degrees of alterations if present occurs along edges and cracks. A small percentage, less than 10 %, of pyroxene (primarily pigeonite) crystals display exsolution lamellae.

3.6. Geochronology

The $^{40}Ar/^{39}Ar$ geochronological data from this study can be found in Table 3.1. New whole rock major and trace element data is presented in Table 3.2 with Sr-Nd-Pb isotopic results presented in Table 3.3.

3.6.1. $^{40}Ar/^{39}Ar$ geochronology

Four samples (TAS-01, TAS-14, TAS-19, and TAS, 21) yielded statistically significant plagioclase $^{40}Ar/^{39}Ar$ plateau ages (Figure 3.4; Table 3.1). Plateau ages for these four samples ranged from 182.69 ± 0.54 to 184.27 ± 0.24 Ma with an MSWD range from 0.45 – 1.45 and probabilities that ranged from 0.11 – 0.98. The plateaus are defined by a 71 – 84 % of cumulative ^{39}Ar released (Table 3.1). The age spectra for samples TAS-01, TAS-19, and TAS-21 display minor disturbances in the first 5 to

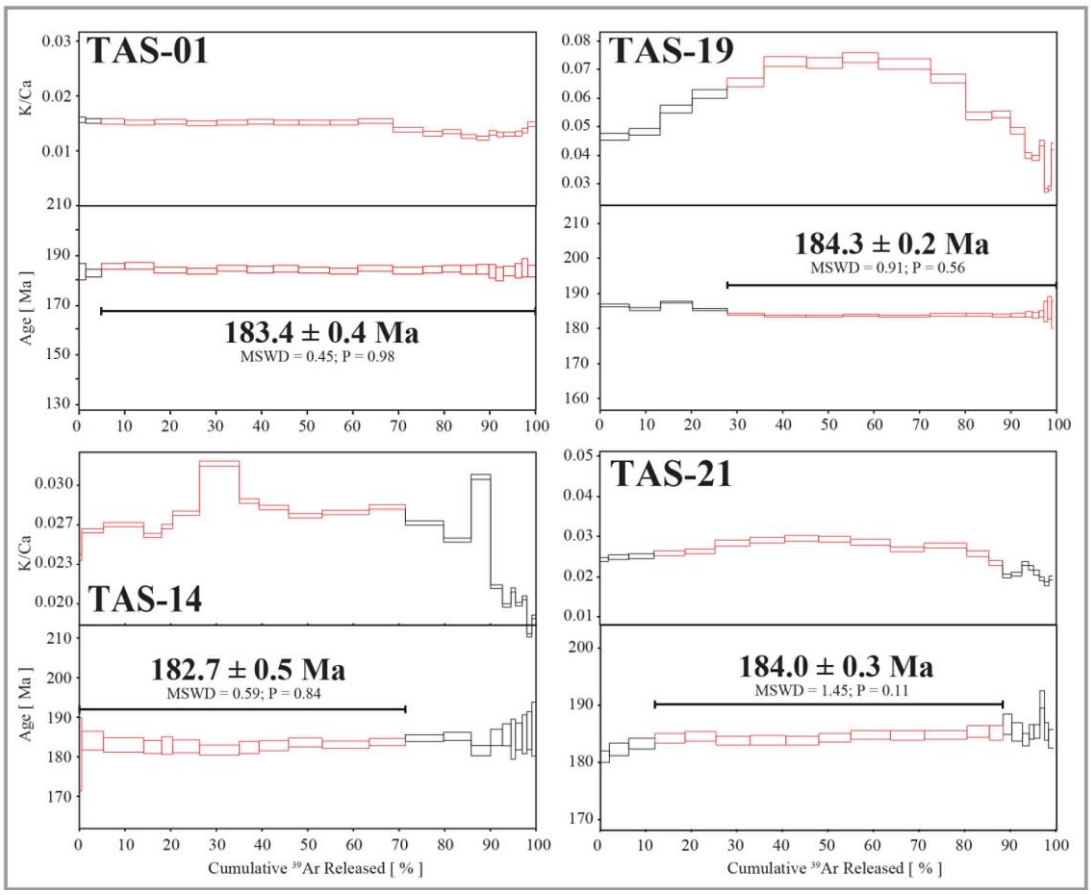

Figure 3.4: $^{40}Ar/^{39}Ar$ apparent age and related K/Ca ratio spectra for pyroxene and plagioclase separates plotted against the cumulative percentage of ^{39}Ar released. Mean squared weighted deviation (MSWD) and probability of fit (P) is indicated. Errors on plateau ages are quoted at 2σ and do not include systematic errors (i.e. uncertainties on the age of the monitor and on the decay constant).

25 % of ^{39}Ar released before reaching the plateau requirements. Sample TAS-14 display disturbances primarily to slightly older results after 70 % of ^{39}Ar released. Sample TAS-21, on top of displaying a slight age spectra disturbance within the first 12 % of ^{39}Ar released, also has a disturbance after about 88 % of ^{39}Ar released. Due to a cluster of the data close to the $^{39}Ar/^{40}Ar$ axis, the samples yielded poorly defined initial $^{40}Ar/^{36}Ar$ values (Table 3.1) preventing the determination of statistically meaningful isochron ages. Therefore, plateau ages were calculated using the air ratio of 298.56 ± 0.31 of (Lee *et al.*, 2006b; Mark *et al.*, 2011).

The K/Ca mean ratio values for these samples range from 0.017 to 0.031 in three of the four samples and a slightly higher range of 0.027 to 0.073 for TAS-19 (Figure 3.4). The shape of the K/Ca spectra varies from sample to sample, with TAS-

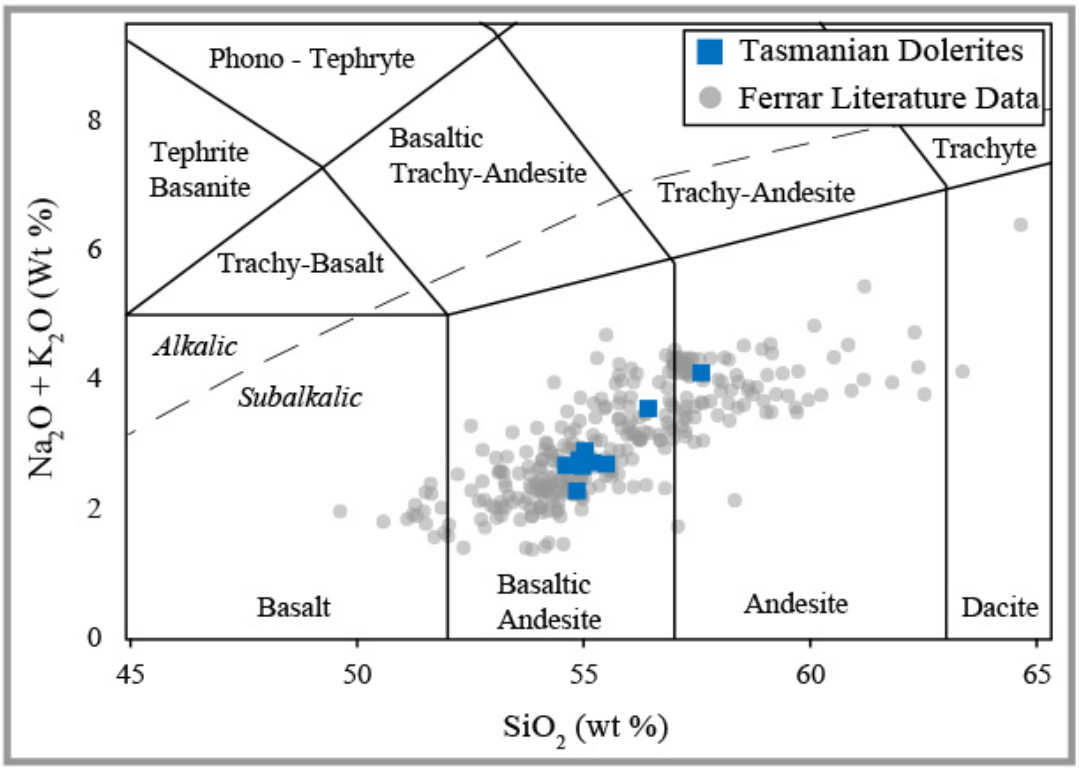

Figure 3.5: Total alkalis-silica (TAS) Diagram (Bas *et al.*, 1986). Alkalic-subalkalic line from Irvine and Baragar (1971). All major element data for the Ferrar CFBs are from the GEOROC database.

01 having a flat spectrum until greater than to 70 % ^{39}Ar released where the ratios display a concave dip (Figure 3.4). TAS-19 and TAS-21 both display convex K/Ca

spectra with low ratios in the low temperature heating step, high ratios in the middle heating steps, before decreasing as well as display more disturbance in the highest heating steps (Figure 3.4). TAS-14 contains a slightly disturbed K/Ca spectrum with two steps jumping out of the trend at 30 and 90 % of ^{39}Ar released. TAS-19 has the greatest precision of these Tasmanian Dolerite samples (± 0.24 Ma) most likely due to

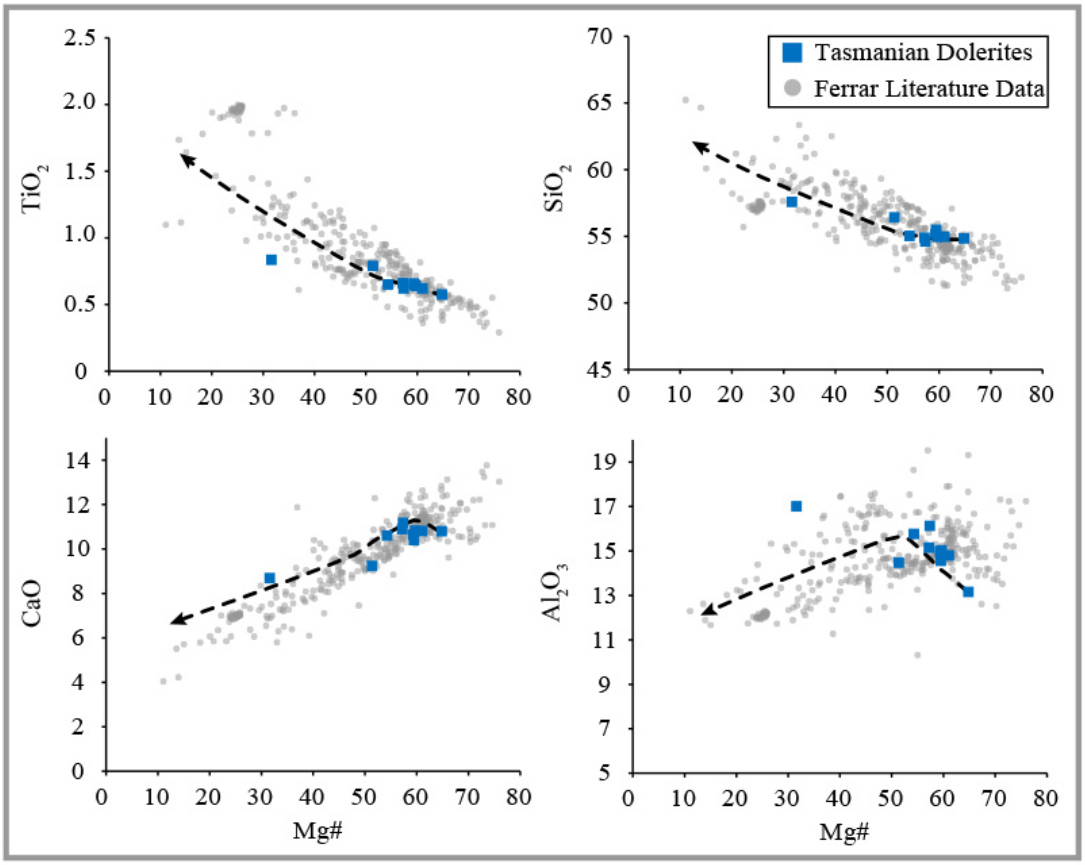

Figure 3.6: Major element (wt. %) vs. Mg-number [100 x atomic ratio of Mg/ (Mg + Fe_2^+) with Fe_2O_3/FeO normalized to 0.15] diagrams. MELTS fractional crystallization modeling curves plotted as well. Moderate pressure (3 kbar) anhydrous (0 % H_2O) calculations are displayed. A QFM (Quartz – Fayalite – Magnetite) buffer was used for fO_2 (Ghiorso and Sack, 1995). All major element data for the Ferrar CFBs are from the GEOROC database.

the higher K contents (average K/Ca ratio of 0.05) compared with other samples (Figure 3.4).

3.7. Geochemistry

3.7.1. Major elements

Samples analyzed for major element geochemistry display subalkalic (tholeiitic) basaltic andesite bulk rock compositions, with the exception of one sample (TAS-07) that falls within the andesite field using a total alkali silica (TAS) diagram (Bas *et al.*, 1986) (Figure 3.5). The results of the Tasmanian dolerites from this study plot within the range of data available for the rest of the Ferrar CFB province. As with all other Ferrar tholeiites, samples from this study are classified as low-Ti with TiO_2 contents < 2 weight percent (wt. %). The major element patterns display a negative covariance in regards to Mg # with TiO_2, FeO_{total} (FeO_t), Na_2O, K_2O, P_2O_5, and MnO and a positive co-variation with Al_2O_3 and CaO wt. %'s (Figure 3.6; Table 3.2).

3.7.2. Trace elements

The Tasmanian Dolerites display an enrichment in light rare earth elements (LREEs) compared to heavy rare earth elements (HREEs) normalized to chondrite (Sun & McDonough, 1989) (Figure 3.7). The REE patterns have a negative slope for the LREEs and a near horizontal slope for the HREEs. A minor negative Eu anomaly is apparent for the dolerites, likely representing plagioclase fractionation. As with the major elements, REE results for all Tasmanian Dolerites from this study fall within the range of the Ferrar CFBs. Trace elements display pronounced negative Nb and Ta (all samples except the most enriched sample; TAS-07) anomalies as well as a positive Pb anomaly (normalized to premitive mantle; Sun & McDonough, 1989) consistent with the Ferrar province (Figure 3.7). Two samples display a slightly higher enrichment in REEs and incompatible trace elements from the rest of the suite. These two samples are the most evolved of the samples analyzed, with the highest SiO_2 and lowest MgO wt. % (Table 3.2).

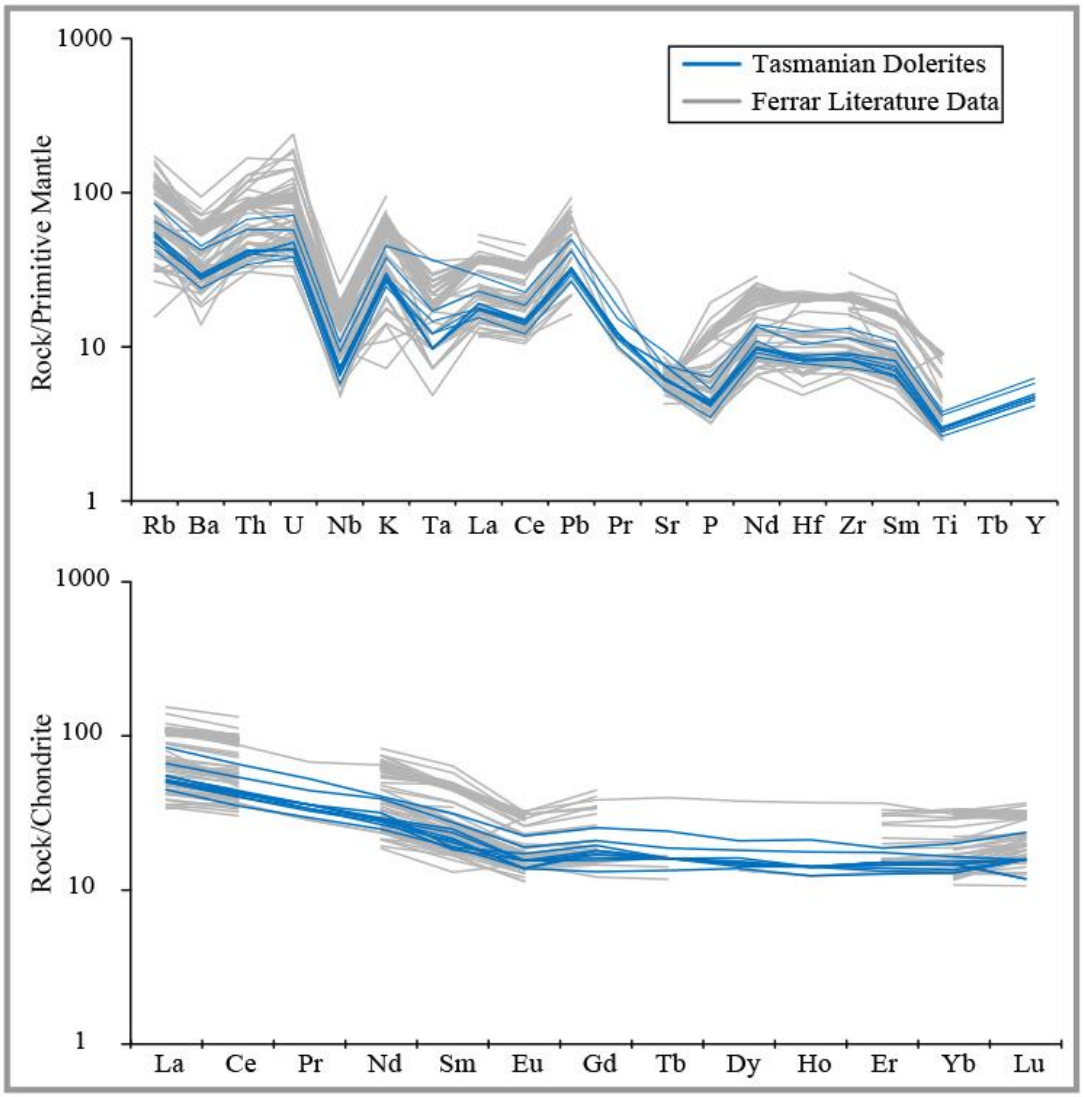

Figure 3.7: Primitive mantle-normalized incompatible trace elements patterns and Chondrite-normalized REE patterns for the Tasmanian Dolerites. Normalization parameters from Sun and McDonough (1989). All trace element data for the Ferrar CFBs are from the GEOROC database.

3.7.3. Isotopes

Sr-Nd-Pb isotope analyses were conducted on nine samples from the collected Tasmanian Dolerites. Measured isotopic ratios were corrected from the in-situ decay of the parent elements using an average age of 183 Ma (high precision $^{40}Ar/^{39}Ar$ plagioclase ages presented above) and parent/daughter ratios derived from the elemental concentrations measured by ICP-MS (Table 3.3). Results show little variation in Nd and Pb ratios to more variable Sr isotopic ratios ($^{143}Nd/^{144}N_i$ = 0.51177 – 0.51187; $^{87}Sr/^{86}Sr_i$ = 0.7092 – 0.7103; $^{206}Pb/^{204}Pb_i$ = 18.178 – 18.85; $^{207}Pb/^{204}Pb_i$ =

15.67 – 15.81; $^{208}Pb/^{204}Pb_i$ = 38.20 – 38.89) (Figure 3.8). As this suite of samples was collected across the whole island of Tasmania, results provide a regional representative collection of Tasmanian Dolerites. Isotope ratios for results presented here fall within the range previously established for the Ferrar CFBs (Hergt *et al.*, 1989b; Molzahn *et al.*, 1996) (Figure 3.8).

Neodymium isotopic ratios display nearly a horizontal trend from a slight variation for a larger Sr isotope ratio variation (Figure 3.8). Lead isotope data plot above the Northern Hemisphere Reference Line (NHRL) (Figure 3.8b and c) for both $^{208}Pb/^{204}Pb_i$ and $^{207}Pb/^{204}Pb_i$ ratios. In diagrams of $^{208}Pb/^{204}Pb_i$ vs. $^{206}Pb/^{204}Pb_i$ the ratios plot parallel and near to the NHRL (Figure 3.8b). However, in $^{207}Pb/^{204}Pb_i$ vs. $^{206}Pb/^{204}Pb_i$ diagrams, Tasmanian Dolerite data plot well above the NHRL (Figure 3.8c). The Tasmanian Dolerites are much less variable in $^{206}Pb/^{204}Pb_i$ ratios than other samples from the Ferrar CFBs (Figure 3.8). One sample, TAS-10, has much lower Sr isotopic ratios (0.7091) compared to the rest of the samples suite (~ 0.7108). These low Sr isotopes for this suite of Tasmanian Dolerite samples still plot within the range of results from Ferrar (0.7083 – 0.7112; Hergt *et al.*, 1989a; Molzahn *et al.*, 1996). Elements Rb, Sr, U, Th, and Pb are more susceptible to alteration due to being generally more mobile elements, compared with Sm and Nd, in standard igneous processes.

The spread in Sr values, particularly from sample TAS-10, could therefore represent a small degree of alteration within this sample at least. However, Pb isotope variation within these Tasmanian samples is minimal, indicating no mobility of Pb within this system. Coupling these observations with all samples having less than 2 % loss on ignition (LOI), similar trace element trends, and no observable degree of alteration petrographically indicate little alteration has affected these samples.

Sample	**TAS-02**	**TAS-07**	**TAS-08**	**TAS-10**	**TAS-12**	**TAS-14**	**TAS-15**	**TAS-18**	**TAS-21**	**TAS-24**
Rock Type	Dolerite	Granophyre	Dolerite	Dolerite	Dolerite	Dolerite	Dolerite	Dolerite	Dolerite	Dolerite
Description	Medium-Fine	Very Coarse	Medium	Medium	Medium	Medium	Medium	Medium-Fine	Medium Coarse	Coarse
Zone	55	55	55	55	55	55	55	55	55	55
Northing	5183731.9	5230971.5	5228927.3	5268692.2	5319057.3	5345402.7	5372894.4	5407041.9	5355722.9	5284622.8
Easting	490325.5	519183.6	521917.9	497942.2	454324.8	461359.1	473323.6	519399.4	572504.9	565581.5
Major Elements (wt. %):										
SiO_2	54.68	56.53	54.31	55.74	54.17	54.07	54.00	54.16	53.66	54.50
Al_2O_3	14.34	16.70	13.03	14.30	15.52	14.92	14.54	14.81	15.85	14.81
Fe_2O_3	10.26	10.24	10.58	11.10	10.30	10.26	9.91	9.98	9.65	10.04
MgO	6.46	2.03	8.36	5.03	5.25	5.88	6.66	6.34	5.57	6.28
CaO	10.25	8.53	10.69	9.13	10.44	10.73	10.62	10.67	10.99	10.51
Na_2O	1.83	2.70	1.54	2.40	1.96	1.91	1.82	1.85	1.85	1.81
K_2O	0.85	1.36	0.74	1.14	0.92	0.83	0.82	0.85	0.80	0.90
TiO_2	0.64	0.82	0.57	0.78	0.64	0.65	0.61	0.63	0.61	0.65
P_2O_5	0.09	0.14	0.08	0.12	0.10	0.10	0.09	0.09	0.09	0.10
MnO	0.16	0.14	0.18	0.17	0.17	0.17	0.16	0.17	0.16	0.17
LOI	0.25	0.71	0.13	0.20	0.63	0.61	0.41	0.47	0.66	0.50
H_2O-										
Total	99.81	99.90	100.21	100.11	100.10	100.13	99.64	100.02	99.89	100.27
Mg#	59.47	31.60	64.80	51.36	54.29	57.18	61.03	59.68	57.36	59.31
Trace Elements (ppm):										
La	12.2	19.9	10.6	15.7	13.0	12.3	11.9	12.0	11.9	13.1
Ce	25.5	40.1	21.5	33.0	27.1	26.5	24.8	26.2	24.6	26.3
Pr	3.40	5.00	2.80	4.20	3.40	3.40	3.20	3.40	3.10	3.20
Nd	13.3	18.9	11.6	18.3	13.7	13.3	12.4	14.8	13.0	13.4
Sm	3.10	4.80	2.90	4.20	3.80	3.30	3.20	2.90	2.80	3.60
Eu	0.90	1.30	0.80	1.10	0.90	0.80	0.80	1.00	0.90	0.90
Gd	3.30	5.20	2.70	4.30	3.50	3.70	3.50	4.00	3.20	3.70
Tb	0.60	0.90	0.50	0.70	0.60	0.60	0.60	0.60	0.60	0.60
Dy	3.80	5.30	3.50	4.60	3.80	4.10	3.80	3.90	3.60	3.70
Ho	0.80	1.20	0.70	1.00	0.80	0.80	0.80	0.80	0.80	0.80
Er	2.40	3.10	2.10	2.90	2.40	2.20	2.50	2.50	2.30	2.50
Yb	2.50	3.40	2.20	2.80	2.50	2.20	2.50	2.50	2.30	2.60
Lu	0.40	0.60	0.40	0.40	0.40	0.40	0.30	0.30	0.40	0.40
Rb	30.4	53.8	27.1	41.4	36.6	30.2	32.7	34.0	33.0	34.7
Ba	199	315	167	297	210	198	192	207	193	206
Th	3.30	5.70	2.90	4.90	3.70	3.50	3.40	3.60	3.30	3.50
U	1.00	1.50	0.80	1.20	1.00	0.90	0.80	0.90	1.00	0.90
Nb	5.30	7.60	4.10	6.60	5.20	5.20	4.60	4.80	4.70	5.00

Sample	**TAS-02**	**TAS-07**	**TAS-08**	**TAS-10**	**TAS-12**	**TAS-14**	**TAS-15**	**TAS-18**	**TAS-21**	**TAS-24**
Rock Type	Dolerite	Granophyre	Dolerite	Dolerite	Dolerite	Dolerite	Dolerite	Dolerite	Dolerite	Dolerite
Description	Medium-Fine	Very Coarse	Medium	Medium	Medium	Medium	Medium	Medium-Fine	Medium Coarse	Coarse
Zone	55	55	55	55	55	55	55	55	55	55
Northing	5183731.9	5230971.5	5228927.3	5268692.2	5319057.3	5345402.7	5372894.4	5407041.9	5355722.9	5284622.8
Easting	490325.5	519183.6	521917.9	497942.2	454324.8	461359.1	473323.6	519399.4	572504.9	565581.5
Trace Element (ppm): Continued										
K	7056	11290	6143	9464	7637	6890	6807	7056	6641	7471
Ta	0.60	1.50	0.50	0.70	0.70	0.50	0.40	0.40	0.40	0.40
Pb	6.00	9.20	4.90	7.70	6.20	6.00	5.70	5.70	5.40	6.00
Sr	132	160	112	197	139	131	134	128	130	161
P	402	602	332	506	423	419	388	410	397	423
Hf	2.60	3.90	2.40	3.20	2.70	2.50	2.50	2.50	2.60	2.70
Zr	94.0	147.0	82.0	127.0	101.0	98.0	92.0	93.0	92.0	101.0
Ti	3837	4916	3417	4676	3837	3897	3657	3777	3657	3897
Tb										
Y	21.6	28.4	18.8	26.3	22.7	21.3	20.7	21.5	20.5	22.4
Ag	0.05	0.06	0.03	0.03	0.03	0.03	0.04	0.06	0.05	0.02
Co	45.2	34.0	49.7	44.6	44.6	43.2	44.5	42.7	41.2	44.1
Cr	148.0	35.0	187.0	65.0	51.0	85.0	124.0	104.0	54.0	90.0
Cs	1.20	2.70	1.00	1.20	1.40	1.40	1.40	1.20	1.30	1.20
Cu	80.6	120.0	66.9	101.2	89.6	84.1	81.4	82.3	81.2	70.9
Ga	16.0	19.8	14.5	17.1	16.9	16.5	15.0	15.6	17.8	15.7
Mo	0.50	0.50	0.50	0.40	0.50	0.40	0.50	0.30	0.30	0.40
Ni	71.5	11.7	92.0	47.4	52.0	60.9	73.4	68.9	60.5	65.7
Sn	1.00	2.00	2.00	2.00	1.00	2.00	2.00	2.00	2.00	1.00
Tl	0.20	0.30	0.17	0.24	0.22	0.18	0.20	0.18	0.17	0.20
V	246	197	261	248	233	243	241	239	239	237
Zn	80.0	90.0	74.0	88.0	79.0	77.0	74.0	77.0	76.0	75.0

Table 3.2: Major and trace element analyses of dolerite dykes and sills from the Tasmanian Dolerites, Ferrar CFB province. Major and trace element analyses for the Kalkarindji CFB province. Major element analysis: X-ray fluorescence (XRF). Trace element analysis: inductively coupled plasma mass spectrometry (ICP-MS). Sc and V analysis: inductively coupled plasma optical (atomic) emission spectrometry (ICP-OES). For the remaining elements a four acid digest was implemented with ICP-MS and ICP-OES analyses. LOI, loss on ignition. GPS Datum: AGD84 unless otherwise noted.

3.8. Discussion

3.8.1. High precision $^{40}Ar/^{39}Ar$ geochronology of the Tasmanian Dolerites

Previous $^{40}Ar/^{39}Ar$ ages from Ferrar ranged from 180.3 ± 1.0 Ma to 182.5 ± 1.0 Ma (recalculated from Fleming *et al.*, 1997), although pioneering at the time of publication, results were rather imprecise compared to the 0.11 % (2σ) U-Pb results recently obtained for Ferrar in Burgess *et al.* (2015). Furthermore, $^{40}Ar/^{39}Ar$ ages (Heimann *et al.*, 1994; Fleming *et al.*, 1997; Minor & Mukasa, 1997) were calibrated using the heterogeneous MMhb-1 standard thus questioning the strict accuracy of those results. Our $^{40}Ar/^{39}Ar$ results provide the highest precision plagioclase geochronology dataset for Tasmanian Dolerites and the Ferrar CFB province (uncertainties as low as ± 0.1 % at 2σ; Table 3.1). Increased precision for $^{40}Ar/^{39}Ar$ ages using the mineral plagioclase is largely due to new-generation multi-collector machines (e.g. ARGUS VI) over older generation single collector machines (e.g. MAP 215-50), making precision comparable with that currently attainable by U-Pb ages, especially when the uncertainties on the decay constant are included in the calculation.

The older Ferrar province ages thus far are limited to the Dufek layered mafic intrusion at 183.9 ± 0.3 Ma (Minor & Mukasa, 1997) and a weighted mean of two dolerite sills at 183.6 ± 1.0 Ma and 183.4 ± 1.4 Ma (Encarnacion *et al.*, 1996). An extensive array of new U/Pb CA-TIMS analyses conducted across the whole Ferrar province, including one sample from the Tasmanian Dolerite, have prompted Burgess *et al.* (2015) to constrain the activity of the Ferrar CFBs to an even tighter magmatic duration of 349 ± 49 Ka. When considering previous ID-TIMs results from the Dufek

intrusion (Figure 3.2) by Minor and Mukasa (1997), the magmatic activity range can be extended to 1.47 ± 50 Ma.

Our new results offer an uncertainty ranging from ± 0.1 to 0.2 % providing a duration for the emplacement of the Tasmanian Dolerites to be ca. 1.58 ± 0.78 Ma (Figure 3.4). Increased precision of $^{40}Ar/^{39}Ar$ ages reveals a high degree of complexity to the Tasmanian Dolerites intrusion, distinguishing differing emplacement ages between various intrusions (Figure 3.9). Although all the results together display a continuous emplacement of magma from ca. 184.3 – 182.7 Ma; the age of samples TAS-14 (182.19 ± 0.52 Ma) and TAS-19 (184.27 ± 0.24 Ma) can statistically be distinguished from each other (Figure 3.4). These new ages are further distinguished from

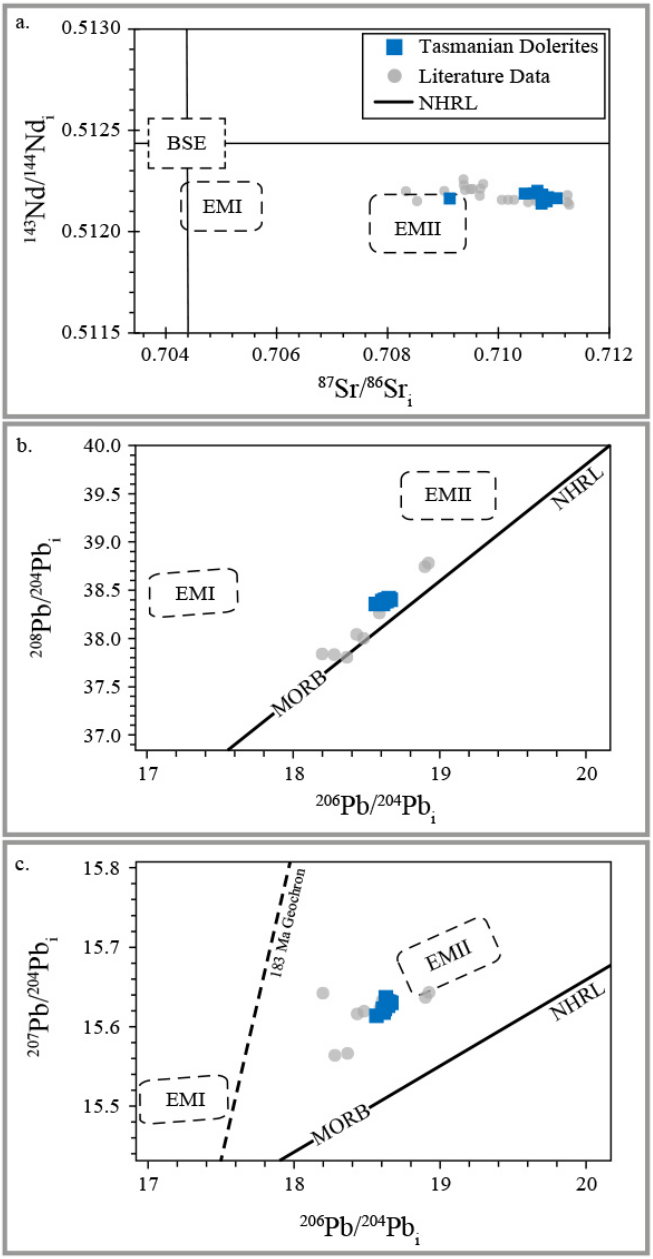

Figure 3.8: Initial (183 Ma) Sr, Nd, and Pb isotopic compositions of Tasmanian Dolerites. In the two Pb vs. Pb isotope diagrams, the Northern Hemisphere Reference Line (NHRL); (Hart, 1984) is shown. Approximate locations of mantle end-members age-calculated to 183 Ma (Zindler and Hart, 1986) are indicated for reference. BSE = Bulk Silicate Earth, EMI = Enriched Mantle I, EMII = Enriched Mantle II, MORB = Mid-Ocean Ridge Basalt, DMM = Depleted MORB Mantle. All isotope data for the Ferrar CFBs are from the GEOROC database, Pb isotopic data for Ferrar are from Hergt *et al.* (1989b).

Sample	Sr (ppm)	Rb (ppm)	$^{87}Rb/^{86}Sr$	$^{87}Sr/^{86}Sr_{meas}$	± 1σ	$(^{87}Sr/^{86}Sr)_{i.}$	Nd (ppm)	Sm (ppm)	$^{147}Sm/^{144}Nd$	$^{143}Nd/^{144}Nd_{meas}$	± 1σ	$(^{143}Nd/^{144}Nd)_{i.}$	εNd
TAS – 02	30.4	132.3	0.66451	0.71252	0.0000046	0.71079	13.3	3.1	0.123761	0.512331	0.0000023	0.512183	-5.98
TAS – 07	53.8	160.2	0.97129	0.71339	0.0000056	0.71087	18.9	4.8	0.134851	0.512329	0.0000023	0.512168	-6.02
TAS – 08	27.1	112.0	0.69973	0.71230	0.0000025	0.71047	11.6	2.9	0.132744	0.512347	0.0000018	0.512188	-5.68
TAS – 10	41.4	197.3	0.60672	0.71070	0.0000032	0.70912	18.3	4.2	0.121863	0.512310	0.0000020	0.512164	-6.41
TAS – 12	36.6	139.3	0.75986	0.71275	0.0000045	0.71078	13.7	3.8	0.147278	0.512314	0.0000021	0.512138	-6.31
TAS – 14	30.2	130.9	0.66722	0.71278	0.0000041	0.71105	13.3	3.3	0.131746	0.512323	0.0000018	0.512165	-6.15
TAS – 15	32.7	134.0	0.70574	0.71273	0.0000044	0.71089	12.4	3.2	0.137026	0.512334	0.0000022	0.512170	-5.93
TAS – 18	34.0	128.1	0.76759	0.71270	0.0000041	0.71070	14.8	2.9	0.104043	0.512326	0.0000021	0.512201	-6.09
TAS – 21	33.0	129.5	0.73695	0.71255	0.0000037	0.71063	13.0	2.8	0.114364	0.512326	0.0000020	0.512189	-6.08
TAS – 24	34.7	160.9	0.62368	0.71249	0.0000032	0.71087	13.4	3.6	0.142650	0.512321	0.0000021	0.512150	-6.19

Sample	Pb (ppm)	U (ppm)	Th (ppm)	$^{206}Pb/^{204}Pb_{meas}$	± 1σ	$^{206}Pb/^{204}Pb_i$	$^{207}Pb/^{204}Pb_{meas}$	± 1σ	$^{207}Pb/^{204}Pb_i$	$^{208}Pb/^{204}Pb_{meas}$	± 1σ	$^{208}Pb/^{204}Pb_i$
TAS – 02	6.0	1.0	3.3	18.924	0.001287	18.621	15.655	0.001062	15.639	38.770	0.002566	38.443
TAS – 07	9.2	1.5	5.7	18.939	0.001238	18.641	15.656	0.001021	15.641	38.812	0.002509	38.444
TAS – 08	4.9	0.8	2.9	18.924	0.001109	18.627	15.649	0.000906	15.634	38.765	0.002307	38.413
TAS – 10	7.7	1.2	4.9	18.926	0.001227	18.642	15.668	0.001012	15.654	38.835	0.002495	38.456
TAS – 12	6.2	1.0	3.7	18.928	0.001188	18.634	15.654	0.000990	15.639	38.797	0.002406	38.442
TAS – 14	6.0	0.9	3.5	18.940	0.001081	18.667	15.662	0.000858	15.648	38.819	0.002233	38.472
TAS – 15	5.7	0.8	3.4	18.935	0.000884	18.679	15.660	0.000759	15.647	38.812	0.001879	38.458
TAS – 18	5.7	0.9	3.6	18.937	0.001218	18.649	15.663	0.001000	15.649	38.820	0.002484	38.444
TAS – 21	5.4	1.0	3.3	18.914	0.001372	18.577	15.648	0.001149	15.631	38.776	0.002811	38.412
TAS – 24	6.0	0.9	3.5	18.930	0.000671	18.657	15.657	0.000550	15.643	38.805	0.001351	38.458

Table 3.3: Sr-Nd-Pb isotope data for the Tasmanian Dolerites, Ferrar CFB province. Initial calculations are age-corrected to 183 Ma. Uncertainties on initial ratios include in-run errors and uncertainties on blank corrections. Sample locations can be found with major and trace element data (Table 3.2).

plagioclase and pyroxene $^{40}Ar/^{39}Ar$ ages from the Tasmanian Dolerites presented in Chapter 5; 181.69 ± 0.36 Ma (plagioclase) and 182.36 ± 0.75 Ma (pyroxene).

New high precision $^{40}Ar/^{39}Ar$ results from plagioclase within the Tasmanian Dolerites, presented here, fall within the range of the duration indicated by results from

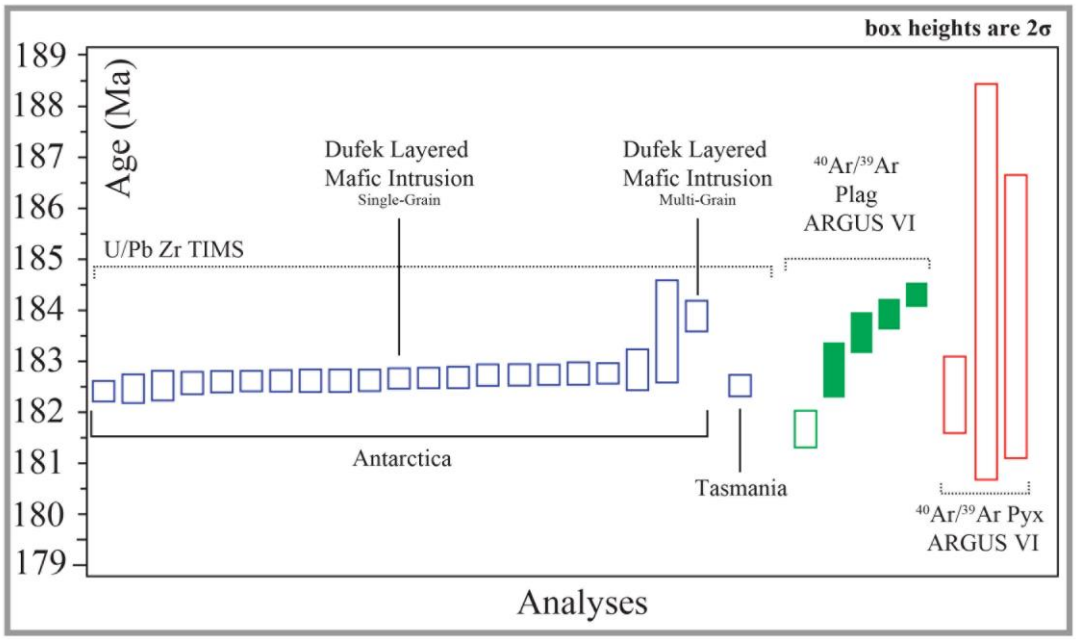

Figure 3.9: New plagioclase geochronology data compared with literature data from the Ferrar province. Previous geochronological results from Encarnacion *et al.* (1996); Minor and Mukasa (1997); Burgess *et al.* (2015).

(Minor & Mukasa, 1997) and (Burgess *et al.*, 2015) (Figure 3.9). One result (TAS-14, Figure 3.4) is within uncertainty of the upper range from Burgess *et al.* (2015); another is within this young range when considering a plagioclase $^{40}Ar/^{39}Ar$ result from data presented in Chapter 5 (TAS-17; Figure 3.9). The other three results from this study show an age progression to an older age of 184.27 ± 0.24 Ma (TAS-19) all overlapping with the age of the Dufek intrusion of 183.9 ± 0.3 Ma from Minor and Mukasa (1997) (Figure 3.9).

Considering the ca. 184.3 – 182.7 Ma ages and the range they represent in the larger context of the Ferrar CFB province; ages of the Dufek layered mafic intrusion indicate magmatic activity began at least by ca. 183.9 Ma in the western most regions

of the Ferrar province (Minor & Mukasa, 1997) (Figure 3.2). A new age on the Lexington granophyre of 182.54 ± 0.21 Ma from Burgess *et al.* (2015) challenges the evidence of older zircons present within Ferrar. The quoted age of Minor and Mukasa (1997) is the weighted mean of three multigrain analyses (sample 1: 1.28 mg, $^{206}Pb/^{238}U$ age of 183.8 ± 1.1 Ma; sample 2: 1.27 mg, $^{206}Pb/^{238}U$ age of 183.5 ± 0.7 Ma; sample 3: 0.99 mg, $^{206}Pb/^{238}U$ age of 184.0 ± 0.7 Ma). Each of these individual ages are closer within uncertainty with the ca. 182 Ma age of Burgess *et al.* (2015). This could be the result of analytical differences in the analyses; i.e. only one uncertainty is quoted for the results of Minor and Mukasa (1997) making inter-laboratory comparisons difficult. Another plausible scenario to explain the age discrepancy from the same unit, is comparison of multigrain and single-grain analyses being made. Due to the plausibility of inherited grains within multigrain analyses, single-grain analyses consequently provide the closest crystallization age of the intrusion. Regardless, the new plagioclase $^{40}Ar/^{39}Ar$ ages further indicate magmatism was synchronous throughout the Ferrar province (Figure 3.9). Thus, providing no evidence to suggest there is an age progression apparent within the Ferrar CFB province. Furthermore, results are synchronous with the earliest appearances of the Karoo CFB province; e.g. the 183.25 ± 0.21 Ma U/Pb zircon CA-TIMS age from the New Amalfi Sheet in the Eastern Karoo Basin (Burgess *et al.*, 2015) and plagioclase plateau ages from sills of the Western Cape Province (Western Karoo Basin) ranging from 182.11 ± 0.83 Ma and 183.99 ± 1.09 Ma; Chapter 4).

3.8.2. Evidence of Crystal Inheritance?

The precision of our results provide more insight into the plumbing system of the Tasmanian Dolerites region, from the Ferrar Province. Both TAS-14 ($^{40}Ar/^{39}Ar$ plagioclase plateau; 182. 91 ± 0.52 Ma) and TAS-17 ($^{40}Ar/^{39}Ar$ plagioclase plateau;

181.69 ± 0.36 Ma; Chapter 5), as well as a U/Pb zircon age from the Red Hill Dolerite dyke (CA-TIMS weighted mean of 182.54 ± 0.21 Ma; Burgess *et al.*, 2015) give the youngest ages of the Tasmanian Dolerites (Figure 3.9). All other ages obtained, from the Tasmanian Dolerites, are older, yielding $^{40}Ar/^{39}Ar$ plagioclase plateau ages ca. 184 Ma. Sample TAS-21 ($^{40}Ar/^{39}Ar$ plagioclase plateau; 183.98 ± 0.33 Ma) falls between these two groups (Figure 3.9), indicating the Tasmanian Dolerite magmatism cannot be divided strictly into two distinct pulses. However, these results do display that local areas of the island were experiencing magmatism at distinguishably different ages. Therefore, these results indicate that some sills and dykes may contain multiple phases of magma injection throughout ca. 2 Ma.

Is such apparent long duration an artifact of the $^{40}Ar/^{39}Ar$ data, or could there be additional evidence that this value is a true representation of the duration of the magmatic system? Within the age spectra of the younger ca. 182 Ma sills and dykes a slight perturbation to older ages is apparent within the higher heating steps ramping up to ca. 185.5 Ma (Figure 3.4). Typically this trend and a saddle shaped age spectra, are interpreted to simply be the presence of excess Ar in the sample (e.g. Lanphere & Dalrymple, 1976; Kelley, 2002). In older single-collector $^{40}Ar/^{39}Ar$ such fine scale detail within age spectra would be mostly masked by the uncertainties associate with individual steps. However, with the increase in precision from multi-collector analyses, as used in this study, such a trend becomes evident.

We suggest that excess Ar could be an overly simplified interpretation, instead, this trend to older ages could be evidence of a younger pulse of magma utilizing a previously established conduit. The younger pulse would entrain some xenocrysts from slightly older sills or dykes into this new fresh magma batch. These entrained crystals cannot be antecrysts, as is the case sometimes with zircon grains, because Ar

within the plagioclase crystal would not survive long within the new magma before the system completely resets; activation energies of 155 – 187 kJ/mol and pre-exponential factor frequency factors D_0 ranging from 4.1 x 10^{-4} to 5.4 x 10^3 cm^2/s which correspond to closure temperatures of 225 – 300 °C for a 10 °C/Ma cooling rate (Cassata *et al.*, 2009; Cassata & Renne, 2013). Evidenced by the older ages in the highest heating steps of the age spectra, these inherited crystals from previous magmatic pulses would then either make up; (1) "core" like zones within some of the plagioclase grains or (2) have slightly different diffusion characteristics than the younger magmatic plagioclase crystals. Therefore, the older trend at the end of the 182 Ma age spectra indicate an inheritance of crystals from the oldest (i.e. 184 – 185 Ma) generation of magma activity.

To further test the plausibility of crystal inheritance resulting in older ages at the end of the heating spectra, a numerical mixing + diffusion model was conducted using the ArArDIFF (Jourdan & Eroglu, 2017) algorithm. This diffusion model attempts to reproduce the old age tail that can develop in some of the age spectra (Figure 3.10). In the numerical model, the first magma generation has plagioclase crystallize occurring at 185 Ma. A fresh batch of magma is then emplaced at 182 Ma through many of the same conduits, entertaining some of the 185 Ma plagioclase crystals. The model calculated theoretical age spectra for a crystallization age of 185 Ma (magma generation 1) and a separate crystallization age of 182 Ma (magma generation 2) (Figure 3.10a; Table 3.4). When the rock of the younger batch of magma solidifies it comprises a mixture of plagioclase crystals from the 182 Ma magmatic event (providing 70 % of the crystals) and plagioclase crystals from the 185 Ma (providing 30 % of the crystals). This estimate of a mixture of plagioclase crystals within the younger magma batches is in agreement with the observed K/Ca ratios that suggest

two populations; a K/Ca value of ~ 0.023 (generation 1) and 0.030 (generation 2) (Figure 3.4). More Ca could mean more resistance to diffusion, although clear evidence for this has not yet been established (Cassata and Renne, 2013). For the numerical + diffusion model to reproduce the older ages in the later heating steps, the first generation of plagioclase must be slightly more resistant to diffusion than the second generation of plagioclase crystals. As stated above, this can be achieved by a lower D_o or by the first generation being enclosed in the second generation, affecting the diffusion time scale. The models utilizes the first scenario of differing diffusion coefficients, assuming that the two populations of plagioclase do not "interact" to any great extent. Therefore, the model assumes two linear cooling periods, a rapid initial duration of cooling for the 182 Ma magmatic event of 22 hours to cool from 1100 °C to 400 °C (Figure 3.10a; Table 3.4); followed by a cooling duration of 10 Ka to fully solidify from 400 °C to 0 °C (Figure 3.10a; Table 3.4).

Our model age spectrum successfully reproduces the step-heating data from sample TAS-14 (Figure 3.10), suggesting a mixture between 185 Ma plagioclase xenocrysts entrained in a young 182 Ma magma batch can explain the presence of older heating steps in some of the age spectra. Such a model alone cannot rule out that the late stage older ages are associated with excess Ar incorporated during the early (core) crystallization phase. However, it would be remarkable that excess ^{40}Ar systematically shift the old age toward 184 – 185 Ma, the age of older dykes and sills, and not to anonymously older apparent ages. Furthermore, we have shown above that our suite of samples yielded a range of age from 182 Ma to 184.3 Ma supporting the existence of an old generation of intrusions. Altogether, these theoretical results coupled with the observed data from the younger generation of intrusions indicate that

Diffusion Parameters

	D_0 (cm^2/s)	E_a (J/mol)	Radius (μm)	K_2O contribution (mixed phase)
Anorthite (Max)	5400	240000	200	70 %
Anorthite (Min)	0.0004	164000	200	30 %

Thermal History: Crystallization 185 Ma

	Start (Ma)	End (Ma)	Duration	Starting temp. (°C)	Ending temp. (°C)
Period 1	182	182	22 hours	1100	400
Period 2	182	182	10 Ka	400	0

Table 3.4: $^{40}Ar/^{39}Ar$ Thermochronology Diffusion Model of Inherited Plagioclase Diffusion parameters from (Cassata & Renne, 2013) and time-temperature history used in the ArArDiff models (Jourdan & Eroglu, 2017) to generate synthetic age spectra.

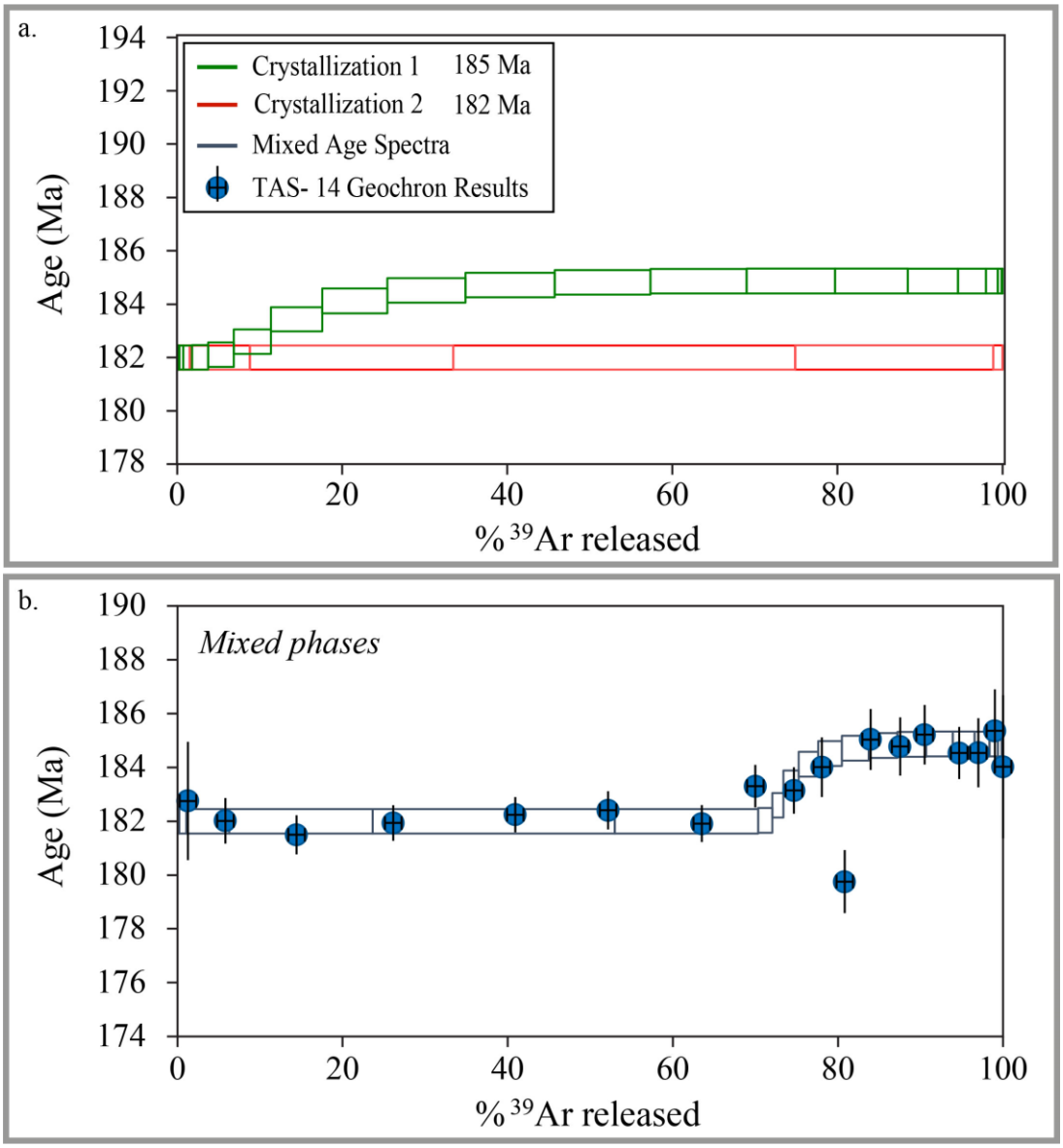

Figure 3.10: (a) Time-temperature path used to calculate the simulated age spectra. (b) Modeled age spectra resulting from a metamorphic cooling path for 150 µm radius crystals of biotite, orthopyroxene, and clinopyroxene compositions. Diffusion parameters and thermal history are given in Table 3.4.

the $^{40}Ar/^{39}Ar$ (system) can identify older generations of plagioclase. Therefore, both through full plateau ages and slightly older ages, of the higher heating steps within the age spectrum, indicate that the magmatic activity starts earlier (i.e. 184 –185 Ma) than has been recently proposed (Burgess *et al.*, 2015) based on U-Pb zircon age alone.

3.8.3. Zircons do not tell the whole story?

In the geochronological investigation of CFBs, in some instances, a divergence in duration estimates is apparent between those using the U/Pb zircon method and the

$^{40}Ar/^{39}Ar$ plagioclase method. Zircon U/Pb CA-TIMS results on sills within the Karoo Basin constrain the duration of the emplacement of these sills to about 470 Ka with ages ranging from 182.9 ± 0.5 Ma to 182.3 ± 0.6 Ma (Svensen *et al.*, 2007; Svensen *et al.*, 2012). However, $^{40}Ar/^{39}Ar$ results for sills within the same basin provide a more prolonged duration of ca. 3 Ma with ages ranging from 182.4 ± 0.5 Ma to 185.6 ± 0.5 Ma (recalculated from Jourdan *et al.*, 2008). This wider spread trend in $^{40}Ar/^{39}Ar$ results compared to U/Pb results is continued here, with new results of the Tasmanian Dolerites from this study indicate a duration of at least 0.8 Ma, whereas U/Pb CA-TIMS analyses estimate a duration of 349 ± 49 Ka (Burgess *et al.*, 2015).

Typically this discrepancy has been attributed to the heterogeneous monitors used during analyses or the Ar system suffering from alteration, recoil, or excess Ar that can at times be difficult to discriminate (Jourdan *et al.*, 2007c; Svensen *et al.*, 2012). However, utilizing the U/Pb zircon method for mafic sills suffers from many notable issues as well. Zircon is not a common crystallizing phase in mafic rocks; yet, mafic compositions compose the vast majority of LIPs. Zircon crystals utilized for U/Pb analyses of CFB basalts are typically relegated to being sourced from isolated lenses of coarse grained pegmatites, hosted in the finer grained dolerite dykes and sills, or thick pooled lava piles (Elliot & Fleming, 2008; Svensen *et al.*, 2012; Burgess *et al.*, 2015). Therefore, the differences in the two systems could be that zircon U/Pb are bias either geographically or even temporally.

With the advancement in precision capabilities for the $^{40}Ar/^{39}Ar$ technique in the case of plagioclase allows for results that approach that of the CA-TIMS method (e.g. Belica *et al.*, 2017). Advancements in precision also provide better calibration on monitors, indicating the probability of differences in ages being systematic becoming less and less. This is evidenced by recent results from the Deccan province

in India where the zircon U-Pb (Schoene *et al.*, 2015) and plagioclase $^{40}Ar/^{39}Ar$ yield indistinguishable results for the same stratigraphic units. Furthermore, our high precision results from the Tasmanian Dolerites display a range of plateau ages from ca. 184.3 ± 0.2 – 182.7 ± 0.5 Ma rather than displaying a systematic offset from the ca. 182 Ma age data from the U/Pb results (Burgess *et al.*, 2015) (Figure 3.9). The $^{40}Ar/^{39}Ar$ Tasmanian Dolerite results also overlap completely with all high precision U/Pb data available for the Ferrar LIPs; 183.9 ± 0.3 Ma – 182.4 ± 0.2 Ma (Encarnacion *et al.*, 1996; Minor & Mukasa, 1997; Burgess *et al.*, 2015). As a result, we propose the inconsistency between the U-Pb and $^{40}Ar/^{39}Ar$ ages obtained for Ferrar samples is not the product of analytical discrepancies but represents a true geologically significance, with each method providing different facets of the emplacement story.

3.8.4. Coupling Geochemistry with the Geochronology

The Tasmanian Dolerites mineral assemblage is dominated by plagioclase and clinopyroxenes. These minerals are expected to form early, or throughout, the evolution of the mafic magmas. Rhyolite-MELTS models using the program and code of (Ghiorso & Sack, 1995; Gualda *et al.*, 2012) were used to provide estimates of a plausible fractionation assemblage of these tholeiites to comment on mineral phases that would appear first during the magmatic evolution of the province. The isenthalpic calculations made applied initial parameters of 3 kbar (pressure), anhydrous (H_2O = 0 %), and a liquidus temperature of ~ 1200 °C, utilizing the QFM (quartz-fayalite-magnetite) oxygen fugacity (fO_2). Sample TAS-08 was chosen as an initial starting composition for the MELTS models due to containing the highest MgO of the sampled suite (Figure 3.6; Table 3.2). The MELTS model displays a mineral assemblage in agreement with petrographic observations: plagioclase (38 wt. %), augite (46 wt. %), pigeonite (7 wt. %), quartz (7 wt. %), and magnetite (3 wt. %). The MELTS models

predict a crystallization sequences of augite + plagioclase → augite + pigeonite + plagioclase → augite + pigeonite + plagioclase + titano-magnetite → augite + pigeonite + plagioclase + titano-magnetite + quartz, indicating plagioclase and pyroxene are the first phases to crystallize during the fractional crystallization process of these tholeiites. The MELTS models accurately reproduce the trend of all the previous data from Ferrar as well as all the data from this study except sample TAS-07. Sample TAS-07 has a discrepancy from the MELTS modelled curves due to high Al_2O_3 compared to the rest of the Tasmanian Dolerite and Ferrar geochemical data. The MELTS models are not able to reproduce this as well as the rest of the data due to the extreme degrees of differentiation the core of this thick dyke (Red Hill Dolerite Dyke) has undergone. Pegmatites are typically attributed to the last vestiges of a magmatic system when the residual liquid is saturated enough with volatiles to permit the formation of coarser grained zones. Late stage pegmatite formation is corroborated by the MELTS models with the "quartz" appearance at the end of the fractionation sequence, indicating an over saturation of Silicon in the final fractionation stages. As the geochemical data do not have ages attached to them, MELTS models can inform two scales of magmatic evolution; small scale crystallization of each of these phases within a sill, and the constituents of the evolution of the whole magmatic system.

When considering small scale observations, zircon crystal appear exclusively within pegmatitic and granophyric features found within dolerite dykes and sills, and thick lava piles. Within a single thick dyke or sill, the zircon crystals should be younger than the plagioclase because plagioclase and pyroxene phases dominate early formed crystals within the system. Pegmatitic and granophyric textures would be the final zones forming within thick sills and dykes, when the system is oversaturated with silica. Furthermore, the cooling rate and crystallization of each phase can affect and

complicate these small scale difference. If the cooling of a thick sill has an extended slow cooling, the plagioclase will remain open until the sills cooled below ~ 250 °C (Cassata & Renne, 2013) and the zircon would close ~ 1000 °C (Flowers *et al.*, 2005), again assuming a modest average cooling rate of 10 °C/Ma (e.g. Cassata *et al.*, 2011; Cassata & Renne, 2013). Therefore, if zircon was already crystallized when these pegmatitic and granophyric zones of the intrusion went below these respective temperatures then plagioclase near the granophyre should be younger than the zircon, whereas the plagioclase outside of the pegmatite or granophyric zones should be slightly older. Regardless, within this small scale consideration, the difference between the two crystals should be younger by few 1,000's to 10,000's of years required by the time of crystallization. Therefore, these small scale crystallization differences between the two crystals cannot explain a difference in the ages between the U/Pb zircon analyses and the $^{40}Ar/^{39}Ar$ plagioclase analyses that is at times up to 2 Ma.

If the clustering of U/Pb zircon ages at 182 Ma cannot be explained by simple differentiation of a thick intrusion, then the answer must be within the geochemical evolution of the magmatic system. The element Zr is an incompatible high field strength element (HFSE), incompatibility concentrates this element into the melt phases of magmas. Therefore, during the crystal fractionation and evolution of the Tasmanian Dolerite magmas HFSEs, and thus Zr, would become more concentrated into the residual melt as plagioclase and pyroxene crystallize first. This process is evident in the variations in the concentration of Zr (ppm) of these rocks; e.g. TAS-07 has 147 ppm Zr while sample TAS-08 has 82 ppm Zr (Table 3.2). If Zr is then concentrated in the late-stage magmatic fluid during the evolution of this magmatic system, the younger sills and dykes should contain more Zr than the older generation sills and dykes.

To test this theory, two samples that successfully yielded $^{40}Ar/^{39}Ar$ plagioclase ages were analyzed for major, trace, and Sr, Nd, and Pb geochemical data (samples TAS-14 and TAS-21). Sample TAS-14 yielded a $^{40}Ar/^{39}Ar$ plagioclase plateau age of 182.91 ± 0.52 Ma while TAS-21 returned a $^{40}Ar/^{39}Ar$ plagioclase plateau age of 183.98 ± 0.33 Ma (Figure 3.4). The younger sample (TAS-14; SiO_2 = 54.07 %, MgO = 5.88 %, Zr = 98 ppm) displays more differentiated and slightly increased incompatible trace element geochemical signatures than the older generation sample (TAS-21; SiO_2 = 53.66 %, MgO = 5.57 %, Zr = 92 ppm). The evolved geochemistry of sample TAS-07 (SiO_2 = 56.53 %, MgO = 2.03 %, Zr = 147 ppm) from the Red Hill Granophyre which has a U/Pb zircon age of 182.54 ± 0.21 Ma further implicates a possible geochemical difference between the older magmatic activity ca. 184 Ma and the younger magmatic activity ca. 182 Ma.

One interesting discrepancy to the idea of geochemical differences between the early and later generations is the different ages obtained for the Lexington granophyre of the Dufek layered mafic intrusion; 183.9 ± 0.3 Ma (Minor & Mukasa, 1997) and 182.5 ± 0.2 Ma (Burgess *et al.*, 2015) (Figure 3.9). The differences in these results are most likely the result of multi-grain analyses (Minor & Mukasa, 1997) versus single-grain analyses (Burgess *et al.*, 2015). Furthermore, due to no geochemical data available for this unit within the Dufek intrusion, the above test cannot be made. The multigrain results may contain slightly older generations of zircon that were mitigated in the single-grain picking process, offsetting the ages of minor Minor and Mukasa (1997) and Burgess *et al.* (2015). If this were the case, it further indicates an older generation of magmatism through inherited grains corroborating results of the older heating steps discussed in section 3.8.2.

Unfortunately, the inability to find zircon within these samples, as well as having only two $^{40}Ar/^{39}Ar$ plagioclase plateau results that overlap with the geochemical data, do not allow for a proper conclusion to be deduced. However, the residual liquid being concentrated in incompatible elements as well as Si oversaturation, evidenced by the MELTS models, in the final magmatic stages of the system present a plausible probability of a geochemical control on why zircon ages are younger than associated plagioclase ages within the Ferrar CFB province. The two samples (TAS-14 and TAS-21) that contain both geochemical and geochronological data further indicate this possibility, however, more data will be needed to fully develop this hypothesis. Most importantly is the new $^{40}Ar/^{39}Ar$ plagioclase plateau ages presented here, used in tandem with other high precision methods such as the CA-TIMS, are arriving at previously unattained high level precision, allowing for minute scale magmatic processes to begin to be addressed.

3.9. Conclusions

1. The high-precision $^{40}Ar/^{39}Ar$ plagioclase geochronology of Tasmanian Dolerites presents a protracted duration of magmatic activity of ca. 1.6 Ma for the Ferrar CFB province.

2. Results display continues magmatism throughout ca. 1.6 Ma, however, ages for the youngest and oldest intrusion generations is distinguishable.

3. The $^{40}Ar/^{39}Ar$ geochronology ages overlap with the present cluster of U/Pb zircon at ca. 182 Ma (Burgess *et al.*, 2015) but are, at time, almost 2 Ma older, indicating a more complex emplacement history than that concluded from zircon results.

4. Precision of these results provide evidence for possible crystal inheritance from older generation intrusions (ca. 184 – 185 Ma) entrained within the younger generation intrusions (ca 182 Ma).

5. Geochemical comparison between the older generation sills and dykes with younger generations display a geochemical evolution of the magma source that could be responsible for the absence of zircon within the older generation magmatism.

3.10. References

Baksi, A. K., Archibald, D. A. & Farrar, E. (1996). Intercalibration of 40 Ar 39 Ar dating standards. *Chemical Geology* **129**, 307-324.

Bas, M. J. L., Maitre, R. W. L., Streckeisen, A. & Zanettin, B. (1986). A Chemical Classification of Volcanic Rocks Based on the Total Alkali-Silica Diagram. *Journal of Petrology* **27**, 745-750.

Béguelin, P., Chiaradia, M., Beate, B. & Spikings, R. (2015). The Yanaurcu volcano (Western Cordillera, Ecuador): A field, petrographic, geochemical, isotopic and geochronological study. *Lithos* **218-219**, 37-53.

Brauns, C. M., Hergt, J. M., Woodhead, J. D. & Maas, R. (2000). Os Isotopes and the Origin of the Tasmanian Dolerites. *Journal of Petrology* **41**, 905-918.

Brotzu, P., Capaldi, G., Civetta, L., Orsi, G., Gallo, G. & Melluso, L. (1992). Geochronology and geochemistry of Ferrar rocks from North Victoria Land, Antarctica. *European Journal of Mineralogy*, 605-617.

Burgess, S. D., Bowring, S. A., Fleming, T. H. & Elliot, D. H. (2015). High-precision geochronology links the Ferrar Large Igneous Province with early-Jurassic ocean anoxia and biotic crisis. *Earth and Planetary Science Letters* **415**, 90-99.

Cassata, W. S. & Renne, P. R. (2013). Systematic variations of argon diffusion in feldspars and implications for thermochronometry. *Geochimica et Cosmochimica Acta* **112**, 251-287.

Cassata, W. S., Renne, P. R. & Shuster, D. L. (2009). Argon diffusion in plagioclase and implications for thermochronometry: A case study from the Bushveld Complex, South Africa. *Geochimica et Cosmochimica Acta* **73**, 6600-6612.

Compston, W., McDougall, I. & Heier, K. S. (1968). Geochemical comparison of the mesozoic basaltic rocks of Antarctica, South Africa, South America and Tasmania. *Geochimica et Cosmochimica Acta* **32**, 129-149.

Courtillot, V., Gallet, Y., Rocchia, R., Féraud, G., Robin, E., Hofmann, C., Bhandari, N. & Ghevariya, Z. G. (2000). Cosmic markers, 40Ar/39Ar dating and paleomagnetism of the KT sections in the Anjar Area of the Deccan Large Igneous Province. *Earth and Planetary Science Letters* **182**, 137-156.

Courtillot, V. E. & Renne, P. R. (2003). On the ages of flood basalt events. *Comptes Rendus Geoscience* **335**, 113-140.

Edwards, A. B. (1942a). Differentiation of the Dolerites of Tasmania. I. *The Journal of Geology* **50**, 451-480.

Edwards, A. B. (1942b). Differentiation of the Dolerites of Tasmania. II. *The Journal of Geology* **50**, 579-610.

Elliot, D. H. & Fleming, T. H. (2004). Occurrence and Dispersal of Magmas in the Jurassic Ferrar Large Igneous Province, Antarctica. *Gondwana Research* **7**, 223-237.

Elliot, D. H. & Fleming, T. H. (2008). Physical volcanology and geological relationships of the Jurassic Ferrar Large Igneous Province, Antarctica. *Journal of Volcanology and Geothermal Research* **172**, 20-37.

Encarnacion, J., Fleming, T. H., Elliot, D. H. & Eales, H. V. (1996). Synchronous emplacement of Ferrar and Karoo dolerites and the early breakup of Gondwana. *Geology (Boulder)* **24**, 535-538.

Faure, G. & Mensing, T. M. (2011). The Ferrar Group: Kirkpatrick Basalt. 373-414.

Fleming, T., Heimann, A., Foland, K. & Elliot, D. (1997). Ar-40/Ar-39 geochronology of Ferrar Dolerite sills from the Transantarctic mountains, Antarctica: Implications for the age and origin of the Ferrar magmatic province. *Geol. Soc. Am. Bull.* **109**, 533-546.

Foland, K. A., Fleming, T. H., Heimann, A. & Elliot, D. H. (1993). Potassium-argon dating of fine-grained basalts with massive Ar loss: Application of the 40 Ar 39 Ar technique to plagioclase and glass from the Kirkpatrick Basalt, Antarctica. *Chemical Geology* **107**, 173-190.

Ghiorso, M. S. & Sack, R. O. (1995). Chemical mass transfer in magmatic processes IV. A revised and internally consistent thermodynamic model for the interpolation and extrapolation of liquid-solid equilibria in magmatic systems at elevated temperatures and pressures. *Contributions to Mineralogy and Petrology* **119**, 197-212.

Hart, S. R. (1984). A large-scale isotope anomaly in the Southern Hemisphere mantle. *Nature* **309**, 753-757.

Heimann, A., Fleming, T. H., Elliot, D. H. & Foland, K. A. (1994). A short interval of Jurassic Continental Flood Basalt volcanism in Antarctica as demonstrated by 40 Ar 39 Ar geochronology. *Earth and Planetary Science Letters* **121**, 19-41.

Hergt, J. M. & Brauns, C. M. (2001). On the origin of Tasmanian dolerites. *Australian Journal of Earth Sciences* **48**, 543-549.

Hergt, J. M., Chappell, B. W., Faure, G. & Mensing, T. M. (1989a). The geochemistry of Jurassic dolerites from Portal Peak, Antarctica. *Contributions to Mineralogy and Petrology* **102**, 298-305.

Hergt, J. M., Chappell, B. W., McCulloch, M. T., McDougall, I. & Chivas, A. R. (1989b). Geochemical and isotopic constraints on the origin of the Jurassic dolerites of Tasmania. *Journal of Petrology* **30**, 841-883.

Hofmann, C., Courtillot, V., Feraud, G., Rochette, P., Yirgu, G., Ketefo, E. & Pik, R. (1997). Timing of the Ethiopian flood basalt event and implications for plume birth and global change. *Nature* **389**, 838-841.

Hooper, P., Widdowson, M. & Kelley, S. (2010). Tectonic setting and timing of the final Deccan flood basalt eruptions. *Geology* **38**, 839-842.

Irvine, T. & Baragar, W. (1971). A guide to the chemical classification of the common volcanic rocks. *Canadian Journal of Earth Sciences* **8**, 523-548.

Jourdan, F. & Eroglu, E. (2017). 40Ar/39Ar and (U-Th)/He model age signatures of elusive Mercurian and Venusian meteorites. *Meteoritics & Planetary Science*, n/a-n/a.

Jourdan, F., Féraud, G., Bertrand, H., Watkeys, M. K. & Renne, P. R. (2008). The40Ar/39Ar ages of the sill complex of the Karoo Large Igneous Province: Implications for the Pliensbachian-Toarcian climate change. *Geochemistry, Geophysics, Geosystems* **9**, n/a-n/a.

Jourdan, F., Matzel, J. P. & Renne, P. R. (2007). 39Ar and 37Ar recoil loss during neutron irradiation of sanidine and plagioclase. *Geochimica et Cosmochimica Acta* **71**, 2791-2808.

Jourdan, F. & Renne, P. R. (2007). Age calibration of the Fish Canyon sanidine $^{40}Ar/^{39}Ar$ dating standard using primary K–Ar standards. *Geochimica et Cosmochimica Acta* **71**, 387-402.

Kelley, S. (2002). Excess Argon in K-Ar and Ar-Ar Geochronology. *Chemical Geology* **188**, 1-22.

Koppers, A. A. P. (2002). ArArCALC - software for Ar-40/Ar-39 age calculations. *Computers & Geosciences* **28**, 605-619.

Lanphere, M. A. & Dalrymple, G. **B.** (1976). Identification of excess 40Ar by the 40Ar/39Ar age spectrum technique. *Earth and Planetary Science Letters* **32**, 141-148.

Lee, J. K. W., Onstott, T. C., Cashman, K. V., Cumbest, R. J. & Johnson, D. (1991). Incremental heating of hornblende in vacuo: implications for (super 40) Ar/ (super 39) Ar geochronology and the interpretation of thermal histories. *Geology (Boulder)* **19**, 872-876.

Lee, J. Y., Marti, K., Severinghaus, J. P., Kawamura, K., Yoo, H. S., Lee, J. B. & Kim, J. S. (2006). A redetermination of the isotopic abundances of atmospheric Ar. *Geochimica Et Cosmochimica Acta* **70**, 4507-4512.

Mark, D. F., Stuart, F. M. & de Podesta, M. (2011). New high-precision measurements of the isotopic composition of atmospheric argon. *Geochimica et Cosmochimica Acta* **75**, 7494-7501.

Marzoli, A., Jourdan, F., Puffer, J. H., Cuppone, T., Tanner, L. H., Weems, R. E., Bertrand, H., Cirilli, S., Bellieni, G. & De Min, A. (2011). Timing and duration of the Central Atlantic magmatic province in the Newark and Culpeper basins, eastern U.S.A. *Lithos* **122**, 175-188.

McArthur, J. M., Howarth, R. J. & Bailey, T. R. (2001). Strontium Isotope Stratigraphy: LOWESS Version 3: Best Fit to the Marine Sr-Isotope Curve for 0–509 Ma and Accompanying Look-up Table for Deriving Numerical Age. *The Journal of Geology* **109**, 155-170.

McClintock, M. & White, J. D. L. (2005). Large phreatomagmatic vent complex at Coombs Hills, Antarctica: Wet, explosive initiation of flood basalt volcanism in the Ferrar-Karoo LIP. *Bulletin of Volcanology* **68**, 215-239.

McDougall, I. (1962). Differentiation of the Tasmanian dolerites

Red Hill dolerite-granophyre association. Boulder, CO: Boulder, CO, United States: Geological Society of America (GSA), 279-315.

Merle, R., Marzoli, A., Bertrand, H., Reisberg, L., Verati, C., Zimmermann, C., Chiaradia, M., Bellieni, G. & Ernesto, M. (2011). 40Ar/39Ar ages and Sr–Nd–Pb–Os geochemistry of CAMP tholeiites from Western Maranhão basin (NE Brazil). *Lithos* **122**, 137-151.

Minor, D. R. & Mukasa, S. B. (1997). Zircon U/Pb and hornblende 40Ar/39Ar ages for the Dufek layered mafic intrusion, Antarctica: Implications for the age of the Ferrar Large Igneous Province. *Geochimica et Cosmochimica Acta* **61**, 2497-2504.

Molzahn, M., Reisberg, L. & Wörner, G. (1996). Os, Sr, Nd, Pb, O isotope and trace element data from the Ferrar flood basalts, antarctica: evidence for an enriched

subcontinental lithospheric source. *Earth and Planetary Science Letters* **144**, 529-545.

Olierook, H. K. H., Jourdan, F., Merle, R. E., Timms, N. E., Kusznir, N. & Muhling, J. R. (2016). Bunbury Basalt: Gondwana breakup products or earliest vestiges of the Kerguelen mantle plume? *Earth and Planetary Science Letters* **440**, 20-32.

Onstott, T. C., Phillips, D. & Pringle-Goodell, L. (1991). Laser microprobe measurement of chlorine and argon zonation in biotite. *Chemical Geology* **90**, 145-168.

Oostingh, K. F., Jourdan, F., Merle, R. & Chiaradia, M. (2016). Spatio-temporal Geochemical Evolution of the SE Australian Upper Mantle Deciphered from the Sr, Nd and Pb Isotope Compositions of Cenozoic Intraplate Volcanic Rocks. *Journal of Petrology* **57**, 1509-1530.

Phillips, D. & Matchan, E. L. (2013). Ultra-high precision 40Ar/39Ar ages for Fish Canyon Tuff and Alder Creek Rhyolite sanidine: New dating standards required? *Geochimica et Cosmochimica Acta* **121**, 229-239.

Pin, C., Briot, D., Bassin, C. & Poitrasson, F. (1994). Concomitant separation of strontium and samarium-neodymium for isotopic analysis in silicate samples, based on specific extraction chromatography. *Analytica Chimica Acta* **298**, 209-217.

Renne, P. R. (2014). Some footnotes to the optimization-based calibration of the 40Ar/39Ar system. *Geological Society, London, Special Publications* **378**, 21-31.

Renne, P. R., Balco, G., Ludwig, K. R., Mundil, R. & Min, K. (2011). Response to the comment by W.H. Schwarz et al. on "Joint determination of K-40 decay constants and Ar-40*/K-40 for the Fish Canyon sanidine standard, and improved accuracy for Ar-40/Ar-39 geochronology" by PR Renne et al. (2010). *Geochimica Et Cosmochimica Acta* **75**, 5097-5100.

Renne, P. R. & Norman, E. B. (2001). Determination of the half-life of 37Ar by mass spectrometry. *Physical Review C* **63**, 047302.

Renne, P. R., Swisher, C. C., Deino, A. L., Karner, D. B., Owens, T. L. & Depaolo, D. J. (1998). Intercalibration of standards, absolute ages and uncertainties in 40Ar/39Ar dating. *Chemical Geology* **145**, 117-152.

Schmidt, P. W. & McDougall, I. (1977). Palaeomagnetic and potassium-argon dating studies of the Tasmanian Dolerites. *Journal of the Geological Society of Australia* **24**, 321-328.

Schoene, B., Guex, J., Bartolini, A., Schaltegger, U. & Blackburn, T. J. (2010). Correlating the end-Triassic mass extinction and flood basalt volcanism at the 100 ka level. *Geology* **38**, 387-390.

Schoene, B., Samperton, K. M., Eddy, M. P., Keller, G., Adatte, T., Bowring, S. A., Khadri, S. F. R. & Gertsch, B. (2015). U-Pb geochronology of the Deccan Traps and relation to the end-Cretaceous mass extinction. *Science* **347**, 182-184.

Spell, T. L. & McDougall, I. (2003). Characterization and calibration of 40Ar/ 39Ar dating standards. *Chemical Geology* **198**, 189-211.

Sun, S. s. & McDonough, W. F. (1989). Chemical and isotopic systematics of oceanic basalts: implications for mantle composition and processes. *Geological Society, London, Special Publications* **42**, 313-345.

Svensen, H., Corfu, F., Polteau, S., Hammer, Ø. & Planke, S. (2012). Rapid magma emplacement in the Karoo Large Igneous Province. *Earth and Planetary Science Letters* **325-326**, 1-9.

Svensen, H., Planke, S., Chevallier, L., Malthe-Sørenssen, A., Corfu, F. & Jamtveit, B. (2007). Hydrothermal venting of greenhouse gases triggering Early Jurassic global warming. *Earth and Planetary Science Letters* **256**, 554-566.

Tanaka, T., Togashi, S., Kamioka, H., Amakawa, H., Kagami, H., Hamamoto, T., Yuhara, M., Orihashi, Y., Yoneda, S., Shimizu, H., Kunimaru, T., Takahashi, K., Yanagi, T., Nakano, T., Fujimaki, H., Shinjo, R., Asahara, Y., Tanimizu, M. & Dragusanu, C. (2000). JNdi-1: a neodymium isotopic reference in consistency with LaJolla neodymium. *Chemical Geology* **168**, 279-281.

Villa, I. M., Grobéty, B., Kelley, S. P., Trigila, R. & Wieler, R. (1996). Assessing Ar transport paths and mechanisms in the McClure Mountains hornblende. *Contributions to Mineralogy and Petrology* **126**, 67-80.

Zindler, A. & Hart, S. (1986). Chemical geodynamics. A*nnual review of earth and planetary sciences* **14**, 493-571.

3.11. Figure Captions

Figure 3.1: Outcrop map of the Tasmanian Dolerites. Sample locations are represented in white dots while the samples chosen for $^{40}Ar/^{39}Ar$ geochronology analyses are represented in red.

Figure 3.2: Present day location of the constituents of the Ferrar Continental Flood Basalt Province. Locations created and modified from Bryan and Ernst (2008) and Burgess *et al.* (2015).

Figure 3.3: Photomicrographs of select samples from the Tasmanian Dolerite.

Figure 3.4: $^{40}Ar/^{39}Ar$ apparent age and related K/Ca ratio spectra for pyroxene and plagioclase separates plotted against the cumulative percentage of ^{39}Ar released. Mean squared weighted deviation (MSWD) and probability of fit (P) is indicated. Errors on plateau ages are quoted at 2σ and do not include systematic errors (i.e. uncertainties on the age of the monitor and on the decay constant).

Figure 3.5: Total alkalis-silica (TAS) Diagram (Bas *et al.*, 1986). Alkalic-subalkalic line from Irvine and Baragar (1971). All major element data for the Ferrar CFBs are from the GEOROC database.

Figure 3.6: Major element (wt. %) vs. Mg-number [100 x atomic ratio of Mg/ (Mg + Fe_2^+) with Fe_2O_3/FeO normalized to 0.15] diagrams. MELTS fractional crystallization modeling curves plotted as well. Moderate pressure (3 kbar) anhydrous (0 % H_2O) calculations are displayed. A QFM (Quartz – Fayalite – Magnetite) buffer was used for fO_2 (Ghiorso and Sack, 1995). All major element data for the Ferrar CFBs are from the GEOROC database.

Figure 3.7: Primitive mantle-normalized incompatible trace elements patterns and Chondrite-normalized REE patterns for the Tasmanian Dolerites. Normalization parameters from Sun and McDonough (1989). All trace element data for the Ferrar CFBs are from the GEOROC database.

Figure 3.8: Initial (183 Ma) Sr, Nd, and Pb isotopic compositions of Tasmanian Dolerites. In the two Pb vs. Pb isotope diagrams, the Northern Hemisphere Reference Line (NHRL); (Hart, 1984) is shown. Approximate locations of mantle end-members age-calculated to 183 Ma (Zindler and Hart, 1986) are indicated for reference. BSE = Bulk Silicate Earth, EMI = Enriched Mantle I, EMII = Enriched Mantle II, MORB = Mid-Ocean Ridge Basalt, DMM = Depleted MORB Mantle. All isotope data for the Ferrar CFBs are from the GEOROC database, Pb isotopic data for Ferrar are from Hergt *et al.* (1989b).

Figure 3.9: New plagioclase geochronology data compared with literature data from the Ferrar province. Previous geochronological results from Encarnacion *et al.* (1996); Minor and Mukasa (1997); Burgess *et al.* (2015).

Figure 3.10: (a) Time-temperature path used to calculate the simulated age spectra. (b) Modeled age spectra resulting from a metamorphic cooling path for 150 µm radius crystals of biotite, orthopyroxene, and clinopyroxene compositions. Diffusion parameters and thermal history are given in Table 3.4.

Chapter 4: Primary Hydrous Minerals from the Karoo LIP magmas: Evidence for a Hydrated Source component.

Bryant Ware[1], Fred Jourdan[1], Eric Tohver[2], Kamila Fernandes[2], Massimo Chiaradia[3]

[1]*Western Australian Argon Isotope Facility, Department of Applied Geology and JdL-CMS, Curtin University, Perth, WA 6845, Australia.*

[2] *University of Western Australia, School of Earth and Environment, 35 Stirling Highway, Crawley, WA, Australia*

[3] *Department of Earth Sciences, University of Geneva, 13 Rue de Maraîchers, 1205, Geneva, Switzerland*

4.1. Abstract

The Karoo Continental Flood Basalt (CFB) Province is primarily located in Southern Africa with minor exposures in Antarctica and the Falkland Islands. This ~ 180 Ma province is composed of tholeiitic lava flows and sills as well as a large radiating dyke swarm. The origin of the Karoo CFBs is still debated, with many different and conflicting models proposed. Disparities in these models can often be traced down to the degree of influence a plume and/or the sub-continental lithospheric mantle (SCLM) had during the genesis of this magmatic province.

Nine sills intruded into the Western Cape Province of the Karoo Basin were investigated using $^{40}Ar/^{39}Ar$ geochronology, whole rock geochemistry, and Sr, Nd, Pb isotopes. These sills are peculiar as they contain hydrated minerals (biotite and hornblende), an unusual feature for Karoo basalts. For five of these samples, biotite and/or hornblende separates yielded statistically indistinguishable $^{40}Ar/^{39}Ar$ ages as

plagioclase separates; indicating that the biotite and hornblende found within these samples are primary features requiring that water was present in the magma during the crystallization of those sills.

Major and trace element geochemistry place these rocks into the low-Ti suite of the Karoo CFBs. Trace elements indicate the involvement of fluids over sediment within the source region for these Karoo magmas. All samples from the Western Cape Province display enriched Sr-Nd-Pb initial values with large variations in elemental concentrations for a restricted range of isotopic ratios. Assimilation models indicate these enriched isotopic contents and observed trends are not the result of crustal contamination and are representative of the composition of the source. The trace element and isotopic geochemistry as well as the primary hydrated minerals indicate that water present in the system at the time of formation came directly from one of the mantle sources, supporting the hypothesis that the SCLM was metasomatized by fluids plausibly as a result of the Proterozoic Kibaran Orogeny and/or the Permian Cape Orogeny.

4.2. Introduction

The Karoo Large Igneous Province (LIP) represents one of the largest Continental Flood Basalts (CFBs) on the planet with an estimated area greater than 3 x 10^6 km^2 with exposures Africa (Figure 4.1), along the Princess Martha Coast of Western Dronning Maud Land in Antarctica, and dykes throughout the Falkland Islands (Duncan *et al.*, 1984; Encarnacion *et al.*, 1996; Jourdan *et al.*, 2005; Riley, 2005a; Jourdan *et al.*, 2007a; Jourdan *et al.*, 2008; Stone *et al.*, 2008; Heinonen *et al.*, 2010; Svensen *et al.*, 2012; Heinonen *et al.*, 2014; Luttinen *et al.*, 2015). The province consists of a vast cover of lava flows throughout southern Africa, a huge network of sills and dykes (including giant dyke swarms), as well as localized intrusive centers.

The Karoo Province has been the subject of extensive geochronology studies conducted over the last decade with currently over 100 precise geochronologic data (Encarnacion *et al.*, 1996; Duncan *et al.*, 1997; Jones *et al.*, 2001; Jourdan *et al.*, 2005; Jourdan *et al.*, 2006; Jourdan *et al.*, 2008; Svensen *et al.*, 2012; Sell *et al.*, 2014; Luttinen *et al.*, 2015). The estimated duration of the main volume of the Karoo Province has been constrained by $^{40}Ar/^{39}Ar$ (Jourdan *et al.*, 2008, recalibrated with the ^{40}K constants of Renne *et al.*, 2011) and chemical abrasion thermal ionization mass spectrometry (CA-TIMS) U-Pb (Svensen *et al.*, 2012; Sell *et al.*, 2014) results to an interval from ~ 179 to 184 Ma.

Many different models have been proposed to explain the formation of the Karoo LIP. The differences between the models revolve around the relative contributions of a deep mantle plume and the uppermost mantle (Duncan *et al.*, 1984; Sweeney & Watkeys, 1990; Sweeney *et al.*, 1994; Jourdan *et al.*, 2007a; Heinonen *et al.*, 2014). An important constraint on these models is the ability for heat transfer from the ascending plume or asthenospheric mantle to cause sub-continental lithospheric mantle (SCLM) melting, or if previous charging by fluids provides a fertile and/or relatively hydrated SCLM that can melt via decompression processes. Many studies have proposed that the SCLM, below southern Africa, has been substantially hydrated/metasomatized (Grégoire *et al.*, 2003; Jourdan *et al.*, 2007a; Hopp *et al.*, 2008; Wang *et al.*, 2016); however, no *direct* evidence has been found of these fluids in the rocks of the Karoo LIP. Recent studies suggesting that degassing of volcanic rocks can occur at the surface indicate that some rocks, which appear to contain little water, can in fact arise from hydrated sources (Aubaud *et al.*, 2005). $^{40}Ar/^{39}Ar$ geochronology and major-element, trace-element, and Sr, Nd, Pb geochemical data of biotite and hornblende-bearing sills from the Karroo Province are presented, all

together demonstrating that the hydrous minerals (biotite and hornblende) are primary in nature and suggest the first direct evidence of the presence of water in the mantle source.

4.3. Geologic Setting and Previous Results

4.3.1. Karoo Large Igneous Province

The African portion of the province encompasses much of southern Africa and comprises a range of rock types from nephelinites, picrites, tholeiites, rhyolites, to mid-ocean ridge basalts (Figure 4.1) (Duncan *et al.*, 1984; Jourdan *et al.*, 2007a). The tholeiites constitute the majority of the Karoo rocks and have been subsequently divided into two subgroups; a high-Ti and low-Ti suite. The two suites have been divided based on TiO_2 contents (high-Ti > 2 – 2.5 %; low-Ti < 2 – 2.5 %) as well as P_2O_5 and incompatible trace element concentrations (Duncan *et al.*, 1984). The two tholeiite suites are strongly controlled by location; the high-Ti suite is localized along the craton boundaries of the Kaapvaal and Zimbabwe cratons (Figure 4.1). The low-Ti suite is more widespread and voluminous than the high-Ti suite and is primarily concentrated in southern Africa; southern Lebombo, the Lesotho flows, Namibia, and Botswana (Figure 4.1).

4.3.2. The Karoo Basin igneous rocks

The Karoo sedimentary basin (greater than 0.6×10^6 km^2) dominates the surface geology of the Western Cape Province. The Karoo sedimentary basin is primarily composed of Late Carboniferous to Jurassic non-marine sediments with thicknesses up to 6 km (Eales *et al.*, 1983; Smith *et al.*, 1993). The Karoo Basin have been divided into four groups of sedimentary packages: (1) the ~ 1200 m thick Dwyka Group constitutes the basal depositional package of the Karoo Basin and is dominated

by glacial deposits of the late Paleozoic ice-age that were deposited directly onto the Cape Supergroup after a temporally protracted hiatus; (2) the organic rich Permian Ecca Group overlies the Dwyka Group with a maximum thickness of 3000 m in southern portions of the basin; (3) Permian to Triassic fluvial sediments of the Beaufort Group conformably overlie the Ecca Group and represent the thickest portions of the basin with a maximum thickness greater than 5000 m; (4) the uppermost portion of the basin is composed of the Stormberg Group, which is capped by lavas of the Drakensberg Group (Eales *et al.*, 1983; Smith *et al.*, 1993; Jourdan *et al.*, 2008; Svensen *et al.*, 2012; Lanci *et al.*, 2013; Tohver *et al.*, 2015). The Karoo CFBs intruded into and throughout the Karoo sedimentary basin with some flows forming coevally with the latest stages of sedimentary deposition. Thick sills (up to 200 m thick) are emplaced as extensive sheets throughout much of the Ecca Group of the Karoo Basin (Svensen *et al.*, 2012). The dense network of sills throughout the Karoo sedimentary basin reaches its maximum abundance within the Beaufort Group where the sill system is structured into more saucer-like shapes (Jourdan *et al.*, 2008; Svensen *et al.*, 2012). In the uppermost groups of the Karoo Basin the sills become much less common (Stormberg Group), to even nonexistent in the Drakensberg Group lavas, suggesting this intrusive network were feeders to the lava group. The sills are estimated to comprise roughly 30 % of the Karoo Basin's thickness, representing a large volume of dolerite within a relatively localized area of the Karoo Province (Svensen *et al.*, 2012). The geochemistry of the dolerite intrusions through the Karoo sedimentary basin are all low-Ti tholeiites with major and trace elements similar to the low-Ti suite found elsewhere in the Karoo LIP (Neumann *et al.*, 2011). The geochronology for this region of dolerites within the Karoo CFB Province is mostly relegated to a small number of

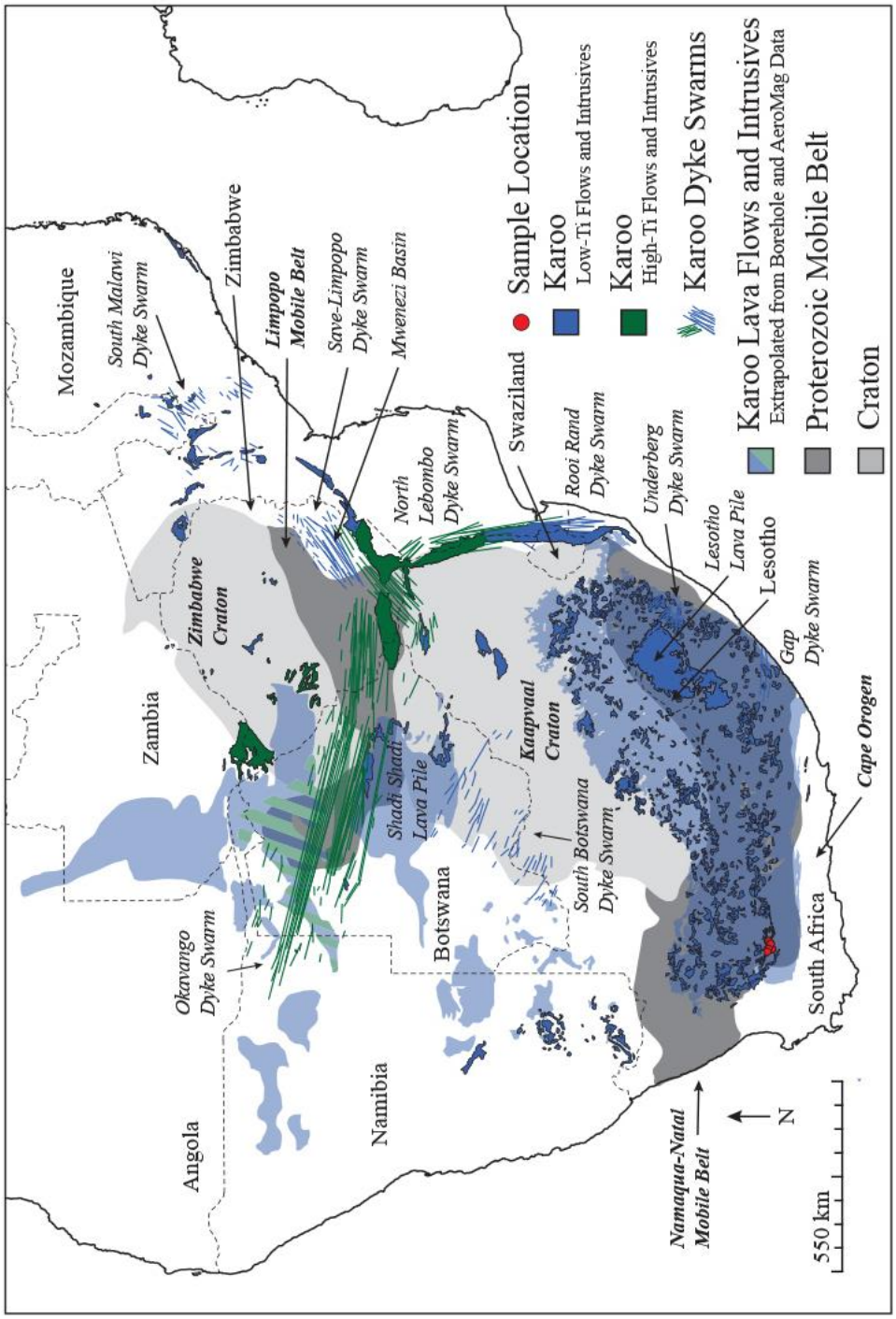

Figure 4.1: Sketch map of the African portion of the Karoo Continental Flood Basalt (CFB) Province's distribution and constituent suites. Modified and created after Jourdan *et al.* (2006); Jourdan *et al.* (2007a); and Svensen *et al.* (2012). Bold italics indicate relevant lithosphere types, labels in italics indicate relevant flows and intrusions of the Karoo CFBs, and countries of the African continent are labeled in a normal font.

studies (Encarnacion *et al.*, 1996; Duncan *et al.*, 1997; Riley, 2005b; Jourdan *et al.*, 2008; Svensen *et al.*, 2012) focusing on the sills and dykes located in the eastern region of the Karoo Basin. Four sills from the western Karoo Basin have been dated by zircon U/Pb geochronology, with ages ranging from 182.5 ± 0.4 Ma to 182.9 ± 0.5 Ma (Svensen *et al.*, 2007; Svensen *et al.*, 2012). Results from the eastern margins of the Karoo sedimentary basin based on zircon U/Pb data and full $^{40}Ar/^{39}Ar$ plateau ages (including over 70 % of ^{39}Ar released) suggests a more extended emplacement duration of ~ 3 Ma (Encarnacion *et al.*, 1996; Jourdan *et al.*, 2008; Sell *et al.*, 2014). It must be noted that one sample (SA101) from Jourdan *et al.* (2008) contained biotite that gave an $^{40}Ar/^{39}Ar$ plateau age of 184.4 ± 1.6 Ma, indicating the only instance from the literature of primary hydrous minerals within the sills of the Karoo sedimentary basin.

4.4. Sample Selection and Analytical Methods

Nine biotite or hornblende-bearing dolerite sills intruded into the Western Cape Province of the Karoo Basin were the focus of this study (Figure 4.1). The whole rock major and trace element and the Sr-Nd-Pb isotopic results are displayed in the supplementary material. The $^{40}Ar/^{39}Ar$ geochronological data from this study can be found in Table 4.1.

4.4.1. Major and trace element analyses

For this study all of the major and trace element analyses were conducted at Genalysis Laboratory Services Pty Ltd in Perth (Australia). The samples were crushed with a steel hydraulic press where rock chips were hand chosen based on how fresh they appeared, avoiding weathered and saw cut surfaces. These chips were then crushed into a powder using an agate mortar and pestle. Major element analysis was performed by XRF on fused discs. These discs were produced by a lithium borate

fusion technique in platinum crucibles (Genalysis Laboratory Services Pty Ltd method code FB1/XRF20). Trace element analysis was conducted using the inductively coupled plasma mass spectrometry (ICP-MS) method on samples dissolved using a lithium metaborate/tetraborate fusion (Genalysis Laboratory Services Pty Ltd method code FB6/MS). Sc and V underwent analysis by inductively coupled plasma optical (atomic) emission spectrometry (ICP-OES). For the remaining elements Ag, As, Be, Bi, Cd, Co, Ge, In, Li, Mo, Pb, Re, Sb, Se, Te, Tl (ICP-MS analyses; method code 4A/MS) and Cu, Ni, Zn (ICP-OES analyses: method code 4A/OE) a four acid digestion (Hydrofluoric, Nitric, Perchloric and Hydrochloric acids in Teflon Tubes) was implemented. To obtain reproducibility, analyses of sample KB was duplicated. Three procedural blank analyses were also performed: one control blank for every major and trace element analysis and two other control blanks for trace element analyses. One acid blank analysis was performed for the trace element measurements. Internal standards OREAS 24b, OREAS 45d, and OREAS 45d for the trace element analyses and SY-4 for the major element analyses were used to monitor the accuracy of the instruments (Appendix F). To obtain reproducibility each analysis was duplicated along with performing analyses of three control blanks and an acid blank per sample analysis.

4.4.2. Sr-Nd-Pb isotope analyses

Sr, Nd, and Pb isotope analyses were completed at the Department of Earth Sciences, University of Geneva (Switzerland). The nine samples were crushed into small chips using a hydraulic press. The chips were rinsed with distilled H_2O and selected under a binocular microscope to avoid any saw marks or weathered surfaces. The clean chips were then powdered by hand using an agate mortar and pestle and ca. 150 mg of powder were attacked during 7 days in Savillex® Teflon vials using 4

ml of concentrated HF and 1 ml of HNO_3 15 M, at a temperature of 140 °C and with the help of ultrasonication for 30 min twice a day (Chiaradia *et al.*, 2011). Subsequently, samples were dried and re-dissolved for 3 days (also with 30 min ultrasonication twice a day) in 3 ml of HNO_3 15 M and dried again. Sr, Nd and Pb were purified from the sample matrix using cascade columns with Sr-Spec, TRU-Spec and Ln-Spec resins according to a protocol modified after Pin *et al.* (1994). Finally, the separates were re-dissolved in 2% HNO3 solutions and ratios were measured using a Thermo Neptune PLUS multicollector ICP-MS on Faraday cups in static mode using the virtual amplifier mode. Ratios used to correct instrumental fractionation were: $^{88}Sr/^{86}Sr = 8.375209$ for the $^{87}Sr/^{86}Sr$ ratio, $^{146}Nd/^{144}Nd = 0.7219$ for the $^{143}Nd/^{144}Nd$ ratio and $^{203}Tl/^{205}Tl = 0.418922$ for the three Pb ratios (a Tl standard was added to the solution). Interferences at masses 84 (^{84}Kr), 86 (^{86}Kr) and 87 (^{87}Rb) were corrected by monitoring ^{83}Kr and ^{85}Rb, ^{144}Sm interference on ^{144}Nd was monitored on the mass ^{147}Sm and corrected by using a $^{144}Sm/^{147}Sm$ value of 0.206700 and ^{204}Hg interference on ^{204}Pb was corrected by monitoring ^{202}Hg.

Used external standards were SRM987 ($^{87}Sr/^{86}Sr = 0.710248$: MacArthur et al., 2001; long-term external reproducibility: 10 ppm, 1σ), JNdi-1 ($^{143}Nd/^{144}Nd = 0.512115$; Tanaka et al., 2000; long-term external reproducibility: 10 ppm, 1σ), and SRM981 (Baker et al., 2004) for Pb (long-term external reproducibility was 0.0048% for $^{206}Pb/^{204}Pb$, 0.0049% for $^{207}Pb/^{204}Pb$ and 0.0062% for $^{208}Pb/^{204}Pb$, all at the 1σ level). $^{87}Sr/^{86}Sr$, $^{143}Nd/^{144}Nd$ and Pb isotope ratios were further corrected for external fractionation (due to a systematic difference between measured and accepted standard ratios from the above references) by − 0.025‰, + 0.049‰, and + 0.36‰ respectively. Total procedural blanks were < 500 pg for Pb and < 100 pg for Sr and

Nd which are insignificant compared to the amounts of these elements purified from the whole rock samples investigated.

4.4.3. $^{40}Ar/^{39}Ar$ Geochronology Analyses

Five low-Ti samples from sills intruded into the Western Cape Province that contained either biotite or hornblende were selected for $^{40}Ar/^{39}Ar$ geochronology analyses. Due to the primary aim of this study to test if the hydrous minerals present within these Karoo dolerites are primary features; the mineral preparation and mineral picking were not optimized for high-precision analyses. These samples were crushed using the same methods as discussed above for the geochemical analyses. Crushed samples sieved to a size fraction of 125 – 212 μm were subsequently separated using a Frantz magnetic separator. The plagioclase separates were concentrated in the non-magnetic fraction and further picked using a binocular microscope. The most unaltered and optically transparent grains were selected for further analysis. The plagioclase crystals were subhedral (primarily) to anhedral, vitreous, and transparent. Some samples displayed evidence for slight alteration with small inclusions. These slightly altered grains were avoided when selecting the plagioclase grains for geochronology analyses. Between 5 and 7 mg were picked for each of the 8 samples chosen for population geochronological analyses.

The biotite and hornblende minerals were concentrated within the magnetic fraction. From this magnetic fraction the minerals were further separated by hand picking the cleanest and freshest looking grains under a binocular microscope. As with the plagioclase the 125 – 212 μm size fraction was used to pick from for further analyses. Biotite grains chosen for geochronological analyses were subhedral, with a brownish color, and platy habit. Some grains display slight alteration, and were avoided when picking. Between 12 and 31 grains were picked for irradiation from each

sample. Only one sample contained hornblende for analysis (KF), from which no biotite was observed. Both the biotite and hornblende samples were analyzed as population analyses with all of the cleanest grains irradiated loaded for biotite and 5 mg of the 14 mg irradiated loaded for the hornblende.

The separated plagioclase and hornblende grains were leached using dilute 5 N HF for one minute per aliquot then rinsed in distilled H_2O in an ultrasonic cleaner. The biotite grains were not leached in HF due to the crystal structure, which risks being broken down and disaggregated into thin sheets when exposed to HF. A lack of an HF leach for biotite is acceptable due to the high amount of K within this mineral as well as the fact that sericite does not affect biotite. The samples were loaded into several 1.9 cm diameter by 0.3 cm depth aluminum discs and irradiated in Cadmium-Lined In-Core Irradiation Tubes (Cd shielded to minimize undesirable nuclear interference reactions) in the TRIGA Reactor at Oregon State University for 40 hours in two different irradiation batches.

The $^{40}Ar/^{39}Ar$ geochronological analyses were conducted at the Western Australian Argon Isotope Facility at Curtin University. All samples were analyzed in static mode using a Thermofisher© (Oostingh *et al.*, 2017) ARGUS VI mass spectrometer. The samples were step-heated using a continuous 100 W PhotonMachine© CO_2 (IR, 10.4 μm) laser fired on the crystals during 60 seconds. Each of the standard crystals were fused in a single step. The gas was purified in an extra low-volume stainless steel extraction line of 240cc utilizing two SAES AP10 and one GP50 getters. Measurements were carried out using four faradays to measure mass 40 to 37 and a low background compact discrete dynode ion counter to measure mass 36. The relative abundance of each mass was measured simultaneously using 10 cycles of peak-hopping and 33 seconds of integration time for each mass. Detectors were

calibrated to each other electronically first then using air shot beam signals. Blanks were monitored every 3 to 4 steps. The raw data were processed using the ArArCALC software (Koppers, 2002). The ages were calculated with the GA1550 (age of 99.738 ± 0.104 Ma) neutron flux monitor (Renne *et al.*, 2011b). The J-values computed from the standard grains were 0.01062800 ± 0.00000500 and 0.01131200 ± 0.00001131, for each of the irradiation. The mass discrimination was monitored on an automated air pipette providing a range of values from 0.993417 ± 0.03 to 0.997411 ± 0.06 per dalton. For interfering isotopes the following correction factors, with 1 sigma errors, were implemented ($^{39}Ar/^{37}Ar$) Ca = 6.95×10^{-4} (± 1.3 %), ($^{36}Ar/^{37}Ar$) Ca = 2.65×10^{-4} (± 0.84 %) and ($^{40}Ar/^{39}Ar$) K = 7.30×10^{-4} (± 12.4 %) (Renne *et al.*, 2013).

4.5. Petrography

All of the samples were derived from fine to medium-grained dolerite dykes and sills and comprise plagioclase, clinopyroxene, and Fe-Ti oxides with ca. 5 % or less of hydrous minerals (biotite or hornblende). These dykes and sills are typically phenocryst-poor (Figure 4.2) and are characterized by an ophitic to almost seriate texture with grain sizes ranging from less than a millimeter to some plagioclase and clinopyroxene crystals measuring up to 7 millimeters. In all the samples the columnar to prismatic plagioclase displaying excellent multiple and Carlsbad twinning. Some of the large plagioclase grains display zoning. The clinopyroxene occurs as subhedral to anhedral augite in all samples. In some clinopyroxene grains twinning is readily apparent. The augite crystals on occasion display an intergrowth texture within the gaps of the columnar plagioclase grains. In many of these samples a minor amount of 0.5 – 2 mm sized biotite crystals are present. The majority of the biotite grains display well-defined grain boundaries with the plagioclase and augite (Figure 4.2a, b). The grains are all pleochroic brown to a deep dark brown in plain polarized light (PPL) and

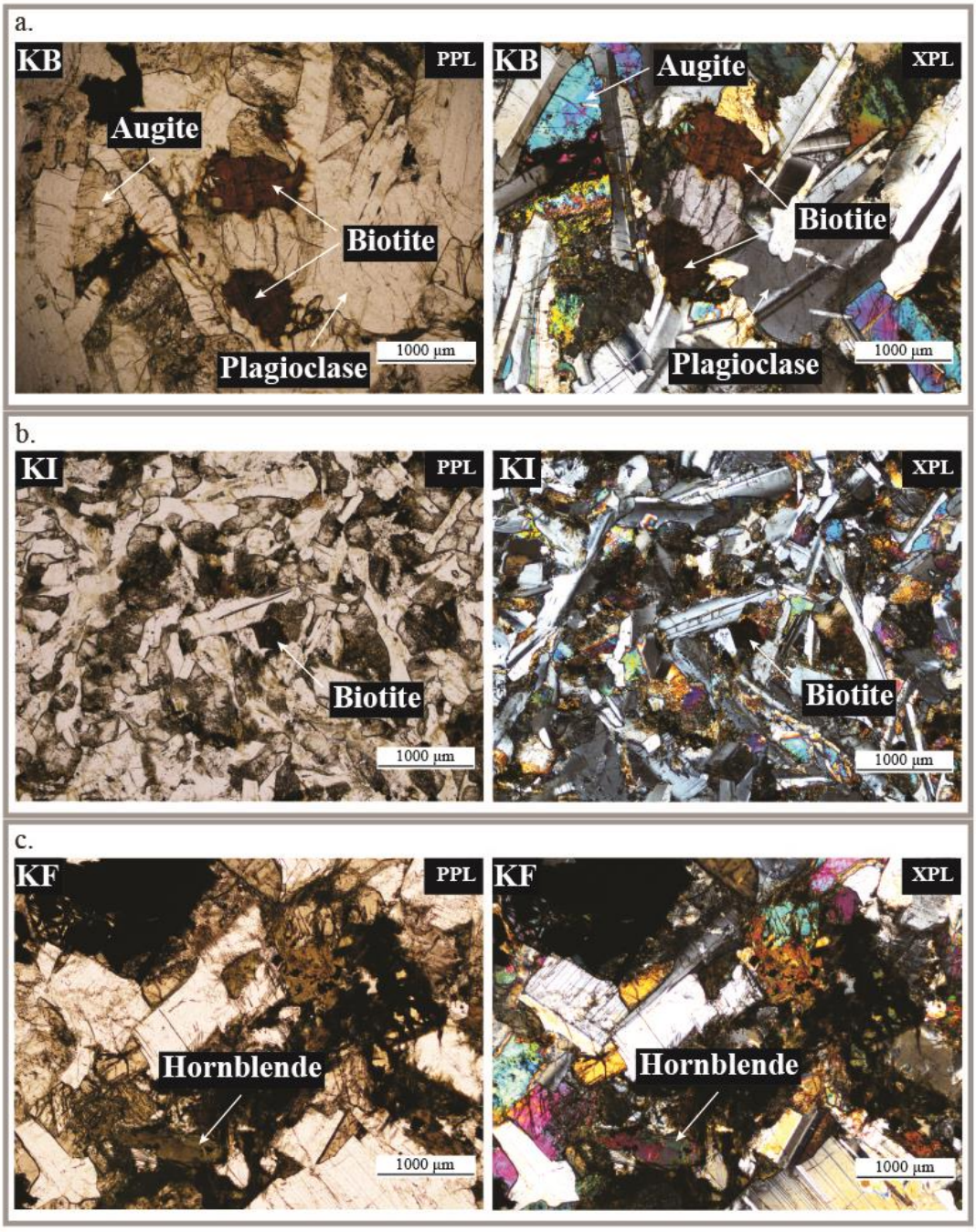

Figure 4.2: Photomicrograph of selected samples displaying petrography, freshness, and hydrous mineral crystal textures. Mineral phases labeled for convenience. Scale bar represents 1000 µm.

a dark brown in cross polarized light (XPL). One sample (KF) that contained no biotite displayed roughly 3 % modal amount of hornblende (Figure 4.2c). Petrographically the hornblende crystals displayed less defined grain boundaries than the biotite crystals of other samples. The hornblende was a green to brown in both PPL and XPL, displaying pleochroism from darker to lighter of the aforementioned colors in PPL.

Some of these hornblende grains within this sample appear as well defined crystals suggesting a primary crystal relationship with the plagioclase and pyroxenes (Figure 4.2c). However, a small minority of the amphibole present within these dolerites display a minor degree of alteration and less defined boundaries around the borders of pyroxene grains. The augite within sample KF also appear to have alteration products of rutile in an accessory mineral abundance.

All of the samples display only minor to nearly no degree of alteration. Alteration that does occur is most evident within some of the pyroxene grains with a slightly mottled look (most apparent in PPL) causing darker patches obscuring the grains. Sample KF displays the greatest degree of alteration within the hornblende and rutile alteration of augite. The overall excellent quality of the plagioclase with still strongly developed twin's and minor to no patches of sericite (Verati & Jourdan, 2013) provides the greatest visual measure on the low amount of alteration of these samples from the Western Cape Province.

4.6. Geochronology

4.6.1. $^{40}Ar/^{39}Ar$ geochronology

Five samples (KB, KC, KD, KF, and KG) were chosen for plagioclase $^{40}Ar/^{39}Ar$ analyses using the ARGUS VI (Figure 4.3, Table 4.1). Two plagioclase samples (KB and KF) produced precise plateau ages of 182.11 ± 0.83 (MSWD = 0.38, P = 1.00) and 183.27 ± 0.62 Ma (MSWD = 0.25, P = 1.00). Plagioclase separates from samples KC and KG produced less precise plateau ages of 182.92 ± 2.11 (MSWD = 0.07, P = 1.00) and 183.97 ± 1.09 Ma (MSWD = 0.50, P = 0.97). All plateau ages include more than 88 % of ^{39}Ar released. One plagioclase sample (KD) produced a mini-plateau age of 182.54 ± 0.84 Ma, including 45 % of the total ^{39}Ar released with

an MSWD of 0.52 and a probability of 0.93. For all samples a dip in the K/Ca ratio is observed roughly around the 70 % ^{39}Ar release mark, with ratios ranging from 0.01 to 0.04 (Figure 4.3).

The five samples analyzed contained hydrous minerals that were also dated using the ^{40}Ar/^{39}Ar technique to assess if these crystals were primary or an alteration product (Figure 4.3, Table 4.1). Sample KB, KC and KG yielded biotite plateau ages of 184.59 ± 0.72 Ma (MSWD = 1.27; P = 0.21), 184.56 ± 0.63 Ma (MSWD = 1.27; P = 0.24), and 184.45 ± 1.93 Ma (MSWD = 0.15; P = 1.00), respectively. All of these samples have a hump-shape spectrum with younger low-temperature steps that suggest either diffusive Ar loss or recoil redistribution. Since the plagioclase from the same samples do not show any sign of Ar loss and some of the steps in all three biotite spectra are older than the plateau age, it is concluded that these crystals most likely suffered from recoil redistribution (Turner & Cadogan, 1974; Hess & Lippolt, 1986; Villa, 1997; Paine *et al.*, 2006; Jourdan *et al.*, 2007c; Jourdan & Renne, 2013). In the instance of recoil, the total fusion ages (integrating all steps in one age) ranging from 181.6 ± 2.2 Ma to 183.8 ± 1.2 Ma might be closer to the crystallization age of the sills (Encarnacion *et al.*, 1996; Svensen *et al.*, 2007; Jourdan *et al.*, 2008; Svensen *et al.*, 2012; Sell *et al.*, 2014), compared to the plateau ages.

One of the biotite (KD) samples and the hornblende (KF) sample did not return any plateau ages (Figure 4.3). The first few heating steps of the biotite sample (KD) yielded a relatively old apparent age (ca. 900 Ma) with nearly a steady decrease after the first five steps suggesting the presence of excess ^{40}Ar. Therefore, the youngest steps converging towards ~ 200 Ma likely indicate a minimum age for this sample. The hornblende sample has likely been affected by alteration as apparent in the petrographic observations and confirmed by variable K/Ca ratios for each step.

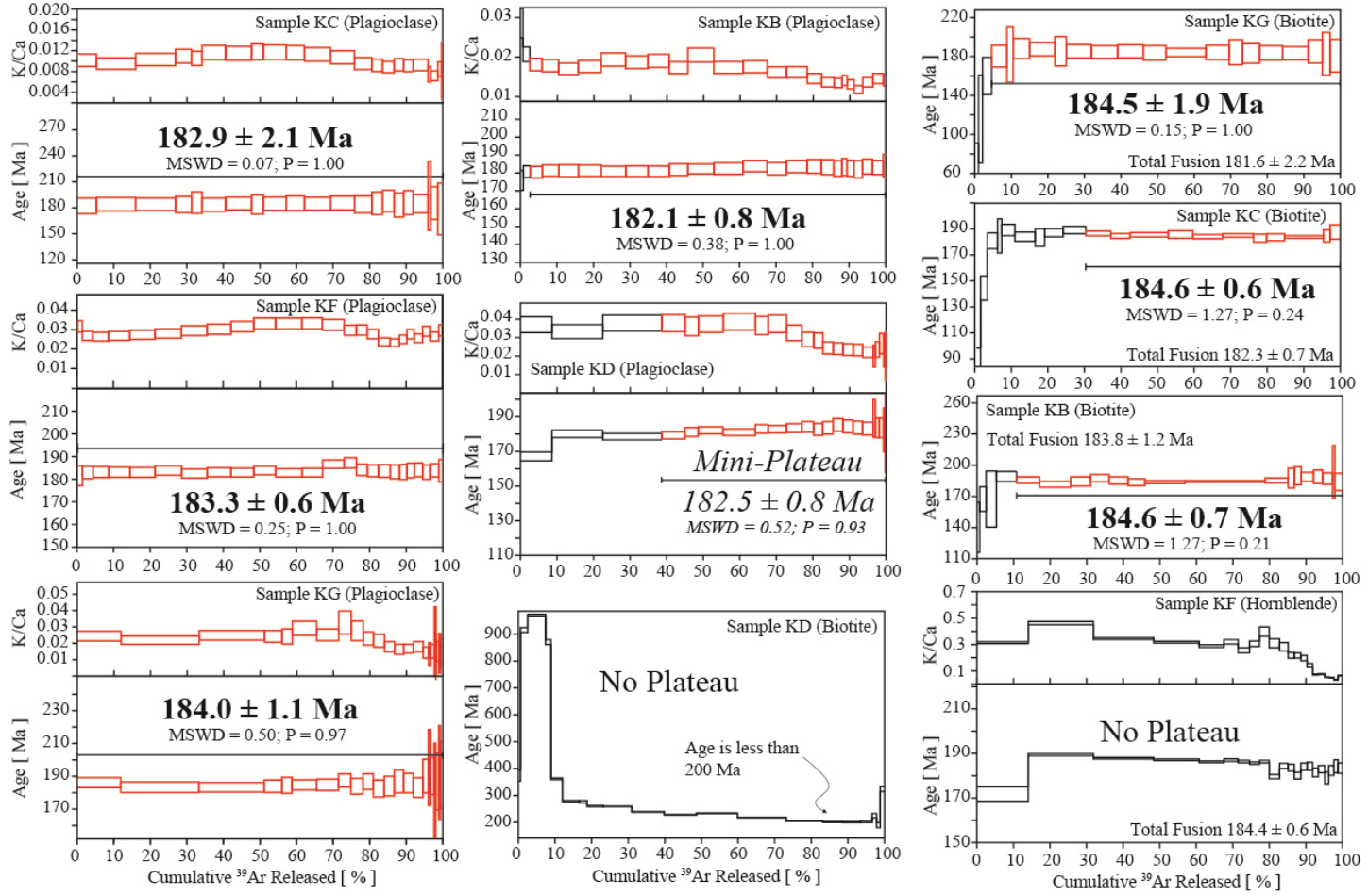

Figure 4.3: $^{40}Ar/^{39}Ar$ apparent age and related K/Ca ratio spectra for plagioclase, biotite, and hornblende separates plotted against the cumulative percentage of ^{39}Ar released (the K/Ca ratios were not plotted for samples that did not yield concordant plateau ages or biotite analyses due to a low concentration of Ca). Errors on plateau ages are quoted at 2σ. Bold fonts indicate plateau ages and italics font for sample KD indicate a mini-plateau age.

Sample	Coordinates Zone 55 (UTM)	Mineral	Total Fusion Age (Ma)	Plateau (Ma)	Total ^{39}Ar Released (%,n)	MSWD	P	Isochron Age (Ma)	Spreading Factor (%)	^{40}Ar/^{36}Ar Intercept	MSWD	P
KB	32.4483 S	Plagioclase	182.09 ± 0.83	182.11 ± 0.83	97.33 (22)	0.38	1.00	182.0 ± 1.81	15.4	301.0 ± 36.2	0.40	0.99
	20.6604 E	Biotite	183.85 ± 1.19	184.59 ± 0.72	89.18 (16)	1.27	0.21	184.5 ± 0.87	67.3	302.3 ± 2.2	1.60	0.07
KC	32.4443 S	Plagioclase	182.84 ± 2.18	182.92 ± 2.11	100.00 (22)	0.07	1.00	183.33 ± 2.33	85.6	293.8 ± 12.0	0.05	1.00
	20.6591 E	Biotite	182.28 ± 0.74	184.56 ± 0.63	69.64 (11)	1.27	0.24	183.83 ± 1.19	42.1	300.6 ± 2.9	1.16	0.31
KD	32.3596 S	Plagioclase	179.75 ± 0.66	*182.54 ± 0.84*	44.58 (16)	0.52	0.93	182.55 ± 0.98	74.1	298.5 ± 11.6	0.56	0.90
	20.8800 E	Biotite	-	-	-	-	-	-	-	-	-	-
KF	32.4108 S	Plagioclase	183.58 ± 0.61	183.27 ± 0.62	90.74 (23)	0.25	1.00	183.21 ± 0.67	80.5	299.8 ± 5.3	0.25	1.00
	20.8063 E	Hornblende	184.34 ± 0.59	-	-	-	-	-	-	-	-	-
KG	32.3185 S	Plagioclase	183.97 ± 1.15	183.97 ± 1.09	88.09 (21)	0.50	0.97	182.78 ± 1.91	40.3	328.7 ± 38.1	0.37	0.99
	20.6609 E	Biotite	181.57 ± 2.16	184.45 ± 1.93	95.38 (18)	0.15	1.00	184.45 ± 2.31	15.0	299.9 ± 89.9	0.16	100

Table 4.1: ^{40}Ar/^{39}Ar Geochronology of Primary Hydrous Minerals from Dolerite Sills of the Western Cape Province**.** Plateau ages are the preferred ages for interpretation. The calculated J values relative to an age of GA1550 of 99.74 ± 0.10 % Ma. MSWD and probability (P), percentage of ^{39}Ar degassed used in the plateau calculation, number of analyses included in the isochron, and ^{40}Ar/^{36}Ar intercept are indicated. Analytical uncertainties on the ages are quoted at 2 sigma (2σ) confidence levels and at 1σ for the ^{40}Ar/^{36}Ar intercept. Age in italics for KD (plagioclase) is a mini-plateau calculated with 45 % of the total ^{39}Ar released and therefore is not statistically reliable but are listed for information only.

The majority of the heating steps are, however, hovering around 185 Ma. Although these results do not give a precise age, they do strongly suggest a primary nature as the

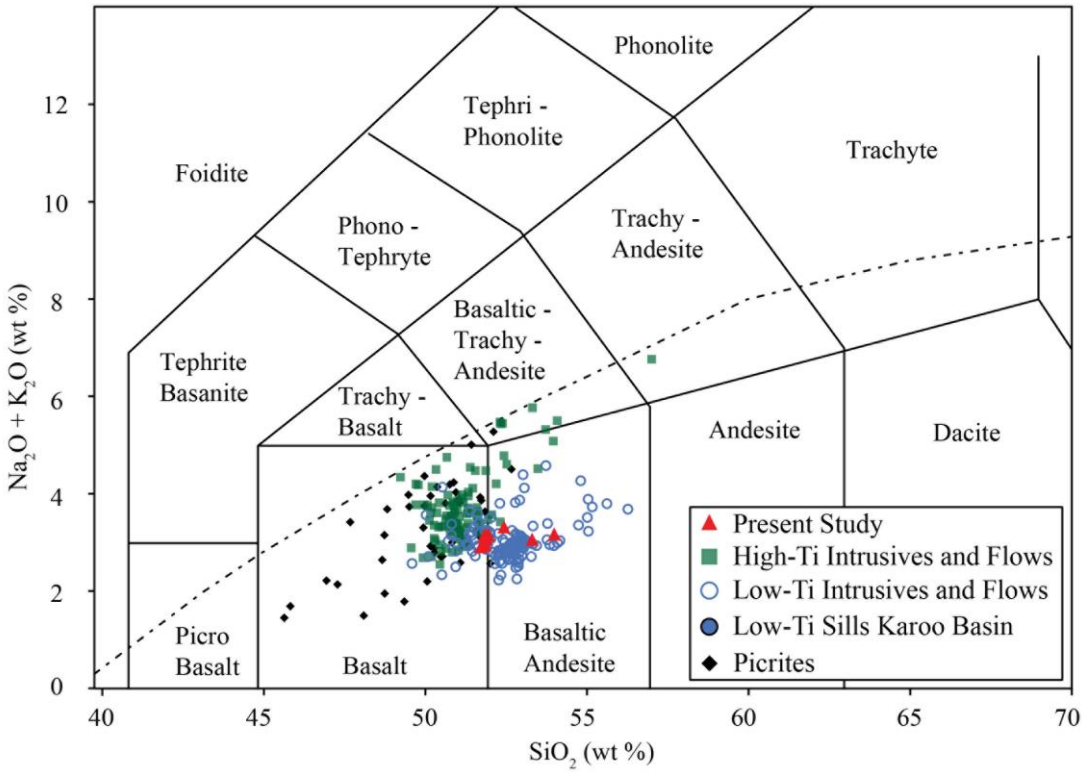

Figure 4.4: Total alkalis-silica (TAS) Diagram, (Bas *et al.*, 1986). Alkalic-subalkalic line from Irvine and Baragar (1971).

obtained age is similar to other plagioclase and zircon results from Karoo.

4.7. Geochemistry

4.7.1. Major and trace elements

All nine samples bulk rock compositions are subalkalic (tholeiitic) falling into the basaltic andesite field or right on the border between the basalt and basaltic andesite field in the total alkali silica (TAS) (Bas *et al.*, 1986) diagram (Figure 4.4d). All samples are classified as low-Ti with TiO_2 contents < 2 weight percent (wt. %) falling within the well-defined majority of tholeiitic rocks from the Karoo CFBs. However, these samples represent some of the most evolved samples from the low-Ti suite with MgO content of 7.2 or less wt. % and Mg #'s ranging from 58 to 40 (Table F1). The major element patterns display a negative covariance in regards to Mg # with TiO_2,

FeO_{total} (FeO_t), Na_2O, K_2O, P_2O_5, and MnO and a positive co-variation with Al_2O_3 and CaO wt. %'s (Figure 4.5a – c).

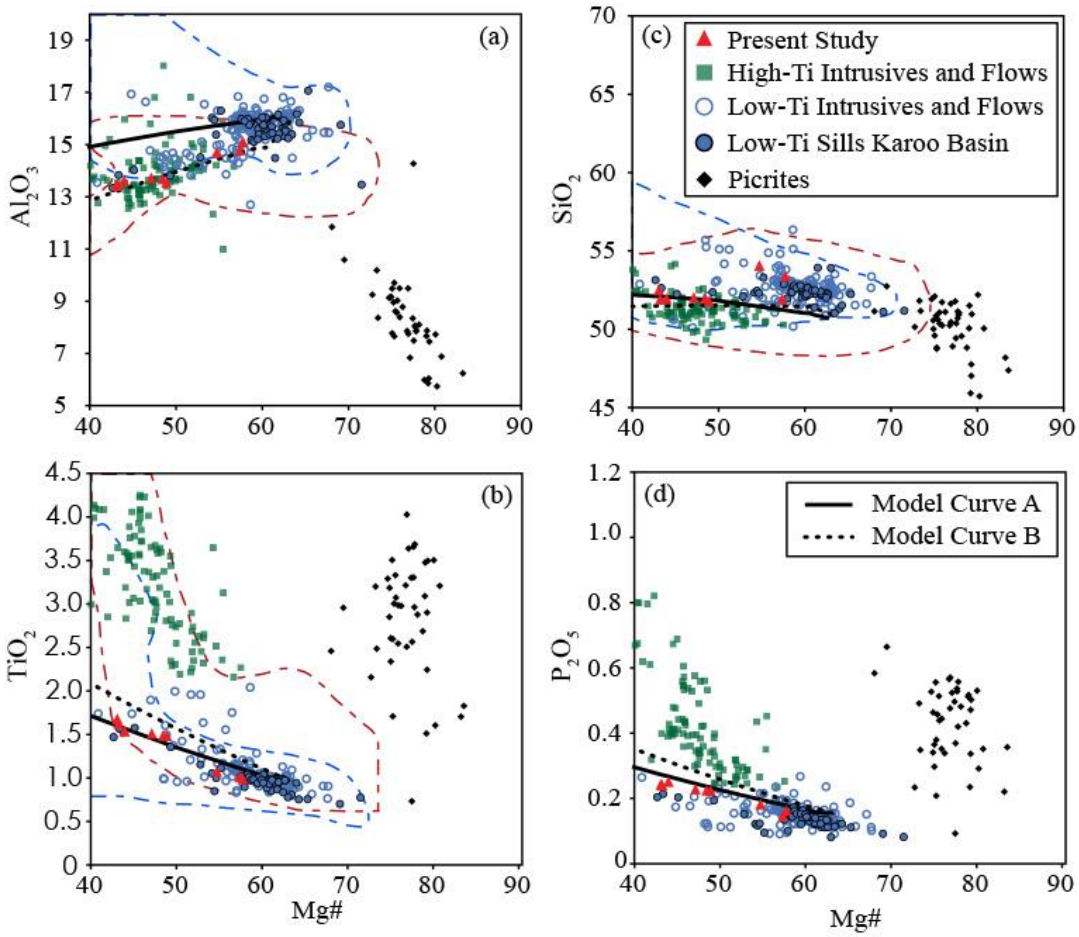

Figure 4.5: (a – d) Major element (wt. %) vs Mg-number [100 x atomic ratio of Mg/ (Mg + Fe_2^+) with Fe_2O_3/FeO normalized to 0.15] diagrams with MELTS fractional crystallization modeling curves for selected major element trends for the Karoo Continental Flood Basalt. MELTS parameters: Model Curve A – low pressure (1 kbar) hydrous (0.5 % H_2O) and Model Curve B – low pressure (1 kbar) anhydrous. A QFM (Quartz – Fayalite – Magnetite) buffer was used for fO_2 (Ghiorso & Sack, 1995). Dashed red lines represent anhydrous and blue dashed lines represent hydrous experimental data compiled by (Wang *et al.*, 2016). All geochemical data for the Karoo CFBs are from the GEOROC database.

The REE and trace element patterns of the Karoo CFBs have a negative slope when plotted in variation diagrams normalized to chondrite and primitive mantle, respectively (Figure 4.6a and b). The samples from this study plot in the range of the low-Ti suite of Karoo. The slight negative slope in both the REE and trace element variation diagrams is related to a low incompatible trace element concentration with a slight LREE enrichment as well as a small ratio between LREE and HREE, and La/Sm

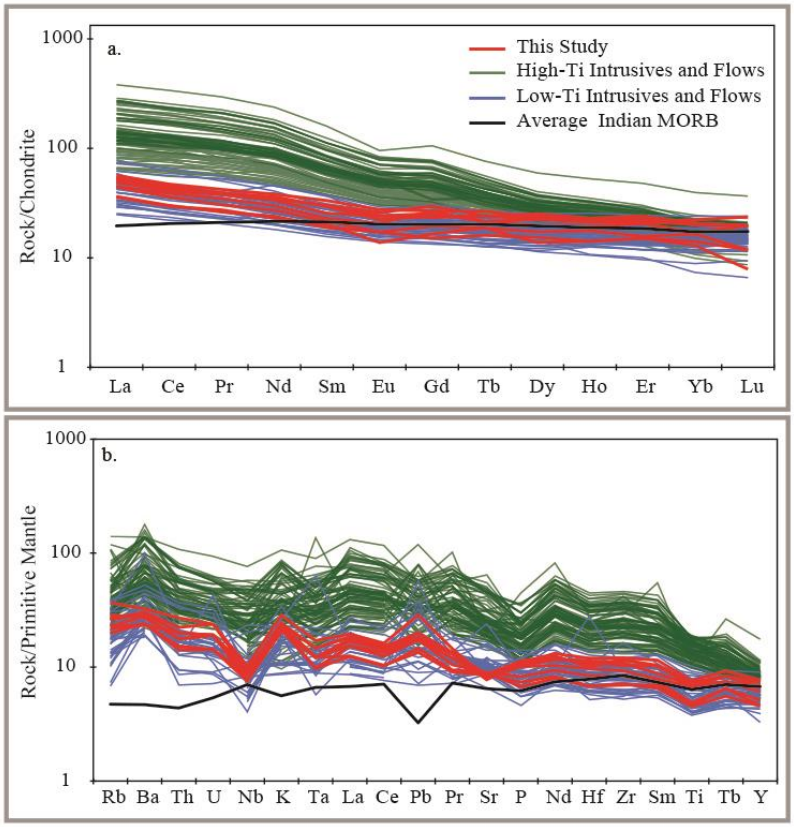

Figure 4.6: (a) Primitive mantle normalized incompatible trace elements patterns. (b) Chondrite normalized REE patterns. Normalization parameters from Sun and McDonough (1989). All geochemical data for the Karoo CFBs are from the GEOROC database.

chondrite normalized (cn) values of 1.63 – 2.05. The low-Ti Karoo suite contains LREE concentrations higher than Indian MORB (mid-ocean ridge basalt) and lower than Indian MORB in the HREE patterns (Figure 4.6a and b). The trace element patterns for these Karoo samples display a pronounced negative Nb and Ta anomalies and a positive Pb anomaly (normalized to primitive mantle).

4.7.2. Sr-Nd-Pb isotopes

The isotope results for the analyzed samples display a tight cluster with only minor variations ($^{143}Nd/^{144}N_i$ = 0.51233 – 0.51237; $^{87}Sr/^{86}Sr_i$ = 0.7054 – 0.7059; $^{206}Pb/^{204}Pb_i$ = 18.009 – 18.119; $^{207}Pb/^{204}Pb_i$ = 15.584 – 15.599; $^{208}Pb/^{204}Pb_i$ = 37.614 – 37.985) (Figure 4.7 and Table H1). Reported isotopic ratios have been corrected to initial values for in situ decay of the parent isotope from emplacement at 183 Ma to the present.

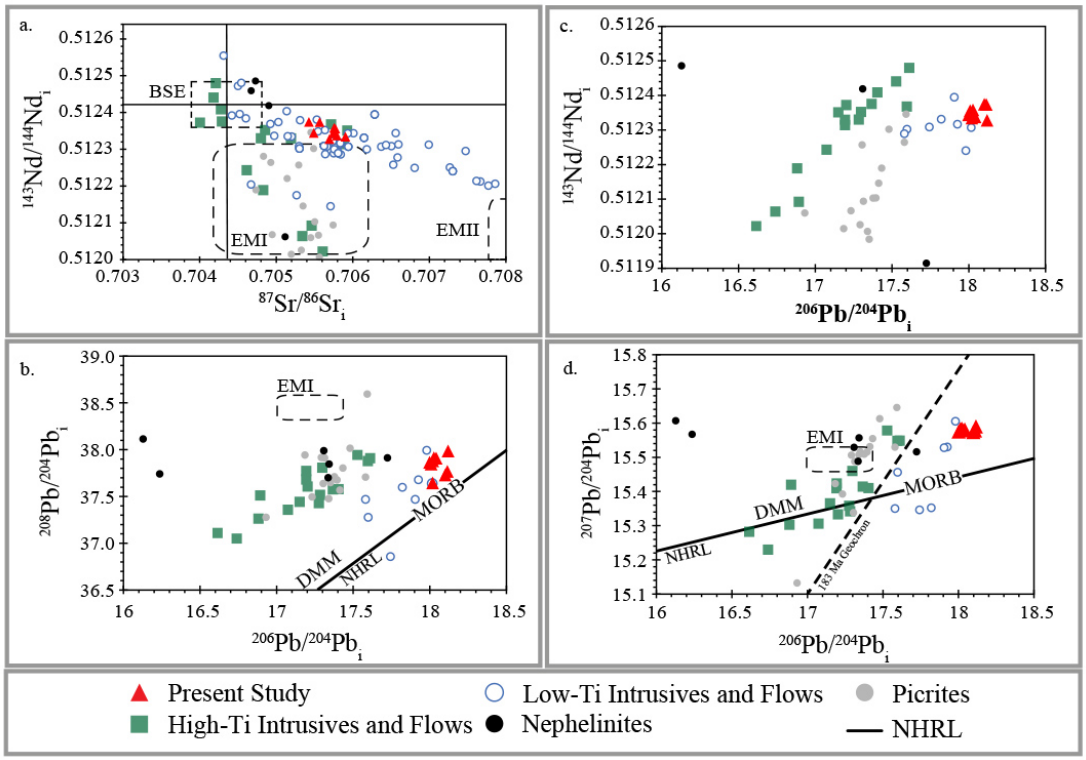

Figure 4.7: Initial (183 Ma) Sr, Nd, and Pb isotopic compositions of the Karoo Continental Flood Basalt (CFB) Province. The Northern Hemisphere Reference Line (NHRL); (Hart, 1984) is shown in Pb vs Pb isotope diagrams. Approximate locations of mantle end-members (Zindler & Hart, 1986) are indicated for reference. BSE = Bulk Silicate Earth, EMI = Enriched Mantle I, EMII = Enriched Mantle II, MORB = Mid-Ocean Ridge Basalt, DMM = Depleted MORB Mantle. All geochemical data for the Karoo CFBs are from the GEOROC database.

$^{87}Sr/^{86}Sr_i$ compositions as a whole for all nine samples do not display a correlation with the Mg # (Figure 4.8). The $^{143}Nd/^{144}Nd_i$ values for all nine samples form a slightly negative trend with decreasing Mg numbers. However, this apparent negative trend is more pronounced with two differing vectors, one defined between samples KA and KG and another defined between samples KA and KD (Figure 4.8). When $^{143}Nd/^{144}Nd_i$ and $^{87}Sr/^{86}Sr_i$ ratios are plotted against each other a slight negative slope is defined with the same vector as the rest of the low-Ti suite of Karoo (Figure 4.7a). These samples from the Western Cape Province lie within the overlapping ranges of the low-Ti and high-Ti suites.

For the Pb isotope results, all of the data plot above the Northern Hemisphere Reference Line (NHRL) (Figure 4.7) and have a small degree of variability in the isotopic ratios. The $^{206}Pb/^{204}Pb_i$ compositions for these Western Cape Karoo sills

exhibit the highest values from all the Karoo mafic rocks (Figure 4.7). The $^{207}Pb/^{204}Pb_i$ isotope ratios for these samples are comparable to other values from the rest of the low-Ti suite. There is little variability in the $^{207}Pb/^{204}Pb_i$ isotope ratios, plotting as a tight cluster in the $^{207}Pb/^{204}Pb_i$ vs $^{206}Pb/^{204}Pb_i$ diagrams. The $^{208}Pb/^{204}Pb_i$ ratios display more variability then the other Pb isotopes (Figure 4.7). These Western Cape sills have $^{208}Pb/^{204}Pb_i$ values comparable with the highest values in the rest of the low-Ti suite (Figure 4.7).

4.8. Discussion

4.8.1. Contemporaneity between plagioclase, biotite, and hornblende.

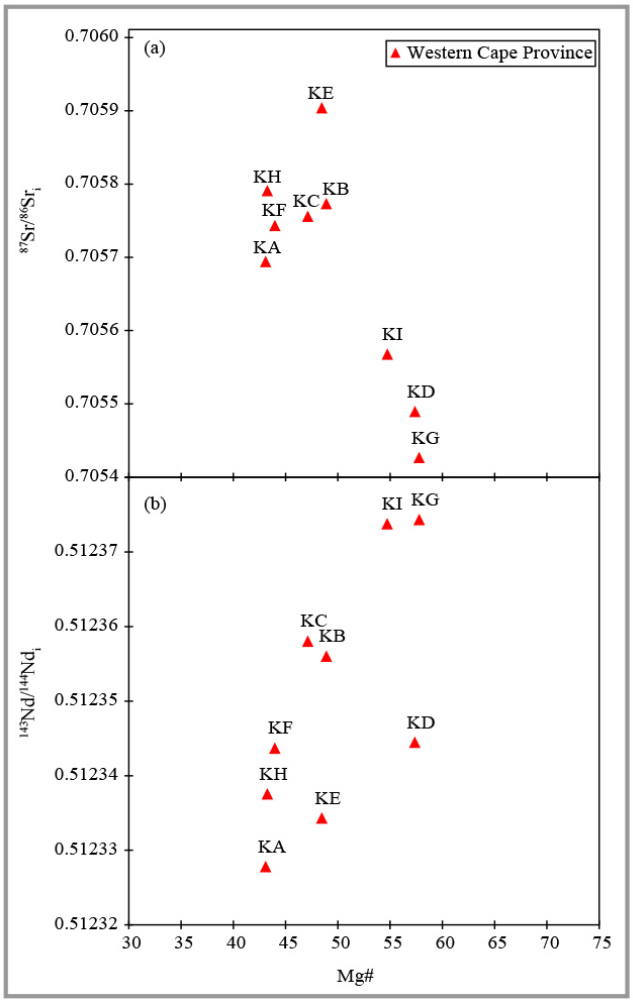

Figure 4.8: (a) $^{87}Sr/^{86}Sr$ initial isotopic composition vs Mg-number and (b) $^{143}Nd/^{144}Nd$ initial isotopic composition vs Mg-number. All isotopic data has been age-corrected to 183 Ma.

Five samples from the nine acquired were distinctive as they contain primary hydrated minerals (biotite and hornblende), an unusual feature for Karoo low-Ti basalts; previously observed in only one large sill in the eastern Karoo Basin (Jourdan *et al.*, 2008). Plagioclase $^{40}Ar/^{39}Ar$ plateau (and mini-plateau) ages range from 182.1 ± 0.8 to 184.0 ± 1.5 Ma. Three of the biotite-bearing samples yielded $^{40}Ar/^{39}Ar$ biotite plateau ages ranging from 184.5 ± 1.9 to 184.6 ± 0.7 Ma and

integrated ages of 181.6 ± 2.2 to 183.8 ± 1.2 Ma, that may or may not be more relevant if irradiation-induced ^{39}Ar recoil has affected the internal ^{39}Ar distribution. Regardless of the fine-tuned accuracy of these ages (see discussion hereafter), these results show that the plagioclase and biotite yielded the same $^{40}Ar/^{39}Ar$ ages within uncertainty (Figure 4.9), hence providing direct evidence of the primary nature of the hydrous minerals within these dolerites.

Two other samples (one hornblende and one with biotite) yielded perturbed $^{40}Ar/^{39}Ar$ spectra. The lack of a plateau age for samples KF (hornblende) and KD

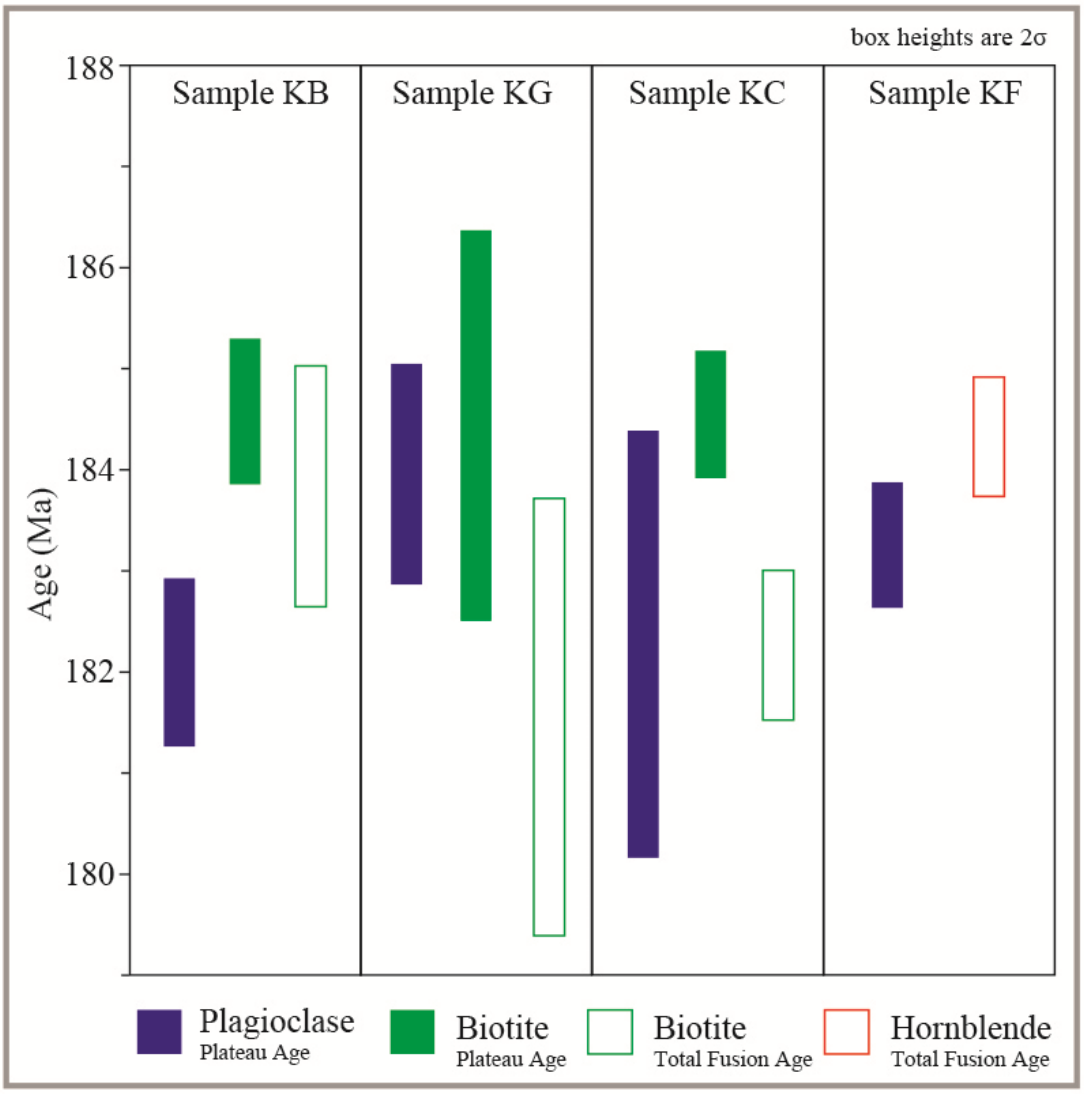

Figure 4.9: Bar graph comparing the plagioclase $^{40}Ar/^{39}Ar$ plateau ages with the $^{40}Ar/^{39}Ar$ biotite plateau and total fusion (error) ages for samples KB, KC, and KG. For sample KF the $^{40}Ar/^{39}Ar$ plagioclase plateau age is compared to the total fusion (error) age of the hornblende.

(biotite) cannot be utilized for precise geochronology of the Karoo Province; however, these semi-quantitative results are still useful to indicate likely contemporaneity between the plagioclase and hydrous minerals. Petrographically the biotite or hornblende grains within these selected samples appeared to be primary. Sample KF did not produce a plateau age due to the alteration apparent in some of the hornblende crystals, which was observed during petrography but was harder to avoid during picking due to the semi-opaque nature of hornblende. However, the step ages are converging to an age ca. 183 – 184 Ma (Figure 4.3). An approximate hornblende $^{40}Ar/^{39}Ar$ age of ca. 183 – 184 Ma is similar to the plateau age of 183.3 ± 0.6 Ma obtained on the plagioclase separates from the same sample (Figure 4.9). The results for the biotite found in sample KD indicate the crystallization age is less than 200 Ma (the youngest heating step). Although results such as this cannot be used to demonstrate the primary nature of the biotite in this particular sample, the results are compatible with such an interpretation and corroborate observations from petrography. Therefore, the $^{40}Ar/^{39}Ar$ geochronology from the sills of the Western Cape Province indicate the plagioclase, biotite, and hornblende within these dolerites crystallized at the same time.

4.8.2. Precise timing of the emplacement of hydrous magmas within the sequence of the Karoo LIP

The apparent age results presented above demonstrate the biotite and hornblende are primary features of the sills. Due to the possibility of the biotite plateau ages being affected by recoil redistribution and possibility of the equivalent total fusion age affected by ^{39}Ar and/or ^{40}Ar loss, the biotite age data cannot be used to place the exact timing of these sills into the context of the rest of the Karoo sequence. The same is true for the two relatively imprecise plateau ages of 184.0 ± 1.1 and 182.9 ± 2.1 Ma

as, although likely accurate, it means that the emplacement age could be anytime between 181 Ma and 185 Ma, which is not as precise as U-Pb ages obtained from other sills within the Karoo sedimentary basin (precision ca. ± 0.5 Ma). Rather, the

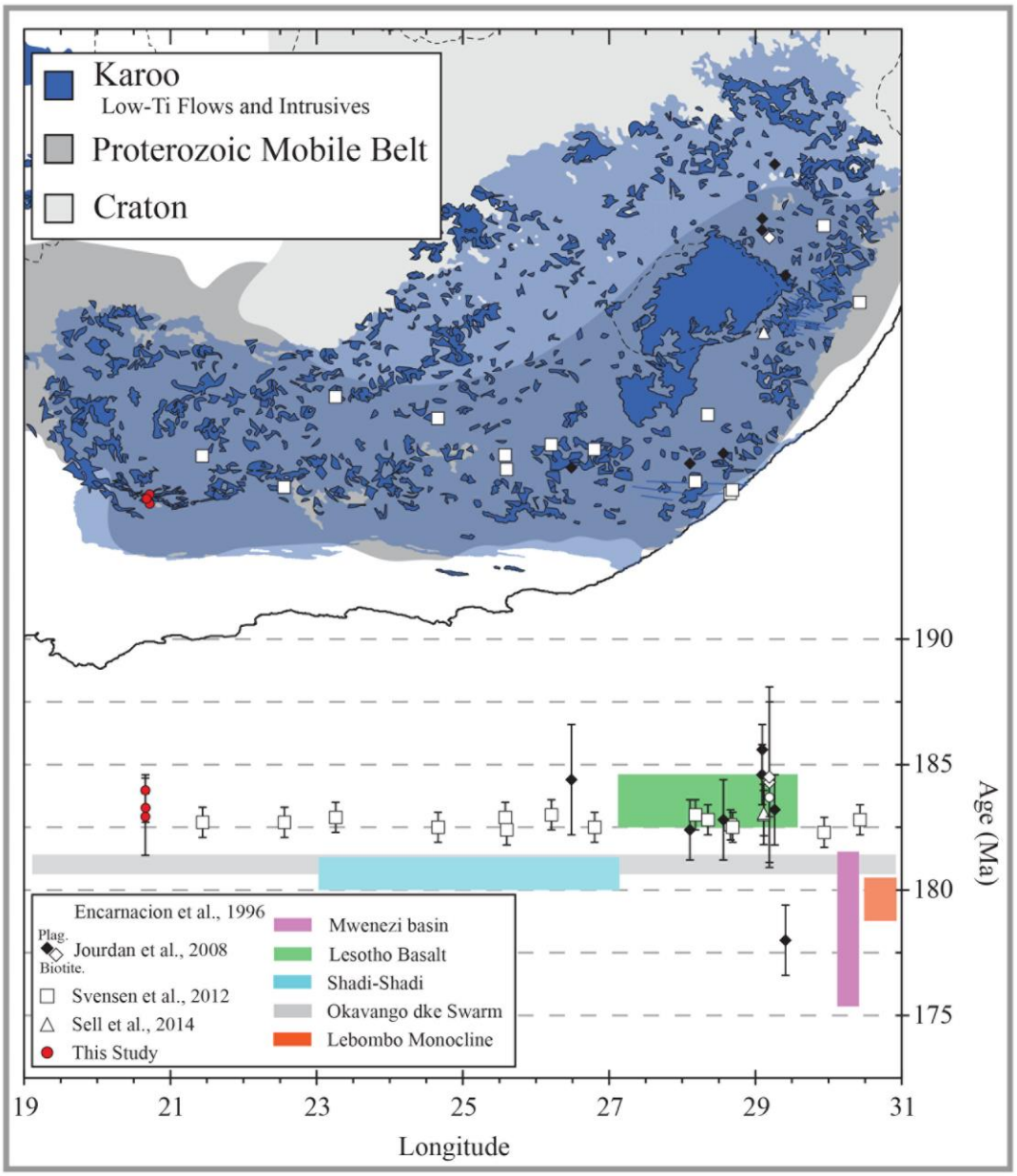

Figure 4.10: Age vs longitude plot of selected geochronological data from sills of the Karoo sedimentary basin. Also represented are ranges or weighted means of available data from: the Menezes Basin (Jourdan *et al.*, 2007b); the Lebombo Monocline (Jourdan *et al.*, 2005 [plagioclase]); (Sell *et al.*, 2014 [zircon]); the Okavango dyke Swarm (Jourdan *et al.*, 2006); the Shadi-Shadi lava pile (Jourdan *et al.*, 2005); the Lesotho Basalt (Jourdan *et al.*, 2007b).

emplacement age of the sills is therefore best approximated by the two plagioclase plateau ages of 182.1 ± 0.8 and 183.3 ± 0.6 Ma (Figure 4.3). Compared to other sills in the area (182.5 ± 0.5 to 182.9 ± 0.5 Ma; Svensen *et al.* (2007); Svensen *et al.* (2012),

the plagioclase ages are slightly older by a few hundred thousand years (Figure 4.10). The two plagioclase ages are indistinguishable from a U-Pb zircon age of 183.7 ± 0.6 Ma obtained on the New Amalfi sill cropping out in the eastern part of the basin (Encarnacion *et al.*, 1996) and slightly older than another sill with a zircon and baddeleyite U-Pb age of 183.0 ± 0.1 Ma (Sell *et al.*, 2014) (Figure 4.10). The plagioclase ages are also similar within uncertainty to a weighted mean age of 183.8 ± 0.6 Ma (MSWD = 1.5; P = 0.11) calculated by pooling eleven $^{40}Ar/^{39}Ar$ full plateau (i.e. > 70 % ^{39}Ar released) ages obtained on plagioclase from sills from the eastern part of the basin (Jourdan *et al.*, 2008) and recalculated using the decay constants and standard ages of Renne *et al.* (2011b) (Figure 4.10). It is also similar to the eruption age of the Lesotho basaltic pile (183.3 ± 0.8 Ma; n = 5 plateaus; P = 0.97), also located in the eastern part of the basin. Those ages, however, are older than the weighted mean ages of 180.5 ± 0.5 Ma (n = 7 plagioclase $^{40}Ar/^{39}Ar$ plateaus; P = 0.35) from e.g.: (1) the 700 m thick Shadi-Shadi lava pile in Botswana (recalculated from Jourdan *et al.*, 2005); (2) the Okavango giant dyke swarm 180.9 ± 0.3 Ma; n = 11 plagioclase $^{40}Ar/^{39}Ar$ plateaus; P = 0.17 (recalculated from Jourdan *et al.*, 2006 reference therein); (3) rhyolite and sills from the Lebombo monocline with one plagioclase $^{40}Ar/^{39}Ar$ age of 179.6 ± 0.6 Ma (recalculated from Jourdan *et al.*, 2007b) and two zircon U-Pb ages of 179.3 ± 0.2 Ma and 180.3 ± 0.2 Ma (Sell *et al.*, 2014); (4) and silicic to gabbroic intrusions from the Mwenezi Basin with $^{40}Ar/^{39}Ar$ ages ranging from 176.2 ± 0.7 to 180.0 ± 1.7 Ma (recalculated from Jourdan *et al.*, 2007b) (Figure 4.1 and Figure 4.10). This shows that the hydrated sills from the Karoo sedimentary basin have been emplaced very early in the Karoo magmatic sequence of the province, and based on the current age database, are among the first magmas to have been emplaced. Thus, the geochronological results of these Western Cape sills suggest water “rich” magmas

will be expelled early in the sequence of intrusions and eruptions and more dry magmas to be emplaced or erupted in the later stages of activity for the Karoo province.

4.8.3. Origin of the water within the sills and dykes of the Karoo Basin

The geochronological data indicate that the biotite and hornblende found within these samples are primary crystals and imply that water (and thus likely other volatiles such as F, Cl, and CO_2) must have been present in the magma during the crystallization of the earliest sills emplaced in the Karoo Province. Two explanations are possible regarding the origin of the water: (1) the water present in the system at the time of formation came from assimilation of sediments from the surrounding basin and/or upper crust during the ascent of the magma from the mantle to the sub-surface; or (2) the water present in the system is inherent to one of the mantle sources inferred in the genesis of the Karoo CFB Province. These hypotheses will be examined using major and trace element and Sr-Nd-Pb isotope geochemistry data.

4.8.3.1. Water in the petrogenesis of the Western Cape Province Dykes and Sills

The dolerites of the Western Cape Province are among the most differentiated rocks of the low-Ti suite with MgO values ranging from 7.2 – 5.0 (Mg # 57 – 43; Figure 4.4a – c). The literature data extends the range of MgO for the low-Ti suite across the whole province to 11.5 – 1.3 (Mg # 74 – 40.9; Figure 4.4a – c); however, only two samples from the literature have a lower MgO value than the hydrated sills. These samples also represent some of the most evolved samples from the available geochemistry of the sills intruded into the Karoo sedimentary basin (Neumann *et al.*, 2011). Rhyolite-MELTS models were calculated using the program and code of Ghiorso and Sack (1995) and Gualda *et al.* (2012) to further test the observed fractionation trend of the low-Ti suite. Model curve A uses the same input parameters and samples as those calculated in Jourdan *et al.* (2007a) [P = 1 kbar, 0.5 % H_2O, fO_2

= QFM] (Figure 4.4a – c; Model Curve A). Model curve A reproduces the rest of the low-Ti suite quite well in many of the major oxides; however, fails to correctly reproduce all of the trends found in the low-Ti Western Cape sills, particularly Al_2O_3 (Figure 4.4a). Although many other models with varying initial compositions and physicochemical parameters were calculated, the resulting model curves were still unable to reproduce the trends observed for these dolerites completely. Dry MELTS modeled liquid line of descents are able to reproduce the Al_2O_3 and FeO_t trends better than curves with initial H_2O present, however, fall short in reproducing all other oxides for the low-Ti suite (Figure 4.4a – c; Model Curve B). The unexplained fractionation trend of the dolerites found in the Karoo Basin was also noted by Neumann *et al.* (2011). The discrepancy could be the result of more complex processes than fractional crystallization (e.g. melt flow through large sills) or even problems with the MELTS model itself (Neumann *et al.*, 2011). The new evidence of primary hydrous minerals within these dolerites could offer a simple explanation for this inconsistency: the role of hydrous minerals during fractional crystallization. The MELTS models calculated from the low-Ti literature dataset and the Western Cape sample collection fractionate biotite late in the evolution. Due to the differentiated nature of even the most 'primitive' low-Ti tholeiites of the Karoo CFBs, the starting composition used in the MELTS models have in fact already undergone some level of differentiation. Regardless, the MELTS models indicate that for the Western Cape sills and the low-Ti suite as a whole, water was integral to create the best fit liquid line of descent for the fractionation of the Karoo magmas.

4.8.3.2. Is the water coming from the assimilation of sedimentary or upper crustal material?

Previous studies of the Karoo LIP low-Ti suite have demonstrated a varying amount of crustal contamination (e.g. Jourdan *et al.*, 2007a; Neumann *et al.*, 2011).

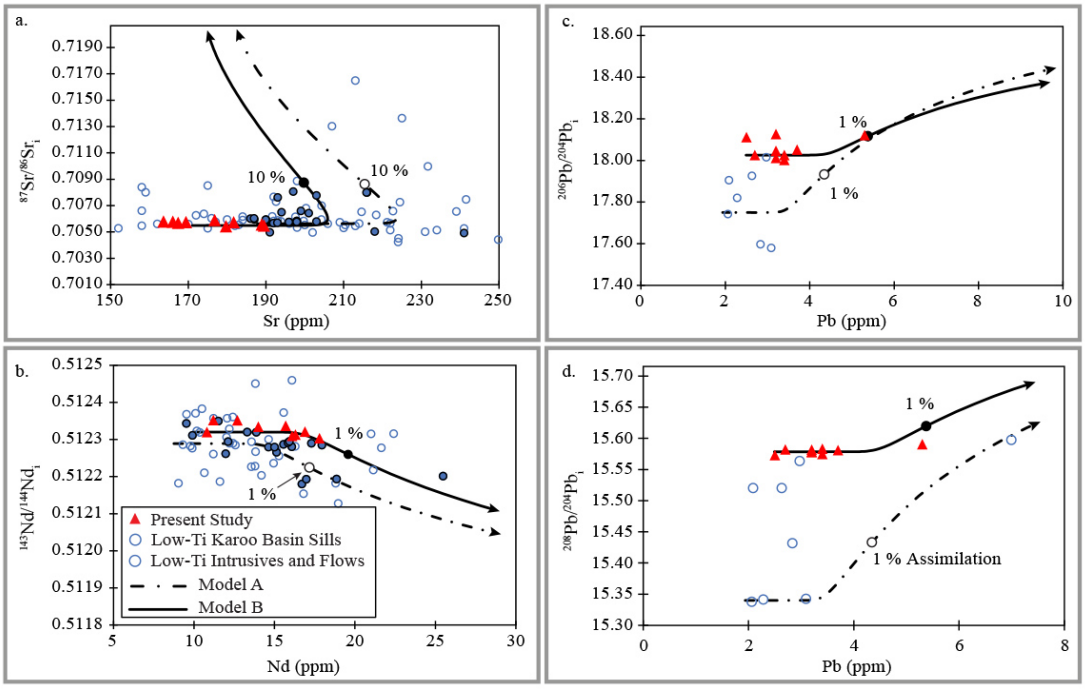

Figure 4.11: Diagrams with energy constrained assimilation and fractional crystallization (EC-AFC) model curves; (a) Initial $^{87}Sr/^{86}Sr$ vs Sr (ppm), (b) initial $^{143}Nd/^{144}Nd$ vs Nd (ppm), (c) initial $^{206}Pb/^{204}Pb$ vs Pb (ppm), and (d) initial $^{208}Pb/^{204}Pb$ vs Pb (ppm) calculated using the code of Spera and Bohrson (2001). Small circles on curves indicate percentage of assimilated contaminant. All isotopic data has been age-corrected to 183 Ma. Parameters given in Appendix I; Table I1.

Investigating the dolerites of the Karoo Basin directly, Neumann *et al.* (2011) found evidence for a multistage evolution of the dolerites within the basin consisting of variable degrees of localized crustal contamination in some sills. Due to the evidence present for some of the low-Ti rocks of the Karoo CFBs displaying evidence for crustal contamination, it is important to address if assimilation affected the Western Cape dolerites and thus could have contributed to injecting sufficient amount of water in the low-Ti magmas. When comparing the Western Cape sills with the rest of the sills within the Karoo Basin, the Western Cape sills display Sr (ppm) concentrations lower than much of the sills from Neumann *et al.* (2011) but falling within the range of other

values from the larger low-Ti suite of Karoo (Figure 4.11a). The Nd (ppm) concentration for the Western Cape sills fall within the range of values defined by both other sills from the Karoo Basin as well as the larger low-Ti suite (Figure 4.11b). Although, no Pb isotopic results are presented for other sills within the Karoo Basin, the Western Cape samples fall within the range of Pb (ppm) concentrations found within the other sills of the Karoo Basin (Neumann *et al.*, 2011) as well as within the range of rest of the low-Ti suite. Collectively, the geochemistry data from the Western Cape Province sills display a larger variation in elemental concentrations for little variations in isotopic ratios (Figure 4.11) and thus do not follow the same trends as the contaminated samples from Neumann *et al.* (2011).

To further test the degree of crustal contamination of the Western Cape sills and the proposed assimilation of water rich sediments into the sills, energy-constrained assimilation and fractional crystallization (EC-AFC) models were conducted using the models of Bohrson and Spera (2001). An initial model (Model A, Figure 4.11; Table I1) was calculated with initial sample composition values from a sample within the low-Ti suite from Jourdan *et al.* (2007a). The assimilant introduced to the Karoo magmas in Model A was upper continental crust from Bohrson and Spera (2001). This assimilant was chosen as average values of the upper continental crust would sufficiently represent the average found within the primarily clastic sediments of the Karoo sedimentary basin. The modeled trends for Modal A agree well with the Sr concentrations and isotopic ratios; however, is isotopically too low for the Nd and Pb isotopic ratios of the Western Cape sills (Figure 4.11). Therefore, a second model (Model B, Figure 4.11) curve was calculated using initial concentrations from a sample of the Western Cape (KD); sample KD is the most primitive sample within the Western Cape Province sample set of this study. With these models it is important to note that

the samples for the Western Cape sills display large variations in elemental concentrations in all isotopic systems for a small range of isotopic ratios (Figure 4.11). The data agree well with the initial flat trajectories of the calculated assimilation curves for either Model A and Model B. The lack of any production of anatectic melt from the delay of the country rock reaching the solidus temperature controls the early stages of the model (Figure 4.11). This trend is in stark difference to the sills of the Karoo Basin that have been contaminated by crust, which display large variation of isotopic ratios along a given elemental concentration (as displayed by data from the sills of the Karoo Basin from Neumann *et al.*, 2011; blue filled circles in Figure 4.11a and b); following the model trends that are defined by assimilation resulting in changes to the isotopic ratios. The trend in the isotopic data for these Western Cape sills suggest a minute degree of crustal contamination (less than 1 % when referencing the Pb data), if any (less than 0.1 % when referencing the Sr and Nd data) (Figure 4.11). Although the crystals within these dolerites would not have crystallized until emplacement of the sills within the shallow crust, the lack of evidence for strong crustal contamination indicates the H_2O signature, apparent in the form of primary hydrous minerals, is not from the crust. This observation is supported by the complete lack of hydrous minerals (outside of alteration products of biotite and chlorite from pyroxene) in strongly contaminated low-Ti rocks (Jourdan *et al.*, 2007a; Neumann *et al.*, 2011).

4.8.3.3. Is the water coming from the mantle source?

Some trace element ratios are negligibly affected by crustal contamination allowing investigation of the parental magmas to complement the Sr, Nd, and Pb isotope analyses of the Western Cape sills. The La/Nb (1.57 – 2.02) and Ba/Nb (27.8 – 33.7) ratios indicate all of these samples have values above the ratios given for Primitive Mantle by Sun and McDonough (1989) (La/Nb: 0.9 and Ba/Nb: 9; Figure

4.12) further indicating the evolved nature of these low-Ti rocks. The Karoo rocks display low Nb/La values similar to subduction related magmatism (Nb/La < 1; Figure 4.12c). Due to Nb and La having similar partition coefficients during partial melting in the upper mantle, this "arc-like" signature in CFBs has been classically suggested to represent segments of the SCLM that have been modified by earlier subduction events (Hergt *et al.*, 1991; Hawkesworth *et al.*, 1999); suggesting in turn the presence of significant amount of water present within the sources of these LIPs (e.g. Anderson, 1994; Wang *et al.*, 2016). In arc magma, trace element ratios such as Th/Yb and Ba/La can be reliable indicators to distinguish between sediment or fluid contributions into magma source regions (Woodhead *et al.*, 2001). The low Th/Yb and high Ba/La contents of the Western Cape Province sills as well as the rest of the low-Ti suite of Karoo suggest that fluids played an important role in the development of these low-Ti tholeiites (Figure 4.12b). If water doesn't come from assimilation of upper crustal material or sediments from the Karoo Basin, then it's likely that it comes from the mantle source itself as hinted at by the trace element results. The mantle rich reservoir could thus be located; (1) in a mixing zone between a plume and the SCLM; (2) the

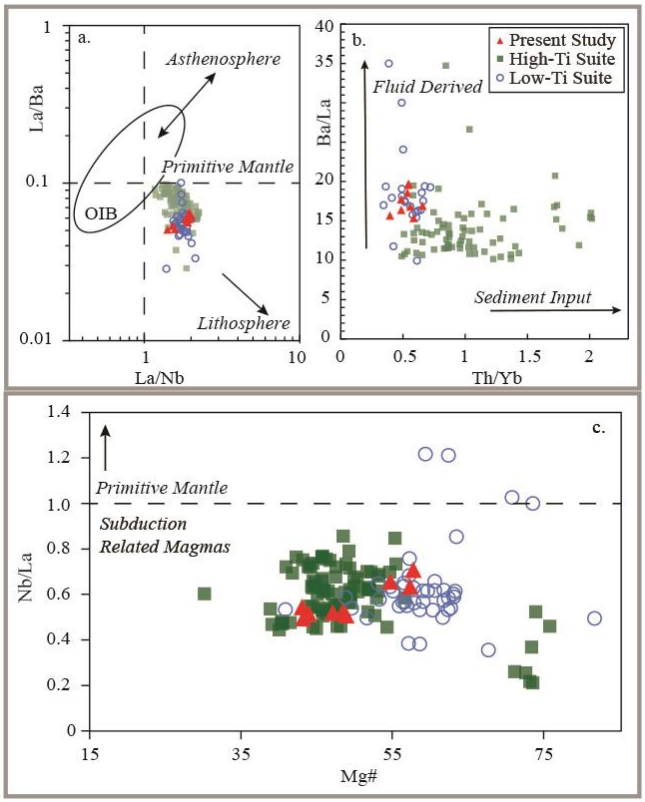

Figure 4.12: (a – c) Selected trace element graphs for the Karoo Continental Flood Basalt (CFB) Province. Karoo low-Ti and high-Ti suite compositions from the GEOROC database. Primitive mantle shaded areas from Hawkesworth *et al.* (1999) and Chauvel *et al.* (1995).

mantle transition zone as suggested by Wang *et al.* (2016); or (3) in a veined SCLM as the main and only source of Karoo magmatism.

The Karoo CFBs display an impressive dyke swarm forming a "triple-junction" geometry that is typically attributed to the impact of a mantle plume (Duncan *et al.*, 1984; Sweeney & Watkeys, 1990; Sweeney *et al.*, 1994). The presence of a dyke swarm, however, has been demonstrated to not be as conclusively linked to mantle plumes as previously thought. Instead dyke swarm orientation can correspond to lithospheric discontinuities that can be unrelated to mantle plumes (Jourdan *et al.*, 2006). The strongly enriched (continental-like) geochemical signature of the Karoo CFBs (particularly the low Nd isotopic ratios observed for the high-Ti basalts and picrites; Jourdan *et al.*, 2007a) suggest that it is unlikely that a mantle plume would be the sole contributor (if a contributor at all) to the generation of the Karoo CFBs without a contribution from the SCLM. In the plume-lithosphere mixing models an ascending plume provides heat to melt the SCLM allowing mixing between a mantle plume and the SCLM (e.g. Ellam *et al.*, 1992; Jourdan *et al.*, 2007a). The similarity of the HREE patterns between these Western Cape sills and MORB could indicate the involvement of a plume; however, the enriched LREE and isotopic ratios cannot be explained by a plume alone without strong continental contamination. The isotopic ratios of the Western Cape Province indicate a long and stable environment is required to produce the observed Pb isotopic ratios corroborated by other geochemical studies of the Karoo CFBs (e.g. Jourdan *et al.*, 2007a; Neumann *et al.*, 2011). Therefore, primary hydrous minerals within the sills of the Karoo Basin alone do not preclude a plume as one of several mantle sources of the Karoo CFBs, but they do provide evidence that an additional hydrated source is needed to explain the Karoo magma.

Thermomechanical modelling of the interactions between a plume and dry lithosphere by Arndt and Christensen (1992) concluded that the lithosphere was too cold and dry to provide any significant contribution of magma to CFBs; suggesting that crustal contamination strictly from the crust in various amounts and processes must account for the crustal signatures evident in CFB provinces. However, more recent studies, primarily addressing the isotopic signatures of CFBs, have demonstrated that a fertile or hydrous SCLM and/or upper asthenosphere could melt and provide a significant melt contribution (Hergt *et al.*, 1989b; Anderson, 1994; Molzahn *et al.*, 1996; Merle *et al.*, 2013). The lithosphere could melt and plausibly contribute the majority of magma to the genesis of CFBs containing as little as 0.3 % H_2O (Gallagher & Hawkesworth, 1992). Thus, the presence of primary hydrated material within the source of the Karoo magmas provides a means to facilitate the lithospheric mantle to melt and be involved to an appreciable degree in the petrogenesis of the province. As mentioned in regards to a plume SCLM mixture, the Western Cape Province display enriched Sr-Nd-Pb initial values and trace element signatures indicating a strong SCLM geochemical signal. If these hydrated minerals are from an SCLM source, the fact that these samples are located only in this portion of the Karoo Province complements the models of a heterogeneous SCLM. Other authors have recognized a slight geochemical change from north to south in the Karoo CFBs as well (more arc-like chemical signatures in the south and more intra-continental chemical signatures in the north; Duncan, 1987; Wang *et al.*, 2016). In this model the SCLM would be the sole source of the Karoo CFBs with the geochemical heterogeneity of the province from an overall metasomatized SCLM by fluids with discreet sediment enriched veins (Figure 4.13).

Another, possibility is the mantle transition zone water-filtering model (e.g. Wang *et al.*, 2016). The study by Wang *et al.* (2016) utilized a geochemical database of six LIPs to investigate the distinguishing characteristics of arc basalts and intra-continental basalts that display arc-like geochemical characteristics. The results demonstrate that many CFBs display arc-like hydrous geochemical characteristics indicating the importance of water flux melting in the generation of CFBs. Experimental petrology supports this hypothesis and suggests that fractional crystallization trends observed for the low-Ti samples of the Western Cape sills are due to water in the magma, and that this water is present within *all* low-Ti rocks of Karoo (Figure 4.4) (Wang *et al.*, 2016). Furthermore, Wang *et al.* (2016) used the results from the experimental petrology study to advance the discussion of water in deep-Earth water cycling and how fluids modify and thus trigger/control CFB partial melting events. The arc-like geochemical signatures of CFBs suggest the SCLM most likely is not the dominate source for these large scale intra-continental magmatic events (Merle *et al.*, 2013; Heinonen *et al.*, 2014; Wang *et al.*, 2016). In the mantle transition zone water-filtering model, subducted materials stagnate and hydrate the mantle transition zone during the building of supercontinents (Wang *et al.*, 2016). "Hydrous upwelling" occurs from the the top of the mantle transition zone that is focused to thinner cratonal boundaries, possibly by edge driven convection, where subsequent large scale melting of a now fertilized cratonic lithosphere occurs (Wang *et al.*, 2016). This model still involves a fertilized SCLM that would be geochemically similar to the hydrated SCLM discussed above, the difference is the means of hydrating the SCLM.

4.8.3.4. Why water is observed in the sills of the Karoo Basin

The primary hydrous minerals found within the sills and dykes of the Karoo Basin provide direct evidence of water, confirming the theoretical predictions from the MELTS models of Jourdan *et al.* (2007a) and the experimental data synthesis of Wang *et al.* (2016). However, hydrous minerals have been observed only in the sills from the Karoo Basin. Therefore, the possible reason why water is preferentially incorporated into the Cape Fold Basin sills could be the result of (1) magma degassing, either from a lower degassing efficiency during emplacement of the older sills or a temporal relation to magma degassing as the magmatic system evolves, and/or (2) a slightly different mantle source composition.

The lack of hydrous minerals throughout the overwhelming majority of the Karoo Province could be related to degassing of the volatile content of the magmas prior to reaching the surface. This process is a common occurrence for CFBs and large scale degassing has been extensively studied in regards to the environmental consequences of LIPs (Aubaud *et al.*, 2005; Black *et al.*, 2012). Magmatic events experience changes in volatile contents through degassing as the magmas respond to decompression during ascent or through crystallization if the magma stays below water saturation depths (Westrich *et al.*, 1988). In the case of these Karoo basalts the volatiles and thus H_2O content in the volcanic expressions of the magmas could have degassed quickly upon eruption, hampering the crystallization of hydrous minerals. Studies of H_2O degassing of rhyolite magmas indicate that the crystallization behavior of the magma can be significantly affected by water exsolution, particularly crystal phase stability, nucleation rates, and growth rates (Westrich *et al.*, 1988). The intrusive expressions of the Karoo magmas can contain more of the initial water content, through the presence of hydrous minerals, due to deeper crustal levels facilitating a

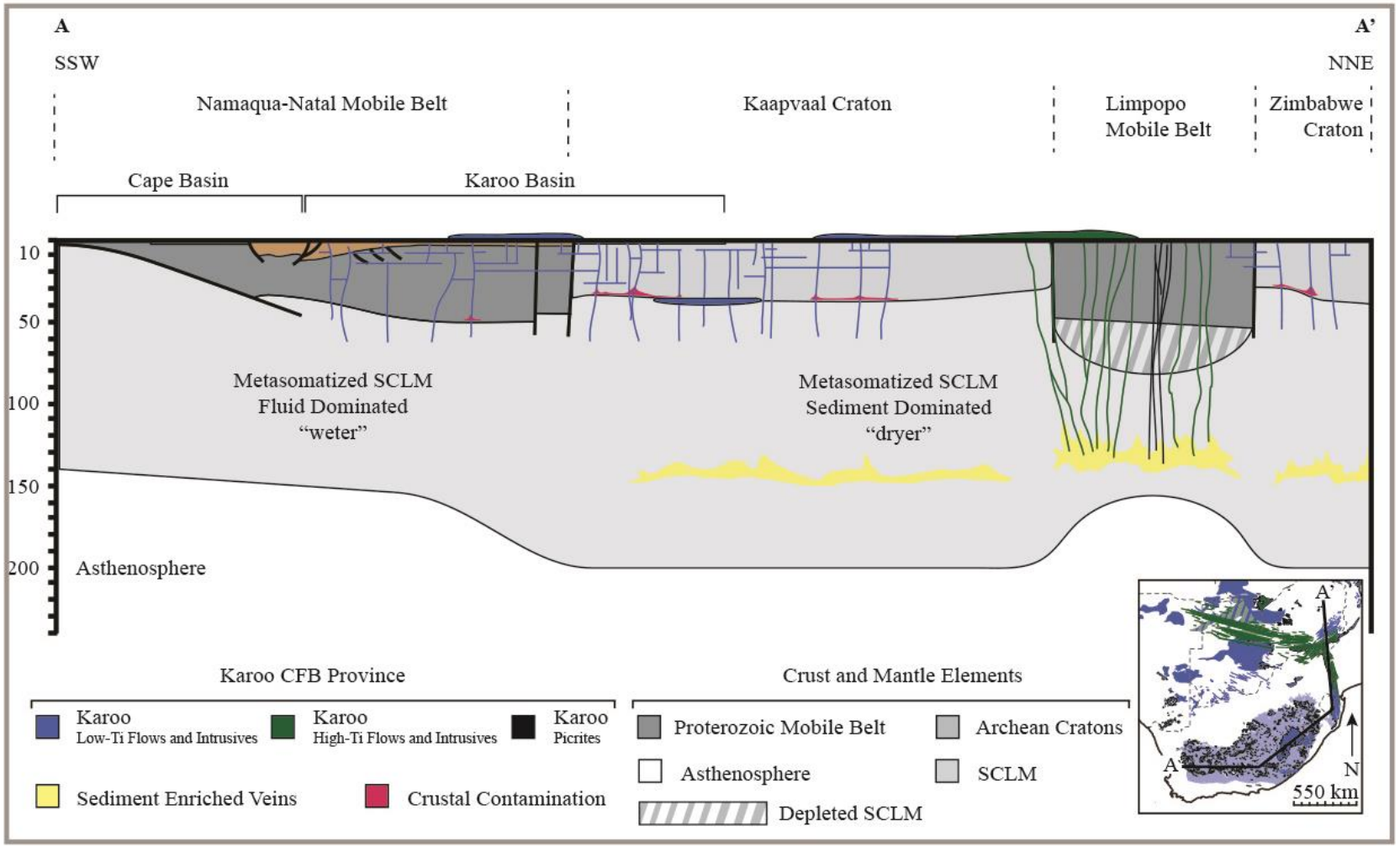

Figure 4.13: Schematic cross section of the proposed geodynamic model of the Karoo large igneous Province in Africa. Lithosphere structure sketched from results and conclusions of Nguuri et al. (2001), Tankard et al. (2009), and Youssof et al. (2013).

slower degassing rate and thus crystallization occurring within a thermodynamically stable melt (Westrich *et al.*, 1988).

The MELTS models calculated above indicate that water must be present within the Karoo magmas to create the best fit liquid line of descent. The experimental petrology study of Wang *et al.* (2016) suggests that Karoo low-Ti melts should contain around 1.9 wt. % H_2O during differentiation. Nevertheless, even when incorporating 1.9 wt. % of water, the MELTS model curves could not evolve sufficiently to crystallize biotite in all scenarios causing discontinuities between the models and observed data for (e.g.) Al_2O_3 (Figure 4.4a – d). If water is not the problem in these MELTS models of the Karoo material that do not contain primary hydrous minerals, the problem must be in the composition of the starting material from which these magmas fractionate. Wang *et al.* (2016) recognized a slight change in arc-like geochemical signatures that correlates with distance from the proposed Gondwana assembly subduction zone to the south of the Cape Fold Belt (Figure 4.1). The Karoo CFBs display more arc-like chemical signatures in the south that transition to more "within-plate" chemical signatures in the north (Duncan, 1987; Wang *et al.*, 2016). The hydrous minerals recognized so far within the Karoo Province have all been localized over the Namaqua-Natal mobile belt (Figure 4.10). Therefore, for the results that did not experience extreme crustal contamination, these geochemical differences represent compositional differences inherent to the source region, suggesting different degrees of lithospheric fertilization.

4.8.4. A Fresh/Revised Look at the Generation of the Karoo LIP

4.8.4.1 The introduction of water into the source region the Karoo CFBs

The location of the hydrated minerals within the Karoo Province currently appears to be restricted to localities directly overlying the Mesoproterozoic Namaqua-Natal mobile belt and the Cape Orogeny south of the Kaapvaal craton (Figure 4.1). The rest of the low-Ti suite located north of the Namaqua-Natal mobile belt contain no hydrous minerals including those that intrude the Limpopo mobile belt and the Kaapvaal and Zimbabwe cratons. The geochemical similarity between Proterozoic sills and dykes from the 1.1 Ga Umkondo Province and those from the overlapping 183 Ma Karoo Province suggest that the source might be located in the African lithospheric mantle (refer to discussion by Jourdan *et al.*, 2009a).

The deformation observed along the Namaqua-Natal mobile belt has been constrained to the Kibaran Orogeny, 1.2 – 1.0 Ga (Eglington, 2006; Hopp *et al.*, 2008). The Kibaran Orogeny is a likely candidate for providing the enriched material fertilizing and hydrating the SCLM below southern Africa through various subduction events (Jourdan *et al.*, 2009a). Further studies into the kimberlites within the Kaapvaal craton suggest an enrichment age around 1.0 Ga ± 300 Ma based on Nd model ages (Becker & Roex, 2006). Phlogopite $^{40}Ar/^{39}Ar$ ages of 1.0 – 1.2 Ga from within xenoliths in kimberlites of the Kaapvaal Craton suggest metasomatism of the SCLM below the craton (Hopp *et al.*, 2008).

The elevated ^{207}Pb to moderate ^{206}Pb isotopic ratios further suggest an ancient enrichment followed by a stable lithospheric environment evidenced by the decoupling of these two systems (Jourdan *et al.*, 2007a). As the trace element results do not suggest Pb mobility, this study used the new Pb isotopic data from the dolerites of the Western Cape Province to estimate the age of the SCLM enrichment from the Pb growth curve

calculations of Stacey and Kramers (1975) with a two-stage Pb growth curve (refer to supplementary material for details on calculation; Appendix I, Table I2). The composition of the enriched material is that of GLOSS given by Plank and Langmuir (1998). These Pb enrichment calculations indicate that the Pb isotopic ratios for the ^{207}Pb and ^{208}Pb systems can successfully both be reproduced with an enrichment event at 1.0 Ga, although we note that the $^{206}Pb/^{204}Pb$ isotopic ratios calculated from the model are low compared to the measured and calculated initial values.

Therefore, the Cape Orogeny to the south of the Namaqua-Natal mobile belt and the Karoo Basin intrusives may have provided a further influx of fluids around 261 Ma (Hansma *et al.*, 2016). Whether the Cape Orogeny was in conjunction with a subduction zone or not is still debated (Hansma *et al.*, 2016 and references therein). Thus, we model an additional enrichment event to the lithosphere at 261 Ma with the introduction of the upper continental crust compositions of Zartman and Haines (1988) like $^{238}U/^{204}Pb$ and $^{232}Th/^{238}U$ ratios. However, due to the short duration between the Cape Orogeny and the Karoo CFB event the isotope ratios were not affected greatly by this enrichment. However, a second enrichment phase has the benefit of providing an even tighter fit between the modeled and measured Pb isotope ratios (Table I1). These results suggest that the SCLM enrichment below the Karoo CFB Province resulted primarily from subduction processes during the Mesoproterozoic Kibaran Orogeny and possibly the Cape Orogeny (Jourdan *et al.*, 2009a).

4.8.4.2. Emplacement of the Karoo LIP with an H_2O consideration

Even with the consideration of these early hydrated sills into the evolutional history of the Karoo LIP, a unique model cannot be established. However, these results can place further constraints on the petrogenetic evolution of the Karoo magmas. The geochemistry of these Western Cape sills in conjunction with geochemical results from

the rest of the Karoo Province indicate the hydrated material was introduced into the system by subduction related to the Kibaran Orogeny during the assembly of Gondwana. The geochemical results of the Western Cape sills along with the calculations for the time of source enrichment further indicate a mantle plume was not the only contributor to the Karoo CFB magmatism. The mantle transition zone water-filtering model of Wang *et al.* (2016) suggests that melting of LIPs in general occurs within a fertilized SCLM after interactions with the hydrous upwelling from the mantle transition zone. Due to primary melting for LIP generation in the mantle transition zone model occuring at the base of the lithosphere, fertilized asthenorshperic and lithospheric mantle, the means of involvment of a hydrated mantle transition zone or solely a fertilized SCLM is difficult to constrain geochemically. However, the isotope enrichment calculations can place constraints on the plausibilities of these two models, as the 1.0 Ga enrichment of the Pb isotopes indicates that the fertilization of the SCLM did not occur just prior to melting. Therefore, unless these observed isotopic ratios evolved within the stable mantle transition zone and retained these values through the large scale melting that occurs within the cratonic lithosphere the mantle transition zone water-filtering model could not have played a significant role in the petrogenesis of the Karoo magmas.

When coupling the geographic localizations of hydrous minerals and the variably geochemical signatures across the province the control on hydrated mineral crystallization could be the result of a combination of different degrees of hydration (due to degassing variability) and lithosphere compositional differences. For instance, the low-Ti suite displays more fluid influence where the high-Ti suite display more involment from sediments. This compositional difference is also apparent in the south to north geochemical transition from more arc-like geochemical signatures to “within-

plate" geochemical sinatures to along the north/south mobile belt to craton transitions. These geochemical signatures further demonstrate a strong role of a heterogeneously fertilized SCLM in the petrogenesis of the Karoo magmas. Whereas the mantle transition zone may cause more hydrated zones (e.g. more arc-like geochemical characteristics vs. intr-contentental geochemical characterisitcs) during the hydrous upwelling, the differences in sediment (high-Ti suite, Figure 4.6b) and fluid (low-Ti suite, Figure 4.6b) fertilization is more likely an SCLM feature (Figure 4.13). Therefore, these hydrated minerals coupled with the geochemical data of the Western Cape intrusions indicate fluid over sediment involvement in the source of the Karoo LIP was controlled by the proximity or distance from the subduction zone that introduced the enriched material to the SCLM (Figure 4.13).

4.9. Conclusions

1. The Western Cape dolerite sills are some of the first magma to be emplaced in the Karoo magmatic event (~183.5 Ma).

2. The hydrous minerals present within these low-Ti tholeiites of the Western Cape Province sills are primary features, crystallizing at the same time as plagioclase. The primary biotite and hornblende crystals provide the *first* direct evidence of H_2O in the Karoo magmas.

3. The lack of geochemical evidence for upper crustal contamination indicate the required H_2O content is representative of a hydrated source.

4. The geochemical data, particularly the Sr, Nd, and Pb isotopes, signify the source region for these Western Cape dolerites is a hydrated SCLM that was fertilized from subduction during the Mesoproterozoic Kibaran Orogeny.

5. The hydrous minerals are only apparent in sills sourced at the base of the Namaqua-Natal Mobile belt indicating the geochemical variations controlling the presence of hydrous minerals is driven by different lithosphere types (craton vs. mobile belts) experiencing different degrees of fertilization. Thus suggesting that the hydration of the lithosphere is most prevalent in close proximity to the ancient subduction zone.

4.10. References

Anderson, D. L. (1994). The sublithospheric mantle as the source of Continental Flood Basalts; the case against the continental lithosphere and plume head reservoirs. *Earth and Planetary Science Letters* **123**, 269-280.

Arndt, N. T. & Christensen, U. (1992). The role of lithospheric mantle in continental flood volcanism: Thermal and geochemical constraints. *Journal of Geophysical Research* **97**, 10967.

Aubaud, C., Pineau, F., Hékinian, R. & Javoy, M. (2005). Degassing of CO 2 and H 2 O in submarine lavas from the Society hotspot. *Earth and Planetary Science Letters* **235**, 511-527.

Bas, M. J. L., Maitre, R. W. L., Streckeisen, A. & Zanettin, B. (1986). A Chemical Classification of Volcanic Rocks Based on the Total Alkali-Silica Diagram. *Journal of Petrology* **27**, 745-750.

Becker, M. & Roex, A. P. L. (2006). Geochemistry of South African on-and off-craton, Group I and Group II kimberlites: petrogenesis and source region evolution. *Journal of Petrology* **47**, 673-704.

Black, B. A., Elkins-Tanton, L. T., Rowe, M. C. & Peate, I. U. (2012). Magnitude and consequences of volatile release from the Siberian Traps. *Earth and Planetary Science Letters* **317-318**, 363-373.

Bohrson, W. A. & Spera, F. J. (2001). Energy-constrained open-system magmatic processes II: application of energy-constrained assimilation–fractional crystallization (EC-AFC) model to magmatic systems. *Journal of Petrology* **42**, 1019-1041.

Chauvel, C., Goldstein, S. & Hofmann, A. (1995). Hydration and dehydration of oceanic crust controls Pb evolution in the mantle. *Chemical Geology* **126**, 65-75.

Chiaradia, M., Müntener, O. & Beate, B. (2011). Enriched basaltic andesites from mid-crustal fractional crystallization, recharge, and assimilation (Pilavo Volcano, Western Cordillera of Ecuador). *Journal of Petrology* **52**, 1107-1141.

Duncan, A., Erlank, A. & Marsh, J. (1984). Regional geochemistry of the Karoo igneous province. In: Erlank, A. (ed.) *Duncan, A. R., Erlank, A. J. & Marsh, J. S. (1984). Regional Geochemistry of the Karoo igneous province. In: Erlank, A. J. (ed.) Petrogenesis of the Volcanic Rocks of the Karoo Province. Special Publication of the Geological Society of South Africa, 355–388.*: Special Publication of the Geological Society of South Africa, 355–388.

Duncan, A. R. (1987). The Karoo igneous province—a problem area for inferring tectonic setting from basalt geochemistry. *Journal of Volcanology and Geothermal Research* **32**, 13-34.

Duncan, R. A., Hooper, P., Rehacek, J., Marsh, J. & Duncan, A. (1997). The timing and duration of the Karoo igneous event, southern Gondwana.

Eales, H. V., Marsh, J. S. & Cox, K. G. (1983). The Karoo Igneous Province: An Introduction. In: Erlank, A. J. (ed.) *Petrogenesis of the Volcanic Rocks of the Karoo Province*. Johannesburg: Special Publication No. 13 The Geological Society of South Africa, 1-26.

Eglington, B. (2006). Evolution of the Namaqua-Natal Belt, southern Africa–A geochronological and isotope geochemical review. *Journal of African Earth Sciences* **46**, 93-111.

Ellam, R., Carlson, R. & Shirey, S. (1992). Evidence from Re–Os isotopes for plume–lithosphere mixing in Karoo flood basalt genesis. *Nature* **359**, 718-721.

Encarnacion, J., Fleming, T. H., Elliot, D. H. & Eales, H. V. (1996). Synchronous emplacement of Ferrar and Karoo dolerites and the early breakup of Gondwana. *Geology (Boulder)* **24**, 535-538.

Gallagher, K. & Hawkesworth, C. (1992). Dehydration melting and the generation of Continental Flood Basalts. *Nature* **358**, 57-59.

Gerstenberger, H. & Haase, G. (1997). A highly effective emitter substance for mass spectrometric Pb isotope ratio determinations. *Chemical Geology* **136**, 309-312.

Ghiorso, M. S. & Sack, R. O. (1995). Chemical mass transfer in magmatic processes IV. A revised and internally consistent thermodynamic model for the interpolation and extrapolation of liquid-solid equilibria in magmatic systems at elevated temperatures and pressures. *Contributions to Mineralogy and Petrology* **119**, 197-212.

Grégoire, M., Bell, D. & Le Roex, A. (2003). Garnet lherzolites from the Kaapvaal Craton (South Africa): trace element evidence for a metasomatic history. *Journal of Petrology* **44**, 629-657.

Gualda, G. A. R., Ghiorso, M. S., Lemons, R. V. & Carley, T. L. (2012). Rhyolite-MELTS: a Modified Calibration of MELTS Optimized for Silica-rich, Fluid-bearing Magmatic Systems. *Journal of Petrology* 53, 875-890.

Hansma, J., Tohver, E., Schrank, C., Jourdan, F. & Adams, D. (2016). The timing of the Cape Orogeny: New 40 Ar/39 Ar age constraints on deformation and cooling of the Cape Fold Belt, South Africa. *Gondwana Research* **32**, 122-137.

Hart, S. R. (1984). A large-scale isotope anomaly in the Southern Hemisphere mantle. *Nature* **309**, 753-757.

Hawkesworth, C., Kelley, S., Turner, S., Le Roex, A. & Storey, B. (1999). Mantle processes during Gondwana break-up and dispersal. *Journal of African Earth Sciences* **28**, 239-261.

Heinonen, J. S., Carlson, R. W. & Luttinen, A. V. (2010). Isotopic (Sr, Nd, Pb, and Os) composition of highly magnesian dikes of Vestfjella, western Dronning Maud Land, Antarctica: A key to the origins of the Jurassic Karoo Large Igneous Province? *Chemical Geology* **277**, 227-244.

Heinonen, J. S., Carlson, R. W., Riley, T. R., Luttinen, A. V. & Horan, M. F. (2014). Subduction-modified oceanic crust mixed with a depleted mantle reservoir in the sources of the Karoo Continental Flood Basalt province. *Earth and Planetary Science Letters* **394**, 229-241.

Hergt, J., Peate, D. & Hawkesworth, C. (1991). The petrogenesis of Mesozoic Gondwana low-Ti flood basalts. *Earth and Planetary Science Letters* **105**, 134-148.

Hergt, J. M., Chappell, B. W., McCulloch, M. T., McDougall, I. & Chivas, A. R. (1989). Geochemical and isotopic constraints on the origin of the Jurassic dolerites of Tasmania. *Journal of Petrology* **30**, 841-883.

Hess, J. & Lippolt, H. (1986). Kinetics of Ar isotopes during neutron irradiation: 39Ar loss from minerals as a source of error in 40Ar/39Ar dating. *Chemical Geology: Isotope Geoscience section* **59**, 223-236.

Hopp, J., Trieloff, M., Brey, G. P., Woodland, A. B., Simon, N. S. C., Wijbrans, J. R., Siebel, W. & Reitter, E. (2008). 40Ar/39Ar-ages of phlogopite in mantle xenoliths from South African kimberlites: Evidence for metasomatic mantle impregnation during the Kibaran orogenic cycle. *Lithos* **106**, 351-364.

Irvine, T. & Baragar, W. (1971). A guide to the chemical classification of the common volcanic rocks. *Canadian Journal of Earth Sciences* **8**, 523-548.

Jones, D., Duncan, R. A., Briden, J., Randall, D. & MacNiocaill, C. (2001). Age of the Batoka basalts, northern Zimbabwe, and the duration of Karoo Large Igneous Province magmatism. *Geochemistry, Geophysics, Geosystems* **2**.

Jourdan, F., Bertrand, H., Féraud, G., Le Gall, B. & Watkeys, M. (2009). Lithospheric mantle evolution monitored by overlapping Large Igneous Provinces: case study in southern Africa. *Lithos* **107**, 257-268.

Jourdan, F., Bertrand, H., Scharer, U., Blichert-Toft, J., Feraud, G. & Kampunzu, A. B. (2007a). Major and Trace Element and Sr, Nd, Hf, and Pb Isotope Compositions of the Karoo Large Igneous Province, Botswana-Zimbabwe: Lithosphere vs Mantle Plume Contribution. *Journal of Petrology* **48**, 1043-1077.

Jourdan, F., Féraud, G., Bertrand, H., Kampunzu, A. B., Tshoso, G., Watkeys, M. K. & Le Gall, B. (2005). Karoo Large Igneous Province: Brevity, origin, and relation to mass extinction questioned by new 40Ar/39Ar age data. *Geology* **33**, 745.

Jourdan, F., Féraud, G., Bertrand, H., Watkeys, M., Kampunzu, A. & Le Gall, B. (2006). Basement control on dyke distribution in Large Igneous Provinces: case study of the Karoo triple junction. *Earth and Planetary Science Letters* **241**, 307-322.

Jourdan, F., Féraud, G., Bertrand, H., Watkeys, M. & Renne, P. (2007b). Distinct brief major events in the Karoo Large Igneous Province clarified by new 40 Ar/39 Ar ages on the Lesotho basalts. *Lithos* **98**, 195-209.

Jourdan, F., Féraud, G., Bertrand, H., Watkeys, M. K. & Renne, P. R. (2008). The40Ar/39Ar ages of the sill complex of the Karoo Large Igneous Province: Implications for the Pliensbachian-Toarcian climate change. *Geochemistry, Geophysics, Geosystems* **9**, n/a-n/a.

Jourdan, F., Matzel, J. P. & Renne, P. R. (2007c). 39Ar and 37Ar recoil loss during neutron irradiation of sanidine and plagioclase. *Geochimica et Cosmochimica Acta* **71**, 2791-2808.

Jourdan, F. & Renne, P. R. (2013). Neutron-induced 37Ar recoil ejection in Ca-rich minerals and implications for 40Ar/39Ar dating. *Geological Society, London, Special Publications* **378**, 33-52.

Koppers, A. A. P. (2002). ArArCALC—software for 40 Ar/39 Ar age calculations. *Computers & Geosciences* **28**, 605-619.

Lanci, L., Tohver, E., Wilson, A. & Flint, S. (2013). Upper Permian magnetic stratigraphy of the lower Beaufort group, Karoo basin. *Earth and Planetary Science Letters* **375**, 123-134.

Luttinen, A. V., Heinonen, J. S., Kurhila, M., Jourdan, F., Manttari, I., Vuori, S. K. & Huhma, H. (2015). Depleted Mantle-sourced CFB Magmatism in the Jurassic

Africa-Antarctica Rift: Petrology and 40Ar/39Ar and U/Pb Chronology of the Vestfjella Dyke Swarm, Dronning Maud Land, Antarctica. *Journal of Petrology* **56**, 919-952.

McArthur, J. M., Howarth, R. J. & Bailey, T. R. (2001). Strontium Isotope Stratigraphy: LOWESS Version 3: Best Fit to the Marine Sr-Isotope Curve for 0–509 Ma and Accompanying Look-up Table for Deriving Numerical Age. *The Journal of Geology* **109**, 155-170.

Merle, R., Marzoli, A., Reisberg, L., Bertrand, H., Nemchin, A., Chiaradia, M., Callegaro, S., Jourdan, F., Bellieni, G., Kontak, D., Puffer, J. & McHone, J. G. (2013). Sr, Nd, Pb and Os Isotope Systematics of CAMP Tholeiites from Eastern North America (ENA): Evidence of a Subduction-enriched Mantle Source. *Journal of Petrology* **55**, 133-180.

Molzahn, M., Reisberg, L. & Wörner, G. (1996). Os, Sr, Nd, Pb, O isotope and trace element data from the Ferrar flood basalts, antarctica: evidence for an enriched subcontinental lithospheric source. *Earth and Planetary Science Letters* **144**, 529-545.

Neumann, E.-R., Svensen, H., Galerne, C. Y. & Planke, S. (2011). Multistage evolution of dolerites in the Karoo Large Igneous Province, Central South Africa. *Journal of Petrology* **52**, 959-984.

Nguuri, T., Gore, J., James, D., Webb, S., Wright, C., Zengeni, T., Gwavava, O. & Snoke, J. (2001). Crustal structure beneath southern Africa and its implications for the formation and evolution of the Kaapvaal and Zimbabwe cratons. *Geophysical Research Letters* **28**, 2501-2504.

Oostingh, K. F., Jourdan, F., Matchan, E. L. & Phillips, D. (2017). 40Ar/39Ar geochronology reveals rapid change from plume-assisted to stress-dependent volcanism in the Newer Volcanic Province, SE Australia. *Geochemistry, Geophysics, Geosystems* **Under Review**.

Paine, J. H., Nomade, S. & Renne, P. R. (2006). Quantification of 39 Ar recoil ejection from GA1550 biotite during neutron irradiation as a function of grain dimensions. *Geochimica et Cosmochimica Acta* **70**, 1507-1517.

Pin, C., Briot, D., Bassin, C. & Poitrasson, F. (1994). Concomitant separation of strontium and samarium-neodymium for isotopic analysis in silicate samples, based on specific extraction chromatography. *Analytica Chimica Acta* **298**, 209-217.

Plank & Langmuir. (1998). The chemical composition of subducting sediment and its consequences for the crust and mantle. *Chemical Geology* **145**.

Renne, P. R., Balco, G., Ludwig, K. R., Mundil, R. & Min, K. (2011). Response to the comment by WH Schwarz et al. on "Joint determination of 40 K decay constants

and 40 Ar∗/40 K for the Fish Canyon sanidine standard, and improved accuracy for 40 Ar/39 Ar geochronology" by PR Renne et al.(2010). *Geochimica et Cosmochimica Acta* **75**, 5097-5100.

Renne, P. R., Deino, A. L., Hilgen, F. J., Kuiper, K. F., Mark, D. F., Mitchell, W. S., Morgan, L. E., Mundil, R. & Smit, J. (2013). Time scales of critical events around the Cretaceous-Paleogene boundary. *Science* **339**, 684-687.

Riley, T. R. (2005a). Early-Middle Jurassic Dolerite Dykes from Western Dronning Maud Land (Antarctica): Identifying Mantle Sources in the Karoo Large Igneous Province. *Journal of Petrology* **46**, 1489-1524.

Riley, T. R. (2005b). Overlap of Karoo and Ferrar Magma Types in KwaZulu-Natal, South Africa. *Journal of Petrology* **47**, 541-566.

Sell, B., Ovtcharova, M., Guex, J., Bartolini, A., Jourdan, F., Spangenberg, J. E., Vicente, J.-C. & Schaltegger, U. (2014). Evaluating the temporal link between the Karoo LIP and climatic–biologic events of the Toarcian Stage with high-precision U–Pb geochronology. *Earth and Planetary Science Letters* **408**, 48-56.

Smith, R., Eriksson, P. & Botha, W. (1993). A review of the stratigraphy and sedimentary environments of the Karoo-aged basins of Southern Africa. *Journal of African Earth Sciences (and the Middle East)* **16**, 143-169.

Stacey, J. t. & Kramers, J. (1975). Approximation of terrestrial lead isotope evolution by a two-stage model. *Earth and Planetary Science Letters* **26**, 207-221.

Stone, P., Richards, P., Kimbell, G., Esser, R. & Reeves, D. (2008). Cretaceous dykes discovered in the Falkland Islands: implications for regional tectonics in the South Atlantic. *Journal of the Geological Society* **165**, 1-4.

Sun, S. s. & McDonough, W. F. (1989). Chemical and isotopic systematics of oceanic basalts: implications for mantle composition and processes. *Geological Society, London, Special Publications* **42**, 313-345.

Svensen, H., Corfu, F., Polteau, S., Hammer, Ø. & Planke, S. (2012). Rapid magma emplacement in the Karoo Large Igneous Province. *Earth and Planetary Science Letters* **325-326**, 1-9.

Svensen, H., Planke, S., Chevallier, L., Malthe-Sørenssen, A., Corfu, F. & Jamtveit, B. (2007). Hydrothermal venting of greenhouse gases triggering Early Jurassic global warming. *Earth and Planetary Science Letters* **256**, 554-566.

Sweeney, R., Duncan, A. & Erlank, A. (1994). Geochemistry and petrogenesis of central Lebombo basalts of the Karoo igneous province. *Journal of Petrology* **35**, 95-125.

Sweeney, R. & Watkeys, M. (1990). A possible link between Mesozoic lithospheric architecture and Gondwana flood basalts. *Journal of African Earth Sciences (and the Middle East)* **10**, 707-716.

Tanaka, T., Togashi, S., Kamioka, H., Amakawa, H., Kagami, H., Hamamoto, T., Yuhara, M., Orihashi, Y., Yoneda, S., Shimizu, H., Kunimaru, T., Takahashi, K., Yanagi, T., Nakano, T., Fujimaki, H., Shinjo, R., Asahara, Y., Tanimizu, M. & Dragusanu, C. (2000). JNdi-1: a neodymium isotopic reference in consistency with LaJolla neodymium. *Chemical Geology* **168**, 279-281.

Tankard, A., Welsink, H., Aukes, P., Newton, R. & Stettler, E. (2009). Tectonic evolution of the Cape and Karoo basins of South Africa. *Marine and Petroleum Geology* **26**, 1379-1412.

Todt, W., Cliff, R. A., Hanser, A. & Hofmann, A. (1996). Evaluation of a 202Pb–205Pb Double Spike for High-Precision Lead Isotope Analysis. *Earth processes: reading the isotopic code*, 429-437.

Tohver, E., Lanci, L., Wilson, A., Hansma, J. & Flint, S. (2015). Magnetostratigraphic constraints on the age of the lower Beaufort Group, western Karoo basin, South Africa, and a critical analysis of existing U-Pb geochronological data. *Geochemistry, Geophysics, Geosystems* **16**, 3649-3665.

Turner, G. & Cadogan, P. (1974). Possible effects of 39Ar recoil in 40Ar-39Ar dating. *Lunar and Planetary Science Conference Proceedings*, 1601-1615.

Verati, C. & Jourdan, F. (2013). Modelling effect of sericitization of plagioclase on the 40K/40Ar and 40Ar/39Ar chronometers: implication for dating basaltic rocks and mineral deposits. *Geological Society, London, Special Publications* **378**, 155-174.

Villa, I. M. (1997). Direct determination of 39 Ar recoil distance. *Geochimica et Cosmochimica Acta* **61**, 689-691.

Wang, X.-C., Wilde, S. A., Xu, B. & Pang, C.-J. (2016). Origin of arc-like continental basalts: Implications for deep-Earth fluid cycling and tectonic discrimination. *Lithos* **261**, 5-45.

Westrich, H., Stockman, H. & Eichelberger, J. (1988). Degassing of rhyolitic magma during ascent and emplacement. *Journal of Geophysical Research: Solid Earth* **93**, 6503-6511.

Woodhead, J., Hergt, J., Davidson, J. & Eggins, S. (2001). Hafnium isotope evidence for 'conservative'element mobility during subduction zone processes. *Earth and Planetary Science Letters* **192**, 331-346.

Youssof, M., Thybo, H., Artemieva, I. & Levander, A. (2013). Moho depth and crustal composition in Southern Africa. *Tectonophysics* **609**, 267-287.

Zartman, R. E. & Haines, S. M. (1988). The plumbotectonic model for Pb isotopic systematics among major terrestrial reservoirs. A case for bi-directional transport. . *Geochimica et Cosmochimica Acta* **52**, 1327-1339.

Zindler, A. & Hart, S. (1986). Chemical geodynamics. *Annual review of earth and planetary sciences **14***, 493-571.

4.11 Figure Captions

Figure 4.1: Sketch map of the African portion of the Karoo Continental Flood Basalt (CFB) Province's distribution and constituent suites. Modified and created after Jourdan *et al.* (2006); Jourdan *et al.* (2007a); and Svensen *et al.* (2012). Bold italics indicate relevant lithosphere types, labels in italics indicate relevant flows and intrusions of the Karoo CFBs, and countries of the African continent are labeled in a normal font.

Figure 4.2: Photomicrograph of selected samples displaying petrography, freshness, and hydrous mineral crystal textures. Mineral phases labeled for convenience. Scale bar represents 1000 μm.

Figure 4.3: $^{40}Ar/^{39}Ar$ apparent age and related K/Ca ratio spectra for plagioclase, biotite, and hornblende separates plotted against the cumulative percentage of ^{39}Ar released (the K/Ca ratios were not plotted for samples that did not yield concordant plateau ages or biotite analyses due to a low concentration of Ca). Errors on plateau ages are quoted at 2σ. Bold fonts indicate plateau ages and italics font for sample KD indicate a mini-plateau age.

Figure 4.4: Total alkalis-silica (TAS) Diagram, (Bas *et al.*, 1986). Alkalic-subalkalic line from Irvine and Baragar (1971).

Figure 4.5: (a – d) Major element (wt. %) vs Mg-number [100 x atomic ratio of Mg/ ($Mg + Fe_2^+$) with Fe_2O_3/FeO normalized to 0.15] diagrams with MELTS fractional crystallization modeling curves for selected major element trends for the Karoo Continental Flood Basalt. MELTS parameters: Model Curve A – low pressure (1 kbar) hydrous (0.5 % H_2O) and Model Curve B – low pressure (1 kbar) anhydrous. A QFM (Quartz – Fayalite – Magnetite) buffer was used for fO_2 (Ghiorso & Sack, 1995). Dashed red lines represent anhydrous and blue dashed lines represent hydrous experimental data compiled by (Wang *et al.*, 2016). All geochemical data for the Karoo CFBs are from the GEOROC database.

Figure 4.6: (a) Primitive mantle normalized incompatible trace elements patterns. (b) Chondrite normalized REE patterns. Normalization parameters from Sun and McDonough (1989). All geochemical data for the Karoo CFBs are from the GEOROC database.

Figure 4.7: Initial (183 Ma) Sr, Nd, and Pb isotopic compositions of the Karoo Continental Flood Basalt (CFB) Province. The Northern Hemisphere Reference Line (NHRL); (Hart, 1984) is shown in Pb vs Pb isotope diagrams. Approximate locations of mantle end-members (Zindler & Hart, 1986) are indicated for reference. BSE = Bulk Silicate Earth, EMI = Enriched Mantle I, EMII = Enriched Mantle II, MORB =

Mid-Ocean Ridge Basalt, DMM = Depleted MORB Mantle. All geochemical data for the Karoo CFBs are from the GEOROC database.

Figure 4.8: (a) $^{87}Sr/^{86}Sr$ initial isotopic composition vs Mg-number and (b) $^{143}Nd/^{144}Nd$ initial isotopic composition vs Mg-number. All isotopic data has been age-corrected to 183 Ma.

Figure 4.9: Bar graph comparing the plagioclase $^{40}Ar/^{39}Ar$ plateau ages with the $^{40}Ar/^{39}Ar$ biotite plateau and total fusion (error) ages for samples KB, KC, and KG. For sample KF the $^{40}Ar/^{39}Ar$ plagioclase plateau age is compared to the total fusion (error) age of the hornblende.

Figure 4.10: Age vs longitude plot of selected geochronological data from sills of the Karoo sedimentary basin. Also represented are ranges or weighted means of available data from: the Menezes Basin (Jourdan *et al.*, 2007b); the Lebombo Monocline (Jourdan *et al.*, 2005 [plagioclase]); (Sell *et al.*, 2014 [zircon]); the Okavango dyke Swarm (Jourdan *et al.*, 2006); the Shadi-Shadi lava pile (Jourdan *et al.*, 2005); the Lesotho Basalt (Jourdan *et al.*, 2007b).

Figure 4.11: Diagrams with energy constrained assimilation and fractional crystallization (EC-AFC) model curves; (a) Initial $^{87}Sr/^{86}Sr$ vs Sr (ppm), (b) initial $^{143}Nd/^{144}Nd$ vs Nd (ppm), (c) initial $^{206}Pb/^{204}Pb$ vs Pb (ppm), and (d) initial $^{208}Pb/^{204}Pb$ vs Pb (ppm) calculated using the code of Spera and Bohrson (2001). Small circles on curves indicate percentage of assimilated contaminant. All isotopic data has been age-corrected to 183 Ma. Parameters given in Appendix I; Table I1.

Figure 4.12: (a – c) Selected trace element graphs for the Karoo Continental Flood Basalt (CFB) Province. Karoo low-Ti and high-Ti suite compositions from the GEOROC database. Primitive mantle shaded areas from Hawkesworth *et al.* (1999) and Chauvel *et al.* (1995).

Figure 4.13: Schematic cross section of the proposed geodynamic model of the Karoo large igneous Province in Africa. Lithosphere structure sketched from results and conclusions of Nguuri *et al.* (2001), Tankard *et al.* (2009), and Youssof *et al.* (2013).

Chapter 5: $^{40}Ar/^{39}Ar$ Geochronology of Terrestrial Pyroxene

Bryant Ware[1] and Fred Jourdan[1]

[1]Western Australian Argon Isotope Facility, Department of Applied Geology and JdL-CMS, Curtin University, Perth, WA 6845, Australia.

5.1. Abstract

The ability to precisely provide geologically meaningful ages to a wide range of minerals is principle to obtaining a comprehensive understanding of the diverse geologic processes shaping the Earth through 4.56 Ga of evolution. Geochronological techniques such as U/Pb in minerals such as zircon and baddeleyite and $^{40}Ar/^{39}Ar$ on a vast range of minerals such as sanidine, plagioclase, and biotite provide means to address an array of different geologic processes. Many of these minerals, however, are not abundant in mafic or completely lacking in ultramafic rocks. The gap in ability to date mafic/ultramafic rocks is exacerbated particularly if plagioclase has altered to the high K mineral sericite eliminating the ability to use the $^{40}Ar/^{39}Ar$ technique on these rock types. Pyroxene is a primary rock forming mineral for both mafic and ultramafic rocks. This ability to obtain statistically meaningful and accurate ages with the mineral pyroxene provide unprecedented geochronological opportunities to all Large Igneous Provinces, dredged rocks, metamorphic geochronology, and thermochronology applications.

Multi-collector noble gas mass spectrometer (ARGUS VI) provide step-wise advancements in the sensitivity and precision on smaller sample volume requirements than previous single-collector mass spectrometer. The use of these multi-collector

arrays on clinopyroxene crystals from two different Large Igneous Provinces display the ability to procure geologically meaningful and relatively precise ages. Results from the Tasmanian Dolerites of the island state of Tasmania, Australia yield ages that are statistically the same as high-precision plagioclase $^{40}Ar/^{39}Ar$ plateau ages from the same sample. The method is also successful on clinopyroxene separates from the Kalkarindji Continental Flood Basalt province located in Australia with a pyroxene plateau age overlapping with all previous geochronological results from a variety of other studies. These results present the first ever geologically meaningful and accurate ages of terrestrial pyroxene.

5.2. Introduction

With the advancement of mass spectrometers, the ability to obtain robust and precise geochronological data provides the opportunity to push the methods to unprecedented limits. Felsic rocks have a plethora of minerals that have been developed as viable candidates for varying methods of geochronology analyses (e.g. $^{238}U/^{206}Pb$ dating of zircon and baddeleyite and $^{40}Ar/^{39}Ar$ dating of sanidine and biotite). Mafic rocks, however, and in particular ultramafic rocks, suffer from a lack of mineral types available for geochronology. Although neo-formed zircon can crystallize in thick intrusions (e.g. Sills within the Karoo Basin: Svensen et al, 2007; 2012; Sills of the Ferrar Large Igneous Province: Burgess *et al.*, 2015), it is completely lacking in fine-grained mafic rocks. As such, plagioclase is currently the common mineral utilized to date fine to medium-grained mafic rocks yielding relatively precise ages thanks to the new generation of noble gas multi-collector machines (e.g. 265.05 ± 0.35 Ma; Belica *et al.*, 2017). However, both plagioclase and zircon are completely lacking as primary crystallizing phases in ultramafic rocks, thus making it extremely challenging to date those rocks. Furthermore, plagioclase unfortunately alters into

sericite (a high K micaceous hydrothermal alteration mineral of feldspars), which at times, can make $^{40}Ar/^{39}Ar$ geochronology of plagioclase impossible (Verati & Jourdan, 2013). Pyroxene, however, is an abundant and essential mineral found in all mafic and ultramafic rocks. Both orthopyroxene and clinopyroxene mineral varieties do not alter to high K minerals. Therefore, the ability to date pyroxene would be particularly useful for dating volcanic flows that constitute the bulk of Large Igneous Provinces.

Previous attempts of dating pyroxene from terrestrial rocks recognized tremendous difficulties when using the K-Ar decay system (Hart & Dodd, 1962; McDougall, 1963; McDougall & Green, 1964; Rama *et al.*, 1965; Lanphere & Dalrymple, 1976; Harrison & McDougall, 1981). Initial attempts at $^{40}Ar/^{39}Ar$ analyses on terrestrial pyroxene displayed saddle shaped age spectra, which were typically attributed to the presence of excess ^{40}Ar (Lanphere & Dalrymple, 1976; Harrison & McDougall, 1981). Although plateau ages could not be calculated, each individual heating step produced results with standard deviations of 0.7 – 17 % (Lanphere & Dalrymple, 1976; Harrison & McDougall, 1981). As a consequence, dating pyroxene from terrestrial rocks was abandoned by the $^{40}Ar/^{39}Ar$ community quite quickly. On the other hand, dating pyroxene with the $^{40}Ar/^{39}Ar$ technique has been shown to be feasible for meteorites due to their old age and thus significant $^{40}Ar^*$ accumulation (Wang *et al.*, 1980; Kunz *et al.*, 1997; Trieloff *et al.*, 2003; Cassata *et al.*, 2010) although the precision obtained is generally relatively poor; e.g., 3313 ± 174 Ma (Kennedy *et al.*, 2013). As with pure pyroxene, the method has been utilized on whole rock samples that are primarily composed of pyroxene (Wang *et al.*, 1980; Kunz *et al.*, 1997). These studies differentiated different phases in these whole rock analyses through the K/Ca ratios (i.e. a low K/Ca ratio was attributed to pyroxene where a high

K/Ca ratio was attributed to plagioclase or any other higher K phase was present in the respective material being dated).

Failures in obtaining geologically meaningful results have been attributed to the low concentrations of K within the pyroxene mineral structure as well as high amounts of excess ^{40}Ar. All previous attempts described above were made using single collector machines (e.g., MAP 215-50, VG5400). New-generation machines provide a step-wise advancement in the sensitivity, precision, and smaller sample volume requirements compared to previous single collector instruments and thus, can mitigate many of the problems mentioned above. The ARGUS VI multi-collector mass spectrometer incorporation of five faraday cups in the detection array allows for the simultaneous collection of all five argon isotopes that provide an accurate $^{40}Ar/^{39}Ar$ age determination at significantly increased levels of precision (e.g. Olierook *et al.*, 2016; Oostingh *et al.*, 2017). The multi-collector array not only allows for heightened sensitivity to accurately detect and measure such small concentrations of K (irradiated to ^{39}Ar) but also provides a much greater ability to accurately measure the trapped $^{40}Ar/^{36}Ar$ ratio; which is very important for dating pyroxene due to high $^{40}Ar/^{36}Ar$ ratios. These high values typically result in plateau age calculations using the $^{40}Ar/^{36}Ar$ measured ratios determined from the inverse isochron (Oostingh *et al.*, 2016), or taking directly the inverse isochron age itself.

In this study, the viability of using the $^{40}Ar/^{39}Ar$ technique on the mineral pyroxene is tested using mineral separates from dolerites collected from two different Large Igneous Provinces (LIPs) located in Australia. Using the ARGUS VI mass spectrometer, we show that pyroxene can provide meaningful and relatively precise ages, even when plagioclase failed and the rock is altered. Results from this study yield ages that are statistically the same as high precision plagioclase $^{40}Ar/^{39}Ar$ plateau ages

from the same samples (e.g. TAS-17: 182.2 ± 0.4 Ma, plagioclase; 182.1 ± 0.7 Ma, pyroxene) as well as with all previous geochronological results from a variety of other methods (e.g. plagioclase $^{40}Ar/^{39}Ar$ geochronology, U/Pb results from zircon and baddeleyite).

5.3. Dating pyroxene with the $^{40}Ar/^{39}Ar$ method.

5.3.1. Terrestrial applications

In the early 1960's, studies utilizing the K-Ar method on pyroxenes (Hart, 1961; McDougall, 1961; Hart & Dodd, 1962; McDougall & Green, 1964) and later followed by the $^{40}Ar/^{39}Ar$ method in the 70's (Lanphere & Dalrymple, 1976; Harrison & McDougall, 1981) were being conducted. Initially, pyroxene was targeted as a possible candidate mineral for the K-Ar method due to the lack of structural vacancies within the mineral structure that would mitigate the likelihood of excess Ar (Dalrymple & Lanphere, 1969). Ironically, despite no structural site suitable within the crystal lattice for K, excess argon was shown to have greatly affected these initial analyses (Lanphere & Dalrymple, 1976; Harrison & McDougall, 1981). Therefore, it was concluded that $^{40}Ar^*$ could, however, be housed in crystal dislocations or defects as well as attributed to small fluid or gas inclusions (Hart & Dodd, 1962; McDougall & Green, 1964; Rama *et al.*, 1965; McDougall *et al.*, 1969). Along with the potential for excess argon, $^{40}Ar/^{39}Ar$ geochronology of pyroxene is further complicated by the very low abundances of K within the mineral. Such low abundances make the measurement of ^{39}Ar to close to the blank levels, even for very long irradiations, leading to difficulties in obtaining precise and meaningful results.

The quality of the K-Ar results from studies by Hart (1961) and McDougall (1961) is difficult to assess, as errors on the age calculations are not provided. In

addition, composite grains of plagioclase and pyroxene (McDougall, 1961) and pyroxene and biotite (Hart, 1961) were analyzed due to the difficulty of separating these various phases at the time. Although these impurities accounted for "less than 5 %" of the total amount of grains, the much higher K content of these "impurities" would most likely have dominated the signal (a simple mass balance calculation show that 5 % plagioclase with 0.1% K_20 within 95% pyroxene with 0.01% K_20 would still contribute to 1/3 of the total ^{40}Ar [and ^{39}Ar] signal). Another major problem was excess ^{40}Ar. The age spectra consistently displayed complex "saddle" shape age spectra with older ages in the lower heating steps, minima ages in the middle heating steps that approach the known crystallization age, before rising again to ages in excess of 4 Ga at times (Lanphere & Dalrymple, 1976; Harrison & McDougall, 1981). Errors on the individual steps for these analyses display a wide range of 0.7 % to 17 %. Interestingly, even in these initial studies that could not produce plateau ages, the K/Ca ratios displayed decreases of two orders of magnitude throughout the course of gas released (Harrison & McDougall, 1981). These authors interpreted these K/Ca spectra shapes to indicate that the excess ^{40}Ar is dominantly held in the Ca sites, which then outgassed in higher heating steps.

These obstacles have led to the application of the K-Ar and $^{40}Ar/^{39}Ar$ methods for terrestrial samples to nearly be absent from practice by the 1970's. Imaoka and Itaya (2004) utilize the K-Ar method on pyroxene and plagioclase from andesites using the flame photometry method (Itaya *et al.*, 1996) that has the capability of analyzing low concentrations of potassium. The coexisting clinopyroxene and plagioclase reported ages of 16.5 ± 1.5 Ma and 14.2 ± 0.8 Ma, respectively, identical within error, but showing the relatively poor precision on the pyroxene age (± 9%) (Imaoka & Itaya, 2004). The $^{40}Ar/^{39}Ar$ method more recently was applied to pyroxene inclusions in

diamonds; however, these results were calculated from typically less than three heating steps providing statistically unreliable results (Phillips *et al.*, 1989; Burgess *et al.*, 2004; Phillips *et al.*, 2004).

5.3.2. Extraterrestrial applications

In some (yet relatively rare) instances, $^{40}Ar/^{39}Ar$ thermochronology of pyroxene has been utilized to study extraterrestrial materials, probably due to the relatively large abundance of this mineral in planetary bodies (e.g. basaltic meteorites and chondrites; Pellas *et al.*, 1997; Trieloff *et al.*, 2003; Korochantseva *et al.*, 2005; Cassata & Renne, 2010; Cassata *et al.*, 2011), and the old age of most of meteorites. Pyroxene $^{40}Ar/^{39}Ar$ geochronology has been successfully applied (with poor precision) to constraining the timing of shock features of chondrites and Martian meteorites (Wang *et al.*, 1980; Kunz *et al.*, 1997; Trieloff *et al.*, 2003; Cassata *et al.*, 2010). The method is also typically utilized on whole rock samples that are primarily composed of pyroxene rather than mineral separates, with the various phases being differentiated through the K/Ca ratios. Plagioclase or K rich phases were interpreted through high K/Ca ratios whereas low K/Ca ratio were attributed to pyroxenes. Plateau ages of pyroxenes were then quoted from only the heating steps that correlated with the low K/Ca ratios (Wang *et al.*, 1980; Kunz *et al.*, 1997).

5.4. Geologic Setting and Previous Results

The pyroxene examined for this study was collected from two different Continental Flood Basalt (CFB) provinces; the Kalkarindji CFB province and the Tasmanian Dolerites, part of the Ferrar CFB province (Table 5.1). Four of the six samples utilized for this study were collected from the Kalkarindji CFB province found throughout the western half of Australia. These samples are composed of fine-medium to medium grained dolerite dykes and sills found within the Officer Basin (Figure 5.1).

The second group of samples is from the medium to coarse-grained Tasmanian Dolerite dykes and sills that are extensively outcropped throughout the island state of

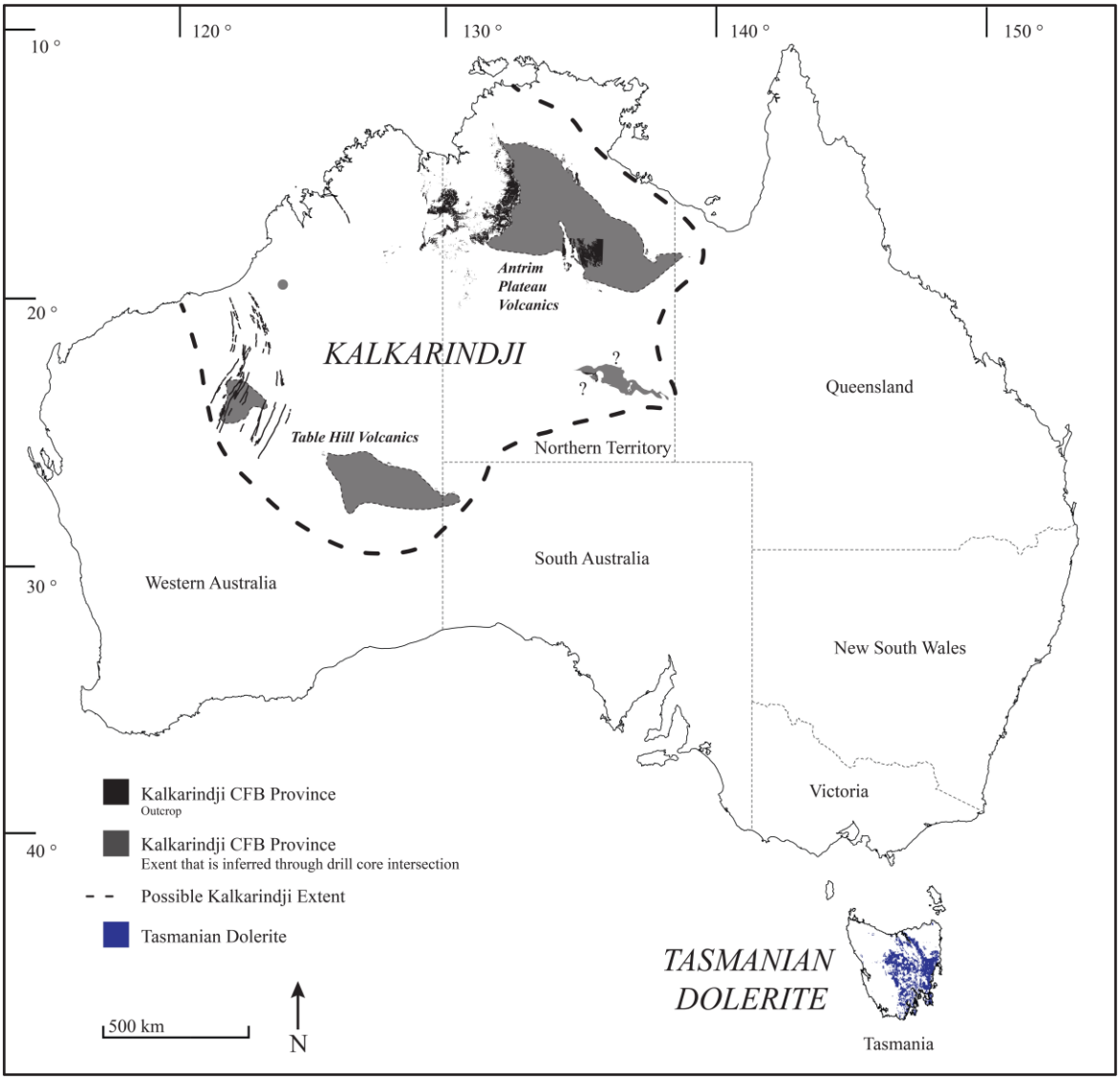

Figure 5.1: Sketch map of the Australian Kalkarindji Continental Flood Basalt (CFB) province's distribution and constituent suites. Modified after Figure 2.1. Outcrop of the Tasmanian Dolerite also represented.

Tasmania, Australia (Figure 5.1). These two CFBs were targeted for pyroxene analyses to test the method with provinces emplaced at different ages (Kalkarindji at 511 Ma and the Tasmanian Dolerites at 184 Ma) as well as with rocks affected by different degrees of alteration.

5.4.1. Ferrar CFB Province

The Ferrar CFB province is composed of dolerite sills and dykes, a layered mafic intrusion, and a minor amount of basaltic flows outcropping in Antarctica and in the Australian state of Tasmania. In Tasmania, intrusions of tholeiitic magmas are exposed over approximately 30,000 km² of the island (Figure 5.1) (Edwards, 1942a; Edwards, 1942b; McDougall, 1962; Compston *et al.*, 1968; Hergt *et al.*, 1989b). Many of these intrusions are thick enough to observe a grain size increase toward the cores of the intrusions, in some cases developing a granophyre zone (McDougall, 1962). The database of reliable isotopic ages for Ferrar province is largely lacking, in particular in Tasmania. Plagioclase $^{40}Ar/^{39}Ar$ geochronology of the dolerites from Antarctica gave three plateau ages ranging from 180.3 ± 1.0 Ma to 182.5 ± 1.0 Ma (recalculated from Fleming *et al.*, 1997 using the constants and standard age from Renne *et al.*, 2011) although it must be noted that these ages have been measured using the MMhb hornblende standards, which has been shown to be heterogeneous (e.g. Renne *et al.*, 1998) . U/Pb zircon and baddeleyite analyses of the Dufek layered mafic intrusion (183.9 ± 0.3 Ma) and two dolerite sills (183.6 ± 1.0 Ma) provide the first high precision ages of the Ferrar province (Encarnacion *et al.*, 1996; Minor & Mukasa, 1997). More recently, a series of zircon U/Pb ages from 20 sills of the Ferrar LIP provided a range from 182.85 – 182.43 Ma including a single age of 182.54 ± 0.21 Ma from the Tasmanian Dolerite (Burgess *et al.*, 2015).

5.4.2. Kalkarindji CFB Province

The Kalkarindji CFB province is 2.1 x 10^6 km^2 LIP with exposures in Western Australia, Northern Territory, Queensland, and South Australia (Figure 5.1). The Kalkarindji CFB province can be grouped into two large, region controlled, groups; the Antrim Plateau Volcanics group in the north and the Table Hill Volcanics in the

south; see discussion in Chapter 2 (Figure 5.1). Geochronological analyses of the Kalkarindji CFB province have constrained the emplacement age to ca. 511 Ma (Jourdan *et al.*, 2014b) although these authors note that the overall advanced alteration of plagioclase, prevent a proper coverage of the entire province. The geochronological approaches have been quite diverse thus far for the Kalkarindji CFB province, with four $^{40}Ar/^{39}Ar$ plateau ages ranging from of 509.0 ± 2.6 Ma to 511.9 ± 1.9 Ma (data from Glass and Phillips, 2006 and Evins *et al.*, 2009 recalculated by Jourdan *et al.*, 2014b using the constants of Renne *et al.*, 2011) , baddeleyite crystals inductively coupled thermal ionization mass spectrometry (ID-TIMS) results with a concordant upper intercept of 511 ± 5 Ma, and zircon chemical abrasion thermal ionization mass spectrometry (CA-TIMS) analyses with a weighted $^{238}U/^{206}Pb$ mean age of 510.7 ± 0.6 Ma (Jourdan *et al.*, 2014b).

5.5. Sample Selection and Analytical Methods

5.5.1. Petrography

5.5.1.1. Tasmanian Dolerites

The Tasmanian samples were collected from the thick Red Hill Dolerite dyke in southern Tasmania (TAS-07) as well as a sill located in northern Tasmania (TAS-17). Both samples collected are medium grained dolerites; however, TAS-07 has differentiated to the point of displaying a granophyric texture in areas (Figure 5.2a, b). The mineralogy for all the samples is remarkably similar, dominated by plagioclase feldspar and clinopyroxene (augite and pigeonite) with varying amounts of Fe-Ti oxide (primarily ilmenite) minerals and minor degrees of secondary biotite and hornblende. Both samples are primarily characterized by an ophitic and seriate texture containing a grain size range of less than a millimeter to some plagioclase and clinopyroxene

crystals up to 4 millimeters. TAS-17 has a higher abundance of crystal size fractions around a millimeter or less with only about 5 % of the grains falling in the greater than 1 mm size fraction. TAS-07 is nearly the opposite compared to TAS-17, with a higher

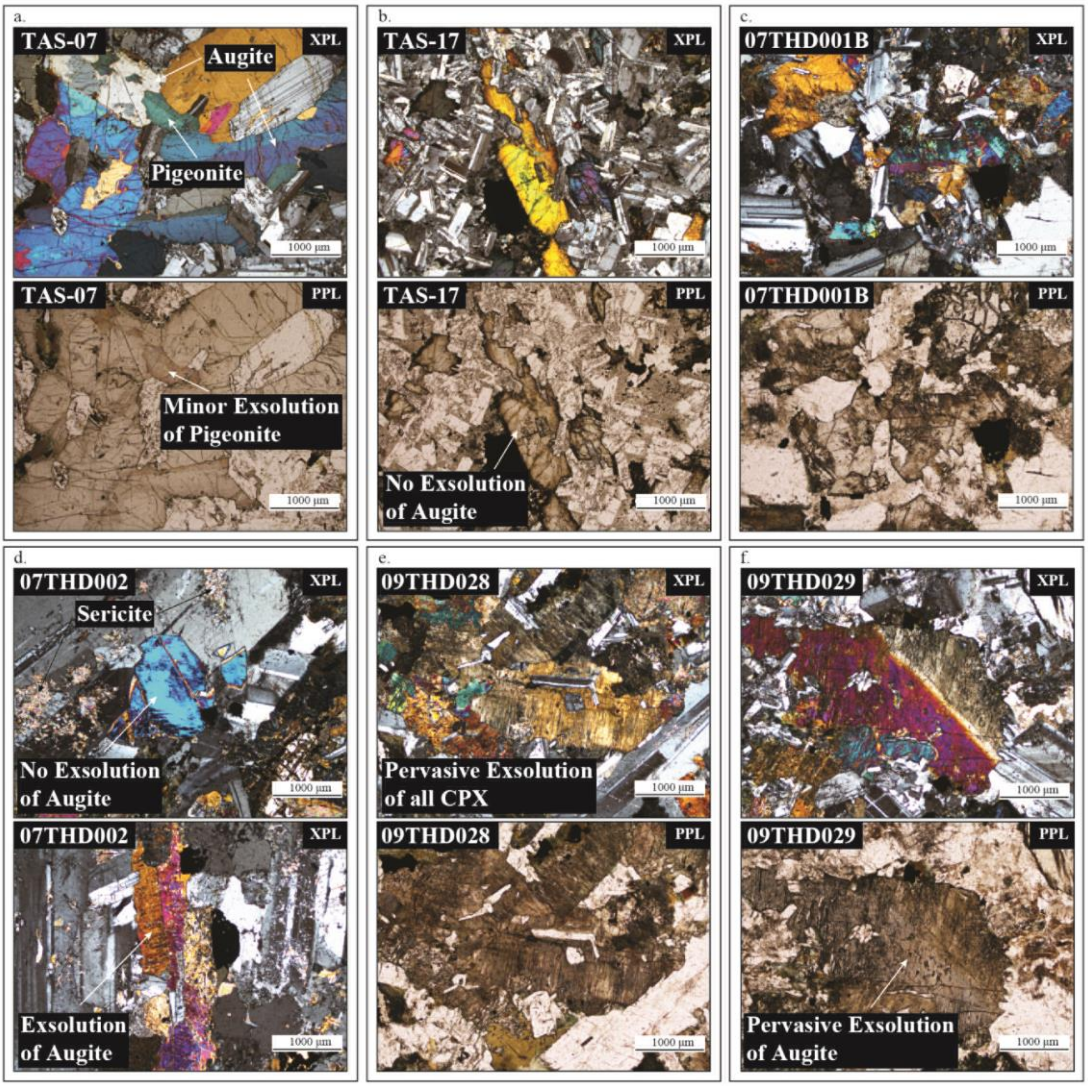

Figure 5.2: Photomicrographs of all samples. Selected examples of exsolution features, pigeonite, augite, and sericite are labelled. CPX – clinopyroxene; OPX – Orthopyroxene.

abundance of crystal sizes greater than 1 mm. In both samples the plagioclase crystals are columnar to prismatic in habit and euhedral, displaying well-developed multiple and Carlsbad twinning. Nearly all the plagioclase grains of TAS-07 display a minor degree of sericite alteration. The majority of the plagioclase crystals of TAS-17 show severe sericite alteration, however, roughly 40 % of the grains are completely unaffected by the alteration (Figure 5.2). The clinopyroxene crystals in these two

samples are of the augite (70 %) and pigeonite (30 %) variety. The clinopyroxene crystal habit for TAS-17 is dominated by subhedral to anhedral grains while TAS-07 displays euhedral to subhedral grains. TAS-07 clinopyroxene displays an intergrowth texture within the gaps of the columnar plagioclase grains. The pyroxene grains for both samples contain a minor amount of grains with simple twins as well as slight zoning from the center to the outer edges of the crystals primarily evident in differences in the degree of birefringence. TAS-17 contains a higher abundance of pyroxene crystals that display this zoning than TAS-07. A low degree of exsolution lamellae is apparent in roughly 1 % of the pigeonite crystals. The pyroxene grains are primarily unaltered fresh crystals, the minor degrees of alterations that is present occurs along edges and cracks.

5.5.1.2. Table Hill Volcanics (Kalkarindji)

The Kalkarindji samples chosen for this study were from a suite of dolerite sills collected from borehole intersections of the Table Hill Volcanics within the Officer Basin. All four samples are medium to coarse-grained dolerites (Figure 5.2c-f). Plagioclase feldspar and clinopyroxene (augite and pigeonite) are the most abundant mineral phases present with Fe-Ti oxide minerals (ilmenite), orthopyroxene, and secondary biotite and hornblende comprising the next highest abundances of mineral phases observed. These samples contain a range of grain sizes from less than a millimeter to some plagioclase and clinopyroxene crystals up to 3 and 4 millimeters; in the case of sample 07THD002 the plagioclase crystals can be greater than 5 millimeters. In all samples the columnar and prismatic plagioclase crystals are primarily euhedral with a minor abundance of grains displaying a more subhedral crystal form. Multiple and Carlsbad twins are observed in most plagioclase crystals; however, the grains are highly variable in how developed the twins appear. This is in

most part due to the high degree of sericite alteration affecting all the samples (Figure 5.2c-f). The crystal habit of the pyroxene for all samples is dominantly subhedral to anhedral. Twinning is apparent in a low abundance of the pyroxene grains for all samples. Unlike the Tasmanian Dolerites, however, these samples do not display as high an abundance of the center to edge pyroxene zoning and rather show a high abundance of exsolution lamellae (at times present in the clinopyroxenes and orthopyroxene). Sample 07THD002 displays a discernibly lower abundance of pyroxene crystals riddled with exsolution lamellae than samples 07THD001B, 09THD028, and 09THD029, which all display a large degree of exsolution lamellae in some 95 % of the crystals (Figure 5.2d).

5.5.1.3. Scanning electron microscope (SEM) analyses

SEM analyses were conducted on the Tasmanian Dolerite and Kalkarindji samples to investigate further the extent and nature of the exsolution observed within the petrography (Figure 5.3). The pyroxene variety of the Tasmanian Dolerites is strictly relegated to clinopyroxenes (augite and pigeonite). The two clinopyroxene varieties in the Tasmanian Dolerites is apparent as completely separate crystals throughout the sample as well as a more complex relationship showing a more "patchy" texture (Figure 5.3a and b). The presence of these two pyroxene types is a common occurrence in basaltic magmas, the crystallization of pyroxene, as well as the exsolution of pyroxene, within basaltic magmas is discussed extensively in Poldervaart and Hess (1951) where observations similar to those observed within this study are discussed. Minor degrees of exsolution is present within some clinopyroxene crystals from the Tasmanian Dolerites primarily affecting pigeonite crystals over augite (Figure 5.2a). However, exsolution is not all together absent within the augite, although these exsolution features are revealed only in the SEM images (Figure 5.3c).

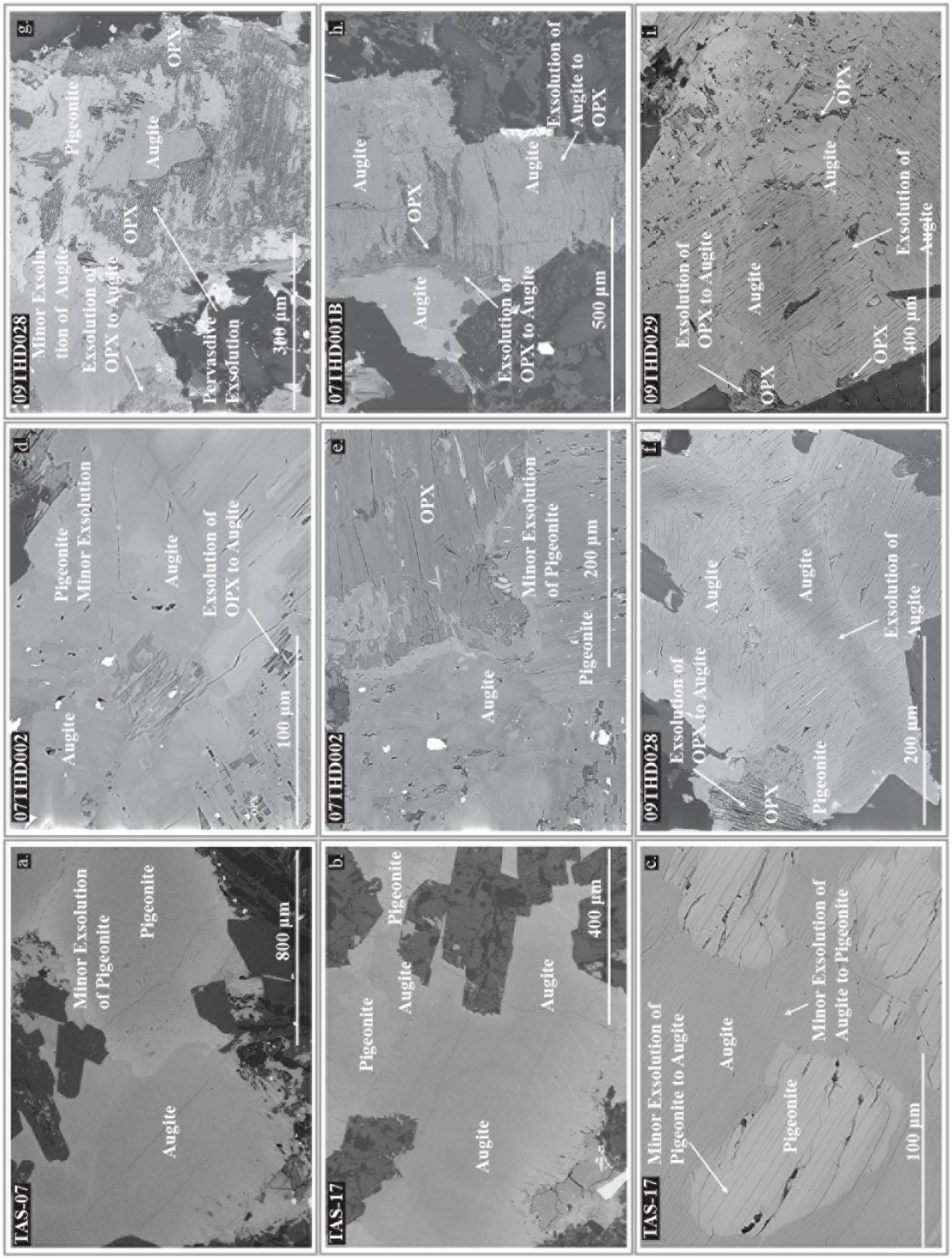

Figure 5.3: Representative SEM Images of pyroxene crystals from the Tasmanian Dolerites and sills of the Table Hill Volcanics (Kalkarindji). Selected examples of exsolution features, pigeonite, augite, and sericite are labelled. OPX – orthopyroxene.

When minor exsolution is present in a pyroxene crystal, the lamellae are only minute in width (micron to submicron scales; Figure 5.3). The nature of the exsolution within the Tasmanian Dolerites is lamellae of augite exsolving from pigeonite and pigeonite exsolving from augite. Overall, the Tasmanian Dolerite pyroxene is largely devoid of exsolution, with lamellae only being observed in less than 3 % of the crystals.

The pyroxenes within the Kalkarindji sills display both varieties of clinopyroxenes as well as a minor amount of orthopyroxene (no more that 10 % of the modal abundance in any of the samples) (Figure 5.3d – i). As with the Tasmanian Dolerites the different pyroxene varieties are present as completely different crystals (e.g. Figure 5.3e) as well as a more patchy relationship (e.g. Figure 5.3f). The exsolution observed within the Kalkarindji sample suite is more pervasive and complex than the Tasmanian Dolerites (Figure 5.3d – i). In sample 07THD002, exsolution lamellae is largely lacking within the augite crystals (Figure 5.3d and e) with minor degrees of exsolution appearing within the pigeonite crystals (Figure 5.3e). Most apparent within the pyroxene from sample 07THD002, is the abundance of inclusions of a variety of different minerals (primarily orthopyroxene and ilmenite) compared to pyroxene from the other samples of the Kalkarindji suite. Exsolution within the other three samples from the Kalkarindji suite is strongly pervasive with lamellae present in nearly every pyroxene crystal (Figure 5.3f – i). At times the relationship between the orthopyroxene present and the clinopyroxenes is difficult to discern. The orthopyroxene and clinopyroxenes display the same "patchy" interactions that are represented more prevalently between augite and pigeonite (e.g. Figure 5.3g) as well as distinct grains (e.g. Figure 5.3i). However, in some grains the relationship between crystals that are all together a different grain or advanced exsolution features is complex and unclear (e.g. Figure 5.3g – h).

5.6.2. Sample preparation and $^{40}Ar/^{39}Ar$ analytical conditions

5.6.2.1. Sample preparation

The samples were first crushed with a rigorously cleaned steel hydraulic press. Once crushed the material was sieved to a size fraction of 125 – 212 μm (hence forth referred to as the fine size fraction) and 212 – 350 μm (hence referred to as the coarse size fraction). The sample fractions were rinsed in distilled H_2O to remove any dust or powder from the desired grains. Each size fraction was first separated using heavy liquid (LST from Central Chemical Consulting; density = 2.85) where pyroxene is concentrated into the heavy fraction. This approach is primarily aimed at removing the plagioclase crystals from the separate as plagioclase constitutes roughly half the mineral abundance for these dolerite. Electron microprobe values from the central Atlantic magmatic province showed that plagioclase contains roughly 0.05 % to 0.1 % of K_2O and is below detection limit (< 0.01 wt. %) for pyroxene. Once thoroughly drained and rinsed of any LST, the heavy fraction containing pyroxene was separated further using a Frantz magnetic separator concentrating the pyroxene in the magnetic fraction (0.3 – 0.4 Å). The plagioclase was separated from the light fraction of the LST stage and further concentrated using the Frantz magnetic separator concentrating in the non-magnetic fraction (up to 1.6 Å).

Samples were handpicked under a binocular microscope into multiple aliquots to test for any possible effect related to the crystal size as well as to test how rigorously the sample needed to be picked. For the Kalkarindji and Tasmanian Dolerite, plagioclase and pyroxene samples were either picked around 10 mg (10 pyroxene aliquots and all of the plagioclase samples) or around 20 mg (6 pyroxene aliquots). For most samples the small size fraction provided the opportunity to pick grains that were translucent to transparent with a tan/amber/dark orange color whereas the coarse size

fraction for the Kalkarindji suite of samples had very few of these types of grains (or the grains that were semi-transparent were riddled with inclusion) (Figure 5.4). The inability to clearly observe if inclusions were present within the darkest colored grains required these coarse size fraction grains to be picked using preferentially the morphology. The coarse size fraction also presented problems in most samples by the

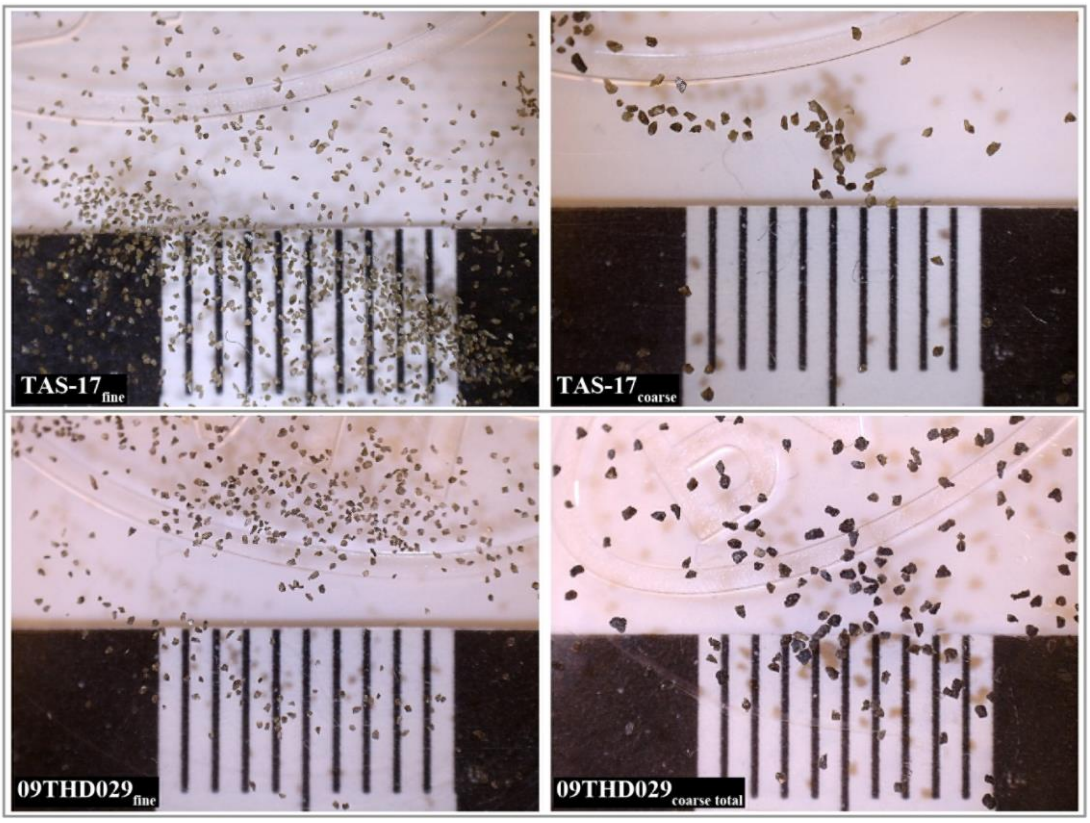

Figure 5.4: Photographs of selected examples of pyroxene separates. Ruler measurement displayed is in 1 cm increments.

amount of plagioclase that was adhered to the surface of the grains. Grains with plagioclase stuck to the surface were avoided as much as possible; however, with the dark opaque color this was sometimes difficult if the grains could not be flipped to reveal all sides easily. To alleviate further the possibility that the coarse pyroxene fraction incorporate plagioclase, all coarse grained samples were leached for one minute per aliquot using dilute 5 N HF. All aliquots from the Kalkarindji samples were leached with HF while the Tasmanian sample TAS-17 was not leached due to the translucent fresh appearance of all the pyroxene crystals (Figure 5.4). Once each

sample aliquot had been leached with HF, the samples were rinsed in distilled H_2O in an ultrasonic cleaner. All plagioclase aliquots were leached with HF to remove any potential adhering alteration product within superficial cracks that were not removed during hand picking (Jourdan *et al.*, 2009b). Some samples were further duplicated to test how rigorous the picking strategy needed to be for pyroxene. For this test, rather than the rigid picking criteria discussed above (i.e. transparent/translucent for the fine or morphology for the coarse size fraction), samples were picked by discarding any non-pyroxene grains, pyroxene with visible inclusions, or plagioclase adhered to the crystal sides. All of the aliquots that were not rigorously picked were leached for one minute using dilute 5 N HF.

The various aliquots separated from each sample are as follows: *fine* = 125 – 212 μm size fraction picked rigorously; *fine total* = 125 – 212 μm size fraction picked with less rigor (ALL pure pyroxene selected, any grains with obvious signs of plagioclase or inclusions picked out); *coarse* = 212 – 350 μm size fraction picked rigorously; *coarse total* = 212 – 350 μm size fraction picked with less rigor (ALL pure pyroxene selected, any grains with obvious signs of plagioclase or inclusions picked out). TAS-07 had one aliquot of coarse pyroxene picked for analysis. Sample TAS-17 had all four aliquots (sample denoted e.g. TAS-17_{fine}). Two samples (07THD002 and 07THD028) with four aliquots each (*fine, fine total, coarse, coarse total*) and two samples (07THD001b and 09THD029) with two aliquots each (*fine and coarse*) from the Kalkarindji CFB province were analyzed for $^{40}Ar/^{39}Ar$ geochronology.

5.6.2.2. Sample irradiation and analysis

The cleaned plagioclase and pyroxene separates were then loaded into several 1.9 cm in diameter by 0.3 cm depth aluminum discs. The discs were then stacked together and placed in quartz tubes. Samples were irradiated in Cadmium-Lined In-

Core Irradiation Tubes (Cd shielded to minimize undesirable nuclear interference reactions) at the TRIGA Reactor at Oregon State University. Each disk was irradiated for 40 hours throughout four different irradiations. All $^{40}Ar/^{39}Ar$ geochronological analyses of the plagioclase and pyroxene were conducted at Curtin University within the Western Australian Argon Isotope Facility of the John de Laeter Centre. The mineral populations were analyzed using a low volume (600 cc) ARGUS VI mass spectrometer from Thermofisher© (Phillips & Matchan, 2013; Olierook *et al.*, 2016; Oostingh *et al.*, 2017). Fully inter-calibrated standards irradiated together with the samples are GA1550 (age of 99.738 ± 0.104 Ma), FCs (age of 28.294 ± 0.037 Ma), and WA1ms (age of 2613.0 ± 2.4 Ma) (Jourdan & Renne, 2007; Renne *et al.*, 2011a; Jourdan *et al.*, 2014a). The plagioclase samples for both Tasmanian samples were irradiated together in the first irradiation batch (irradiation 18); with a J-value computed as 0.0111675 ± 0.04 % (1σ). For the second irradiation, the TAS-07 pyroxene sample had an average J-value computed to be 0.010602 ± 0.125 %. For the third irradiation, that included all of the Kalkarindji samples and the TAS-17 pyroxene samples, the J-values computed were 0.010502 ± 0.055 % for all samples except for two aliquots ($09THD028_{coarse}$ and $09THD029_{coarse\ total}$) that had computed J-values of 0.01055 ± 0.047 %. The mass discrimination was monitored on an automated air pipette providing a range of values from 0.992179 ± 0.08 to 0.994335 ± 0.04 per dalton. Both the plagioclase and pyroxene crystals were analyzed as populations step-heated by a continuous 100 W PhotoMachine© CO_2 (IR, 10.4 μm) laser that was fired and rastered onto the sample populations during 60 seconds. The standard analyses were all fused in a single step.

During analyses the gas was purified through an extra low-volume stainless steel extraction line of 240cc, using two SAES AP10 and one GP50 getter. Argon

isotopes were measured in static mode set with a permanent resolution of ~200. The multi-collection Ar isotope measurements were made using four faraday cups (three 10^{12} ohm resistors for masses ^{40}Ar, ^{38}Ar, ^{37}Ar and a 10^{13} ohm resistor for mass ^{39}Ar, thus providing a less noise/signal ratio) as well as a low background compact discrete dynode ion counter to measure mass ^{36}Ar. The relative abundance of each mass was measured simultaneously using 10 cycles of peak-hopping with 33 seconds of integration time for each mass. Detectors were calibrated to each other electronically followed by Air shot beam signals. The raw data were processed using the ArArCALC software (Koppers, 2002). For all analyses the interfering isotopes were corrected, with 1 sigma errors, with $(^{39}Ar/^{37}Ar)$ Ca = 6.95×10^{-4} (± 1.3 %), $(^{36}Ar/^{37}Ar)$ Ca = 2.65×10^{-4} (± 0.84 %) and $(^{40}Ar/^{39}Ar)$ K = 7.30×10^{-4} (± 12.4 %) correction factors (Renne *et al.*, 2013). The ages were then calculated using the decay constants recommended by Renne *et al.* (2011a). Blanks were monitored every 3 to 4 steps. All parameters and relative abundance values are provided in Table 5.1 with individual errors given at the 1σ level.

The criteria for the determination of a plateau were as follows; the analyses must include at least 70 % of ^{39}Ar, should be distributed over a minimum of 3 consecutive steps agreeing at 95 % confidence level, and must satisfy a probability of fit (P) of at least 0.05. The plateau ages are calculated using the mean of all plateau steps, each weighted by the inverse variance of their individual analytical error and then listed at the 2σ level. Uncertainties quoted do not include analytical and J-value errors.

5.6.2.3. Note on the error propagation of the $^{40}Ar/^{36}Ar$ ratio

When using the $^{40}Ar/^{39}Ar$ technique plateau age calculations correct the contribution of ^{40}Ar from the atmosphere using a $^{40}Ar/^{36}Ar$ constant of 298.56 (Lee *et*

al., 2006a; Mark *et al.*, 2011). When this constant is used the assumption is made that the initial trapped ratio is the same as the atmospheric composition. Multiple measurements of the various pyroxene separates indicate that this assumption is not always valid, with ratios sometimes below but more often above this atmospheric $^{40}Ar/^{36}Ar$ constant, typically no more than ± 1.6 %. This discrepancy usually indicates excess ^{40}Ar or air fractionation during cooling. The standard plateau age calculations using the $^{40}Ar/^{36}Ar$ constant do not propagate the uncertainty of the measured trapped argon ratio likely underestimating the true age uncertainty. The inverse isochron ($^{40}Ar/^{39}Ar$ vs. $^{40}Ar/^{36}Ar$) age accounts for both the trapped ratio and its uncertainty, which in the case of knowing the ratio to an acceptably confident degree provides a more accurate representation of the crystallization age of the rock. Due to the differing $^{40}Ar/^{36}Ar$ ratios between the constant and measured values, both (1) the inverse isochron ages and (2) plateau ages calculated using the inverse isochron $^{40}Ar/^{36}Ar$ intercept value (and its uncertainty) are presented following the approach of Oostingh *et al.* (2017). The corrected plateau age approach allows an easier comparison in terms of uncertainty with published ages, all calculated using the standard plateau approach, but result in a statistically more accurate age due to the propagation of the uncertainty of the trapped ratio. In addition, using the plateau representation provides an easier assessment of the amount of gas included in the age calculation. One downside is that using this approach tends to artificially yield better χ^2 statistics due to larger errors on each step. Therefore, intercept values derived from the inverse isochron were only used for the correction if the isochron probability of fit was greater than 5 %, thus avoiding the calculation of plateau ages with insignificant inverse isochrones (Oostingh *et al.*, 2017). A full summary of the step-heating analyses can be found in the supplementary material.

Sample	Coordinates (UTM)	Mineral	Total Fusion Age (Ma)	Plateau Age (Ma)	Total ^{39}Ar Released (%,n)	MSWD	P	Isochron Age (Ma)	Spreading Factor (%)	$^{40}Ar/^{36}Ar$ Intercept	MSWD	P
Tasmanian Dolerites												
TAS-07	519183 S	Plagioclase	181.95 ± 0.58	-		-	-	-	-	-	-	-
	5230971 E	Plagioclase (dup)	181.47 ± 0.28	-		-	-	-	-	-	-	-
		Pyroxene (c)	184.24 ± 11.35	183.89 ± 2.77	80.74 (12)	0.41	0.95	183.10 ± 5.13	31.8	302.6 ± 4.3	0.60	0.82
TAS-17	519528 S	Plagioclase	182.13 ± 0.26	181.69 ± 0.36	74.67 (11)	1.69	0.08	183.32 ± 1.29	83.6	274.9 ± 18.3	1.17	0.31
	5411978 E	Pyroxene (c)	177.15 ± 7.13	184.57 ± 3.87	94.99 (20)	0.59	0.92	184.96 ± 5.92	15.3	295.4 ± 1.0	0.68	0.83
		Pyroxene (ct)	180.53 ± 1.53	182.36 ± 0.75	69.62 (12)	1.37	0.18	181.75 ± 2.26	54.3	299.9 ± 4.5	1.53	0.12
Kalkarindji: Table Hill Volcanics												
07THD001B	32.3596 S	Pyroxene (f)	503.98 ± 5.45	-	-	-	-	-	-	-	-	-
	20.8800 E	Pyroxene (c)	512.02 ± 1.55	-	-	-	-	-	-	-	-	-
07THD002	32.4108 S	Pyroxene (f)	505.04 ± 5.11	507.53 ± 3.42	90.67 (17)	0.55	0.92	503.87 ± 5.41	47.7	296.6 ± 1.2	0.94	0.53
	20.8063 E	Pyroxene (c)	517.33 ± 1.12	-		-	-	-	-	-	-	-
		Pyroxene (ct)	508.67 ± 1.15	-	-	-	-	-	-	-	-	-
09THD028	32.3185 S	Pyroxene (f)	499.88 ± 2.14	-	-	-	-	-	-	-	-	-
	20.6609 E	Pyroxene (c)	515.40 ± 0.80	-	-	-	-	-	-	-	-	-
09THD029	32.3185 S	Pyroxene (ft)	515.75 ± 0.68	-	-	-	-	-	-	-	-	-
	20.6609 E	Pyroxene (c)	517.67 ± 0.88	-	-	-	-	-	-	-	-	-
		Pyroxene (ct)	496.24 ± 0.83	-	-	-	-	-	-	-	-	-

Table 5.1: $^{40}Ar/^{39}Ar$ Geochronology of Plagioclase and Pyroxene Crystals from the Tasmanian Dolerites and Kalkarindji CFB Province. The calculated J values relative to FCs with an age of 28.294 ± 0.037 % Ma [all pyroxene samples from Kalkarindji as well as pyroxene for TAS-07 and TAS-17], GA1550 with an age of 99.74 ± 0.104 Ma [TAS-07 plagioclase], and WA1ms with an age of 2613.0 ± 2.4 Ma [TAS-17 plagioclase] (Jourdan & Renne, 2007; Renne *et al.*, 2011b; Jourdan *et al.*, 2014a). MSWD and probability (P), percentage of ^{39}Ar degassed used in the plateau calculation, number of analyses included in the isochron, and $^{40}Ar/^{36}Ar$ intercept are indicated. Analytical uncertainties on the ages are quoted at 2 sigma (2σ) confidence levels and at 1σ for the $^{40}Ar/^{36}Ar$ intercept. Dup = duplicate; f = fine, ft = fine total, c = coarse, ct = coarse total.

5.7. Geochronological results

5.7.1. $^{40}Ar/^{39}Ar$ Geochronology

5.7.1.1. Tasmanian Dolerites geochronology

Two samples from the Tasmanian Dolerites were chosen for $^{40}Ar/^{39}Ar$ geochronological analyses. Two aliquots of sample TAS-17 ($TAS\text{-}17_{coarse\ total}$ and $TAS\text{-}17_{coarse}$) and the one analyzed from sample TAS-07 yielded statistically significant pyroxene plateau ages (the two aliquots from sample TAS-17 that did not return results suffered from outside mechanical issues not related to the ARGUS VI or the samples selected). Sample $TAS\text{-}17_{coarse\ total}$ yielded a plateau age of 182.4 ± 0.8 Ma (MSWD = 1.37; P = 0.18) including 69.6 % of ^{39}Ar and calculated using a $^{40}Ar/^{39}Ar$ intercept that was equal to the atmospheric ratio from Lee *et al.* (2006a) (Figure 5.5a). Samples $TAS\text{-}17_{coarse}$ and TAS-07 yielded $^{40}Ar/^{36}Ar$ trapped ratios of 295.4 ± 0.9 and 301.5 ± 4.9, respectively. The inverse isochron for both samples display large amounts of trapped argon ($^{36}Ar/^{40}Ar$) to low radiogenic argon ($^{39}Ar/^{40}Ar$) ratios (e.g. TAS-07; $^{36}Ar/^{40}Ar$ of 0.0027 for a $^{39}Ar/^{40}Ar$ of 0.017; Figure 5.6a – c). Therefore, inverse isochron corrected plateau ages were calculated for these two samples ($TAS\text{-}17_{coarse}$ and TAS-07). $TAS\text{-}17_{coarse}$ gave an age of 184.6 ± 3.8 Ma (MSWD = 0.59, P = 0.92) including 95.0 % of ^{39}Ar released. TAS-07 yielded an age of 183.9 ± 2.8 Ma (MSWD = 0.41, P = 0.95), which includes 80.7 % ^{39}Ar (Figure 5.5a).

Plagioclase from $TAS\text{-}17_{(plagioclase)}$ produced a plateau age of 181.69 ± 0.36 Ma (MSWD = 1.7; P = 0.08) including 75 % ^{39}Ar released (Figure 5.5a). Sample TAS-07 was picked twice for plagioclase $^{40}Ar/^{39}Ar$ geochronological analyses, neither attempt produced plateau ages. The age spectra for these two plagioclase analyses from TAS-07 are particularly perturbed in the higher heating steps

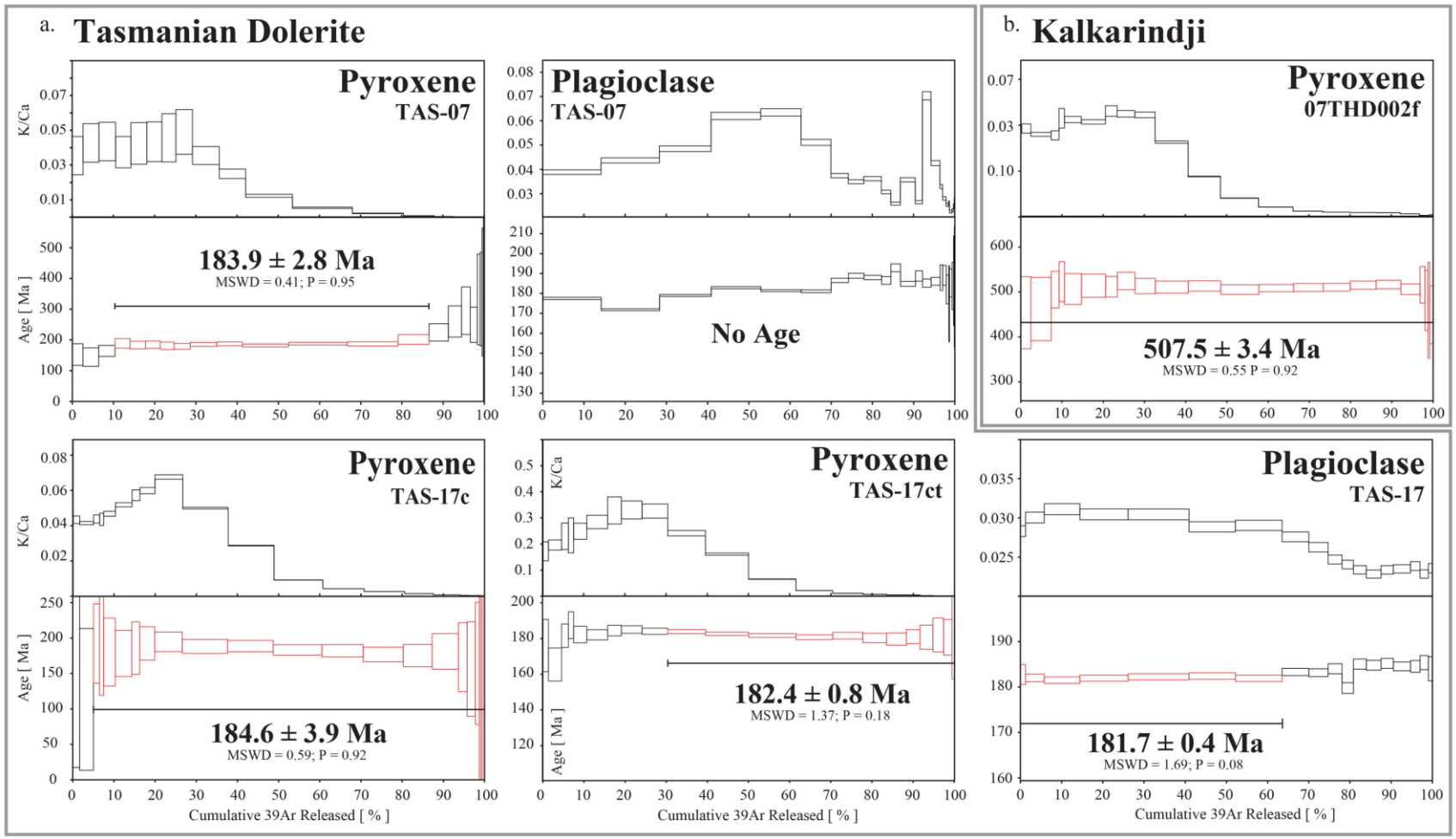

Figure 5.5: $^{40}Ar/^{39}Ar$ apparent age and related K/Ca ratio spectra for pyroxene and plagioclase separates plotted against the cumulative percentage of ^{39}Ar released. Mean squared weighted deviation (MSWD) and probability of fit (P) are indicated. Errors on plateau ages are quoted at 2σ and do not include systematic errors (i.e. uncertainties on the age of the monitor and on the decay constant).

(Figure 5.5a). Total fusion error ages for the two samples are 181.95 ± 0.58 and 181.47 ± 0.28 Ma.

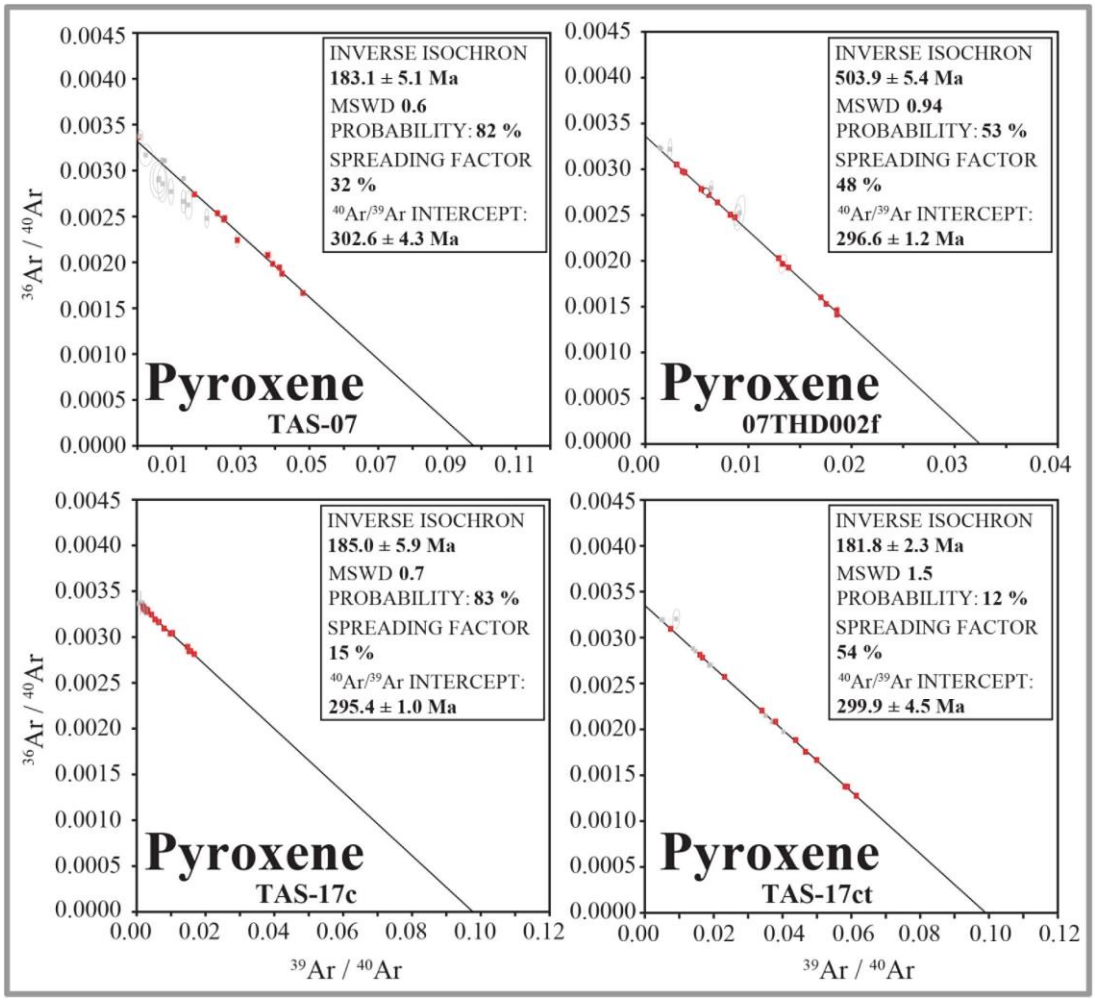

Figure 5.6: Inverse isochons for the $^{40}Ar/^{39}Ar$ geochronology results. Inverse isochron atmospheric ratio used in calculations made for the age quoted.

5.7.1.2. Kalkarindji geochronology

Sample $07THD002_{fine}$ from the Kalkarindji CFB province was the only aliquot from the Kalkarindji sample set to produce a statistically significant pyroxene plateau age. As with the samples that yielded plateau ages for the Tasmanian Dolerites, the inverse isochron for 07THD002 displays high atmospheric argon compared to radiogenic argon (Figure 5.6d). This sample yielded a $^{40}Ar/^{36}Ar$ trapped ratio of 295.5 ± 0.9 so therefore the plateau age was corrected and calculated using the inverse isochron trapped ratio, yielding an age of 507.5 ± 3.4 Ma (MSWD = 0.55,

P = 0.92) (Figure 5.5b). The calculated plateau age includes 90 % of the ^{39}Ar released where the excluded steps overlap completely with the included steps, however, with much larger uncertainties. Three of the four samples from the Kalkarindji CFB province did not return plateau ages (07THD001B, 09THD028, and 09THD029) (Figure 5.7). All results from the aliquots of these three samples returned age spectra that are nearly identical in shape (Figure 5.7); displaying older ages in the lower heating steps (after an initial step or two of young ages) with a then steady decrease to younger ages in the higher heating steps. The two coarse grained aliquots from sample 07THD002 did not yield plateau ages instead displaying the more "sigmoidal" shape observed in all of the other Kalkarindji samples after around 10 % of ^{39}Ar released (Figure 5.7). The initial heating steps for $07THD002_{\text{coarse and coarse total}}$ (< 10 % ^{39}Ar released) display the youngest steps from this study.

5.7.1.3. K/Ca ratio results

The K/Ca ratio for the plagioclase from TAS-17 is around 0.03 until about 70 % of the ^{39}Ar released when the ratio begins to decrease to around 0.024 by 80 % ^{39}Ar released, where the ratio remains for the rest of the heating steps. The K/Ca spectra for the plagioclase separated from TAS-07 are erratic step-to-step, producing a wide range in K/Ca ratios from 0.029 – 0.072 for one analysis and 0.022 – 0.069 for another suggesting the presence of sericite (Verati and Jourdan, 2014).

The K/Ca for all pyroxene separates (Kalkarindji and the Tasmanian Dolerite) display remarkably the same trend. All K/Ca ratios are high in the low heating steps (0.01 to 0.33) with a drastic yet steady decrease in K/Ca ratios between about 30 and 50 % ^{39}Ar released across all samples. From 50 % ^{39}Ar released the K/Ca ratio steadily decreases to ca. 0.0002 (Figure 5.5 and Figure 5.7).

The K/Ca ratios even for these samples that did not return plateau ages continue to display the trend of high K/Ca ratios within the lower heating steps that drop

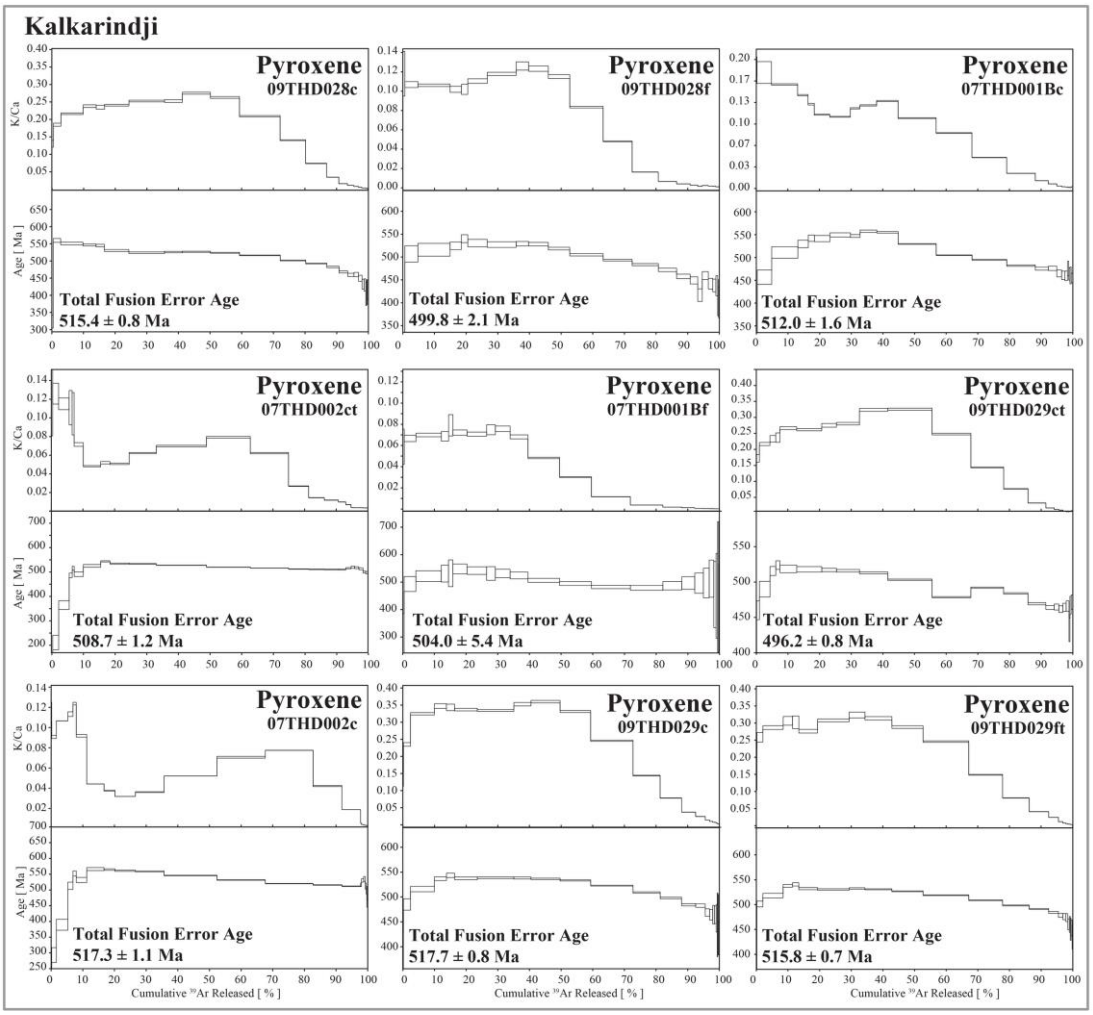

Figure 5.7: $^{40}Ar/^{39}Ar$ and related K/Ca ratio spectra for pyroxene analyses that did not return plateau ages; plotted against the cumulative percentage of ^{39}Ar released. Total fusion error ages quoted. Note that the error ages are *not* providing the age of crystallization and should be considered rather as a semi-quantitative age information.

drastically to near zero within the higher heating steps. Sample 07THD002 from the Kalkarindji sample suite display a more erratic K/Ca spectrum than the other samples from the province (Figure 5.7). This sample displays high K/Ca ratios in heating steps < 10 % ^{39}Ar released correlating with the youngest ages of any analyses from this province before displaying a K/Ca spectra trend that is similar to the rest of the province's results (Figure 5.7).

5.8. Discussion

5.8.1. Pyroxene $^{40}Ar/^{39}Ar$ geochronology of CFBs

This study not only shows that the $^{40}Ar/^{39}Ar$ systematics can be measured in pyroxene, but it shows that pyroxene can yield well-developed plateau ages with a relatively good precision ranging from ± 1.8 % to 0.4 % (2σ) when a new generation multi-collection mass spectrometer is used to measure the isotopic abundances. This is most likely due to the ability to measure very low signal of ^{39}Ar thanks to the 10^{13} ohm resistor faraday located on mass 39, as well as the ability to precisely measure the $^{40}Ar/^{36}Ar$ trapped ratio value. To test the geologic viability of these plateau ages, the pyroxene data will be compared to $^{40}Ar/^{39}Ar$ plateau ages from plagioclase and zircon $^{238}U/^{206}Pb$ age data from the same samples, where applicable, or to results from the literature of the chosen CFB's investigated.

5.8.1.1. Comparison between plagioclase and pyroxene plateau ages

Fresh plagioclase and pyroxene were separated and analyzed from sample TAS-17 allowing the results to be directly compared. The two pyroxene aliquots yielded plateau ages of 184.6 ± 3.9 Ma (10 mg aliquot, TAS-17_{coarse}) and 182.4 ± 0.8 Ma (20 mg aliquot, TAS-$17_{coarse\ total}$) (Figure 5.5a) and the plagioclase separate yielded a plateau age of 181.67 ± 0.4 Ma (Figure 5.5a), in full agreement, within uncertainties. This demonstrates that pyroxene can yield meaningful geologic ages when the samples are fresh. Although the pyroxene does not achieve the precision of plagioclase when comparable amounts of material are analyzed (~ 10 mg for the TAS-17_{coarse} and TAS-$17_{(plagioclase)}$ ages), it still provides statistically reliable ages with satisfactory errors < 2 % when high-precision is not the goal of the study. However, the ± 0.4 % uncertainty on the age of TAS-$17_{coarse\ total}$ approaches the precision obtained for plagioclase (± 0.2

% error), showing that more precise results can be obtained by simply analyzing twice as much material.

5.8.1.2. Comparison between plagioclase and pyroxene from a mildly altered rock.

Plagioclase from sample TAS-07 was separated and analyzed twice. The plagioclase in both instances did not return a plateau age for this sample (results for one of the attempts shown in Figure 5.5a). The age spectra and particularly the tilde-shape of the K/Ca spectrum of the two aliquots suggest evidence for sericite alteration (Verati & Jourdan, 2013) (Figure 5.5a). Sericite is a common alteration product of plagioclase and contains a significantly higher concentration of K than the unaltered plagioclase. Therefore, only a minute amount of sericite (e.g. 0.1%) within the selected grains can perturbed an age spectrum greatly (Verati & Jourdan, 2013). As a consequence, plagioclase grains must be rigorously picked for the most unaltered and optically transparent grains and in some cases, even the most stringent picks fail to produce plateau age. However, the pyroxene aliquot yielded a plateau age of 183.9 ± 2.8 Ma (Figure 5.5). This sample perfectly exemplifies the strengths in using the mineral pyroxene for $^{40}Ar/^{39}Ar$ geochronology of CFBs.

5.8.1.3. Comparison between pyroxene and plagioclase $^{40}Ar/^{39}Ar$ and zircon U-Pb age data

Previous investigations into the age of the Tasmanian Dolerites as well as the greater Ferrar CFB province have primarily been regulated to the U/Pb system. The high precision data available for the province returns an age for the Ferrar CFBs around 182.4 ± 0.2 – 182.9 ± 0.4 Ma (Burgess *et al.*, 2015) to 183.6 ± 1.0 – 183.9 ± 0.3 Ma (Encarnacion *et al.*, 1996; Minor & Mukasa, 1997). Our pyroxene results range from 182.4 to 184.6 and overlap completely with this range of ages from the literature for the Ferrar province (Figure 5.8a).

The previous argon geochronology results for the Kalkarindji province have come from the basalt flows in the north (one results) as well as the Table Hill Volcanics (two results; one of which is a plagioclase plateau from 07THD002, Jourdan *et al.*, 2014b). The pyroxene separated from 07THD002 returned a plateau age of 507.5 ± 3.4 Ma (Figure 5.5b), overlapping within uncertainties with the plagioclase plateau age of the same sample (510 ± 4 Ma; Jourdan *et al.*, 2014). The precision difference of the two results is due to the plagioclase result being obtained on an older generation MAP215-50 mass spectrometer. The pyroxene plateau age also overlap with all of the three plagioclase $^{40}Ar/^{39}Ar$ ages ranging from 509.0 ± 2.6 to 511.9 ± 1.9 Ma, the

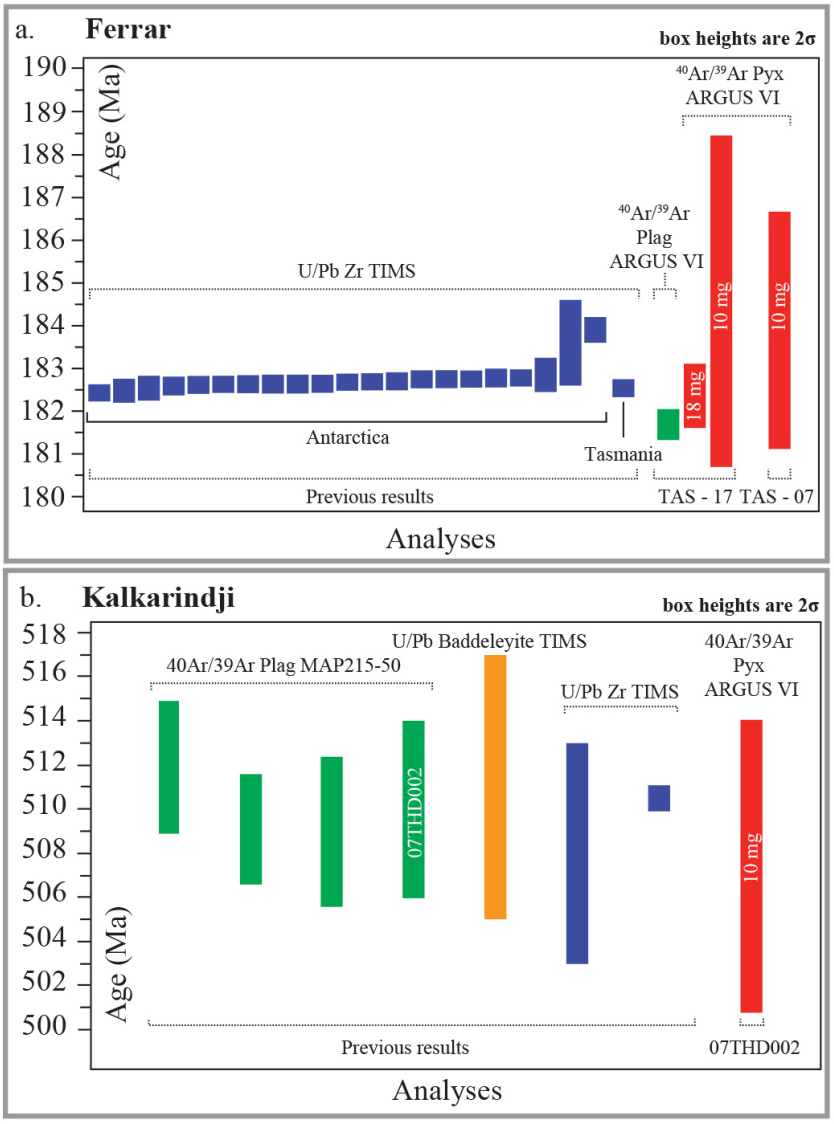

Figure 5.8: Pyroxene data compared with literature data and in the case of the results from TAS-17 the plagioclase ages of the same sample as well. Kalkarindji data compiled in Jourdan *et al.* (2014b). Literature results from the Ferrar province from Minor and Mukasa (1997) and Burgess *et al.* (2015).

baddeleyite U-Pb age of 511 ± 5 Ma, a sensitive high-resolution ion microprobe U-Pb zircon age of 508 ± 5 Ma, and the high precision zircon CA-TIMS U-Pb age of 510.7 ± 1.9 Ma (Figure 5.8b) (Jourdan *et al.*, 2014b and references therein), demonstrating how robust the pyroxene plateau age is that was obtained on the Kalkarindji sample.

Pyroxene aliquots from the Kalkarindji CFB province were separated and analyzed due to the systematic lack of unaltered plagioclase within these rocks evidenced from petrography and previous $^{40}Ar/^{39}Ar$ analyses (Glass & Phillips, 2006; Evins *et al.*, 2009; Jourdan *et al.*, 2014b), explaining why only 7 reliable U/Pb and $^{40}Ar/^{39}Ar$ ages have been published (see compilation by Jourdan *et al.*, 2014b). Furthermore, of the seven reliable ages from previous studies, only one is from the basaltic flows of the Kalkarindji province whereas all the other ages come from intrusive bodies, which are generally fresher than their extrusive counterparts. This is particularly significant because, the highest proportions of igneous material from the Kalkarindji province is basalt flows, particularly in the northern region, and thus are (1) naturally devoid of zircon and (2) and contain primarily altered plagioclase. Therefore, pyroxene appear a viable and perhaps the only alternative to date plagioclase-altered zircon-free mafic hypabyssal and (especially) volcanic rocks.

5.8.1.4. Was pure pyroxene dated?

We have shown that analyzing pyroxene concentrate yield robust plateau ages and can be therefore applied to pyroxene-bearing rocks. However, is the contributor of K (and thus $^{40}Ar^*$) truly pure pyroxene, or does the K come from other phases? The K/Ca ratio for all samples, regardless of whether a plateau age could be calculated or not, have a distinct "stair step" shape (Figure 5.5 and Figure 5.7). These K/Ca spectra show low temperature steps with values ranging from 0.01 to 0.33 to very low values of ca. 0.0002 for high temperature steps, after roughly around 50 – 70 % released ^{39}Ar

and greater (Figure 5.5 and Figure 5.7). Due to the extremely low K content of pyroxene as well as the high Ca content of clinopyroxene, the K/Ca ratio for clinopyroxene would be low, comparable to the values obtained for high temperature steps (Figure 5.5). However, the K/Ca ratios in the low temperature steps are orders of magnitude higher than 0.0002. Whereas there is little doubt that the very low K/Ca observed for the high temperature steps reflect degassing of clinopyroxene crystals, questions remain on the origin of the high K/Ca ratio of early temperature steps. The high K/Ca ratios for the low temperature steps could be attributed to (1) degassing of plagioclase inclusions throughout the crystals analyzed; or (2) being indicative of K and/or Ca concentration differences within one or several pyroxene crystal types. We will demonstrate in three points that multi components of pyroxene were analyzed.

(1) Experimental studies show that Ar diffusion in plagioclase occurs at lower temperatures than pyroxene simply due to the different diffusion characteristics of the two phases (Cassata *et al.*, 2009; Cassata *et al.*, 2011). Therefore, plagioclase inclusions could diffuse before the pyroxene causing the observed K/Ca signature within the lower temperature heating steps. However, if the observed K/Ca ratios were obtained from plagioclase inclusions within pyroxene grains and not from the pyroxene crystal at all, these initial heating steps would contain the majority of the ^{39}Ar released, hence be much wider than the high-temperature steps in an age spectrum. In other words, high K/Ca ratio steps would correspond to larger % of ^{39}Ar released steps. However, the observed ^{39}Ar released throughout the analysis is nearly constant (Figure 5.5) with high K/Ca and low K/Ca steps releasing roughly the same magnitude of ^{39}Ar. In some instances the larger % of ^{39}Ar release steps come from low

K/Ca steps (Figure 5.9). When considering if the plagioclase inclusions followed the diffusion rules of pyroxene due to being completely enclosed within the pyroxene crystal, then the signal would be revealed in the latest heating steps. Although the pyroxene crystals were dark and opaque for most of the Kalkarindji samples making the observation of inclusions within the crystal difficult to discern with a binocular microscope, the pyroxene picked from the Tasmanian Dolerites as well as the fine fraction from 07THD002 was translucent enough to observe if any inclusions were present within the grains and thus be avoided during sample processing. These observations are corroborated by the SEM images that show little inclusions in all samples except some large grains in 07THD002.

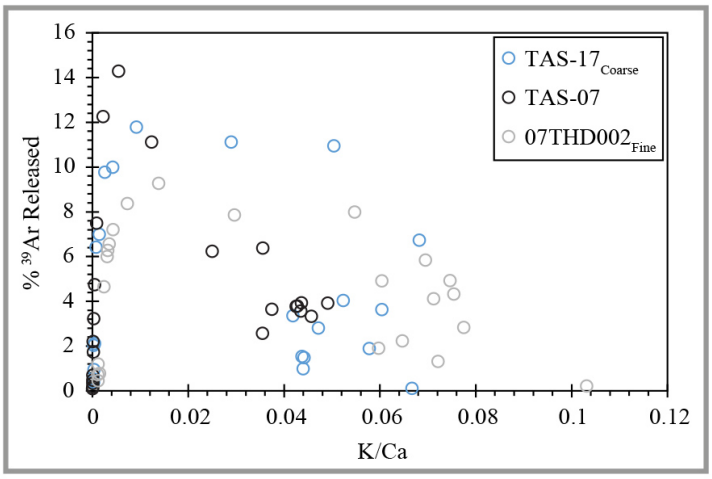

Figure 5.9: % ^{39}Ar released vs K/Ca ratio for each respective step for three representative pyroxene analyses.

(2) The intensity of the signal was plotted versus the laser power from sample TAS-17 (TAS-17_{coarse} and TAS-$17_{plagioclase}$) (Figure 5.10). A noble gas mass spectrometer does not measure K and Ca content directly so proxies created during the irradiation process are measured; ^{39}Ar for K and ^{37}Ar for Ca. The signal for $^{37}Ar_{(Ca)}$ from the plagioclase and pyroxene analyses are noticeably different. The plagioclase $^{37}Ar_{(Ca)}$ is degassed primarily within the first 15 % of laser power (up to a signal intensity peak of 1.1 fA) before nearly levelling out with a signal intensity less than 0.02 fA after 20 % of laser power (Figure 5.10a). Whereas the pyroxene signal does not increase to significant values until the intensity of the plagioclase signal

levels out (Figure 5.10a). The K/Ca curve of pyroxene mirrors that of the ^{37}Ar pyroxene curve. The ^{37}Ar curve for pyroxene displays nearly no Ca (signal less than

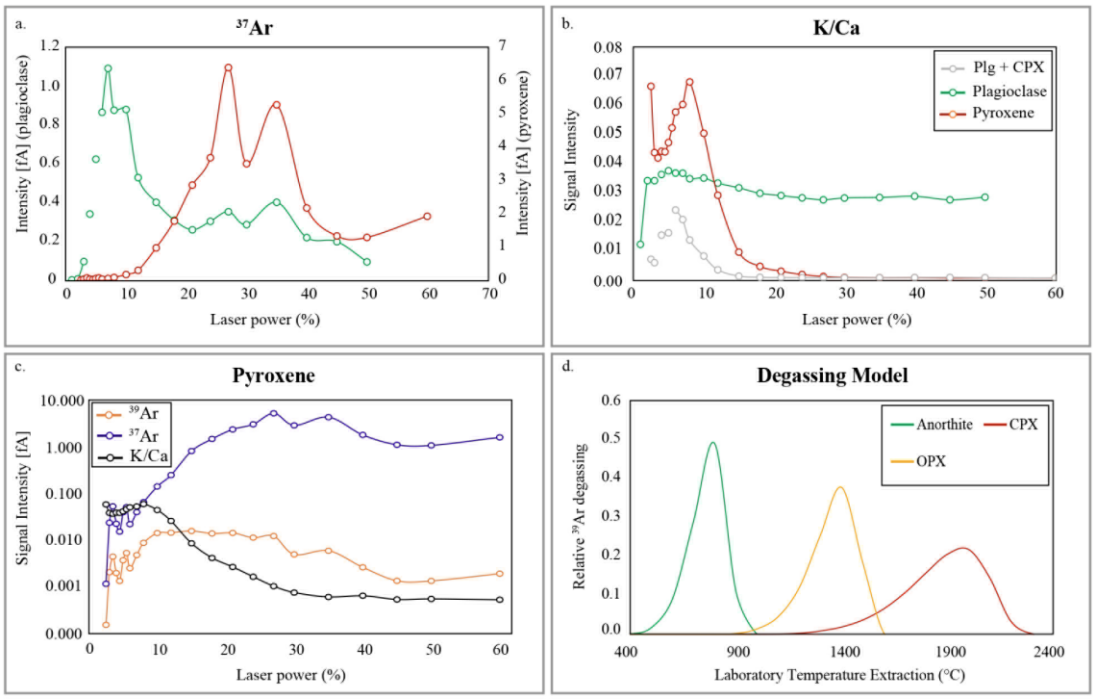

Figure 5.10: (a – c) Selected graphs of laser power vs signal intensity for analyses of pyroxene separates (coarse fraction) and plagioclase separates from TAS-17. d) Degassing model calculated with experimentally derived activation energies (E_a) and diffusion coefficients (D_0) for anorthite, clinopyroxene (CPX), and orthopyroxene (OPX).

0.02 fA until 10 % laser power) in early heating steps (high K/Ca ratios) until an increase in the ^{37}Ar signal for laser power greater than 10 % (low K/Ca ratios); however, during the whole analysis the ^{39}Ar signal stays at a nearly consistent signal intensity ranging from 0.002 – 0.02 fA (heating step 2 to the end of analyses) (Figure 5.10c). These plots of the intensity of the signal indicate that the signal of the plagioclase analyses behave differently than the signals observed for the pyroxene analyses. The maximum K/Ca value of the pure plagioclase (here TAS-$17_{plagioclase}$; 0.031) is lower than the pyroxene (TAS-17_{coarse}; 0.068) from the same sample. A simple mass balance calculation of a 0.5:0.95 mixture of plagioclase (0.035) and high-temperature step pyroxene (0.0002) show that the K/Ca ratio of the mixture will be significantly lower than the high K/Ca ratios observed in most pyroxene analyses (Figure 5.10b). Therefore, not only demonstrate that these analyses are not controlled

by plagioclase but also show that the control on the K/Ca spectrum is Ca related rather than from changes in K content.

(3) A possible explanation for this observed K/Ca spectrum is Ca concentration difference in the pyroxene varieties present within the sample. Petrographic observations of the pyroxene within these CFBs display both augite (high-Ca) and pigeonite (low-Ca) clinopyroxene types, as well as a minor amount of (no-Ca) orthopyroxene in the case of the Kalkarindji sills (Figure 5.2). The diffusion parameters for Ar in pyroxene have been experimentally measured by (Cassata *et al.*, 2011). Here we model the behavior of the expected degassing curves for plagioclase, clinopyroxene, and orthopyroxene during a conventional step heating analysis by using the ArArDIFF algorithm (see Jourdan & Eroglu, 2017) based on the equations of Crank and Gupta (1975). We use average activation energies (E_a) of 381 kJ/mol and diffusion coefficients (D_0) of 1.8 cm^2/s for clinopyroxene, Ea of 371 kJ/mol and D_0 of 600 cm^2/s for orthopyroxene, and Ea of 196 kJ/mol and D_0 of 0.05 cm^2/s for anorthite corresponding to closure temperatures of ca. 750 °C (clinopyroxene), 610 °C (orthopyroxene), and 320 °C (plagioclase) for a cooling rate of 10°C/Ma (Cassata *et al.*, 2011) and crystal (sphere) radius of 10 µm (anorthite), 175 µm (clinopyroxene), 150 µm (orthopyroxene). Since no data are available for pure pigeonite, we used the diffusion parameters of orthopyroxene for our models since pigeonite (a Ca-poor clinopyroxene) is compositionally closer to orthopyroxene than augite. Our model (Figure 5.10d) shows that both plagioclase and pigeonite would degas their Ar at lower heating steps than the augite crystals. The theoretical model shows no overlap between plagioclase and augite, but a significant overlap between pigeonite and augite. If the material analyzed was characterized by a mixture between plagioclase inclusions and clinopyroxene, two distinct K/Ca populations should be apparent due to the absence

of degassing curve overlap (Figure 5.10d) which would be exacerbated even more by the small crystal size of the plagioclase inclusions. Rather, the K/Ca spectra all show a progressive change from high K/Ca to low K/Ca ratios in the spectrum (Figure 5.5 and Figure 5.7) instead of two distinct K/Ca plateaus.

The pigeonite crystals produce a higher K/Ca ratio due to low Ca domains that degas earlier than the augite crystals with high Ca contents accounting for the sigma shape of the curve. Therefore, we conclude that the high K/Ca values associated with the low temperature steps are associated with a deficit in Ca in pigeonite (or pigeonite + orthopyroxene for some of the Kalkarindji samples) with a quasi-constant K concentration. As the temperature step increases along the experiment, the Ar in pigeonite (or pigeonite + orthopyroxene) get progressively exhausted and progressively replaced by the Ar from the augite. Therefore, we have dated a mixture between low-Ca and high-Ca pyroxene. Since the samples come from rapidly cooled intrusions these crystals crystallized simultaneously, as further evidenced by the "patchy" relationship between the various pyroxene types. Therefore, the slight differences in diffusion characteristics of the two pyroxene types will give the same ages in these rock types and thus be adequate for geochronology of igneous rocks. However, these different diffusion characteristics may have significant consequences for thermochronological studies of metamorphic rocks (see discussion below).

5.8.2. Argon recoil redistribution within pyroxene

Several of the samples from the Kalkarindji LIP did not return any plateau ages, and yet, they all display nearly the same tilde shaped age spectrum (Figure 5.7). The age spectra for these samples have slightly younger low-temperature steps compared to the age expected for the province (ca. 511 Ma), with rising ages for the low to mid-temperature steps returning apparent step-ages older than the ca. 511 Ma and high

temperature heating steps with ages younger than 511 Ma (Figure 5.7). These Kalkarindji samples display the same overall K/Ca trend than the samples that did return plateau ages. The shape of these age spectra does not suggest the presence of excess ^{40}Ar (Kelley, 2002). Such a tilde-shaped age spectrum has been observed from the effect of alteration on plagioclase (Verati and Jourdan, 2014), or irradiation-induced recoil redistribution (Jourdan & Renne, 2013). As we have seen above, no plagioclase is present in the pyroxene separates and pyroxene does not alter into sericite thus pointing toward a recoil issue.

In short, recoil is caused by the kinetic energy acted upon the ^{39}Ar atom by the emission of a proton during neutron bombardment of the irradiation process (Turner & Cadogan, 1974; Hess & Lippolt, 1986; Villa, 1997; Paine *et al.*, 2006; Jourdan *et al.*, 2007c; Jourdan & Renne, 2013). In the case of recoil, two effects can occur during the irradiation process: (1) net ^{39}Ar loss can occur due to the ejection of ^{39}Ar from the crystal lattice which is usually a problem for crystals with a size lower than 50 µm (Paine *et al.,* 2006; Jourdan *et al.,* 2007) and/or (2) ^{39}Ar redistribution from low-temperature, high potassium minerals to high-temperature, low potassium minerals (whole rock analyses); or (in the case of one mineral type population analyses) this same process could occur within the lattice of the grains (e.g. ^{39}Ar between K rich and poor zones and ^{37}Ar between Ca rich and poor zones within the grains) (Jourdan and Renne, 2014). The ^{37}Ar recoil becomes particularly problematic and important for clinopyroxene due to the high Ca contents of the mineral.

The aliquots from the samples chosen for analyses were selected from two different size fractions the 125 – 212 µm and 212 – 355 µm. The size of these grains should be too large to be drastically affected by recoil (typically problematic less than 50 µm, Paine *et al.,* 2006; Jourdan *et al.,* 2007). Furthermore, the age spectra are

identical across these two different grain size aliquots (e.g. sample 09THD029, where both the coarse [$09THD029_{coarse}$] and the fine [$09THD029_{fine\ total}$] fractions display nearly identical age spectra's; Figure 5.7). These results and the similar degree of age offsets from the tilde-shaped age spectra do not appear to be grain size dependent.

Comparative analysis of petrographic and SEM images of the pyroxene crystals from the Tasmanian and the Kalkarindji samples show that exsolution lamellae in the pyroxene crystals are present in all samples to varying degrees. Well developed and extensive exsolution lamellae are present in three (07THD001b, 09THD028, and 09THD029) out of the four samples in the Kalkarindji pyroxenes, whereas the Tasmanian Dolerite clinopyroxenes display no discernable exsolution features in augite and a minor degree of alteration in around 1 % of the pigeonite grains (Figure 5.2). Further inspection with SEM reveals minor degrees of exsolution within augite crystals as well as a slightly higher abundance of exsolution in pigeonite crystals than the abundance observed from thin sections of the Tasmanian Dolerites (Figure 5.3). All of the pyroxene aliquots from the Tasmanian Dolerites returned plateau ages ($TAS\text{-}07_{pyx}$, $TAS\text{-}17_{coarse}$, and $TAS\text{-}17_{coarse\ total}$), whereas only the aliquot with the least amount of exsolution from the Kalkarindji sample suite returned a pyroxene $^{40}Ar/^{39}Ar$ plateau age ($07THD002_{fine}$), suggesting a correlation between exsolution lamellae and structured age spectra. Altogether, these results and observations suggest that the exsolution lamellae could have induced recoil redistribution between the pyroxene crystals and the exsolution lamellae, which in turn cause the tilde-shape age spectrum. If exsolution lamellae caused recoil redistribution, then one would expect that the ^{39}Ar and ^{37}Ar atoms have been shuffled around to some degree, but with a minimum loss to the system. Therefore, to further test if these age spectra patterns are the result of

recoil distribution, total fusion (error) ages have been calculated. If there has only been a reshuffling of argon atoms rather than a net loss to the system the total fusion (error) ages should be approximately similar to the age expected for those rocks. We stress that those integrated ages are geologically meaningless even within uncertainty, but they have the potential to shed some light on the recoil hypothesis. The total fusion (error) age is calculated by summing all the gas for each isotope and calculating the age based on the ratio between all masses (i.e. summing all the steps in a giant step). The nine samples yielded total fusion (error) ages relatively evenly distributed between 496.2 ± 0.8 Ma to 527.7 ± 1.0 Ma.

These total fusion (error) ages overlap or display only a maximum of ca. 3 % difference from the 511 Ma age of Kalkarindji (Figure 5.11b), indicating that there

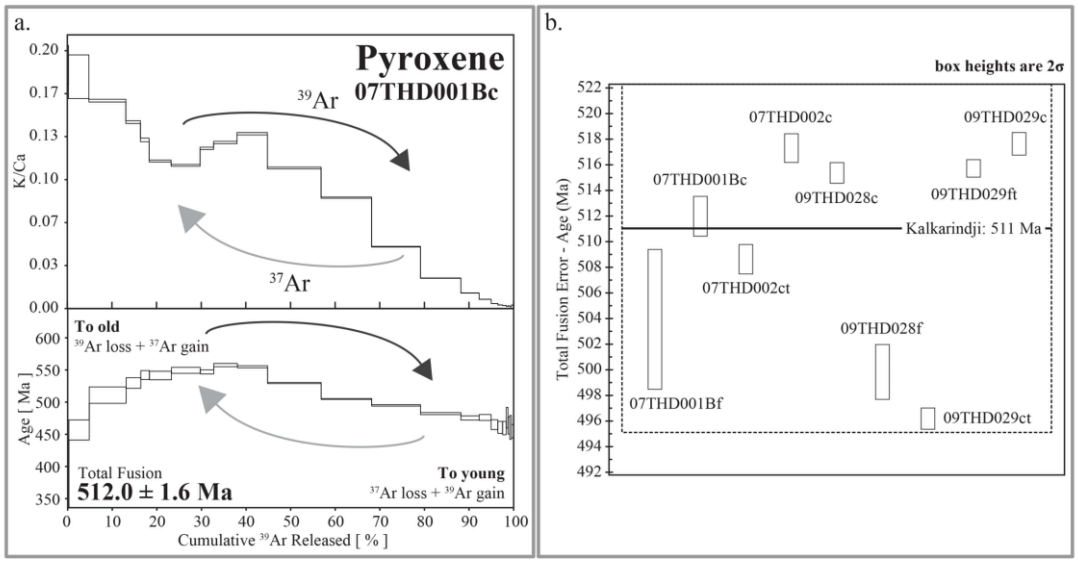

Figure 5.11: (a) Schematic diagram explaining the effect of recoil redistribution on age and K/Ca spectra; modified from Jourdan and Renne (2013) using results from 07THD001Bc. (b) Graph displaying the total fusion (error) age of the recoil-plagued samples (Figure 5.7) compared to the emplacement age. Dotted box represents a ± 18 Ma age difference from 511 Ma (Jourdan *et al.*, 2014b). Note that the error ages are *not* providing the age of crystallization and should be considered rather as a semi-quantitative age information.

was only a minimal argon loss to the system or that the wrong trapped ratio has been used in the calculation (here assumed to have an atmospheric composition) since the inverse isochron cannot be used to measure the $^{40}Ar/^{36}Ar$ intercept. In any case, those

results further support that these age patterns are the product of recoil redistribution. Total fusion (error) ages when associated with recoil, however, must be used under a great degree of caution as they are not an accurate representation of the actual crystallization age. If recoil can be convincingly shown to be the cause of a structured pyroxene age spectrum, the total fusion age will most certainly approach the true age and could help to approximately constrain crystallization age on a semi-quantitative basis for an area that is devoid of any other datable material (Figure 5.11b).

Furthermore, the presence of exsolution lamellae only within the pigeonite crystals for the Tasmanian Dolerites could also have affected why recoil redistribution preferentially affected the Kalkarindji samples. If the recoil redistribution is heavily controlled by the redistribution of $^{37}Ar_{(ca)}$ rather than the ^{39}Ar then those pyroxene phases with higher Ca contents would be more susceptible. Therefore, if exsolution is only apparent in low-Ca phases of pyroxene (as is the case for the Tasmania samples) then the samples could potentially yield statistically reliable ages. This observation requires further testing and analyses of different types and exsolution affected pyroxene crystals to be fully resolved.

These observations of the exsolution lamellae and argon recoil correlation indicate the importance of a thorough petrographic and/or SEM examination of the samples prior to $^{40}Ar/^{39}Ar$ geochronology. Exsolution is solid solution phase unmixing that can occur in minerals which have compositions that vary between two or more pure endmembers. This unmixing or exsolution is typically apparent through the growth of crystallographically controlled lamellae within the host crystal during cooling. The exsolution process is impeded by rapid cooling and is thus not usually observed in crystals within volcanic rocks formed close to the surface. Therefore, exsolution and thus recoil redistribution associated with relatively thick intrusive

bodies should not be a problem in volcanic rocks. The presence of minor exsolution features within the Tasmanian Dolerites demonstrate that the recoil redistribution only disturbs the ability to obtain meaningful ages when a pervasive degree of exsolution has occurred or occurs extensively in high Ca phases. The ability to readily recognize exsolution lamellae and inclusion abundance in thin section and SEM images offers a means of pre-screening rocks that comprise pyroxene with a high likelihood of success for $^{40}Ar/^{39}Ar$ geochronology.

5.8.3. Further application of the pyroxene $^{40}Ar/^{39}Ar$ dating approach

5.8.3.1. Mafic rocks affected by hydrothermal alteration

We have shown above that pyroxene in mafic rocks can yield robust plateau ages, even when plagioclase analyses fail, due to substantial sericite alteration. Therefore, similarly to zircon, pyroxene offer the ability to date altered mafic rocks. Although this is important for continental igneous rocks, this might be particularly relevant for submarine volcanic rocks (e.g. volcanic seamounts, LIPs, mid-oceanic ridge basalts) where plagioclase and basaltic groundmass, currently the two phases commonly dated with the $^{40}Ar/^{39}Ar$ technique, are often substantially altered by seawater. In many cases, this results in the authors dating fully sericitized plagioclase in order to provide minimum eruption ages (e.g. Olierook *et al.*, 2015; Olierook *et al.*, 2017). Although the alteration processes of pyroxene and plagioclase is complex and well out of the scope of this project, some studies do show that pyroxene appears unaffected by hydrothermal fluids in oceanic basalts when plagioclase and basalt glass show a high degree of alteration (e.g. Mortimer *et al.*, 1998; Zeng *et al.*, 2015). Pyroxene, although significantly more robust than plagioclase, is not completely resistant to all types of hydrothermal alteration. When the alteration level is quite advanced, the most common type of alteration product is the replacement of pyroxene

minerals with amphiboles, particularly hornblende and actinolite (e.g. Humphris & Thompson, 1978), which can cause problems with the $^{40}Ar/^{39}Ar$ technique. However, for hydrothermally altered rocks, the degree of pyroxene alteration can be quite variable (e.g. Fawcett, 1965; Mahoney *et al.*, 1993). As with plagioclase sample processing, altered or damaged pyroxene grains can be avoided during sample processing using the same procedures that are implemented for mitigating sericite alteration of plagioclase (e.g. thin section observations, implementing a rigorous picking method of only fresh grains, and leaching each sample population with HF). Therefore, the ability to date pyroxene with the $^{40}Ar/^{39}Ar$ method will provide a more reliable and greater chance of obtaining meaningful results in oceanic basalt and oceanic LIP studies.

5.8.3.2. Mafic rocks affected by greenschist metamorphism

Greenschist facies metamorphism is a low grade metamorphic facies that typically represents between ca. 300 and 500 °C for pressures of 2 to 10 kbars (Winter, 2010). Provided that no amphibilitization occurs due to significant fluid circulation during metamorphism, diffusion characteristics experimentally determined on clinopyroxene and orthopyroxene suggest that these minerals will remain close to Ar diffusion during greenschist facies metamorphism temperatures. To demonstrate the resilience of pyroxene to some types of greenschist metamorphism over plagioclase, modeled age spectra were calculated using ArArDIFF (Jourdan & Eroglu, 2017) algorithm.

As an exercise, the mineralogy and metamorphic history of the 1.1 Ga Umkondo dykes located in southern Africa (Jourdan *et al.*, 2009a) were used to constrain the model parameters. The model calculated a 100 Myr prograde and

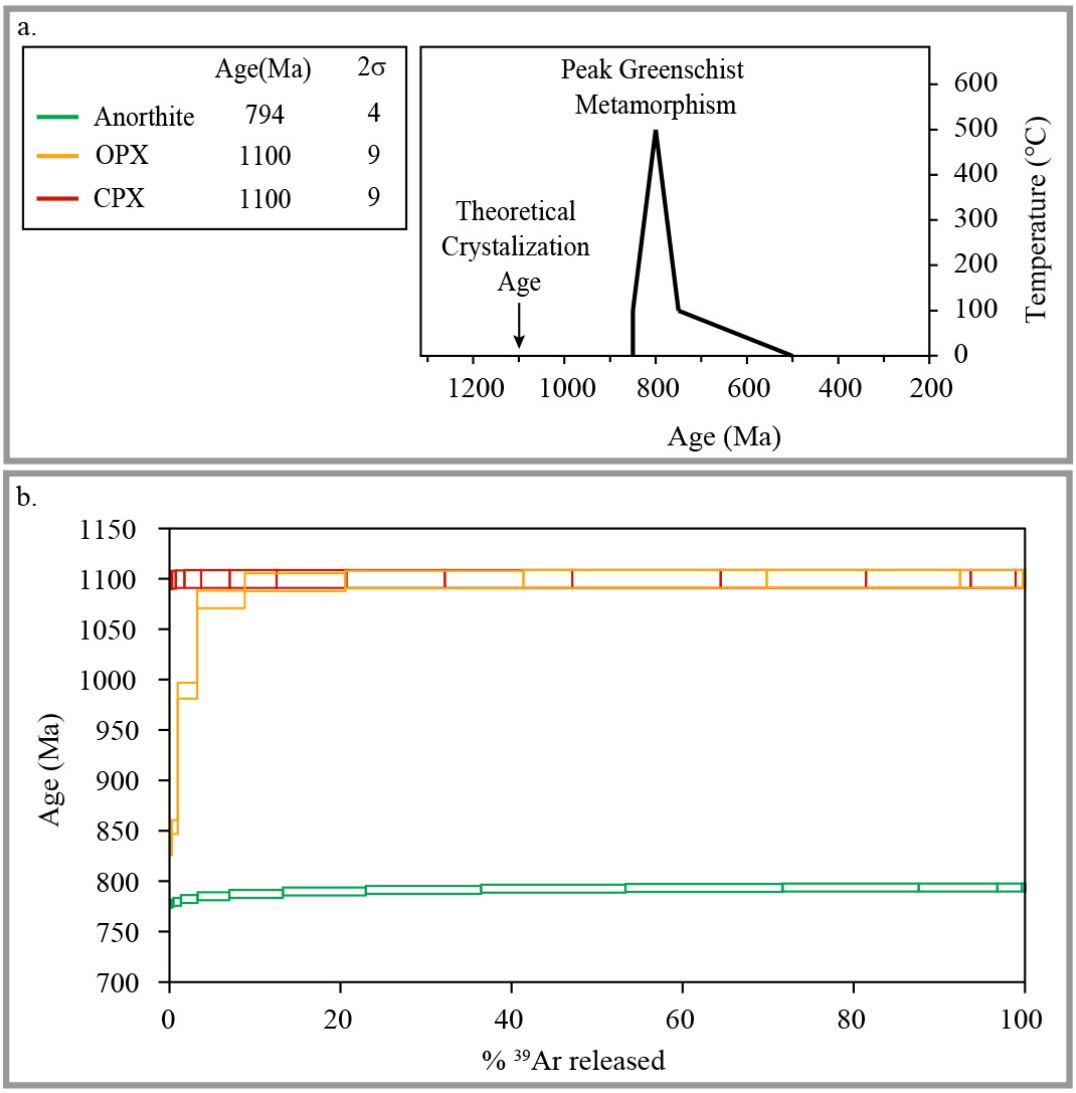

Figure 5.12: (a) Time-temperature path used to calculate the simulated age spectra. (b) Modeled age spectra from material subjected to a greenschist metamorphic event around 800 Ma. Metamorphic history of the 1.1 Ga Umkondo dykes used to constrain model parameters (Jourdan *et al.*, 2009a). A 100 Ma prograde and retrograde event was calculated for 150 µm radius crystals of anorthite, orthopyroxene (OPX), and clinopyroxene (CPX) compositions. Diffusion parameters and thermal history are given in Table 5.2.

retrograde greenschist metamorphic event with peak temperatures of 500 °C at 800 Ma (Figure 5.12a; Table 5.2). Assuming no sericitization (which is probably not very realistic), the theoretical age spectra show that the plagioclase would not withstand the metamorphic event yielding reset ages around the time of peak metamorphism ~ 794 Ma (Figure 5.12b). However, both orthopyroxene and clinopyroxene, yielded plateaus and retained the crystallization age of 1.1 Ga. This simple model displays the ability

for pyroxene to retain its argon (and crystallization age) at temperature conditions associated with greenschist metamorphism.

Nevertheless, when greenschist metamorphism is associated with hydrothermal circulation, pyroxene tends to partially turn to amphibole as is observed for the Umkondo dykes (Jourdan *et al.*, 2009a). The effect of 1% uralitization (which occurred during the onset of metamorphism at 850 Ma) on a 1.1 Ga pyroxene age spectrum yields a structured age spectra, however in this case, fails to provide the crystallization age of the rock. Since the K_2O concentration of amphibole (here set at 0.5 wt. %) is usually significantly higher than pyroxene, the effect on the age spectrum is quite dramatic, and mimic the effect of sericite on plagioclase (Verati & Jourdan, 2013). Again, careful petrographic observations should allow to easily identify the presence of amphibole and it remains to be seen if stringent picking can isolate pure pyroxene phase for such rocks.

5.8.3.3. $^{40}Ar/^{39}Ar$ thermochronology of pyroxene

Thermochronology is based on the capacity of different minerals to retain a given element within the mineral structure once the system has cooled to slow any significant diffusion. This concept is known as closure temperature (Dodson, 1973), which is used in metamorphic studies to determine dates of events or rates of geologic processes. Clinopyroxene and orthopyroxene have closure temperatures around 600°C and 750 °C (for cooling rates of 10°C/Ma), respectively as measured on meteorite samples (Cassata *et al.*, 2011). Diffusion studies provide evidence that at crustal conditions the mineral pyroxene has the ability to retain Ar more efficiently than both amphibole and plagioclase (Cassata *et al.*, 2011). Thus, the capability of obtaining cooling ages from a mineral within this range of temperatures has the potential to greatly benefit time-temperature studies of metamorphic terrains.

Diffusion Parameters

				Mixed phases		
	D_0 (cm^2/s)	**E_a (J/mol)**	**Radius (μm)**	**Modal composition**	**% K_2O (each mineral)**	**K_2O contribution (mixed phase)**
Anorthite	0.05	240000	150	30%	10%	37%
CPX	1.80	381000	150	50%	0.01%	13%
OPX	600.00	371000	150	20%	0.10%	50%

Thermal History: Crystallization 1100 Ma

	Start (Ma)	**End (Ma)**	**Duration (Ma)**	**Starting temp. (°C)**	**Ending temp. (°C)**	**Cooling rate (°C/Ma)**
Period 1	850	800	50	100	500	-8
Period 2	800	750	50	500	100	8
Period 3	750	500	250	100	0	0
Period 4	500	0	500	0	0	0

Table 5.2: $^{40}Ar/^{39}Ar$ Greenschist Metamorphism Diffusion Model of Pyroxene. Diffusion parameters and time-temperature history used in the ArArDiff models (Jourdan & Eroglu, 2017) to generate synthetic age spectra. The mineralogy and metamorphic history of the 1.1 Ga Umkondo dykes of Africa (Jourdan *et al.*, 2009a) were used to constrain the model parameters.

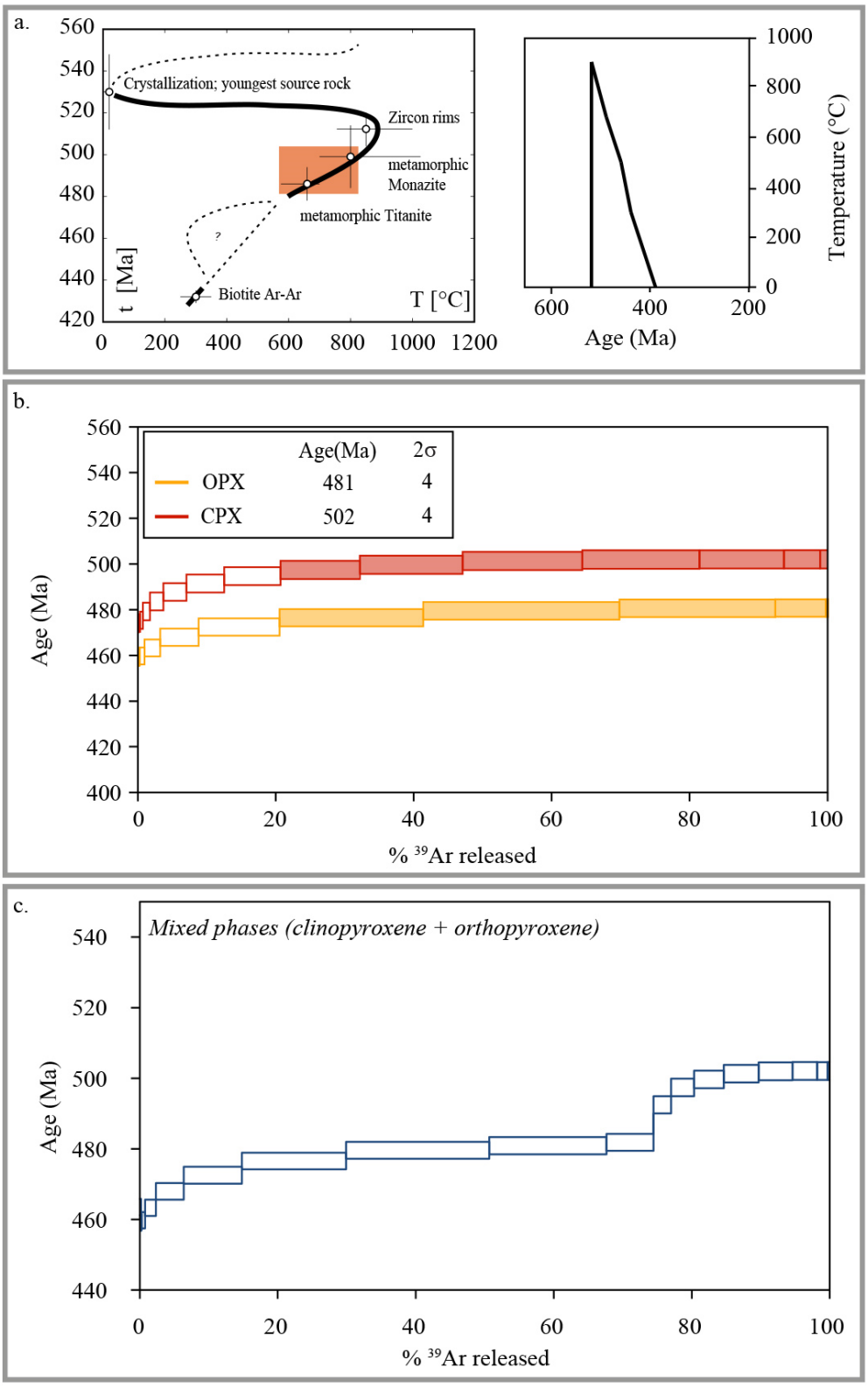

Figure 5.13: (a) Time-temperature path used to calculate the simulated age spectra. (b) Modeled age spectra resulting from a metamorphic cooling path for 150 µm radius crystals of Biotite, orthopyroxene (OPX), and clinopyroxene (CPX) compositions. Cooling history parameters constrained from the metamorphic history of the Nampula Complex in Mozambique (Ueda *et al.*, 2012). Diffusion parameters and thermal history are given in Table 5.3. Heating steps used to calculate plateau age are shaded. Approximate T-t path of the Ticué structure redrafted from data and figure presented in Ueda *et al.* (2012), approximate location of the theoretical modeled pyroxene is displayed by the orange box.

There are a reasonable selection of minerals with various closure temperatures that are currently used for thermochronology studies, however these minerals tend to trend toward mid to low-temperatures; e.g., hornblende, muscovite, biotite, rutile, titanite and apatite with closure temperature for Ar or Pb ranging from ~ 240 to 600 °C at typical crustal pressures (Flowers *et al.*, 2005; Scibiorski *et al.*, 2015) or high Pb closure temperatures such as for monazite (ca. 800°C) and zircon (> 1000 °C) (e.g. Flowers *et al.*, 2005). As such, orthopyroxene and clinopyroxene, quite abundant in mafic and intermediate rocks, can potentially bridge the 600 – 1000 °C gap, in particular for rocks devoid of monazite.

We take the opportunity to illustrate the potential of pyroxene for thermochronology by testing the response of the K/Ar systems for clinopyroxenes, orthopyroxene and a 2:1 mixture of orthopyroxene and clinopyroxene to a simple metamorphic history. Again, using the ArArDIFF (Jourdan & Eroglu, 2017) algorithm, we have calculated synthetic age spectra associated with the thermal history of the Nampula Complex in Mozambique (Ueda *et al.*, 2012). The Nampula Complex was chosen because of its relatively well constrained rapid cooling history with slow monotonous cooling of 7 – 8 °C/Ma (Ueda *et al.*, 2012). We modeled a cooling path of 520 to 390 Ma from peak temperatures of 900 °C over 4 periods of various cooling rates that approximate the cooling history presented by Ueda *et al.* (2012). The model age spectra show that, for such a cooling rate, clinopyroxene and orthopyroxene are expected to yield plateau ages and cool down below their respective closure temperatures at ca. 502 Ma and 481 Ma (Figure 5.13b). The clinopyroxene model age agree with the monazite age of ca. 500 Ma and (Thomas *et al.*, 2010; Ueda *et al.*, 2012). We conclude that using *pure* orthopyroxene and clinopyroxene have the

potential to yield robust cooling ages in a temperature range currently only dominated by monazite and titanite (Figure 5.13a; Table 5.3).

However, as seen previously, pyroxene from two LIPs were both composed of a mixture between orthopyroxene and two phases of clinopyroxene rather than pure isolated phases. Modeling the effect of the Nampula complex thermal history on a 2:1 orthopyroxene and clinopyroxene mixture show that the mixture *will not* yield a plateau (Figure 5.13c). Rather a sigmoid shape age spectrum result from a mixture between the cooling ages of the two phases. Only the highest temperature steps yielding step ages around 500 Ma similar to that of the pure clinopyroxene spectrum, most likely because the orthopyroxene reservoir was exhausted by these high heating steps (Figure 5.9d). It remains to be seen if such a complex spectrum can be reverted to calculating the T-t history of the host rock, but prompt us to encourage a thorough characterization of the metamorphic pyroxene phase(s) before $^{40}Ar/^{39}Ar$ analysis.

5.9. Conclusions

1. Using multi-collector noble gas mass spectrometers such as the ARGUS VI provide the ability to obtain geologically meaning $^{40}Ar/^{39}Ar$ pyroxene plateau ages.

2. The ability to attain $^{40}Ar/^{39}Ar$ pyroxene plateau results provide meaningful geologic ages to an important phase in mafic and ultramafic rocks, which until now has been largely unattainable.

3. These results from two different CFBs in both age and degree of alteration, although indicate the importance of a thorough petrographic and sample pre-screen, demonstrate the broad applicability of using pyroxene with the $^{40}Ar/^{39}Ar$ technique.

Diffusion Parameters

	D_0 (cm^2/s)	E_a (J/mol)	Radius (μm)	*Mixed phases* Modal composition	% K_2O (each mineral)	K_2O contribution (mixed phase)
CPX	1.80	381000	150	80%	0.01%	29%
OPX	600	371000	150	20%	0.10%	71%

Thermal History: Crystallization 900 Ma

	Start (Ma)	End (Ma)	Duration (Ma)	Starting temp. (°C)	Ending temp. (°C)	Cooling rate (°C/Ma)
Period 1	520	490	30	900	680	7
Period 2	490	460	30	680	500	6
Period 3	460	440	20	500	300	10
Period 4	440	390	50	300	0	6

Table 5.3: $^{40}Ar/^{39}Ar$ Thermochronology Diffusion Model of Pyroxene. Diffusion parameters and time-temperature history used in the ArArDiff models (Jourdan & Eroglu, 2017) to generate synthetic age spectra. Time-temperature parameters constrained using the thermal history of the Nampula Complex in Mozambique (Ueda *et al.*, 2012).

4. The capability of utilizing the $^{40}Ar/^{39}Ar$ technique establishes unprecedented geochronological opportunities not only within the field of LIP research but also in the fields of metamorphic and thermochronologic applications.

5.10. References

Belica, M., Tohver, E., Pisarevsky, S., Jourdan, F., Denyszyn, S. & George, A. (2017). Middle Permian paleomagnetism of the Sydney Basin, Eastern Gondwana: Testing Pangea models and the timing of the end of the Kiaman Reverse Superchron. *Tectonophysics* **699**, 178-198.

Burgess, R., Kiviets, G. & Harris, J. (2004). Ar–Ar age determinations of eclogitic clinopyroxene and garnet inclusions in diamonds from the Venetia and Orapa kimberlites. *Lithos* **77**, 113-124.

Burgess, S. D., Bowring, S. A., Fleming, T. H. & Elliot, D. H. (2015). High-precision geochronology links the Ferrar Large Igneous Province with early-Jurassic ocean anoxia and biotic crisis. *Earth and Planetary Science Letters* **415**, 90-99.

Cassata, W. & Renne, P. (2010). Ar-37 diffusion in pyroxene: Implications for thermochronometry and mantle degassing. *Geochim. Cosmochim. Acta* **74**, A148-A148.

Cassata, W. S., Renne, P. R. & Shuster, D. L. (2009). Argon diffusion in plagioclase and implications for thermochronometry: A case study from the Bushveld Complex, South Africa. *Geochimica et Cosmochimica Acta* **73**, 6600-6612.

Cassata, W. S., Renne, P. R. & Shuster, D. L. (2011). Argon diffusion in pyroxenes: Implications for thermochronometry and mantle degassing. *Earth and Planetary Science Letters* **304**, 407-416.

Cassata, W. S., Shuster, D. L., Renne, P. R. & Weiss, B. P. (2010). Evidence for shock heating and constraints on Martian surface temperatures revealed by 40Ar/ 39Ar thermochronometry of Martian meteorites. *Geochimica et Cosmochimica Acta* **74**, 6900-6920.

Compston, W., McDougall, I. & Heier, K. S. (1968). Geochemical comparison of the mesozoic basaltic rocks of Antarctica, South Africa, South America and Tasmania. *Geochimica et Cosmochimica Acta* **32**, 129-149.

Crank, J. & Gupta, R. S. (1975). Isotherm migration method in two dimensions. *International Journal of Heat and Mass Transfer* **18**, 1101-1107.

Dalrymple, G. B. & Lanphere, M. A. (1969). Potassium-argon dating: Principles, techniques and applications to geochronology. *(Freeman) San Francisco, California*, 258.

Dodson, M. H. (1973). Closure temperature in cooling geochronological and petrological systems. *Contributions to Mineralogy and Petrology* **40**, 259-274.

Edwards, A. B. (1942a). Differentiation of the Dolerites of Tasmania. I. *The Journal of Geology* **50**, 451-480.

Edwards, A. B. (1942b). Differentiation of the Dolerites of Tasmania. II. *The Journal of Geology* **50**, 579-610.

Encarnacion, J., Fleming, T. H., Elliot, D. H. & Eales, H. V. (1996). Synchronous emplacement of Ferrar and Karoo dolerites and the early breakup of Gondwana. *Geology (Boulder)* **24**, 535-538.

Evins, L. Z., Jourdan, F. & Phillips, D. (2009). The Cambrian Kalkarindji Large Igneous Province: Extent and characteristics based on new 40Ar/39Ar and geochemical data. *Lithos* **110**, 294-304.

Fawcett, J. J. (1965). Alteration Products of Olivine and Pyroxene in Basalt Lavas from the Isle of Mull1. *Mineralogical Magazine* **35**, 55-68.

Fleming, T., Heimann, A., Foland, K. & Elliot, D. (1997). Ar-40/Ar-39 geochronology of Ferrar Dolerite sills from the Transantarctic mountains, Antarctica: Implications for the age and origin of the Ferrar magmatic province. *Geol. Soc. Am. Bull.* **109**, 533-546.

Flowers, R., Bowring, S., Tulloch, A. & Klepeis, K. (2005). Tempo of burial and exhumation within the deep roots of a magmatic arc, Fiordland, New Zealand. *Geology* **33**, 17-20.

Glass, L. M. & Phillips, D. (2006). The Kalkarindji Continental Flood Basalt province: A new Cambrian Large Igneous Province in Australia with possible links to faunal extinctions. *Geology* **34**, 461.

Harrison, T. M. & McDougall, I. (1981). Excess40Ar in metamorphic rocks from Broken Hill, New South Wales: implications for40Ar/39Ar age spectra and the thermal history of the region. *Earth and Planetary Science Letters* **55**, 123-149.

Hart, S. & Dodd, R. T. (1962). Excess Radiogenic Argon in Pyroxenes. *Journal of Geophysical Research* **67**, 2998-2999.

Hart, S. R. (1961). The use of hornblendes and pyroxenes for K-Ar dating. *Journal of Geophysical Research* **66**, 2995-3001.

Hergt, J. M., Chappell, B. W., McCulloch, M. T., McDougall, I. & Chivas, A. R. (1989). Geochemical and isotopic constraints on the origin of the Jurassic dolerites of Tasmania. *Journal of Petrology* **30**, 841-883.

Hess, J. & Lippolt, H. (1986). Kinetics of Ar isotopes during neutron irradiation: 39Ar loss from minerals as a source of error in 40Ar/39Ar dating. *Chemical Geology: Isotope Geoscience section* **59**, 223-236.

Humphris, S. E. & Thompson, G. (1978). Hydrothermal alteration of oceanic basalts by seawater. *Geochimica et Cosmochimica Acta* **42**, 107-125.

Imaoka, T. & Itaya, T. (2004). KAr geochronology of a middle Miocene submarine volcano-plutonic complex in southwest Japan. *Geol. Mag.* **141**, 1-13.

Itaya, T., Doi, M. & Ohira, T. (1996). Very low potassium analysis by flame photometry using ultra low blank chemical lines: an application of K-Ar method to ophiolites. *Geochemical Journal* **30**, 31-39.

Jourdan, F., Bertrand, H., Féraud, G., Le Gall, B. & Watkeys, M. (2009a). Lithospheric mantle evolution monitored by overlapping Large Igneous Provinces: case study in southern Africa. *Lithos* **107**, 257-268.

Jourdan, F. & Eroglu, E. (2017). 40Ar/39Ar and (U-Th)/He model age signatures of elusive Mercurian and Venusian meteorites. *Meteoritics & Planetary Science*, n/a-n/a.

Jourdan, F., Frew, A., Joly, A., Mayers, C. & Evans, N. J. (2014a). WA1ms: A~ 2.61 Ga muscovite standard for 40 Ar/39 Ar dating. *Geochimica et Cosmochimica Acta* **141**, 113-126.

Jourdan, F., Hodges, K., Sell, B., Schaltegger, U., Wingate, M. T. D., Evins, L. Z., Soderlund, U., Haines, P. W., Phillips, D. & Blenkinsop, T. (2014b). High-precision dating of the Kalkarindji Large Igneous Province, Australia, and synchrony with the Early-Middle Cambrian (Stage 4-5) extinction. *Geology* **42**, 543-546.

Jourdan, F., Marzoli, A., Bertrand, H., Cirilli, S., Tanner, L. H., Kontak, D. J., McHone, G., Renne, P. R. & Bellieni, G. (2009b). 40Ar/39Ar ages of CAMP in North America: Implications for the Triassic–Jurassic boundary and the 40K decay constant bias. *Lithos* **110**, 167-180.

Jourdan, F., Matzel, J. P. & Renne, P. R. (2007). 39Ar and 37Ar recoil loss during neutron irradiation of sanidine and plagioclase. *Geochimica et Cosmochimica Acta* **71**, 2791-2808.

Jourdan, F. & Renne, P. R. (2007). Age calibration of the Fish Canyon sanidine $^{40}Ar/^{39}Ar$ dating standard using primary K–Ar standards. *Geochimica et Cosmochimica Acta* **71**, 387-402.

Jourdan, F. & Renne, P. R. (2013). Neutron-induced 37Ar recoil ejection in Ca-rich minerals and implications for 40Ar/39Ar dating. *Geological Society, London, Special Publications* **378**, 33-52.

Kelley, S. (2002). Excess Argon in K-Ar and Ar-Ar Geochronology. *Chemical Geology* **188**, 1-22.

Kennedy, T., Jourdan, F., Bevan, A. W., Gee, M. M. & Frew, A. (2013). Impact history of the HED parent body (ies) clarified by new 40 Ar/39 Ar analyses of four HED meteorites and one anomalous basaltic achondrite. *Geochimica et Cosmochimica Acta* **115**, 162-182.

Koppers, A. A. P. (2002). ArArCALC - software for Ar-40/Ar-39 age calculations. *Computers & Geosciences* **28**, 605-619.

Korochantseva, E. V., Trieloff, M., Buikin, A. I., Hopp, J. & Meyer, H.-P. (2005). 40Ar/39Ar dating and cosmic-ray exposure time of desert meteorites: Dhofar 300 and Dhofar 007 eucrites and anomalous achondrite NWA 011. *Meteoritics & Planetary Science* **40**, 1433-1454.

Kunz, J., Falter, M. & Jessberger, E. K. (1997). Shocked meteorites: Argon-40-argon-39 evidence for multiple impacts. *Meteoritics & Planetary Science* **32**, 647-670.

Lanphere, M. A. & Dalrymple, G. **B.** (1976). Identification of excess 40Ar by the 40Ar/39Ar age spectrum technique. *Earth and Planetary Science Letters* **32**, 141-148.

Lee, J. Y., Marti, K., Severinghaus, J. P., Kawamura, K., Yoo, H. S., Lee, J. B. & Kim, J. S. (2006). A redetermination of the isotopic abundances of atmospheric Ar. *Geochimica et Cosmochimica Acta* **70**, 4507-4512.

Mahoney, J. J., Storey, M., Duncan, R. A., Spencer, K. J. & Pringle, M. (1993). Geochemistry and geochronology of Leg 130 basement lavas: nature and origin of the Ontong Java Plateau. *Proceedings of the Ocean Drilling Program, Scientific Results*: Ocean Drilling Program, Texas A&M University College Station, TX, 3-22.

Mark, D. F., Stuart, F. M. & de Podesta, M. (2011). New high-precision measurements of the isotopic composition of atmospheric argon. *Geochimica et Cosmochimica Acta* **75**, 7494-7501.

McDougall, I. (1961). Determination of the age of a basic igneous intrusion by the potassium–argon method. *Nature* **190**, 1184-1186.

McDougall, I. (1962). Differentiation of the Tasmanian dolerites: Red Hill dolerite-granophyre association. Boulder, CO: Boulder, CO, United States: Geological Society of America (GSA), 279-315.

McDougall, I. (1963). Potassium-argon age measurements on dolerites from Antarctica and South Africa. *Journal of Geophysical Research* **68**, 1535-1545.

McDougall, I. & Green, D. (1964). Excess radiogenic argon in pyroxenes and isotopic ages on minerals from Norwegian eclogites. *Norsk Geologisk Tidsskrift* **44**, 183-196.

McDougall, I., Polach, H. & Stipp, J. (1969). Excess radiogenic argon in young subaerial basalts from the Auckland volcanic field, New Zealand. *Geochimica et Cosmochimica Acta* **33**, 1485-1520.

Minor, D. R. & Mukasa, S. B. (1997). Zircon U□Pb and hornblende 40Ar□ 39Ar ages for the Dufek layered mafic intrusion, Antarctica: Implications for the age of the Ferrar Large Igneous Province. *Geochimica et Cosmochimica Acta* **61**, 2497-2504.

Mortimer, N., Herzer, R., Gans, P., Parkinson, D. & Seward, D. (1998). Basement geology from Three Kings Ridge to West Norfolk Ridge, southwest Pacific Ocean: evidence from petrology, geochemistry and isotopic dating of dredge samples. *Marine Geology* **148**, 135-162.

Olierook, H. K., Merle, R. E. & Jourdan, F. (2017). Toward a Greater Kerguelen Large Igneous Province: Evolving mantle source contributions in and around the Indian Ocean. *Lithos*.

Olierook, H. K., Merle, R. E., Jourdan, F., Sircombe, K., Fraser, G., Timms, N. E., Nelson, G., Dadd, K. A., Kellerson, L. & Borissova, I. (2015). Age and geochemistry of magmatism on the oceanic Wallaby Plateau and implications for the opening of the Indian Ocean. *Geology* **43**, 971-974.

Olierook, H. K. H., Jourdan, F., Merle, R. E., Timms, N. E., Kusznir, N. & Muhling, J. R. (2016). Bunbury Basalt: Gondwana breakup products or earliest vestiges of the Kerguelen mantle plume? *Earth and Planetary Science Letters* **440**, 20-32.

Oostingh, K. F., Jourdan, F., Matchan, E. L. & Phillips, D. (2017). 40Ar/39Ar geochronology reveals rapid change from plume-assisted to stress-dependent volcanism in the Newer Volcanic Province, SE Australia. *Geochemistry, Geophysics, Geosystems* **18,** doi:10.1002/2016GC006601.

Oostingh, K. F., Jourdan, F., Merle, R. & Chiaradia, M. (2016). Spatio-temporal Geochemical Evolution of the SE Australian Upper Mantle Deciphered from the Sr, Nd and Pb Isotope Compositions of Cenozoic Intraplate Volcanic Rocks. *Journal of Petrology* **57**, 1509-1530.

Paine, J. H., Nomade, S. & Renne, P. R. (2006). Quantification of 39 Ar recoil ejection from GA1550 biotite during neutron irradiation as a function of grain dimensions. *Geochimica et Cosmochimica Acta* **70**, 1507-1517.

Pellas, P., Fiéni, C., Trieloff, M. & Jessberger, E. K. (1997). The cooling history of the Acapulco meteorite as recorded by the 244 Pu and 40 Ar-39 Ar chronometers. *Geochimica et Cosmochimica Acta* **61**, 3477-3501.

Phillips, D., Harris, J. & Kiviets, G. (2004). 40 Ar/39 Ar analyses of clinopyroxene inclusions in African diamonds: implications for source ages of detrital diamonds. *Geochimica et Cosmochimica Acta* **68**, 151-165.

Phillips, D. & Matchan, E. L. (2013). Ultra-high precision 40Ar/39Ar ages for Fish Canyon Tuff and Alder Creek Rhyolite sanidine: New dating standards required? *Geochimica Et Cosmochimica Acta* **121**, 229-239.

Phillips, D., Onstott, T. & Harris, J. (1989). 40Ar/39Ar laser-probe dating of diamond inclusions from the Premier Kimberlite.

Poldervaart, A. & Hess, H. H. (1951). Pyroxenes in the crystallization of basaltic magma. *The Journal of Geology* **59**, 472-489.

Rama, S., Hart, S. & Roedder, E. (1965). Excess radiogenic argon in fluid inclusions. *Journal of Geophysical Research* **70**, 509-511.

Renne, P. R., Balco, G., Ludwig, K. R., Mundil, R. & Min, K. (2011). Response to the comment by W.H. Schwarz et al. on "Joint determination of K-40 decay constants and Ar-40*/K-40 for the Fish Canyon sanidine standard, and improved accuracy for Ar-40/Ar-39 geochronology" by PR Renne et al. (2010). *Geochimica Et Cosmochimica Acta* **75**, 5097-5100.

Renne, P. R., Deino, A. L., Hilgen, F. J., Kuiper, K. F., Mark, D. F., Mitchell, W. S., Morgan, L. E., Mundil, R. & Smit, J. (2013). Time scales of critical events around the Cretaceous-Paleogene boundary. *Science* **339**, 684-687.

Renne, P. R., Swisher, C. C., Deino, A. L., Karner, D. B., Owens, T. L. & Depaolo, D. J. (1998). Intercalibration of standards, absolute ages and uncertainties in 40Ar/ 39Ar dating. *Chemical Geology* **145**, 117-152.

Scibiorski, E., Tohver, E. & Jourdan, F. (2015). Rapid cooling and exhumation in the western part of the Mesoproterozoic Albany-Fraser Orogen, Western Australia. *Precambrian Research* **265**, 232-248.

Svensen, H., Corfu, F., Polteau, S., Hammer, Ø. & Planke, S. (2012). Rapid magma emplacement in the Karoo Large Igneous Province. *Earth and Planetary Science Letters* **325-326**, 1-9.

Svensen, H., Planke, S., Chevallier, L., Malthe-Sørenssen, A., Corfu, F. & Jamtveit, B. (2007). Hydrothermal venting of greenhouse gases triggering Early Jurassic global warming. *Earth and Planetary Science Letters* **256**, 554-566.

Thomas, R., Jacobs, J., Horstwood, M., Ueda, K., Bingen, B. & Matola, R. (2010). The Mecubúri and Alto Benfica groups, NE Mozambique: Aids to unravelling ca. 1 and 0.5 Ga events in the east African orogen. *Precambrian Research* **178**, 72-90.

Trieloff, M., Jessberger, E. K., Herrwerth, I., Hopp, J., Fiéni, C., Ghélis, M., Bourot-Denise, M. & Pellas, P. (2003). Structure and thermal history of the H-chondrite parent asteroid revealed by thermochronometry. *Nature* **422**, 502-506.

Turner, G. & Cadogan, P. (1974). Possible effects of 39Ar recoil in 40Ar-39Ar dating. *Lunar and Planetary Science Conference Proceedings*, 1601-1615.

Ueda, K., Jacobs, J., Thomas, R. J., Kosler, J., Jourdan, F. & Matola, R. (2012). Delamination-induced late-tectonic deformation and high-grade metamorphism of the Proterozoic Nampula Complex, northern Mozambique. *Precambrian Research* **196**, 275-294.

Verati, C. & Jourdan, F. (2013). Modelling effect of sericitization of plagioclase on the 40K/40Ar and 40Ar/39Ar chronometers: implication for dating basaltic rocks and mineral deposits. *Geological Society, London, Special Publications* **378**, 155-174.

Villa, I. M. (1997). Direct determination of 39 Ar recoil distance. *Geochimica et Cosmochimica Acta* **61**, 689-691.

Wang, S., McDougall, I., Tetley, N. & Harrison, T. M. (1980). 40Ar/39Ar age and thermal history of the Kirin chondrite. *Earth and Planetary Science Letters* **49**, 117-131.

Winter, J. D. N. (2010). *Principles of Igneous and Metamorphic Petrology*: Prentice Hall.

Zeng, Z., Niedermann, S., Chen, S., Wang, X. & Li, Z. (2015). Noble gases in sulfide deposits of modern deep-sea hydrothermal systems: Implications for heat fluxes and hydrothermal fluid processes. *Chemical Geology* **409**, 1-11

5.11 Figure captions

Figure 5.1: Sketch map of the Australian Kalkarindji Continental Flood Basalt (CFB) province's distribution and constituent suites. Modified after Figure 2.1. Outcrop of the Tasmanian Dolerite also represented.

Figure 5.2: Photomicrographs of all samples. Selected examples of exsolution features, pigeonite, augite, and sericite are labelled. CPX – clinopyroxene; OPX – Orthopyroxene.

Figure 5.3: Representative SEM Images of pyroxene crystals from the Tasmanian Dolerites and sills of the Table Hill Volcanics (Kalkarindji). Selected examples of exsolution features, pigeonite, augite, and sericite are labelled. OPX – orthopyroxene.

Figure 5.4: Photographs of selected examples of pyroxene separates. Ruler measurement displayed is in 1 cm increments.

Figure 5.5: $^{40}Ar/^{39}Ar$ apparent age and related K/Ca ratio spectra for pyroxene and plagioclase separates plotted against the cumulative percentage of ^{39}Ar released. Mean

squared weighted deviation (MSWD) and probability of fit (P) are indicated. Errors on plateau ages are quoted at 2σ and do not include systematic errors (i.e. uncertainties on the age of the monitor and on the decay constant).

Figure 5.6: Inverse isochons for the $^{40}Ar/^{39}Ar$ geochronology results. Inverse isochron atmospheric ratio used in calculations made for the age quoted.

Figure 5.7: $^{40}Ar/^{39}Ar$ and related K/Ca ratio spectra for pyroxene analyses that did not return plateau ages; plotted against the cumulative percentage of ^{39}Ar released. Total fusion error ages quoted. Note that the error ages are *not* providing the age of crystallization and should be considered rather as a semi-quantitative age information.

Figure 5.8: Pyroxene data compared with literature data and in the case of the results from TAS-17 the plagioclase ages of the same sample as well. Kalkarindji data compiled in Jourdan *et al.* (2014b). Literature results from the Ferrar province from Minor and Mukasa (1997) and Burgess *et al.* (2015).

Figure 5.9: % ^{39}Ar released vs K/Ca ratio for each respective step for three representative pyroxene analyses.

Figure 5.10: (a – c) Selected graphs of laser power vs signal intensity for analyses of pyroxene separates (coarse fraction) and plagioclase separates from TAS-17. d) Degassing model calculated with experimentally derived activation energies (E_a) and diffusion coefficients (D_0) for anorthite, clinopyroxene (CPX), and orthopyroxene (OPX).

Figure 5.11: (a) Schematic diagram explaining the effect of recoil redistribution on age and K/Ca spectra; modified from Jourdan and Renne (2013) using results from 07THD001Bc. (b) Graph displaying the total fusion (error) age of the recoil-plagued samples (Figure 5.7) compared to the emplacement age. Dotted box represents a ± 18 Ma age difference from 511 Ma (Jourdan *et al.*, 2014b). Note that the error ages are *not* providing the age of crystallization and should be considered rather as a semi-quantitative age information.

Figure 5.12: (a) Time-temperature path used to calculate the simulated age spectra. (b) Modeled age spectra from material subjected to a greenschist metamorphic event around 800 Ma. Metamorphic history of the 1.1 Ga Umkondo dykes used to constrain model parameters (Jourdan *et al.*, 2009a). A 100 Ma prograde and retrograde event was calculated for 150 µm radius crystals of anorthite, orthopyroxene (OPX), and clinopyroxene (CPX) compositions. Diffusion parameters and thermal history are given in Table 5.2.

Figure 5.13: (a) Time-temperature path used to calculate the simulated age spectra. (b) Modeled age spectra resulting from a metamorphic cooling path for 150 µm radius crystals of Biotite, orthopyroxene (OPX), and clinopyroxene (CPX) compositions. Cooling history parameters constrained from the metamorphic history of the Nampula Complex in Mozambique (Ueda *et al.*, 2012). Diffusion parameters and thermal history are given in Table 5.3. Heating steps used to calculate plateau age are shaded. Approximate T-t path of the Ticué structure redrafted from data and figure presented in Ueda *et al.* (2012), approximate location of the theoretical modeled pyroxene is displayed by the orange box.

Chapter 6: Thesis Conclusions

The multidiscipline approach displayed within the various projects of this PhD research, demonstrates the benefit of an integrated geochemical and high precision geochronological approach to understanding the origin of Large Igneous Provinces (LIPs). The results of this study indicate the ability to provide high precision ages to mafic/silica poor rocks with the $^{40}Ar/^{39}Ar$ technique using plagioclase and through the development of pyroxene (not yet at the levels of precision of plagioclase but a now viable option) allow for a more extensive and complete understanding of the duration of LIPs. The ability to now place concise ages to the mafic endmember of LIP geochronology broaden the minute detail achievable to understanding the magmatic systems of LIPs, available particularly when used in tandem with high precision U/Pb results. Furthermore, coupling the deeper understanding of the timing and duration of LIP magma emplacement with geochemical data is paramount to understanding the geodynamics of LIP petrogenesis.

The Kalkarindji Continental Flood Basalt (CFB) Province is the oldest known LIP in the Phanerozoic. The geochemistry of this CFB province is unparalleled in the homogeneity of the geochemical data across the whole areal extent of the province. Crustal contamination once the magma exited the source cannot explain the continental-like geochemical characteristics of the Kalkarindji. An extensive geochemical data set of major, trace, and Sr, Nd, and Pb indicate an ancient enrichment event ca. 2.5 Ga into the source region of the Kalkarindji magmas. Numerical models in conjunction with the geochemical data are used to propose a dominantly anciently enriched sub-continental lithospheric mantle (SCLM) source component. The lithospheric and asthenospheric mantle of the Kalkarindji magmas were warmed under

a ca. 700 Ma stability of the Australian continent during the period of Gondwana. During a large scale rotation of Gondwana ca. 500 Ma, resulting in considerable extension, within the Australian continent caused decompression melting of the fertilized source of the Kalkarindji magmas.

A protracted duration of ca. 1.6 Ma is revealed for the Tasmanian Dolerite through high-precision $^{40}Ar/^{39}Ar$ plagioclase geochronology. The magmatism represented by these intrusive bodies reveals nearly continuous emplacement throughout. The precision of the results, however, do allow for the oldest intrusions (ca. 184 Ma) of the sample suite to be temporally distinguished from the youngest intrusions (ca. 182 Ma). Furthermore, a slight inflection of the age spectra to older ages (trending toward 185 Ma) within the younger generation of intrusions provides the first evidence of possible crystal inheritance using the $^{40}Ar/^{39}Ar$ technique. These ages for the Tasmanian Dolerites ranging from 182 – 184 Ma contain some of the oldest ages thus far for the Ferrar province. The geochemistry of the younger generation intrusions display a slightly more evolved characteristic (i.e. higher SiO_2 and lower MgO contents; higher incompatible element signatures) than the geochemical characteristics of the older generation of intrusions. This slight geochemical difference represents a geochemical evolution of the magma source over the ca 1.6 Ma duration of the event. The geochemical progression to more silica rich compositions of the magmas could be responsible for the absence of zircon in the 184 – 185 Ma generation of magmatism. The new $^{40}Ar/^{39}Ar$ plagioclase plateau ages presented in this study are arriving at previously unattained high levels of precision allowing for more minute scale magmatic processes than ever before.

The Karoo province was emplaced into Gondwana contemporaneously with the Ferrar Province. $^{40}Ar/^{39}Ar$ plagioclase geochronology indicate sills from the

Western Cape Province intruded into the Karoo Basin ca 183.5 Ma as some of the first magmatic expressions of the Karoo LIP. These sills of the Western Cape Province contain hydrated minerals (biotite and hornblende) that crystallized contemporaneously with plagioclase from the same samples. The presence of primary biotite and hornblende within low-Ti tholeiites provide the first direct evidence of H_2O amidst the Karoo magmas. A major, trace, and Sr, Nd, and Pb isotope geochemical investigation of these Western Cape Province intrusions preclude a considerable involvement of crustal contamination processes. Therefore, the integration of $^{40}Ar/^{39}Ar$ geochronology and major, trace, and isotopic geochemical data of these hydrous sills indicate the H_2O content is representative of a hydrated source. Considering the geochemical and geochronological results as well as the geographic location of the Western Cape intrusions with the other low-Ti rocks of the Karoo LIP, argue for involvement of a fertilized heterogeneous SCLM during the genesis of the Karoo magmas. The geochemical data signify the most probable tectonic event for fertilizing/hydrating the SCLM source region of the Western Cape dolerites was subduction during the Mesoproterozoic Kibaran Orogeny. Subduction associated with the Kibaran Orogeny introduced hydrated material preferentially to the base of the lithosphere most proximal to the subduction zone; evidenced by the exclusive appearance of the hydrous minerals in sills emplaced in the Namaqua-Natal Mobile belt. Therefore, the SCLM below the Karoo LIP displays geochemical evidence for more fluid involvement in the magmas sourced more proximal to the ancient subduction zone and more sediment involvement in the magmas sourced distal to the ancient subduction zone.

As discussed in chapter's three and four, to develop a complete understanding of the geochronological framework of a CFB province high-precision geochronology

is essential. However, the ability to obtain geochronological data is determinant on the availability of datable material. In the case of LIP research, the dominant mafic rock type precludes the consistent availability of zircon and the alteration of plagioclase to the high K mineral sericite can make the application of the $^{40}Ar/^{39}Ar$ technique impossible. Therefore, new geochronology methods must be developed to obtain a truly comprehensive understanding of the magmatic systems of LIPs across all of the variable rock types generated during these large scale magmatic events. This study presents the *first* geologically meaningful $^{40}Ar/^{39}Ar$ plateau ages for terrestrial pyroxene. The ability to now produce statistically important $^{40}Ar/^{39}Ar$ ages to the mineral pyroxene is accomplished by the use of multi-collector noble gas mass spectrometers such as the ARGUS VI. The ability to simultaneously collect all argon isotopes as well as the heightened sensitivity to measure low ^{39}Ar resulting from a 10^{13} ohm resistor to the faraday cup that measures mass 39 provide the means to obtain plateau ages from low K minerals such as pyroxene. A thorough investigation of the $^{40}Ar/^{39}Ar$ pyroxene plateau ages compared to $^{40}Ar/^{39}Ar$ plateau ages from plagioclase of the same samples as well as $^{40}Ar/^{39}Ar$ plagioclase and $^{238}U/^{206}Pb$ zircon data from the literature indicate the pyroxene plateau ages represent a true geological event. Evidence of irradiation induced recoil for pyroxene grains that contain pervasive exsolution lamellae indicate a thorough petrographic and sample pre-screening process is essential to assure geologic analytical success. Numerical models demonstrate the capability of utilizing $^{40}Ar/^{39}Ar$ pyroxene plateau ages in the fields of metamorphic and thermochronologic applications. The availability of utilizing the $^{40}Ar/^{39}Ar$ technique with the mineral pyroxene establishes unprecedented geochronological opportunities to all geologic studies dominated with mafic/ultramafic rocks or with pyroxene as a dominant unaltered phase.

Although the focus of these various studies are on three CFBs found in the southern hemisphere, the conclusions and deeper understanding of these geochemically and geochronologically variable CFBs provide important insights into the origin of LIPs. The results provide examples for the importance of more accurate geochronology techniques for obtaining a better understanding of the anomalous melting conditions that are characteristic of large igneous provinces. The first direct evidence of cogenetic hydrous minerals within tholeiites of the Karoo CFBs is of considerable importance to the determination of viable petrogenetic models for LIPs as many of these hypotheses are reliant on the presence or absence of volatiles in the magmas. In general these studies emphasize the importance of combining accurate geochronology of magma emplacement during LIP events with geochemical data to obtain unprecedented insights into the petrogenesis of LIPs.

Chapter 7: Bibliography

Aitken, A. R. A. & Betts, P. G. (2009). Constraints on the Proterozoic supercontinent cycle from the structural evolution of the south-central Musgrave Province, central Australia. *Precambrian Research* 168, 284-300.

Allègre, C. J., Treuil, M., Minster, J.-F., Minster, B. & Albarède, F. (1977). Systematic use of trace element in igneous process. *Contributions to Mineralogy and Petrology* 60, 57-75.

Anderson, D. L. (1994). The sublithospheric mantle as the source of continental flood basalts; the case against the continental lithosphere and plume head reservoirs. *Earth and Planetary Science Letters* 123, 269-280.

Anderson, D. L. (2005). Scoring hotspots: The plume and plate paradigms. In: Foulger, G. R., Natland, J. H., Presnall, D. C. & Anderson, D. L. (eds.) *Plate, Plumes, and Paradigms*: Geological Society of America Special Paper 388, 31-54.

Anderson, D. L., Zhang, Y.-S. & Tanimoto, T. (1992). Plume heads, continental lithosphere, flood basalts and tomography. *Geological Society, London, Special Publications* 68, 99-124.

Arndt, N. T. & Christensen, U. (1992). The role of lithospheric mantle in continental flood volcanism: Thermal and geochemical constraints. *Journal of Geophysical Research* 97, 10967.

Arndt, N. T., Czamanske, G. K., Wooden, J. L. & Fedorenko, V. A. (1993). Mantle and crustal contributions to continental flood volcanism. *Tectonophysics* 223, 39-52.

Aubaud, C., Pineau, F., Hékinian, R. & Javoy, M. (2005). Degassing of CO 2 and H 2 O in submarine lavas from the Society hotspot. *Earth and Planetary Science Letters* 235, 511-527.

Baier, J., Audétat, A. & Keppler, H. (2008). The origin of the negative niobium tantalum anomaly in subduction zone magmas. *Earth and Planetary Science Letters* 267, 290-300.

Baksi, A. K., Archibald, D. A. & Farrar, E. (1996). Intercalibration of 40 Ar 39 Ar dating standards. *Chemical Geology* 129, 307-324.

Bas, M. J. L., Maitre, R. W. L., Streckeisen, A. & Zanettin, B. (1986). A Chemical Classification of Volcanic Rocks Based on the Total Alkali-Silica Diagram. *Journal of Petrology* 27, 745-750.

Becker, M. & Roex, A. P. L. (2006). Geochemistry of South African on-and off-craton, Group I and Group II kimberlites: petrogenesis and source region evolution. *Journal of Petrology* 47, 673-704.

Béguelin, P., Chiaradia, M., Beate, B. & Spikings, R. (2015). The Yanaurcu volcano (Western Cordillera, Ecuador): A field, petrographic, geochemical, isotopic and geochronological study. *Lithos* 218-219, 37-53.

Belica, M., Tohver, E., Pisarevsky, S., Jourdan, F., Denyszyn, S. & George, A. (2017). Middle Permian paleomagnetism of the Sydney Basin, Eastern Gondwana: Testing Pangea models and the timing of the end of the Kiaman Reverse Superchron. *Tectonophysics* 699, 178-198.

Ben Othman, D., White, W., M. & Patchett, J. (1989). The geochemistry of marine sediments, island arc magma genesis, and crust-mantle recycling. *Earth and Planetary Science Letters* 94, 1-21.

Betts, P. G., Giles, D., Lister, G. S. & Frick, L. R. (2002). Evolution of the Australian lithosphere. *Australian Journal of Earth Sciences* 49, 661-695.

Bezard, R., Davidson, J. P., Turner, S., Macpherson, C. G., Lindsay, J. M. & Boyce, A. J. (2014). Assimilation of sediments embedded in the oceanic arc crust: myth or reality? *Earth and Planetary Science Letters* 395, 51-60.

Black, B. A., Elkins-Tanton, L. T., Rowe, M. C. & Peate, I. U. (2012). Magnitude and consequences of volatile release from the Siberian Traps. *Earth and Planetary Science Letters* 317-318, 363-373.

Bohrson, W. A. & Spera, F. J. (2001). Energy-constrained open-system magmatic processes II: application of energy-constrained assimilation–fractional crystallization (EC-AFC) model to magmatic systems. *Journal of Petrology* 42, 1019-1041.

Bond, G. C., Nickeson, P. A. & Kominz, M. A. (1984). Breakup of a supercontinent between 625 Ma and 555 Ma: new evidence and implications for continental histories. *Earth and Planetary Science Letters* 70, 325-345.

Brauns, C. M., Hergt, J. M., Woodhead, J. D. & Maas, R. (2000). Os Isotopes and the Origin of the Tasmanian Dolerites. *Journal of Petrology* 41, 905-918.

Briqueu, L., Bougault, H. & Joron, J. L. (1984). Quantification of Nb, Ta, Ti and V anomalies in magmas associated with subduction zones: petrogenetic implications. *Earth and Planetary Science Letters* 68, 297-308.

Bryan, S. E. & Ernst, R. E. (2008). Revised definition of Large Igneous Provinces (LIPs). *Earth-Science Reviews* 86, 175-202.

Bultitude, R. (1976). Flood basalts of probable early Cambrian age in northern Australia. *Volcanism in Australasia*, 1-20.

Burgess, R., Kiviets, G. & Harris, J. (2004). Ar–Ar age determinations of eclogitic clinopyroxene and garnet inclusions in diamonds from the Venetia and Orapa kimberlites. *Lithos* 77, 113-124.

Burgess, S. D., Bowring, S. A., Fleming, T. H. & Elliot, D. H. (2015). High-precision geochronology links the Ferrar large igneous province with early-Jurassic ocean anoxia and biotic crisis. *Earth and Planetary Science Letters* 415, 90-99.

Campbell, I. H. (2001). Identification of ancient mantle plumes. *Special Papers-Geological Society of America*, 5-22.

Campbell, I. H. & Griffiths, R. W. (1990). Implications of mantle plume structure for the evolution of flood basalts. *Earth and Planetary Science Letters* 99, 79-93.

Carlson, R., Lugmair, G. & Macdougall, J. (1981). Crustal influence in the generation of continental flood basalts. *Nature* 289, 160-162.

Cassata, W. & Renne, P. (2010). Ar-37 diffusion in pyroxene: Implications for thermochronometry and mantle degassing. *Geochim. Cosmochim. Acta* 74, A148-A148.

Cassata, W. S. & Renne, P. R. (2013). Systematic variations of argon diffusion in feldspars and implications for thermochronometry. *Geochimica et Cosmochimica Acta* 112, 251-287.

Cassata, W. S., Renne, P. R. & Shuster, D. L. (2009). Argon diffusion in plagioclase and implications for thermochronometry: A case study from the Bushveld Complex, South Africa. *Geochimica et Cosmochimica Acta* 73, 6600-6612.

Cassata, W. S., Renne, P. R. & Shuster, D. L. (2011). Argon diffusion in pyroxenes: Implications for thermochronometry and mantle degassing. *Earth and Planetary Science Letters* 304, 407-416.

Cassata, W. S., Shuster, D. L., Renne, P. R. & Weiss, B. P. (2010). Evidence for shock heating and constraints on Martian surface temperatures revealed by 40Ar/ 39Ar thermochronometry of Martian meteorites. *Geochimica et Cosmochimica Acta* 74, 6900-6920.

Cawood, P. A. & Korsch, R. J. (2008). Assembling Australia: Proterozoic building of a continent. *Precambrian Research* 166, 1-35.

Chauvel, C., Goldstein, S. & Hofmann, A. (1995). Hydration and dehydration of oceanic crust controls Pb evolution in the mantle. *Chemical Geology* 126, 65-75.

Chiaradia, M., Müntener, O. & Beate, B. (2011). Enriched basaltic andesites from mid-crustal fractional crystallization, recharge, and assimilation (Pilavo Volcano, Western Cordillera of Ecuador). *Journal of Petrology* 52, 1107-1141.

Chung, S.-L. & Jahn, B.-m. (1995). Plume-lithosphere interaction in generation of the Emeishan flood basalts at the Permian-Triassic boundary. *Geology* 23, 889-892.

Class, C. & Goldstein, S. L. (1997). Plume-lithosphere interactions in the ocean basins: constraints from the source mineralogy. *Earth and Planetary Science Letters* 150, 245-260.

Coffin, M. F. & Eldholm, O. (1994). Large igneous provinces: Crustal structure, dimensions, and external consequences. *Reviews of Geophysics* 32, 1-36.

Coltice, N., Bertrand, H., Rey, P., Jourdan, F., Phillips, B. R. & Ricard, Y. (2009). Global warming of the mantle beneath continents back to the Archaean. *Gondwana Research* 15, 254-266.

Coltice, N., Phillips, B. R., Bertrand, H., Ricard, Y. & Rey, P. (2007). Global warming of the mantle at the origin of flood basalts over supercontinents. *Geology* 35, 391.

Compston, W., McDougall, I. & Heier, K. S. (1968). Geochemical comparison of the mesozoic basaltic rocks of Antarctica, South Africa, South America and Tasmania. *Geochimica et Cosmochimica Acta* 32, 129-149.

Courtillot, V., Davaille, A., Besse, J. & Stock, J. (2003). Three distinct types of hotspots in the Earth's mantle. *Earth and Planetary Science Letters* 205, 295-308.

Courtillot, V., Jaupart, C., Manighetti, I., Tapponnier, P. & Besse, J. (1999). On causal links between flood basalts and continental breakup. *Earth and Planetary Science Letters* 166, 177-195.

Courtillot, V. E. & Renne, P. R. (2003). On the ages of flood basalt events. *Comptes Rendus Geoscience* 335, 113-140.

Crank, J. & Gupta, R. S. (1975). Isotherm migration method in two dimensions. *International Journal of Heat and Mass Transfer* 18, 1101-1107.

Dalrymple, G. B. & Lanphere, M. A. (1969). Potassium-argon dating: Principles, techniques and applications to geochronology. *(Freeman) San Francisco, California*, 258.

Deckart, K., Bertrand, H. & Liégeois, J.-P. (2005). Geochemistry and Sr, Nd, Pb isotopic composition of the Central Atlantic Magmatic Province (CAMP) in Guyana and Guinea. *Lithos* 82, 289-314.

Dessai, A. G. & Viegas, A. (2009). Petrogenesis of alkaline rocks from Murud-Janjira, in the Deccan Traps, Western India. *Mineralogy and Petrology* 98, 297-311.

Dietz, R. S. & Holden, J. C. (1970). Reconstruction of Pangaea: Breakup and dispersion of continents, Permian to Present. *Journal of Geophysical Research* 75, 4939-4956.

Dodson, M. H. (1973). Closure temperature in cooling geochronological and petrological systems. *Contributions to Mineralogy and Petrology* 40, 259-274.

Doucet, S., Moreira, M., Weis, D., Scoates, J. S., Giret, A. & Allègre, C. (2006). Primitive neon and helium isotopic compositions of high-MgO basalts from the Kerguelen Archipelago, Indian Ocean. *Earth and Planetary Science Letters* 241, 65-79.

Doucet, S., Scoates, J. S., Weis, D. & Giret, A. (2005). Constraining the components of the Kerguelen mantle plume: A Hf-Pb-Sr-Nd isotopic study of picrites and high-MgO basalts from the Kerguelen Archipelago. *Geochemistry, Geophysics, Geosystems* 6, n/a-n/a.

Drüppel, K., McCready, A. J. & Stumpfl, E. F. (2009). High-K granites of the Rum Jungle Complex, N-Australia: Insights into the Late Archean crustal evolution of the North Australian Craton. *Lithos* 111, 203-219.

Duncan, A., Erlank, A. & Marsh, J. (1984). Regional geochemistry of the Karoo igneous province. In: Erlank, A. (ed.) *Duncan, A. R., Erlank, A. J. & Marsh, J. S. (1984). Regional Geochemistry of the Karoo igneous province. In: Erlank, A. J. (ed.) Petrogenesis of the Volcanic Rocks of the Karoo Province. Special Publication of the Geological Society of South Africa, 355–388.*: Special Publication of the Geological Society of South Africa, 355–388.

Duncan, A. R. (1987). The Karoo igneous province—a problem area for inferring tectonic setting from basalt geochemistry. *Journal of Volcanology and Geothermal Research* 32, 13-34.

Duncan, R. & Pyle, D. (1988). Rapid eruption of the Deccan flood basalts at the Cretaceous/Tertiary boundary. *Nature* 333, 841-843.

Duncan, R. A., Hooper, P., Rehacek, J., Marsh, J. & Duncan, A. (1997). The timing and duration of the Karoo igneous event, southern Gondwana.

Duncan, R. A. & Richards, M. (1991). Hotspots, mantle plumes, flood basalts, and true polar wander. *Reviews of Geophysics* 29, 31-50.

Eales, H. V., Marsh, J. S. & Cox, K. G. (1983). The Karoo Igneous Province: An Introduction. In: Erlank, A. J. (ed.) *Petrogenesis of the Volcanic Rocks of the Karoo Province*. Johannesburg: Special Publication No. 13 The Geological Society of South Africa, 1-26.

Edwards, A. B. (1942a). Differentiation of the Dolerites of Tasmania. I. *The Journal of Geology* 50, 451-480.

Edwards, A. B. (1942b). Differentiation of the Dolerites of Tasmania. II. *The Journal of Geology* 50, 579-610.

Eglington, B. (2006). Evolution of the Namaqua-Natal Belt, southern Africa–A geochronological and isotope geochemical review. *Journal of African Earth Sciences* 46, 93-111.

Ellam, R., Carlson, R. & Shirey, S. (1992). Evidence from Re–Os isotopes for plume–lithosphere mixing in Karoo flood basalt genesis. *Nature* 359, 718-721.

Elliot, D. H. & Fleming, T. H. (2004). Occurrence and Dispersal of Magmas in the Jurassic Ferrar Large Igneous Province, Antarctica. *Gondwana Research* 7, 223-237.

Elliot, D. H. & Fleming, T. H. (2008). Physical volcanology and geological relationships of the Jurassic Ferrar Large Igneous Province, Antarctica. *Journal of Volcanology and Geothermal Research* 172, 20-37.

Encarnacion, J., Fleming, T. H., Elliot, D. H. & Eales, H. V. (1996). Synchronous emplacement of Ferrar and Karoo dolerites and the early breakup of Gondwana. *Geology (Boulder)* 24, 535-538.

Ernst, R. E. (2014). *Large igneous provinces*: Cambridge University Press.

Ernst, R. E. & Youbi, N. (2017). How Large Igneous Provinces affect global climate, sometimes cause mass extinctions, and represent natural markers in the geological record. *Palaeogeography, Palaeoclimatology, Palaeoecology*.

Evins, L. Z., Jourdan, F. & Phillips, D. (2009). The Cambrian Kalkarindji Large Igneous Province: Extent and characteristics based on new 40Ar/39Ar and geochemical data. *Lithos* 110, 294-304.

Ewart, A., Marsh, J., Milner, S., Duncan, A., Kamber, B. S. & Armstrong, R. (2004). Petrology and geochemistry of Early Cretaceous bimodal continental flood volcanism of the NW Etendeka, Namibia. Part 2: Characteristics and petrogenesis of the high-Ti latite and high-Ti and low-Ti voluminous quartz latite eruptives. *Journal of Petrology* 45, 107-138.

Faure, G. (1986). Principles of isotope geochemistry. *John Wiley and Sons. chapters* 6, 8.

Faure, G. & Mensing, T. M. (2011). The Ferrar Group: Kirkpatrick Basalt. 373-414.

Fawcett, J. J. (1965). Alteration Products of Olivine and Pyroxene in Basalt Lavas from the Isle of Mull1. *Mineralogical Magazine* 35, 55-68.

Fleming, T., Heimann, A., Foland, K. & Elliot, D. (1997). Ar-40/Ar-39 geochronology of Ferrar Dolerite sills from the Transantarctic mountains, Antarctica: Implications for the age and origin of the Ferrar magmatic province. *Geol. Soc. Am. Bull.* 109, 533-546.

Flowers, R., Bowring, S., Tulloch, A. & Klepeis, K. (2005). Tempo of burial and exhumation within the deep roots of a magmatic arc, Fiordland, New Zealand. *Geology* 33, 17-20.

Foulger, G. R. (2007). The "plate" model for the genesis of melting anomalies. *Geological Society of America Special Papers* 430, 1-28.

Gallagher, K. & Hawkesworth, C. (1992). Dehydration melting and the generation of continental flood basalts. *Nature* 358, 57-59.

Gerstenberger, H. & Haase, G. (1997). A highly effective emitter substance for mass spectrometric Pb isotope ratio determinations. *Chemical Geology* 136, 309-312.

Ghiorso, M. S. & Sack, R. O. (1995). Chemical mass transfer in magmatic processes IV. A revised and internally consistent thermodynamic model for the interpolation and extrapolation of liquid-solid equilibria in magmatic systems at elevated temperatures and pressures. *Contributions to Mineralogy and Petrology* 119, 197-212.

Gibbons, A. D., Whittaker, J. M. & Müller, R. D. (2013). The breakup of East Gondwana: assimilating constraints from Cretaceous ocean basins around India into a best-fit tectonic model. *Journal of Geophysical Research: Solid Earth* 118, 808-822.

Gibson, S., Thompson, R., Dickin, A. P. & Leonardos, O. (1995). High-Ti and low-Ti mafic potassic magmas: Key to plume-lithosphere interactions and continental flood-basalt genesis. *Earth and Planetary Science Letters* 136, 149-165.

Gibson, S. A., Thompson, R. N. & Day, J. A. (2006). Timescales and mechanisms of plume–lithosphere interactions: 40Ar/39Ar geochronology and geochemistry of alkaline igneous rocks from the Paraná–Etendeka large igneous province. *Earth and Planetary Science Letters* 251, 1-17.

Glass, L. M. & Phillips, D. (2006). The Kalkarindji continental flood basalt province: A new Cambrian large igneous province in Australia with possible links to faunal extinctions. *Geology* 34, 461.

Graham, S., Lambert, D. D., Shee, S. R., Smith, C. B. & Reeves, S. (1999). Re-Os isotopic evidence for Archean lithospheric mantle beneath the Kimberley block, Western Australia. *Geology* 27, 431-434.

Gray, D. R., Foster, D. A., Meert, J. G., Goscombe, B. D., Armstrong, R., Trouw, R. A. J. & Passchier, C. W. (2008). A Damara orogen perspective on the assembly of southwestern Gondwana. *Geological Society, London, Special Publications* 294, 257-278.

Green, D. & Ringwood, A. (1967). The genesis of basaltic magmas. *Contributions to Mineralogy and Petrology* 15, 103-190.

Grégoire, M., Bell, D. & Le Roex, A. (2003). Garnet lherzolites from the Kaapvaal Craton (South Africa): trace element evidence for a metasomatic history. *Journal of Petrology* 44, 629-657.

Grey, K., Hocking, R., Stevens, M., Bagas, L., Carlsen, G., Irimies, F., Pirajno, F., Haines, P. & Apak, S. (2005). Lithostratigraphic nomenclature of the Officer Basin and correlative parts of the Paterson Orogen, Western Australia. *Geological Survey of Western Australia Report* 93, 89.

Gualda, G. A. R., Ghiorso, M. S., Lemons, R. V. & Carley, T. L. (2012). Rhyolite-MELTS: a Modified Calibration of MELTS Optimized for Silica-rich, Fluid-bearing Magmatic Systems. *Journal of Petrology* 53, 875-890.

Gurnis, M. (1988). Large-scale mantle convection and the aggregation and dispersal of supercontinents. *Nature* 332, 695-699.

Hansma, J., Tohver, E., Schrank, C., Jourdan, F. & Adams, D. (2016). The timing of the Cape Orogeny: New 40 Ar/39 Ar age constraints on deformation and cooling of the Cape Fold Belt, South Africa. *Gondwana Research* 32, 122-137.

Harrison, T. M. & McDougall, I. (1981). Excess40Ar in metamorphic rocks from Broken Hill, New South Wales: implications for40Ar/39Ar age spectra and the thermal history of the region. *Earth and Planetary Science Letters* 55, 123-149.

Hart, S. & Dodd, R. T. (1962). Excess Radiogenic Argon in Pyroxenes. *Journal of Geophysical Research* 67, 2998-2999.

Hart, S. R. (1961). The use of hornblendes and pyroxenes for K-Ar dating. *Journal of Geophysical Research* 66, 2995-3001.

Hart, S. R. (1984). A large-scale isotope anomaly in the Southern Hemisphere mantle. *Nature* 309, 753-757.

Hawkesworth, C., Kelley, S., Turner, S., Le Roex, A. & Storey, B. (1999). Mantle processes during Gondwana break-up and dispersal. *Journal of African Earth Sciences* 28, 239-261.

Heimann, A., Fleming, T. H., Elliot, D. H. & Foland, K. A. (1994). A short interval of Jurassic continental flood basalt volcanism in Antarctica as demonstrated by 40 Ar 39 Ar geochronology. *Earth and Planetary Science Letters* 121, 19-41.

Heinonen, J. S., Carlson, R. W. & Luttinen, A. V. (2010). Isotopic (Sr, Nd, Pb, and Os) composition of highly magnesian dikes of Vestfjella, western Dronning Maud Land, Antarctica: A key to the origins of the Jurassic Karoo large igneous province? *Chemical Geology* 277, 227-244.

Heinonen, J. S., Carlson, R. W., Riley, T. R., Luttinen, A. V. & Horan, M. F. (2014). Subduction-modified oceanic crust mixed with a depleted mantle reservoir in the sources of the Karoo continental flood basalt province. *Earth and Planetary Science Letters* 394, 229-241.

Hergt, J., Peate, D. & Hawkesworth, C. (1991). The petrogenesis of Mesozoic Gondwana low-Ti flood basalts. *Earth and Planetary Science Letters* 105, 134-148.

Hergt, J. M. & Brauns, C. M. (2001). On the origin of Tasmanian dolerites. *Australian Journal of Earth Sciences* 48, 543-549.

Hergt, J. M., Chappell, B. W., Faure, G. & Mensing, T. M. (1989a). The geochemistry of Jurassic dolerites from Portal Peak, Antarctica. *Contributions to Mineralogy and Petrology* 102, 298-305.

Hergt, J. M., Chappell, B. W., McCulloch, M. T., McDougall, I. & Chivas, A. R. (1989b). Geochemical and isotopic constraints on the origin of the Jurassic dolerites of Tasmania. *Journal of Petrology* 30, 841-883.

Hess, J. & Lippolt, H. (1986). Kinetics of Ar isotopes during neutron irradiation: 39Ar loss from minerals as a source of error in 40Ar/39Ar dating. *Chemical Geology: Isotope Geoscience section* 59, 223-236.

Hill, R. I. (1991). Starting plumes and continental break-up. *Earth and Planetary Science Letters* 104, 398-416.

Hill, R. I. (1993). Mantle plumes and continental tectonics. *Lithos* 30, 193-206.

Hoatson, D. M., Jaireth, S. & Claoue-Long, J. (2008). *Guide to using the 1: 5 000 000 map of Australian proterozoic mafic-ultramafic magmatic events*: Geoscience Australia.

Hofmann, C., Courtillot, V., Feraud, G., Rochette, P., Yirgu, G., Ketefo, E. & Pik, R. (1997). Timing of the Ethiopian flood basalt event and implications for plume birth and global change. *Nature* 389, 838-841.

Hooper, P. R. (1982). The Columbia river basalts. *Science* 215, 1463-1468.

Hooper, P. R., Camp, V. E., Reidel, S. P. & Ross, M. E. (2007). The origin of the Columbia River flood basalt province: Plume versus nonplume models. *Geological Society of America Special Papers* 430, 635-668.

Hopp, J., Trieloff, M., Brey, G. P., Woodland, A. B., Simon, N. S. C., Wijbrans, J. R., Siebel, W. & Reitter, E. (2008). 40Ar/39Ar-ages of phlogopite in mantle xenoliths from South African kimberlites: Evidence for metasomatic mantle impregnation during the Kibaran orogenic cycle. *Lithos* 106, 351-364.

Houseman, G. & Molnar, P. (2001). Mechanisms of lithospheric rejuvenation associated with continental orogeny. *Geological Society, London, Special Publications* 184, 13-38.

Humphris, S. E. & Thompson, G. (1978). Hydrothermal alteration of oceanic basalts by seawater. *Geochimica et Cosmochimica Acta* 42, 107-125.

Imaoka, T. & Itaya, T. (2004). KAr geochronology of a middle Miocene submarine volcano-plutonic complex in southwest Japan. *Geol. Mag.* 141, 1-13.

Irvine, T. & Baragar, W. (1971). A guide to the chemical classification of the common volcanic rocks. *Canadian Journal of Earth Sciences* 8, 523-548.

Itaya, T., Doi, M. & Ohira, T. (1996). Very low potassium analysis by flame photometry using ultra low blank chemical lines: an application of K-Ar method to ophiolites. *Geochemical Journal* 30, 31-39.

Jacobsen, S. B. & Wasserburg, G. J. (1980). Sm-Nd isotopic evolution of chondrites. *Earth and Planetary Science Letters* 50, 139-155.

Jaques, A., O'Neill, H. S. C., Smith, C., Moon, J. & Chappell, B. (1990). Diamondiferous peridotite xenoliths from the Argyle (AK1) lamproite pipe, Western Australia. *Contributions to Mineralogy and Petrology* 104, 255-276.

Jones, D., Duncan, R. A., Briden, J., Randall, D. & MacNiocaill, C. (2001). Age of the Batoka basalts, northern Zimbabwe, and the duration of Karoo Large Igneous Province magmatism. *Geochemistry, Geophysics, Geosystems* 2.

Jones, M. T., Jerram, D. A., Svensen, H. H. & Grove, C. (2016). The effects of large igneous provinces on the global carbon and sulphur cycles. *Palaeogeography, Palaeoclimatology, Palaeoecology* 441, Part 1, 4-21.

Jourdan, F., Bertrand, H., Féraud, G., Le Gall, B. & Watkeys, M. (2009a). Lithospheric mantle evolution monitored by overlapping large igneous provinces: case study in southern Africa. *Lithos* 107, 257-268.

Jourdan, F., Bertrand, H., Scharer, U., Blichert-Toft, J., Feraud, G. & Kampunzu, A. B. (2007a). Major and Trace Element and Sr, Nd, Hf, and Pb Isotope Compositions of the Karoo Large Igneous Province, Botswana-Zimbabwe: Lithosphere vs Mantle Plume Contribution. *Journal of Petrology* 48, 1043-1077.

Jourdan, F. & Eroglu, E. (2017). 40Ar/39Ar and (U-Th)/He model age signatures of elusive Mercurian and Venusian meteorites. *Meteoritics & Planetary Science*, n/a-n/a.

Jourdan, F., Féraud, G., Bertrand, H., Kampunzu, A. B., Tshoso, G., Watkeys, M. K. & Le Gall, B. (2005). Karoo large igneous province: Brevity, origin, and relation to mass extinction questioned by new 40Ar/39Ar age data. *Geology* 33, 745.

Jourdan, F., Féraud, G., Bertrand, H., Watkeys, M., Kampunzu, A. & Le Gall, B. (2006). Basement control on dyke distribution in Large Igneous Provinces: case study of the Karoo triple junction. *Earth and Planetary Science Letters* 241, 307-322.

Jourdan, F., Féraud, G., Bertrand, H., Watkeys, M. & Renne, P. (2007b). Distinct brief major events in the Karoo large igneous province clarified by new 40 Ar/39 Ar ages on the Lesotho basalts. *Lithos* 98, 195-209.

Jourdan, F., Féraud, G., Bertrand, H., Watkeys, M. K. & Renne, P. R. (2008). The40Ar/39Ar ages of the sill complex of the Karoo large igneous province: Implications for the Pliensbachian-Toarcian climate change. *Geochemistry, Geophysics, Geosystems* 9, n/a-n/a.

Jourdan, F., Frew, A., Joly, A., Mayers, C. & Evans, N. J. (2014a). WA1ms: A~ 2.61 Ga muscovite standard for 40 Ar/39 Ar dating. *Geochimica et Cosmochimica Acta* 141, 113-126.

Jourdan, F., Hodges, K., Sell, B., Schaltegger, U., Wingate, M. T. D., Evins, L. Z., Soderlund, U., Haines, P. W., Phillips, D. & Blenkinsop, T. (2014b). High-precision dating of the Kalkarindji large igneous province, Australia, and synchrony with the Early-Middle Cambrian (Stage 4-5) extinction. *Geology* 42, 543-546.

Jourdan, F., Marzoli, A., Bertrand, H., Cirilli, S., Tanner, L. H., Kontak, D. J., McHone, G., Renne, P. R. & Bellieni, G. (2009b). 40Ar/39Ar ages of CAMP in North America: Implications for the Triassic–Jurassic boundary and the 40K decay constant bias. *Lithos* 110, 167-180.

Jourdan, F., Matzel, J. P. & Renne, P. R. (2007c). 39Ar and 37Ar recoil loss during neutron irradiation of sanidine and plagioclase. *Geochimica et Cosmochimica Acta* 71, 2791-2808.

Jourdan, F. & Renne, P. R. (2007). Age calibration of the Fish Canyon sanidine $^{40}Ar/^{39}Ar$ dating standard using primary K–Ar standards. *Geochimica et Cosmochimica Acta* 71, 387-402.

Jourdan, F. & Renne, P. R. (2013). Neutron-induced 37Ar recoil ejection in Ca-rich minerals and implications for 40Ar/39Ar dating. *Geological Society, London, Special Publications* 378, 33-52.

Kelley, S. (2002). Excess Argon in K-Ar and Ar-Ar Geochronology. *Chemical Geology* 188, 1-22.

Kennedy, T., Jourdan, F., Bevan, A. W., Gee, M. M. & Frew, A. (2013). Impact history of the HED parent body (ies) clarified by new 40 Ar/39 Ar analyses of four HED meteorites and one anomalous basaltic achondrite. *Geochimica et Cosmochimica Acta* 115, 162-182.

King, S. D. & Anderson, D. L. (1995). An alternative mechanism of flood basalt formation. *Earth and Planetary Science Letters* 136, 269-279.

Kinman, W. S., Neal, C. R., Davidson, J. P. & Font, L. (2009). The dynamics of Kerguelen Plateau magma evolution: New insights from major element, trace element and Sr isotope microanalysis of plagioclase hosted in Elan Bank basalts. *Chemical Geology* 264, 247-265.

Koppers, A. A. P. (2002). ArArCALC—software for 40 Ar/39 Ar age calculations. *Computers & Geosciences* 28, 605-619.

Korochantseva, E. V., Trieloff, M., Buikin, A. I., Hopp, J. & Meyer, H.-P. (2005). 40Ar/39Ar dating and cosmic-ray exposure time of desert meteorites: Dhofar 300 and Dhofar 007 eucrites and anomalous achondrite NWA 011. *Meteoritics & Planetary Science* 40, 1433-1454.

Kunz, J., Falter, M. & Jessberger, E. K. (1997). Shocked meteorites: Argon-40-argon-39 evidence for multiple impacts. *Meteoritics & Planetary Science* 32, 647-670.

Lanci, L., Tohver, E., Wilson, A. & Flint, S. (2013). Upper Permian magnetic stratigraphy of the lower Beaufort group, Karoo basin. *Earth and Planetary Science Letters* 375, 123-134.

Lanphere, M. A. & Dalrymple, G. B. (1976). Identification of excess 40Ar by the 40Ar/39Ar age spectrum technique. *Earth and Planetary Science Letters* 32, 141-148.

Lassiter, J. C. & DePaolo, D. J. (1997). Plume/lithosphere interaction in the generation of continental and oceanic flood basalts: chemical and isotopic constraints. *Large igneous provinces: Continental, oceanic, and planetary flood volcanism*, 335-355.

Lee, J.-Y., Marti, K., Severinghaus, J. P., Kawamura, K., Yoo, H.-S., Lee, J. B. & Kim, J. S. (2006a). A redetermination of the isotopic abundances of atmospheric Ar. *Geochimica et Cosmochimica Acta* 70, 4507-4512.

Lee, J. K. W., Onstott, T. C., Cashman, K. V., Cumbest, R. J. & Johnson, D. (1991). Incremental heating of hornblende in vacuo: implications for (super 40) Ar/(super 39) Ar geochronology and the interpretation of thermal histories. *Geology (Boulder)* 19, 872-876.

Lee, J. Y., Marti, K., Severinghaus, J. P., Kawamura, K., Yoo, H. S., Lee, J. B. & Kim, J. S. (2006b). A redetermination of the isotopic abundances of atmospheric Ar. *Geochimica Et Cosmochimica Acta* 70, 4507-4512.

Li, Z. X., Zhang, L. & Powell, C. M. (1996). Positions of the East Asian cratons in the Neoproterozoic supercontinent Rodinia. *Australian Journal of Earth Sciences* 43, 593-604.

Luguet, A., Jaques, A. L., Pearson, D. G., Smith, C. B., Bulanova, G. P., Roffey, S. L., Rayner, M. J. & Lorand, J. P. (2009). An integrated petrological, geochemical and Re–Os isotope study of peridotite xenoliths from the Argyle lamproite, Western Australia and implications for cratonic diamond occurrences. *Lithos* 112, 1096-1108.

Luttinen, A. V., Heinonen, J. S., Kurhila, M., Jourdan, F., Manttari, I., Vuori, S. K. & Huhma, H. (2015). Depleted Mantle-sourced CFB Magmatism in the Jurassic Africa-Antarctica Rift: Petrology and 40Ar/39Ar and U/Pb Chronology of the Vestfjella Dyke Swarm, Dronning Maud Land, Antarctica. *Journal of Petrology* 56, 919-952.

Mahoney, J. J., Storey, M., Duncan, R. A., Spencer, K. J. & Pringle, M. (1993). Geochemistry and geochronology of Leg 130 basement lavas: nature and origin of the Ontong Java Plateau. *Proceedings of the Ocean Drilling Program, Scientific Results*: Ocean Drilling Program, Texas A&M University College Station, TX, 3-22.

Mark, D. F., Stuart, F. M. & de Podesta, M. (2011). New high-precision measurements of the isotopic composition of atmospheric argon. *Geochimica et Cosmochimica Acta* 75, 7494-7501.

Marshall, P. E., Widdowson, M. & Murphy, D. T. (2016). The Giant Lavas of Kalkarindji: rubbly pāhoehoe lava in an ancient continental flood basalt province. *Palaeogeography, Palaeoclimatology, Palaeoecology* 441, 22-37.

McArthur, J. M., Howarth, R. J. & Bailey, T. R. (2001). Strontium Isotope Stratigraphy: LOWESS Version 3: Best Fit to the Marine Sr-Isotope Curve for 0–509 Ma and Accompanying Look-up Table for Deriving Numerical Age. *The Journal of Geology* 109, 155-170.

McClintock, M., Marsh, J. S. & White, J. D. L. (2007). Compositionally diverse magmas erupted close together in space and time within a Karoo flood basalt crater complex. *Bulletin of Volcanology* 70, 923-946.

McClintock, M. & White, J. D. L. (2005). Large phreatomagmatic vent complex at Coombs Hills, Antarctica: Wet, explosive initiation of flood basalt volcanism in the Ferrar-Karoo LIP. *Bulletin of Volcanology* 68, 215-239.

McDougall, I. (1961). Determination of the age of a basic igneous intrusion by the potassium–argon method. *Nature* 190, 1184-1186.

McDougall, I. (1962). Differentiation of the Tasmanian dolerites: Red Hill dolerite-granophyre association. Boulder, CO: Boulder, CO, United States: Geological Society of America (GSA), 279-315.

McDougall, I. (1963). Potassium-argon age measurements on dolerites from Antarctica and South Africa. *Journal of Geophysical Research* 68, 1535-1545.

McDougall, I. & Green, D. (1964). Excess radiogenic argon in pyroxenes and isotopic ages on minerals from Norwegian eclogites. *Norsk Geologisk Tidsskrift* 44, 183-196.

McDougall, I., Polach, H. & Stipp, J. (1969). Excess radiogenic argon in young subaerial basalts from the Auckland volcanic field, New Zealand. *Geochimica et Cosmochimica Acta* 33, 1485-1520.

McKenzie, D. & Bickle, M. (1988). The volume and composition of melt generated by extension of the lithosphere. *Journal of Petrology* 29, 625-679.

McKenzie, D. & O'Nions, R. (1983). Mantle reservoirs and ocean island basalts. *Nature* 301, 229-231.

Menzies, M., Rogers, N., Tindle, A. & Hawkesworth, C. (1987). Metasomatic and enrichment processes in lithospheric peridotites, an effect of asthenosphere-lithosphere interaction. In: Menzies, M. & Hawkesworth, C. (eds.) *Mantle Metasomatism*: Academic Press, 313-364.

Merle, R., Marzoli, A., Bertrand, H., Reisberg, L., Verati, C., Zimmermann, C., Chiaradia, M., Bellieni, G. & Ernesto, M. (2011). 40Ar/39Ar ages and Sr–Nd–Pb–Os geochemistry of CAMP tholeiites from Western Maranhão basin (NE Brazil). *Lithos* 122, 137-151.

Merle, R., Marzoli, A., Reisberg, L., Bertrand, H., Nemchin, A., Chiaradia, M., Callegaro, S., Jourdan, F., Bellieni, G., Kontak, D., Puffer, J. & McHone, J. G. (2013). Sr, Nd, Pb and Os Isotope Systematics of CAMP Tholeiites from Eastern North America (ENA): Evidence of a Subduction-enriched Mantle Source. *Journal of Petrology* 55, 133-180.

Minor, D. R. & Mukasa, S. B. (1997). Zircon U□Pb and hornblende 40Ar□ 39Ar ages for the Dufek layered mafic intrusion, Antarctica: Implications for the age of the Ferrar large igneous province. *Geochimica et Cosmochimica Acta* 61, 2497-2504.

Molzahn, M., Reisberg, L. & Wörner, G. (1996). Os, Sr, Nd, Pb, O isotope and trace element data from the Ferrar flood basalts, antarctica: evidence for an enriched subcontinental lithospheric source. *Earth and Planetary Science Letters* 144, 529-545.

Morgan, W. J. (1983). Hotspot tracks and the early rifting of the Atlantic. *Tectonophysics* 94, 123-139.

Mortimer, N., Herzer, R., Gans, P., Parkinson, D. & Seward, D. (1998). Basement geology from Three Kings Ridge to West Norfolk Ridge, southwest Pacific Ocean: evidence from petrology, geochemistry and isotopic dating of dredge samples. *Marine Geology* 148, 135-162.

Mory, A. J. & Beere, G. M. (1988). *Geology of the onshore Bonaparte and Ord basins in Western Australia*: State Print. Division.

Müntener, O., Manatschal, G., Desmurs, L. & Pettke, T. (2010). Plagioclase peridotites in ocean–continent transitions: refertilized mantle domains generated by melt stagnation in the shallow mantle lithosphere. *Journal of Petrology* 51, 255-294.

Mutter, J. C., Buck, W. R. & Zehnder, C. M. (1988). Convective partial melting: 1. A model for the formation of thick basaltic sequences during the initiation of spreading. *Journal of Geophysical Research* 93, 1031.

Myers, J. S., Shaw, R. D. & Tyler, I. M. (1996). Tectonic evolution of proterozoic Australia. *Tectonics* 15, 1431-1446.

Neumann, E.-R., Svensen, H., Galerne, C. Y. & Planke, S. (2011). Multistage evolution of dolerites in the Karoo large igneous province, Central South Africa. *Journal of Petrology* 52, 959-984.

Nguuri, T., Gore, J., James, D., Webb, S., Wright, C., Zengeni, T., Gwavava, O. & Snoke, J. (2001). Crustal structure beneath southern Africa and its implications for the formation and evolution of the Kaapvaal and Zimbabwe cratons. *Geophysical Research Letters* 28, 2501-2504.

O'Reilly, S. Y. & Griffin, W. (2013). Mantle Metasomatism. In: Harlov, D. E. & Austrheim, H. (eds.) *Metasomatism and the chemical transformation of rock*: Springer, 471-533.

Olierook, H. K., Merle, R. E. & Jourdan, F. (2017). Toward a Greater Kerguelen Large Igneous Province: Evolving mantle source contributions in and around the Indian Ocean. *Lithos*.

Olierook, H. K., Merle, R. E., Jourdan, F., Sircombe, K., Fraser, G., Timms, N. E., Nelson, G., Dadd, K. A., Kellerson, L. & Borissova, I. (2015). Age and geochemistry of magmatism on the oceanic Wallaby Plateau and implications for the opening of the Indian Ocean. *Geology* 43, 971-974.

Olierook, H. K. H., Jourdan, F., Merle, R. E., Timms, N. E., Kusznir, N. & Muhling, J. R. (2016). Bunbury Basalt: Gondwana breakup products or earliest vestiges of the Kerguelen mantle plume? *Earth and Planetary Science Letters* 440, 20-32.

Onstott, T. C., Phillips, D. & Pringle-Goodell, L. (1991). Laser microprobe measurement of chlorine and argon zonation in biotite. *Chemical Geology* 90, 145-168.

Oostingh, K. F., Jourdan, F., Matchan, E. L. & Phillips, D. (2017). 40Ar/39Ar geochronology reveals rapid change from plume-assisted to stress-dependent volcanism in the Newer Volcanic Province, SE Australia. *Geochemistry, Geophysics, Geosystems* **18,** doi:10.1002/2016GC006601.

Oostingh, K. F., Jourdan, F., Merle, R. & Chiaradia, M. (2016). Spatio-temporal Geochemical Evolution of the SE Australian Upper Mantle Deciphered from the Sr, Nd and Pb Isotope Compositions of Cenozoic Intraplate Volcanic Rocks. *Journal of Petrology* 57, 1509-1530.

Paine, J. H., Nomade, S. & Renne, P. R. (2006). Quantification of 39 Ar recoil ejection from GA1550 biotite during neutron irradiation as a function of grain dimensions. *Geochimica et Cosmochimica Acta* 70, 1507-1517.

Pearce, J. A. (1982). Trace element characteristics of lavas from destructive plate boundaries. *Andesites* 8, 525-548.

Pellas, P., Fiéni, C., Trieloff, M. & Jessberger, E. K. (1997). The cooling history of the Acapulco meteorite as recorded by the 244 Pu and 40 Ar-39 Ar chronometers. *Geochimica et Cosmochimica Acta* 61, 3477-3501.

Phillips, D., Harris, J. & Kiviets, G. (2004). 40 Ar/39 Ar analyses of clinopyroxene inclusions in African diamonds: implications for source ages of detrital diamonds. *Geochimica et Cosmochimica Acta* 68, 151-165.

Phillips, D. & Matchan, E. L. (2013). Ultra-high precision 40Ar/39Ar ages for Fish Canyon Tuff and Alder Creek Rhyolite sanidine: New dating standards required? *Geochimica Et Cosmochimica Acta* 121, 229-239.

Phillips, D., Onstott, T. & Harris, J. (1989). 40Ar/39Ar laser-probe dating of diamond inclusions from the Premier Kimberlite.

Pin, C., Briot, D., Bassin, C. & Poitrasson, F. (1994). Concomitant separation of strontium and samarium-neodymium for isotopic analysis in silicate samples, based on specific extraction chromatography. *Analytica Chimica Acta* 298, 209-217.

Pirajno, F. & Bagas, L. (2008). A review of Australia's Proterozoic mineral systems and genetic models. *Precambrian Research* 166, 54-80.

Pirajno, F. & Hoatson, D. M. (2012). A review of Australia's Large Igneous Provinces and associated mineral systems: Implications for mantle dynamics through geological time. *Ore Geology Reviews* 48, 2-54.

Plank & Langmuir. (1998). The chemical composition of subducting sediment and its consequences for the crust and mantle. *Chemical Geology* 145.

Poldervaart, A. & Hess, H. H. (1951). Pyroxenes in the crystallization of basaltic magma. *The Journal of Geology* 59, 472-489.

Powell, C. M., Li, Z. X., McElhinny, M. W., Meert, J. G. & Park, J. K. (1993). Paleomagnetic constraints on timing of the Neoproterozoic breakup of Rodinia and the Cambrian formation of Gondwana. *Geology*. 21, 889.

Puffer, J. (2001). Contrasting high field strength element contents of continental flood basalts from plume versus reactivated-arc sources. *Geology* 29, 675-678.

Rama, S., Hart, S. & Roedder, E. (1965). Excess radiogenic argon in fluid inclusions. *Journal of Geophysical Research* 70, 509-511.

Rao, N. V. C. & Lehmann, B. (2011). Kimberlites, flood basalts and mantle plumes: New insights from the Deccan Large Igneous Province. *Earth-Science Reviews* 107, 315-324.

Ray, J. S. (2005). Rapid emplacement of the Kerguelen plume–related Sylhet Traps, eastern India: Evidence from40Ar-39Ar geochronology. *Geophysical Research Letters* 32.

Renne, P. R. (2014). Some footnotes to the optimization-based calibration of the 40Ar/39Ar system. *Geological Society, London, Special Publications* 378, 21-31.

Renne, P. R., Balco, G., Ludwig, K. R., Mundil, R. & Min, K. (2011a). Response to the comment by W.H. Schwarz et al. on "Joint determination of K-40 decay constants and Ar-40*/K-40 for the Fish Canyon sanidine standard, and improved accuracy for Ar-40/Ar-39 geochronology" by PR Renne et al. (2010). *Geochimica Et Cosmochimica Acta* 75, 5097-5100.

Renne, P. R., Balco, G., Ludwig, K. R., Mundil, R. & Min, K. (2011b). Response to the comment by WH Schwarz et al. on “Joint determination of 40 K decay constants and 40 Ar∗/40 K for the Fish Canyon sanidine standard, and improved accuracy for 40 Ar/39 Ar geochronology” by PR Renne et al.(2010). *Geochimica et Cosmochimica Acta* 75, 5097-5100.

Renne, P. R., Deino, A. L., Hilgen, F. J., Kuiper, K. F., Mark, D. F., Mitchell, W. S., Morgan, L. E., Mundil, R. & Smit, J. (2013). Time scales of critical events around the Cretaceous-Paleogene boundary. *Science* 339, 684-687.

Renne, P. R. & Norman, E. B. (2001). Determination of the half-life of 37Ar by mass spectrometry. *Physical Review C* 63, 047302.

Renne, P. R., Swisher, C. C., Deino, A. L., Karner, D. B., Owens, T. L. & Depaolo, D. J. (1998). Intercalibration of standards, absolute ages and uncertainties in 40Ar/ 39Ar dating. *Chemical Geology* 145, 117-152.

Richards, M. A. & Duncan, R. A. (1988). Flood basalts and hotspot tracks plume heads and tails. Washington, DC: Washington, DC, United States: American Geophysical Union, 1421.

Riley, T. R. (2005a). Early-Middle Jurassic Dolerite Dykes from Western Dronning Maud Land (Antarctica): Identifying Mantle Sources in the Karoo Large Igneous Province. *Journal of Petrology* 46, 1489-1524.

Riley, T. R. (2005b). Overlap of Karoo and Ferrar Magma Types in KwaZulu-Natal, South Africa. *Journal of Petrology* 47, 541-566.

Ringwood, A. & Green, D. (1966). An experimental investigation of the gabbro-eclogite transformation and some geophysical implications. *Tectonophysics* 3, 383-427.

Robinson, J. A. C. & Wood, B. J. (1998). The depth of the spinel to garnet transition at the peridotite solidus. *Earth and Planetary Science Letters* 164, 277-284.

Roex, A. P. & Reid, D. L. (1978). Geochemistry of Karroo dolerite sills in the Calvinia district, western Cape Province, South Africa. *Contributions to Mineralogy and Petrology* 66, 351-360.

Rollinson, H. R. (1993). *Using geochemical data : evaluation, presentation, interpretation / Hugh R. Rollinson*. Harlow, Essex, England : New York: Longman Scientific & Technical ; Copublished in the U.S. with J. Wiley & Sons.

Royer, J.-Y. & Sandwell, D. T. (1989). Evolution of the eastern Indian Ocean since the Late Cretaceous: Constraints from Geosat altimetry. *Journal of Geophysical Research: Solid Earth* 94, 13755-13782.

Rudnick, R. L. & Fountain, D. M. (1995). Nature and composition of the continental crust: a lower crustal perspective. *Reviews of Geophysics* 33, 267-309.

Saunders, A. D., Storey, M., Kent, R. & Norry, M. (1992). Consequences of plume-lithosphere interactions. *Geological Society, London, Special Publications* 68, 41-60.

Sayers, J., Symonds, P. A., Direen, N. G. & Bernardel, G. (2001). Nature of the continent-ocean transition on the non-volcanic rifted margin of the central Great Australian Bight. *Geological Society, London, Special Publications* 187, 51-76.

Schmidt, P. W. & McDougall, I. (1977). Palaeomagnetic and potassium-argon dating studies of the Tasmanian Dolerites. *Journal of the Geological Society of Australia* 24, 321-328.

Schoene, B., Guex, J., Bartolini, A., Schaltegger, U. & Blackburn, T. J. (2010). Correlating the end-Triassic mass extinction and flood basalt volcanism at the 100 ka level. *Geology* 38, 387-390.

Schoene, B., Samperton, K. M., Eddy, M. P., Keller, G., Adatte, T., Bowring, S. A., Khadri, S. F. R. & Gertsch, B. (2015). U-Pb geochronology of the Deccan Traps and relation to the end-Cretaceous mass extinction. *Science* 347, 182-184.

Scibiorski, E., Tohver, E. & Jourdan, F. (2015). Rapid cooling and exhumation in the western part of the Mesoproterozoic Albany-Fraser Orogen, Western Australia. *Precambrian Research* 265, 232-248.

Sell, B., Ovtcharova, M., Guex, J., Bartolini, A., Jourdan, F., Spangenberg, J. E., Vicente, J.-C. & Schaltegger, U. (2014). Evaluating the temporal link between the Karoo LIP and climatic–biologic events of the Toarcian Stage with high-precision U–Pb geochronology. *Earth and Planetary Science Letters* 408, 48-56.

Shaw, D. M. (1970). Trace element fractionation during anatexis. *Geochimica et Cosmochimica Acta* 34, 237-243.

Shaw, R., Wellman, P., Gunn, P., Whitaker, A., Tarlowski, C. & Morse, M. (1995). Australian crustal elements map. *AGSO Res. Newslett* 23, 1-3.

Sheppard, S., Tyler, I. M., Griffin, T. J. & Taylor, W. R. (1999). Palaeoproterozoic subduction-related and passive margin basalts in the Halls Creek Orogen, northwest Australia. *Australian Journal of Earth Sciences* 46, 679-690.

Simpson, E. (1954). On the graphical representation of differentiation trends in igneous rocks. *Geological Magazine* 91, 238-244.

Smith, R., Eriksson, P. & Botha, W. (1993). A review of the stratigraphy and sedimentary environments of the Karoo-aged basins of Southern Africa. *Journal of African Earth Sciences (and the Middle East)* 16, 143-169.

Smithies, R. H., Kirkland, C. L., Korhonen, F. J., Aitken, A. R. A., Howard, H. M., Maier, W. D., Wingate, M. T. D., Quentin de Gromard, R. & Gessner, K. (2015). The Mesoproterozoic thermal evolution of the Musgrave Province in central Australia — Plume vs. the geological record. *Gondwana Research* 27, 1419-1429.

Sobolev, S. V., Sobolev, A. V., Kuzmin, D. V., Krivolutskaya, N. A., Petrunin, A. G., Arndt, N. T., Radko, V. A. & Vasiliev, Y. R. (2011). Linking mantle plumes, large igneous provinces and environmental catastrophes. *Nature* 477, 312-316.

Spell, T. L. & McDougall, I. (2003). Characterization and calibration of 40Ar/ 39Ar dating standards. *Chemical Geology* 198, 189-211.

Spera, F. J. & Bohrson, W. A. (2001). Energy-constrained open-system magmatic processes I: General model and energy-constrained assimilation and fractional crystallization (EC-AFC) formulation. *Journal of Petrology* 42, 999-1018.

Stacey, J. t. & Kramers, J. (1975). Approximation of terrestrial lead isotope evolution by a two-stage model. *Earth and Planetary Science Letters* 26, 207-221.

Stevens, M. & Apak, S. (1999). Empress 1 and 1A well completion report, Savory Sub-basin, Western Australia, with notes on petroleum and mineral potential. *Geological Survey of Western Australia Record* 4.

Stone, P., Richards, P., Kimbell, G., Esser, R. & Reeves, D. (2008). Cretaceous dykes discovered in the Falkland Islands: implications for regional tectonics in the South Atlantic. *Journal of the Geological Society* 165, 1-4.

Storey, M., Saunders, A., Tarney, J., Gibson, I., Norry, M., Thirlwall, M., Leat, P., Thompson, R. & Menzies, M. (1989). Contamination of Indian Ocean asthenosphere by the Kerguelen–Heard mantle plume. *Nature* 338, 574-576.

Storey, M., Saunders, A., Tarney, J., Leat, P., Thirlwall, M., Thompson, R., Menzies, M. & Marriner, G. (1988). Geochemical evidence for plume—mantle interactions beneath Kerguelen and Heard Islands, Indian Ocean. *Nature* 336, 371-374.

Sun, S. s. & McDonough, W. F. (1989). Chemical and isotopic systematics of oceanic basalts: implications for mantle composition and processes. *Geological Society, London, Special Publications* 42, 313-345.

Svensen, H., Corfu, F., Polteau, S., Hammer, Ø. & Planke, S. (2012). Rapid magma emplacement in the Karoo Large Igneous Province. *Earth and Planetary Science Letters* 325-326, 1-9.

Svensen, H., Planke, S., Chevallier, L., Malthe-Sørenssen, A., Corfu, F. & Jamtveit, B. (2007). Hydrothermal venting of greenhouse gases triggering Early Jurassic global warming. *Earth and Planetary Science Letters* 256, 554-566.

Sweeney, R., Duncan, A. & Erlank, A. (1994). Geochemistry and petrogenesis of central Lebombo basalts of the Karoo igneous province. *Journal of Petrology* 35, 95-125.

Sweeney, R. & Watkeys, M. (1990). A possible link between Mesozoic lithospheric architecture and Gondwana flood basalts. *Journal of African Earth Sciences (and the Middle East)* 10, 707-716.

Sweet, I., Mendum, J., Bultitude, R. & Morgan, C. (1974). The geology of the southern Victoria River region, Northern Territory. *Bur. Miner. Resour. Aust. Rep* 167.

Takahahshi, E., Nakajima, K. & Wright, T. L. (1998). Origin of the Columbia River basalts: melting model of a heterogeneous plume head. *Earth and Planetary Science Letters* 162, 63-80.

Tanaka, T., Togashi, S., Kamioka, H., Amakawa, H., Kagami, H., Hamamoto, T., Yuhara, M., Orihashi, Y., Yoneda, S., Shimizu, H., Kunimaru, T., Takahashi, K., Yanagi, T., Nakano, T., Fujimaki, H., Shinjo, R., Asahara, Y., Tanimizu, M. & Dragusanu, C. (2000). JNdi-1: a neodymium isotopic reference in consistency with LaJolla neodymium. *Chemical Geology* 168, 279-281.

Tankard, A., Welsink, H., Aukes, P., Newton, R. & Stettler, E. (2009). Tectonic evolution of the Cape and Karoo basins of South Africa. *Marine and Petroleum Geology* 26, 1379-1412.

Taylor, S. R. & McLennan, S. M. (1985). *The continental crust: its composition and evolution*. Palo Alto, CA: Blackwell Scientific Publisher.

Thomas, R., Jacobs, J., Horstwood, M., Ueda, K., Bingen, B. & Matola, R. (2010). The Mecubúri and Alto Benfica groups, NE Mozambique: Aids to unravelling ca. 1 and 0.5 Ga events in the east African orogen. *Precambrian Research* 178, 72-90.

Todt, W., Cliff, R. A., Hanser, A. & Hofmann, A. (1996). Evaluation of a 202Pb–205Pb Double Spike for High-Precision Lead Isotope Analysis. *Earth processes: reading the isotopic code*, 429-437.

Tohver, E., Lanci, L., Wilson, A., Hansma, J. & Flint, S. (2015). Magnetostratigraphic constraints on the age of the lower Beaufort Group, western Karoo basin, South Africa, and a critical analysis of existing U-Pb geochronological data. *Geochemistry, Geophysics, Geosystems* 16, 3649-3665.

Trieloff, M., Jessberger, E. K., Herrwerth, I., Hopp, J., Fiéni, C., Ghélis, M., Bourot-Denise, M. & Pellas, P. (2003). Structure and thermal history of the H-chondrite parent asteroid revealed by thermochronometry. *Nature* 422, 502-506.

Turner, G. & Cadogan, P. (1974). Possible effects of 39Ar recoil in 40Ar-39Ar dating. *Lunar and Planetary Science Conference Proceedings*, 1601-1615.

Turner, S. & Hawkesworth, C. (1995). The nature of the sub-continental mantle: constraints from the major-element composition of continental flood basalts. *Chemical Geology* 120, 295-314.

Turner, S., Hawkesworth, C., Gallagher, K., Stewart, K., Peate, D. & Mantovani, M. (1996). Mantle plumes, flood basalts, and thermal models for melt generation beneath continents: assessment of a conductive heating model and application to the Parana. *Journal of Geophysical Research: Solid Earth* 101, 11503-11518.

Ueda, K., Jacobs, J., Thomas, R. J., Kosler, J., Jourdan, F. & Matola, R. (2012). Delamination-induced late-tectonic deformation and high-grade metamorphism of the Proterozoic Nampula Complex, northern Mozambique. *Precambrian Research* 196, 275-294.

Veevers, J. (2001). Atlas of billion-year earth history of Australia and neighbours in Gondwanaland.

Veevers, J. J. (2004). Gondwanaland from 650–500 Ma assembly through 320 Ma merger in Pangea to 185–100 Ma breakup: supercontinental tectonics via stratigraphy and radiometric dating. *Earth-Science Reviews* 68, 1-132.

Veevers, J. J. (2006). Updated Gondwana (Permian–Cretaceous) earth history of Australia. *Gondwana Research* 9, 231-260.

Veevers, J. J. (2012). Reconstructions before rifting and drifting reveal the geological connections between Antarctica and its conjugates in Gondwanaland. *Earth-Science Reviews* 111, 249-318.

Verati, C., Bertrand, H. & Feraud, G. (2005). The farthest record of the Central Atlantic Magmatic Province into West Africa craton: Precise Ar/Ar dating and geochemistry of Taoudenni basin intrusives (northern Mali). *Earth and Planetary Science Letters* 235, 391-407.

Verati, C. & Jourdan, F. (2013). Modelling effect of sericitization of plagioclase on the 40K/40Ar and 40Ar/39Ar chronometers: implication for dating basaltic rocks and mineral deposits. *Geological Society, London, Special Publications* 378, 155-174.

Villa, I. M. (1997). Direct determination of 39 Ar recoil distance. *Geochimica et Cosmochimica Acta* 61, 689-691.

Villa, I. M., Grobéty, B., Kelley, S. P., Trigila, R. & Wieler, R. (1996). Assessing Ar transport paths and mechanisms in the McClure Mountains hornblende. *Contributions to Mineralogy and Petrology* 126, 67-80.

Wade, B. P., Kelsey, D. E., Hand, M. & Barovich, K. M. (2008). The Musgrave Province: Stitching north, west and south Australia. *Precambrian Research* 166, 370-386.

Walker, F. & Poldervaart, A. (1949). Karroo dolerites of the Union of South Africa. *Geological Society of America Bulletin* 60, 591-706.

Wang, S., McDougall, I., Tetley, N. & Harrison, T. M. (1980). 40Ar/39Ar age and thermal history of the Kirin chondrite. *Earth and Planetary Science Letters* 49, 117-131.

Wang, X.-C., Wilde, S. A., Xu, B. & Pang, C.-J. (2016). Origin of arc-like continental basalts: Implications for deep-Earth fluid cycling and tectonic discrimination. *Lithos* 261, 5-45.

Westrich, H., Stockman, H. & Eichelberger, J. (1988). Degassing of rhyolitic magma during ascent and emplacement. *Journal of Geophysical Research: Solid Earth* 93, 6503-6511.

White, R. & McKenzie, D. (1989a). Magmatism at rift zones: The generation of volcanic continental margins and flood basalts. *Journal of Geophysical Research: Solid Earth (1978–2012)* 94, 7685-7729.

White, R. S. & McKenzie, D. P. (1989b). Volcanism at Rifts. *Scientific American* 261, 62-71.

White, R. V. & Saunders, A. D. (2005). Volcanism, impact and mass extinctions: incredible or credible coincidences?☆. *Lithos* 79, 299-316.

Wingate, M. T. D., Pirajno, F. & Morris, P. A. (2004). Warakurna large igneous province: A new Mesoproterozoic large igneous province in west-central Australia. *Geology* 32, 105.

Winter, J. D. N. (2010). *Principles of Igneous and Metamorphic Petrology*: Prentice Hall.

Woodhead, J., Hergt, J., Davidson, J. & Eggins, S. (2001). Hafnium isotope evidence for 'conservative'element mobility during subduction zone processes. *Earth and Planetary Science Letters* 192, 331-346.

Youssof, M., Thybo, H., Artemieva, I. & Levander, A. (2013). Moho depth and crustal composition in Southern Africa. *Tectonophysics* 609, 267-287.

Zartman, R. E. & Haines, S. M. (1988). The plumbotectonic model for Pb isotopic systematics among major terrestrial reservoirs. A case for bi-directional transport. . *Geochimica et Cosmochimica Acta* 52, 1327-1339.

Zeng, Z., Niedermann, S., Chen, S., Wang, X. & Li, Z. (2015). Noble gases in sulfide deposits of modern deep-sea hydrothermal systems: Implications for heat fluxes and hydrothermal fluid processes. *Chemical Geology* 409, 1-11.

Zhao, J.-x. & McCulloch, M. T. (1993). Melting of a subduction-modified continental lithospheric, mantle: Evidence from Late Proterozoic mafic dike swarms, in central Australia. *Geology* 21, 463-466.

Zhao, X., Coe, R. S., Gilder, S. A. & Frost, G. M. (1996). Palaeomagnetic constraints on the palaeogeography of China: Implications for Gondwanaland∗. *Australian Journal of Earth Sciences* 43, 643-672.

Zindler, A. & Hart, S. (1986). Chemical geodynamics. *Annual review of earth and planetary sciences* 14, 493-571.

APPENDIX A: First Author Journal Publications

This Appendix presents all Statement of Authorship forms for all submitted papers.

Statement of Authorship

Title of Paper	The Kalkarindji Large Igneous Province, Australia: Petrogenesis of the oldest and most compositionally homogenous province of the Phanerozoic	
Publication Status	Published	Accepted for Publication
	Submitted for Publication	Publication Style
Publication Details	Bryant D. Ware, Fred Jourdan, Renaud Merle, Massimo Chiaradia, Kyle Hodges (2017a). The Kalkarindji Large Igneous Province, Australia: Petrogenesis of the oldest and most compositionally homogenous province of the Phanerozoic. *Journal of Petrology*; under review.	

Author Contributions

By signing the Statement of Authorship, each author certifies that their stated contribution to the publication is accurate and that permission is granted for the publication to be included in the candidate's thesis.

Name of Principal Author (Candidate)	Bryant Ware		
Contribution to the Paper	Bryant Ware produced the majority of the data, did most of the drafting of the manuscript, and the interpretation of the results.		
Overall percentage (%)	70		
Signature	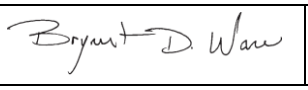	Date	April 27th, 2017

Name of Principal Author (Candidate)	Fred Jourdan		
Contribution to the Paper	Fred Jourdan is principal supervisor and assisted with the experiments, the drafting of the document, and the interpretation of the results.		
Overall percentage (%)	10		
Signature	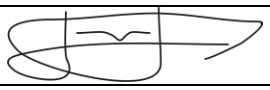	Date	April 27th, 2017

Name of Principal Author (Candidate)	Renaud Merle		
Contribution to the Paper	Renaud Merle assisted with the interpretation of the results.		
Overall percentage (%)	10		
Signature	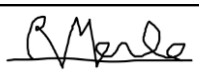	Date	April 27th, 2017

Name of Principal Author (Candidate)	Massimo Chiaradia		
Contribution to the Paper	Massimo Chiaradia was responsible for the Sr, Nd and Pb isotope analysis		
Overall percentage (%)	5		
Signature		Date	April 27th, 2017

Name of Principal Author (Candidate)	Kyle Hodges		
Contribution to the Paper	Kyle Hodges processed some of the samples for isotope analysis during his honours project		
Overall percentage (%)	5		
Signature		Date	April 27th, 2017

Statement of Authorship

Title of Paper	High Precision $^{40}Ar/^{39}Ar$ Geochronology of Large Igneous Provinces: The Tasmanian Dolerites of the Ferrar Continental Flood Basalt.	
Publication Status	Published	Accepted for Publication
	Submitted for Publication	Publication Style
Publication Details	Bryant D. Ware, Fred Jourdan, Massimo Chiaradia. High Precision $^{40}Ar/^{39}Ar$ Geochronology of Large Igneous Provinces: The Tasmanian Dolerites of the Ferrar Continental Flood Basalt. *Journal of Petrology*; To be Submitted.	

Author Contributions

By signing the Statement of Authorship, each author certifies that their stated contribution to the publication is accurate and that permission is granted for the publication to be included in the candidate's thesis.

Name of Principal Author (Candidate)	Bryant Ware		
Contribution to the Paper	Bryant Ware produced the majority of the data, did most of the drafting of the manuscript, and the interpretation of the results.		
Overall percentage (%)	70		
Signature	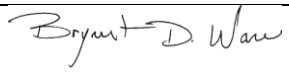	Date	April 27th, 2017

Name of Principal Author (Candidate)	Fred Jourdan		
Contribution to the Paper	Fred Jourdan is principal supervisor and assisted with the experiments, the drafting of the document, and the interpretation of the results.		
Overall percentage (%)	25		
Signature	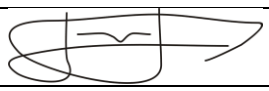	Date	April 27th, 2017

Name of Principal Author (Candidate)	Massimo Chiaradia		
Contribution to the Paper	Massimo Chiaradia was responsible for the Sr, Nd and Pb isotope analysis		
Overall percentage (%)	5		
Signature		Date	April 27th, 2017

Statement of Authorship

Title of Paper	Primary Hydrous Minerals from the Karoo LIP magmas: Evidence for a Hydrated Source component.	
Publication Status	Published	Accepted for Publication
	Submitted for Publication	Publication Style
Publication Details	Bryant D. Ware, Fred Jourdan, Eric Tohver, Kamila Fernandes, Massimo Chiaradia. Primary Hydrous Minerals from the Karoo LIP magmas: Evidence for a Hydrated Source component. *Earth and Planetary Science Letters*; To be Submitted.	

Author Contributions

By signing the Statement of Authorship, each author certifies that their stated contribution to the publication is accurate and that permission is granted for the publication to be included in the candidate's thesis.

Name of Principal Author (Candidate)	Bryant Ware		
Contribution to the Paper	Bryant Ware produced the majority of the data, did most of the drafting of the manuscript, and the interpretation of the results.		
Overall percentage (%)	70		
Signature	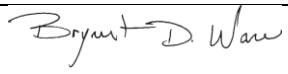	Date	April 27th, 2017

Name of Principal Author (Candidate)	Fred Jourdan		
Contribution to the Paper	Fred Jourdan is principal supervisor and assisted with the experiments, the drafting of the document, and the interpretation of the results.		
Overall percentage (%)	10		
Signature	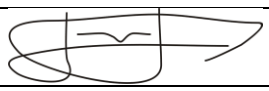	Date	April 27th, 2017

Name of Principal Author (Candidate)	Eric Tohver		
Contribution to the Paper	Eric Tohver collected the samples and assisted with the interpretation of the results		
Overall percentage (%)	10		
Signature		Date	April 27th, 2017

Name of Principal Author (Candidate)	Kamila Fernandes		
Contribution to the Paper	Kamila Fernandes processed the samples for $^{40}Ar/^{39}Ar$ geochronology analysis during her honours project		
Overall percentage (%)	5		
Signature		Date	April 27th, 2017

Name of Principal Author (Candidate)	Massimo Chiaradia		
Contribution to the Paper	Massimo Chiaradia was responsible for the Sr, Nd and Pb isotope analysis		
Overall percentage (%)	5		
Signature		Date	April 27th, 2017

Statement of Authorship

Title of Paper	$^{40}Ar/^{39}Ar$ Geochronology of Terrestrial Pyroxene.	
Publication Status	Published	Accepted for Publication
	Submitted for Publication	Publication Style
Publication Details	Bryant D. Ware and Fred Jourdan. $^{40}Ar/^{39}Ar$ Geochronology of Terrestrial Pyroxene. *Geochimica et Cosmochimica Acta*; To be Submitted.	

Author Contributions

By signing the Statement of Authorship, each author certifies that their stated contribution to the publication is accurate and that permission is granted for the publication to be included in the candidate's thesis.

Name of Principal Author (Candidate)	Bryant Ware		
Contribution to the Paper	Bryant Ware produced the majority of the data, did most of the drafting of the manuscript, and the interpretation of the results.		
Overall percentage (%)	75		
Signature	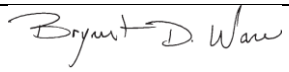	Date	April 27th, 2017

Name of Principal Author (Candidate)	Fred Jourdan		
Contribution to the Paper	Fred Jourdan is principal supervisor and assisted with the experiments, models, the drafting of the document, and the interpretation of the results.		
Overall percentage (%)	25		
Signature	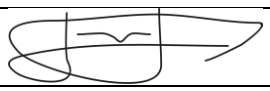	Date	April 27th, 2017

APPENDIX B: Supplementary Data Chapter 2 – Major and Trace Element Data, Kalkarindji Continental Flood Basalt Province

Table B1: Major and trace element analyses of basaltic and doleritic dykes, lavas, and sills from the Kalkarindji CFB province (Antrim Plateau Volcanics).

Type: Antrim Drill Core ANTD001 (Basalt)				Location: WGS 84	Zone 52	572022mN 7978167mE						
Sample	**A001-104.3**	**A001-149.5**	**A001-198.65**	**A001-250.25**	**A001-308.4**	**A001-348.7**	**A001-395.05**	**A001-415.8**	**A001-450.2**	**A001-465.6**	**A001-432.7**	**A002-117.95**
Major Elements (wt. %):												
SiO_2	52.71	54.9	55.66	54.51	52.66	54.58	52.54	50.96	52.88	53.03	53.23	52.46
Al_2O_3	14.99	15.46	14.23	15.67	14.23	13.4	14.22	12.73	13.46	13.31	13.27	14.72
FeO_{tot}	10.42	9.32	9.57	9.25	11.22	12.4	11.23	13.09	13.25	13.63	13.68	10.85
MgO	5.10	5.04	4.98	5.01	5.08	3.95	5.55	4.04	4.41	4.26	4.04	5.7
CaO	7.88	8.17	7.13	9.02	6.92	6.04	6.96	7.5	7.29	7.26	6.76	6.29
Na_2O	3.33	3.03	3.46	2.48	4.33	4.74	4.94	4.71	3.72	3.34	4.17	4.44
K_2O	1.72	1.7	1.95	1.54	2.27	1.49	1.56	1.65	1.77	1.78	1.95	1.87
TiO_2	1.28	0.98	1.07	1.02	1.35	1.43	1.11	1.48	1.48	1.55	1.59	1.25
P_2O_5	0.15	0.14	0.16	0.14	0.16	0.13	0.1	0.17	0.17	0.18	0.19	0.14
MnO	0.19	0.13	0.15	0.14	0.18	0.17	0.16	0.18	0.2	0.2	0.2	0.16
LOI	1.65	1.24	1.37	0.85	1.5	1.62	1.93	2.82	1.41	1.24	1.39	2.13
H_2O-Total	99.42	100.11	99.73	99.63	99.9	99.95	100.3	99.33	100.04	99.78	100.47	100.01
Mg #	53.28	55.75	54.80	55.79	51.34	42.60	53.52	41.83	43.68	42.14	40.76	55.04
Trace Elements (ppm):												
La	20.50	22.02	25.51	21.87	21.95	22.83	15.97	24.07	23.73	25.26	24.94	19.03
Ce	44.11	46.34	53.52	46.22	46.32	49.2	34.38	51.44	50.61	54.18	54.07	40.58
Pr	5.27	5.327	6.225	5.45	5.549	5.634	4.121	6.087	6.012	6.396	6.472	4.80
Nd	20.85	20.94	24.45	21.43	22.47	22.51	16.9	24.2	24.2	25.72	26.24	19.63
Sm	4.82	4.61	5.46	4.77	5.15	5.24	3.88	5.55	5.51	5.87	5.97	4.47
Eu	1.38	1.26	1.32	1.27	1.53	1.3	1.16	1.51	1.54	1.65	1.6	1.34
Gd	5.18	4.98	5.96	5.04	5.53	5.5	4.39	6.12	6.29	6.38	6.63	4.93
Tb	0.92	0.83	1.02	0.88	0.97	0.93	0.75	1.05	1.07	1.10	1.11	0.85
Dy	6.03	5.6	6.52	5.78	6.68	6.23	4.97	6.99	7.11	7.3	7.5	5.54
Ho	1.17	1.08	1.26	1.07	1.25	1.19	0.98	1.34	1.35	1.4	1.43	1.07
Er	3.33	3.16	3.67	3.11	3.67	3.44	2.82	3.84	3.85	4.06	4.29	3.2
Yb	3.18	2.91	3.34	2.97	3.48	3.16	2.63	3.73	3.56	3.73	3.88	2.99
Lu	0.45	0.435	0.482	0.433	0.514	0.46	0.384	0.509	0.513	0.534	0.569	0.425
Rb	65.45	77.02	87.09	69.49	97.61	64.03	73.08	60.08	73.48	60.78	84.98	63.46
Ba	311.4	303.6	340	303.1	359.8	315.9	245.7	240.8	252	285.7	262	256.5
Th	7.85	9.59	11.2	9.24	8.15	11.67	8.14	9.85	9.27	10.09	9.99	6.88
U	1.23	1.7	2.07	1.56	1.35	1.83	1.3	1.63	1.58	1.79	1.67	1.12
Nb	9.45	8.77	9.87	8.73	9.16	9.03	6.84	10.09	9.88	10.66	10.86	7.58
K	14762	14410	16620	13065	19372	12740	13317	14388	15101	15206	16568	16038
Ta	0.92	0.8	0.9	0.73	0.68	0.74	0.59	0.71	0.7	0.78	0.75	0.57

Table B1: Continued

Type: Antrim Drill Core ANTD001(Basalt)												
Sample	**A001-104.3**	**A001-149.5**	**A001-198.65**	**A001-250.25**	**A001-308.4**	**A001-348.7**	**A001-395.05**	**A001-415.8**	**A001-450.2**	**A001-465.6**	**A001-432.7**	**A002-117.95**
Trace Element (ppm): Continued												
Pb												
Sr	160	159	146	161	147	158	139	144	123	140	101	151
P	676.7	623.8	716.9	624.4	717.8	584.3	448.8	779.3	762.4	808.3	848.6	631.2
Hf	4.45	4.05	4.74	4.17	4.76	4.47	3.24	4.6	4.55	5.02	5.05	3.94
Zr	160.9	153	169.7	151.5	173.7	150.5	114.4	166.2	164.6	177.6	177.8	145.7
Ti	7933	5998	6585	6248	8319	8829	6842	9319	9118	9562	9755	7741
Tb	0.917	0.83	1.015	0.877	0.969	0.926	0.748	1.046	1.07	1.098	1.109	0.848
Y	29.1	27.75	30.4	27.9	31.3	30.22	24.55	33.8	33.7	35.58	36.76	27.84
Co	37	30	32	32	37	40	41		42	40	41	
Cr	85	134	113	125	69	19	71		24	16	20	
Cu	49	38	71	57	41	27	52		62	27	57	
Ni	50	70	49	47	43	20	46		21	16	20	
V	262	187	200	188	287	359	292		309	311	316	
Zn	87	97	105	87	74	91	85		147	115	128	

Table B1: Continued

Type: Antrim Drill Core ANTD002 (Basalt)				Location: WGS 84	Zone 52	564818mN	7995173mE					
Sample	**A002-157.8**	**A002-179.4**	**A002-201.75**	**A002-224.8**	**A002-247.5**	**A002-274**	**A002-302.4**	**A002-327.4**	**A002-334.0**	**A002-349.8**	**A002-379.5**	**A002-404.05**
Major Elements (wt. %):												
SiO_2	55.48	55.57	56.31	55.61	52.51	52.51	52.94	52.92	53.25	52.7	52.99	53.24
Al_2O_3	15.51	14.31	14.73	15.12	15.57	15.49	15.03	14.17	14.23	14.01	14.3	14.26
FeO_{tot}	9.26	9.34	9.05	8.61	10.47	10.43	11.03	11.33	11.64	10.98	11.46	11.34
MgO	4.35	5.05	4.63	6.02	6.11	6.12	5.68	5.32	4.95	6.69	5.67	5.67
CaO	7.61	7.77	7.43	8.35	9.71	9.71	9.41	6.83	4.88	4.71	7.16	8.82
Na_2O	3.29	3.09	3.05	2.69	2.36	2.39	2.44	4.27	4.46	5.06	3.73	2.7
K_2O	1.84	1.85	1.95	1.57	1.14	1.14	1.29	1.81	3.23	1.7	1.8	1.37
TiO_2	1.07	0.99	0.95	0.83	1.09	1.08	1.23	1.37	1.32	1.05	1.16	1.1
P_2O_5	0.15	0.14	0.15	0.12	0.13	0.13	0.15	0.17	0.17	0.11	0.11	0.11
MnO	0.13	0.15	0.16	0.14	0.15	0.15	0.17	0.2	0.25	0.27	0.17	0.18
LOI	1.62	1.6	1.5	1.13	0.35	0.41	0.4	1.7	1.58	2.56	1.57	0.77
H_2O-												
Total	100.31	99.86	99.91	100.19	99.59	99.56	99.77	100.09	99.96	99.84	100.12	99.56
Mg #	52.26	55.75	54.38	61.96	57.62	57.76	54.54	52.25	49.77	58.67	53.55	53.81
Trace Elements (ppm):												
La	23.9	25.05	25.61	21.06	20.93	16.97	19.13	20.04	27.24	14.46	18.99	17.46
Ce	50.04	51.09	52.15	45.04	43.66	36.78	40.61	43.86	54.95	32.23	38.75	37.19
Pr	5.861	5.909	6.176	5.143	5.169	4.267	4.819	5.254	6.22	3.793	4.625	4.207
Nd	23.44	23.21	23.65	20.22	20.21	17.79	19.4	21.88	24.01	15.61	18.05	16.94
Sm	5.15	5.16	5.22	4.54	4.56	4.11	4.53	5.08	5.18	3.67	4.2	3.89
Eu	1.3	1.32	1.31	1.19	1.22	1.18	1.33	1.4	1.37	1.02	1.18	1.1
Gd	5.43	5.48	5.45	4.71	5.03	4.36	4.95	5.66	5.44	3.98	4.43	4.42
Tb	0.906	0.915	0.914	0.83	0.84	0.769	0.85	0.947	0.923	0.682	0.763	0.745
Dy	6.01	5.9	6.1	5.15	5.54	5.01	5.66	6.38	5.9	4.66	5.34	4.89
Ho	1.17	1.17	1.14	0.99	1.07	1	1.11	1.26	1.15	0.9	1.02	0.96
Er	3.34	3.35	3.31	2.86	3.11	2.96	3.2	3.59	3.42	2.57	2.95	2.86
Yb	3.24	3.16	3.19	2.77	2.89	2.79	2.98	3.37	3.09	2.48	2.71	2.59
Lu	0.469	0.456	0.461	0.395	0.428	0.395	0.454	0.504	0.453	0.375	0.398	0.372
Rb	82.04	84.46	90.99	71.72	69.19	46.8	49.81	58.09	78.53	31.6	78.22	58.96
Ba	322.2	321	337.4	281	279.5	262.9	273.1	280.8	326.2	135.9	241.7	216.1
Th	10.64	10.57	11.56	9.51	9.19	6.13	6.76	8.17	9.53	7.48	8.67	8.05
U	1.89	1.96	2.1	1.76	1.68	1	1.08	1.31	1.59	1.31	1.52	1.45
Nb	8.86	8.44	9.85	8.09	8.12	7.08	7.7	8.92	8.73	6.13	6.98	6.61
K	15625	15780	16603	13273	9638	9646	10898	15450	27583	14673	15341	11646
Ta	0.71	0.67	0.73	0.64	0.65	0.53	0.54	0.64	0.98	0.48	0.58	0.52

Table B1: Continued

Type: Antrim Drill Core ANTD002 (Basalt)												
Sample	**A002-157.8**	**A002-179.4**	**A002-201.75**	**A002-224.8**	**A002-247.5**	**A002-274**	**A002-302.4**	**A002-327.4**	**A002-334.0**	**A002-349.8**	**A002-379.5**	**A002-404.05**
Trace Element (ppm): Continued												
Pb												
Sr	162	146	145	144	153	168	169	147	233	238	157	148
P	669.6	627.7	671.4	533.3	577.8	578.3	666.1	762.8	763.1	499.1	492.8	491.6
Hf	4.55	4.4	4.47	4.04	4	3.67	3.88	4.7	4.22	3.02	3.29	3.23
Zr	165	160.5	167	143.4	143.2	134	141.8	169.4	145	106.1	119.2	110.2
Ti	6561	6098	5841	5067	6654	6599	7503	8444	8140	6544	7139	6752
Tb	0.906	0.915	0.914	0.83	0.84	0.769	0.85	0.947	0.923	0.682	0.763	0.745
Y	29.69	29.77	29.56	25.99	27.12	26.37	28.34	30.83	29.37	22.26	25.85	24.52
Co	28	29	29	30	32	39	37	36	37		40	41
Cr	85	121	121	188	151	111	93	62	71		54	68
Cu	22	41	42	38	33	37	40	42	56		52	58
Ni	42	48	48	57	61	61	52	40	38		36	44
V	180	177	174	165	194	239	257	270	287		303	292
Zn	72	79	73	70	72	87	79	76	81		90	83

Table B1: Continued

						Type: AusQuest Antrim Rock Chip Basaltic Outcrop Samples						
Sample	**A002-416.4**	**A002-431.2**	**A002-465.7**	**A002-499.0**	**A002-529.0**	**ANT001**	**ANT002**	**ANT005**	**ANT006**	**ANT008**	**ANT009**	**ANT010**
Rock Type						Basalt	Basalt	Basalt	Basalt	Basalt	Basalt	Basalt
Location						Outcrop	Outcrop	Outcrop	Outcrop	Outcrop	Outcrop	Outcrop
Zone						52	52	52	52	52	52	52
Northing						8319840	8318365	8222530	8206730	8189640	8196370	8196370
Easting						785395	783805	509015	505835	532405	534915	534915
Major Elements (wt. %):												
SiO_2	51.41	52.56	51.61	52.64	53.39	50.7	51.22	52.78	52.54	52.3	53.99	54.29
Al_2O_3	13.82	14.03	13.2	13.45	13.63	14.34	14.23	14.12	13.97	14.07	13.51	13.72
FeO_{tot}	12.32	12.8	13.17	13.42	13.49	10.75	10.97	12.44	11.61	11.83	12.75	12.63
MgO	6.16	5.67	4.46	4.44	4.6	6.71	6.64	5.22	5.77	5.42	4.23	4.58
CaO	3.6	4.57	7.22	7.53	8.37	6.42	6.12	7.59	6.31	6.61	6.26	7.09
Na_2O	4.22	4.71	4.9	3.38	2.77	4.41	2.72	2.94	3.4	3.77	3.83	3.45
K_2O	3	1.8	1.2	1.6	1.44	1.87	3.94	1.81	2.11	1.93	2.02	1.63
TiO_2	1.43	1.43	1.46	1.49	1.52	1.01	1.05	1.27	1.24	1.23	1.37	1.35
P_2O_5	0.14	0.13	0.17	0.17	0.18	0.11	0.1	0.12	0.13	0.13	0.12	0.12
MnO	0.21	0.15	0.17	0.2	0.18	0.13	0.18	0.17	0.14	0.15	0.17	0.17
LOI	3.14	2.31	2.57	1.55	0.69	3.6	2.57	1.12	2.28	2.3	1.37	1.37
H_2O-												
Total	99.45	100.16	100.13	99.87	100.26	100.05	99.74	99.58	99.50	99.74	99.62	100.4
Mg #	53.81	50.79	44.11	43.53	44.28	59.26	58.51	49.43	53.66	51.63	43.60	45.80
Trace Elements (ppm):												
La	19.95	22.86	21.76	23.65	23.98	13.97	12.7	20.46	21.04	22.83	22.94	21.14
Ce	43.3	47.75	47.87	49.91	50.57	28.9	27.06	42.02	43.52	44.67	47.05	43.35
Pr	5.165	5.576	5.668	5.968	6.079	3.585	3.423	5.014	5.251	5.184	5.567	5.174
Nd	20.78	22.35	23.11	24.47	24.6	14.65	13.94	19.77	20.56	20.52	21.69	20.34
Sm	4.84	5	5.29	5.53	5.77	3.49	3.59	4.46	4.5	4.47	4.87	4.58
Eu	1.29	1.36	1.5	1.55	1.56	1.11	1.17	1.22	1.21	1.4	1.32	1.3
Gd	5.4	5.51	6.09	6.19	6.33	4	3.79	4.84	4.95	4.99	5.21	4.97
Tb	0.948	0.911	1.02	1.053	1.118	0.668	0.649	0.804	0.818	0.837	0.869	0.844
Dy	6.39	6.16	6.69	7.15	7.19	4.54	4.36	5.49	5.66	5.62	5.93	5.6
Ho	1.28	1.18	1.32	1.33	1.4	0.89	0.87	1.04	1.08	1.09	1.13	1.08
Er	3.54	3.58	3.92	3.86	3.92	2.54	2.51	3.01	3.09	3.1	3.3	3.11
Yb	3.32	3.23	3.54	3.67	3.67	2.4	2.32	2.88	2.95	2.89	3	2.9
Lu	0.479	0.478	0.515	0.55	0.562	0.348	0.343	0.412	0.434	0.418	0.43	0.422
Rb	85.86	61.29	35.71	71.97	62.26	60.33	57.88	70.84	66.41	67.03	86.84	68.87
Ba	196.1	205.4	214.5	263.1	260.7	190	1234	243	281	327	270	240

Table B1: Continued

						Type: AusQuest Antrim Rock Chip Basaltic Samples						
Sample	**A002-416.4**	**A002-431.2**	**A002-465.7**	**A002-499.0**	**A002-529.0**	**ANT001**	**ANT002**	**ANT005**	**ANT006**	**ANT008**	**ANT009**	**ANT010**
Rock Type						Basalt	Basalt	Basalt	Basalt	Basalt	Basalt	Basalt
Location						Outcrop	Outcrop	Outcrop	Outcrop	Outcrop	Outcrop	Outcrop
Zone						52	52	52	52	52	52	52
Northing						8319840	8318365	8222530	8206730	8189640	8196370	8196370
Easting						785395	783805	509015	505835	532405	534915	534915
Trace Element (ppm): Continued												
Th	10.82	10.55	8.91	9.2	9.56	4.46	4.24	8.49	8.46	7.52	9.32	8.78
U	1.98	1.9	1.43	1.54	1.7	0.78	0.71	1.53	1.56	1.33	1.69	1.55
Nb	8.46	8.16	9.38	9.93	10.16	5.67	5.43	7.19	7.84	7.5	8.01	7.75
K	26195	15474	10351	13697	12171	16277	34046	15456	18235	16645	17293	13841
Ta	0.63	0.63	0.69	1.08	0.68	0.58	0.47	0.54	0.58	0.56	0.61	0.58
Pb												
Sr	98	152	143	126	145	136	743	148	174	287	160	147
P	642.6	587.5	770.8	765.0	799.7	503.3	454.2	538.7	590.6	589.4	540.0	535.6
Hf	4.11	4.08	4.6	4.68	4.76	2.9	2.79	3.51	3.9	3.71	3.82	3.66
Zr	141.8	140.3	160.9	164.8	168.1	99	97	119	133	136	130	137
Ti	9016	8877	9094	9210	9277	6348	6552	7831	7738	7660	8469	8278
Tb	0.948	0.911	1.02	1.053	1.118	0.668	0.649	0.804	0.818	0.837	0.869	0.844
Y	30.92	30.62	33.35	34.49	35.3	23.48	22.77	27.25	28.46	29.09	29.81	28.73
Co				42	40			47.5			43.8	44.7
Cr				19	22			111			52	88
Cu				22	23			16			27	18
Ni				20	21			33			26	28
V				306	306			359			372	383
Zn				107	88			96			100	92

Table B1: Continued

Type: AusQuest Antrim Rock Chip Basaltic Samples

Sample	**ANT011**	**ANT012**	**ANT013**	**ANT015**	**ANT016**	**ANT017**	**ANT020**	**ANT021**	**ANT022**	**ANT023**	**ANT024**	**ANT025**
Rock type	Basalt	Basalt	Basalt	Basalt	Basalt	Basalt	Basalt	Basalt	Basalt	Basalt	Basalt	Basalt
Location	Outcrop	Outcrop	Outcrop	Outcrop	Outcrop	Outcrop	Outcrop	Outcrop	Outcrop	Outcrop	Outcrop	Outcrop
Zone	52	52	52	52	52	52	52	52	52	52	52	52
Northing	8198450	8203280	8203280	8188060	8186720	8162760	8131380	8119350	8038840	8035690	8031315	8026734
Easting	536595	529005	529005	505670	505550	494810	486900	486840	484160	486290	487875	488490
Major Elements (wt. %):												
SiO_2	53.1	52.69	52.17	54.1	54.07	52.78	53.34	52.74	51.78	52.66	52.66	53.61
Al_2O_3	13.9	14.19	14.27	14.11	14.18	14.86	14.79	14.73	13.99	14.11	13.98	13.86
FeO_{tot}	11.45	11.88	10.76	10.64	10.71	9.69	9.88	9.99	12.22	11.59	12.33	11.79
MgO	5.57	5.86	5.52	4.79	5.08	7.3	6.26	6.95	6.46	6.2	5.82	5.63
CaO	7.28	5.17	8.12	7.23	5.88	6.93	8.92	8.48	6.88	7.54	6.87	9.03
Na_2O	3.48	4.43	3.6	3.4	4	3.3	2.08	3.09	2.85	2.95	3.67	2.26
K_2O	1.56	2.08	1.93	2.02	2.18	2.45	1.76	1.28	1.97	2.19	2.02	1.17
TiO_2	1.15	1.21	1.11	1.21	1.16	0.88	0.95	0.91	1.31	1.2	1.32	1.29
P_2O5	0.11	0.12	0.11	0.18	0.17	0.1	0.1	0.1	0.13	0.12	0.13	0.13
MnO	0.18	0.18	0.18	0.16	0.16	0.15	0.14	0.15	0.16	0.16	0.17	0.17
LOI	1.78	2.11	1.77	1.64	2	1.73	1.29	1.28	2.05	0.99	1.07	0.62
H_2O-												
Total	99.56	99.92	99.54	99.48	99.59	100.17	99.51	99.7	99.8	99.71	100.04	99.56
Mg #	53.13	53.47	54.45	51.20	52.50	63.71	59.62	61.85	55.19	55.49	52.38	52.67
Trace Elements (ppm):												
La	18.81	19.16	18.25	32.21	32.01	15.28	18.07	16.41	16.95	15.8	17.66	17.52
Ce	38.28	39.94	37.41	66.23	60.87	31.65	37.26	34.46	35.86	32.98	36.5	35.78
Pr	4.544	4.732	4.441	7.626	7.289	3.75	4.399	4.072	4.378	4.008	4.409	4.291
Nd	18.17	19.1	17.68	28.98	27.66	14.91	17.18	16.05	17.67	15.87	17.83	17.34
Sm	4.13	4.41	4.1	5.8	5.67	3.35	3.91	3.61	4.08	3.72	4.18	4.02
Eu	1.14	1.26	1.17	1.58	1.52	1	0.99	1.02	1.25	1.16	1.27	1.23
Gd	4.48	4.81	4.4	5.83	5.77	3.7	4.2	3.97	4.67	4.18	4.74	4.63
Tb	0.762	0.802	0.749	0.924	0.92	0.61	0.687	0.673	0.782	0.734	0.802	0.769
Dy	5.13	5.44	5	6.01	5.96	4.18	4.7	4.51	5.3	4.87	5.41	5.29
Ho	0.98	1.04	0.95	1.14	1.11	0.81	0.92	0.89	1.02	0.96	1.06	1.04
Er	2.82	2.98	2.77	3.2	3.16	2.37	2.69	2.54	3.02	2.76	3.12	2.91
Yb	2.6	2.77	2.6	3.02	2.85	2.25	2.48	2.32	2.84	2.59	2.83	2.81
Lu	0.377	0.417	0.375	0.435	0.434	0.333	0.354	0.344	0.4	0.388	0.421	0.418
Rb	49.41	74.48	70.74	76.49	76.28	70.23	73.21	48.69	45.56	57.94	59.01	25.08
Ba	216	413	345	351	375	436	243	182	279	272	260	497

Table B1: Continued

Type: AusQuest Antrim Rock Chip Basaltic Samples

Sample	**ANT011**	**ANT012**	**ANT013**	**ANT015**	**ANT016**	**ANT017**	**ANT020**	**ANT021**	**ANT022**	**ANT023**	**ANT024**	**ANT025**
Rock type	Basalt	Basalt	Basalt	Basalt	Basalt	Basalt	Basalt	Basalt	Basalt	Basalt	Basalt	Basalt
Location	Outcrop	Outcrop	Outcrop	Outcrop	Outcrop	Outcrop	Outcrop	Outcrop	Outcrop	Outcrop	Outcrop	Outcrop
Zone	52	52	52	52	52	52	52	52	52	52	52	52
Northing	8198450	8203280	8203280	8188060	8186720	8162760	8131380	8119350	8038840	8035690	8031315	8026734
Easting	536595	529005	529005	505670	505550	494810	486900	486840	484160	486290	487875	488490
Trace Element (ppm): Continued												
Th	7.59	7.93	7.47	10.99	10.46	5.61	7.29	6.95	6.23	5.66	6.33	6.23
U	1.37	1.44	1.34	1.3	1.25	0.82	1.16	1.08	1.13	1.03	1.13	1.11
Nb	6.81	6.96	6.71	10.54	9.85	5.58	6.56	6.03	6.42	5.94	6.32	6.53
K	13402	17871	16570	17328	18751	20867	15027	10907	16943	18635	17158	9935
Ta	0.51	0.55	0.5	0.65	0.62	0.39	0.63	0.46	0.5	0.46	0.51	0.47
Pb												
Sr	142	196	153	167	155	458	137	193	194	187	156	166
P	496.8	542.0	496.5	811.7	768.6	447.7	448.8	448.0	587.7	536.8	580.5	580.3
Hf	3.28	3.51	3.25	4.84	4.69	2.8	3.26	3.03	3.51	3.26	3.57	3.53
Zr	114	117	115	180	169	113	118	126	120	116	123	127
Ti	7134	7507	6882	7495	7205	5412	5857	5599	8135	7373	8096	7910
Tb	0.762	0.802	0.749	0.924	0.92	0.61	0.687	0.673	0.782	0.734	0.802	0.769
Y	25.99	27.01	25.96	29.48	31.18	21.66	24.82	23.16	27.25	25.28	29.98	26.98
Co	44.7		42.7	37.3	38.1	40.7	38.6	40.8		46.1	45.3	43.1
Cr	122		90	111	67	184	228	165		65	150	73
Cu	56		52	36	33	65	22	82		58	29	88
Ni	40		47	30	29	62	75	62		45	44	43
V	323		288	234	240	232	229	238		315	333	333
Zn	160		99	70	81	66	66	89		89	99	113

Table B1: Continued

Type: AusQuest Antrim Rock Chip Basaltic Samples

Sample	**ANT026A**	**ANT027**	**ANT028**	**ANT029**	**ANT044**	**ANT054**	**ANT055**	**ANT056**	**ANT057**	**ANT058**	**ANT060**	**ANT061**
Rock Type	Basalt	Basalt	Basalt	Basalt		Basalt	Basalt	Basalt	Basalt	Basalt	Basalt	Basalt
Location	Outcrop	Outcrop	Outcrop	Outcrop		Outcrop	Outcrop	Outcrop	Outcrop	Outcrop	Outcrop	Outcrop
Zone	52	52	52	52		52	52	52	52	52	52	52
Northing	7989320	7964120	7979210	7983090		8222730	8230460	8281895	8282560	8287988	8256790	8265330
Easting	488000	411270	427000	430680		435890	438580	413450	412860	406900	461890	466600
Major Elements (wt. %):												
SiO_2	52.96	53.36	50.68	53.45	52.92	50.46	52.65	50.17	53.14	56.18	50	50.64
Al_2O_3	14.29	13.62	14.9	14.54	14.22	15.39	14.5	14.77	14.28	13.45	15.39	14.68
FeO_{tot}	11.61	10.46	9.5	10.8	11.15	8.33	9.98	9	11.64	11.86	8.53	8.66
MgO	5.63	4.79	8.02	6.18	5.97	8.46	6.37	8.04	5.57	3.79	8.3	8.12
CaO	8.73	7.97	7.38	9.37	8.05	7.97	6.79	8.26	8.21	5.54	9.22	7.94
Na_2O	2.66	2.17	3.6	2.4	2.93	2.63	3.96	2.57	3.01	3.58	2.49	4.1
K_2O	1.39	1.81	1.9	1.4	1.62	2.76	2.34	2.99	1.49	2.53	2.26	1.51
TiO_2	1.25	1.4	0.8	1.04	1.22	0.71	0.87	0.73	1.14	1.31	0.69	0.75
P_2O_5	0.15	0.22	0.08	0.12	0.13	0.07	0.1	0.08	0.13	0.16	0.07	0.08
MnO	0.17	0.15	0.14	0.18	0.15	0.14	0.13	0.13	0.17	0.15	0.14	0.19
LOI	0.77	3.69	2.94	0.48	1.57	3.14	2.12	2.8	1.15	1.45	2.8	3.11
H_2O-												
Total	99.61	99.64	99.94	99.96	99.93	100.06	99.81	99.54	99.93	100	99.89	99.78
Mg #	53.05	51.62	66.30	57.14	55.51	70.30	59.80	67.55	52.72	42.68	69.39	68.60
Trace Elements (ppm):												
La	19.81	34.71	12.25	16.53	20.38	9.72	15.66	9.25	18.72	29.18	9.21	9.23
Ce	41.65	70.86	25.58	33.93	41.79	20.6	32.32	19.57	39.17	59.55	19.37	19.86
Pr	5.058	8.146	3.084	4.061	4.9	2.542	3.909	2.404	4.649	7.006	2.426	2.464
Nd	20.43	31.3	12.73	16.36	19.57	10.34	15.11	9.98	18.75	27.16	9.85	10.27
Sm	4.63	6.34	2.96	3.78	4.36	2.52	3.47	2.39	4.29	5.86	2.41	2.54
Eu	1.38	1.74	0.89	1.14	1.24	0.8	0.99	0.79	1.24	1.45	0.77	0.77
Gd	5.06	6.34	3.2	4.16	4.79	2.83	3.74	2.92	4.66	6.31	2.77	2.81
Tb	0.877	1.027	0.553	0.704	0.808	0.484	0.632	0.481	0.769	1.036	0.459	0.481
Dy	5.8	6.65	3.86	4.76	5.38	3.23	4.32	3.23	5.24	6.95	3.19	3.35
Ho	1.13	1.26	0.74	0.93	1.05	0.66	0.83	0.65	0.99	1.33	0.64	0.67
Er	3.28	3.6	2.11	2.68	3.01	1.87	2.39	1.85	2.89	3.82	1.81	1.89
Yb	2.98	3.2	2.02	2.46	2.89	1.77	2.36	1.75	2.83	3.62	1.7	1.81
Lu	0.423	0.481	0.294	0.377	0.405	0.262	0.332	0.258	0.399	0.52	0.255	0.266
Rb	51.47	66.67	54.95	51.23	64.21	103.04	81.59	155.31	60.86	102.34	79.27	60.73
Ba	323	454	270	315	311	197	321	201	249	352	152	137

Table B1: Continued

Type: AusQuest Antrim Rock Chip Basaltic Samples

Sample	**ANT026A**	**ANT027**	**ANT028**	**ANT029**	**ANT044**	**ANT054**	**ANT055**	**ANT056**	**ANT057**	**ANT058**	**ANT060**	**ANT061**
Rock Type	Basalt	Basalt	Basalt	Basalt		Basalt	Basalt	Basalt	Basalt	Basalt	Basalt	Basalt
Location	Outcrop	Outcrop	Outcrop	Outcrop		Outcrop	Outcrop	Outcrop	Outcrop	Outcrop	Outcrop	Outcrop
Zone	52	52	52	52		52	52	52	52	52	52	52
Northing	7989320	7964120	7979210	7983090		8222730	8230460	8281895	8282560	8287988	8256790	8265330
Easting	488000	411270	427000	430680		435890	438580	413450	412860	406900	461890	466600
Trace Element (ppm): Continued												
Th	6.56	12.18	4.49	5.48	6.8	3.71	5.95	2.93	7.05	12.69	3.56	3.11
U	1.2	1.5	0.73	0.98	1.3	0.51	0.94	0.48	1.28	2.42	0.49	0.47
Nb	7.46	11.76	4.19	6.51	7.51	3.93	5.72	3.23	7.14	10.77	3.46	3.63
K	11814	15833	16422	11811	13830	23846	20091	25900	12672	21572	19496	13085
Ta	0.54	0.72	0.32	0.45	0.53	0.26	0.4	0.24	0.51	0.8	0.25	0.27
Pb												
Sr	181	173	292	162	156	397	216	559	172	156	319	248
P	670.2	1011.6	363.5	532.2	583.4	317.9	451.3	364.3	581.2	717.1	317.4	364.4
Hf	3.67	5.38	2.5	3.23	3.74	1.98	2.89	1.93	3.46	4.88	1.93	2.04
Zr	130	191	87	115	128	73	99	70	118	169	66	68
Ti	7671	8843	4993	6336	7521	4429	5394	4566	7001	8066	4298	4693
Tb	0.877	1.027	0.553	0.704	0.808	0.484	0.632	0.481	0.769	1.036	0.459	0.481
Y	28.86	34.14	19.64	24.04	27.26	17.07	22.62	17.16	26.87	35.89	16.66	17.42
Co	42.2			41.2	41.4				44.9	36.8		
Cr	77			137	119				83	0		
Cu	56			25	23				89	21		
Ni	39			57	46				48	25		
V	277			262	286				291	258		
Zn	88			77	81				98	106		

Table B1: Continued

					Type: AusQuest Antrim Rock Chip Dolerite Samples							
Sample	**ANT063**	**ANT064**	**ANT065**	**ANT066**	**ANT046**	**ANT047**	**ANT048**	**ANT030**	**ANT031**	**ANT067**	**ANT068**	**ANT069**
Rock Type	Outcrop	NTGS Drill Hole	NTGS Drill Hole	NTGS Drill Hole								
Location	B'dudu1	B'dudu1	B'dudu1	B'dudu1								
Zone	52	52	52	52								
Northing	7970500	7970500	7970500	7970500								
Easting	567500	567500	567500	567500								
Major Elements (wt. %):												
SiO_2	54.1	54.08	53.1	53.09	52.63	52.65	52.67	52.95	52.85	49.4	48.03	46.92
Al_2O_3	14.44	14.55	14.81	14.91	13.67	13.73	13.73	14.01	14.12	15.75	16.08	13.47
FeO_{tot}	10.89	10.53	10.87	10.74	14.6	14.64	14.51	13.5	13.83	11.83	13.52	14.86
MgO	5.28	5.28	5.96	5.58	4.66	4.67	4.83	5.32	5.06	8.28	8.84	8.53
CaO	8.31	5.35	4.65	9.42	8.79	8.75	8.91	8.78	8.41	1.74	1.81	0.82
Na_2O	2.48	4.51	5.09	2.64	2.56	2.41	2.44	2.44	2.37	2.41	1.8	2.75
K_2O	1.64	2.51	1.26	0.66	1.23	1.16	1.18	0.98	1.15	0.18	0.28	0.5
TiO_2	1.13	1.11	1.12	1.19	1.45	1.47	1.44	1.32	1.35	1.24	1.55	3.33
P_2O_5	0.16	0.16	0.15	0.14	0.19	0.18	0.18	0.17	0.17	0.03	0.2	0.47
MnO	0.16	0.2	0.24	0.15	0.19	0.19	0.19	0.17	0.18	6.91	5.88	6.56
LOI	1.06	2.19	2.45	1.16	0.35	0.28	0.38	0.48	0.47	2.56	2.34	2.05
H_2O-												
Total	99.65	100.47	99.7	99.68	100.32	100.13	100.46	100.12	99.96	100.33	100.33	100.26
Mg #	53.05	53.88	56.09	54.76	42.65	42.64	43.68	47.87	46.02	61.99	60.37	57.22
Trace Elements (ppm):												
La	26.4	26.08	23.15	19.11	20.16	19.85	20.18	18.16	19.73	12.64	30.47	34.18
Ce	53.53	53.26	55	39.85	44.14	42.96	44.14	38.99	41.65	27.89	61.78	79.69
Pr	6.224	6.206	6.637	4.808	5.599	5.455	5.553	5.021	5.308	3.492	7.301	10.457
Nd	24.03	23.88	25.55	19.06	23.31	22.7	23.16	21.07	22.25	14.73	27.5	44.14
Sm	4.95	4.9	5.17	4.29	5.22	5.1	5.19	4.65	4.98	3.49	5.62	9.2
Eu	1.39	1.4	1.42	1.29	1.58	1.53	1.57	1.43	1.48	1.31	1.76	2.77
Gd	5.15	5.01	5.15	4.81	5.61	5.49	5.61	5.07	5.24	3.86	5.66	9.31
Tb	0.84	0.826	0.826	0.806	0.92	0.892	0.934	0.841	0.873	0.635	0.927	1.456
Dy	5.35	5.32	5.37	5.4	5.99	5.84	6.01	5.43	5.64	4.17	5.86	8.9
Ho	1.06	1.02	1.04	1.07	1.14	1.15	1.16	1.05	1.11	0.8	1.16	1.64
Er	2.94	2.98	2.95	3.07	3.31	3.26	3.32	2.98	3.17	2.38	3.26	4.48
Yb	2.69	2.76	2.79	2.86	3.02	3.01	2.92	2.74	2.98	2.02	2.76	3.9
Lu	0.398	0.405	0.4	0.405	0.455	0.432	0.439	0.413	0.41	0.301	0.412	0.531
Rb	63.65	86.35	37.08	35.28	39.03	38.52	38.11	33.13	38.76	207.65	148.91	278.49
Ba	333	393	343	260	497	346	305	363	599	501.6	424.6	174.4

Table B1: Continued

					Type: AusQuest Antrim Rock Chip Dolerite Samples							
Sample	**ANT063**	**ANT064**	**ANT065**	**ANT066**	**ANT046**	**ANT047**	**ANT048**	**ANT030**	**ANT031**	**ANT067**	**ANT068**	**ANT069**
Rock Type	Outcrop	NTGS Drill Hole	NTGS Drill Hole	NTGS Drill Hole								
Location	B'dudu1	B'dudu1	B'dudu1	B'dudu1								
Zone	52	52	52	52								
Northing	7970500	7970500	7970500	7970500								
Easting	567500	567500	567500	567500								
Trace Element (ppm): Continued												
Th	9.41	9.31	9.46	6.27	3.25	3.24	3.24	3.12	3.3	1.23	3.72	2.46
U	1.14	1.13	1.15	1.02	0.8	0.81	0.82	0.63	0.76	0.33	0.47	0.64
Nb	9.49	9.32	9.49	7.86	7.94	7.94	7.77	7.07	7.35	8.04	14.22	29.76
K	13964	21432	10877	5622	10365	9788	9932	8277	9731	1547	2405	4291
Ta	0.58	0.55	0.57	0.52	0.5	0.47	0.47	0.44	0.46	0.49	0.81	1.71
Pb												
Sr	191	159	217	182	166	187	175	193	179	218	297	172
P	716.1	718.2	680.7	627.0	841.7	798.4	796.4	754.8	756.2	135.5	903.2	2120.5
Hf	4.3	4.28	4.51	3.99	3.85	3.85	3.66	3.32	3.59	2	3.35	3.55
Zr	166	165	166	148	135	148	139	133	132	60.1	117.4	116.6
Ti	6948	6844	6982	7321	8824	8957	8752	8051	8249	7696	9615	20639
Tb	0.84	0.826	0.826	0.806	0.92	0.892	0.934	0.841	0.873	0.635	0.927	1.456
Y	27.64	27.84	27.7	27.75	30.05	30.07	30.04	27.28	28.66	21.31	29.66	42.06
Co	40.2			39.8	47.9	47.3	48.6	45.9	46.2			
Cr	113			132	92	87	96	98	81			
Cu	28			41	156	153	153	116	119			
Ni	28			47	51	54	54	55	51			
V	241			245	313	316	315	293	284			
Zn	87			76	120	125	122	111	111			

Table B1: Continued

		Type: Antrim Plateau Volcanics Samples Collected Specifically for this Study							
Sample	**ANT070**	**036** (25)	**ANT-333** (26)	**K03** (27)	**052** (28)	**109** (29)	**111** (30)	**112** (31)	**P04** (32)
Rock Type		Basalt	Coarse Basalt	Basalt	Basalt	Basalt	Basalt	Basalt	Basalt
Location		Kirrikimbie	ANTD-002	Bungle Bungle	Kirrikimbie	Spring Creek	Spring Creek	Spring Creek	Bungle Bungle
Zone		52	52	52	52	52	52	52	52
Northing		8055508		8080181	8069121	8143676	8142640	8142424	8080318
Easting		554080		427646	543159	480282	481086	481266	427461
Major Elements (wt. %):									
SiO_2	47.2	52.48	53.38	52.07	53.37	52.91	55.02	53.56	53.62
Al_2O_3	14.22	15.27	14.18	14.31	13.82	13.93	13.05	14.02	13.65
FeO_{tot}	14.95	11.27	11.48	12.28	12.77	12.63	14.37	12.77	12.2
MgO	8.91	4.71	5	5.4	4.65	4.81	3.62	4.91	5.47
CaO	1.81	5.94	4.89	5.85	6.65	6.38	5.59	7.15	7.01
Na_2O	0.99	4.33	4.57	3.94	3.38	3.59	3.07	3.39	3.07
K_2O	0.42	2.66	3.21	2.27	2.12	2.98	2.26	1.9	1.95
TiO_2	2.68	1.19	1.3	1.46	1.23	1.18	1.54	1.21	1.21
P_2O_5	0.02	0.129	0.172	0.175	0.141	0.135	0.172	0.137	0.154
MnO	5.66	0.17	0.2	0.24	0.18	0.2	0.36	0.17	0.13
LOI	2.97	1.79	1.46	1.86	1.34	1.08	0.72	0.66	1.31
H_2O-									
Total	99.83	99.939	99.842	99.855	99.651	99.825	99.772	99.877	99.774
Mg #	58.14	49.34	50.37	50.61	45.90	47.02	36.98	47.26	51
Trace Elements (ppm):									
La	32.88	21.5	21.6	20.6	21.3	20.4	29.6	21.1	19.2
Ce	70.04	44.8	44.8	45.9	45	42.4	60.9	42.9	39.8
Pr	8.848	5.15	5.24	5.56	5.26	4.94	7.01	4.91	4.83
Nd	35.26	21.5	21.9	22.9	21.9	20.4	28.7	20.8	20.2
Sm	7.2	4.68	5.04	5.41	4.99	4.54	6.29	4.58	4.36
Eu	2.28	1.24	1.39	1.52	1.33	1.23	1.56	1.27	1.3
Gd	7.76	4.82	5.4	5.96	5.24	5.03	6.45	5.2	4.6
Tb	1.186	0.8	0.85	0.98	0.85	0.82	1.08	0.85	0.83
Dy	7.56	5.25	5.5	6.06	5.67	5.13	6.59	5.4	5.24
Ho	1.43	1.08	1.11	1.21	1.16	1.09	1.34	1.09	1.09
Er	4.11	3.07	3.21	3.64	3.46	3.2	4.02	3.29	3.07
Yb	3.61	2.97	2.97	3.26	3.19	3.04	3.72	2.99	2.89
Lu	0.545	0.43	0.46	0.54	0.51	0.47	0.57	0.44	0.45
Rb	68.96	77.8	74.1	72.8	69.5	63.1	89.3	62.9	61.1
Ba	246.6	314.9	288.1	303.2	276	303.6	266	202.8	277.2

Table B1: Continued

		Type: Antrim Plateau Volcanics Samples Collected Specifically for this Study							
Sample	**ANT070**	**036** (25)	**ANT-333** (26)	**K03** (27)	**052** (28)	**109** (29)	**111** (30)	**112** (31)	**P04** (32)
Rock Type		Basalt	Coarse Basalt	Basalt	Basalt	Basalt	Basalt	Basalt	Basalt
Location		Kirrikimbie	ANTD-002	Bungle Bungle	Kirrikimbie	Spring Creek	Spring Creek	Spring Creek	Bungle Bungle
Zone		52	52	52	52	52	52	52	52
Northing		8055508		8080181	8069121	8143676	8142640	8142424	8080318
Easting		554080		427646	543159	480282	481086	481266	427461
Trace Element (ppm): Continued									
Th	3.41	8.7	9.18	7.18	9.28	8.22	13.32	8.51	7.05
U	0.58	1.43	1.64	1.12	1.55	1.33	2.28	1.4	1.17
Nb	19	7.3	7.2	7.9	8.1	7.3	10.1	7.4	6.8
K	3656	22714	27346	19428	18104	25320	19178	16077	16619
Ta	1.09	0.6	0.7	0.6	0.6	0.6	0.8	0.6	0.5
Pb		15.8	3.6	7.7	9.9	8	13.5	7.4	9.7
Sr	250	183.2	264.2	212.4	123.5	337.1	126	174.7	170.2
P	91.5	579.0	770.2	787.3	633.0	603.0	767.2	609.4	689.9
Hf	4.94	3.4	3.6	3.9	3.7	3.2	4.6	3.4	3.3
Zr	162.2	143	151	168	148	140	182	141	138
Ti	16847	7337	7997	9023	7585	7240	9436	7393	7446
Tb	1.186	0.8	0.85	0.98	0.85	0.82	1.08	0.85	0.83
Y	37.79	28.8	30.2	33.1	31.2	30.4	36.8	30.6	28.4
Co									
Cr									
Cu									
Ni									
V									
Zn									

Major and trace element analyses for the Kalkarindji continental flood basalt province Analysis information can be found in Table B3 and B4. LOI, loss on ignition. GPS Datum: AGD84 unless otherwise noted. Sample information left blank did not have information provided by AusQuest Limited. Results left blank were not analyzed for those particular trace elements.

Table B2: Major and trace element analyses of basaltic and doleritic dykes, lavas, and sills from the Kalkarindji CFB province (Table Hill Volcanics).

Amadeus Petroleum Boondawari, Akabura, and Akubra

Sample	**AOB06**	**AOB21**	**AOB07**	**AOB08**	**AOB09**	**AOB01**	**AOB02**	**AOB26**	**AOB27**	**AOB28**	**AOB03**	**AOB04**
Rock Type	Basalt	Basalt	Dolerite	Gabbro	Gabbro	Basalt	Diorite	Dolerite	Diorite	Mafic Diorite	Dolerite	Gabbro
Location	Boondawari 1	Boondawari 1	Boondawari 1	Boondawari 1	Boondawari 1	Akubra 1	Akubra 1	Akabura 1	Akabura 1	Akabura 1	Akubra 1	Akubra 1
Zone	51	51	51	51	51	51	51	51	51	51	51	51
Northing	7398348	7398348	7398348	7398348	7398348	7401112	7401112	7401112	7401112	7401112	7401112	7401112
Easting	349097	349097	349097	349097	349097	334400	334400	334400	334400	334400	334400	334400
Major Elements (wt. %):												
SiO_2	52.41	52.28	52.1	52.22	51.79	54.66	54.64	61.5	60.55	58.74	53.12	53.69
Al_2O_3	14.57	14.67	14.66	15.36	13.89	13.69	14.45	12.75	12.97	12.91	15.01	16.55
FeO_{tot}	9.83	9.76	9.63	9.33	9.14	11.06	11.11	10.14	10.28	11.36	11.96	9.00
MgO	6.88	7.14	7.19	6.47	8.73	4.58	3.5	1.63	1.82	2.08	3.12	4.3
CaO	10.06	10.83	10.93	11	11.33	4.88	6.87	2.75	2.82	3.5	6.93	9.37
Na_2O	2.29	2.29	2.26	2.41	2.01	4.86	3.19	5.05	4.83	4.2	3.06	2.59
K_2O	1.16	0.83	0.74	0.81	0.7	1.89	2.03	2.55	2.66	2.68	2.14	1.44
TiO_2	0.92	0.91	0.89	0.87	0.72	1.36	1.39	1.28	1.44	1.56	1.61	0.95
P_2O_5	0.12	0.12	0.12	0.12	0.09	0.17	0.18	0.31	0.27	0.26	0.15	0.12
MnO	0.17	0.17	0.17	0.17	0.17	0.16	0.17	0.15	0.16	0.16	0.2	0.16
LOI	0.56	0.37	0.4	0.37	0.28	1.4	1.45	0.59	0.65	0.84	1.26	1.04
H_2O-												
Total	98.97	99.37	99.09	99.13	98.85	98.71	98.98	98.70	98.45	98.29	98.56	99.21
Mg #	61.98	63.02	63.51	61.77	68.99	49.11	42.33	27.45	29.21	29.90	37.81	52.69
Trace Elements (ppm):												
La	18.58	17.28	16.54	17.21	12.9	29.46	29.63	49.67	43.56	46.46	27.42	21.05
Ce	38.86	32.88	35.21	38.27	27.22	62.73	64.97	99.2	86.94	91.4	59.22	47.6
Pr	4.234	3.838	3.964	4.366	3.191	7.14	7.224	11.406	10.115	10.474	6.718	5.403
Nd	16.87	15.21	15.73	16.9	12.52	27.3	28.39	44.07	38.71	40.3	26.22	21.39
Sm	3.76	3.39	3.49	3.72	2.75	6.01	6.32	9.64	8.57	9.04	5.84	4.5
Eu	1.16	1.03	1.09	1.18	0.91	1.56	1.6	2.03	1.89	2.02	1.55	1.33
Gd	4.06	3.87	3.66	3.91	3.02	6.09	6.41	10.38	9.12	9.52	5.91	4.77
Tb	0.704	0.656	0.638	0.67	0.525	1.083	1.119	1.729	1.518	1.574	1.05	0.816
Dy	4.46	4.25	4.16	4.35	3.58	6.68	7.09	10.58	9.76	9.8	6.64	5.28
Ho	0.86	0.89	0.82	0.87	0.7	1.24	1.37	2.23	1.96	2.02	1.29	0.98
Er	2.37	2.4	2.32	2.42	1.92	3.59	3.81	5.9	5.37	5.55	3.47	2.64
Yb	2.31	2.34	2.31	2.26	1.93	3.44	3.61	5.65	5.2	5.19	3.4	2.68
Lu	0.342	0.375	0.354	0.353	0.283	0.54	0.559	0.897	0.808	0.803	0.547	0.422
Rb	56.24	34.62	30.22	33.41	29.89	73.74	90.5	77.15	82.32	110.92	91.38	61.44
Ba	236.6	236.8	230.3	225.5	185.2	281.5	334.4	378.3	418.6	440.2	362.6	260.5

Table B2: Continued

Amadeus Petroleum Boondawari, Akabura, and Akubra

Sample	**AOB06**	**AOB21**	**AOB07**	**AOB08**	**AOB09**	**AOB01**	**AOB02**	**AOB26**	**AOB27**	**AOB28**	**AOB03**	**AOB04**
Rock Type	Basalt	Basalt	Dolerite	Gabbro	Gabbro	Basalt	Diorite	Dolerite	Diorite	Mafic Diorite	Dolerite	Gabbro
Location	Boondawari 1	Boondawari 1	Boondawari 1	Boondawari 1	Boondawari 1	Akubra 1	Akubra 1	Akabura 1	Akabura 1	Akabura 1	Akubra 1	Akubra 1
Zone	51	51	51	51	51	51	51	51	51	51	51	51
Northing	7398348	7398348	7398348	7398348	7398348	7401112	7401112	7401112	7401112	7401112	7401112	7401112
Easting	349097	349097	349097	349097	349097	334400	334400	334400	334400	334400	334400	334400
Trace Element (ppm): Continued												
Th	5.73	5.38	5.19	5.39	3.98	13.08	13.64	22.12	19.92	20.57	11.96	10.06
U	1.05	0.87	0.92	0.9	0.67	2.54	2.66	4.04	3.22	3.74	2.28	1.94
Nb	5.13	4.9	4.91	4.58	3.43	9.93	10.25	16.24	15.18	14.59	9.69	7.1
K	9785	6960	6225	6809	5895	16124	17279	21577	22581	22830	18259	12178
Ta	0.41	0.6	0.38	0.35	0.27	0.92	0.88	1.27	1.18	1.18	0.79	0.66
Pb												
Sr	210	178	198	203	179	268	191	86	94	124	233	183
P	532.1	529.0	530.6	530.3	398.4	762.4	805.4	1378.9	1204.8	1164.3	672.8	533.5
Hf	2.95	2.56	2.65	1.84	1.45	4.62	5.04	7.46	6.91	6.92	4.46	3.48
Zr	98.7	91.2	95.5	57.8	56.2	152.9	171.8	263.3	251.5	237.6	146.1	111
Ti	5604	5510	5406	5281	4378	8378	8543	7821	8827	9596	9920	5801
Tb	0.704	0.656	0.638	0.67	0.525	1.083	1.119	1.729	1.518	1.574	1.05	0.816
Y	22.53	23.45	22.05	21.7	18.15	33.9	35.6	58.35	50.99	51.69	33.63	25.18
Co	41	37	40	38	41	37	36	19	23	27	39	33
Cr	77	83	106	83	184	15	7	5	6	3	4	40
Cu	98	91	101	109	91	61	50	11	17	24	67	66
Ni	62	63	72	64	91	21	14	1	1	1	14	25
V	248	234	234	240	216	287	279	60	103	134	469	217
Zn	73	81	73	71	69	61	71	85	106	92	158	94

Table B2: Continued

			Type: AusQuest Akubra o/c, Boondawari o/c and Trainor Hills									
Sample	**AOB05**	**AOB22**	**TH1**	**TH2**	**TH3**	**TH4**	**TH5**	**TH6**	**TH8**	**TH9**	**ECP74**	**122601**
Rock Type	Gabbro	Gabbro	Gabbro	Gabbro	Gabbro	Gabbro	Gabbro	Gabbro	Gabbro	Gabbro	Gabbro	Gabbro
Location	AKUBRA 1	Akabura 1	Nyianinya RH	20k SW Akubra	Akubra o/c	Akubra o/c	Boondawari o/c	Boondawari o/c	Trainor Hills o/c	Trainor Hills o/c	Trainor Hills o/c	M. Jilyili Sill
Zone	51	51	51	51	51	51	51	51	51	51	51	51
Northing	7401112	7401112	7406548	7397328	7403988	7405350	7390830	7391765	7333755	7312085	411083	7265369
Easting	334400	334400	287374	319930	333471	335330	342764	343605	405420	419452	7327315	262834
Major Elements (wt. %):												
SiO_2	53.67	54.32	52.22	53.62	53.44	53.28	55	53.52	53.65	53.64	53.86	53.79
Al_2O_3	15.65	14.09	15.5	12.88	16.82	17.16	14.7	16.64	14.9	13.38	13.33	15.97
FeO_{tot}	8.53	10.11	9.47	13.24	8.13	8.24	11.30	9.46	10.46	11.17	11.71	12.41
MgO	5.39	5.73	6.82	3.59	4.72	4.68	2.8	3.92	4.76	6.06	5.5	2.88
CaO	9.35	8.48	10.61	7.05	9.57	9.63	6.53	9.22	8.66	8.22	7.74	7.45
Na_2O	2.69	2.61	2.15	2.76	2.44	2.32	3.12	2.4	2.65	2.38	2.54	2.9
K_2O	1.31	1.5	0.86	1.9	1.31	1.43	2.15	1.56	1.45	1.45	1.6	1.6
TiO_2	0.91	1.06	0.9	1.81	0.84	0.81	1.52	0.98	1.13	1.16	1.32	1.49
P_2O_5	0.12	0.12	0.09	0.17	0.11	0.11	0.18	0.12	0.13	0.14	0.15	0.16
MnO	0.12	0.18	0.16	0.19	0.13	0.17	0.19	0.17	0.18	0.19	0.19	0.16
LOI	1.3	0.99	0.37	1.18	1.27	1.17	1.48	0.78	1.21	0.92	1.12	1.08
H_2O-												
Total	99.04	99.19	99.15	98.39	98.78	99.00	98.97	98.77	99.18	98.71	99.06	99.89
Mg #	59.56	56.90	62.67	38.73	57.49	56.95	36.6	49.13	51.45	55.84	52.26	52.26
Trace Elements (ppm):												
La	22.12	22.3	14.04	28.29	18.03	18.94	29.82	21.4	21.44	22.64	26.67	25.93
Ce	45.9	44	29.18	59.14	36.77	38.37	61.33	45.01	44.73	45.91	52.24	52.92
Pr	5.117	5.071	3.446	6.916	4.3	4.443	7.161	5.32	5.309	5.429	5.907	6.132
Nd	19.62	20.24	13.28	25.96	16.28	16.69	27.51	19.45	19.68	20.6	23.74	24.82
Sm	4.16	4.67	3.26	6	3.76	3.78	5.99	4.43	4.49	4.67	5.26	5.59
Eu	1.14	1.22	1.01	1.49	0.98	1.02	1.61	1.31	1.3	1.33	1.38	1.45
Gd	4.32	4.85	3.67	6.43	4.11	4.11	6.7	4.95	4.79	5.14	5.55	6
Tb	0.763	0.859	0.682	1.118	0.698	0.705	1.125	0.867	0.851	0.881	0.948	0.988
Dy	5.01	5.4	4.53	7.19	4.59	4.53	7.21	5.69	5.85	6.15	6.26	6.29
Ho	0.97	1.12	0.86	1.38	0.85	0.83	1.36	1.09	1.04	1.11	1.2	1.28
Er	2.71	3.05	2.49	4.01	2.52	2.5	4.11	3.19	3.11	3.24	3.41	3.71
Yb	2.49	3.05	2.34	3.8	2.39	2.46	3.8	2.82	2.91	3.05	3.25	3.38
Lu	0.406	0.454	0.371	0.546	0.334	0.335	0.551	0.427	0.422	0.477	0.514	0.511
Rb	59.4	74.96	37.03	92.7	57.29	68.1	100.01	79.02	66.53	68.45	78.81	77.03
Ba	223.1	257.4	167	329.2	228.6	244.4	416.9	282	253.5	261.8	296.5	343.8

Table B2: Continued

			Type: AusQuest Akubra o/c, Boondawari o/c and Trainor Hills									GDA94
Sample	**AOB05**	**AOB22**	**TH1**	**TH2**	**TH3**	**TH4**	**TH5**	**TH6**	**TH8**	**TH9**	**ECP74**	**122601**
Rock Type	Gabbro	Gabbro	Gabbro	Gabbro	Gabbro	Gabbro	Gabbro	Gabbro	Gabbro	Gabbro	Gabbro	Gabbro
Location	AKUBRA 1	Akabura 1	Nyianinya RH	20k SW Akubra	Akubra	Akubra	Boondawari	Boondawari	Trainor Hills	Trainor Hills	Trainor Hills	M. Jilyili Sill
Zone	51	51	51	51	51	51	51	51	51	51	51	51
Northing	7401112	7401112	7406548	7397328	7403988	7405350	7390830	7391765	7333755	7312085	411083	7265369
Easting	334400	334400	287374	319930	333471	335330	342764	343605	405420	419452	7327315	262834
Trace Element (ppm): Continued												
Th	9.59	10.09	5.43	12.14	8.08	8.24	12.87	9.26	9.24	9.65	11.78	10.87
U	1.84	1.88	0.96	2.31	1.58	1.52	2.38	1.79	1.69	1.73	2.22	1.78
Nb	7.17	7.21	5.08	10.1	6.56	6.44	10.72	7.42	7.77	7.68	9.11	9.93
K	11127	12680	7228	16227	11152	12134	18308	13217	12286	12310	13563	13614
Ta	0.6	0.68	0.5	0.8	0.57	0.57	0.82	0.67	0.64	0.64	0.7	
Pb												
Sr	157	140	144	139	162	164	171	171	166	145	155	203
P	535.8	533.3	397.6	763.2	492.3	490.7	805.7	534.4	579.0	624.8	668.4	707.1
Hf	3.34	3.52	2.55	4.59	2.97	2.89	4.86	3.41	3.54	3.59	3.99	
Zr	119.7	127	97.3	166.8	111.3	109.6	171.8	120.4	132.8	137	134.9	148
Ti	5581	6470	5462	11162	5164	4963	9346	5995	6914	7111	8080	9155
Tb	0.763	0.859	0.682	1.118	0.698	0.705	1.125	0.867	0.851	0.881	0.948	0.988
Y	25.24	29.68	22.63	37.47	23.1	23.48	37.28	26.42	28.48	29.57	33.18	34.77
Co	32	37	39	45	33	33	37	34	39	44	44	54
Cr	95	39	142	19	71	75	12	21	24	37	39	7
Cu	35	44	68	30	35	51	53	63	54	46	48	53
Ni	37	28	68	20	40	40	14	26	30	36	27	26
V	207	231	235	529	207	195	354	224	261	276	316	395
Zn	40	90	66	99	57	125	136	118	89	89	103	148

Table B2: Continued

Type: Table Hill Chopper Rock Chips AQ												
	GDA94	GDA94	GDA94	GDA94	GDA94	GDA94	GDA94	GDA94	GDA94	GDA94	GDA94	GDA94
Sample	**122602**	**122603**	**122604**	**122605**	**122606**	**122609**	**122610**	**122611**	**122612**	**122613**	**122614**	**122615**
Rock Type	Gabbro	Gabbro	Dolerite	Basalt	Gabbro	Dolerite	Dolerite	Dolerite	Gabbro	Leucogabbro	Dolerite	Gabbro
Location	U. Jilyili Sill	U. Jilyili Sill	U. Jilyili Sill	U. Jilyili Sill	L. Jilyili Sill	Jilyili Dyke	Jilyili Dyke	Jilyili Dyke	Jilyili Dyke	Jilyili Dyke	Jilyili Dyke	M. Jilyili Sill
Zone	51	51	51	51	51	51	51	51	51	51	51	51
Northing	7265800	7266110	7266201	7266243	7264838	7267538	7267533	7267573	7271798	7272056	7271933	7254032
Easting	262902	263255	263586	263611	263034	261941	261945	261911	262002	261849	261868	275926
Major Elements (wt. %):												
SiO_2	56.99	61.54	54.11	50.26	53.73	54.61	55.18	54	58.65	53.96	53.73	54.33
Al_2O_3	14.7	13.17	13.39	12.7	15.79	13.64	13.63	14.03	14.61	15.68	14.88	16.88
FeO_{tot}	12.26	10.8	12.19	17.08	10.9	12.46	12.43	12.48	11.42	13.3	12.99	10.28
MgO	1.72	1.11	4.52	5.16	3.67	4.22	3.86	4.74	1.47	2.77	2.3	3.61
CaO	5.96	3.96	5.97	5.12	8.37	6.89	5.55	8.07	5.6	7.82	6.97	8.89
Na_2O	3.05	3.29	3.13	2.26	2.66	2.65	2.97	2.67	3.17	2.83	2.63	2.55
K_2O	2.5	3.29	2.25	1.64	1.65	2.06	2.8	1.64	2.56	1.77	2.2	1.55
TiO_2	1.64	1.26	1.34	3.16	1.13	1.37	1.41	1.28	1.47	1.7	1.71	1.07
P_2O_5	0.220	0.307	0.170	0.325	0.140	0.172	0.179	0.151	0.243	0.158	0.188	0.135
MnO	0.182	0.172	0.160	0.068	0.164	0.158	0.114	0.160	0.156	0.159	0.152	0.158
LOI	0.81	1.17	1.8	0.95	1.09	1.37	1.52	0.91	0.78	0.85	1.18	1.17
H_2O-												
Total	100.03	100.07	99.03	98.72	99.29	99.60	99.64	100.13	100.13	101.00	98.93	100.62
Mg #	35.09	24.64	19.32	46.35	41.31	43.96	44.11	41.98	46.95	23.07	32.67	45.00
Trace Elements (ppm):												
La	36.56	49.66	30.78	37.45	22.05	27.14	29.54	22.93	38.33	24.14	28	20.62
Ce	73.4	102.55	61.05	74.4	44.51	55.28	59	47.08	77.32	49.54	56.9	42.32
Pr	8.626	11.575	6.989	9.879	5.169	6.41	6.837	5.541	8.967	5.827	6.798	4.937
Nd	34.97	46.68	28.24	45.04	21.31	25.47	27.3	22.39	36.36	24.08	28.11	20
Sm	7.47	10.05	5.89	10.74	4.73	5.62	5.93	5.04	7.99	5.32	6.23	4.4
Eu	1.83	2.16	1.39	3.17	1.23	1.38	1.33	1.27	1.87	1.43	1.62	1.2
Gd	8.1	10.64	6.29	12.55	5.02	6	6.23	5.57	8.52	5.8	6.85	4.85
Tb	1.296	1.705	1.008	1.867	0.814	0.971	1.009	0.922	1.404	0.971	1.079	0.796
Dy	8.37	10.89	6.3	11.05	5.3	6.26	6.45	5.93	8.71	6.17	7.03	5.06
Ho	1.72	2.2	1.29	2.12	1.08	1.29	1.32	1.23	1.78	1.26	1.42	1.02
Er	4.89	6.36	3.72	5.6	3.16	3.77	3.86	3.55	5.13	3.69	4.05	2.94
Yb	4.49	5.8	3.53	4.07	2.99	3.47	3.61	3.28	4.73	3.41	3.71	2.7
Lu	0.661	0.858	0.53	0.559	0.436	0.522	0.535	0.498	0.71	0.507	0.551	0.391
Rb	128.59	169.61	90.54	88.77	81.44	96.34	83.89	67.22	127.44	79.15	114.62	75.49

Table B2: Continued

Type: Table Hill Chopper Rock Chips AQ												
	GDA94	GDA94	GDA94	GDA94	GDA94	GDA94	GDA94	GDA94	GDA94	GDA94	GDA94	GDA94
Sample	**122602**	**122603**	**122604**	**122605**	**122606**	**122609**	**122610**	**122611**	**122612**	**122613**	**122614**	**122615**
Rock Type	Gabbro	Gabbro	Dolerite	Basalt	Gabbro	Dolerite	Dolerite	Dolerite	Gabbro	Leucogabbro	Dolerite	Gabbro
Location	U. Jilyili Sill	U. Jilyili Sill	U. Jilyili Sill	U. Jilyili Sill	L. Jilyili Sill	Jilyili Dyke	Jilyili Dyke	Jilyili Dyke	Jilyili Dyke	Jilyili Dyke	Jilyili Dyke	M. Jilyili Sill
Zone	51	51	51	51	51	51	51	51	51	51	51	51
Northing	7265800	7266110	7266201	7266243	7264838	7267538	7267533	7267573	7271798	7272056	7271933	7254032
Easting	262902	263255	263586	263611	263034	261941	261945	261911	262002	261849	261868	275926
Trace Element (ppm): Continued												
Ba	573.4	599.2	593.8	384.3	298.7	436.8	868.8	337.1	443.4	326	393.3	293.1
Th	15.54	21.96	12.95	6.15	9.05	11.89	13.15	9.71	16.7	10.12	11.79	8.75
U	2.05	4.01	2.48	0.75	1.85	2.2	2.84	1.82	3.35	1.9	1.98	1.59
Nb	13.75	18.85	10.14	10.24	8.8	10.3	10.31	8.84	14.59	9.74	11.35	8.32
K	21179	27922	19455	14172	14105	17634	23994	13896	21641	14870	18936	13074
Ta												
Pb												
Sr	188.54	151.08	198.05	236.95	182.01	169.53	231.64	175.63	173.23	192.23	189.56	180.59
P	979.4	1369.6	770.6	1477.8	628.0	773.2	805.0	673.5	1079.1	698.1	850.0	599.32
Hf												
Zr	200.3	265.3	174.5	150.4	122.5	155.3	173.9	141.8	214.1	133.6	163.8	120.4
Ti	10032	7722	8367	19720	6975	8468	8725	7832	8973	10313	10628	6517.3
Tb	1.296	1.705	1.008	1.867	0.814	0.971	1.009	0.922	1.404	0.971	1.079	0.796
Y	45.77	60.13	34.45	61.86	30.5	34.85	36.48	33.18	46.83	33.99	38.43	27.55
Co	53	37	47	50	50	47	50	49	39	47	48	40
Cr	5	0	51	50	8	11	25	11	0	5	0	17
Cu	29	28	35	40	43	46	32	30	33	39	41	50
Ni	10	10	43	64	25	24	31	29	8	20	16	36
V	218	50	284	376	241	283	294	283	115	470	384	223
Zn	200.3	265.3	174.5	150.4	122.5	155.3	173.9	141.8	214.1	133.6	163.8	120.4

Table B2: Continued

Type: Table Hill Chopper Rock Chips AQ												
	GDA94	GDA94	GDA94	GDA94	GDA94	GDA94	GDA94	GDA94	GDA94	GDA94		
Sample	**122616**	**122617**	**122618**	**122619**	**122620**	**122621**	**122622**	**122623**	**122624**	**122625**	**AOB010**	**AOB011**
Rock Type	Mesogabbro	Leucogabbro	Gabbro	Mesogabbro	Dolerite	Gabbro	Gabbro	Gabbro	Gabbro	Gabbro	Basalt	Basalt
Location	M. Jilyili Sill	Jilyili Sill	Jilyili Sill	Jilyili Sill	Jilyili Sill	Dyke Blake Hills	MN 5	Dyke S of MN 5	TSHLA	TSHLA	Empress 1A	Empress 1A
Zone	51	51	51	51	51	51	51	51	51	51	51	51
Northing	7254104	7254187	7254433	7254735	7254848	7263528	7317436	7317143	7334428	7333914	7005943	7005943
Easting	276066	276248	276323	276408	276418	324480	353138	353200	403189	402382	714042	714042
Major Elements (wt. %):												
SiO_2	54.28	53.71	56.82	54.35	54.29	54.47	57.64	55.95	53.57	57.29	52.17	51.63
Al_2O_3	15.77	14.56	12.66	14.64	14.46	14.79	15.24	14.41	14.52	15.23	14.84	14.46
FeO_{tot}	11.19	13.24	13.25	12.47	12.50	10.90	9.10	11.34	11.14	8.95	9.56	9.03
MgO	3.89	3.04	2.01	3.35	3.6	2.42	2.04	3.04	5.22	4.08	7.13	6.3
CaO	8.49	7.29	4.89	7.04	7.29	6.78	5.09	5.84	8.41	6.41	9.71	6.42
Na_2O	2.39	2.57	2.8	2.7	2.67	5.7	3.4	2.55	2.41	2.57	2.13	3.12
K_2O	1.76	2.01	2.88	2.05	1.94	0.81	1.98	1.69	1.46	1.64	0.96	4.01
TiO_2	1.15	1.55	1.67	1.39	1.39	1.69	1.65	1.19	1.08	1.36	0.82	0.76
P_2O_5	0.142	0.170	0.241	0.170	0.170	0.190	0.179	0.151	0.133	0.156	0.070	0.070
MnO	0.198	0.234	0.241	0.227	0.172	0.152	0.108	0.147	0.174	0.129	0.140	0.160
LOI	0.94	0.96	1.23	1.29	1	1.63	2.55	3.28	1.33	2.49	1.41	2.73
H_2O-												
Total	100.20	99.33	98.69	99.68	99.48	99.53	98.98	99.59	99.45	100.30	98.94	98.69
Mg #	44.75	34.85	26.12	38.50	40.16	34.09	34.31	38.45	52.20	51.51	63.46	61.90
Trace Elements (ppm):												
La	21.71	26.97	37.26	26.64	25.67	22.55	77.15	30.08	20.61	20.08	13.84	14.45
Ce	44.78	55.21	76.49	55.14	52.4	49.05	68.79	46.02	41.57	39.38	29.92	31.81
Pr	5.236	6.357	8.946	6.345	6.162	6.175	16.559	6.21	4.926	4.636	3.268	3.584
Nd	21.19	25.3	35.76	26	24.88	26.46	67.09	25.65	20.22	18.5	12.91	13.91
Sm	4.73	5.62	7.86	5.74	5.44	6.15	13.23	5.42	4.55	3.98	3.15	3.56
Eu	1.22	1.46	1.92	1.48	1.4	1.65	3.15	1.35	1.19	1.24	0.93	0.95
Gd	5.14	6.1	8.33	6.15	6.08	6.71	12.59	6.1	4.95	4.07	3.61	3.99
Tb	0.831	0.975	1.354	1.007	0.987	1.092	1.805	0.933	0.82	0.654	0.674	0.681
Dy	5.36	6.27	8.71	6.4	6.2	6.87	10.14	5.74	5.2	4.03	4.51	4.82
Ho	1.1	1.27	1.8	1.3	1.28	1.44	1.95	1.19	1.06	0.82	0.88	0.93
Er	3.13	3.71	5.1	3.81	3.73	4.12	5.17	3.36	3.05	2.26	2.42	2.72
Yb	2.92	3.49	4.71	3.48	3.55	3.79	4.49	2.9	2.81	2.13	2.47	2.53
Lu	0.432	0.508	0.688	0.533	0.529	0.575	0.653	0.442	0.425	0.3	0.363	0.381
Rb	86.06	102.09	155.33	98.56	96.37	58.08	100.4	108.77	69.44	74.7	37.57	56.78

Table B2: Continued

Type: Table Hill Chopper Rock Chips AQ												
	GDA94	GDA94	GDA94	GDA94	GDA94	GDA94	GDA94	GDA94	GDA94	GDA94		
Sample	**122616**	**122617**	**122618**	**122619**	**122620**	**122621**	**122622**	**122623**	**122624**	**122625**	**AOB010**	**AOB011**
Rock Type	Mesogabbro	Leucogabbro	Gabbro	Mesogabbro	Dolerite	Gabbro	Gabbro	Gabbro	Gabbro	Gabbro	Basalt	Basalt
Location	M. Jilyili Sill	Jilyili Sill	Jilyili Sill	Jilyili Sill	Jilyili Sill	Dyke Blake Hills	MN 5	Dyke S of MN 5	TSHLA	TSHLA	Empress 1A	Empress 1A
Zone	51	51	51	51	51	51	51	51	51	51	51	51
Northing	7254104	7254187	7254433	7254735	7254848	7263528	7317436	7317143	7334428	7333914	7005943	7005943
Easting	276066	276248	276323	276408	276418	324480	353138	353200	403189	402382	714042	714042
Trace Element (ppm): Continued												
Ba	325	368.1	539.2	403.3	350.2	549.4	575.9	478.9	245.8	319.7	174.8	190.8
Th	9.51	11.09	16.67	11.42	10.85	11.62	13.01	10.19	8.73	10.39	7.58	9.05
U	1.77	2.22	3.4	2.12	2.11	2.44	1.84	1.84	1.64	1.94	1.26	1.49
Nb	8.7	10.35	14.95	10.57	10.28	11.44	12.53	8.44	7.94	9.39	4.28	4.07
K	14888	17194	24870.5	17520	16564	6946	17209	14741	12495	14048	8171	34691
Ta											0.43	0.44
Pb												
Sr	167.96	169.36	140.91	181.17	180.84	159.02	189.73	170.54	155.09	165.4	101	343
P	631.6	762.3	1092.0	761.6	760.9	857.1	816.4	693.3	597.8	701.5	313.2	318.3
Hf											2.54	2.63
Zr	129.3	140.5	222.2	159.7	165	168.3	170.4	122	123.9	124.1	85.2	88.5
Ti	7024	9574	10413	8578	8570	10465	10356	7495	6674	8412	5040	4747
Tb	0.831	0.975	1.354	1.007	0.987	1.092	1.805	0.933	0.82	0.654	0.674	0.681
Y	29.72	34.89	48.21	35.59	35.28	39.75	50.84	34.34	28.75	21.09	23.22	24.99
Co	46	46	43	43	46	32	31	36	44	56	42	43
Cr	15	0	0	5	0	0	9	16	28	34	93	59
Cu	73	81	41	69	73	14	51	59	61	65	67	40
Ni	18	10	0	11	13	13	18	35	24	27	52	34
V	245	397	188	295	286	348	288	220	244	281	242	239
Zn	129.3	140.5	222.2	159.7	165	168.3	170.4	122	123.9	124.1	73	67

Table B2: Continued

Type: GSWA Empress 1A Drill Core					Type: Hunt Oil Yowalga 2 drill core				Type: AusQuest Various Basalt, Dolerite, Gabbro			
Sample	**AOB012**	**AOB013**	**AOB014**	**AOB015**	**AOB016**	**AOB017**	**AOB018**	**AOB019**	**AK2-6**	**AK2-9**	**BW2-02**	**BW2-04**
Rock Type	Basalt	Basalt	Basalt	Basalt-altered	Basalt-altered	Basalt	Basalt	Basalt	Gabbro	Dolerite	Dolerite	Dolerite
Location	Empress 1A	Empress 1A	Empress 1A	Empress 1A	Yowalga 2	Yowalga 2	Yowalga 2	Yowalga 2	Akubra	Akubra	Boondawari	Boondawari
Zone	51	51	51	51	51	51	51	51	51	51	51	51
Northing	7005943	7005943	7005943	7005943	7102250	7102250	7102250	7102250	7405205	7403804	7393144	7393315
Easting	714042	714042	714042	714042	796690	796690	796690	796690	336541	333415	344600	344590
Major Elements (wt. %):												
SiO_2	52.69	54.39	54.47	49.98	48.3	52.88	52.88	53.42	53.79	51.87	54.28	54.39
Al_2O_3	15.06	15.47	15.9	17.32	13.78	15.64	15.64	15.25	14.36	14.59	13.51	13.71
FeO_{tot}	9.24	8.27	7.64	7.58	12.58	9.09	9.09	9.33	10.95	9.70	11.36	11.55
MgO	6.56	6.37	6.34	9.08	8.38	6.87	6.87	6.51	4.19	7.16	4.49	4.11
CaO	9.11	7.77	8.78	7.35	1.9	9.37	9.37	9.35	7.53	11	5.86	6.48
Na_2O	2.91	2.29	2.04	2.45	1.95	2.11	2.11	2.11	2.78	2.06	3.1	2.81
K_2O	1.5	1.89	1.16	0.55	5.72	1.2	1.2	1.25	1.87	0.72	2.02	2.63
TiO_2	0.79	0.79	0.89	0.83	0.98	0.76	0.76	0.81	1.23	0.9	1.36	1.36
P_2O_5	0.07	0.08	0.08	0.07	0.09	0.06	0.06	0.07	0.15	0.12	0.17	0.17
MnO	0.17	0.15	0.14	0.02	0.31	0.14	0.14	0.14	0.2	0.17	0.19	0.2
LOI	1.35	1.61	1.72	4.13	4.32	0.85	0.85	0.65	1.39	0.56	1.64	1.21
H_2O-												
Total	99.45	99.08	99.16	99.36	98.31	98.97	98.97	98.89	98.44	98.85	97.98	98.62
Mg #	62.32	64.22	65.91	73.63	60.82	63.79	63.79	61.91	47.13	63.24	47.93	45.32
Trace Elements (ppm):												
La	14.3	19.97	22.89	17.43	14.72	11.64	16.83	17.63	22.99	15.12	26.11	25.7
Ce	31.67	42.28	48.11	39.9	28.65	22.81	33	35.43	49.78	31.25	55.87	55.46
Pr	3.596	4.745	5.342	4.461	3.237	2.559	3.73	3.926	5.815	3.71	6.681	6.492
Nd	14.41	18.39	20.54	17.23	12.84	10.05	14.62	15.38	22.87	14.66	26.11	25.56
Sm	3.46	4.24	4.7	3.83	3.15	2.43	3.34	3.58	5.45	3.35	6.07	5.97
Eu	0.98	1.02	1.11	0.99	1.01	0.85	0.98	1	1.35	0.94	1.38	1.34
Gd	3.94	4.51	4.92	4.14	3.95	3.1	3.69	4.09	5.57	3.58	6.05	6.13
Tb	0.722	0.83	0.874	0.737	0.767	0.596	0.682	0.721	0.927	0.612	1.016	0.999
Dy	4.69	5.14	5.85	4.93	5.42	4.23	4.48	4.77	6.69	4.42	6.98	6.9
Ho	0.93	1.01	1.1	0.99	1.14	0.88	0.93	1.01	1.09	0.76	1.2	1.19
Er	2.57	2.81	3.04	2.77	3.37	2.58	2.68	2.81	3.45	2.27	3.67	3.72
Yb	2.46	2.82	2.98	2.78	3.32	2.73	2.65	2.78	3.2	2.12	3.45	3.37
Lu	0.408	0.42	0.457	0.453	0.517	0.434	0.411	0.42	0.461	0.321	0.475	0.463
Rb	61.68	57.54	31.36	13.94	133.63	112.49	65.35	65.57	73.48	24.52	94.67	110.5
Ba	206.2	272.6	291.2	142	380	225	200.6	211.7	326.1	228.3	290	363.2

Table B2: Continued

Type: GSWA Empress 1A Drill Core					Type: Hunt Oil Yowalga 2 drill core				Type: AusQuest Various Basalt, Dolerite, Gabbro			
Sample	**AOB012**	**AOB013**	**AOB014**	**AOB015**	**AOB016**	**AOB017**	**AOB018**	**AOB019**	**AK2-6**	**AK2-9**	**BW2-02**	**BW2-04**
Rock Type	Basalt	Basalt	Basalt	Basalt-altered	Basalt-altered	Basalt-altered	Basalt	Basalt	Gabbro	Dolerite	Dolerite	Dolerite
Location	Empress 1A	Empress 1A	Empress 1A	Empress 1A	Yowalga 2	Yowalga 2	Yowalga 2	Yowalga 2	Akubra	Akubra	Boondawari	Boondawari
Zone	51	51	51	51	51	51	51	51	51	51	51	51
Northing	7005943	7005943	7005943	7005943	7102250	7102250	7102250	7102250	7405205	7403804	7393144	7393315
Easting	714042	714042	714042	714042	796690	796690	796690	796690	336541	333415	344600	344590
Trace Element (ppm): Continued												
Th	8.55	12.89	14.36	11.64	8.04	6.69	10.38	11.31	9.84	4.77	11.96	11.59
U	1.45	1.78	1.99	1.66	1.56	1.47	1.25	1.31	3.41	2.33	3.77	3.74
Nb	4.12	6.21	7.05	5.22	4.9	4.39	4.32	4.84	9	5.5	10.92	10.9
K	12694	16098	9883	4795	50524	10153	10153	10563	15996	6081	17406	22414
Ta	0.45	0.66	0.73	0.58	0.45	0.46	0.5	0.51	0.68	0.41	0.83	0.8
Pb												
Sr	125	108	119	154	579	203	89	95	201	187	208	230
P	311.4	358.2	358.3	320.8	417.9	266.9	266.9	310.9	674.5	532.8	770.0	761.6
Hf	2.64	3.29	3.67	3.09	3.07	2.91	2.77	3.09	4.03	2.67	4.87	4.57
Zr	81.3	111.8	126	99.3	104.7	92	91.3	97.9	144.4	104.4	184.7	178.2
Ti	4827	4859	5475	5225	6250	4643	4643	4942	7597	5489	8462	8369
Tb	0.722	0.83	0.874	0.737	0.767	0.596	0.682	0.721	0.927	0.612	1.016	0.999
Y	23.8	27.23	30.92	24.76	31.82	25.68	25.71	25.35	28.88	20.6	32.55	33.02
Co	42	34	34	41	53	62	42	43	38	40	39	40
Cr	65	171	123	78	17	18	98	91	8	70	14	16
Cu	42	67	48	41	41	28	33	37	68	108	51	60
Ni	36	63	57	45	57	75	60	53	18	74	20	20
V	239	196	207	231	254	268	239	268	273	248	302	303
Zn	76	73	78	105	96	71	70	76	136	75	111	122

Table B2: Continued

Type: AusQuest Various Basalt, Dolerite, Gabbro Samples

Sample	**BW2-12**	**BN02**	**BN04**	**BN06**	**389057**	**389059**	**389060**	**389061**	**389062**	**389067**	**389068**	**AOB020**
Rock Type	Basalt dyke	Mafic chips	Mafic chips	Mafic chips	Basalt	Mesogabbro	Mesogabbro	Mesogabbro	Mesogabbro	Dolerite	Dolerite	Basalt
Location	Boondawari	CRA drill hole	CRA drill hole	CRA drill hole	MD-1A	TRR1	TRR2	TRR3	TRR6	NYI 1	SCR 1	153995
Zone	51	51	51	51	51	51	51	51	51	51	51	51
Northing	7388169	7396494	7395745	7395964	7404962	7331546	7333122	7332626	7331430	7406514	7366498	6873823
Easting	342287	335116	336408	333783	319217	406939	403959	403220	406564	287352	292156	739112
Major Elements (wt. %):												
SiO_2	51.25	47.77	46.24	48.76	52.7	54	54	54.3	54.2	51.9	55.7	52.88
Al_2O_3	14.77	14.26	14.65	14.63	15	14.2	15.2	13.7	13.9	15.6	14.45	14.28
FeO_{tot}	10.16	11.36	11.72	12.03	9.36	10.44	10.26	11.25	10.89	9.63	10.57	9.20
MgO	7.11	10.33	10.13	9.33	6.96	5.73	4.62	5.21	5.59	6.82	3.62	6.4
CaO	9.3	1.39	2.44	0.64	9.51	8.57	8.49	7.9	8.3	10.7	6.47	6.73
Na_2O	2.7	3.05	2.28	3.04	2.12	2.41	2.7	2.54	2.46	2.18	3.04	3.01
K_2O	1.33	1	1.02	1.14	1.16	1.41	1.58	1.66	1.51	0.84	2.04	3.59
TiO_2	0.94	2.53	2.55	1.98	0.95	1.11	1.17	1.27	1.23	0.95	1.36	0.81
P_2O_5	0.12	0.26	0.28	0.19	0.13	0.13	0.14	0.15	0.14	0.1	0.17	0.07
MnO	0.17	0.12	0.16	0.1	0.16	0.18	0.17	0.19	0.19	0.17	0.17	0.18
LOI	1.26	5.98	6.43	6.12	1.01	0.56	0.61	0.52	0.5	0.27	1.25	1.56
H_2O-Total	99.11	98.05	97.90	97.96	99.06	98.74	98.94	98.69	98.91	99.16	98.84	98.71
Mg #	61.99	67.95	66.83	64.38	63.41	56.12	51.21	51.91	54.47	62.27	44.38	61.83
Trace Elements (ppm):												
La	18.88	19.18	17.76	15.38	18.39	23.34	23.63	26.74	24.47	15.11	31.59	14.29
Ce	33.96	46.77	41.37	35.11	36.93	48.23	49.06	54.57	50.7	31.96	65.42	28.93
Pr	4.655	5.968	5.38	4.621	4.304	5.707	5.832	6.483	5.88	3.794	7.599	3.361
Nd	18.97	25.38	23.24	19.52	15.54	20.55	20.88	22.72	21.62	14.17	26.67	13.35
Sm	4.33	5.94	5.6	4.69	3.61	4.87	4.89	5.38	4.98	3.43	6.25	3.15
Eu	1.09	1.4	1.5	1.32	1.15	1.36	1.43	1.47	1.43	1.07	1.61	0.96
Gd	4.46	6.03	5.8	5.19	3.8	5.06	5.01	5.61	5.26	3.72	6.44	3.64
Tb	0.724	0.938	0.919	0.804	0.614	0.829	0.826	0.934	0.9	0.64	1.019	0.684
Dy	5.18	6.07	5.93	5.3	4.32	5.75	5.83	6.45	6.11	4.43	7.05	4.49
Ho	0.9	1.01	1.01	0.88	0.88	1.15	1.16	1.3	1.23	0.9	1.43	0.88
Er	2.73	2.94	2.91	2.55	2.42	3.17	3.17	3.53	3.41	2.55	3.94	2.42
Yb	2.47	2.62	2.52	2.2	2.35	2.94	3.14	3.27	3.08	2.4	3.57	2.39
Lu	0.359	0.359	0.371	0.308	0.4	0.515	0.497	0.553	0.526	0.375	0.591	0.38
Rb	49.49	21.27	21.01	22.12	34.33	69.16	74.88	79.1	72.6	37.73	96	49.01
Ba	387	151.1	426.7	46	246.1	255.9	259.6	268.6	279.5	153.3	346.4	295.3

Table B2: Continued

Type: AusQuest Various Basalt, Dolerite, Gabbro Samples

Sample	**BW2-12**	**BN02**	**BN04**	**BN06**	**389057**	**389059**	**389060**	**389061**	**389062**	**389067**	**389068**	**AOB020**
Rock Type	Basalt dyke	Mafic chips	Mafic chips	Mafic chips	Basalt	Mesogabbro	Mesogabbro	Mesogabbro	Mesogabbro	Dolerite	Dolerite	Basalt
Location	Boondawari	CRA drill hole	CRA drill hole	CRA drill hole	MD-1A	TRR1	TRR2	TRR3	TRR6	NYI 1	SCR 1	153995
Zone	51	51	51	51	51	51	51	51	51	51	51	51
Northing	7388169	7396494	7395745	7395964	7404962	7331546	7333122	7332626	7331430	7406514	7366498	6873823
Easting	342287	335116	336408	333783	319217	406939	403959	403220	406564	287352	292156	739112
Trace Element (ppm): Continued												
Th	5.2	4.8	4.52	3.74	5.86	10.18	10.25	11.55	10.67	5.95	14.24	8.39
U	2.42	2.46	2.67	2.43	1.31	1.81	1.85	2.05	1.91	1.04	2.68	1.39
Nb	5.92	15.54	15.42	12.68	6.41	9.29	9.53	10.35	9.64	6.47	12.59	4.31
K	11284	9017	9258	10305	9822	11923	13340	14038	12738	7052	17353	30677
Ta	0.47	1.01	1.02	0.91	0.49	0.75	0.76	0.84	0.81	0.55	1.03	0.44
Pb												
Sr	210	45	89	55	208	150	171	154	150	146	166	400
P	535.2	1232.4	1335.9	902.8	578.6	577.9	621.4	666.8	620.8	441.3	760.2	314.4
Hf	2.99	5	5.11	4.12	3.03	3.78	3.99	4.32	3.93	2.74	4.96	2.65
Zr	112.9	193.9	197.7	156.9	107.2	134.5	145.3	156.2	142.7	95.7	178.4	84.8
Ti	5759	16474	16713	12924	5808	6778	7133	7755	7493	5759	8354	4998
Tb	0.724	0.938	0.919	0.804	0.614	0.829	0.826	0.934	0.9	0.64	1.019	0.684
Y	25.2	26.07	26.56	22.77	23.24	30.46	31.25	34.45	32.2	23.81	37.18	23.47
Co	40	43	44	44	39	40	37	41	42	39	34	41
Cr	56	94	136	57	63	35	19	30	31	128	12	82
Cu	112	78	69	44	106	52	55	48	47	76	42	57
Ni	64	59	66	53	68	33	25	28	30	65	13	45
V	256	348	356	310	255	266	269	287	285	252	287	255
Zn	103	146	176	122	72	88	95	93	96	74	103	71

Table B2: Continued

Type: Table Hill Volcanics Samples Collected Specifically for this Study												
	07THD-001B	07THD-001B	07THD-001B	07THD-001B	07THD-001B	THD-008	THD-008	THD-008	THD-008	THD-008	09THD-029	09THD-029
Sample	**1**	**2**	**3**	**4**	**5**	**6**	**7**	**8**	**9**	**10**	**11**	**12**
Rock Type	Dolerite	Dolerite	Dolerite	Dolerite	Dolerite	Dolerite	Dolerite	Dolerite	Dolerite	Dolerite	Dolerite	Dolerite
Location	MN1	MN1	MN1	MN1	MN1	MN1	MN1	MN1	MN1	MN1	MN5	MN5
Zone	51	51	51	51	51	51	51	51	51	51	51	51
Northing	7367674	7367674	7367674	7367674	7367674	7367809	7367809	7367809	7367809	7367809	7332952	7332952
Easting	340154	340154	340154	340154	340154	340828	340828	340828	340828	340828	366034	366034
Major Elements (wt. %):												
SiO_2	59.99	54.01	53.76	54.31	54.55	55.53	53.98	53.7	54.32	55.22	53.82	54.06
Al_2O_3	12.81	15.17	15.08	13.93	13.46	13.75	15.5	13.73	13.22	13.6	13.68	14.39
FeO_{tot}	12.7	12.07	10.92	11.95	12.76	13.75	11.23	11.62	12	12.7	11.89	11.46
MgO	1.29	3.77	5.44	5.71	4.93	2.88	4.15	6.78	6.33	4.05	6.21	5.73
CaO	3.26	7.34	8.97	8.16	5.71	6.08	8.91	9.18	8.14	4.39	8.56	8.66
Na_2O	3.14	2.87	2.27	2.3	2.67	3.08	2.5	2.18	2.26	4.14	2.32	2.41
K_2O	2.96	1.63	1.17	1.58	2.58	2.24	1.59	1.23	1.48	1.86	1.33	1.4
TiO_2	1.4	1.2	0.94	1.06	1.33	1.54	1.1	0.92	1.06	1.36	1.03	1.03
P_2O_5	0.297	0.148	0.114	0.133	0.163	0.174	0.135	0.105	0.129	0.17	0.121	0.126
MnO	0.17	0.17	0.17	0.19	0.17	0.18	0.16	0.2	0.18	0.11	0.19	0.18
LOI	1.42	1.41	1.12	0.72	1.47	1.28	0.71	0.81	0.68	1.91	0.7	0.6
H_2O-												
Total	99.44	99.79	99.95	100.04	99.79	100.48	99.97	100.46	99.80	99.51	99.85	100.05
Mg #	19.14	42.12	53.72	52.68	47.38	32.80	46.26	57.62	55.14	42.63	54.89	53.81
Trace Elements (ppm):												
La	50.5	25.3	19.7	22.3	27.7	32	23.7	18.5	22	28.6	20.4	21.8
Ce	103.2	51.5	40.4	46	56.3	65.2	47.5	37.5	45.8	57.7	41.5	44.4
Pr	11.93	5.92	4.68	5.3	6.59	7.52	5.47	4.3	5.19	6.71	4.81	5.22
Nd	46.9	23.9	19	21.5	26.3	30.3	22.4	18.1	21.5	26.9	19.8	21.3
Sm	10.26	5.15	3.98	4.74	5.73	6.52	4.71	3.86	4.66	5.72	4.33	4.38
Eu	2.14	1.31	1.1	1.19	1.44	1.62	1.26	1.08	1.17	1.48	1.09	1.19
Gd	10.35	5.37	4.46	4.88	5.94	6.82	5.18	4.2	5.15	6.08	4.62	4.85
Tb	1.59	0.9	0.75	0.79	0.94	1.09	0.81	0.72	0.81	0.99	0.75	0.8
Dy	10.26	5.55	4.64	4.9	6.18	6.98	5.19	4.51	5.25	6.22	4.85	5.03
Ho	2.03	1.12	0.93	0.99	1.22	1.41	1.06	0.9	1.05	1.31	0.98	1.04
Er	5.69	3.28	2.7	2.95	3.59	3.93	3.06	2.52	3.07	3.64	2.86	3.03
Yb	5.24	2.93	2.62	2.74	3.26	3.72	2.82	2.45	2.88	3.4	2.7	2.72
Lu	0.81	0.46	0.39	0.42	0.49	0.58	0.44	0.4	0.46	0.54	0.44	0.39
Rb	110.7	70.7	49.9	67.1	87.1	95.2	69.6	54.1	66.3	58.3	56.9	60.8

Table B2: Continued

Type: Table Hill Volcanics Samples Collected Specifically for this Study												
	07THD-001B	07THD-001B	07THD-001B	07THD-001B	07THD-001B	08THD-008	08THD-008	08THD-008	08THD-008	08THD-008	09THD-029	09THD-029
Sample	**1**	**2**	**3**	**4**	**5**	**6**	**7**	**8**	**9**	**10**	**11**	**12**
Rock Type	Dolerite	Dolerite	Dolerite	Dolerite	Dolerite	Dolerite	Dolerite	Dolerite	Dolerite	Dolerite	Dolerite	Dolerite
Location	MN1	MN1	MN1	MN1	MN1	MN1	MN1	MN1	MN1	MN1	MN5	MN5
Zone	51	51	51	51	51	51	51	51	51	51	51	51
Northing	7367674	7367674	7367674	7367674	7367674	7367809	7367809	7367809	7367809	7367809	7332952	7332952
Easting	340154	340154	340154	340154	340154	340828	340828	340828	340828	340828	366034	366034
Trace Element (ppm): Continued												
Ba	515.8	297.8	243.6	259.5	449.7	360.8	267.3	216.4	227.5	293.5	226.1	241.8
Th	20.45	10.08	8.25	8.93	11.37	13.06	9.54	7.37	9.45	12.12	8.45	8.9
U	3.95	1.91	1.67	1.73	2.13	2.52	1.81	1.42	1.78	2.42	1.57	1.7
Nb	14.2	8.3	6.9	7.3	9.1	11.5	8	6.2	7.5	9.6	7.1	7.3
K	25344	13898	9916	13332	22023	18963	13423	10345	12518	16001	11246	11799
Ta	1.2	0.7	0.5	0.6	0.7	0.9	0.6	0.5	0.6	0.8	0.6	0.6
Pb	14.5	9.5	7.3	16.5	10.4	9.5	8.5	12.2	8.7	4.3	13.4	11.5
Sr	122	158.5	147.2	147.1	180.3	145.2	156.5	138.4	136.6	160.1	154.1	150.3
P	1336	663.4	507.9	589.9	731.4	774.3	599.1	464.2	573.6	768.8	537.8	558.2
Hf	6.2	3.5	2.9	3.2	3.9	4.6	3.4	2.8	3.3	3.9	3.2	3.1
Zr	276	148	125	129	167	197	138	112	137	169	129	129
Ti	8656	7388	5753	6459	8198	9414	6706	5587	6474	8448	6289	6268
Tb	1.59	0.9	0.75	0.79	0.94	1.09	0.81	0.72	0.81	0.99	0.75	0.8
Y	54.5	30.9	26.4	27.6	34	38.7	29	25	28.5	34.4	27.5	28.2
Co												
Cr												
Cu												
Ni												
V												
Zn												

Table B2: Continued

Type: Table Hill Volcanics Samples Collected Specifically for this Study											
	09THD-029	09THD-029	09THD-028	09THD-028	09THD-028	07THD-002	07THD-002	07THD-002	07THD-002	07THD-002	07THD-002
Sample	**13**	**14**	**15**	**16**	**17**	**18**	**19**	**20**	**21**	**22**	**23**
Rock Type	Dolerite	Dolerite	Dolerite	Dolerite	Dolerite	Dolerite	Dolerite	Dolerite	Dolerite	Dolerite	Dolerite
Location	MN5	MN5	MN5	MN5	MN5	Boondawari	Boondawari	Boondawari	Boondawari	Boondawari	Boondawari
Zone	51	51	51	51	51	51	51	51	51	51	51
Northing	7332952	7332952	7333542	7333542	7333542	7392547	7392547	7392547	7392547	7392547	7392547
Easting	366034	366034	367563	367563	367563	342847	342847	342847	342847	342847	342847
Major Elements (wt. %):											
SiO_2	54.16	55.39	54.33	53.91	55.15	53.53	53.40	53.37	53.30	54.14	54.66
Al_2O_3	13.15	13.67	13.31	13.21	13.91	16.31	16.42	16.70	16.31	14.19	13.59
FeO_{tot}	12.79	13.24	12.04	13.09	12.35	10.16	9.88	9.61	8.92	11.68	12.82
MgO	5.67	4.12	6.38	5.55	5.12	4.10	4.68	4.89	5.34	5.65	4.46
CaO	8.00	3.27	8.39	7.66	3.73	8.98	9.49	9.59	9.87	8.54	6.79
Na_2O	2.51	2.63	2.24	2.36	3.36	3.09	2.35	2.52	2.70	2.31	2.89
K_2O	1.53	3.81	1.50	1.45	2.77	1.26	1.46	1.19	1.01	1.62	2.06
TiO_2	1.23	1.39	1.03	1.24	1.41	0.94	0.85	0.83	0.82	1.01	1.35
P_2O_5	0.15	0.17	0.13	0.15	0.17	0.12	0.11	0.10	0.11	0.13	0.17
MnO	0.19	0.14	0.20	0.20	0.12	0.14	0.17	0.14	0.13	0.18	0.19
LOI	0.56	1.81	0.67	0.63	1.65	1.21	0.82	1.18	1.31	0.41	1.03
H_2O-											
Total	99.94	99.64	100.22	99.45	99.74	99.84	99.63	100.12	99.82	99.86	100.01
Trace Elements (ppm):											
La	22.90	28.60	20.70	21.20	28.90	21.40	19.40	19.20	19.40	22.60	29.30
Ce	46.80	58.20	42.70	44.10	59.90	43.50	38.90	38.30	38.20	46.10	58.10
Pr	5.32	6.67	5.00	5.10	6.80	5.00	4.50	4.34	4.29	5.33	6.61
Nd	22.20	27.10	20.60	20.80	27.70	20.20	18.40	18.60	17.80	21.30	26.80
Sm	4.80	5.82	4.29	4.41	5.87	4.35	4.00	3.97	3.66	4.64	6.04
Eu	1.31	1.42	1.20	1.24	1.50	1.19	1.06	0.98	0.95	1.23	1.43
Gd	5.16	6.13	4.67	4.87	6.21	4.66	4.28	3.97	3.92	4.93	6.36
Tb	0.83	1.00	0.80	0.79	0.99	0.76	0.72	0.66	0.66	0.81	1.00
Dy	5.29	6.07	5.09	5.21	6.22	4.78	4.38	4.20	4.19	5.09	6.21
Ho	1.11	1.24	1.05	1.04	1.29	0.99	0.90	0.87	0.85	1.06	1.31
Er	3.10	3.55	3.01	3.00	3.65	2.88	2.56	2.53	2.37	3.00	3.69
Yb	2.84	3.36	2.75	2.85	3.33	2.73	2.46	2.26	2.32	2.69	3.30
Lu	0.43	0.52	0.42	0.45	0.60	0.50	0.43	0.35	0.34	0.46	0.49
Rb	66.10	112.40	62.30	56.70	108.20	53.60	66.40	50.00	46.30	79.60	92.50
Ba	250.10	586.10	260.00	231.30	339.80	249.40	259.30	220.40	168.90	271.00	321.00

Table B2: Continued

Type: Table Hill Volcanics Samples Collected Specifically for this Study											
	09THD-029	09THD-029	09THD-028	09THD-028	09THD-028	07THD-002	07THD-002	07THD-002	07THD-002	07THD-002	07THD-002
Sample	**13**	**14**	**15**	**16**	**17**	**18**	**19**	**20**	**21**	**22**	**23**
Rock Type	Dolerite	Dolerite	Dolerite	Dolerite	Dolerite	Dolerite	Dolerite	Dolerite	Dolerite	Dolerite	Dolerite
Locations	MN5	MN5	MN5	MN5	MN5	Boondawari	Boondawari	Boondawari	Boondawari	Boondawari	Boondawari
Zone	51	51	51	51	51	51	51	51	51	51	51
Northing	7332952	7332952	7333542	7333542	7333542	7392547	7392547	7392547	7392547	7392547	7392547
Easting	366034	366034	367563	367563	367563	342847	342847	342847	342847	342847	342847
Trace Element (ppm): Continued											
Th	9.21	12.51	8.81	8.55	12.36	8.51	8.00	7.79	7.84	9.03	11.93
U	1.72	2.34	1.74	1.66	2.41	1.63	1.61	1.58	1.51	1.76	2.25
Nb	7.40	9.80	7.40	7.30	9.70	6.80	6.40	6.30	6.10	7.10	9.50
K	12911	32694	12624	12317	23672	10692	12348	10061	8573	13634	17466
Ta	0.60	0.80	0.60	0.60	0.80	0.60	0.50	0.50	0.50	0.60	0.70
Pb	8.80	14.90	17.50	11.00	14.40	9.20	10.80	9.20	31.70	10.90	16.20
Sr	133.80	219.90	138.70	133.10	134.00	182.40	163.60	166.10	164.50	152.50	196.70
P	660.94	748.79	566.26	665.33	768.18	544.20	489.03	457.74	468.49	561.86	748.74
Hf	3.40	4.20	3.20	3.10	4.10	3.10	2.80	2.70	2.60	3.10	4.20
Zr	139.00	177.00	134.00	135.00	175.00	124.00	112.00	114.00	112.00	130.00	171.00
Ti	7495	8613	6260	7606	8701	5760	5191	5067	5026	6138	8265
Tb	0.83	1.00	0.80	0.79	0.99	0.76	0.72	0.66	0.66	0.81	1.00
Y	29.30	34.70	28.30	29.00	34.40	27.00	24.50	24.40	23.60	28.50	35.20
Co											
Cr											
Cu											
Ni											
V											
Zn											

Major and trace element analyses for the Kalkarindji continental flood basalt province. Analysis information can be found in Table B3 and B4. LOI, loss on ignition. GPS Datum: AGD84 unless otherwise noted. Sample information left blank did not have information provided by AusQuest. Results left blank were not analyzed for those particular trace elements. L – Lower, M – Middle, U – Upper Jilyili Sill; TSHLA – Trainer Sill Helix Lag Anomaly; TRR_ – Trainor Sill; NYR – Niyaninya sill; SCR – Savory Creek. Rock Type descriptions for the data received from AusQuest Limited are as provided, these samples were not observed by the author.

Table B3: Raw Major and Trace Element Results from Genalysis

Sample				07THD-001B					08THD-008					09THD-029
Element	Unit	Detection	Method	SAMPLE1	SAMPLE2	SAMPLE3A	SAMPLE4	SAMPLE5	SAMPLE6	SAMPLE7	SAMPLE8	SAMPLE9B	SAMPLE10	SAMPLE11
Major Elements:														
Al2O3	%	0.01	FB1/XRF20	12.81	15.17	15.08	13.93	13.46	13.75	15.5	13.73	13.22	13.6	13.68
BaO	ppm	1	/CALC	576	333	272	290	502	403	298	242	254	328	252
BaO	%	0.01	FB1/XRF20	0.07	0.03	0.03	0.04	0.05	0.04	0.03	0.03	0.03	0.04	0.03
CaO	%	0.01	FB1/XRF20	3.26	7.34	8.97	8.16	5.71	6.08	8.91	9.18	8.14	4.39	8.56
Cr2O3	%	0.01	FB1/XRF20	X	X	0.02	X	X	X	X	0.01	X	X	X
Fe2O3	%	0.01	FB1/XRF20	12.7	12.07	10.92	11.95	12.76	13.75	11.23	11.62	12	12.7	11.89
K2O	%	0.01	FB1/XRF20	2.96	1.63	1.17	1.58	2.58	2.24	1.59	1.23	1.48	1.86	1.33
MgO	%	0.01	FB1/XRF20	1.29	3.77	5.44	5.71	4.93	2.88	4.15	6.78	6.33	4.05	6.21
MnO	%	0.01	FB1/XRF20	0.17	0.17	0.17	0.19	0.17	0.18	0.16	0.2	0.18	0.11	0.19
Na2O	%	0.01	FB1/XRF20	3.14	2.87	2.27	2.3	2.67	3.08	2.5	2.18	2.26	4.14	2.32
P2O5	%	0.002	FB1/XRF20	0.297	0.148	0.114	0.133	0.163	0.174	0.135	0.105	0.129	0.17	0.121
SO3	%	0.01	FB1/XRF20	0.16	0.24	0.22	0.24	0.22	0.28	0.22	0.22	0.24	0.2	0.1
SiO2	%	0.01	FB1/XRF20	59.99	54.01	53.76	54.31	54.55	55.53	53.98	53.7	54.32	55.22	53.82
TiO2	%	0.01	FB1/XRF20	1.4	1.2	0.94	1.06	1.33	1.54	1.1	0.92	1.06	1.36	1.03
LOI	%	0.01	/TGA	1.42	1.41	1.12	0.72	1.47	1.28	0.71	0.81	0.68	1.91	0.7
Total	%	0.01	FB1/XRF20	99.65	99.98	100.16	100.3	100	100.72	100.17	100.68	100.03	99.68	100.07
Trace Elements:														
Ag	ppm	0.01	4A/MS	0.17	0.07	0.1	0.06	0.04	0.06	0.1	0.07	0.14	0.12	0.07
As	ppm	0.5	4A/MS	3.1	1.9	0.6	0.9	0.7	X	X	X	0.9	1.9	0.9
Ba	ppm	0.5	FB6/MS	515.8	297.8	243.6	259.5	449.7	360.8	267.3	216.4	227.5	293.5	226.1
Be	ppm	0.05	4A/MS	2.92	1.6	1.26	1.31	1.8	1.76	1.43	1.23	1.39	1.98	1.3
Bi	ppm	0.01	4A/MS	0.09	0.08	0.09	0.2	0.09	0.08	0.1	0.13	0.17	0.15	0.1
C	%	0.01	/CSA	0.09	0.03	0.02	0.04	0.02	0.02	0.04	0.03	0.03	0.05	0.03
Cd	ppm	0.02	4A/MS	0.26	0.09	0.19	0.18	0.15	0.18	0.17	0.15	0.17	0.13	0.21
Ce	ppm	0.5	FB6/MS	103.2	51.5	40.4	46	56.3	65.2	47.5	37.5	45.8	57.7	41.5
Co	ppm	0.1	4A/MS	22.3	37.2	37.4	40.3	43.2	35.7	38.7	42.3	45.6	42.7	45.4
Cr	ppm	20	FB6/MS	29	X	112	57	32	X	38	77	68	X	67
Cs	ppm	0.05	FB6/MS	1.67	1.32	2.09	2.18	1.3	1.45	2.09	2.35	2.39	0.97	1.44
Cu	ppm	1	4A/OE	12	41	54	66	46	47	62	68	71	16	40
Dy	ppm	0.05	FB6/MS	10.26	5.55	4.64	4.9	6.18	6.98	5.19	4.51	5.25	6.22	4.85
Er	ppm	0.05	FB6/MS	5.69	3.28	2.7	2.95	3.59	3.93	3.06	2.52	3.07	3.64	2.86
Eu	ppm	0.05	FB6/MS	2.14	1.31	1.1	1.19	1.44	1.62	1.26	1.08	1.17	1.48	1.09
Ga	ppm	0.1	FB6/MS	21.9	20.9	19.1	19.1	20.8	22.2	20.7	17.9	18.7	20.9	19.2

Table B3: Continued

Sample				07THD-001B					08THD-008					09THD-029
Element	Unit	Detection	Method	SAMPLE1	SAMPLE2	SAMPLE3A	SAMPLE4	SAMPLE5	SAMPLE6	SAMPLE7	SAMPLE8	SAMPLE9B	SAMPLE10	SAMPLE11
Trace Element: Continued														
Gd	ppm	0.05	FB6/MS	10.35	5.37	4.46	4.88	5.94	6.82	5.18	4.2	5.15	6.08	4.62
Ge	ppm	0.05	4A/MS	1.11	1.14	0.79	0.86	1.09	1.14	1.07	0.95	1.31	1.35	1.11
Hf	ppm	0.1	FB6/MS	6.2	3.5	2.9	3.2	3.9	4.6	3.4	2.8	3.3	3.9	3.2
Ho	ppm	0.02	FB6/MS	2.03	1.12	0.93	0.99	1.22	1.41	1.06	0.9	1.05	1.31	0.98
In	ppm	0.005	4A/MS	0.126	0.088	0.071	0.068	0.09	0.108	0.067	0.069	0.082	0.086	0.064
La	ppm	0.2	FB6/MS	50.5	25.3	19.7	22.3	27.7	32	23.7	18.5	22	28.6	20.4
Li	ppm	0.1	4A/MS	9.6	9.1	11.3	10.6	16.6	8.1	9.7	13.4	10.8	14	11.3
Lu	ppm	0.02	FB6/MS	0.81	0.46	0.39	0.42	0.49	0.58	0.44	0.4	0.46	0.54	0.44
Mo	ppm	0.1	4A/MS	1.7	1.1	0.8	0.8	1.1	0.9	1.1	0.6	1	0.7	0.9
Nb	ppm	0.1	FB6/MS	14.2	8.3	6.9	7.3	9.1	11.5	8	6.2	7.5	9.6	7.1
Nd	ppm	0.1	FB6/MS	46.9	23.9	19	21.5	26.3	30.3	22.4	18.1	21.5	26.9	19.8
Ni	ppm	1	4A/OE	X	13	32	32	22	5	18	41	34	13	29
Pb	ppm	0.5	4A/MS	14.5	9.5	7.3	16.5	10.4	9.5	8.5	12.2	8.7	4.3	13.4
Pr	ppm	0.05	FB6/MS	11.93	5.92	4.68	5.3	6.59	7.52	5.47	4.3	5.19	6.71	4.81
Rb	ppm	0.1	FB6/MS	110.7	70.7	49.9	67.1	87.1	95.2	69.6	54.1	66.3	58.3	56.9
Re	ppm	0.002	4A/MS	0.006	X	0.007	X	0.006	X	X	X	0.002	0.005	X
S	%	0.01	/CSA	0.06	0.1	0.1	0.11	0.09	0.11	0.09	0.08	0.1	0.08	0.05
Sb	ppm	0.05	4A/MS	0.44	0.21	0.18	0.14	0.12	0.13	0.18	0.14	0.15	0.11	0.13
Sc	ppm	10	FB6/OE	23	31	34	35	36	32	33	39	38	35	39
Se	ppm	0.5	4A/MS	X	X	X	X	X	X	X	X	X	X	X
Sm	ppm	0.05	FB6/MS	10.26	5.15	3.98	4.74	5.73	6.52	4.71	3.86	4.66	5.72	4.33
Sn	ppm	1	FB6/MS	4	2	2	2	2	3	2	2	2	2	2
Sr	ppm	0.2	FB6/MS	122	158.5	147.2	147.1	180.3	145.2	156.5	138.4	136.6	160.1	154.1
Ta	ppm	0.1	FB6/MS	1.2	0.7	0.5	0.6	0.7	0.9	0.6	0.5	0.6	0.8	0.6
Tb	ppm	0.02	FB6/MS	1.59	0.9	0.75	0.79	0.94	1.09	0.81	0.72	0.81	0.99	0.75
Te	ppm	0.05	4A/MS	X	0.05	X	X	X	X	X	X	X	0.07	X
Th	ppm	0.05	FB6/MS	20.45	10.08	8.25	8.93	11.37	13.06	9.54	7.37	9.45	12.12	8.45
Tl	ppm	0.02	4A/MS	0.58	0.33	0.25	0.38	0.57	0.45	0.35	0.27	0.43	0.59	0.32
Tm	ppm	0.05	FB6/MS	0.87	0.48	0.42	0.46	0.54	0.62	0.44	0.39	0.46	0.57	0.41
U	ppm	0.05	FB6/MS	3.95	1.91	1.67	1.73	2.13	2.52	1.81	1.42	1.78	2.42	1.57
V	ppm	10	FB6/OE	75	268	234	253	298	387	256	243	260	298	262
W	ppm	1	FB6/MS	2	X	X	1	X	X	X	X	X	1	X
Y	ppm	0.5	FB6/MS	54.5	30.9	26.4	27.6	34	38.7	29	25	28.5	34.4	27.5
Yb	ppm	0.05	FB6/MS	5.24	2.93	2.62	2.74	3.26	3.72	2.82	2.45	2.88	3.4	2.7
Zn	ppm	1	4A/OE	117	74	70	118	58	101	76	96	85	36	97
Zr	ppm	1	FB6/MS	276	148	125	129	167	197	138	112	137	169	129

Table B3: Continued

Sample				09THD-029			09THD-028			07THD-002				
Element	Unit	Detection	Method	SAMPLE12A	SAMPLE13	SAMPLE14	SAMPLE15	SAMPLE16B	SAMPLE17	SAMPLE18	SAMPLE19	SAMPLE20	SAMPLE21	SAMPLE22
Major Elements:														
Al2O3	%	0.01	FB1/XRF20	14.39	13.15	13.67	13.31	13.21	13.91	16.31	16.42	16.7	16.31	14.19
BaO	ppm	1	/CALC	270	279	654	290	258	379	278	289	246	189	303
BaO	%	0.01	FB1/XRF20	0.03	0.04	0.07	0.03	0.03	0.04	0.03	0.03	0.03	0.02	0.03
CaO	%	0.01	FB1/XRF20	8.66	8	3.27	8.39	7.66	3.73	8.98	9.49	9.59	9.87	8.54
Cr2O3	%	0.01	FB1/XRF20	X	X	X	0.01	X	X	X	0.02	0.01	0.02	X
Fe2O3	%	0.01	FB1/XRF20	11.46	12.79	13.24	12.04	13.09	12.35	10.16	9.88	9.61	8.92	11.68
K2O	%	0.01	FB1/XRF20	1.4	1.53	3.81	1.5	1.45	2.77	1.26	1.46	1.19	1.01	1.62
MgO	%	0.01	FB1/XRF20	5.73	5.67	4.12	6.38	5.55	5.12	4.1	4.68	4.89	5.34	5.65
MnO	%	0.01	FB1/XRF20	0.18	0.19	0.14	0.2	0.2	0.12	0.14	0.17	0.14	0.13	0.18
Na2O	%	0.01	FB1/XRF20	2.41	2.51	2.63	2.24	2.36	3.36	3.09	2.35	2.52	2.7	2.31
P2O5	%	0.002	FB1/XRF20	0.126	0.149	0.166	0.128	0.149	0.171	0.122	0.11	0.103	0.105	0.127
SO3	%	0.01	FB1/XRF20	0.2	0.24	0.02	0.19	0.23	0.27	0.2	0.2	0.18	0.09	0.19
SiO2	%	0.01	FB1/XRF20	54.06	54.16	55.39	54.33	53.91	55.15	53.53	53.4	53.37	53.3	54.14
TiO2	%	0.01	FB1/XRF20	1.03	1.23	1.39	1.03	1.24	1.41	0.94	0.85	0.83	0.82	1.01
LOI	%	0.01	/TGA	0.6	0.56	1.81	0.67	0.63	1.65	1.21	0.82	1.18	1.31	0.41
Total	%	0.01	FB1/XRF20	100.25	100.22	99.88	100.52	99.67	100.03	100.06	99.97	100.34	100.01	100.22
Trace Elements:														
Ag	ppm	0.01	4A/MS	0.04	0.05	0.04	0.08	0.07	0.12	0.16	0.34	0.08	0.18	0.18
As	ppm	0.5	4A/MS	0.9	0.6	X	X	X	X	1.5	1.5	3.5	1.3	X
Ba	ppm	0.5	FB6/MS	241.8	250.1	586.1	260	231.3	339.8	249.4	259.3	220.4	168.9	271
Be	ppm	0.05	4A/MS	1.4	1.42	1.92	1.32	1.47	1.96	1.35	1.23	1.16	1.25	1.39
Bi	ppm	0.01	4A/MS	0.08	0.1	0.12	0.11	0.08	0.1	0.08	0.21	0.1	0.07	0.21
C	%	0.01	/CSA	0.01	0.02	0.01	0.05	0.01	0.02	0.04	0.03	0.04	0.03	0.02
Cd	ppm	0.02	4A/MS	0.11	0.17	0.12	0.18	0.18	0.19	0.14	0.22	0.12	0.18	0.26
Ce	ppm	0.5	FB6/MS	44.4	46.8	58.2	42.7	44.1	59.9	43.5	38.9	38.3	38.2	46.1
Co	ppm	0.1	4A/MS	42	42.3	39.6	42.1	46.3	43.1	35.8	35.3	34.2	35.7	43.6
Cr	ppm	20	FB6/MS	45	38	26	70	23	31	X	104	100	140	55
Cs	ppm	0.05	FB6/MS	1.96	2.01	2.24	2.27	1.69	2.04	1.75	1.8	1.28	1.01	2.41
Cu	ppm	1	4A/OE	43	47	15	45	42	62	32	64	52	14	86
Dy	ppm	0.05	FB6/MS	5.03	5.29	6.07	5.09	5.21	6.22	4.78	4.38	4.2	4.19	5.09
Er	ppm	0.05	FB6/MS	3.03	3.1	3.55	3.01	3	3.65	2.88	2.56	2.53	2.37	3
Eu	ppm	0.05	FB6/MS	1.19	1.31	1.42	1.2	1.24	1.5	1.19	1.06	0.98	0.95	1.23
Ga	ppm	0.1	FB6/MS	19.2	18.5	20.8	18.4	18.1	21.2	20.5	18.7	18.8	18.5	18.7

Table B3: Continued

Sample				09THD-029			09THD-028			07THD-002				
Element	Unit	Detection	Method	SAMPLE12A	SAMPLE13	SAMPLE14	SAMPLE15	SAMPLE16B	SAMPLE17	SAMPLE18	SAMPLE19	SAMPLE20	SAMPLE21	SAMPLE22
Trace Elemen): Continued														
Gd	ppm	0.05	FB6/MS	4.85	5.16	6.13	4.67	4.87	6.21	4.66	4.28	3.97	3.92	4.93
Ge	ppm	0.05	4A/MS	1.13	1.16	1.08	0.96	1.08	1.12	1.12	1.1	1.12	1.21	1.17
Hf	ppm	0.1	FB6/MS	3.1	3.4	4.2	3.2	3.1	4.1	3.1	2.8	2.7	2.6	3.1
Ho	ppm	0.02	FB6/MS	1.04	1.11	1.24	1.05	1.04	1.29	0.99	0.9	0.87	0.85	1.06
In	ppm	0.005	4A/MS	0.069	0.079	0.079	0.062	0.075	0.09	0.066	0.08	0.078	0.062	0.075
La	ppm	0.2	FB6/MS	21.8	22.9	28.6	20.7	21.2	28.9	21.4	19.4	19.2	19.4	22.6
Li	ppm	0.1	4A/MS	9.8	14.1	18.6	10.3	9.8	16.9	12.6	16.1	11.4	11.5	14.2
Lu	ppm	0.02	FB6/MS	0.39	0.43	0.52	0.42	0.45	0.6	0.5	0.43	0.35	0.34	0.46
Mo	ppm	0.1	4A/MS	0.7	1	0.9	0.8	0.9	1.2	0.6	1.4	0.7	0.9	0.9
Nb	ppm	0.1	FB6/MS	7.3	7.4	9.8	7.4	7.3	9.7	6.8	6.4	6.3	6.1	7.1
Nd	ppm	0.1	FB6/MS	21.3	22.2	27.1	20.6	20.8	27.7	20.2	18.4	18.6	17.8	21.3
Ni	ppm	1	4A/OE	26	23	20	30	21	17	17	29	34	37	32
Pb	ppm	0.5	4A/MS	11.5	8.8	14.9	17.5	11	14.4	9.2	10.8	9.2	31.7	10.9
Pr	ppm	0.05	FB6/MS	5.22	5.32	6.67	5	5.1	6.8	5	4.5	4.34	4.29	5.33
Rb	ppm	0.1	FB6/MS	60.8	66.1	112.4	62.3	56.7	108.2	53.6	66.4	50	46.3	79.6
Re	ppm	0.002	4A/MS	X	X	X	X	0.002	0.004	0.004	0.005	0.004	0.003	X
S	%	0.01	/CSA	0.09	0.09	0.01	0.08	0.09	0.11	0.09	0.08	0.08	0.03	0.08
Sb	ppm	0.05	4A/MS	0.11	0.13	0.11	0.14	0.11	0.16	0.16	0.2	0.19	0.18	0.17
Sc	ppm	10	FB6/OE	35	37	35	38	34	33	32	30	30	31	37
Se	ppm	0.5	4A/MS	X	X	X	X	X	X	X	X	X	X	X
Sm	ppm	0.05	FB6/MS	4.38	4.8	5.82	4.29	4.41	5.87	4.35	4	3.97	3.66	4.64
Sn	ppm	1	FB6/MS	2	2	3	2	2	3	2	2	2	2	2
Sr	ppm	0.2	FB6/MS	150.3	133.8	219.9	138.7	133.1	134	182.4	163.6	166.1	164.5	152.5
Ta	ppm	0.1	FB6/MS	0.6	0.6	0.8	0.6	0.6	0.8	0.6	0.5	0.5	0.5	0.6
Tb	ppm	0.02	FB6/MS	0.8	0.83	1	0.8	0.79	0.99	0.76	0.72	0.66	0.66	0.81
Te	ppm	0.05	4A/MS	X	X	X	X	X	X	0.07	X	0.06	X	0.06
Th	ppm	0.05	FB6/MS	8.9	9.21	12.51	8.81	8.55	12.36	8.51	8	7.79	7.84	9.03
Tl	ppm	0.02	4A/MS	0.34	0.38	0.64	0.4	0.35	0.94	0.27	0.31	0.22	0.23	0.38
Tm	ppm	0.05	FB6/MS	0.45	0.46	0.55	0.43	0.44	0.53	0.43	0.38	0.36	0.36	0.44
U	ppm	0.05	FB6/MS	1.7	1.72	2.34	1.74	1.66	2.41	1.63	1.61	1.58	1.51	1.76
V	ppm	10	FB6/OE	250	278	307	256	271	305	237	204	200	208	258
W	ppm	1	FB6/MS	1	1	1	1	X	1	X	2	X	X	2
Y	ppm	0.5	FB6/MS	28.2	29.3	34.7	28.3	29	34.4	27	24.5	24.4	23.6	28.5
Yb	ppm	0.05	FB6/MS	2.72	2.84	3.36	2.75	2.85	3.33	2.73	2.46	2.26	2.32	2.69
Zn	ppm	1	4A/OE	91	101	96	99	103	112	65	154	64	55	127
Zr	ppm	1	FB6/MS	129	139	177	134	135	175	124	112	114	112	130

Table B3: Continued

Sample				07THD-002	060	036	ANT-D002	K03	052	109	111	112	P04	Check
Element	Unit	Detection	Method	SAMPLE23	SAMPLE24	SAMPLE25	SAMPLE26	SAMPLE27	SAMPLE28	SAMPLE29	SAMPLE30	SAMPLE31	SAMPLE32	07THD-001B
Major Elements:														
Al2O3	%	0.01	FB1/XRF20	13.59	14.52	15.27	14.18	14.31	13.82	13.93	13.05	14.02	13.65	16.44
BaO	ppm	1	/CALC	358	200	352	322	339	308	339	297	226	310	185
BaO	%	0.01	FB1/XRF20	0.04	0.02	0.04	0.03	0.04	0.04	0.04	0.03	0.03	0.04	0.02
CaO	%	0.01	FB1/XRF20	6.79	9.22	5.94	4.89	5.85	6.65	6.38	5.59	7.15	7.01	9.9
Cr2O3	%	0.01	FB1/XRF20	X	0.02	0.01	0.01	X	X	X	X	X	X	0.02
Fe2O3	%	0.01	FB1/XRF20	12.82	10.09	11.27	11.48	12.28	12.77	12.63	14.37	12.77	12.2	8.96
K2O	%	0.01	FB1/XRF20	2.06	4.8	2.66	3.21	2.27	2.12	2.98	2.26	1.9	1.95	1.01
MgO	%	0.01	FB1/XRF20	4.46	6.87	4.71	5	5.4	4.65	4.81	3.62	4.91	5.47	5.35
MnO	%	0.01	FB1/XRF20	0.19	0.17	0.17	0.2	0.24	0.18	0.2	0.36	0.17	0.13	0.14
Na2O	%	0.01	FB1/XRF20	2.89	0.85	4.33	4.57	3.94	3.38	3.59	3.07	3.39	3.07	2.7
P2O5	%	0.002	FB1/XRF20	0.168	0.087	0.129	0.172	0.175	0.141	0.135	0.172	0.137	0.154	0.107
SO3	%	0.01	FB1/XRF20	0.28	0.02	X	0.15	0.02	0.02	0.05	X	X	X	0.09
SiO2	%	0.01	FB1/XRF20	54.66	50.01	52.48	53.38	52.07	53.37	52.91	55.02	53.56	53.62	53.45
TiO2	%	0.01	FB1/XRF20	1.35	0.87	1.19	1.3	1.46	1.23	1.18	1.54	1.21	1.21	0.82
LOI	%	0.01	/TGA	1.03	2.39	1.79	1.46	1.86	1.34	1.08	0.72	0.66	1.31	1.28
Total	%	0.01	FB1/XRF20	100.23	100.2	100.14	100.06	100.09	99.83	100.05	99.99	100.05	99.94	100.34
Trace Elements:														
Ag	ppm	0.01	4A/MS	0.09	0.06	0.04	0.09	0.2	0.22	0.14	0.11	0.04	0.13	0.09
As	ppm	0.5	4A/MS	X	X	X	0.8	2	X	1.6	1.1	4	X	1
Ba	ppm	0.5	FB6/MS	321	178.7	314.9	288.1	303.2	276	303.6	266	202.8	277.2	165.4
Be	ppm	0.05	4A/MS	1.89	0.79	1.21	1.34	1.16	1.41	1.26	1.93	1.38	1.2	1.15
Bi	ppm	0.01	4A/MS	0.16	0.07	0.05	0.06	0.06	0.08	0.08	0.09	0.08	0.04	0.06
C	%	0.01	/CSA	0.03	0.04	0.04	0.06	0.03	0.03	0.02	0.01	0.02	0.04	0.04
Cd	ppm	0.02	4A/MS	0.17	0.11	0.11	0.13	0.2	0.12	0.14	0.13	0.24	0.18	0.16
Ce	ppm	0.5	FB6/MS	58.1	25	44.8	44.8	45.9	45	42.4	60.9	42.9	39.8	38.1
Co	ppm	0.1	4A/MS	41.5	39.9	36.9	38.3	41.6	42.1	43.2	40.9	45.6	39.5	35.2
Cr	ppm	20	FB6/MS	35	172	91	85	47	X	X	X	X	52	136
Cs	ppm	0.05	FB6/MS	2.26	0.6	6.47	0.96	0.28	0.72	0.36	1.27	0.47	0.77	0.98
Cu	ppm	1	4A/OE	48	77	15	44	128	18	14	34	17	6	15
Dy	ppm	0.05	FB6/MS	6.21	3.75	5.25	5.5	6.06	5.67	5.13	6.59	5.4	5.24	4.14
Er	ppm	0.05	FB6/MS	3.69	2.2	3.07	3.21	3.64	3.46	3.2	4.02	3.29	3.07	2.45
Eu	ppm	0.05	FB6/MS	1.43	0.96	1.24	1.39	1.52	1.33	1.23	1.56	1.27	1.3	0.95
Ga	ppm	0.1	FB6/MS	20.9	16.6	18.9	18.4	19.3	19.8	19.3	21.1	19.3	18.2	18

Table B3: Continued

Sample				07THD-002	060	036	ANT-D002	K03	052	109	111	112	P04	Check
Element	Unit	Detection	Method	SAMPLE23	SAMPLE24	SAMPLE25	SAMPLE26	SAMPLE27	SAMPLE28	SAMPLE29	SAMPLE30	SAMPLE31	SAMPLE32	07THD-001B
Trace Element: Continued														
Gd	ppm	0.05	FB6/MS	6.36	3.38	4.82	5.4	5.96	5.24	5.03	6.45	5.2	4.6	4.22
Ge	ppm	0.05	4A/MS	0.96	0.96	1.23	0.81	1.05	1.15	1.28	1.37	1.42	0.9	0.87
Hf	ppm	0.1	FB6/MS	4.2	2.2	3.4	3.6	3.9	3.7	3.2	4.6	3.4	3.3	2.8
Ho	ppm	0.02	FB6/MS	1.31	0.78	1.08	1.11	1.21	1.16	1.09	1.34	1.09	1.09	0.82
In	ppm	0.005	4A/MS	0.091	0.052	0.058	0.073	0.081	0.065	0.07	0.096	0.08	0.093	0.062
La	ppm	0.2	FB6/MS	29.3	12.1	21.5	21.6	20.6	21.3	20.4	29.6	21.1	19.2	19.8
Li	ppm	0.1	4A/MS	21.6	33.1	31.5	27.6	15.7	16.4	21.9	16	12	25.2	11.5
Lu	ppm	0.02	FB6/MS	0.49	0.33	0.43	0.46	0.54	0.51	0.47	0.57	0.44	0.45	0.37
Mo	ppm	0.1	4A/MS	1.2	0.5	0.8	0.6	0.8	0.6	1	0.9	1.1	0.4	0.8
Nb	ppm	0.1	FB6/MS	9.5	4.2	7.3	7.2	7.9	8.1	7.3	10.1	7.4	6.8	6.3
Nd	ppm	0.1	FB6/MS	26.8	13	21.5	21.9	22.9	21.9	20.4	28.7	20.8	20.2	17.5
Ni	ppm	1	4A/OE	15	71	35	34	23	15	16	2	15	29	41
Pb	ppm	0.5	4A/MS	16.2	9.5	15.8	3.6	7.7	9.9	8	13.5	7.4	9.7	30.7
Pr	ppm	0.05	FB6/MS	6.61	3.01	5.15	5.24	5.56	5.26	4.94	7.01	4.91	4.83	4.38
Rb	ppm	0.1	FB6/MS	92.5	50.2	77.8	74.1	72.8	69.5	63.1	89.3	62.9	61.1	45
Re	ppm	0.002	4A/MS	X	X	X	0.005	0.007	0.006	0.002	X	X	0.005	X
S	%	0.01	/CSA	0.12	0.01	0.01	0.06	0.01	0.01	0.02	0.01	0.01	X	0.03
Sb	ppm	0.05	4A/MS	0.17	0.13	0.17	0.14	0.14	0.16	0.14	0.16	0.16	0.14	0.2
Sc	ppm	10	FB6/OE	34	36	33	33	34	37	39	34	38	35	34
Se	ppm	0.5	4A/MS	X	X	X	X	X	X	X	X	X	X	X
Sm	ppm	0.05	FB6/MS	6.04	2.9	4.68	5.04	5.41	4.99	4.54	6.29	4.58	4.36	3.81
Sn	ppm	1	FB6/MS	3	1	2	2	2	2	2	3	2	2	2
Sr	ppm	0.2	FB6/MS	196.7	1131.2	183.2	264.2	212.4	123.5	337.1	126	174.7	170.2	165.2
Ta	ppm	0.1	FB6/MS	0.7	0.3	0.6	0.7	0.6	0.6	0.6	0.8	0.6	0.5	0.5
Tb	ppm	0.02	FB6/MS	1	0.58	0.8	0.85	0.98	0.85	0.82	1.08	0.85	0.83	0.66
Te	ppm	0.05	4A/MS	0.05	X	X	X	X	X	X	X	X	X	X
Th	ppm	0.05	FB6/MS	11.93	4.22	8.7	9.18	7.18	9.28	8.22	13.32	8.51	7.05	7.84
Tl	ppm	0.02	4A/MS	0.47	0.13	0.17	0.22	0.17	0.2	0.14	0.32	0.18	0.2	0.2
Tm	ppm	0.05	FB6/MS	0.54	0.32	0.45	0.48	0.54	0.51	0.49	0.6	0.48	0.47	0.36
U	ppm	0.05	FB6/MS	2.25	0.71	1.43	1.64	1.12	1.55	1.33	2.28	1.4	1.17	1.54
V	ppm	10	FB6/OE	296	248	266	298	303	296	291	345	292	278	220
W	ppm	1	FB6/MS	1	X	X	X	X	1	X	2	1	X	X
Y	ppm	0.5	FB6/MS	35.2	21.5	28.8	30.2	33.1	31.2	30.4	36.8	30.6	28.4	23.1
Yb	ppm	0.05	FB6/MS	3.3	1.98	2.97	2.97	3.26	3.19	3.04	3.72	2.99	2.89	2.25
Zn	ppm	1	4A/OE	110	78	90	73	198	94	112	200	90	109	57
Zr	ppm	1	FB6/MS	171	90	143	151	168	148	140	182	141	138	117

Method codes: /CSA - Induction Furnace Analyzed by Infrared Spectrometry; /TGA - No digestion or other pre-treatment undertaken. Analyzed by Thermal Gravimetric Analyzer; 4A/MS - Multi-acid digest including Hydrofluoric, Nitric, Perchloric and Hydrochloric acids in Teflon Tubes. Analyzed by Inductively Coupled Plasma Mass Spectrometry (ICP-MS); 4A/OE - Multi-acid digest including Hydrofluoric, Nitric, Perchloric and Hydrochloric acids in Teflon Tubes; Analyzed by Inductively Coupled Plasma Optical (Atomic) Emission Spectrometry (ICP-OES); FB1/XRF - Fused Disk preparation for XRF analysis Analyzed by XRF Spectrometry; FB6/MS - Lithium metaborate/tetraborate fusion Analyzed by Inductively Coupled Plasma Mass Spectrometry; FB6/OE - Lithium metaborate/tetraborate fusion Analyzed by ICP-OES.

Table B4: Raw Major and Trace Element Results of Standards and Blanks from Genalysis

				Standards										
Element	Unit	Detection	Method	40100	GenFe-3	OREAS 45P	OREAS 45P	SARM1	GenFe-5	MA-1b	SARM4	WPR-1	WPR-1	SY-4
Major Elements:														
Al2O3	%	0.01	FB1/XRF20					11.99			16.28			20.53
BaO	ppm	1	/CALC				303						23	
BaO	%	0.01	FB1/XRF20					0.01			0.01			0.04
CaO	%	0.01	FB1/XRF20					0.76			11.35			7.93
Cr2O3	%	0.01	FB1/XRF20					X			X			X
Fe2O3	%	0.01	FB1/XRF20					1.97			9.09			6.31
K2O	%	0.01	FB1/XRF20					5			0.24			1.67
MgO	%	0.01	FB1/XRF20					0.02			7.41			0.51
MnO	%	0.01	FB1/XRF20					0.02			0.18			0.11
Na2O	%	0.01	FB1/XRF20					3.35			2.47			7.24
P2O5	%	0.002	FB1/XRF20					0.004			0.014			0.13
SO3	%	0.01	FB1/XRF20					0.02			0.01			0.04
SiO2	%	0.01	FB1/XRF20					75.44			52.44			49.8
TiO2	%	0.01	FB1/XRF20					0.09			0.19			0.28
LOI	%	0.01	/TGA		4.38				9.38					
Total	%	0.01	FB1/XRF20					99.33			99.73			100.12
Trace Elements:														
Ag	ppm	0.01	4A/MS			0.4						0.73		
As	ppm	0.5	4A/MS			13						1.4		
Ba	ppm	0.5	FB6/MS				271.5						20.4	
Be	ppm	0.05	4A/MS			0.84						0.14		
Bi	ppm	0.01	4A/MS			0.22						0.15		
C	%	0.01	/CSA	1.02						2.46				
Cd	ppm	0.02	4A/MS			0.16						0.2		
Ce	ppm	0.5	FB6/MS				48.4						5.6	
Co	ppm	0.1	4A/MS			118.1						182.4		
Cr	ppm	20	FB6/MS				1153						3989	
Cs	ppm	0.05	FB6/MS				2.06						0.61	
Cu	ppm	1	4A/OE			764						1707		
Dy	ppm	0.05	FB6/MS				3.92						0.71	
Er	ppm	0.05	FB6/MS				2.09						0.43	
Eu	ppm	0.05	FB6/MS				1.15						0.27	
Ga	ppm	0.1	FB6/MS				22						4.4	

Table B4: Continued

Element	Unit	Detection	Method	Standards										
				40100	GenFe-3	OREAS 45P	OREAS 45P	SARM1	GenFe-5	MA-1b	SARM4	WPR-1	WPR-1	SY-4
Trace Element: Continued														
Gd	ppm	0.05	FB6/MS				3.91						0.76	
Ge	ppm	0.05	4A/MS			1.62						0.6		
Hf	ppm	0.1	FB6/MS				6.3						0.6	
Ho	ppm	0.02	FB6/MS				0.76						0.16	
In	ppm	0.005	4A/MS			0.098						0.035		
La	ppm	0.2	FB6/MS				24.5						2	
Li	ppm	0.1	4A/MS			13.6						5		
Lu	ppm	0.02	FB6/MS				0.3						0.09	
Mo	ppm	0.1	4A/MS			2.2						0.3		
Nb	ppm	0.1	FB6/MS				21.3						1.9	
Nd	ppm	0.1	FB6/MS				21.7						3.5	
Ni	ppm	1	4A/OE			387						3077		
Pb	ppm	0.5	4A/MS			21						5.8		
Pr	ppm	0.05	FB6/MS				5.45						0.67	
Rb	ppm	0.1	FB6/MS				21.7						4.2	
Re	ppm	0.002	4A/MS			0.002						0.013		
S	%	0.01	/CSA	1.13						1.21				
Sb	ppm	0.05	4A/MS			0.85						0.81		
Sc	ppm	10	FB6/OE				64						11	
Se	ppm	0.5	4A/MS			1.6						4.3		
Sm	ppm	0.05	FB6/MS				4.48						0.79	
Sn	ppm	1	FB6/MS				3						X	
Sr	ppm	0.2	FB6/MS				31.1						7.8	
Ta	ppm	0.1	FB6/MS				1.5						0.1	
Tb	ppm	0.02	FB6/MS				0.64						0.13	
Te	ppm	0.05	4A/MS			0.21						0.48		
Th	ppm	0.05	FB6/MS				9.71						0.31	
Tl	ppm	0.02	4A/MS			0.24						0.09		
Tm	ppm	0.05	FB6/MS				0.31						0.06	
U	ppm	0.05	FB6/MS				2.33						0.24	
V	ppm	10	FB6/OE				267						90	
W	ppm	1	FB6/MS				1						X	
Y	ppm	0.5	FB6/MS				17.8						4.5	
Yb	ppm	0.05	FB6/MS				2.03						0.4	
Zn	ppm	1	4A/OE			140						93		
Zr	ppm	1	FB6/MS				268						22	

Table B4: Continued

				Standards							Blanks				Check
Element	Unit	Detection	Method	CD-1	SY-4	SY-4	WGB-1	WGB-1	AMIS0076	AMIS0076	Control Blank	Control Blank	Control Blank	Acid Blank	THB-001B
Major Elements:															
Al2O3	%	0.01	FB1/XRF20								X				12.83
BaO	ppm	1	/CALC			384		916		111	X		2		591
BaO	%	0.01	FB1/XRF20								X				0.07
CaO	%	0.01	FB1/XRF20								X				3.27
Cr2O3	%	0.01	FB1/XRF20								X				X
Fe2O3	%	0.01	FB1/XRF20								X				12.71
K2O	%	0.01	FB1/XRF20								X				2.98
MgO	%	0.01	FB1/XRF20								X				1.3
MnO	%	0.01	FB1/XRF20								X				0.17
Na2O	%	0.01	FB1/XRF20								X				3.18
P2O5	%	0.002	FB1/XRF20								X				0.298
SO3	%	0.01	FB1/XRF20								X				0.15
SiO2	%	0.01	FB1/XRF20								99.11				60.3
TiO2	%	0.01	FB1/XRF20								X				1.42
LOI	%	0.01	/TGA								0.04				1.39
Total	%	0.01	FB1/XRF20								99.14				100.04
Trace Elements:															
Ag	ppm	0.01	4A/MS		0.07		0.16		4.11		0.04	0.04		0.02	0.07
As	ppm	0.5	4A/MS		0.6		1.9		578.8		X	0.6		X	2.2
Ba	ppm	0.5	FB6/MS			344.1		820.2		99.3	0.8		1.9		529.4
Be	ppm	0.05	4A/MS		2.96		0.39		0.82		X	X		X	2.86
Bi	ppm	0.01	4A/MS		0.03		0.05		2.49		0.01	0.02		0.02	0.08
C	%	0.01	/CSA	0.21							X				0.09
Cd	ppm	0.02	4A/MS		0.12		0.08		0.94		X	X		X	0.24
Ce	ppm	0.5	FB6/MS			124.7		17.1		84.4	0.5		0.5		103.2
Co	ppm	0.1	4A/MS		2.6		27.7		124.6		0.1	0.2		X	23.4
Cr	ppm	20	FB6/MS			X		307		1119	X		X		26
Cs	ppm	0.05	FB6/MS			1.56		0.46		1.97	X		X		1.71
Cu	ppm	1	4A/OE		5		93		94		1	1		X	11
Dy	ppm	0.05	FB6/MS			18.86		2.75		17.53	0.07		X		9.92
Er	ppm	0.05	FB6/MS			14.37		1.54		9.51	X		X		5.81
Eu	ppm	0.05	FB6/MS			2.02		1.18		1.83	X		X		2.12
Ga	ppm	0.1	FB6/MS			35.8		12		3.8	0.1		X		21.7

Table B4: Continued

				Standards							Blanks				Check
Element	Unit	Detection	Method	CD-1	SY-4	SY-4	WGB-1	WGB-1	AMIS0076	AMIS0076	Control Blank	Control Blank	Control Blank	Acid Blank	THB-001B
Trace Element: Continued															
Gd	ppm	0.05	FB6/MS			14.49		2.85		13.41	0.07		X		10.04
Ge	ppm	0.05	4A/MS		0.67		1.2		0.51		X	X		X	0.89
Hf	ppm	0.1	FB6/MS			10.6		1.6		5.1	X		0.2		6.6
Ho	ppm	0.02	FB6/MS			4.33		0.54		3.36	X		X		2.09
In	ppm	0.005	4A/MS		0.042		0.056		0.024		X	X		X	0.114
La	ppm	0.2	FB6/MS			59.6		7.8		42	X		X		49.9
Li	ppm	0.1	4A/MS		38.1		44		7.7		X	X		X	10.4
Lu	ppm	0.02	FB6/MS			2.07		0.23		0.93	0.02		0.02		0.8
Mo	ppm	0.1	4A/MS		0.2		0.8		8.8		X	X		X	1.7
Nb	ppm	0.1	FB6/MS			13.6		5.8		10.1	0.3		0.3		16
Nd	ppm	0.1	FB6/MS			61.3		10.4		36.6	0.1		X		47.1
Ni	ppm	1	4A/OE		9		71		200		X	X		X	X
Pb	ppm	0.5	4A/MS		10.1		7.4		666.3		X	X		X	13.3
Pr	ppm	0.05	FB6/MS			15.11		2.16		9.37	0.06		X		11.74
Rb	ppm	0.1	FB6/MS			52.8		18.5		17.2	X		0.4		121.4
Re	ppm	0.002	4A/MS		X		0.005		0.003		X	X		X	X
S	%	0.01	/CSA	3.13							X				0.06
Sb	ppm	0.05	4A/MS		0.17		2.14		51.54		0.12	0.09		0.07	0.22
Sc	ppm	10	FB6/OE			X		38		X	X		X		23
Se	ppm	0.5	4A/MS		X		X		X		X	X		X	X
Sm	ppm	0.05	FB6/MS			12.8		2.49		10.93	X		X		9.76
Sn	ppm	1	FB6/MS			7		4		3	X		1		4
Sr	ppm	0.2	FB6/MS			1243.3		117		34.1	1.1		1.4		128.2
Ta	ppm	0.1	FB6/MS			0.9		0.4		5.2	X		0.1		1.3
Tb	ppm	0.02	FB6/MS			2.67		0.45		2.71	X		X		1.61
Te	ppm	0.05	4A/MS		0.07		X		0.34		X	X		0.05	0.06
Th	ppm	0.05	FB6/MS			1.81		1.13		151.86	X		0.17		20.52
Tl	ppm	0.02	4A/MS		0.31		0.39		0.26		X	X		X	0.6
Tm	ppm	0.05	FB6/MS			2.29		0.23		1.34	X		X		0.86
U	ppm	0.05	FB6/MS			1.24		1.1		1550.43	0.13		0.92		3.88
V	ppm	10	FB6/OE			X		235		24	X		X		74
W	ppm	1	FB6/MS			X		2		1	X		X		1
Y	ppm	0.5	FB6/MS			124.5		15.2		76.1	X		X		56.7
Yb	ppm	0.05	FB6/MS			14.8		1.41		7.74	X		X		5.35
Zn	ppm	1	4A/OE		92		31		465		X	X		X	114
Zr	ppm	1	FB6/MS			641		68		232	X		7		302

Method codes: /CSA - Induction Furnace Analyzed by Infrared Spectrometry; /TGA - No digestion or other pre-treatment undertaken. Analyzed by Thermal Gravimetric Analyzer; 4A/MS - Multi-acid digest including Hydrofluoric, Nitric, Perchloric and Hydrochloric acids in Teflon Tubes. Analyzed by Inductively Coupled Plasma Mass Spectrometry (ICP-MS); 4A/OE - Multi-acid digest including Hydrofluoric, Nitric, Perchloric and Hydrochloric acids in Teflon Tubes; Analyzed by Inductively Coupled Plasma Optical (Atomic) Emission Spectrometry (ICP-OES); FB1/XRF - Fused Disk preparation for XRF analysis Analyzed by XRF Spectrometry; FB6/MS - Lithium metaborate/tetraborate fusion Analyzed by Inductively Coupled Plasma Mass Spectrometry; FB6/OE - Lithium metaborate/tetraborate fusion Analyzed by ICP-OES.

APPENDIX C: Supplementary Data Chapter 3 – Major and Trace Element Raw Data, Tasmanian Dolerites

Table C1: Raw Major and Trace Element Results from Genalysis

				Tasmanian Dolerite Samples									
Element	Unit	Detection	Method	TAS-02	TAS-07	TAS-08	TAS-10	TAS-12	TAS-14	TAS-15	TAS-18	TAS-21	TAS-24
Major Elements:													
Al2O3	%	0.01	FB1/XRF	14.34	16.7	13.03	14.3	15.52	14.92	14.54	14.81	15.85	14.81
BaO	%	0.005	FB1/XRF	0.029	0.033	0.026	0.034	0.029	0.02	0.024	0.021	0.025	0.028
CaO	%	0.01	FB1/XRF	10.25	8.53	10.69	9.13	10.44	10.73	10.62	10.67	10.99	10.51
Cr2O3	%	0.005	FB1/XRF	0.022	0.007	0.029	0.01	0.009	0.016	0.018	0.017	0.009	0.015
Fe2O3	%	0.01	FB1/XRF	10.26	10.24	10.58	11.1	10.3	10.26	9.91	9.98	9.65	10.04
K2O	%	0.01	FB1/XRF	0.85	1.36	0.74	1.14	0.92	0.83	0.82	0.85	0.8	0.9
MgO	%	0.01	FB1/XRF	6.46	2.03	8.36	5.03	5.25	5.88	6.66	6.34	5.57	6.28
MnO	%	0.01	FB1/XRF	0.16	0.14	0.18	0.17	0.17	0.17	0.16	0.17	0.16	0.17
Na2O	%	0.01	FB1/XRF	1.83	2.7	1.54	2.4	1.96	1.91	1.82	1.85	1.85	1.81
P2O5	%	0.001	FB1/XRF	0.092	0.138	0.076	0.116	0.097	0.096	0.089	0.094	0.091	0.097
SO3	%	0.002	FB1/XRF	0.049	0.135	0.077	0.035	0.099	0.033	0.073	0.076	0.074	0.09
SiO2	%	0.01	FB1/XRF	54.68	56.53	54.31	55.74	54.17	54.07	54	54.16	53.66	54.5
TiO2	%	0.01	FB1/XRF	0.64	0.82	0.57	0.78	0.64	0.65	0.61	0.63	0.61	0.65
Total	%	0.01	FB1/XRF	99.98	100.06	100.38	100.3	100.26	100.29	99.79	100.19	100.06	100.44
LOI	%	0.01	/TGA	0.25	0.71	0.13	0.2	0.63	0.61	0.41	0.47	0.66	0.5
Trace Elements:													
Ag	ppm	0.01	4A/MS	0.05	0.06	0.03	0.03	0.03	0.03	0.04	0.06	0.05	0.02
As	ppm	0.5	4A/MS	0.9	1.1	0.9	1.2	0.9	0.8	0.8	0.8	0.6	1
Ba	ppm	0.5	FB6/MS	198.6	314.8	167	296.7	209.8	197.6	191.9	207	193.2	205.5
Be	ppm	0.05	4A/MS	0.79	0.95	0.63	0.97	0.93	0.69	0.67	0.69	0.78	0.68
Bi	ppm	0.01	4A/MS	0.17	0.16	0.11	0.11	0.07	0.07	0.06	0.06	0.04	0.04
C	%	0.01	/CSA	0.05	0.01	0.02	0.01	X	0.01	0.01	0.01	0.01	0.01
Cd	ppm	0.02	4A/MS	0.08	0.09	0.08	0.1	0.07	0.09	0.1	0.1	0.1	0.08
Ce	ppm	0.5	FB6/MS	25.5	40.1	21.5	33	27.1	26.5	24.8	26.2	24.6	26.3
Co	ppm	0.1	4A/MS	45.2	34	49.7	44.6	44.6	43.2	44.5	42.7	41.2	44.1
Cr	ppm	20	FB6/OE	148	35	187	65	51	85	124	104	54	90
Cs	ppm	0.1	FB6/MS	1.2	2.7	1	1.2	1.4	1.4	1.4	1.2	1.3	1.2
Cu	ppm	0.5	4A/OE	80.6	120	66.9	101.2	89.6	84.1	81.4	82.3	81.2	70.9
Dy	ppm	0.1	FB6/MS	3.8	5.3	3.5	4.6	3.8	4.1	3.8	3.9	3.6	3.7
Er	ppm	0.1	FB6/MS	2.4	3.1	2.1	2.9	2.4	2.2	2.5	2.5	2.3	2.5
Eu	ppm	0.1	FB6/MS	0.9	1.3	0.8	1.1	0.9	0.8	0.8	1	0.9	0.9
Ga	ppm	0.1	FB6/MS	16	19.8	14.5	17.1	16.9	16.5	15	15.6	17.8	15.7

Table C1: Continued

				Tasmanian Dolerite Samples									
Element	Unit	Detection	Method	TAS-02	TAS-07	TAS-08	TAS-10	TAS-12	TAS-14	TAS-15	TAS-18	TAS-21	TAS-24
Trace Element: Continued													
Gd	ppm	0.1	FB6/MS	3.3	5.2	2.7	4.3	3.5	3.7	3.5	4	3.2	3.7
Ge	ppm	0.05	4A/MS	0.76	0.99	1.12	1.36	1.23	1.05	1.27	0.92	1.04	0.85
Hf	ppm	0.1	FB6/MS	2.6	3.9	2.4	3.2	2.7	2.5	2.5	2.5	2.6	2.7
Ho	ppm	0.1	FB6/MS	0.8	1.2	0.7	1	0.8	0.8	0.8	0.8	0.8	0.8
In	ppm	0.01	4A/MS	0.06	0.09	0.07	0.07	0.07	0.08	0.07	0.06	0.06	0.06
La	ppm	0.2	FB6/MS	12.2	19.9	10.6	15.7	13	12.3	11.9	12	11.9	13.1
Li	ppm	0.1	4A/MS	8.2	13.4	8.9	15.1	9.6	11	9.8	10.6	9.7	9.8
Lu	ppm	0.1	FB6/MS	0.4	0.6	0.4	0.4	0.4	0.4	0.3	0.3	0.4	0.4
Mo	ppm	0.1	4A/MS	0.5	0.5	0.5	0.4	0.5	0.4	0.5	0.3	0.3	0.4
Nb	ppm	0.1	FB6/MS	5.3	7.6	4.1	6.6	5.2	5.2	4.6	4.8	4.7	5
Nd	ppm	0.1	FB6/MS	13.3	18.9	11.6	18.3	13.7	13.3	12.4	14.8	13	13.4
Ni	ppm	0.5	4A/OE	71.5	11.7	92	47.4	52	60.9	73.4	68.9	60.5	65.7
Pb	ppm	0.5	4A/MS	6	9.2	4.9	7.7	6.2	6	5.7	5.7	5.4	6
Pr	ppm	0.1	FB6/MS	3.4	5	2.8	4.2	3.4	3.4	3.2	3.4	3.1	3.2
Rb	ppm	0.1	FB6/MS	30.4	53.8	27.1	41.4	36.6	30.2	32.7	34	33	34.7
Re	ppm	0.002	4A/MS	X	X	0.002	X	X	X	X	X	X	X
S	%	0.01	/CSA	0.02	0.06	0.03	0.02	0.04	0.02	0.03	0.03	0.03	0.04
Sb	ppm	0.05	4A/MS	0.11	0.18	0.17	0.25	0.15	0.15	0.13	0.14	0.13	0.14
Sc	ppm	10	FB6/OE	42	30	45	40	40	41	41	41	41	40
Se	ppm	0.5	4A/MS	X	X	X	X	X	X	X	X	X	X
Sm	ppm	0.1	FB6/MS	3.1	4.8	2.9	4.2	3.8	3.3	3.2	2.9	2.8	3.6
Sn	ppm	1	FB6/MS	1	2	2	2	1	2	2	2	2	1
Sr	ppm	0.2	FB6/MS	132.3	160.2	112	197.3	139.3	130.9	134	128.1	129.5	160.9
Ta	ppm	0.1	FB6/MS	0.6	1.5	0.5	0.7	0.7	0.5	0.4	0.4	0.4	0.4
Tb	ppm	0.1	FB6/MS	0.6	0.9	0.5	0.7	0.6	0.6	0.6	0.6	0.6	0.6
Te	ppm	0.1	4A/MS	X	X	X	X	X	X	X	X	X	X
Th	ppm	0.1	FB6/MS	3.3	5.7	2.9	4.9	3.7	3.5	3.4	3.6	3.3	3.5
Tl	ppm	0.02	4A/MS	0.2	0.3	0.17	0.24	0.22	0.18	0.2	0.18	0.17	0.2
Tm	ppm	0.1	FB6/MS	0.4	0.6	0.3	0.6	0.4	0.4	0.3	0.4	0.4	0.4
U	ppm	0.1	FB6/MS	1	1.5	0.8	1.2	1	0.9	0.8	0.9	1	0.9
V	ppm	10	FB6/OE	246	197	261	248	233	243	241	239	239	237
W	ppm	1	FB6/MS	X	X	X	X	X	X	X	X	X	X
Y	ppm	0.5	FB6/MS	21.6	28.4	18.8	26.3	22.7	21.3	20.7	21.5	20.5	22.4
Yb	ppm	0.1	FB6/MS	2.5	3.4	2.2	2.8	2.5	2.2	2.5	2.5	2.3	2.6
Zn	ppm	1	4A/OE	80	90	74	88	79	77	74	77	76	75
Zr	ppm	1	FB6/MS	94	147	82	127	101	98	92	93	92	101

Method codes: /CSA - Induction Furnace Analyzed by Infrared Spectrometry; /TGA - No digestion or other pre-treatment undertaken. Analyzed by Thermal Gravimetric Analyzer; 4A/MS - Multi-acid digest including Hydrofluoric, Nitric, Perchloric and Hydrochloric acids in Teflon Tubes. Analyzed by Inductively Coupled Plasma Mass Spectrometry (ICP-MS); 4A/OE - Multi-acid digest including Hydrofluoric, Nitric, Perchloric and Hydrochloric acids in Teflon Tubes; Analyzed by Inductively Coupled Plasma Optical (Atomic) Emission Spectrometry (ICP-OES); FB1/XRF - Fused Disk preparation for XRF analysis Analyzed by XRF Spectrometry; FB6/MS - Lithium metaborate/tetraborate fusion Analyzed by Inductively Coupled Plasma Mass Spectrometry; FB6/OE - Lithium metaborate/tetraborate fusion Analyzed by ICP-OES.

Table C2: Raw Major and Trace Element Results of Standards and Blanks from Genalysis

				Check	Standards									
Element	Unit	Detection	Method	TAS-02	GBW07104	OREAS 45e	SARM1	SY-4	GBW07105	GBW07105	OREAS 24b	SARM1	GBW07122	GBW07122
Major Elements:														
Al2O3	%	0.01	FB1/XRF	14.38				20.69				12.06		
BaO	%	0.005	FB1/XRF	0.025				0.036				0.019		
CaO	%	0.01	FB1/XRF	10.23				7.92				0.76		
Cr2O3	%	0.005	FB1/XRF	0.023				X				X		
Fe2O3	%	0.01	FB1/XRF	10.27				6.21				1.97		
K2O	%	0.01	FB1/XRF	0.86				1.66				4.99		
MgO	%	0.01	FB1/XRF	6.47				0.53				0.03		
MnO	%	0.01	FB1/XRF	0.16				0.1				0.01		
Na2O	%	0.01	FB1/XRF	1.84				7.16				3.31		
P2O5	%	0.001	FB1/XRF	0.095				0.134				0.008		
SO3	%	0.002	FB1/XRF	0.05				0.039				0.021		
SiO2	%	0.01	FB1/XRF	54.65				49.8				75.7		
TiO2	%	0.01	FB1/XRF	0.63				0.29				0.09		
LOI	%	0.01	/TGA	0.28										
Total	%	0.01	FB1/XRF	100.04				99.57				99.64		
Trace Elements:														
Ag	ppm	0.01	4A/MS	0.06	0.07				0.03				0.07	
As	ppm	0.5	4A/MS	0.7	2.4				X				25	
Ba	ppm	0.5	FB6/MS	202.8			120.3			540.4				53.9
Be	ppm	0.05	4A/MS	0.78	1.09				2.71				0.38	
Bi	ppm	0.01	4A/MS	0.03	0.09				0.02				0.12	
C	%	0.01	/CSA	0.05		0.53					0.2			
Cd	ppm	0.02	4A/MS	0.09	0.08				0.05				0.12	
Ce	ppm	0.5	FB6/MS	25.9			208.5			104				7.8
Co	ppm	0.1	4A/MS	45.7	12.7				49.8				54.9	
Cr	ppm	20	FB6/OE	147			X			139				133
Cs	ppm	0.1	FB6/MS	1.3			1			0.5				1.8
Cu	ppm	0.5	4A/OE	79.5	54.6				44.3				83.3	
Dy	ppm	0.1	FB6/MS	3.8			18.7			5.3				3.8
Er	ppm	0.1	FB6/MS	2.4			13.4			2				2.6
Eu	ppm	0.1	FB6/MS	0.9			0.3			3.4				0.8
Ga	ppm	0.1	FB6/MS	16.2			30			23.7				17.2

Table C2: Continued

				Check	Standards									
Element	Unit	Detection	Method	TAS-02	GBW07104	OREAS 45e	SARM1	SY-4	GBW07105	GBW07105	OREAS 24b	SARM1	GBW07122	GBW07122
Trace Element: Continued														
Gd	ppm	0.1	FB6/MS	3.5			15.1			8.5				3.4
Ge	ppm	0.05	4A/MS	0.63	0.75				0.46				0.8	
Hf	ppm	0.1	FB6/MS	2.5			12.4			6				1.7
Ho	ppm	0.1	FB6/MS	0.8			4.3			0.9				0.8
In	ppm	0.01	4A/MS	0.07	0.03				0.08				0.08	
La	ppm	0.2	FB6/MS	11.8			117			55.4				3.3
Li	ppm	0.1	4A/MS	8.6	18.1				9.6				11.6	
Lu	ppm	0.1	FB6/MS	0.3			2.2			0.2				0.4
Mo	ppm	0.1	4A/MS	0.5	0.6				2.7				X	
Nb	ppm	0.1	FB6/MS	5.1			56.7			73.2				2.6
Nd	ppm	0.1	FB6/MS	12.7			71.4			50.9				6.8
Ni	ppm	0.5	4A/OE	70	15.7				144.5				111.2	
Pb	ppm	0.5	4A/MS	5.9	10.4				4.9				4.1	
Pr	ppm	0.1	FB6/MS	3.2			21.8			12.3				1.3
Rb	ppm	0.1	FB6/MS	31			330.4			38.4				27.9
Re	ppm	0.002	4A/MS	X	X				X				X	
S	%	0.01	/CSA	0.02		0.04					0.2			
Sb	ppm	0.05	4A/MS	0.12	0.24				0.18				1.15	
Sc	ppm	10	FB6/OE	42			X			13				42
Se	ppm	0.5	4A/MS	X	X				X				X	
Sm	ppm	0.1	FB6/MS	3.3			14.6			10.1				2.6
Sn	ppm	1	FB6/MS	2			6			3				1
Sr	ppm	0.2	FB6/MS	135.6			10.6			1135				148.9
Ta	ppm	0.1	FB6/MS	0.4			4.7			4.3				0.2
Tb	ppm	0.1	FB6/MS	0.6			2.7			1.1				0.6
Te	ppm	0.1	4A/MS	X	X				X				X	
Th	ppm	0.1	FB6/MS	3.4			52.2			5.8				0.3
Tl	ppm	0.02	4A/MS	0.19	0.14				0.03				0.12	
Tm	ppm	0.1	FB6/MS	0.4			2.2			0.3				0.4
U	ppm	0.1	FB6/MS	0.9			17.6			1.4				0.2
V	ppm	10	FB6/OE	245			X			175				310
W	ppm	1	FB6/MS	X			2			X				X
Y	ppm	0.5	FB6/MS	21.9			130.3			22.1				21.9
Yb	ppm	0.1	FB6/MS	2.6			14.2			1.4				2.5
Zn	ppm	1	4A/OE	78	71				155				97	
Zr	ppm	1	FB6/MS	98			307			277				55

Table C2: Continued

				Standards				Blanks				
Element	Unit	Detection	Method	OREAS 24b	OREAS 24b	OREAS 25a	OREAS 25a	Control Blank	Control Blank	Control Blank	Acid Blank	Acid Blank
Major Elements:												
Al2O3	%	0.01	FB1/XRF									
BaO	%	0.005	FB1/XRF									
CaO	%	0.01	FB1/XRF									
Cr2O3	%	0.005	FB1/XRF									
Fe2O3	%	0.01	FB1/XRF									
K2O	%	0.01	FB1/XRF									
MgO	%	0.01	FB1/XRF									
MnO	%	0.01	FB1/XRF									
Na2O	%	0.01	FB1/XRF									
P2O5	%	0.001	FB1/XRF									
SO3	%	0.002	FB1/XRF									
SiO2	%	0.01	FB1/XRF									
TiO2	%	0.01	FB1/XRF									
LOI	%	0.01	/TGA									
Total	%	0.01	FB1/XRF									
Trace Elements:												
Ag	ppm	0.01	4A/MS	0.07		0.05		X	0.02		X	
As	ppm	0.5	4A/MS	8.8		10.6		X	X		X	
Ba	ppm	0.5	FB6/MS		754		158.9	1.7		2		X
Be	ppm	0.05	4A/MS	2.72		0.94		X	X		X	
Bi	ppm	0.01	4A/MS	0.69		0.34		0.05	X		X	
C	%	0.01	/CSA					X				
Cd	ppm	0.02	4A/MS	0.03		0.07		X	X		X	
Ce	ppm	0.5	FB6/MS		85.5		51.9	X		X		X
Co	ppm	0.1	4A/MS	17.6		8.1		X	X		X	
Cr	ppm	20	FB6/OE		142		125	X		X		X
Cs	ppm	0.1	FB6/MS		10.9		6.5	X		X		X
Cu	ppm	0.5	4A/OE	36.8		30.7		0.8	1.3		X	
Dy	ppm	0.1	FB6/MS		5.9		4	0.1		X		X
Er	ppm	0.1	FB6/MS		3.5		2.7	X		X		X
Eu	ppm	0.1	FB6/MS		1.4		0.7	0.1		X		X
Ga	ppm	0.1	FB6/MS		20.7		24.4	X		0.4		X

Table C2: Continued

				Standards					Blanks				
Element	Unit	Detection	Method	OREAS 24b	OREAS 24b	OREAS 25a	OREAS 25a		Control Blank	Control Blank	Control Blank	Acid Blank	Acid Blank
Trace Element: Continued													
Gd	ppm	0.1	FB6/MS		6.3		4.2	0.1		X		X	
Ge	ppm	0.05	4A/MS	1.61		1.94		X	X		X		
Hf	ppm	0.1	FB6/MS		6.2		10.7	X		0.2		X	
Ho	ppm	0.1	FB6/MS		1.3		0.9	X		X		X	
In	ppm	0.01	4A/MS	0.07		0.11		0.01	X		X		
La	ppm	0.2	FB6/MS		44.4		24.5	0.4		X		X	
Li	ppm	0.1	4A/MS	51.3		35		X	X		X		
Lu	ppm	0.1	FB6/MS		0.5		0.5	X		X		X	
Mo	ppm	0.1	4A/MS	3.9		2.4		X	X		X		
Nb	ppm	0.1	FB6/MS		16.2		28.1	1.7		0.1		X	
Nd	ppm	0.1	FB6/MS		40.8		19.6	0.1		X		0.2	
Ni	ppm	0.5	4A/OE	59		44.9		X	X		X		
Pb	ppm	0.5	4A/MS	23.3		25.4		X	X		X		
Pr	ppm	0.1	FB6/MS		10.5		5.4	X		X		X	
Rb	ppm	0.1	FB6/MS		160.4		62.7	X		0.2		X	
Re	ppm	0.002	4A/MS	X		X		X	X		X		
S	%	0.01	/CSA					X					
Sb	ppm	0.05	4A/MS	0.98		0.66		X	X		0.1		
Sc	ppm	10	FB6/OE		15		14	X		X		X	
Se	ppm	0.5	4A/MS	X		2.6		X	X		X		
Sm	ppm	0.1	FB6/MS		7.4		3.7	X		X		X	
Sn	ppm	1	FB6/MS		5		5	X		X		X	
Sr	ppm	0.2	FB6/MS		122		48.1	1.2		1.1		X	
Ta	ppm	0.1	FB6/MS		1.4		2.2	0.1		X		X	
Tb	ppm	0.1	FB6/MS		1.1		0.6	0.1		X		X	
Te	ppm	0.1	4A/MS	X		0.3		X	X		X		
Th	ppm	0.1	FB6/MS		17		16.7	X		X		X	
Tl	ppm	0.02	4A/MS	0.91		0.36		X	X		X		
Tm	ppm	0.1	FB6/MS		0.5		0.4	0.2		X		X	
U	ppm	0.1	FB6/MS		3.3		3.6	X		X		X	
V	ppm	10	FB6/OE		111		171	X		X		X	
W	ppm	1	FB6/MS		4		3	X		X		X	
Y	ppm	0.5	FB6/MS		32.4		24.8	X		X		X	
Yb	ppm	0.1	FB6/MS		3.2		2.9	X		X		X	
Zn	ppm	1	4A/OE	108		47		X	X		X		
Zr	ppm	1	FB6/MS			641		68		232	X		7

Method codes: /CSA - Induction Furnace Analyzed by Infrared Spectrometry; /TGA - No digestion or other pre-treatment undertaken. Analyzed by Thermal Gravimetric Analyzer; 4A/MS - Multi-acid digest including Hydrofluoric, Nitric, Perchloric and Hydrochloric acids in Teflon Tubes. Analyzed by Inductively Coupled Plasma Mass Spectrometry (ICP-MS); 4A/OE - Multi-acid digest including Hydrofluoric, Nitric, Perchloric and Hydrochloric acids in Teflon Tubes; Analyzed by Inductively Coupled Plasma Optical (Atomic) Emission Spectrometry (ICP-OES); FB1/XRF - Fused Disk preparation for XRF analysis Analyzed by XRF Spectrometry; FB6/MS - Lithium metaborate/tetraborate fusion Analyzed by Inductively Coupled Plasma Mass Spectrometry; FB6/OE - Lithium metaborate/tetraborate fusion Analyzed by ICP-OES.

APPENDIX D: Supplementary Data Chapter 3 – $^{40}Ar/^{39}Ar$ Isotope Abundances Tasmanian Dolerites

Step	36Ar [fA]	%1σ	37Ar [fA]	1‰σ	38Ar [fA]	%1σ	39Ar [fA]	%1σ	40Ar [fA]	%1σ	40(r)/ 39(k)	± 2σ	Age (Ma)	± 2σ	40Ar(r) (%)	39Ar(k) (%)	K/Ca	± 2σ
TAS-01: J = 0.01058900 ± 0.00000635 (1σ) MDF = 0.992802 ± 0.00060 (1σ)																		
0.5	**0.00000**	**282.488**	**0.0004**	**223.500**	**0.0000**	**119.175**	**0.0000**	**312.47**	**0.0001**	**1,287**	**22.22**	**204.97**	**382.02**	**3177.0**	**470.28**	**0.00**	**0.01**	**0.0923**
1	**0.00000**	**382.679**	**0.0008**	**111.527**	**0.0000**	**576.811**	**0.0000**	**93.91**	**0.0002**	**304.1**	**10.88**	**48.55**	**197.12**	**833.62**	**183.52**	**0.00**	**0.02**	**0.0583**
1.5	**0.00001**	**12.234**	**0.0189**	**4.847**	**0.0000**	**42.202**	**0.0008**	**4.321**	**0.0101**	**6.591**	**9.87**	**2.21**	**179.71**	**38.24**	**78.03**	**0.10**	**0.02**	**0.0024**
2	**0.00015**	**1.035**	**0.2337**	**1.243**	**0.0002**	**12.321**	**0.0103**	**0.350**	**0.1289**	**0.515**	**10.04**	**0.18**	**182.68**	**3.19**	**78.90**	**1.33**	**0.02**	**0.0005**
2.5	**0.00035**	**0.571**	**0.6098**	**1.193**	**0.0004**	**5.392**	**0.0266**	**0.145**	**0.3170**	**0.210**	**10.01**	**0.09**	**182.18**	**1.59**	**82.52**	**3.44**	**0.02**	**0.0004**
3	**0.00039**	**0.476**	**0.9187**	**1.188**	**0.0005**	**3.907**	**0.0398**	**0.109**	**0.4426**	**0.150**	**10.17**	**0.07**	**184.85**	**1.27**	**89.91**	**5.15**	**0.02**	**0.0004**
3.5	**0.00041**	**0.473**	**1.1617**	**1.187**	**0.0006**	**3.566**	**0.0498**	**0.095**	**0.5299**	**0.125**	**10.18**	**0.07**	**185.02**	**1.18**	**94.02**	**6.45**	**0.02**	**0.0004**
4	**0.00042**	**0.459**	**1.2625**	**1.187**	**0.0007**	**3.279**	**0.0543**	**0.092**	**0.5653**	**0.118**	**10.08**	**0.07**	**183.39**	**1.15**	**95.24**	**7.03**	**0.02**	**0.0004**
4.5	**0.00039**	**0.560**	**1.2104**	**1.187**	**0.0007**	**2.821**	**0.0515**	**0.093**	**0.5287**	**0.126**	**10.06**	**0.07**	**183.01**	**1.19**	**96.34**	**6.67**	**0.02**	**0.0004**
5	**0.00038**	**0.566**	**1.1999**	**1.188**	**0.0007**	**2.954**	**0.0512**	**0.094**	**0.5283**	**0.126**	**10.11**	**0.07**	**183.92**	**1.19**	**96.40**	**6.63**	**0.02**	**0.0004**
5.5	**0.00033**	**0.559**	**1.0437**	**1.189**	**0.0006**	**3.470**	**0.0451**	**0.099**	**0.4647**	**0.143**	**10.09**	**0.07**	**183.52**	**1.21**	**96.26**	**5.84**	**0.02**	**0.0004**
6	**0.00032**	**0.564**	**0.9748**	**1.189**	**0.0005**	**3.339**	**0.0418**	**0.105**	**0.4325**	**0.154**	**10.11**	**0.07**	**183.87**	**1.25**	**95.99**	**5.41**	**0.02**	**0.0004**
7	**0.00041**	**0.519**	**1.2432**	**1.188**	**0.0007**	**2.935**	**0.0532**	**0.089**	**0.5513**	**0.121**	**10.07**	**0.07**	**183.16**	**1.17**	**95.65**	**6.89**	**0.02**	**0.0004**
8	**0.00035**	**0.537**	**1.0859**	**1.189**	**0.0006**	**3.299**	**0.0465**	**0.097**	**0.4783**	**0.139**	**10.05**	**0.07**	**182.85**	**1.21**	**96.06**	**6.02**	**0.02**	**0.0004**
10	**0.00046**	**0.452**	**1.3715**	**1.188**	**0.0008**	**2.417**	**0.0598**	**0.088**	**0.6248**	**0.106**	**10.13**	**0.06**	**184.20**	**1.12**	**95.40**	**7.75**	**0.02**	**0.0004**
12	**0.00040**	**0.605**	**1.2572**	**1.189**	**0.0006**	**3.792**	**0.0500**	**0.095**	**0.5136**	**0.129**	**10.06**	**0.07**	**183.00**	**1.28**	**96.22**	**6.47**	**0.02**	**0.0004**
15	**0.00027**	**0.664**	**0.8689**	**1.192**	**0.0004**	**5.266**	**0.0331**	**0.123**	**0.3396**	**0.196**	**10.07**	**0.09**	**183.29**	**1.47**	**96.32**	**4.27**	**0.02**	**0.0004**
18	**0.00026**	**0.687**	**0.8353**	**1.192**	**0.0004**	**5.109**	**0.0324**	**0.125**	**0.3338**	**0.199**	**10.10**	**0.08**	**183.71**	**1.47**	**96.40**	**4.19**	**0.02**	**0.0004**
21	**0.00021**	**0.800**	**0.7060**	**1.195**	**0.0003**	**6.214**	**0.0261**	**0.152**	**0.2635**	**0.252**	**10.08**	**0.10**	**183.37**	**1.66**	**97.79**	**3.36**	**0.02**	**0.0004**
24	**0.00017**	**0.938**	**0.5614**	**1.199**	**0.0003**	**6.685**	**0.0204**	**0.186**	**0.2083**	**0.319**	**10.08**	**0.11**	**183.35**	**1.92**	**96.90**	**2.64**	**0.02**	**0.0004**
27	**0.00011**	**1.537**	**0.3319**	**1.219**	**0.0001**	**15.183**	**0.0128**	**0.282**	**0.1321**	**0.503**	**10.06**	**0.16**	**182.98**	**2.71**	**95.54**	**1.65**	**0.02**	**0.0004**
30	**0.00012**	**1.429**	**0.3425**	**1.217**	**0.0002**	**12.589**	**0.0129**	**0.281**	**0.1362**	**0.488**	**9.98**	**0.16**	**181.65**	**2.74**	**93.08**	**1.67**	**0.02**	**0.0004**
35	**0.00016**	**1.067**	**0.5121**	**1.202**	**0.0002**	**11.512**	**0.0194**	**0.193**	**0.1984**	**0.335**	**10.04**	**0.11**	**182.71**	**1.98**	**96.47**	**2.51**	**0.02**	**0.0004**
40	**0.00010**	**1.611**	**0.2981**	**1.227**	**0.0001**	**12.751**	**0.0114**	**0.314**	**0.1189**	**0.559**	**10.05**	**0.17**	**182.90**	**2.99**	**94.48**	**1.47**	**0.02**	**0.0004**
45	**0.00009**	**1.847**	**0.2381**	**1.247**	**0.0001**	**14.209**	**0.0094**	**0.381**	**0.1016**	**0.654**	**10.12**	**0.21**	**184.12**	**3.59**	**91.57**	**1.21**	**0.02**	**0.0004**
50	**0.00013**	**1.172**	**0.3385**	**1.219**	**0.0002**	**11.357**	**0.0143**	**0.254**	**0.1537**	**0.432**	**10.05**	**0.14**	**182.89**	**2.40**	**91.66**	**1.85**	**0.02**	**0.0004**

Step	36Ar [fA]	%1σ	37Ar [fA]	1%σ	38Ar [fA]	%1σ	39Ar [fA]	%1σ	40Ar [fA]	%1σ	40(r)/ 39(k)	± 2σ	Age (Ma)	± 2σ	40Ar(r) (%)	39Ar(k) (%)	K/Ca	± 2σ
TAS-14: J = 0.01058900 ± 0.00000635 (1σ) MDF = 0.992802 ± 0.00060 (1σ)																		
2.5	**0.0001**	**3.895**	**0.0931**	**2.015**	**0.0001**	**40.658**	**0.0044**	**0.354**	**0.0577**	**1.324**	**9.99**	**0.54**	**180.41**	**9.28**	**74.86**	**0.54**	**0.02**	**0.0010**
3	**0.0009**	**0.475**	**0.7496**	**2.000**	**0.0007**	**6.560**	**0.0386**	**0.089**	**0.5788**	**0.132**	**10.20**	**0.15**	**183.97**	**2.58**	**67.06**	**4.74**	**0.03**	**0.0011**
3.5	**0.0013**	**0.400**	**1.3643**	**2.000**	**0.0011**	**3.573**	**0.0715**	**0.083**	**0.9910**	**0.077**	**10.13**	**0.12**	**182.85**	**2.05**	**72.16**	**8.79**	**0.03**	**0.0011**
4	**0.0004**	**0.846**	**0.6301**	**2.001**	**0.0005**	**8.187**	**0.0319**	**0.094**	**0.3800**	**0.201**	**10.09**	**0.11**	**182.19**	**1.92**	**83.68**	**3.92**	**0.03**	**0.0010**
4.5	**0.0002**	**1.376**	**0.3813**	**2.001**	**0.0003**	**14.563**	**0.0199**	**0.113**	**0.2322**	**0.329**	**10.11**	**0.14**	**182.53**	**2.42**	**85.47**	**2.44**	**0.03**	**0.0011**
5	**0.0007**	**0.523**	**0.8766**	**2.001**	**0.0007**	**5.465**	**0.0476**	**0.086**	**0.6212**	**0.123**	**10.11**	**0.11**	**182.46**	**1.90**	**76.50**	**5.86**	**0.03**	**0.0011**
5.5	**0.0009**	**0.491**	**1.1356**	**2.001**	**0.0010**	**3.756**	**0.0709**	**0.083**	**0.8740**	**0.087**	**10.05**	**0.09**	**181.50**	**1.52**	**80.65**	**8.73**	**0.03**	**0.0013**
6	**0.0004**	**0.761**	**0.6246**	**2.002**	**0.0005**	**7.488**	**0.0352**	**0.091**	**0.4263**	**0.179**	**10.09**	**0.11**	**182.12**	**1.81**	**82.22**	**4.33**	**0.03**	**0.0012**
7	**0.0006**	**0.573**	**0.9465**	**2.002**	**0.0008**	**4.934**	**0.0523**	**0.087**	**0.6270**	**0.122**	**10.12**	**0.09**	**182.56**	**1.58**	**83.34**	**6.44**	**0.03**	**0.0011**
8	**0.0006**	**0.601**	**1.1136**	**2.002**	**0.0008**	**4.627**	**0.0601**	**0.086**	**0.6972**	**0.110**	**10.16**	**0.09**	**183.33**	**1.48**	**86.40**	**7.38**	**0.03**	**0.0011**
10	**0.0008**	**0.518**	**1.5368**	**2.002**	**0.0011**	**3.472**	**0.0837**	**0.084**	**0.9413**	**0.081**	**10.13**	**0.08**	**182.77**	**1.33**	**88.86**	**10.29**	**0.03**	**0.0011**
12	**0.0005**	**0.683**	**1.1641**	**2.003**	**0.0008**	**4.528**	**0.0644**	**0.084**	**0.6997**	**0.109**	**10.17**	**0.08**	**183.41**	**1.30**	**92.46**	**7.93**	**0.03**	**0.0011**
15	**0.0005**	**0.665**	**1.2891**	**2.003**	**0.0008**	**4.884**	**0.0680**	**0.086**	**0.7329**	**0.104**	**10.22**	**0.08**	**184.40**	**1.32**	**93.58**	**8.36**	**0.03**	**0.0011**
18	0.0004	0.875	0.9840	2.003	0.0006	6.301	0.0491	0.088	0.5255	0.145	10.25	0.09	184.82	1.47	94.50	6.04	0.03	0.0010
21	0.0002	1.325	0.5754	2.004	0.0005	8.922	0.0347	0.093	0.3662	0.209	10.04	0.09	181.27	1.56	93.96	4.27	0.03	0.0012
24	0.0002	1.480	0.5023	2.004	0.0002	16.027	0.0212	0.106	0.2344	0.326	10.23	0.14	184.54	2.39	91.22	2.60	0.02	0.0009
27	0.0001	2.070	0.3867	2.005	0.0002	21.313	0.0152	0.144	0.1652	0.462	10.27	0.18	185.14	3.08	92.63	1.86	0.02	0.0008
30	0.0001	2.510	0.1928	2.009	0.0001	48.905	0.0081	0.200	0.0994	0.768	10.21	0.30	184.15	5.20	81.36	0.99	0.02	0.0009
35	0.0001	2.348	0.3054	2.006	0.0002	22.854	0.0120	0.144	0.1336	0.571	10.24	0.21	184.74	3.64	90.73	1.47	0.02	0.0008
40	0.0002	1.903	0.2120	2.008	0.0001	26.311	0.0086	0.195	0.1153	0.662	10.28	0.30	185.43	5.07	75.23	1.05	0.02	0.0008
45	0.0001	2.118	0.2523	2.008	0.0001	35.138	0.0087	0.190	0.1083	0.705	10.33	0.29	186.25	5.02	81.00	1.06	0.02	0.0007
50	0.0003	1.004	0.1995	2.010	0.0001	29.964	0.0075	0.223	0.1489	0.513	10.38	0.40	187.07	6.90	50.97	0.91	0.02	0.0008

Step	36Ar [fA]	%1σ	37Ar [fA]	1‰σ	38Ar [fA]	%1σ	39Ar [fA]	%1σ	40Ar [fA]	%1σ	40(r)/ 39(k)	± 2σ	Age (Ma)	± 2σ	40Ar(r) (%)	39Ar(k) (%)	K/Ca	± 2σ
TAS-19: J = 0.01063170 ± 0.00000638 (1σ) MDF = 0.992804 ± 0.00030 (1σ)																		
0.5	0.00000	282.488	0.0004	223.500	0.0000	119.175	0.0000	312.47	0.0001	1,287	22.22	204.97	382.02	3177.0	470.28	0.00	0.01	0.0923
2.5	0.0007	0.194	1.0711	1.205	0.0015	1.071	0.1165	0.033	1.3039	0.053	10.25	0.03	187.10	0.46	91.05	6.36	0.05	0.0011
3	0.0005	0.244	1.0963	1.206	0.0016	1.066	0.1235	0.034	1.3145	0.052	10.18	0.03	185.90	0.44	95.09	6.74	0.05	0.0012
3.5	0.0004	0.277	0.9853	1.206	0.0016	0.814	0.1294	0.034	1.3824	0.050	10.31	0.02	188.05	0.39	95.95	7.07	0.06	0.0014
4	0.0005	0.277	0.9768	1.206	0.0018	0.986	0.1403	0.034	1.4900	0.046	10.19	0.02	185.93	0.37	95.45	7.67	0.06	0.0015
4.5	0.0005	0.294	0.9678	1.207	0.0019	1.065	0.1484	0.033	1.5671	0.044	10.11	0.02	184.64	0.35	95.30	8.11	0.07	0.0016
5	**0.0005**	**0.257**	**0.9926**	**1.207**	**0.0021**	**0.751**	**0.1689**	**0.035**	**1.7750**	**0.039**	**10.08**	**0.02**	**184.07**	**0.31**	**95.52**	**9.24**	**0.07**	**0.0018**
5.5	**0.0004**	**0.247**	**0.8599**	**1.208**	**0.0018**	**1.166**	**0.1453**	**0.033**	**1.5249**	**0.014**	**10.09**	**0.02**	**184.18**	**0.28**	**95.73**	**7.95**	**0.07**	**0.0017**
6	**0.0004**	**0.341**	**0.8326**	**1.208**	**0.0018**	**1.088**	**0.1446**	**0.034**	**1.5169**	**0.015**	**10.09**	**0.02**	**184.33**	**0.29**	**95.81**	**7.91**	**0.07**	**0.0018**
7	**0.0006**	**0.208**	**1.2235**	**1.208**	**0.0025**	**0.862**	**0.2060**	**0.033**	**2.1585**	**0.010**	**10.08**	**0.02**	**184.00**	**0.28**	**95.76**	**11.27**	**0.07**	**0.0017**
8	**0.0004**	**0.325**	**0.9070**	**1.208**	**0.0017**	**1.103**	**0.1417**	**0.035**	**1.4781**	**0.014**	**10.10**	**0.02**	**184.46**	**0.31**	**96.44**	**7.75**	**0.07**	**0.0016**
10	**0.0004**	**0.187**	**0.8365**	**1.209**	**0.0013**	**1.416**	**0.1053**	**0.037**	**1.1039**	**0.020**	**10.10**	**0.02**	**184.39**	**0.36**	**95.77**	**5.75**	**0.05**	**0.0013**
12	**0.0003**	**0.337**	**0.5826**	**1.210**	**0.0009**	**2.036**	**0.0740**	**0.042**	**0.7779**	**0.027**	**10.09**	**0.02**	**184.19**	**0.39**	**95.41**	**4.04**	**0.05**	**0.0013**
15	**0.0002**	**1.734**	**0.5166**	**1.210**	**0.0007**	**3.229**	**0.0585**	**0.042**	**0.6101**	**0.164**	**10.09**	**0.06**	**184.20**	**0.97**	**96.18**	**3.20**	**0.05**	**0.0012**
18	**0.0001**	**2.761**	**0.2901**	**1.214**	**0.0004**	**7.257**	**0.0271**	**0.069**	**0.2860**	**0.350**	**10.10**	**0.11**	**184.42**	**1.92**	**94.97**	**1.48**	**0.04**	**0.0010**
21	**0.0001**	**2.735**	**0.3163**	**1.214**	**0.0004**	**7.319**	**0.0289**	**0.063**	**0.3023**	**0.331**	**10.09**	**0.10**	**184.18**	**1.81**	**95.83**	**1.58**	**0.04**	**0.0009**
24	**0.0001**	**4.066**	**0.1966**	**1.226**	**0.0003**	**10.098**	**0.0203**	**0.098**	**0.2143**	**0.466**	**10.11**	**0.15**	**184.63**	**2.53**	**95.36**	**1.11**	**0.04**	**0.0011**
30	**0.0001**	**3.306**	**0.2281**	**1.222**	**0.0002**	**10.292**	**0.0147**	**0.132**	**0.1606**	**0.623**	**10.13**	**0.20**	**185.02**	**3.51**	**91.88**	**0.80**	**0.03**	**0.0007**
35	**0.0001**	**4.162**	**0.2093**	**1.225**	**0.0002**	**13.417**	**0.0140**	**0.149**	**0.1500**	**0.667**	**10.20**	**0.21**	**186.09**	**3.73**	**94.18**	**0.76**	**0.03**	**0.0007**
40	**0.0001**	**5.772**	**0.1104**	**1.261**	**0.0002**	**18.902**	**0.0111**	**0.171**	**0.1207**	**0.828**	**10.09**	**0.26**	**184.25**	**4.57**	**92.41**	**0.61**	**0.04**	**0.0011**
45	**0.0001**	**6.042**	**0.0558**	**1.398**	**0.0001**	**20.659**	**0.0070**	**0.265**	**0.0820**	**1.220**	**10.01**	**0.42**	**182.85**	**7.28**	**84.56**	**0.38**	**0.05**	**0.0015**
50	**0.0001**	**3.704**	**0.0519**	**1.423**	**0.0001**	**28.305**	**0.0043**	**0.433**	**0.0681**	**1.469**	**10.34**	**0.68**	**188.65**	**11.82**	**64.86**	**0.23**	**0.04**	**0.0011**

Step	36Ar	%1σ	37Ar	1‰σ	38Ar	%1σ	39Ar	%1σ	40Ar	%1σ	40(r)/	± 2σ	Age	± 2σ	40Ar(r)	39Ar(k)	K/Ca	± 2σ

	[fA]		[fA]		[fA]		[fA]		[fA]		39(k)		(Ma)		(%)	(%)		
TAS-21: J = 0.01058900 ± 0.00000635 (1σ) MDF = 0.992802 ± 0.00060 (1σ)																		
0.5	0.0000	49.834	0.0000	371.537	0.0000	334.528	0.0000	161.662	0.0012	52.823	-18.03	203.74	-383.1	4821.6	-14.39	0.00	0.08	0.6884
1	0.0000	56.462	0.0011	16.153	0.0000	2363.843	0.0001	24.694	0.0019	34.839	10.38	28.47	188.53	491.06	38.07	0.01	0.03	0.0153
1.5	0.0000	7.264	0.0452	1.240	0.0000	133.997	0.0025	0.681	0.0302	2.147	9.90	0.80	180.32	13.88	79.71	0.22	0.02	0.0007
2	0.0002	1.309	0.3353	1.176	0.0003	13.474	0.0192	0.109	0.2163	0.300	9.90	0.11	180.32	1.94	86.83	1.73	0.02	0.0006
2.5	0.0004	0.664	0.8208	1.175	0.0007	5.907	0.0480	0.074	0.5305	0.122	9.98	0.06	181.64	1.06	89.22	4.33	0.02	0.0006
3	0.0005	0.590	1.0458	1.175	0.0008	4.542	0.0621	0.066	0.6794	0.096	10.04	0.05	182.67	0.94	90.67	5.60	0.03	0.0006
3.5	0.0006	0.506	1.2243	1.176	0.0010	3.943	0.0747	0.066	0.8150	0.080	10.10	0.05	183.64	0.86	91.50	6.74	0.03	0.0006
4	**0.0005**	**0.512**	**1.1926**	**1.176**	**0.0010**	**3.828**	**0.0738**	**0.065**	**0.8054**	**0.081**	**10.11**	**0.05**	**183.95**	**0.85**	**91.65**	**6.66**	**0.03**	**0.0006**
4.5	**0.0006**	**0.512**	**1.2485**	**1.176**	**0.0011**	**3.363**	**0.0833**	**0.064**	**0.9037**	**0.072**	**10.07**	**0.05**	**183.26**	**0.79**	**91.92**	**7.52**	**0.03**	**0.0007**
5	**0.0006**	**0.271**	**1.2595**	**1.176**	**0.0011**	**1.147**	**0.0865**	**0.085**	**0.9378**	**0.004**	**10.08**	**0.04**	**183.43**	**0.68**	**92.02**	**7.80**	**0.03**	**0.0007**
5.5	**0.0005**	**0.386**	**1.1579**	**1.177**	**0.0010**	**1.476**	**0.0806**	**0.079**	**0.8733**	**0.004**	**10.08**	**0.04**	**183.38**	**0.70**	**92.06**	**7.27**	**0.03**	**0.0007**
6	**0.0005**	**0.305**	**1.1164**	**1.177**	**0.0010**	**1.129**	**0.0772**	**0.062**	**0.8452**	**0.005**	**10.11**	**0.04**	**183.88**	**0.66**	**91.44**	**6.97**	**0.03**	**0.0007**
7	**0.0007**	**0.315**	**1.4414**	**1.177**	**0.0013**	**1.311**	**0.0972**	**0.063**	**1.0691**	**0.005**	**10.13**	**0.04**	**184.32**	**0.68**	**91.14**	**8.77**	**0.03**	**0.0007**
8	**0.0006**	**0.369**	**1.2988**	**1.177**	**0.0011**	**1.859**	**0.0822**	**0.063**	**0.9056**	**0.005**	**10.12**	**0.04**	**184.10**	**0.73**	**90.82**	**7.41**	**0.03**	**0.0006**
10	**0.0008**	**0.285**	**1.5818**	**1.178**	**0.0013**	**1.421**	**0.1034**	**0.061**	**1.1378**	**0.007**	**10.13**	**0.04**	**184.28**	**0.69**	**91.06**	**9.33**	**0.03**	**0.0007**
12	**0.0004**	**0.453**	**0.8867**	**1.178**	**0.0007**	**1.721**	**0.0537**	**0.064**	**0.5851**	**0.005**	**10.16**	**0.05**	**184.76**	**0.78**	**92.23**	**4.84**	**0.03**	**0.0006**
15	**0.0003**	**0.402**	**0.6044**	**1.178**	**0.0004**	**3.252**	**0.0334**	**0.070**	**0.3658**	**0.010**	**10.13**	**0.05**	**184.33**	**0.84**	**91.31**	**3.01**	**0.02**	**0.0006**
18	**0.0002**	**0.940**	**0.4661**	**1.180**	**0.0003**	**20.763**	**0.0221**	**0.120**	**0.2457**	**0.286**	**10.22**	**0.10**	**185.76**	**1.71**	**90.70**	**1.99**	**0.02**	**0.0005**
21	**0.0002**	**0.913**	**0.5201**	**1.180**	**0.0004**	**15.692**	**0.0254**	**0.106**	**0.2774**	**0.253**	**10.15**	**0.09**	**184.52**	**1.56**	**91.54**	**2.28**	**0.02**	**0.0005**
24	**0.0001**	**1.527**	**0.2895**	**1.182**	**0.0003**	**24.056**	**0.0159**	**0.156**	**0.1727**	**0.406**	**10.07**	**0.13**	**183.29**	**2.19**	**91.68**	**1.43**	**0.02**	**0.0006**
27	**0.0001**	**1.618**	**0.2577**	**1.184**	**0.0002**	**28.973**	**0.0135**	**0.183**	**0.1493**	**0.470**	**10.15**	**0.15**	**184.59**	**2.52**	**90.77**	**1.22**	**0.02**	**0.0005**
30	**0.0001**	**1.615**	**0.2803**	**1.183**	**0.0002**	**29.415**	**0.0139**	**0.174**	**0.1517**	**0.463**	**10.15**	**0.14**	**184.67**	**2.47**	**91.95**	**1.25**	**0.02**	**0.0005**
35	0.0001	1.940	0.2320	1.185	0.0002	33.592	0.0106	0.221	0.1201	0.584	10.48	0.18	190.31	3.19	91.32	0.95	0.02	0.0005
40	0.0001	1.605	0.2587	1.184	0.0002	38.024	0.0112	0.213	0.1262	0.556	10.16	0.18	184.68	3.05	88.85	1.01	0.02	0.0004
45	0.0001	1.698	0.2210	1.186	0.0002	38.610	0.0102	0.228	0.1176	0.597	10.09	0.19	183.56	3.32	86.49	0.92	0.02	0.0005
50	0.0001	1.676	0.2000	1.188	0.0001	44.188	0.0083	0.276	0.1029	0.682	10.32	0.24	187.53	4.06	82.18	0.75	0.02	0.0004

APPENDIX E: Supplementary Data Chapter 3 – $^{40}Ar/^{39}Ar$ Results for the Tasmanian Dolerite (Renne and Norman, 2011; ^{37}Ar Irradiation Parameters)

Table E1: $^{40}Ar/^{39}Ar$ Geochronology of Plagioclase Crystals from the Tasmanian Dolerites, Ferrar CFB Province.

	General Characteristics											
Sample	Coordinates Zone 55 (UTM)	Mineral	Integrated Age (Ma)	Plateau Age (Ma)	Total ^{39}Ar Released (%,n)	MSWD	P	Isochron Age (Ma)	Spreading Factor (%)	$^{40}Ar/^{36}Ar$ Intercept	MSWD	P
TAS-01	5183731.9 N 490325.5 E	Plagioclase	183.68 ± 0.33	183.59 ± 0.39	83.59 (19)	0.68	0.84	183.4 ± 1.19	6.6	306.0 ± 47.5	0.71	0.80
TAS-14	5345402.7 N 461359.1 E	Plagioclase	183.36 ± 0.41	182.98 ± 0.44	71.40 (12)	0.92	0.52	182.94 ± 0.95	25.5	285.6 ± 0.64	1.82	0.05
TAS-19	5397933.9 N 519877.5 E	Plagioclase	185.04 ± 0.23	184.31 ± 0.23	72.16 (17)	1.56	0.07	183.91 ± 0.87	33.0	314.7 ± 32.3	1.84	0.02
TAS-21	5355722.9 N 572504.9 E	Plagioclase	183.93 ± 0.27	184.0 ± 0.36	76.32 (11)	2.07	0.02	178.14 ± 5.04	1.5	407.6 ± 97.9	1.26	0.25

$^{40}Ar/^{39}Ar$ Geochronology of Plagioclase Crystals from the Tasmanian Dolerites, Ferrar CFB Province. The calculated J values relative to an age of FCs of 28.294 ± 0.13 % Ma (Turner et al., 1971) [TAS-01, TAS-19, TAS-21] and relative to an age of GA1550 of 99.74 ± 0.10 % Ma [TAS-14]. MSWD and probability (P), percentage of ^{39}Ar degassed used in the plateau calculation, number of analyses included in the isochron, and $^{40}Ar/^{36}Ar$ intercept are indicated. Analytical uncertainties on the ages are quoted at 2 sigma (2σ) confidence levels and at 1σ for the $^{40}Ar/^{36}Ar$ intercept.

APPENDIX F: Supplementary Data Chapter 4 – Major and Trace Element Data, Sills of the Western Cape Province, Karoo Continental Flood Basalt Province

Table F1: Major and trace element analyses of doleritic dykes and sills from the Karoo CFB province (Western Cape Province).

Sample	**KA**	**KB**	**KC**	**KD**	**KE**	**KF**	**KG**	**KH**	**KI**
Rock Type	Dolerite	Dolerite	Dolerite	Dolerite	Dolerite	Dolerite	Dolerite	Dolerite	Dolerite
Latitude	-32.452267	-32.448303	-32.444306	-32.359607	-32.410799	-32.410813	-32.318518	-32.353690	-32.323249
Longitude	20.658190	20.660428	20.659099	20.880039	20.811427	20.806274	20.660862	20.669449	20.581805
Major Elements (wt. %):									
SiO_2	51.58	50.92	51.29	51.37	50.95	51.04	52.78	51.16	53.39
Al_2O_3	13.19	13.32	13.53	14.62	13.41	13.38	14.93	13.25	14.52
FeO_{tot}	15.3	14.54	14.67	12.4	14.45	15.44	11.07	15.87	11.47
MgO	4.97	5.97	5.61	7.16	5.83	5.2	6.5	5.19	5.95
CaO	9.33	10.25	9.88	10.34	9.92	9.65	10.35	9.5	10.01
Na_2O	2.41	2.25	2.41	2.28	2.32	2.37	2.38	2.38	2.48
K_2O	0.86	0.62	0.71	0.65	0.7	0.73	0.66	0.73	0.66
TiO_2	1.65	1.46	1.49	1	1.46	1.51	0.98	1.6	1.06
P_2O_5	0.239	0.22	0.226	0.146	0.221	0.247	0.161	0.237	0.18
MnO	0.23	0.22	0.22	0.18	0.22	0.22	0.17	0.23	0.18
LOI	0.05	0.07	-0.1	-0.5	0.4	0.24	0.05	-0.36	0.14
H_2O-									
Total	99.809	99.84	99.936	99.646	99.881	100.027	100.031	99.787	100.04
Mg #	43.08	48.89	47.12	57.36	48.46	43.97	57.77	43.25	54.73
Trace Elements (ppm):									
La	13.4	10.6	12.1	8.5	11.6	12.6	8.6	12.7	10.5
Ce	28.8	23.8	25.8	18.1	25.1	27.4	18.4	26.5	22
Pr	4	3.3	3.6	2.6	3.6	3.7	2.5	3.7	2.9
Nd	17.8	14	15.7	10.8	16.1	16.9	11.2	16.3	12.7
Sm	5.1	3.5	3.9	3.1	4.6	4.5	2.9	4.6	3.3
Eu	1.6	1.2	1.4	0.8	1.4	1.3	1	1.5	1
Gd	5.5	5.5	5.2	3.4	4.8	4.9	3.1	6.1	4
Tb	1	0.8	0.8	0.7	0.9	0.9	0.6	0.9	0.7
Dy	5.9	5	5.7	3.5	5.7	6.1	3.9	6.4	4.4
Ho	1.3	1.1	1.3	0.8	1.2	1.2	0.8	1.3	1
Er	4	3.4	3.5	2.5	3.5	3.7	2.5	3.7	2.6
Yb	3.5	2.9	3.8	2.4	3.5	3.4	2.2	3.5	2.8
Lu	0.5	0.5	0.6	0.3	0.5	0.5	0.2	0.5	0.3
Rb	23.3	13.9	18.2	14.5	16.5	16.9	12.6	16.9	14.5
Ba	226.9	162.9	189.7	166.4	205.8	211.9	169.4	208.2	195
Th	2.3	1.7	1.5	1.3	1.7	1.9	1.2	1.7	1.5
U	0.5	0.4	0.4	0.3	0.4	0.5	0.3	0.4	0.4
Nb	7.3	5.4	6.3	5.4	6.1	6.5	6.1	6.3	6.9
K	7139.4	5147.0	5894.1	5396.0	5811.1	6060.2	5479.1	6060.2	5479.1

Table F1: Continued

Sample	**KA**	**KB**	**KC**	**KD**	**KE**	**KF**	**KG**	**KH**	**KI**
Rock Type	Dolerite	Dolerite	Dolerite	Dolerite	Dolerite	Dolerite	Dolerite	Dolerite	Dolerite
Latitude	-32.452267	-32.448303	-32.444306	-32.359607	-32.410799	-32.410813	-32.318518	-32.353690	-32.323249
Longitude	20.658190	20.660428	20.659099	20.880039	20.811427	20.806274	20.660862	20.669449	20.581805
Trace Element (ppm): Continued									
Ta	0.7	0.5	0.5	0.4	0.5	0.6	0.5	0.6	0.4
Pb	5.3	3.2	3.2	2.7	3.4	3.4	2.5	3.7	3.2
Sr	167.4	166	169.4	189.5	176.8	181.7	179.7	163.6	188.9
P	1043.0	960.1	986.3	637.2	964.5	1078.0	702.6	1034.3	785.6
Hf	3.7	3	3.5	2.1	3.4	3.1	2.1	3.3	2.6
Zr	135	104	122	78	115	130	80	129	93
Ti	9891.9	8752.8	8932.7	5995.1	8752.8	9052.6	5875.2	9592.2	6354.8
Tb	1	0.8	0.8	0.7	0.9	0.9	0.6	0.9	0.7
Y	35.2	27.8	31.1	20.9	30.4	33.6	20.7	33.4	23.4
Co	45.7	46.5	45.4	43.1	46.3	43.8	39.7	45.9	40
Cr	76	383	215	499	207	191	376	184	288
Cu	228.4	186.8	196.5	90	193.3	204.5	99	212.4	108.8
Ni	45.7	69.2	56.8	86.8	61	53.8	60.9	49.2	50.1
V	362	367	348	274	345	335	248	361	294
Zn	125	110	111	86	110	116	86	117	93

Major and trace element analyses for the Western Cape Sills of the Karoo continental flood basalt province. Major element analysis: X-ray fluorescence. Trace element analysis: inductively coupled plasma mass spectrometry (ICP-MS). Sc and V analysis: inductively coupled plasma optical (atomic) emission spectrometry (ICP-OES). For the remaining elements a four acid digest was implemented with ICP-MS and ICP-OES analyses. LOI, loss on ignition. GPS Datum: AGD84 unless otherwise noted.

Table F2: Raw Major and Trace Element Results from Genalysis

				Western Cape Province Sills								
Element	Unit	Detection	Method	KA	KB	KC	KD	KE	KF	KG	KH	KI
Major Elements:												
Al2O3	%	0.01	FB1/XRF	13.19	13.32	13.53	14.62	13.41	13.38	14.93	13.25	14.52
BaO	%	0.01	FB1/XRF	0.03	0.02	0.02	0.02	0.03	0.03	0.02	0.03	0.02
CaO	%	0.01	FB1/XRF	9.33	10.25	9.88	10.34	9.92	9.65	10.35	9.5	10.01
Cr2O3	%	0.01	FB1/XRF	X	0.05	0.03	0.07	0.03	0.03	0.06	0.02	0.04
Fe2O3	%	0.01	FB1/XRF	15.3	14.54	14.67	12.4	14.45	15.44	11.07	15.87	11.47
K2O	%	0.01	FB1/XRF	0.86	0.62	0.71	0.65	0.7	0.73	0.66	0.73	0.66
MgO	%	0.01	FB1/XRF	4.97	5.97	5.61	7.16	5.83	5.2	6.5	5.19	5.95
MnO	%	0.01	FB1/XRF	0.23	0.22	0.22	0.18	0.22	0.22	0.17	0.23	0.18
Na2O	%	0.01	FB1/XRF	2.41	2.25	2.41	2.28	2.32	2.37	2.38	2.38	2.48
P2O5	%	0.002	FB1/XRF	0.239	0.22	0.226	0.146	0.221	0.247	0.161	0.237	0.18
SO3	%	0.01	FB1/XRF	0.14	0.09	0.12	0.14	0.13	0.13	0.16	0.11	0.19
SiO2	%	0.01	FB1/XRF	51.58	50.92	51.29	51.37	50.95	51.04	52.78	51.16	53.39
TiO2	%	0.01	FB1/XRF	1.65	1.46	1.49	1	1.46	1.51	0.98	1.6	1.06
LOI	%	0.01	/TGA	0.05	0.07	-0.1	-0.5	0.4	0.24	0.05	-0.36	0.14
Total	%	0.01	FB1/XRF	100.06	100.12	100.19	99.93	100.14	100.29	100.29	100.05	100.28
Trace Elements:												
Ag	ppm	0.01	4A/MS	0.07	0.08	0.06	0.04	0.08	0.06	0.04	0.1	0.06
As	ppm	0.5	4A/MS	1.8	1.8	0.8	1.8	0.9	1.4	1.1	1.3	1.1
Ba	ppm	0.5	FB6/MS	226.9	162.9	189.7	166.4	205.8	211.9	169.4	208.2	195
Be	ppm	0.05	4A/MS	1	0.6	0.56	0.56	0.55	0.83	0.76	0.64	0.81
Bi	ppm	0.01	4A/MS	0.11	0.05	0.02	0.02	0.02	0.02	0.02	0.02	0.11
C	%	0.01	/CSA	0.02	0.03	0.02	0.03	0.14	0.14	0.03	0.03	0.02
Cd	ppm	0.02	4A/MS	0.14	0.1	0.09	0.18	0.16	0.1	0.17	0.1	0.15
Ce	ppm	0.5	FB6/MS	28.8	23.8	25.8	18.1	25.1	27.4	18.4	26.5	22
Co	ppm	0.1	4A/MS	45.7	46.5	45.4	43.1	46.3	43.8	39.7	45.9	40
Cr	ppm	20	FB6/OE	76	383	215	499	207	191	376	184	288
Cs	ppm	0.1	FB6/MS	1.8	1	1.2	0.6	1.3	1.5	0.5	0.9	0.7
Cu	ppm	0.5	4A/OE	228.4	186.8	196.5	90	193.3	204.5	99	212.4	108.8
Dy	ppm	0.1	FB6/MS	5.9	5	5.7	3.5	5.7	6.1	3.9	6.4	4.4
Er	ppm	0.1	FB6/MS	4	3.4	3.5	2.5	3.5	3.7	2.5	3.7	2.6
Eu	ppm	0.1	FB6/MS	1.6	1.2	1.4	0.8	1.4	1.3	1	1.5	1
Ga	ppm	0.1	FB6/MS	20.5	18.8	21	16.8	19.2	20.3	16.3	20.7	17.1

Table F2: Continued

				Western Cape Province Sills								
Element	Unit	Detection	Method	KA	KB	KC	KD	KE	KF	KG	KH	KI
Trace Element: Continued												
Gd	ppm	0.1	FB6/MS	5.5	5.5	5.2	3.4	4.8	4.9	3.1	6.1	4
Ge	ppm	0.05	4A/MS	0.4	0.81	0.81	0.69	0.56	0.75	0.48	0.69	0.94
Hf	ppm	0.1	FB6/MS	3.7	3	3.5	2.1	3.4	3.1	2.1	3.3	2.6
Ho	ppm	0.1	FB6/MS	1.3	1.1	1.3	0.8	1.2	1.2	0.8	1.3	1
In	ppm	0.01	4A/MS	0.1	0.09	0.09	0.07	0.09	0.08	0.06	0.09	0.08
La	ppm	0.2	FB6/MS	13.4	10.6	12.1	8.5	11.6	12.6	8.6	12.7	10.5
Li	ppm	0.1	4A/MS	8.2	6.9	6.9	6.5	8.4	7.7	6.4	6.6	9.3
Lu	ppm	0.1	FB6/MS	0.5	0.5	0.6	0.3	0.5	0.5	0.2	0.5	0.3
Mo	ppm	0.1	4A/MS	1.2	1.6	1.2	1.3	1.2	1.3	1	1.3	1.1
Nb	ppm	0.1	FB6/MS	7.3	5.4	6.3	5.4	6.1	6.5	6.1	6.3	6.9
Nd	ppm	0.1	FB6/MS	17.8	14	15.7	10.8	16.1	16.9	11.2	16.3	12.7
Ni	ppm	0.5	4A/OE	45.7	69.2	56.8	86.8	61	53.8	60.9	49.2	50.1
Pb	ppm	0.5	4A/MS	5.3	3.2	3.2	2.7	3.4	3.4	2.5	3.7	3.2
Pr	ppm	0.1	FB6/MS	4	3.3	3.6	2.6	3.6	3.7	2.5	3.7	2.9
Rb	ppm	0.1	FB6/MS	23.3	13.9	18.2	14.5	16.5	16.9	12.6	16.9	14.5
Re	ppm	0.002	4A/MS	X	X	0.002	X	X	X	X	X	X
S	%	0.01	/CSA	0.06	0.05	0.06	0.06	0.06	0.06	0.07	0.06	0.09
Sb	ppm	0.05	4A/MS	0.18	0.13	0.11	0.21	0.14	0.21	0.14	0.14	0.18
Sc	ppm	10	FB6/OE	39	40	39	35	38	38	31	39	35
Se	ppm	0.5	4A/MS	X	X	X	X	X	X	X	X	X
Sm	ppm	0.1	FB6/MS	5.1	3.5	3.9	3.1	4.6	4.5	2.9	4.6	3.3
Sn	ppm	1	FB6/MS	X	X	X	X	1	1	X	X	X
Sr	ppm	0.2	FB6/MS	167.4	166	169.4	189.5	176.8	181.7	179.7	163.6	188.9
Ta	ppm	0.1	FB6/MS	0.7	0.5	0.5	0.4	0.5	0.6	0.5	0.6	0.4
Tb	ppm	0.1	FB6/MS	1	0.8	0.8	0.7	0.9	0.9	0.6	0.9	0.7
Te	ppm	0.1	4A/MS	X	X	X	X	X	X	X	X	X
Th	ppm	0.1	FB6/MS	2.3	1.7	1.5	1.3	1.7	1.9	1.2	1.7	1.5
Tl	ppm	0.02	4A/MS	0.13	0.09	0.1	0.09	0.1	0.1	0.11	0.11	0.12
Tm	ppm	0.1	FB6/MS	0.6	0.5	0.6	0.4	0.5	0.5	0.4	0.5	0.3
U	ppm	0.1	FB6/MS	0.5	0.4	0.4	0.3	0.4	0.5	0.3	0.4	0.4
V	ppm	10	FB6/OE	362	367	348	274	345	335	248	361	294
W	ppm	1	FB6/MS	11	5	1	1	X	X	X	X	X
Y	ppm	0.5	FB6/MS	35.2	27.8	31.1	20.9	30.4	33.6	20.7	33.4	23.4
Yb	ppm	0.1	FB6/MS	3.5	2.9	3.8	2.4	3.5	3.4	2.2	3.5	2.8
Zn	ppm	1	4A/OE	125	110	111	86	110	116	86	117	93
Zr	ppm	1	FB6/MS	135	104	122	78	115	130	80	129	93

Method codes: /CSA - Induction Furnace Analyzed by Infrared Spectrometry; /TGA - No digestion or other pre-treatment undertaken. Analyzed by Thermal Gravimetric Analyzer; 4A/MS - Multi-acid digest including Hydrofluoric, Nitric, Perchloric and Hydrochloric acids in Teflon Tubes. Analyzed by Inductively Coupled Plasma Mass Spectrometry (ICP-MS); 4A/OE - Multi-acid digest including Hydrofluoric, Nitric, Perchloric and Hydrochloric acids in Teflon Tubes; Analyzed by Inductively Coupled Plasma Optical (Atomic) Emission Spectrometry (ICP-OES); FB1/XRF - Fused Disk preparation for XRF analysis Analyzed by XRF Spectrometry; FB6/MS - Lithium metaborate/tetraborate fusion Analyzed by Inductively Coupled Plasma Mass Spectrometry; FB6/OE - Lithium metaborate/tetraborate fusion Analyzed by ICP-OES.

Table F3: Raw Major and Trace Element Results of Standards and Blanks from Genalysis

				Check	Standards					Blanks
Element	Unit	Detection	Method	KB	OREAS 24b	OREAS 45d	OREAS 45d	SY-4	OREAS 24b	Control Blank
Major Elements:										
Al2O3	%	0.01	FB1/XRF					20.68		
BaO	%	0.01	FB1/XRF					0.04		
CaO	%	0.01	FB1/XRF					8.04		
Cr2O3	%	0.01	FB1/XRF					X		
Fe2O3	%	0.01	FB1/XRF					6.24		
K2O	%	0.01	FB1/XRF					1.67		
MgO	%	0.01	FB1/XRF					0.54		
MnO	%	0.01	FB1/XRF					0.11		
Na2O	%	0.01	FB1/XRF					7.08		
P2O5	%	0.002	FB1/XRF					0.131		
SO3	%	0.01	FB1/XRF					0.04		
SiO2	%	0.01	FB1/XRF					49.85		
TiO2	%	0.01	FB1/XRF					0.28		
LOI	%	0.01	/TGA							
Total	%	0.01	FB1/XRF					100.16		
Trace Elements:										
Ag	ppm	0.01	4A/MS	0.05			0.15			X
As	ppm	0.5	4A/MS	2.1			14			X
Ba	ppm	0.5	FB6/MS	166.9		161.7			668.5	X
Be	ppm	0.05	4A/MS	0.65			0.74			X
Bi	ppm	0.01	4A/MS	0.04			0.33			0.01
C	%	0.01	/CSA	0.03	0.19					X
Cd	ppm	0.02	4A/MS	0.09			0.05			X
Ce	ppm	0.5	FB6/MS	23.6		33.9			79.8	X
Co	ppm	0.1	4A/MS	47			30.8			X
Cr	ppm	20	FB6/OE	369		585			158	X
Cs	ppm	0.1	FB6/MS	0.9		3.8			9.3	X
Cu	ppm	0.5	4A/OE	186.4			373.7			X
Dy	ppm	0.1	FB6/MS	5.3		2.7			5.6	X
Er	ppm	0.1	FB6/MS	2.7		1.9			3.4	X
Eu	ppm	0.1	FB6/MS	1.2		0.6			1.1	X
Ga	ppm	0.1	FB6/MS	18.5		20.5			20.2	X

Table F3: Continued

				Check	Standards					Blanks
Element	Unit	Detection	Method	KB	OREAS 24b	OREAS 45d	OREAS 45d	SY-4	OREAS 24b	Control Blank
Trace Element: Continued										
Gd	ppm	0.1	FB6/MS	4.6		2.7			5.7	X
Ge	ppm	0.05	4A/MS	0.81			1.63			X
Hf	ppm	0.1	FB6/MS	2.9		8.3			5.8	X
Ho	ppm	0.1	FB6/MS	1.2		0.7			1.1	X
In	ppm	0.01	4A/MS	0.08			0.11			X
La	ppm	0.2	FB6/MS	10.6		16.1			40.2	X
Li	ppm	0.1	4A/MS	7			20.9			X
Lu	ppm	0.1	FB6/MS	0.5		0.3			0.5	X
Mo	ppm	0.1	4A/MS	1.7			2.5			X
Nb	ppm	0.1	FB6/MS	5.5		16.2			15	X
Nd	ppm	0.1	FB6/MS	13.8		14.7			34.2	X
Ni	ppm	0.5	4A/OE	67.9			230.4			0.5
Pb	ppm	0.5	4A/MS	3.3			20.2			X
Pr	ppm	0.1	FB6/MS	3.2		3.5			9.5	X
Rb	ppm	0.1	FB6/MS	14.3		38.8			163	X
Re	ppm	0.002	4A/MS	0.003			0.003			0.002
S	%	0.01	/CSA	0.05	0.21					X
Sb	ppm	0.05	4A/MS	0.12			0.85			X
Sc	ppm	10	FB6/OE	40		50			14	X
Se	ppm	0.5	4A/MS	X			2.9			X
Sm	ppm	0.1	FB6/MS	3.8		2.2			6.6	X
Sn	ppm	1	FB6/MS	X		2			4	X
Sr	ppm	0.2	FB6/MS	159.8		28.5			113.5	X
Ta	ppm	0.1	FB6/MS	0.4		1.3			1.1	0.1
Tb	ppm	0.1	FB6/MS	0.9		0.5			1	X
Te	ppm	0.1	4A/MS	X			0.1			X
Th	ppm	0.1	FB6/MS	1.7		13			15	X
Tl	ppm	0.02	4A/MS	0.08			0.24			X
Tm	ppm	0.1	FB6/MS	0.5		0.3			0.4	X
U	ppm	0.1	FB6/MS	0.4		2.7			3.2	X
V	ppm	10	FB6/OE	370		261			122	X
W	ppm	1	FB6/MS	5		2			4	X
Y	ppm	0.5	FB6/MS	27.2		16.9			28.9	X
Yb	ppm	0.1	FB6/MS	2.8		2.1			3.1	X
Zn	ppm	1	4A/OE	109			44			2
Zr	ppm	1	FB6/MS	102		322			208	X

Method codes: /CSA - Induction Furnace Analyzed by Infrared Spectrometry; /TGA - No digestion or other pre-treatment undertaken. Analyzed by Thermal Gravimetric Analyzer; 4A/MS - Multi-acid digest including Hydrofluoric, Nitric, Perchloric and Hydrochloric acids in Teflon Tubes. Analyzed by Inductively Coupled Plasma Mass Spectrometry (ICP-MS); 4A/OE - Multi-acid digest including Hydrofluoric, Nitric, Perchloric and Hydrochloric acids in Teflon Tubes; Analyzed by Inductively Coupled Plasma Optical (Atomic) Emission Spectrometry (ICP-OES); FB1/XRF - Fused Disk preparation for XRF analysis Analyzed by XRF Spectrometry; FB6/MS - Lithium metaborate/tetraborate fusion Analyzed by Inductively Coupled Plasma Mass Spectrometry; FB6/OE - Lithium metaborate/tetraborate fusion Analyzed by ICP-OES.

APPENDIX G: Supplementary Data Chapter 4 – $^{40}Ar/^{39}Ar$ Isotope Abundances Karoo Continental Flood Basalt Province

Step	36Ar [fA]	%1σ	37Ar [fA]	1%σ	38Ar [fA]	%1σ	39Ar [fA]	%1σ	40Ar [fA]	%1σ	40(r)/ 39(k)	± 2σ	Age (Ma)	± 2σ	40Ar(r) (%)	39Ar(k) (%)	K/Ca	± 2σ
*KB **plagioclase**: J = 0.01058900 ± 0.00000635 (1σ) MDF = 0.992802 ± 0.00060 (1σ)*																		
0.5	0.00002	3.864	0.0011	156.078	0.0001	41.054	0.0000	226	0.0046	1	-11.31	76.08	-247.6	1784.5	-2.24	0.00	0.00	0.0212
1	0.00007	0.877	0.0066	22.560	0.0001	26.214	0.0004	4	0.0254	0	9.91	1.43	192.12	26.35	16.17	0.12	0.03	0.0124
1.5	0.00012	0.653	0.0352	6.437	0.0001	24.012	0.0024	0.819	0.0534	0.121	9.03	0.30	175.84	5.53	39.49	0.67	0.03	0.0037
2	0.00013	0.595	0.1364	4.441	0.0002	23.643	0.0067	0.326	0.0883	0.073	9.29	0.18	180.71	3.27	69.01	1.88	0.02	0.0018
2.5	**0.00014**	**0.451**	**0.2772**	**4.358**	**0.0002**	**18.152**	**0.0119**	**0.154**	**0.1288**	**0.050**	**9.28**	**0.17**	**180.45**	**3.21**	**84.02**	**3.34**	**0.02**	**0.0016**
3	**0.00016**	**0.434**	**0.3845**	**4.312**	**0.0002**	**18.266**	**0.0162**	**0.109**	**0.1660**	**0.038**	**9.32**	**0.17**	**181.33**	**3.17**	**89.61**	**4.56**	**0.02**	**0.0015**
3.5	**0.00017**	**0.781**	**0.4766**	**4.303**	**0.0002**	**15.946**	**0.0192**	**0.096**	**0.1888**	**0.035**	**9.32**	**0.18**	**181.28**	**3.37**	**93.07**	**5.39**	**0.02**	**0.0015**
4	**0.00017**	**0.428**	**0.5299**	**4.299**	**0.0002**	**15.062**	**0.0221**	**0.113**	**0.2126**	**0.030**	**9.32**	**0.17**	**181.29**	**3.19**	**95.21**	**6.21**	**0.02**	**0.0015**
4.5	**0.00017**	**0.431**	**0.5175**	**4.301**	**0.0003**	**11.157**	**0.0237**	**0.069**	**0.2277**	**0.028**	**9.30**	**0.16**	**180.93**	**2.89**	**95.31**	**6.67**	**0.02**	**0.0017**
5	**0.00016**	**0.444**	**0.4953**	**4.299**	**0.0002**	**19.324**	**0.0219**	**0.084**	**0.2102**	**0.037**	**9.31**	**0.16**	**181.02**	**3.00**	**95.35**	**6.16**	**0.02**	**0.0016**
5.5	**0.00016**	**0.451**	**0.4565**	**4.307**	**0.0002**	**16.605**	**0.0205**	**0.084**	**0.1998**	**0.034**	**9.30**	**0.16**	**180.95**	**2.95**	**94.20**	**5.78**	**0.02**	**0.0016**
6	**0.00015**	**0.673**	**0.4441**	**4.303**	**0.0002**	**15.610**	**0.0182**	**0.127**	**0.1776**	**0.037**	**9.35**	**0.18**	**181.83**	**3.29**	**94.21**	**5.12**	**0.02**	**0.0015**
7	**0.00020**	**0.416**	**0.5189**	**4.306**	**0.0003**	**11.771**	**0.0251**	**0.091**	**0.2520**	**0.027**	**9.37**	**0.15**	**182.24**	**2.75**	**92.03**	**7.07**	**0.02**	**0.0018**
8	**0.00025**	**0.440**	**0.6911**	**4.300**	**0.0003**	**11.277**	**0.0284**	**0.076**	**0.2835**	**0.023**	**9.39**	**0.17**	**182.45**	**3.23**	**92.44**	**7.98**	**0.02**	**0.0015**
10	**0.00021**	**0.416**	**0.5727**	**4.304**	**0.0003**	**12.605**	**0.0238**	**0.076**	**0.2377**	**0.029**	**9.46**	**0.17**	**183.83**	**3.19**	**93.10**	**6.69**	**0.02**	**0.0015**
12	**0.00018**	**0.395**	**0.4886**	**4.302**	**0.0001**	**22.831**	**0.0187**	**0.088**	**0.1862**	**0.034**	**9.38**	**0.19**	**182.35**	**3.47**	**92.52**	**5.25**	**0.02**	**0.0014**
15	**0.00018**	**0.473**	**0.5234**	**4.301**	**0.0002**	**16.486**	**0.0201**	**0.101**	**0.1980**	**0.034**	**9.45**	**0.19**	**183.61**	**3.47**	**93.99**	**5.63**	**0.02**	**0.0014**
18	**0.00013**	**0.491**	**0.4070**	**4.309**	**0.0001**	**31.882**	**0.0141**	**0.119**	**0.1386**	**0.047**	**9.45**	**0.21**	**183.65**	**3.86**	**94.21**	**3.95**	**0.01**	**0.0013**
21	**0.00013**	**0.667**	**0.3711**	**4.315**	**0.0001**	**30.896**	**0.0120**	**0.180**	**0.1191**	**0.056**	**9.43**	**0.23**	**183.21**	**4.20**	**93.10**	**3.36**	**0.01**	**0.0012**
24	**0.00008**	**0.924**	**0.2473**	**4.334**	**0.0001**	**44.721**	**0.0079**	**0.260**	**0.0776**	**0.083**	**9.39**	**0.24**	**182.48**	**4.39**	**93.70**	**2.21**	**0.01**	**0.0012**
27	**0.00005**	**1.646**	**0.1474**	**4.437**	**0.0001**	**54.387**	**0.0049**	**0.475**	**0.0485**	**0.132**	**9.43**	**0.26**	**183.29**	**4.76**	**94.10**	**1.38**	**0.01**	**0.0013**
30	**0.00007**	**0.924**	**0.2175**	**4.371**	**0.0000**	**130.201**	**0.0068**	**0.240**	**0.0669**	**0.096**	**9.39**	**0.24**	**182.62**	**4.52**	**93.19**	**1.90**	**0.01**	**0.0011**
35	**0.00010**	**0.604**	**0.3027**	**4.326**	**0.0001**	**57.781**	**0.0085**	**0.193**	**0.0825**	**0.078**	**9.36**	**0.26**	**182.06**	**4.84**	**94.17**	**2.37**	**0.01**	**0.0010**
40	**0.00010**	**0.693**	**0.3030**	**4.322**	**0.0002**	**18.886**	**0.0098**	**0.160**	**0.0959**	**0.066**	**9.45**	**0.23**	**183.57**	**4.19**	**94.66**	**2.75**	**0.01**	**0.0012**
45	**0.00010**	**0.664**	**0.2978**	**4.323**	**0.0000**	**73.751**	**0.0103**	**0.202**	**0.1008**	**0.064**	**9.42**	**0.21**	**183.09**	**3.95**	**94.40**	**2.89**	**0.01**	**0.0013**
50	**0.00004**	**2.208**	**0.0726**	**4.715**	**0.0000**	**75.961**	**0.0024**	**0.682**	**0.0276**	**0.233**	**9.47**	**0.34**	**184.08**	**6.27**	**81.48**	**0.68**	**0.01**	**0.0013**

Step	36Ar [fA]	%1σ	37Ar [fA]	1%σ	38Ar [fA]	%1σ	39Ar [fA]	%1σ	40Ar [fA]	%1σ	40(r)/ 39(k)	± 2σ	Age (Ma)	± 2σ	40Ar(r) (%)	39Ar(k) (%)	K/Ca	± 2σ
*KC **plagioclase**: J = 0.01058900 ± 0.00000635 (1σ) MDF = 0.992802 ± 0.00060 (1σ)*																		
2.5	**0.0010**	**0.795**	**0.8875**	**5.934**	**0.0004**	**11.164**	**0.0216**	**0.055**	**0.4342**	**0.541**	**9.88**	**0.51**	**180.60**	**8.91**	**47.81**	**5.31**	**0.01**	**0.0012**
3	**0.0007**	**1.032**	**1.9180**	**5.695**	**0.0006**	**6.836**	**0.0439**	**0.048**	**0.4957**	**0.474**	**9.99**	**0.44**	**182.37**	**7.65**	**85.66**	**10.75**	**0.01**	**0.0011**
3.5	**0.0006**	**1.246**	**1.7917**	**5.712**	**0.0006**	**6.679**	**0.0442**	**0.047**	**0.4727**	**0.497**	**9.99**	**0.41**	**182.40**	**7.15**	**90.82**	**10.87**	**0.01**	**0.0012**
4	**0.0002**	**3.483**	**0.6788**	**6.045**	**0.0002**	**17.634**	**0.0178**	**0.075**	**0.1840**	**1.276**	**9.97**	**0.54**	**182.17**	**9.33**	**93.66**	**4.37**	**0.01**	**0.0013**
4.5	**0.0001**	**5.242**	**0.4701**	**6.476**	**0.0002**	**18.797**	**0.0118**	**0.098**	**0.1225**	**1.917**	**10.11**	**0.71**	**184.47**	**12.32**	**94.89**	**2.91**	**0.01**	**0.0014**
5	**0.0003**	**2.362**	**0.9369**	**5.857**	**0.0003**	**13.251**	**0.0261**	**0.052**	**0.2760**	**0.851**	**9.97**	**0.43**	**182.17**	**7.51**	**91.81**	**6.42**	**0.01**	**0.0014**
5.5	**0.0004**	**2.107**	**1.0494**	**5.817**	**0.0004**	**10.827**	**0.0288**	**0.052**	**0.3076**	**0.764**	**10.05**	**0.42**	**183.50**	**7.29**	**91.74**	**7.10**	**0.01**	**0.0013**
6	**0.0002**	**4.947**	**0.4660**	**6.449**	**0.0002**	**26.685**	**0.0131**	**0.089**	**0.1366**	**1.719**	**9.98**	**0.64**	**182.34**	**11.05**	**93.30**	**3.23**	**0.01**	**0.0015**
7	**0.0003**	**2.594**	**0.8989**	**5.889**	**0.0004**	**9.908**	**0.0251**	**0.066**	**0.2630**	**0.893**	**10.04**	**0.44**	**183.32**	**7.60**	**93.59**	**6.20**	**0.01**	**0.0014**
8	**0.0002**	**3.170**	**0.7359**	**5.899**	**0.0003**	**15.098**	**0.0204**	**0.067**	**0.2143**	**1.096**	**10.07**	**0.48**	**183.79**	**8.36**	**93.42**	**5.03**	**0.01**	**0.0014**
10	**0.0003**	**2.220**	**1.0765**	**5.811**	**0.0004**	**9.750**	**0.0290**	**0.054**	**0.3023**	**0.777**	**10.04**	**0.42**	**183.31**	**7.37**	**93.91**	**7.15**	**0.01**	**0.0013**
12	**0.0003**	**2.429**	**1.0336**	**5.853**	**0.0004**	**10.105**	**0.0266**	**0.057**	**0.2733**	**0.859**	**10.08**	**0.45**	**183.94**	**7.88**	**95.25**	**6.53**	**0.01**	**0.0013**
15	**0.0003**	**2.884**	**0.8478**	**6.024**	**0.0003**	**14.574**	**0.0194**	**0.067**	**0.1995**	**1.177**	**9.97**	**0.56**	**182.13**	**9.68**	**94.09**	**4.76**	**0.01**	**0.0012**
18	**0.0002**	**4.305**	**0.5413**	**6.447**	**0.0002**	**20.068**	**0.0120**	**0.089**	**0.1264**	**1.859**	**10.05**	**0.74**	**183.46**	**12.91**	**92.07**	**2.93**	**0.01**	**0.0012**
21	**0.0002**	**3.936**	**0.6155**	**6.129**	**0.0002**	**27.931**	**0.0131**	**0.079**	**0.1386**	**1.694**	**10.20**	**0.70**	**186.04**	**12.18**	**93.36**	**3.21**	**0.01**	**0.0011**
24	**0.0002**	**4.633**	**0.4738**	**6.354**	**0.0002**	**30.515**	**0.0106**	**0.089**	**0.1135**	**2.069**	**9.93**	**0.79**	**181.46**	**13.79**	**89.72**	**2.59**	**0.01**	**0.0012**
27	**0.0002**	**4.588**	**0.4856**	**6.244**	**0.0002**	**24.072**	**0.0106**	**0.103**	**0.1150**	**2.043**	**10.09**	**0.79**	**184.19**	**13.73**	**90.38**	**2.60**	**0.01**	**0.0011**
30	**0.0003**	**3.002**	**0.7434**	**5.931**	**0.0002**	**20.261**	**0.0165**	**0.078**	**0.1779**	**1.320**	**10.01**	**0.60**	**182.86**	**10.45**	**90.24**	**4.05**	**0.01**	**0.0011**
35	**0.0001**	**13.771**	**0.1779**	**9.867**	**0.0000**	**1033.754**	**0.0032**	**0.281**	**0.0350**	**6.711**	**10.52**	**2.29**	**191.60**	**39.65**	**93.14**	**0.78**	**0.01**	**0.0015**
40	**0.0002**	**4.714**	**0.4514**	**6.576**	**0.0000**	**762.790**	**0.0078**	**0.150**	**0.0881**	**2.666**	**10.03**	**1.07**	**183.16**	**18.65**	**85.73**	**1.90**	**0.01**	**0.0009**
45	**0.0002**	**4.612**	**0.2124**	**8.352**	**0.0001**	**39.183**	**0.0043**	**0.227**	**0.0729**	**3.223**	**9.66**	**1.71**	**176.67**	**29.78**	**55.31**	**1.05**	**0.01**	**0.0014**
50	**0.0004**	**1.979**	**0.0596**	**33.062**	**0.0001**	**55.634**	**0.0012**	**0.896**	**0.1212**	**1.938**	**8.57**	**6.49**	**157.59**	**114.25**	**7.94**	**0.28**	**0.01**	**0.0054**

Step	36Ar [fA]	%1σ	37Ar [fA]	1%σ	38Ar [fA]	%1σ	39Ar [fA]	%1σ	40Ar [fA]	%1σ	40(r)/ 39(k)	± 2σ	Age (Ma)	± 2σ	40Ar(r) (%)	39Ar(k) (%)	K/Ca	± 2σ
*KD **plagioclase**: J = 0.01063170 ± 0.00000638 (1σ) MDF = 0.992804 ± 0.00030 (1σ)*																		
2.5	0.0067	0.176	1.0049	5.809	0.0026	1.524	0.0873	0.062	2.7079	0.019	9.08	0.14	166.70	2.51	29.06	8.60	0.04	0.0043
3	0.0011	0.329	1.8065	5.733	0.0018	2.280	0.1412	0.050	1.5653	0.032	9.82	0.12	179.65	2.10	87.82	13.89	0.03	0.0038
3.5	0.0010	0.355	1.8424	5.700	0.0020	1.993	0.1637	0.049	1.7357	0.029	9.74	0.11	178.14	1.83	91.13	16.13	0.04	0.0043
4	0.0003	0.886	0.7312	6.069	0.0008	5.065	0.0649	0.074	0.6721	0.075	9.78	0.12	178.82	2.02	93.64	6.39	0.04	0.0046
4.5	0.0002	1.572	0.4321	7.021	0.0005	8.918	0.0366	0.117	0.3794	0.133	9.89	0.15	180.81	2.55	94.59	3.60	0.04	0.0051
5	0.0004	0.705	0.7889	5.977	0.0009	4.736	0.0691	0.072	0.7438	0.068	9.94	0.12	181.73	2.00	91.62	6.80	0.04	0.0045
5.5	**0.0005**	**0.575**	**0.9885**	**5.867**	**0.0011**	**3.744**	**0.0897**	**0.062**	**0.9633**	**0.052**	**9.88**	**0.11**	**180.67**	**1.88**	**91.29**	**8.84**	**0.04**	**0.0045**
6	**0.0002**	**1.583**	**0.4144**	**6.737**	**0.0004**	**10.721**	**0.0355**	**0.120**	**0.3742**	**0.135**	**9.99**	**0.14**	**182.57**	**2.45**	**94.10**	**3.50**	**0.04**	**0.0049**
7	**0.0003**	**1.056**	**0.5793**	**6.273**	**0.0007**	**6.232**	**0.0510**	**0.089**	**0.5397**	**0.093**	**9.98**	**0.12**	**182.43**	**2.14**	**93.51**	**5.02**	**0.04**	**0.0047**
8	**0.0002**	**1.158**	**0.5499**	**6.451**	**0.0006**	**6.457**	**0.0421**	**0.102**	**0.4482**	**0.112**	**10.02**	**0.15**	**182.98**	**2.53**	**93.27**	**4.14**	**0.03**	**0.0042**
10	**0.0002**	**1.457**	**0.4848**	**6.754**	**0.0005**	**8.843**	**0.0331**	**0.126**	**0.3484**	**0.144**	**10.05**	**0.17**	**183.64**	**3.00**	**94.47**	**3.25**	**0.03**	**0.0039**
12	**0.0002**	**1.854**	**0.3838**	**7.335**	**0.0004**	**10.739**	**0.0256**	**0.162**	**0.2677**	**0.188**	**9.97**	**0.20**	**182.18**	**3.41**	**94.52**	**2.52**	**0.03**	**0.0042**
15	**0.0002**	**1.506**	**0.4935**	**6.646**	**0.0004**	**9.717**	**0.0284**	**0.146**	**0.2981**	**0.169**	**10.01**	**0.20**	**182.95**	**3.51**	**94.36**	**2.79**	**0.02**	**0.0033**
18	**0.0002**	**1.583**	**0.4846**	**6.642**	**0.0004**	**12.304**	**0.0275**	**0.153**	**0.2911**	**0.173**	**10.11**	**0.21**	**184.66**	**3.57**	**94.46**	**2.70**	**0.02**	**0.0032**
21	**0.0002**	**1.450**	**0.5194**	**6.740**	**0.0003**	**11.183**	**0.0289**	**0.149**	**0.3033**	**0.166**	**10.06**	**0.21**	**183.77**	**3.65**	**94.57**	**2.83**	**0.02**	**0.0032**
24	**0.0002**	**1.555**	**0.4761**	**6.649**	**0.0003**	**15.148**	**0.0262**	**0.158**	**0.2770**	**0.182**	**10.02**	**0.21**	**183.00**	**3.70**	**93.59**	**2.57**	**0.02**	**0.0031**
27	**0.0002**	**1.209**	**0.5626**	**6.357**	**0.0004**	**9.309**	**0.0294**	**0.142**	**0.3149**	**0.160**	**9.99**	**0.21**	**182.48**	**3.67**	**91.92**	**2.88**	**0.02**	**0.0028**
30	**0.0001**	**4.872**	**0.1299**	**14.960**	**0.0001**	**33.440**	**0.0061**	**0.649**	**0.0693**	**0.726**	**10.32**	**0.62**	**188.28**	**10.71**	**90.20**	**0.60**	**0.02**	**0.0060**
35	**0.0001**	**3.398**	**0.2015**	**8.840**	**0.0002**	**17.746**	**0.0112**	**0.356**	**0.1190**	**0.423**	**10.01**	**0.32**	**182.93**	**5.51**	**93.30**	**1.10**	**0.02**	**0.0042**
40	**0.0001**	**3.450**	**0.1851**	**10.260**	**0.0002**	**19.904**	**0.0117**	**0.347**	**0.1246**	**0.404**	**10.01**	**0.32**	**182.93**	**5.53**	**92.75**	**1.15**	**0.03**	**0.0055**
45	**0.0001**	**3.439**	**0.0901**	**18.983**	**0.0001**	**38.543**	**0.0048**	**0.824**	**0.0642**	**0.785**	**9.95**	**0.72**	**181.75**	**12.51**	**73.79**	**0.47**	**0.02**	**0.0086**
50	**0.0003**	**0.949**	**0.0496**	**33.286**	**0.0001**	**52.604**	**0.0023**	**1.718**	**0.1102**	**0.457**	**10.03**	**1.50**	**183.29**	**25.98**	**20.70**	**0.23**	**0.02**	**0.0131**

Step	36Ar [fA]	%1σ	37Ar [fA]	1%σ	38Ar [fA]	%1σ	39Ar [fA]	%1σ	40Ar [fA]	%1σ	40(r)/ 39(k)	± 2σ	Age (Ma)	± 2σ	40Ar(r) (%)	39Ar(k) (%)	K/Ca	± 2σ
*KF **plagioclase**: J = 0.01058900 ± 0.00000635 (1σ) MDF = 0.992802 ± 0.00060 (1σ)*																		
0.5	0.0001	1.949	0.0011	162.854	0.0000	196.942	0.0001	20.254	0.0249	2.412	3.13	16.52	63.00	326.30	1.20	0.02	0.04	0.1185
1	**0.0002**	**0.746**	**0.0161**	**13.667**	**0.0000**	**162.790**	**0.0015**	**1.298**	**0.0871**	**0.689**	**10.15**	**1.16**	**196.54**	**21.21**	**17.27**	**0.24**	**0.04**	**0.0109**
1.5	**0.0003**	**0.682**	**0.1036**	**4.600**	**0.0001**	**33.645**	**0.0077**	**0.282**	**0.1394**	**0.431**	**9.34**	**0.24**	**181.56**	**4.41**	**51.04**	**1.26**	**0.03**	**0.0029**
2	**0.0002**	**0.766**	**0.2744**	**4.327**	**0.0002**	**15.104**	**0.0173**	**0.133**	**0.2047**	**0.294**	**9.41**	**0.15**	**182.94**	**2.71**	**78.73**	**2.83**	**0.03**	**0.0023**
2.5	**0.0002**	**0.872**	**0.4291**	**4.297**	**0.0003**	**13.735**	**0.0266**	**0.098**	**0.2740**	**0.220**	**9.42**	**0.13**	**183.17**	**2.40**	**90.58**	**4.35**	**0.03**	**0.0023**
3	**0.0002**	**0.836**	**0.5619**	**4.286**	**0.0004**	**10.710**	**0.0354**	**0.088**	**0.3477**	**0.173**	**9.42**	**0.12**	**183.08**	**2.24**	**94.87**	**5.78**	**0.03**	**0.0023**
3.5	**0.0002**	**0.761**	**0.6582**	**4.285**	**0.0005**	**7.988**	**0.0424**	**0.080**	**0.4108**	**0.146**	**9.42**	**0.12**	**183.03**	**2.15**	**96.05**	**6.92**	**0.03**	**0.0023**
4	**0.0003**	**0.701**	**0.6726**	**4.284**	**0.0006**	**6.261**	**0.0443**	**0.077**	**0.4363**	**0.138**	**9.46**	**0.11**	**183.86**	**2.09**	**95.04**	**7.23**	**0.03**	**0.0024**
4.5	**0.0002**	**0.835**	**0.6178**	**4.288**	**0.0005**	**7.766**	**0.0428**	**0.077**	**0.4148**	**0.145**	**9.39**	**0.11**	**182.50**	**2.02**	**95.88**	**6.99**	**0.03**	**0.0025**
5	**0.0002**	**0.775**	**0.5634**	**4.290**	**0.0004**	**9.233**	**0.0400**	**0.102**	**0.3912**	**0.154**	**9.42**	**0.11**	**183.08**	**2.00**	**95.35**	**6.54**	**0.03**	**0.0026**
5.5	**0.0002**	**0.822**	**0.5104**	**4.291**	**0.0005**	**6.518**	**0.0378**	**0.090**	**0.3738**	**0.161**	**9.41**	**0.10**	**182.93**	**1.94**	**94.40**	**6.19**	**0.03**	**0.0027**
6	**0.0002**	**0.837**	**0.4718**	**4.298**	**0.0004**	**8.907**	**0.0367**	**0.082**	**0.3692**	**0.163**	**9.46**	**0.10**	**183.84**	**1.87**	**93.21**	**6.00**	**0.03**	**0.0029**
7	**0.0002**	**0.723**	**0.5667**	**4.293**	**0.0006**	**5.530**	**0.0441**	**0.082**	**0.4373**	**0.137**	**9.40**	**0.10**	**182.80**	**1.82**	**94.05**	**7.22**	**0.03**	**0.0028**
8	**0.0002**	**1.005**	**0.4380**	**4.295**	**0.0004**	**9.536**	**0.0342**	**0.095**	**0.3358**	**0.179**	**9.41**	**0.10**	**182.92**	**1.90**	**94.90**	**5.59**	**0.03**	**0.0029**
10	0.0002	0.471	0.4779	4.295	0.0005	4.488	0.0364	0.191	0.3652	0.037	9.61	0.10	186.63	1.86	94.85	5.95	0.03	0.0028
12	0.0001	0.573	0.2890	4.312	0.0002	11.747	0.0202	0.343	0.2034	0.064	9.64	0.12	187.19	2.27	94.58	3.29	0.03	0.0026
15	**0.0001**	**1.532**	**0.2613**	**4.352**	**0.0003**	**12.373**	**0.0183**	**0.125**	**0.1832**	**0.328**	**9.48**	**0.13**	**184.16**	**2.49**	**93.77**	**2.99**	**0.03**	**0.0026**
18	**0.0001**	**1.453**	**0.2852**	**4.321**	**0.0002**	**15.275**	**0.0186**	**0.127**	**0.1840**	**0.327**	**9.45**	**0.14**	**183.70**	**2.57**	**94.41**	**3.03**	**0.03**	**0.0024**
21	**0.0001**	**1.242**	**0.3529**	**4.302**	**0.0003**	**15.019**	**0.0197**	**0.130**	**0.1955**	**0.307**	**9.45**	**0.15**	**183.64**	**2.80**	**93.99**	**3.21**	**0.02**	**0.0020**
24	**0.0001**	**1.502**	**0.2902**	**4.315**	**0.0003**	**12.080**	**0.0159**	**0.145**	**0.1571**	**0.382**	**9.43**	**0.16**	**183.25**	**3.04**	**94.11**	**2.59**	**0.02**	**0.0020**
27	**0.0001**	**2.138**	**0.2073**	**4.370**	**0.0002**	**20.495**	**0.0122**	**0.183**	**0.1202**	**0.500**	**9.43**	**0.18**	**183.18**	**3.33**	**94.61**	**1.99**	**0.03**	**0.0022**
30	**0.0001**	**2.411**	**0.1847**	**4.396**	**0.0002**	**16.020**	**0.0120**	**0.179**	**0.1185**	**0.507**	**9.46**	**0.17**	**183.83**	**3.23**	**94.95**	**1.96**	**0.03**	**0.0024**
35	**0.0001**	**2.132**	**0.2402**	**4.348**	**0.0002**	**15.756**	**0.0145**	**0.153**	**0.1397**	**0.430**	**9.48**	**0.16**	**184.12**	**3.01**	**97.03**	**2.36**	**0.03**	**0.0022**
40	**0.0001**	**2.589**	**0.1750**	**4.372**	**0.0002**	**18.297**	**0.0120**	**0.179**	**0.1170**	**0.513**	**9.42**	**0.17**	**183.08**	**3.15**	**95.65**	**1.96**	**0.03**	**0.0026**
45	**0.0001**	**1.735**	**0.2391**	**4.347**	**0.0002**	**16.319**	**0.0149**	**0.143**	**0.1471**	**0.409**	**9.46**	**0.16**	**183.91**	**2.88**	**94.83**	**2.43**	**0.03**	**0.0023**
50	**0.0001**	**2.969**	**0.0951**	**4.846**	**0.0001**	**42.459**	**0.0066**	**0.333**	**0.0705**	**0.852**	**9.45**	**0.27**	**183.73**	**4.95**	**87.86**	**1.08**	**0.03**	**0.0029**

Step	36Ar [fA]	%1σ	37Ar [fA]	1%σ	38Ar [fA]	%1σ	39Ar [fA]	%1σ	40Ar [fA]	%1σ	40(r)/ 39(k)	± 2σ	Age (Ma)	± 2σ	40Ar(r) (%)	39Ar(k) (%)	K/Ca	± 2σ
*KG **plagioclase**: J = 0.01058900 ± 0.00000635 (1σ) MDF = 0.992802 ± 0.00060 (1σ)*																		
2.5	0.0009	0.206	0.9496	6.089	0.0008	3.655	0.0546	0.048	0.7351	0.031	10.17	0.17	185.51	3.01	74.56	11.91	0.02	0.0030
3	**0.0006**	**0.272**	**1.8985**	**5.792**	**0.0011**	**2.824**	**0.0981**	**0.044**	**1.0054**	**0.022**	**10.00**	**0.18**	**182.64**	**3.18**	**96.31**	**21.39**	**0.02**	**0.0025**
3.5	**0.0005**	**0.270**	**1.3972**	**5.834**	**0.0010**	**3.070**	**0.0818**	**0.045**	**0.8466**	**0.026**	**10.00**	**0.16**	**182.64**	**2.82**	**95.48**	**17.85**	**0.02**	**0.0029**
4	**0.0001**	**0.582**	**0.3894**	**7.383**	**0.0003**	**11.576**	**0.0222**	**0.072**	**0.2282**	**0.097**	**10.04**	**0.21**	**183.32**	**3.68**	**96.44**	**4.84**	**0.02**	**0.0036**
4.5	**0.0001**	**0.925**	**0.2236**	**9.610**	**0.0001**	**24.539**	**0.0127**	**0.090**	**0.1314**	**0.168**	**10.07**	**0.28**	**183.87**	**4.82**	**96.31**	**2.77**	**0.02**	**0.0046**
5	**0.0002**	**0.757**	**0.4450**	**7.358**	**0.0004**	**7.687**	**0.0305**	**0.050**	**0.3281**	**0.068**	**10.09**	**0.18**	**184.21**	**3.06**	**92.96**	**6.68**	**0.03**	**0.0043**
5.5	**0.0002**	**0.543**	**0.4667**	**7.089**	**0.0003**	**8.790**	**0.0277**	**0.053**	**0.2999**	**0.074**	**10.09**	**0.20**	**184.19**	**3.40**	**92.02**	**6.04**	**0.03**	**0.0036**
6	**0.0001**	**0.807**	**0.2017**	**10.736**	**0.0002**	**19.459**	**0.0155**	**0.069**	**0.1710**	**0.130**	**10.25**	**0.23**	**187.00**	**3.97**	**91.99**	**3.39**	**0.03**	**0.0070**
7	**0.0001**	**0.820**	**0.2316**	**10.819**	**0.0002**	**20.353**	**0.0151**	**0.070**	**0.1617**	**0.137**	**10.04**	**0.27**	**183.39**	**4.72**	**92.57**	**3.29**	**0.03**	**0.0060**
8	**0.0001**	**0.933**	**0.2410**	**8.846**	**0.0001**	**20.978**	**0.0130**	**0.088**	**0.1392**	**0.159**	**10.20**	**0.27**	**186.11**	**4.69**	**94.21**	**2.84**	**0.02**	**0.0041**
10	**0.0001**	**0.756**	**0.2697**	**8.987**	**0.0001**	**24.301**	**0.0137**	**0.078**	**0.1445**	**0.153**	**9.95**	**0.29**	**181.80**	**5.04**	**93.18**	**2.99**	**0.02**	**0.0039**
12	**0.0001**	**0.775**	**0.2971**	**8.729**	**0.0001**	**96.711**	**0.0126**	**0.092**	**0.1316**	**0.168**	**10.03**	**0.34**	**183.18**	**5.89**	**94.32**	**2.73**	**0.02**	**0.0031**
15	**0.0001**	**0.670**	**0.3052**	**9.290**	**0.0001**	**21.827**	**0.0118**	**0.082**	**0.1238**	**0.180**	**10.19**	**0.39**	**185.94**	**6.83**	**95.35**	**2.56**	**0.02**	**0.0030**
18	**0.0001**	**0.799**	**0.3101**	**7.994**	**0.0002**	**20.161**	**0.0122**	**0.083**	**0.1292**	**0.172**	**10.13**	**0.33**	**184.96**	**5.80**	**94.38**	**2.66**	**0.02**	**0.0027**
21	**0.0001**	**0.765**	**0.2835**	**8.681**	**0.0001**	**29.712**	**0.0120**	**0.085**	**0.1294**	**0.171**	**9.98**	**0.34**	**182.21**	**5.85**	**91.32**	**2.62**	**0.02**	**0.0031**
24	**0.0001**	**1.177**	**0.2013**	**11.928**	**0.0001**	**64.346**	**0.0069**	**0.134**	**0.0755**	**0.293**	**10.37**	**0.58**	**189.04**	**10.03**	**92.15**	**1.48**	**0.01**	**0.0034**
27	**0.0000**	**1.973**	**0.0741**	**25.414**	**0.0000**	**860.221**	**0.0024**	**0.368**	**0.0301**	**0.734**	**10.66**	**1.31**	**194.12**	**22.64**	**82.70**	**0.52**	**0.01**	**0.0069**
30	**0.0001**	**1.134**	**0.1396**	**13.916**	**0.0001**	**50.360**	**0.0050**	**0.198**	**0.0593**	**0.374**	**10.38**	**0.64**	**189.14**	**11.14**	**85.89**	**1.08**	**0.02**	**0.0042**
35	**0.0000**	**2.138**	**0.0414**	**51.142**	**0.0000**	**1970.283**	**0.0020**	**0.445**	**0.0264**	**0.837**	**9.81**	**1.70**	**179.28**	**29.54**	**74.80**	**0.45**	**0.02**	**0.0214**
40	**0.0001**	**1.141**	**0.0900**	**24.305**	**0.0000**	**107.739**	**0.0037**	**0.216**	**0.0547**	**0.405**	**10.19**	**0.98**	**185.97**	**17.05**	**67.43**	**0.80**	**0.02**	**0.0084**
45	**0.0001**	**1.448**	**0.0649**	**35.694**	**0.0000**	**587.925**	**0.0023**	**0.339**	**0.0348**	**0.635**	**10.48**	**1.63**	**191.02**	**28.23**	**68.94**	**0.51**	**0.02**	**0.0108**
50	**0.0001**	**0.913**	**0.0788**	**25.050**	**0.0000**	**86.783**	**0.0028**	**0.354**	**0.0495**	**0.448**	**10.41**	**1.16**	**189.78**	**20.03**	**58.41**	**0.61**	**0.02**	**0.0076**

Step	36Ar [fA]	%1σ	37Ar [fA]	1%σ	38Ar [fA]	%1σ	39Ar [fA]	%1σ	40Ar [fA]	%1σ	40(r)/ 39(k)	± 2σ	Age (Ma)	± 2σ	40Ar(r) (%)	39Ar(k) (%)	K/Ca	± 2σ
*KB **biotite**: J = 0.01058900 ± 0.00000635 (1σ) MDF = 0.992802 ± 0.00060 (1σ)*																		
1	0.00035	0.236	0.0003	39.378	0.0001	25.865	0.0000	52	0.1045	0	-18.82	30.77	-432.7	799.59	-0.70	0.06	0.06	0.0731
2	0.00011	0.633	0.0003	36.174	0.0000	77.877	0.0004	5	0.0352	0	7.12	1.27	140.16	24.08	9.00	0.68	0.55	0.4023
2.7	0.00011	0.788	0.0003	41.695	0.0000	77.595	0.0011	2.070	0.0441	0.075	8.58	0.63	167.43	11.83	22.24	1.74	1.63	1.3617
3.5	0.00112	0.139	0.0009	14.173	0.0002	9.769	0.0019	1.097	0.3536	0.013	8.58	1.45	167.43	26.98	4.52	2.83	0.86	0.2453
4.3	0.00029	0.312	0.0006	19.204	0.0001	19.211	0.0036	0.650	0.1226	0.025	9.74	0.27	189.09	4.90	28.80	5.51	2.46	0.9441
5	**0.00016**	**0.435**	**0.0008**	**20.746**	**0.0001**	**25.041**	**0.0041**	**0.531**	**0.0868**	**0.036**	**9.56**	**0.17**	**185.71**	**3.08**	**45.38**	**6.26**	**2.16**	**0.8978**
5.8	**0.00021**	**0.458**	**0.0010**	**12.801**	**0.0001**	**13.743**	**0.0056**	**0.361**	**0.1160**	**0.027**	**9.34**	**0.15**	**181.60**	**2.77**	**45.29**	**8.56**	**2.51**	**0.6434**
6.5	**0.00027**	**0.262**	**0.0010**	**16.882**	**0.0001**	**19.356**	**0.0036**	**0.621**	**0.1144**	**0.026**	**9.49**	**0.24**	**184.38**	**4.36**	**29.69**	**5.44**	**1.61**	**0.5442**
7.3	**0.00013**	**0.426**	**0.0006**	**23.584**	**0.0001**	**25.790**	**0.0033**	**0.697**	**0.0719**	**0.046**	**9.66**	**0.19**	**187.60**	**3.52**	**45.03**	**5.09**	**2.60**	**1.2281**
8	**0.00008**	**0.889**	**0.0003**	**41.963**	**0.0000**	**41.385**	**0.0034**	**0.660**	**0.0572**	**0.055**	**9.54**	**0.19**	**185.32**	**3.54**	**56.16**	**5.12**	**4.68**	**3.9322**
9	**0.00002**	**2.697**	**0.0002**	**67.713**	**0.0001**	**33.904**	**0.0031**	**0.776**	**0.0346**	**0.090**	**9.45**	**0.18**	**183.70**	**3.30**	**83.91**	**4.66**	**6.38**	**8.6428**
10	**0.00002**	**2.843**	**0.0002**	**72.629**	**0.0001**	**15.087**	**0.0072**	**0.276**	**0.0752**	**0.037**	**9.46**	**0.08**	**183.79**	**1.43**	**90.56**	**10.95**	**17.2**	**24.984**
12	**0.00003**	**2.267**	**0.0004**	**27.714**	**0.0003**	**6.889**	**0.0144**	**0.166**	**0.1443**	**0.028**	**9.49**	**0.04**	**184.48**	**0.74**	**94.77**	**21.89**	**14.4**	**7.9954**
14	**0.00002**	**2.440**	**0.0006**	**21.569**	**0.0001**	**32.416**	**0.0041**	**0.500**	**0.0464**	**0.072**	**9.54**	**0.13**	**185.36**	**2.35**	**85.16**	**6.29**	**2.95**	**1.2729**
16	**0.00003**	**2.263**	**0.0007**	**18.224**	**0.0000**	**93.611**	**0.0011**	**2.099**	**0.0188**	**0.151**	**9.66**	**0.51**	**187.51**	**9.49**	**58.80**	**1.74**	**0.70**	**0.2576**
18	**0.00002**	**2.570**	**0.0003**	**31.887**	**0.0000**	**90.530**	**0.0012**	**1.788**	**0.0193**	**0.148**	**9.79**	**0.47**	**189.86**	**8.64**	**62.32**	**1.87**	**1.54**	**0.9868**
22	**0.00001**	**5.151**	**0.0008**	**15.008**	**0.0000**	**36.247**	**0.0022**	**1.026**	**0.0239**	**0.123**	**9.73**	**0.24**	**188.78**	**4.41**	**88.85**	**3.32**	**1.24**	**0.3721**
26	**0.00000**	**17.188**	**0.0004**	**39.140**	**0.0000**	**64.544**	**0.0016**	**1.372**	**0.0169**	**0.190**	**9.74**	**0.35**	**188.92**	**6.44**	**93.97**	**2.48**	**1.80**	**1.4061**
30	**0.00000**	**11.698**	**0.0003**	**39.923**	**0.0000**	**78.552**	**0.0018**	**1.274**	**0.0189**	**0.169**	**9.64**	**0.30**	**187.10**	**5.54**	**93.14**	**2.77**	**2.38**	**1.9005**
35	**0.00000**	**56.926**	**0.0002**	**56.368**	**0.0000**	**96.778**	**0.0004**	**5.633**	**0.0044**	**0.689**	**9.99**	**1.38**	**193.59**	**25.32**	**93.93**	**0.63**	**0.90**	**1.0234**
40	**0.00000**	**44.911**	**0.0002**	**90.247**	**0.0000**	**106.102**	**0.0014**	**1.725**	**0.0136**	**0.212**	**9.47**	**0.45**	**184.00**	**8.27**	**96.66**	**2.11**	**3.43**	**6.1926**

Step	36Ar [fA]	%1σ	37Ar [fA]	1%σ	38Ar [fA]	%1σ	39Ar [fA]	%1σ	40Ar [fA]	%1σ	40(r)/ 39(k)	± 2σ	Age (Ma)	± 2σ	40Ar(r) (%)	39Ar(k) (%)	K/Ca	± 2σ
*KC **biotite**: J = 0.01058900 ± 0.00000635 (1σ) MDF = 0.992802 ± 0.00060 (1σ)*																		
1	0.00048	0.228	0.0000	2,480.98	0.0001	36	0.0003	2.998	0.1434	0.127	-1.93	2.97	-37.51	58.29	-0.36	0.45	156	7751
2	0.00015	0.555	0.0000	78.780	0.0000	84.590	0.0007	1.146	0.0482	0.376	4.36	0.89	81.95	16.38	6.39	1.17	-10.2	16.215
2.7	0.00012	0.629	0.0000	269.950	0.0001	50.401	0.0011	0.602	0.0459	0.395	7.82	0.53	144.43	9.34	19.54	1.90	-71.4	385.74
3.5	0.00011	0.638	0.0000	398.069	0.0001	94.245	0.0017	0.534	0.0492	0.368	9.90	0.35	180.83	6.09	33.53	2.76	-141	1124
4.3	0.00003	1.804	0.0000	340.604	0.0000	345.997	0.0007	0.985	0.0162	1.121	10.11	0.76	184.58	13.15	42.35	1.12	50.4	343.34
5	0.00009	0.771	0.0000	205.347	0.0000	455.348	0.0022	0.355	0.0493	0.320	10.38	0.25	189.15	4.34	45.81	3.60	101.	416.34
5.8	0.00036	0.240	0.0000	67.288	0.0001	32.877	0.0034	0.291	0.1427	0.112	10.08	0.20	183.99	3.51	23.71	5.55	-58.5	78.748
6.5	0.00011	0.731	0.0000	2,459.21	0.0000	300.663	0.0016	0.546	0.0489	0.323	10.04	0.39	183.26	6.80	31.90	2.57	-1053	51799
7.3	0.00012	0.590	0.0000	580.847	0.0001	37.552	0.0031	0.240	0.0673	0.235	10.25	0.18	187.01	3.14	46.59	5.06	-534	6208
8	0.00017	0.444	0.0000	520.645	0.0001	48	0.0037	0.311	0.0896	0.178	10.37	0.16	189.04	2.83	43.24	6.18	-494	5154.3
9	**0.00013**	**0.487**	**0.0000**	**62.670**	**0.0001**	**41.219**	**0.0041**	**0.194**	**0.0798**	**0.085**	**10.22**	**0.10**	**186.49**	**1.80**	**52.98**	**6.84**	**51.8**	**64.925**
10	**0.00011**	**0.413**	**0.0000**	**226.756**	**0.0001**	**36.172**	**0.0032**	**0.220**	**0.0651**	**0.105**	**10.11**	**0.11**	**184.49**	**1.85**	**49.67**	**5.29**	**-151**	**687.20**
12	**0.00019**	**0.482**	**0.0000**	**134.959**	**0.0001**	**25.280**	**0.0063**	**0.154**	**0.1210**	**0.054**	**10.16**	**0.10**	**185.42**	**1.68**	**52.86**	**10.41**	**208**	**562.18**
14	**0.00019**	**0.556**	**0.0000**	**123.097**	**0.0001**	**32.386**	**0.0041**	**0.176**	**0.0992**	**0.069**	**10.18**	**0.17**	**185.70**	**2.89**	**41.90**	**6.76**	**106**	**262.64**
16	**0.00011**	**0.572**	**0.0000**	**104.997**	**0.0001**	**52.832**	**0.0049**	**0.181**	**0.0834**	**0.081**	**10.08**	**0.09**	**184.02**	**1.59**	**59.58**	**8.15**	**104**	**219.44**
18	**0.00008**	**0.715**	**0.0000**	**543.354**	**0.0001**	**34.991**	**0.0051**	**0.132**	**0.0753**	**0.089**	**10.13**	**0.08**	**184.95**	**1.32**	**68.81**	**8.46**	**655**	**7121.0**
22	**0.00009**	**0.584**	**0.0000**	**95.830**	**0.0001**	**33.228**	**0.0022**	**0.414**	**0.0480**	**0.139**	**10.01**	**0.18**	**182.89**	**3.06**	**45.33**	**3.59**	**50.5**	**96.898**
26	**0.00007**	**0.890**	**0.0000**	**111.880**	**0.0001**	**60.517**	**0.0030**	**0.295**	**0.0516**	**0.130**	**10.05**	**0.15**	**183.53**	**2.61**	**57.92**	**4.92**	**72.8**	**163.08**
30	**0.00004**	**1.203**	**0.0000**	**209.543**	**0.0001**	**27.971**	**0.0064**	**0.117**	**0.0771**	**0.087**	**10.07**	**0.06**	**183.77**	**1.00**	**83.53**	**10.58**	**336**	**1411.9**
35	**0.00002**	**2.199**	**0.0000**	**175.063**	**0.0000**	**118.526**	**0.0011**	**0.554**	**0.0165**	**0.404**	**10.11**	**0.27**	**184.60**	**4.68**	**67.66**	**1.82**	**42.2**	**147.80**
40	**0.00002**	**3.840**	**0.0000**	**374.928**	**0.0001**	**46.988**	**0.0017**	**0.398**	**0.0224**	**0.808**	**10.29**	**0.32**	**187.62**	**5.53**	**78.02**	**2.82**	**162**	**1218.1**

Step	36Ar [fA]	%1σ	37Ar [fA]	1%σ	38Ar [fA]	%1σ	39Ar [fA]	%1σ	40Ar [fA]	%1σ	40(r)/ 39(k)	± 2σ	Age (Ma)	± 2σ	40Ar(r) (%)	39Ar(k) (%)	K/Ca	± 2σ
*KD **biotite**: J = 0.01063170 ± 0.00000638 (1σ) MDF = 0.992804 ± 0.00030 (1σ)*																		
1	0.0001	0.705	0.0000	655.6	-0.000	100.904	0.0001	8.956	0.0283	0.697	7.10	6.00	131.58	107.22	2.38	0.09	13	164
2	0.0001	0.733	0.0000	5567.2	0.0001	32.349	0.0005	1.772	0.0381	0.516	21.63	1.33	374.11	20.76	29.30	0.49	741	82487
2.7	0.0000	2.105	0.0000	272.2	0.0001	42.791	0.0021	0.553	0.1400	0.141	62.02	0.76	915.53	8.79	90.96	1.96	167	907
3.5	0.0001	0.876	0.0000	103.1	0.0001	25.749	0.0051	0.186	0.3672	0.054	66.83	0.28	970.29	3.09	93.00	4.87	123	253
4.3	0.0000	2.151	0.0000	175.2	0.0000	395.674	0.0016	0.567	0.1021	0.193	58.19	0.76	870.58	8.99	90.07	1.51	68	238
5	0.0001	0.748	0.0000	612.5	0.0001	51.700	0.0033	0.253	0.0934	0.212	20.83	0.20	361.66	3.09	73.39	3.14	-480	5877
5.8	0.0001	1.184	0.0000	76.1	0.0001	32.514	0.0048	0.197	0.0956	0.206	15.71	0.14	279.21	2.34	79.18	4.59	101	153
6.5	0.0000	2.895	0.0000	1733.2	0.0000	313.691	0.0022	0.394	0.0412	0.478	15.56	0.28	276.72	4.56	83.85	2.12	747	25904
7.3	0.0000	2.903	0.0000	78.7	0.0001	33.533	0.0047	0.182	0.0753	0.261	14.55	0.13	259.99	2.19	90.74	4.48	100	157
8	0.0000	2.762	0.0000	619.1	0.0001	20.552	0.0081	0.105	0.1242	0.158	14.50	0.07	259.17	1.22	94.66	7.73	-983	12171
9	0.0000	4.328	0.0000	334.4	0.0002	19.810	0.0093	0.106	0.1286	0.153	13.28	0.07	238.78	1.16	96.11	8.87	786	5256
10	0.0000	3.738	0.0000	178.2	0.0002	17.413	0.0093	0.094	0.1216	0.163	12.64	0.06	227.92	1.05	96.18	8.82	519	1851
12	0.0000	3.724	0.0000	221.5	0.0003	11.672	0.0117	0.082	0.1578	0.125	13.00	0.05	234.00	0.91	96.43	11.16	707	3130
14	0.0000	4.266	0.0000	81.6	0.0003	8.660	0.0140	0.084	0.1735	0.113	12.06	0.05	218.15	0.78	97.17	13.33	-253	413
16	0.0000	7.628	0.0000	2835.8	0.0002	12.563	0.0105	0.096	0.1207	0.163	11.31	0.06	205.26	0.97	97.98	9.96	-6428	364602
18	0.0000	7.973	0.0000	198.1	0.0001	31.958	0.0056	0.164	0.0643	0.307	11.10	0.11	201.59	1.88	95.94	5.30	-266	1055
22	0.0000	4.867	0.0000	148.4	0.0001	28.954	0.0053	0.188	0.0620	0.317	11.06	0.11	200.93	1.93	93.68	5.01	-173	514
26	0.0000	4.501	0.0000	654.5	0.0001	48.241	0.0034	0.275	0.0422	0.467	11.13	0.18	202.23	3.07	89.24	3.22	488	6390
30	0.0000	9.786	0.0000	73.8	0.0000	79.135	0.0012	0.768	0.0172	1.149	12.48	0.48	225.19	8.22	88.85	1.17	-26	39
35	0.0000	7.509	0.0000	17965.9	0.0001	67.964	0.0011	0.826	0.0136	1.446	10.39	0.53	189.39	9.13	82.17	1.03	4876	1752102
40	0.0000	6.257	0.0000	111.0	0.0000	110.331	0.0012	0.751	0.0258	0.763	18.45	0.56	323.80	8.95	86.60	1.15	-32	70

Step	36Ar [fA]	%1σ	37Ar [fA]	1%σ	38Ar [fA]	%1σ	39Ar [fA]	%1σ	40Ar [fA]	%1σ	40(r)/ 39(k)	± 2σ	Age (Ma)	± 2σ	40Ar(r) (%)	39Ar(k) (%)	K/Ca	± 2σ
*KF **hornblende**: J = 0.01058900 ± 0.00000635 (1σ) MDF = 0.992802 ± 0.00060 (1σ)*																		
1	0.0040	0.146	0.0040	36.377	0.0013	3.671	0.0091	0.192	1.2587	0.015	8.06	0.47	157.78	8.73	5.81	1.28	0.99	0.7181
2	0.0038	0.136	0.0281	7.182	0.0022	2.131	0.0514	0.061	1.4190	0.014	5.43	0.08	107.73	1.46	19.65	7.25	0.79	0.1129
2.5	0.0012	0.245	0.0139	12.431	0.0007	7.279	0.0228	0.069	0.5640	0.032	9.70	0.08	188.31	1.53	39.25	3.22	0.71	0.1756
3	0.0006	0.394	0.0134	11.744	0.0005	9.393	0.0216	0.087	0.3885	0.046	10.05	0.07	194.64	1.29	55.95	3.05	0.70	0.1635
3.5	0.0006	0.402	0.0185	8.591	0.0005	9.373	0.0246	0.073	0.4054	0.044	9.75	0.06	189.21	1.12	59.08	3.46	0.57	0.0980
4	0.0005	0.444	0.0163	10.966	0.0006	8.739	0.0277	0.067	0.4073	0.044	9.78	0.05	189.65	0.92	66.45	3.91	0.73	0.1598
6	0.0010	0.252	0.0442	5.426	0.0023	2.196	0.0972	0.034	1.3211	0.014	10.62	0.02	205.08	0.34	78.08	13.70	0.95	0.1026
8	0.0005	0.460	0.1035	4.560	0.0034	1.376	0.1103	0.038	1.2599	0.014	10.25	0.02	198.44	0.30	89.68	15.54	0.46	0.0417
10	0.0004	0.540	0.1509	4.390	0.0040	1.156	0.0961	0.036	1.0672	0.018	10.13	0.02	196.22	0.34	91.12	13.54	0.27	0.0240
11	0.0002	1.212	0.0822	4.852	0.0026	1.839	0.0521	0.051	0.5542	0.033	9.82	0.03	190.55	0.53	92.26	7.34	0.27	0.0264
11.8	0.0001	1.771	0.0397	5.861	0.0009	5.128	0.0297	0.070	0.3166	0.057	9.63	0.05	187.03	0.84	90.44	4.19	0.32	0.0377
12.6	0.0001	1.885	0.0323	5.920	0.0006	8.068	0.0227	0.097	0.2442	0.074	9.58	0.06	186.04	1.05	88.87	3.20	0.30	0.0357
13.4	0.0001	2.993	0.0255	7.322	0.0003	14.279	0.0181	0.101	0.1895	0.094	9.52	0.07	184.85	1.33	90.83	2.55	0.31	0.0447
14.2	0.0000	4.163	0.0245	8.562	0.0002	18.942	0.0113	0.183	0.1160	0.154	9.26	0.11	180.22	2.12	89.98	1.59	0.20	0.0339
15	0.0001	3.460	0.0307	6.783	0.0003	16.530	0.0099	0.165	0.1047	0.171	9.20	0.13	179.05	2.42	86.46	1.39	0.14	0.0187
16	0.0001	3.340	0.0400	6.025	0.0004	12.606	0.0099	0.172	0.1073	0.168	9.46	0.13	183.76	2.40	87.28	1.40	0.11	0.0128
17.5	0.0001	2.588	0.0530	5.207	0.0003	15.227	0.0101	0.160	0.1129	0.158	9.48	0.13	184.25	2.37	84.56	1.42	0.08	0.0085
19	0.0001	2.211	0.0673	5.152	0.0004	12.602	0.0125	0.157	0.1355	0.132	9.23	0.11	179.50	2.07	84.50	1.75	0.08	0.0082
20.5	0.0001	2.281	0.0583	5.011	0.0003	14.391	0.0143	0.133	0.1527	0.117	9.34	0.09	181.55	1.70	87.04	2.01	0.11	0.0105
22	0.0000	4.559	0.0353	6.406	0.0001	36.665	0.0057	0.301	0.0619	0.289	9.21	0.23	179.22	4.25	84.13	0.80	0.07	0.0088
24	0.0001	2.518	0.0825	4.595	0.0002	22.926	0.0089	0.192	0.0989	0.181	9.36	0.15	182.04	2.86	83.96	1.25	0.05	0.0042
26	0.0001	3.187	0.0524	5.332	0.0001	32.793	0.0082	0.239	0.0904	0.197	9.46	0.16	183.78	2.96	85.29	1.15	0.07	0.0071
28	0.0000	4.030	0.0392	5.984	0.0001	33.147	0.0092	0.205	0.0991	0.181	9.56	0.14	185.63	2.65	88.65	1.30	0.10	0.0121
32	0.0000	4.054	0.0429	5.857	0.0000	194.822	0.0071	0.278	0.0778	0.230	9.46	0.18	183.79	3.39	86.46	1.00	0.07	0.0084
36	0.0001	2.148	0.0962	4.606	0.0002	23.955	0.0110	0.168	0.1222	0.146	9.52	0.13	184.87	2.41	84.86	1.54	0.05	0.0045
40	0.0001	2.903	0.0660	4.990	0.0002	21.869	0.0084	0.216	0.0938	0.190	9.48	0.16	184.25	2.94	84.94	1.19	0.05	0.0055

Step	36Ar [fA]	%1σ	37Ar [fA]	1%σ	38Ar [fA]	%1σ	39Ar [fA]	%1σ	40Ar [fA]	%1σ	40(r)/ 39(k)	± 2σ	Age (Ma)	± 2σ	40Ar(r) (%)	39Ar(k) (%)	K/Ca	± 2σ
*KG **biotite**: J = 0.01058900 ± 0.00000635 (1σ) MDF = 0.992802 ± 0.00060 (1σ)*																		
1	0.0000	8.529	0.0000	55.03	0.0000	181.105	0.0009	1.052	0.0120	7.397	2.23	2.58	42.39	48.49	17.63	1.04	-15	16
2	0.0000	15.060	0.0000	55.69	0.0000	2974.620	0.0010	0.988	0.0116	7.607	6.22	2.50	115.68	45.06	52.16	1.08	-12	13
2.7	0.0000	9.290	0.0000	40.38	0.0000	209.901	0.0023	0.424	0.0287	3.080	8.70	1.08	159.96	19.04	68.47	2.50	-21	17
3.5	**0.0000**	**10.720**	**0.0000**	**141.97**	**0.0000**	**207.283**	**0.0038**	**0.259**	**0.0453**	**1.952**	**9.87**	**0.64**	**180.31**	**11.17**	**82.79**	**4.20**	**-143**	**406**
4.3	**0.0000**	**41.896**	**0.0000**	**73.25**	**-0.0001**	**60.972**	**0.0015**	**0.611**	**0.0169**	**5.225**	**9.95**	**1.63**	**181.75**	**28.28**	**88.19**	**1.66**	**-26**	**38**
5	**0.0000**	**23.070**	**0.0000**	**138.51**	**-0.0001**	**57.410**	**0.0041**	**0.220**	**0.0457**	**1.935**	**10.31**	**0.60**	**188.06**	**10.41**	**91.99**	**4.50**	**-118**	**326**
5.8	**0.0000**	**27.350**	**0.0000**	**1494.65**	**0.0002**	**38.192**	**0.0063**	**0.180**	**0.0678**	**1.305**	**10.27**	**0.39**	**187.34**	**6.76**	**95.45**	**6.96**	**-2427**	**72550**
6.5	**0.0000**	**93.948**	**0.0000**	**64.83**	**0.0001**	**107.806**	**0.0028**	**0.341**	**0.0294**	**3.010**	**10.16**	**0.87**	**185.41**	**15.09**	**96.97**	**3.10**	**-53**	**68**
7.3	**0.0000**	**49.897**	**0.0000**	**180.27**	**0.0002**	**35.797**	**0.0062**	**0.162**	**0.0647**	**1.366**	**10.15**	**0.39**	**185.32**	**6.84**	**97.42**	**6.86**	**-240**	**864**
8	**0.0000**	**72.174**	**0.0000**	**341.20**	**0.0002**	**36.378**	**0.0065**	**0.141**	**0.0669**	**1.322**	**10.11**	**0.38**	**184.57**	**6.52**	**98.28**	**7.18**	**595**	**4062**
9	**0.0000**	**111.905**	**0.0000**	**443.85**	**0.0001**	**43.696**	**0.0063**	**0.147**	**0.0650**	**1.360**	**10.15**	**0.39**	**185.23**	**6.69**	**98.86**	**7.00**	**-704**	**6251**
10	**0.0000**	**174.628**	**0.0000**	**102.19**	**0.0001**	**39.621**	**0.0056**	**0.162**	**0.0572**	**1.544**	**10.06**	**0.43**	**183.67**	**7.50**	**99.18**	**6.24**	**138**	**282**
12	**0.0000**	**102.778**	**0.0000**	**108.68**	**0.0002**	**31.048**	**0.0099**	**0.106**	**0.1006**	**0.879**	**10.09**	**0.25**	**184.15**	**4.29**	**99.20**	**10.93**	**302**	**657**
14	**0.0000**	**366.645**	**0.0000**	**130.16**	**0.0001**	**92.489**	**0.0057**	**0.162**	**0.0582**	**1.520**	**10.09**	**0.42**	**184.12**	**7.36**	**99.60**	**6.35**	**215**	**561**
16	**0.0000**	**297.431**	**0.0000**	**352.73**	**0.0000**	**139.353**	**0.0033**	**0.267**	**0.0338**	**2.619**	**10.10**	**0.74**	**184.39**	**12.85**	**99.15**	**3.66**	**-272**	**1916**
18	**0.0000**	**174.812**	**0.0000**	**94.08**	**0.0000**	**132.324**	**0.0042**	**0.211**	**0.0427**	**2.068**	**10.02**	**0.58**	**183.02**	**10.06**	**98.88**	**4.66**	**87**	**164**
22	**0.0000**	**90.765**	**0.0000**	**1173.65**	**0.0001**	**44.674**	**0.0057**	**0.160**	**0.0586**	**1.509**	**10.06**	**0.43**	**183.69**	**7.38**	**98.44**	**6.34**	**1531**	**35932**
26	**0.0000**	**109.536**	**0.0000**	**598.42**	**0.0002**	**34.375**	**0.0063**	**0.172**	**0.0636**	**1.390**	**10.03**	**0.39**	**183.22**	**6.77**	**98.82**	**6.92**	**-1028**	**12300**
30	**0.0000**	**702.605**	**0.0000**	**78.63**	**0.0001**	**60.216**	**0.0035**	**0.265**	**0.0359**	**2.461**	**10.15**	**0.69**	**185.19**	**12.00**	**99.69**	**3.90**	**64**	**100**
35	**0.0000**	**178.835**	**0.0001**	**29.52**	**0.0003**	**19.390**	**0.0019**	**0.495**	**0.0197**	**4.491**	**10.00**	**1.27**	**182.65**	**21.99**	**97.91**	**2.13**	**15**	**9**
40	**0.0000**	**112.979**	**0.0001**	**19.93**	**0.0004**	**16.743**	**0.0025**	**0.347**	**0.0257**	**3.435**	**9.89**	**0.96**	**180.76**	**16.77**	**97.36**	**2.80**	**14**	**6**

APPENDIX H: Supplementary Data Chapter 4 – Sr, Nd, and Pb Isotope Data, Sills of the Western Cape Province, Karoo Continental Flood Basalt Province

Table H1: Sr-Nd-Pb isotope data for the Western Cape Province Karoo CFB Sills.

Sample	Sr (ppm)	Rb (ppm)	$^{87}Rb/^{86}Sr$	$^{87}Sr/^{86}Sr_{meas}$	± 1σ	$(^{87}Sr/^{86}Sr)_{i.}$	Nd (ppm)	Sm (ppm)	$^{147}Sm/^{144}Nd$	$^{143}Nd/^{144}Nd_{meas}$	± 1σ	$(^{143}Nd/^{144}Nd)_{i.}$	$\varepsilon Nd_{(0)}$
KA	23.3	167.4	0.40230	0.70674	0.0000023	0.70569	17.8	5.1	0.152134	0.512510	0.0000014	0.512328	-2.50
KB	13.9	166.0	0.24201	0.70640	0.0000025	0.70577	14.0	3.5	0.132744	0.512515	0.0000017	0.512356	-2.40
KC	18.2	169.4	0.31052	0.70656	0.0000022	0.70576	15.7	3.9	0.131899	0.512516	0.0000015	0.512358	-2.40
KD	14.5	189.5	0.22114	0.70607	0.0000025	0.70549	10.8	3.1	0.152410	0.512527	0.0000015	0.512344	-2.20
KE	16.5	176.8	0.26974	0.70661	0.0000024	0.70590	16.1	4.6	0.151708	0.512516	0.0000015	0.512334	-2.40
KF	16.9	181.7	0.26882	0.70644	0.0000024	0.70574	16.9	4.5	0.141384	0.512513	0.0000013	0.512344	-2.40
KG	12.6	179.7	0.20264	0.70595	0.0000027	0.70543	11.2	2.9	0.137485	0.512539	0.0000014	0.512374	-1.90
KH	16.9	163.6	0.29857	0.70657	0.0000028	0.70579	16.3	4.6	0.149846	0.512517	0.0000015	0.512338	-2.40
KI	14.5	188.9	0.22185	0.70615	0.0000024	0.70557	12.7	3.3	0.137970	0.512539	0.0000014	0.512374	-1.90

Sample	Pb (ppm)	U (ppm)	Th (ppm)	$^{206}Pb/^{204}Pb_{meas}$	± 1σ	$^{206}Pb/^{204}Pb_i$	$^{207}Pb/^{204}Pb_{meas}$	± 1σ	$^{207}Pb/^{204}Pb_i$	$^{208}Pb/^{204}Pb_{meas}$	± 1σ	$^{208}Pb/^{204}Pb_i$
KA	5.3	0.5	2.3	18.288	0.000751	18.119	15.599	0.000616	15.590	38.239	0.001551	37.985
KB	3.2	0.4	1.7	18.232	0.001273	18.009	15.593	0.001038	15.582	38.157	0.002574	37.847
KC	3.2	0.4	1.5	18.250	0.001059	18.026	15.590	0.000902	15.579	38.187	0.002213	37.913
KD	2.7	0.3	1.3	18.216	0.001248	18.018	15.592	0.001068	15.582	37.925	0.002574	37.645
KE	3.4	0.4	1.7	18.230	0.000702	18.020	15.594	0.000629	15.583	38.172	0.001479	37.880
KF	3.4	0.5	1.9	18.261	0.000974	17.998	15.588	0.000811	15.575	38.191	0.002004	37.865
KG	2.5	0.3	1.2	18.315	0.000976	18.101	15.584	0.000673	15.573	38.008	0.001660	37.728
KH	3.7	0.4	1.7	18.234	0.001425	18.041	15.591	0.001185	15.581	38.177	0.003000	37.909
KI	3.2	0.4	1.5	18.337	0.000832	18.114	15.589	0.000704	15.578	38.042	0.001718	37.769

Initial calculations are age-corrected to 183 Ma. Uncertainties on initial ratios include in-run errors and uncertainties on blank corrections. Sample locations can be found with major and trace element data (Appendix F).

APPENDIX I: Supplementary Data Chapter 4 – Sr, Nd, and Pb Isotope Models, Sills of the Western Cape Province, Karoo Continental Flood Basalt Province

Table I1: EC-AFC parameters for the Western Cape Province, Karoo LIP and potential contaminants

	T (°C)				
Magma liquidus temperature	1200		Equilibration temperature	999.5	
Magma initial temperature	1300		Crystallization enthalpy (J/kg)	396000	
Assimilant liquidus temperature	1000		Isobaric specific heat of magma (J/kg per K)	1484	
Assimilant initial temperature	300		Fusion enthalpy (J/kg)	270000	
Solidus temperature	900		Isobaric specific heat of assimilant (J/kg per K)	1370	
Composition parameters	Sr	Nd	$^{206}Pb/^{204}Pb$	$^{207}Pb/^{204}Pb$	$^{208}Pb/^{204}Pb$
Karoo Initial Literature C7-2					
Magma initial concentration (ppm)	206	9.3	2.1	2.1	2.1
Magma isotope ratio	0.70563	0.512289	17.75	15.34	36.86
Magma trace element distribution coefficient	0.7	0.25	0.17	0.17	0.17
Karoo Initial Western Cape Province					
Magma initial concentration (ppm)	14.5	10.8	2.7	2.7	2.7
Magma isotope ratio	0.70549	0.51232	18.165	15.589	37.853
Magma trace element distribution coefficient	0.71	0.25	0.17	0.17	0.17
African Crust Assimilant					
Assimilant initial concentration (ppm)	159	26	18.6	18.6	18.6
Assimilant isotope ratio	0.73847	0.5118	18.83	15.89	39.19
Assimilant trace element distribution coefficient	1.5	0.25	0.56	0.56	0.56

Thermodynamic parameters and Sr and Nd distribution coefficients from Bohrson and Spera (2001). Pb distribution coefficients from Jourdan *et al.* (2007a) that were calculated using values reported in the GERM database (http://earthref.org/GERM/). Initial magma compositional parameters: Western Cape, KD; the literature, C7-2 (Jourdan *et al.*, 2007a). Assimilant parameters and composition from Jourdan *et al.* (2007a).

Table I1: Enrichment model parameters for the Western Cape Province Karoo CFB Sills.

Sample	Time (b.y.)	$^{206}Pb/^{204}Pb$	$^{207}Pb/^{204}Pb$	$^{208}Pb/^{204}Pb$	$^{238}U/^{204}Pb$	$^{232}Th/^{204}Pb$	$^{232}Th/^{238}U$
Start of 1st Stage	4.57	9.307	10.294	29.487	7.19	33.21	4.62
Start of 2nd Stage	3.70	11.152	12.998	31.230	9.74	36.84	3.78
Kibaran Orogen Event	1.00	17.069	15.511	36.763	6.24	25.68	4.11
Cape Orogen Event	0.26	17.859	15.579	37.861	13.37	54.30	4.06

Calculations from Stacey and Kramers (1975). Elemental compositions resulting in elemental ratios modified from Zartman and Haines (1989) and Plank and Langmuir (1998).

APPENDIX J: Supplementary Data Chapter 5 – $^{40}Ar/^{39}Ar$ Isotope Abundances for the Tasmanian Dolerites and the Kalkarindji Continental Flood Basalt Province

Step	36Ar [fA]	%1σ	37Ar [fA]	1%σ	38Ar [fA]	%1σ	39Ar [fA]	%1σ	40Ar [fA]	%1σ	40(r)/ 39(k)	± 2σ	Age (Ma)	± 2σ	40Ar(r) (%)	39Ar(k) (%)	K/Ca	± 2σ
TAS-07 ***plagioclase****: J = 0.01116750 ± 0.00000447 (1σ) MDF = 0.993884 ± 0.00030 (1σ)*																		
0.5	0.00000	282.488	0.0004	223.500	0.0000	119.175	0.0000	312.47	0.0001	1,287	22.22	204.97	382.02	3177.0	470.28	0.00	0.01	0.0923
1	0.00246	0.171	0.0153	1.247	0.0005	3.853	0.0010	4	0.7424	0	8.54	3.05	164.74	56.22	1.16	0.12	0.03	0.0025
2	0.00266	0.133	0.2522	1.106	0.0009	2.246	0.0288	0	1.0287	0	8.84	0.10	170.20	1.84	24.59	3.54	0.05	0.0011
3	0.00131	0.184	0.8338	1.106	0.0012	1.687	0.0777	0.063	1.0473	0.032	9.37	0.03	179.95	0.63	68.97	9.52	0.04	0.0009
4	0.00096	0.220	0.8941	1.105	0.0015	1.428	0.1069	0.054	1.2087	0.028	9.34	0.03	179.35	0.46	82.11	13.13	0.05	0.0011
5	0.00082	0.162	0.7409	1.104	0.0016	1.381	0.1250	0.047	1.3429	0.025	9.29	0.02	178.53	0.33	86.11	15.37	0.07	0.0016
6	0.00061	0.201	0.6047	1.104	0.0012	1.631	0.0907	0.057	0.9758	0.035	9.34	0.02	179.40	0.39	86.36	11.15	0.06	0.0014
7	0.00036	0.327	0.4192	1.107	0.0009	2.485	0.0664	0.077	0.6931	0.049	9.36	0.03	179.74	0.46	89.32	8.17	0.07	0.0015
8	0.00026	0.293	0.3449	1.106	0.0007	3.562	0.0534	0.087	0.5463	0.062	9.36	0.03	179.71	0.49	91.03	6.57	0.07	0.0015
10	0.00032	0.333	0.4211	1.108	0.0007	3.302	0.0575	0.081	0.6005	0.056	9.40	0.03	180.53	0.51	89.52	7.06	0.06	0.0013
12	0.00019	0.394	0.2802	1.108	0.0005	4.259	0.0359	0.122	0.3670	0.092	9.35	0.04	179.50	0.67	90.97	4.41	0.05	0.0012
15	0.00016	0.589	0.3916	1.106	0.0004	5.587	0.0326	0.137	0.3291	0.102	9.64	0.05	184.79	0.85	94.63	3.99	0.04	0.0008
18	0.00012	0.601	0.2014	1.107	0.0003	6.832	0.0225	0.188	0.2305	0.146	9.43	0.05	181.09	0.99	91.52	2.76	0.05	0.0011
21	0.00012	0.596	0.2682	1.106	0.0003	10.396	0.0203	0.209	0.2067	0.163	9.58	0.06	183.84	1.16	93.33	2.49	0.03	0.0007
24	0.00010	0.696	0.2228	1.116	0.0003	9.074	0.0196	0.213	0.1990	0.169	9.54	0.06	183.02	1.16	93.13	2.40	0.04	0.0009
27	0.00008	0.867	0.1926	1.106	0.0002	12.036	0.0139	0.311	0.1429	0.235	9.76	0.09	187.03	1.62	94.13	1.70	0.03	0.0007
30	0.00008	1.125	0.2103	1.109	0.0002	13.378	0.0145	0.297	0.1455	0.231	9.63	0.09	184.75	1.64	94.72	1.77	0.03	0.0007
35	0.00012	0.697	0.2764	1.126	0.0002	7.281	0.0193	0.095	0.1946	0.023	9.53	0.05	182.85	0.82	93.40	2.36	0.03	0.0007
40	0.00005	1.163	0.0834	1.129	0.0001	17.878	0.0078	0.215	0.0805	0.050	9.32	0.07	179.12	1.21	89.38	0.95	0.04	0.0009
45	0.00007	0.950	0.1131	1.127	0.0001	14.855	0.0113	0.153	0.1176	0.036	9.49	0.05	182.19	0.93	90.39	1.38	0.04	0.0010
50	0.00005	1.019	0.0838	1.130	0.0001	14.515	0.0093	0.185	0.0952	0.043	9.45	0.05	181.41	0.96	91.55	1.14	0.05	0.0011

Step	36Ar [fA]	%1σ	37Ar [fA]	1%σ	38Ar [fA]	%1σ	39Ar [fA]	%1σ	40Ar [fA]	%1σ	40(r)/ 39(k)	± 2σ	Age (Ma)	± 2σ	40Ar(r) (%)	39Ar(k) (%)	K/Ca	± 2σ
TAS-07 ***plagioclase*** *(duplicate): J = 0.01063200 ± 0.00000478 (1σ) MDF = 0.992804 ± 0.00030 (1σ)*																		
2.5	0.0001	3.895	0.0931	2.015	0.0001	40.658	0.0044	0.354	0.0577	1.324	9.99	0.54	180.41	9.28	74.86	0.54	0.02	0.0010
0.5	0.00000	282.488	0.0004	223.500	0.0000	119.175	0.0000	312	0.0001	1,288	22.22	204.97	382.02	3177.0	470.28	0.00	0.01	0.0923
1	0.00000	382.679	0.0008	111.527	0.0000	576.811	0.0000	94	0.0002	304	10.88	48.55	197.12	833.62	183.52	0.00	0.02	0.0583
1.5	0.00001	12.234	0.0189	4.847	0.0000	42.202	0.0008	4.321	0.0101	6.591	9.87	2.21	179.71	38.24	78.03	0.10	0.02	0.0024
2	0.00015	1.035	0.2337	1.243	0.0002	12.321	0.0103	0.350	0.1289	0.515	10.04	0.18	182.68	3.19	78.90	1.33	0.02	0.0005
2.5	0.00035	0.571	0.6098	1.193	0.0004	5.392	0.0266	0.145	0.3170	0.210	10.01	0.09	182.18	1.59	82.52	3.44	0.02	0.0004
3	0.00039	0.476	0.9187	1.188	0.0005	3.907	0.0398	0.109	0.4426	0.150	10.17	0.07	184.85	1.27	89.91	5.15	0.02	0.0004
3.5	0.00041	0.473	1.1617	1.187	0.0006	3.566	0.0498	0.095	0.5299	0.125	10.18	0.07	185.02	1.18	94.02	6.45	0.02	0.0004
4	0.00042	0.459	1.2625	1.187	0.0007	3.279	0.0543	0.092	0.5653	0.118	10.08	0.07	183.39	1.15	95.24	7.03	0.02	0.0004
4.5	0.00039	0.560	1.2104	1.187	0.0007	2.821	0.0515	0.093	0.5287	0.126	10.06	0.07	183.01	1.19	96.34	6.67	0.02	0.0004
5	0.00038	0.566	1.1999	1.188	0.0007	2.954	0.0512	0.094	0.5283	0.126	10.11	0.07	183.92	1.19	96.40	6.63	0.02	0.0004
5.5	0.00033	0.559	1.0437	1.189	0.0006	3.470	0.0451	0.099	0.4647	0.143	10.09	0.07	183.52	1.21	96.26	5.84	0.02	0.0004
6	0.00032	0.564	0.9748	1.189	0.0005	3.339	0.0418	0.105	0.4325	0.154	10.11	0.07	183.87	1.25	95.99	5.41	0.02	0.0004
7	0.00041	0.519	1.2432	1.188	0.0007	2.935	0.0532	0.089	0.5513	0.121	10.07	0.07	183.16	1.17	95.65	6.89	0.02	0.0004
8	0.00035	0.537	1.0859	1.189	0.0006	3.299	0.0465	0.097	0.4783	0.139	10.05	0.07	182.85	1.21	96.06	6.02	0.02	0.0004
10	0.00046	0.452	1.3715	1.188	0.0008	2.417	0.0598	0.088	0.6248	0.106	10.13	0.06	184.20	1.12	95.40	7.75	0.02	0.0004
12	0.00040	0.605	1.2572	1.189	0.0006	3.792	0.0500	0.095	0.5136	0.129	10.06	0.07	183.00	1.28	96.22	6.47	0.02	0.0004
15	0.00027	0.664	0.8689	1.192	0.0004	5.266	0.0331	0.123	0.3396	0.196	10.07	0.09	183.29	1.47	96.32	4.27	0.02	0.0004
18	0.00026	0.687	0.8353	1.192	0.0004	5.109	0.0324	0.125	0.3338	0.199	10.10	0.08	183.71	1.47	96.40	4.19	0.02	0.0004
21	0.00021	0.800	0.7060	1.195	0.0003	6.214	0.0261	0.152	0.2635	0.252	10.08	0.10	183.37	1.66	97.79	3.36	0.02	0.0004
24	0.00017	0.938	0.5614	1.199	0.0003	6.685	0.0204	0.186	0.2083	0.319	10.08	0.11	183.35	1.92	96.90	2.64	0.02	0.0004
27	0.00011	1.537	0.3319	1.219	0.0001	15.183	0.0128	0.282	0.1321	0.503	10.06	0.16	182.98	2.71	95.54	1.65	0.02	0.0004
30	0.00012	1.429	0.3425	1.217	0.0002	12.589	0.0129	0.281	0.1362	0.488	9.98	0.16	181.65	2.74	93.08	1.67	0.02	0.0004
35	0.00016	1.067	0.5121	1.202	0.0002	11.512	0.0194	0.193	0.1984	0.335	10.04	0.11	182.71	1.98	96.47	2.51	0.02	0.0004
40	0.00010	1.611	0.2981	1.227	0.0001	12.751	0.0114	0.314	0.1189	0.559	10.05	0.17	182.90	2.99	94.48	1.47	0.02	0.0004
45	0.00009	1.847	0.2381	1.247	0.0001	14.209	0.0094	0.381	0.1016	0.654	10.12	0.21	184.12	3.59	91.57	1.21	0.02	0.0004
50	0.00013	1.172	0.3385	1.219	0.0002	11.357	0.0143	0.254	0.1537	0.432	10.05	0.14	182.89	2.40	91.66	1.85	0.02	0.0004

Step	36Ar [fA]	%1σ	37Ar [fA]	1%σ	38Ar [fA]	%1σ	39Ar [fA]	%1σ	40Ar [fA]	%1σ	40(r)/ 39(k)	± 2σ	Age (Ma)	± 2σ	40Ar(r) (%)	39Ar(k) (%)	K/Ca	± 2σ
TAS-17 ***plagioclase****: J = 0.01116750 ± 0.00000447 (1σ) MDF = 0.993406 ± 0.00050 (1σ)*																		
1	**0.0000**	**376.117**	**0.0001**	**152.112**	**0.0000**	**370.540**	**0.0000**	**805.086**	**0.0003**	**50.140**	**71.93**	**1202.0**	**1066.1**	**13460**	**84.50**	**0.00**	**0.01**	**0.1703**
2	**0.0000**	**11.480**	**0.0057**	**3.762**	**0.0000**	**4041.695**	**0.0004**	**7.134**	**0.0050**	**2.690**	**10.20**	**1.95**	**195.13**	**35.34**	**75.25**	**0.07**	**0.03**	**0.0046**
3	**0.0000**	**1.802**	**0.0942**	**1.155**	**0.0001**	**29.553**	**0.0063**	**0.395**	**0.0643**	**0.212**	**9.49**	**0.12**	**182.17**	**2.20**	**91.53**	**1.19**	**0.03**	**0.0007**
4	**0.0002**	**0.571**	**0.3379**	**1.136**	**0.0003**	**10.113**	**0.0239**	**0.115**	**0.2444**	**0.056**	**9.45**	**0.05**	**181.46**	**0.85**	**91.42**	**4.54**	**0.03**	**0.0007**
5	**0.0004**	**0.400**	**0.6195**	**1.135**	**0.0006**	**4.771**	**0.0453**	**0.076**	**0.4863**	**0.028**	**9.43**	**0.04**	**180.96**	**0.73**	**86.95**	**8.62**	**0.03**	**0.0007**
6	**0.0005**	**0.282**	**0.8605**	**1.135**	**0.0008**	**3.960**	**0.0616**	**0.065**	**0.6494**	**0.022**	**9.45**	**0.04**	**181.39**	**0.67**	**88.74**	**11.71**	**0.03**	**0.0007**
7	**0.0006**	**0.268**	**1.0860**	**1.135**	**0.0010**	**2.992**	**0.0777**	**0.062**	**0.8266**	**0.017**	**9.47**	**0.04**	**181.70**	**0.66**	**88.12**	**14.78**	**0.03**	**0.0007**
8	**0.0005**	**0.314**	**0.8710**	**1.135**	**0.0008**	**4.193**	**0.0591**	**0.070**	**0.6277**	**0.022**	**9.47**	**0.04**	**181.83**	**0.72**	**88.32**	**11.24**	**0.03**	**0.0007**
10	**0.0005**	**0.285**	**0.8741**	**1.136**	**0.0008**	**3.566**	**0.0597**	**0.064**	**0.6291**	**0.022**	**9.45**	**0.04**	**181.34**	**0.70**	**88.78**	**11.36**	**0.03**	**0.0007**
12	**0.0002**	**0.408**	**0.5255**	**1.136**	**0.0004**	**6.660**	**0.0341**	**0.092**	**0.3527**	**0.040**	**9.52**	**0.04**	**182.70**	**0.80**	**91.10**	**6.48**	**0.03**	**0.0006**
15	**0.0002**	**0.474**	**0.3984**	**1.137**	**0.0003**	**10.743**	**0.0246**	**0.116**	**0.2453**	**0.056**	**9.51**	**0.05**	**182.51**	**0.87**	**94.40**	**4.68**	**0.03**	**0.0006**
18	0.0001	0.851	0.3067	1.138	0.0002	14.494	0.0178	0.161	0.1769	0.078	9.56	0.06	183.34	1.11	95.22	3.39	0.02	0.0006
21	0.0001	0.917	0.2576	1.139	0.0002	14.300	0.0146	0.180	0.1392	0.098	9.32	0.06	179.07	1.18	96.56	2.77	0.02	0.0006
24	0.0001	0.755	0.3005	1.139	0.0002	14.232	0.0166	0.178	0.1624	0.085	9.61	0.06	184.33	1.14	96.80	3.14	0.02	0.0005
27	0.0001	0.674	0.3502	1.138	0.0002	13.055	0.0189	0.160	0.1851	0.074	9.59	0.06	184.05	1.09	96.54	3.58	0.02	0.0005
30	0.0001	0.728	0.2841	1.139	0.0002	16.662	0.0157	0.166	0.1536	0.089	9.62	0.06	184.50	1.11	96.82	2.97	0.02	0.0005
35	0.0001	0.591	0.3985	1.139	0.0003	10.116	0.0221	0.127	0.2153	0.064	9.58	0.05	183.83	0.98	97.03	4.19	0.02	0.0005
40	0.0001	0.906	0.2171	1.142	0.0002	16.565	0.0122	0.210	0.1213	0.113	9.58	0.07	183.85	1.29	95.24	2.32	0.02	0.0006
45	0.0001	0.856	0.1965	1.143	0.0001	20.272	0.0106	0.282	0.1100	0.124	9.63	0.08	184.63	1.54	91.40	2.01	0.02	0.0005
50	0.0001	1.226	0.0931	1.159	0.0001	45.750	0.0052	0.487	0.0598	0.229	9.55	0.15	183.32	2.66	81.65	0.98	0.02	0.0006

Step	36Ar [fA]	%1σ	37Ar [fA]	1%σ	38Ar [fA]	%1σ	39Ar [fA]	%1σ	40Ar [fA]	%1σ	40(r)/ 39(k)	± 2σ	Age (Ma)	± 2σ	40Ar(r) (%)	39Ar(k) (%)	K/Ca	± 2σ
TAS-07 ***pyroxene*** *(coarse): J = 0.01060200 ± 0.00001325 (1σ) MDF = 0.993088 ± 0.00040 (1σ)*																		
0.5	0.0000	49.834	0.0000	371.537	0.0000	334.528	0.0000	161.662	0.0012	52.823	-18.03	203.74	-383.1	4821.6	-14.39	0.00	0.08	0.6884
2.5	0.00034	0.344	0.0097	15.304	0.0000	8,249	0.0008	2.412	0.1092	0.082	8.29	2.00	152.25	35.18	6.05	2.57	0.04	0.0110
3	0.00046	0.249	0.0118	12.846	0.0000	201.951	0.0012	1.679	0.1472	0.062	7.82	1.70	143.98	30.06	6.25	3.79	0.04	0.0111
3.5	0.00027	0.292	0.0120	12.581	0.0000	121.031	0.0012	1.714	0.0907	0.099	8.96	1.03	164.04	17.95	12.05	3.93	0.04	0.0111
4	**0.00019**	**0.412**	**0.0130**	**11.930**	**0.0000**	**305.193**	**0.0011**	**1.690**	**0.0679**	**0.132**	**10.38**	**0.90**	**188.74**	**15.47**	**17.28**	**3.64**	**0.04**	**0.0090**
4.5	**0.00013**	**0.585**	**0.0119**	**14.002**	**0.0001**	**82.178**	**0.0012**	**1.527**	**0.0502**	**0.177**	**10.05**	**0.72**	**183.16**	**12.41**	**23.45**	**3.77**	**0.04**	**0.0120**
5	**0.00011**	**0.629**	**0.0110**	**13.032**	**0.0000**	**98.790**	**0.0011**	**1.624**	**0.0441**	**0.204**	**10.14**	**0.69**	**184.66**	**11.96**	**25.53**	**3.57**	**0.04**	**0.0114**
5.5	**0.00010**	**0.574**	**0.0097**	**15.037**	**0.0000**	**116.278**	**0.0010**	**1.802**	**0.0407**	**0.219**	**9.90**	**0.69**	**180.55**	**12.05**	**25.13**	**3.33**	**0.05**	**0.0138**
6	**0.00007**	**0.979**	**0.0106**	**12.960**	**0.0000**	**385.769**	**0.0012**	**1.518**	**0.0320**	**0.281**	**9.81**	**0.55**	**178.83**	**9.61**	**37.25**	**3.91**	**0.05**	**0.0128**
7	**0.00011**	**0.634**	**0.0240**	**7.230**	**0.0000**	**386.371**	**0.0020**	**0.823**	**0.0502**	**0.179**	**10.16**	**0.37**	**185.06**	**6.45**	**40.08**	**6.38**	**0.04**	**0.0052**
8	**0.00010**	**0.580**	**0.0333**	**5.366**	**0.0000**	**40,810**	**0.0020**	**0.896**	**0.0460**	**0.195**	**10.28**	**0.36**	**187.06**	**6.16**	**43.29**	**6.24**	**0.03**	**0.0027**
10	**0.00019**	**0.422**	**0.1201**	**3.450**	**0.0000**	**285.629**	**0.0035**	**0.620**	**0.0833**	**0.109**	**9.93**	**0.34**	**181.02**	**5.85**	**41.15**	**11.12**	**0.01**	**0.0009**
12	**0.00025**	**0.339**	**0.3487**	**3.273**	**0.0000**	**923.823**	**0.0047**	**0.397**	**0.0920**	**0.100**	**10.21**	**0.47**	**185.83**	**8.17**	**49.27**	**14.29**	**0.01**	**0.0004**
15	**0.00037**	**0.232**	**0.7298**	**3.252**	**0.0000**	**408.211**	**0.0043**	**0.568**	**0.0900**	**0.100**	**10.02**	**1.07**	**182.58**	**18.49**	**42.37**	**12.26**	**0.00**	**0.0002**
18	**0.00048**	**0.337**	**1.1153**	**3.249**	**0.0000**	**196.218**	**0.0031**	**0.570**	**0.0795**	**0.113**	**10.44**	**2.64**	**189.77**	**45.57**	**30.54**	**7.49**	**0.00**	**0.0001**
21	**0.00055**	**0.298**	**1.3687**	**3.249**	**0.0000**	**105.794**	**0.0024**	**0.714**	**0.0721**	**0.124**	**11.15**	**5.09**	**202.03**	**87.20**	**22.78**	**4.74**	**0.00**	**0.0000**
24	0.00067	0.233	1.7726	3.248	0.0000	101.848	0.0022	0.918	0.0731	0.124	12.03	9.62	217.02	163.57	16.51	3.23	0.00	0.0000
27	0.00069	0.250	1.8460	3.248	0.0000	178.021	0.0020	0.980	0.0679	0.132	12.76	14.69	229.35	248.04	12.87	2.21	0.00	0.0000
30	0.00036	0.367	0.9866	3.251	0.0000	484.299	0.0012	1.400	0.0355	0.251	11.30	10.03	204.59	171.64	17.18	1.74	0.00	0.0000
35	0.00037	0.286	1.0597	3.251	0.0000	1,670.97	0.0010	1.857	0.0284	0.316	11.72	26.44	211.83	450.83	9.04	0.70	0.00	0.0000
40	0.00023	0.333	0.6185	3.257	0.0000	255.772	0.0006	3.441	0.0224	0.401	12.86	23.04	231.03	388.72	8.54	0.48	0.00	0.0000
45	0.00020	0.330	0.5689	3.260	0.0000	616.417	0.0005	3.856	0.0160	0.561	12.23	30.21	220.52	512.58	8.00	0.34	0.00	0.0000
50	0.00016	0.459	0.3430	3.276	0.0000	21,628	0.0003	6.601	0.0203	0.442	8.44	36.98	154.99	650.76	2.21	0.17	0.00	0.0001
60	0.00021	0.458	0.3108	3.280	0.0000	325.101	0.0002	7.618	0.0388	0.232	-34.52	74.37	-823.8	2248.6	-2.79	0.10	0.00	0.0001
40	0.00010	1.611	0.2981	1.227	0.0001	12.751	0.0114	0.314	0.1189	0.559	10.05	0.17	182.90	2.99	94.48	1.47	0.02	0.0004
45	0.00009	1.847	0.2381	1.247	0.0001	14.209	0.0094	0.381	0.1016	0.654	10.12	0.21	184.12	3.59	91.57	1.21	0.02	0.0004
50	0.00013	1.172	0.3385	1.219	0.0002	11.357	0.0143	0.254	0.1537	0.432	10.05	0.14	182.89	2.40	91.66	1.85	0.02	0.0004

Step	36Ar [fA]	%1σ	37Ar [fA]	1%σ	38Ar [fA]	%1σ	39Ar [fA]	%1σ	40Ar [fA]	%1σ	40(r)/ 39(k)	± 2σ	Age (Ma)	± 2σ	40Ar(r) (%)	39Ar(k) (%)	K/Ca	± 2σ
TAS-17 ***pyroxene*** *(coarse): J = 0.01050200 ± 0.00000578 (1σ) MDF = 0.99462 ± 0.00050 (1σ)*																		
2.5	0.0005	1.390	0.0012	53.551	0.0001	32.389	0.0002	5.964	0.1377	1.400	2.67	34.22	50.01	632.11	0.31	0.11	0.07	0.0719
3	0.0110	0.214	0.0264	3.133	0.0021	1.351	0.0022	0.371	3.2692	0.059	8.49	7.87	154.45	137.22	0.58	1.54	0.04	0.0028
3.5	0.0179	0.205	0.0602	2.224	0.0035	0.894	0.0049	0.180	5.3142	0.036	6.16	5.61	113.29	100.03	0.56	3.36	0.04	0.0019
4	**0.0029**	**0.305**	**0.0251**	**3.238**	**0.0006**	**4.751**	**0.0021**	**0.416**	**0.8737**	**0.221**	**10.67**	**3.27**	**192.04**	**55.88**	**2.60**	**1.48**	**0.04**	**0.0029**
4.5	**0.0015**	**0.469**	**0.0169**	**4.307**	**0.0003**	**8.422**	**0.0014**	**0.685**	**0.4665**	**0.413**	**10.52**	**4.13**	**189.53**	**70.66**	**3.22**	**0.99**	**0.04**	**0.0038**
5	**0.0063**	**0.239**	**0.0446**	**2.435**	**0.0013**	**2.646**	**0.0041**	**0.232**	**1.9126**	**0.101**	**9.96**	**2.78**	**179.95**	**47.86**	**2.11**	**2.81**	**0.05**	**0.0023**
5.5	**0.0064**	**0.228**	**0.0578**	**2.245**	**0.0013**	**2.171**	**0.0059**	**0.161**	**1.9299**	**0.100**	**9.86**	**1.88**	**178.11**	**32.42**	**2.97**	**4.04**	**0.05**	**0.0024**
6	**0.0014**	**0.530**	**0.0245**	**3.290**	**0.0003**	**8.708**	**0.0027**	**0.329**	**0.4254**	**0.453**	**10.30**	**2.15**	**185.76**	**36.89**	**6.59**	**1.89**	**0.06**	**0.0038**
7	**0.0031**	**0.293**	**0.0451**	**2.429**	**0.0006**	**4.804**	**0.0053**	**0.186**	**0.9810**	**0.197**	**10.68**	**1.38**	**192.28**	**23.60**	**5.70**	**3.64**	**0.06**	**0.0029**
8	**0.0038**	**0.267**	**0.0738**	**2.141**	**0.0010**	**3.381**	**0.0097**	**0.113**	**1.2151**	**0.159**	**10.82**	**0.81**	**194.64**	**13.82**	**8.63**	**6.73**	**0.07**	**0.0029**
10	**0.0049**	**0.244**	**0.1627**	**1.987**	**0.0013**	**2.542**	**0.0159**	**0.077**	**1.6036**	**0.120**	**10.44**	**0.58**	**188.16**	**9.96**	**10.26**	**10.95**	**0.05**	**0.0020**
12	**0.0031**	**0.311**	**0.2876**	**1.959**	**0.0010**	**3.216**	**0.0162**	**0.077**	**1.0480**	**0.184**	**10.45**	**0.46**	**188.34**	**7.89**	**15.96**	**11.12**	**0.03**	**0.0011**
15	**0.0033**	**0.283**	**0.9578**	**1.948**	**0.0009**	**3.061**	**0.0176**	**0.072**	**1.0798**	**0.179**	**10.11**	**0.47**	**182.52**	**8.07**	**15.89**	**11.78**	**0.01**	**0.0004**
18	**0.0029**	**0.305**	**1.7565**	**1.947**	**0.0008**	**4.210**	**0.0156**	**0.089**	**0.8570**	**0.225**	**10.00**	**0.63**	**180.59**	**10.74**	**16.78**	**9.99**	**0.00**	**0.0002**
21	**0.0035**	**0.277**	**2.8284**	**1.947**	**0.0008**	**3.216**	**0.0160**	**0.096**	**0.9474**	**0.204**	**9.64**	**0.85**	**174.32**	**14.63**	**14.31**	**9.77**	**0.00**	**0.0001**
24	**0.0039**	**0.261**	**3.6477**	**1.948**	**0.0008**	**3.240**	**0.0126**	**0.100**	**0.9662**	**0.200**	**9.43**	**1.42**	**170.83**	**24.60**	**9.83**	**7.00**	**0.00**	**0.0001**
27	**0.0062**	**0.232**	**6.3328**	**1.948**	**0.0012**	**2.391**	**0.0136**	**0.090**	**1.4214**	**0.136**	**9.54**	**2.53**	**172.61**	**43.72**	**6.20**	**6.42**	**0.00**	**0.0000**
30	**0.0032**	**0.293**	**3.4666**	**1.948**	**0.0006**	**4.534**	**0.0054**	**0.199**	**0.6953**	**0.277**	**8.74**	**4.45**	**158.80**	**77.41**	**3.81**	**2.11**	**0.00**	**0.0000**
35	**0.0047**	**0.248**	**5.2247**	**1.948**	**0.0008**	**3.935**	**0.0066**	**0.169**	**0.9985**	**0.193**	**7.32**	**6.59**	**133.91**	**116.16**	**2.15**	**2.04**	**0.00**	**0.0000**
40	**0.0020**	**0.392**	**2.1438**	**1.949**	**0.0004**	**7.761**	**0.0029**	**0.343**	**0.4197**	**0.459**	**7.93**	**6.82**	**144.66**	**119.49**	**2.60**	**0.95**	**0.00**	**0.0000**
45	**0.0013**	**0.553**	**1.3109**	**1.950**	**0.0002**	**12.625**	**0.0015**	**0.564**	**0.2726**	**0.707**	**6.13**	**13.22**	**112.80**	**235.87**	**1.22**	**0.38**	**0.00**	**0.0000**
50	**0.0012**	**0.601**	**1.2671**	**1.950**	**0.0002**	**14.969**	**0.0014**	**0.558**	**0.2491**	**0.774**	**8.54**	**12.56**	**155.34**	**218.83**	**1.94**	**0.39**	**0.00**	**0.0000**
60	**0.0018**	**0.439**	**1.8996**	**1.950**	**0.0003**	**11.017**	**0.0021**	**0.434**	**0.3978**	**0.485**	**6.36**	**11.75**	**116.92**	**209.07**	**1.21**	**0.53**	**0.00**	**0.0000**

Step	36Ar [fA]	%1σ	37Ar [fA]	1%σ	38Ar [fA]	%1σ	39Ar [fA]	%1σ	40Ar [fA]	%1σ	40(r)/ 39(k)	± 2σ	Age (Ma)	± 2σ	40Ar(r) (%)	39Ar(k) (%)	K/Ca	± 2σ
TAS-17 ***pyroxene*** *(coarse total): J = 0.01050200 ± 0.00000578 (1σ) MDF = 0.994323 ± 0.00020 (1σ)*																		
2.5	0.0003	1.047	0.0012	218.204	0.0001	44.813	0.0009	5.604	0.0971	1.294	4.80	3.68	88.89	66.46	4.36	0.14	0.38	1.6653
3	0.0057	0.170	0.0253	10.955	0.0012	3.367	0.0085	0.582	1.7719	0.071	9.73	0.85	176.01	14.68	4.65	1.30	0.17	0.0382
3.5	0.0129	0.100	0.0547	5.865	0.0026	1.414	0.0210	0.242	4.0324	0.031	9.12	0.54	165.37	9.28	4.73	3.20	0.20	0.0234
4	0.0022	0.206	0.0238	11.515	0.0005	9.335	0.0107	0.469	0.7628	0.165	10.06	0.38	181.55	6.56	14.05	1.63	0.23	0.0537
4.5	0.0012	0.326	0.0185	14.682	0.0003	12.035	0.0084	0.585	0.4489	0.280	10.40	0.44	187.45	7.54	19.45	1.29	0.24	0.0694
5	0.0040	0.177	0.0428	6.959	0.0010	4.040	0.0208	0.242	1.4097	0.089	10.09	0.27	182.19	4.64	14.87	3.18	0.25	0.0351
5.5	0.0047	0.135	0.0597	5.519	0.0013	3.281	0.0331	0.153	1.7289	0.073	10.09	0.16	182.03	2.83	19.29	5.07	0.29	0.0318
6	0.0013	0.301	0.0339	8.508	0.0005	7.608	0.0218	0.229	0.6210	0.202	10.22	0.17	184.39	2.95	35.81	3.33	0.33	0.0567
7	0.0019	0.249	0.0511	6.074	0.0008	4.579	0.0330	0.152	0.8917	0.141	10.26	0.12	185.03	2.12	37.88	5.04	0.33	0.0407
8	0.0020	0.218	0.0637	5.206	0.0009	4.433	0.0406	0.132	1.0069	0.125	10.20	0.10	184.07	1.69	41.08	6.21	0.33	0.0344
10	**0.0023**	**0.213**	**0.1270**	**3.821**	**0.0012**	**3.019**	**0.0599**	**0.090**	**1.2809**	**0.098**	**10.19**	**0.07**	**183.85**	**1.23**	**47.58**	**9.16**	**0.24**	**0.0187**
12	**0.0017**	**0.240**	**0.2168**	**3.400**	**0.0015**	**2.520**	**0.0683**	**0.079**	**1.1709**	**0.107**	**10.12**	**0.06**	**182.56**	**1.00**	**58.88**	**10.44**	**0.16**	**0.0111**
15	**0.0017**	**0.330**	**0.5906**	**3.204**	**0.0016**	**1.988**	**0.0757**	**0.068**	**1.2250**	**0.103**	**10.06**	**0.07**	**181.56**	**1.24**	**61.83**	**11.53**	**0.07**	**0.0042**
18	**0.0017**	**0.259**	**1.3679**	**3.178**	**0.0011**	**3.487**	**0.0588**	**0.087**	**0.9827**	**0.128**	**9.98**	**0.14**	**180.27**	**2.41**	**58.81**	**8.87**	**0.02**	**0.0014**
21	**0.0022**	**0.214**	**2.2365**	**3.175**	**0.0011**	**3.950**	**0.0495**	**0.105**	**0.9591**	**0.131**	**10.00**	**0.26**	**180.63**	**4.43**	**50.00**	**7.34**	**0.01**	**0.0007**
24	**0.0023**	**0.210**	**2.6869**	**3.174**	**0.0009**	**4.933**	**0.0396**	**0.127**	**0.8586**	**0.146**	**9.90**	**0.39**	**178.85**	**6.67**	**43.45**	**5.77**	**0.01**	**0.0005**
27	**0.0025**	**0.204**	**3.0775**	**3.174**	**0.0009**	**5.241**	**0.0334**	**0.152**	**0.8210**	**0.153**	**9.83**	**0.53**	**177.63**	**9.15**	**37.39**	**4.78**	**0.01**	**0.0003**
30	**0.0020**	**0.185**	**2.3552**	**3.175**	**0.0006**	**6.736**	**0.0235**	**0.214**	**0.6403**	**0.196**	**9.90**	**0.59**	**178.89**	**10.10**	**33.76**	**3.34**	**0.00**	**0.0003**
35	**0.0034**	**0.175**	**4.3286**	**3.174**	**0.0008**	**4.152**	**0.0232**	**0.223**	**0.8700**	**0.144**	**9.75**	**1.14**	**176.29**	**19.64**	**22.67**	**3.10**	**0.00**	**0.0002**
40	**0.0042**	**0.168**	**5.2526**	**3.174**	**0.0009**	**4.139**	**0.0207**	**0.240**	**1.0157**	**0.124**	**9.71**	**1.63**	**175.57**	**28.14**	**16.34**	**2.62**	**0.00**	**0.0001**
45	**0.0035**	**0.156**	**4.3721**	**3.175**	**0.0008**	**5.190**	**0.0165**	**0.300**	**0.8395**	**0.150**	**9.62**	**1.72**	**173.99**	**29.71**	**15.46**	**2.07**	**0.00**	**0.0001**
50	**0.0023**	**0.194**	**2.7642**	**3.176**	**0.0004**	**9.878**	**0.0058**	**0.842**	**0.5175**	**0.243**	**9.26**	**3.82**	**167.83**	**66.07**	**7.00**	**0.60**	**0.00**	**0.0001**

Step	36Ar [fA]	%1σ	37Ar [fA]	1%σ	38Ar [fA]	%1σ	39Ar [fA]	%1σ	40Ar [fA]	%1σ	40(r)/ 39(k)	± 2σ	Age (Ma)	± 2σ	40Ar(r) (%)	39Ar(k) (%)	K/Ca	± 2σ
07THD001B pyroxene (fine): J = 0.01050200 ± 0.00000578 (1σ) MDF = 0.980756 ± 0.00050 (1σ)																		
2.5	0.0004	2.893	0.0088	14.321	0.0002	19.729	0.0010	2.354	0.1357	2.633	11.94	10.18	213.63	171.74	8.79	0.46	0.06	0.0171
3	0.0078	0.272	0.0632	3.918	0.0019	1.924	0.0081	0.211	2.5537	0.140	29.85	1.88	493.06	27.25	9.46	3.71	0.07	0.0052
3.5	0.0157	0.221	0.1294	3.451	0.0036	1.399	0.0175	0.097	5.2413	0.068	31.87	1.37	521.96	19.56	10.57	7.98	0.07	0.0048
4	0.0025	0.546	0.0382	4.642	0.0006	5.579	0.0051	0.340	0.8935	0.400	32.52	2.17	531.27	30.66	18.31	2.31	0.07	0.0064
4.5	0.0014	0.906	0.0199	7.105	0.0003	14.113	0.0030	0.627	0.5069	0.705	32.58	3.45	532.14	48.81	19.41	1.39	0.08	0.0113
5	0.0052	0.313	0.0703	3.679	0.0013	3.218	0.0098	0.167	1.8864	0.190	33.72	1.29	548.15	18.11	17.41	4.47	0.07	0.0053
5.5	0.0057	0.303	0.0986	3.515	0.0015	3.366	0.0135	0.139	2.1535	0.166	33.29	0.98	542.16	13.81	20.71	6.15	0.07	0.0050
6	0.0018	0.731	0.0420	4.500	0.0005	7.439	0.0061	0.257	0.7221	0.495	32.54	1.76	531.48	24.94	27.21	2.77	0.07	0.0067
7	0.0025	0.531	0.0698	3.667	0.0008	4.570	0.0102	0.156	1.0789	0.331	32.56	1.07	531.76	15.19	30.63	4.66	0.08	0.0056
8	0.0026	0.524	0.0937	3.528	0.0008	4.366	0.0123	0.137	1.1522	0.310	32.02	0.89	524.20	12.66	34.09	5.63	0.07	0.0048
10	0.0031	0.449	0.2352	3.311	0.0013	3.720	0.0220	0.086	1.5756	0.227	30.78	0.52	506.50	7.40	42.60	10.01	0.05	0.0032
12	0.0022	0.581	0.3784	3.284	0.0010	3.640	0.0222	0.104	1.2958	0.276	29.99	0.50	495.01	7.21	50.70	10.06	0.03	0.0020
15	0.0031	0.447	1.1926	3.268	0.0013	2.848	0.0276	0.091	1.6064	0.223	29.11	0.48	482.27	7.03	48.50	12.29	0.01	0.0008
18	0.0053	0.330	3.0400	3.265	0.0018	2.482	0.0244	0.084	1.9910	0.180	28.89	0.95	479.17	13.85	32.41	10.25	0.00	0.0003
21	0.0057	0.295	3.6042	3.265	0.0017	2.037	0.0155	0.122	1.8076	0.198	29.47	1.82	487.51	26.46	21.13	5.95	0.00	0.0001
24	0.0061	0.288	3.6761	3.266	0.0017	2.717	0.0115	0.135	1.7943	0.199	30.14	2.69	497.19	38.84	15.08	4.12	0.00	0.0001
27	0.0067	0.276	4.0623	3.266	0.0018	1.961	0.0087	0.187	1.8665	0.192	30.14	4.47	497.19	64.44	9.51	2.70	0.00	0.0001
30	0.0067	0.278	3.9619	3.266	0.0017	2.157	0.0068	0.237	1.8136	0.197	30.21	6.46	498.23	93.07	6.67	1.84	0.00	0.0000
35	0.0065	0.281	4.0510	3.266	0.0017	2.018	0.0060	0.261	1.7328	0.206	31.34	8.32	514.51	118.82	5.71	1.45	0.00	0.0000
40	0.0043	0.354	2.7829	3.267	0.0010	3.571	0.0035	0.467	1.1154	0.320	27.39	12.53	457.21	184.77	3.80	0.71	0.00	0.0000
45	0.0030	0.465	1.8083	3.268	0.0007	4.854	0.0023	0.571	0.7780	0.459	27.07	13.62	452.40	201.38	3.80	0.50	0.00	0.0000
50	0.0018	0.733	1.1060	3.269	0.0004	9.160	0.0014	1.208	0.4549	0.786	29.33	18.66	485.55	270.88	4.22	0.30	0.00	0.0000
60	0.0022	0.607	1.0778	3.270	0.0006	7.074	0.0014	1.056	0.5710	0.626	17.42	18.50	303.78	296.93	2.01	0.30	0.00	0.0000

Step	36Ar [fA]	%1σ	37Ar [fA]	1%σ	38Ar [fA]	%1σ	39Ar [fA]	%1σ	40Ar [fA]	%1σ	40(r)/ 39(k)	± 2σ	Age (Ma)	± 2σ	40Ar(r) (%)	39Ar(k) (%)	K/Ca	± 2σ
07THD001B pyroxene (coarse): J = 0.01050200 ± 0.00000578 (1σ) MDF = 0.994335 ± 0.00040 (1σ)																		
2.5	0.0016	0.187	0.0072	4.582	0.0004	7.704	0.0026	0.866	0.5270	0.006	16.17	0.83	283.61	13.43	8.11	0.27	0.19	0.0178
3	0.0396	0.168	0.1278	5.317	0.0095	0.532	0.0448	0.117	13.047	0.037	27.37	1.06	456.77	15.63	9.37	4.56	0.18	0.0193
3.5	0.0625	0.165	0.2580	2.483	0.0147	0.293	0.0810	0.045	21.145	0.003	31.10	0.89	510.98	12.76	11.89	8.26	0.16	0.0081
4	0.0160	0.170	0.1153	2.487	0.0040	0.733	0.0325	0.056	5.8040	0.002	32.41	0.58	529.69	8.24	18.09	3.31	0.15	0.0073
4.5	0.0073	0.186	0.0744	2.513	0.0019	2.265	0.0190	0.103	2.8073	0.004	33.30	0.49	542.19	6.92	22.44	1.93	0.13	0.0066
5	0.0197	0.167	0.2164	2.482	0.0050	0.563	0.0483	0.062	7.4740	0.003	33.24	0.48	541.36	6.72	21.41	4.92	0.12	0.0057
5.5	0.0179	0.166	0.2946	2.483	0.0050	0.709	0.0638	0.050	7.4786	0.002	33.81	0.33	549.43	4.60	28.75	6.49	0.11	0.0056
6	0.0056	0.174	0.1228	2.487	0.0018	1.550	0.0297	0.059	2.6643	0.002	33.64	0.23	547.02	3.24	37.44	3.03	0.13	0.0062
7	0.0075	0.177	0.2064	2.487	0.0029	1.222	0.0518	0.056	4.0091	0.003	34.40	0.18	557.64	2.54	44.33	5.28	0.13	0.0065
8	0.0061	0.174	0.2514	2.485	0.0032	1.065	0.0665	0.048	4.0804	0.002	34.21	0.12	554.96	1.63	55.57	6.77	0.14	0.0068
10	0.0054	0.183	0.5552	2.483	0.0048	0.857	0.1181	0.044	5.3739	0.004	32.40	0.07	529.53	0.95	70.94	12.02	0.11	0.0055
12	0.0038	0.198	0.6630	2.482	0.0041	1.010	0.1113	0.045	4.4745	0.003	30.67	0.06	504.80	0.84	75.97	11.32	0.09	0.0043
15	0.0055	0.171	1.1513	2.482	0.0038	0.860	0.1082	0.045	4.7632	0.003	29.97	0.08	494.81	1.16	67.58	10.97	0.05	0.0024
18	0.0079	0.172	1.9313	2.483	0.0036	1.171	0.0899	0.045	4.7924	0.003	29.08	0.14	481.90	2.08	53.73	9.04	0.02	0.0012
21	0.0072	0.173	1.7097	2.483	0.0023	1.446	0.0412	0.054	3.1741	0.003	28.59	0.28	474.74	4.13	36.07	4.09	0.01	0.0006
24	0.0066	0.172	1.9075	2.483	0.0019	2.148	0.0276	0.068	2.5825	0.004	28.61	0.43	475.02	6.28	29.14	2.69	0.01	0.0004
27	0.0053	0.208	1.9470	2.483	0.0015	1.679	0.0162	0.100	1.8399	0.006	27.79	0.74	463.07	10.90	22.47	1.52	0.00	0.0002
30	0.0049	0.181	1.9814	2.484	0.0013	2.377	0.0119	0.120	1.5847	0.006	27.44	0.98	457.81	14.50	18.22	1.07	0.00	0.0001
35	0.0040	0.179	1.7022	2.484	0.0011	3.050	0.0090	0.197	1.2814	0.007	27.34	1.12	456.35	16.48	16.77	0.80	0.00	0.0001
40	0.0026	0.226	1.2348	2.485	0.0007	4.698	0.0047	0.277	0.7776	0.010	28.32	1.69	470.87	24.76	14.02	0.39	0.00	0.0001
45	0.0023	0.203	0.9410	2.485	0.0006	6.609	0.0044	0.283	0.7110	0.008	27.57	1.35	459.78	19.85	14.64	0.39	0.00	0.0001
50	0.0029	0.223	1.4615	2.485	0.0008	4.841	0.0048	0.251	0.8584	0.005	27.22	1.99	454.64	29.37	12.04	0.39	0.00	0.0001
60	0.0016	0.294	0.9236	2.485	0.0005	6.959	0.0055	0.230	0.5483	0.007	27.04	1.04	451.99	15.36	23.82	0.49	0.00	0.0001

Step	36Ar [fA]	%1σ	37Ar [fA]	1%σ	38Ar [fA]	%1σ	39Ar [fA]	%1σ	40Ar [fA]	%1σ	40(r)/ 39(k)	± 2σ	Age (Ma)	± 2σ	40Ar(r) (%)	39Ar(k) (%)	K/Ca	± 2σ
07THD002 pyroxene (fine): J = 0.01050200 ± 0.00000578 (1σ) MDF = 0.992179 ± 0.00080 (1σ)																		
2.5	0.0004	1.325	0.0013	42.052	0.0001	37.647	0.0003	3.827	0.1104	1.196	18.92	14.71	327.65	233.08	4.51	0.22	0.10	0.0871
3	0.0063	0.330	0.0214	3.262	0.0014	2.220	0.0027	0.342	1.9378	0.068	28.36	5.07	471.38	74.16	3.90	2.23	0.06	0.0042
3.5	0.0125	0.329	0.0507	2.263	0.0025	1.183	0.0059	0.220	3.8487	0.035	28.75	4.45	477.12	64.85	4.40	4.92	0.06	0.0027
4	**0.0023**	**0.389**	**0.0199**	**3.402**	**0.0005**	**5.986**	**0.0023**	**0.413**	**0.7475**	**0.177**	**31.00**	**2.70**	**509.56**	**38.74**	**9.48**	**1.91**	**0.06**	**0.0041**
4.5	**0.0013**	**0.492**	**0.0114**	**5.323**	**0.0003**	**8.929**	**0.0016**	**0.580**	**0.4375**	**0.302**	**32.11**	**3.03**	**525.51**	**43.06**	**11.58**	**1.32**	**0.07**	**0.0077**
5	**0.0050**	**0.339**	**0.0359**	**2.528**	**0.0011**	**2.647**	**0.0049**	**0.229**	**1.6254**	**0.081**	**31.09**	**2.24**	**510.84**	**32.12**	**9.42**	**4.12**	**0.07**	**0.0036**
5.5	**0.0055**	**0.332**	**0.0523**	**2.243**	**0.0013**	**2.418**	**0.0070**	**0.172**	**1.8304**	**0.072**	**31.43**	**1.69**	**515.79**	**24.14**	**12.01**	**5.85**	**0.07**	**0.0031**
6	**0.0017**	**0.441**	**0.0227**	**3.140**	**0.0004**	**7.383**	**0.0034**	**0.334**	**0.5916**	**0.223**	**31.13**	**1.55**	**511.42**	**22.21**	**17.81**	**2.83**	**0.08**	**0.0049**
7	**0.0027**	**0.366**	**0.0356**	**2.513**	**0.0007**	**4.403**	**0.0052**	**0.199**	**0.9531**	**0.139**	**32.02**	**1.30**	**524.10**	**18.45**	**17.37**	**4.32**	**0.08**	**0.0038**
8	**0.0026**	**0.368**	**0.0411**	**2.394**	**0.0007**	**4.520**	**0.0059**	**0.180**	**0.9563**	**0.138**	**31.20**	**1.13**	**512.45**	**16.11**	**19.24**	**4.93**	**0.07**	**0.0036**
10	**0.0036**	**0.350**	**0.0909**	**2.072**	**0.0010**	**2.716**	**0.0096**	**0.135**	**1.3653**	**0.097**	**30.98**	**0.89**	**509.29**	**12.73**	**21.69**	**7.99**	**0.05**	**0.0023**
12	**0.0029**	**0.359**	**0.1653**	**2.007**	**0.0008**	**3.431**	**0.0095**	**0.146**	**1.1399**	**0.116**	**31.10**	**0.76**	**511.00**	**10.88**	**25.66**	**7.86**	**0.03**	**0.0012**
15	**0.0033**	**0.354**	**0.4189**	**1.983**	**0.0009**	**3.591**	**0.0114**	**0.124**	**1.2753**	**0.104**	**30.51**	**0.72**	**502.60**	**10.30**	**26.52**	**9.27**	**0.01**	**0.0005**
18	**0.0018**	**0.421**	**0.7159**	**1.980**	**0.0006**	**4.518**	**0.0105**	**0.139**	**0.7729**	**0.171**	**30.63**	**0.59**	**504.34**	**8.48**	**39.68**	**8.37**	**0.01**	**0.0003**
21	**0.0015**	**0.464**	**1.0534**	**1.979**	**0.0006**	**5.518**	**0.0094**	**0.141**	**0.6194**	**0.213**	**30.68**	**0.72**	**504.95**	**10.35**	**42.70**	**7.21**	**0.00**	**0.0002**
24	**0.0011**	**0.535**	**1.1838**	**1.980**	**0.0005**	**5.725**	**0.0087**	**0.139**	**0.4611**	**0.286**	**30.66**	**0.77**	**504.68**	**11.01**	**52.29**	**6.57**	**0.00**	**0.0001**
27	**0.0010**	**0.574**	**1.2134**	**1.980**	**0.0005**	**6.744**	**0.0084**	**0.146**	**0.4276**	**0.309**	**30.96**	**0.81**	**509.07**	**11.61**	**54.40**	**6.28**	**0.00**	**0.0001**
30	**0.0009**	**0.610**	**1.2112**	**1.980**	**0.0004**	**6.486**	**0.0080**	**0.159**	**0.3859**	**0.342**	**31.05**	**0.83**	**510.27**	**11.93**	**57.79**	**6.00**	**0.00**	**0.0001**
35	**0.0008**	**0.675**	**1.2312**	**1.981**	**0.0004**	**7.967**	**0.0064**	**0.194**	**0.2991**	**0.442**	**30.28**	**1.07**	**499.23**	**15.46**	**56.37**	**4.65**	**0.00**	**0.0001**
40	**0.0004**	**1.263**	**0.6125**	**1.983**	**0.0002**	**14.468**	**0.0019**	**0.548**	**0.1078**	**1.225**	**30.83**	**3.10**	**507.12**	**44.51**	**41.17**	**1.20**	**0.00**	**0.0001**
45	0.0004	1.341	0.4098	1.986	0.0001	24.129	0.0012	0.846	0.0977	1.351	28.47	4.76	473.01	69.57	25.46	0.73	0.00	0.0001
50	0.0002	2.141	0.2393	1.996	0.0001	24.532	0.0007	1.438	0.0584	2.262	27.02	7.28	451.72	107.71	24.77	0.45	0.00	0.0001
60	0.0005	0.986	0.3170	1.989	0.0002	20.493	0.0012	0.793	0.1468	0.900	26.45	4.40	443.22	65.43	16.86	0.78	0.00	0.0001

Step	36Ar [fA]	%1σ	37Ar [fA]	1%σ	38Ar [fA]	%1σ	39Ar [fA]	%1σ	40Ar [fA]	%1σ	40(r)/ 39(k)	± 2σ	Age (Ma)	± 2σ	40Ar(r) (%)	39Ar(k) (%)	K/Ca	± 2σ
07THD002 pyroxene (coarse): J = 0.01050200 ± 0.00000578 (1σ) MDF = 0.99358 ± 0.00030 (1σ)																		
2.5	0.0088	0.135	0.0190	22.831	0.0019	2.224	0.0041	0.210	2.6339	0.003	2.15	2.17	40.39	40.29	0.33	0.42	0.11	0.0509
3	0.0322	0.123	0.0722	6.455	0.0072	0.888	0.0205	0.072	9.7932	0.003	8.70	1.49	158.08	25.99	1.81	2.09	0.15	0.0190
3.5	0.0414	0.125	0.1446	5.337	0.0100	0.460	0.0406	0.044	13.181	0.002	20.28	0.98	349.09	15.31	6.23	4.14	0.15	0.0155
4	0.0067	0.131	0.0477	10.094	0.0018	2.654	0.0118	0.072	2.3432	0.005	30.21	0.56	498.32	8.11	15.22	1.21	0.13	0.0260
4.5	0.0025	0.186	0.0210	14.380	0.0007	5.915	0.0061	0.121	0.9396	0.005	32.12	0.53	525.57	7.50	20.84	0.62	0.15	0.0434
5	0.0211	0.125	0.1614	4.802	0.0058	0.592	0.0329	0.047	7.3113	0.003	31.15	0.62	511.77	8.85	13.95	3.35	0.11	0.0101
5.5	0.0145	0.134	0.5553	4.566	0.0068	0.658	0.0577	0.042	6.2193	0.004	33.98	0.26	551.86	3.69	31.31	5.86	0.05	0.0049
6	0.0055	0.156	0.3918	4.587	0.0034	1.020	0.0346	0.050	2.7932	0.004	34.35	0.20	556.93	2.79	42.23	3.51	0.05	0.0042
7	0.0084	0.133	0.8187	4.563	0.0062	0.749	0.0645	0.042	4.6523	0.003	34.57	0.16	560.01	2.30	47.53	6.54	0.04	0.0037
8	0.0055	0.139	1.0993	4.550	0.0075	0.759	0.0952	0.039	4.7625	0.004	33.95	0.11	551.32	1.54	67.30	9.66	0.04	0.0041
10	0.0039	0.150	1.3421	4.549	0.0094	0.356	0.1660	0.034	6.5202	0.003	33.03	0.07	538.46	1.00	83.64	16.89	0.06	0.0058
12	0.0014	0.193	0.7470	4.568	0.0050	0.929	0.1181	0.034	4.2057	0.005	32.60	0.06	532.39	0.79	91.16	12.03	0.08	0.0075
15	0.0013	0.249	0.8118	4.569	0.0042	0.891	0.1146	0.033	3.9591	0.003	31.80	0.06	521.10	0.87	91.64	11.67	0.07	0.0067
18	0.0008	0.314	0.7990	4.565	0.0021	1.665	0.0620	0.046	2.1146	0.005	31.45	0.11	516.02	1.52	91.31	6.28	0.04	0.0036
21	0.0010	0.282	1.1177	4.548	0.0019	2.236	0.0526	0.047	1.8531	0.004	31.48	0.17	516.45	2.43	87.99	5.30	0.02	0.0022
24	0.0006	0.305	0.8200	4.561	0.0012	2.927	0.0216	0.064	0.7749	0.008	31.61	0.30	518.38	4.35	85.83	2.15	0.01	0.0012
27	0.0007	0.277	1.0539	4.553	0.0008	3.721	0.0126	0.114	0.4963	0.012	31.89	0.69	522.25	9.81	76.04	1.21	0.01	0.0005
30	0.0008	0.277	1.2052	4.553	0.0009	4.487	0.0132	0.085	0.5243	0.007	31.80	0.75	521.05	10.73	74.86	1.26	0.01	0.0005
35	0.0008	0.211	1.1963	4.551	0.0009	3.923	0.0163	0.067	0.6271	0.009	31.58	0.59	517.83	8.47	77.92	1.58	0.01	0.0006
40	0.0012	0.251	1.6812	4.547	0.0010	4.021	0.0148	0.087	0.6639	0.007	31.69	0.95	519.43	13.51	65.22	1.40	0.00	0.0004
45	0.0010	0.299	1.6562	4.548	0.0010	3.748	0.0132	0.115	0.5420	0.013	31.78	1.06	520.76	15.07	70.71	1.23	0.00	0.0003
50	0.0007	0.283	1.4101	4.551	0.0007	4.703	0.0113	0.121	0.4279	0.013	31.49	1.05	516.63	15.05	75.60	1.05	0.00	0.0003
60	0.0007	0.233	1.3132	4.554	0.0007	5.707	0.0064	0.196	0.2803	0.015	32.22	1.83	526.96	25.93	63.53	0.57	0.00	0.0002

Step	36Ar [fA]	%1σ	37Ar [fA]	1%σ	38Ar [fA]	%1σ	39Ar [fA]	%1σ	40Ar [fA]	%1σ	40(r)/ 39(k)	± 2σ	Age (Ma)	± 2σ	40Ar(r) (%)	39Ar(k) (%)	K/Ca	± 2σ
07THD002 pyroxene (coarse total): J = 0.01050200 ± 0.00000578 (1σ) MDF = 0.99358 ± 0.00030 (1σ)																		
2.5	0.0092	0.129	0.0204	18.387	0.0024	1.873	0.0050	0.161	2.7661	0.005	6.57	1.79	120.59	31.80	1.19	0.43	0.13	0.0469
3	0.0402	0.122	0.0888	4.450	0.0094	0.572	0.0216	0.087	12.252	0.003	11.81	1.76	211.36	29.76	2.07	1.87	0.13	0.0112
3.5	0.0461	0.122	0.1722	2.719	0.0108	0.331	0.0382	0.059	14.574	0.003	21.26	1.14	364.45	17.73	5.56	3.31	0.12	0.0063
4	0.0062	0.161	0.0514	8.316	0.0015	2.365	0.0110	0.127	2.1754	0.006	29.38	0.65	486.28	9.45	14.80	0.95	0.11	0.0184
4.5	0.0034	0.166	0.0359	10.864	0.0009	4.427	0.0072	0.149	1.2246	0.007	31.41	0.55	515.46	7.92	18.48	0.63	0.10	0.0227
5	0.0216	0.136	0.2425	1.402	0.0058	0.682	0.0335	0.064	7.4220	0.003	29.71	0.65	490.99	9.46	13.34	2.90	0.07	0.0020
5.5	0.0248	0.125	0.6826	0.687	0.0087	0.622	0.0637	0.043	9.3660	0.003	32.09	0.37	525.19	5.32	21.67	5.50	0.05	0.0007
6	0.0046	0.166	0.3346	1.201	0.0025	1.709	0.0337	0.044	2.4738	0.004	33.39	0.16	543.55	2.31	45.16	2.91	0.05	0.0012
7	0.0112	0.135	0.7185	0.685	0.0063	0.699	0.0706	0.042	5.5769	0.003	32.75	0.16	534.46	2.29	41.17	6.09	0.05	0.0007
8	0.0079	0.149	0.8203	0.592	0.0069	0.682	0.0988	0.036	5.5012	0.002	32.68	0.09	533.45	1.27	58.34	8.54	0.06	0.0007
10	0.0053	0.137	1.3612	0.563	0.0097	0.441	0.1835	0.034	7.3537	0.003	32.27	0.04	527.75	0.54	80.13	15.87	0.07	0.0008
12	0.0024	0.157	1.0452	0.580	0.0065	0.585	0.1600	0.038	5.6933	0.003	31.71	0.03	519.79	0.45	88.73	13.85	0.08	0.0009
15	0.0017	0.172	1.1612	0.583	0.0045	0.749	0.1397	0.033	4.7834	0.003	31.47	0.03	516.30	0.41	91.39	12.07	0.06	0.0007
18	0.0014	0.218	1.4183	0.561	0.0026	1.653	0.0742	0.039	2.5848	0.005	31.17	0.05	512.05	0.70	88.32	6.37	0.03	0.0003
21	0.0015	0.200	2.0429	0.527	0.0022	1.939	0.0583	0.038	2.0686	0.003	31.10	0.07	510.99	1.05	85.58	4.95	0.01	0.0002
24	0.0016	0.185	2.2577	0.517	0.0021	1.894	0.0529	0.042	1.9020	0.003	31.06	0.09	510.44	1.24	83.76	4.46	0.01	0.0001
27	0.0010	0.219	1.4174	0.585	0.0011	2.631	0.0278	0.063	1.0078	0.006	31.05	0.11	510.33	1.59	82.64	2.33	0.01	0.0001
30	0.0011	0.255	1.4332	0.581	0.0010	4.078	0.0203	0.052	0.8141	0.007	31.44	0.16	515.90	2.27	74.74	1.68	0.01	0.0001
35	0.0012	0.297	1.7024	0.553	0.0009	3.918	0.0137	0.092	0.6167	0.008	31.68	0.30	519.34	4.21	64.35	1.09	0.00	0.0000
40	0.0013	0.205	2.1569	0.533	0.0009	5.076	0.0167	0.081	0.6932	0.011	31.58	0.27	517.87	3.85	69.11	1.32	0.00	0.0000
45	0.0012	0.308	2.1191	0.536	0.0009	5.067	0.0167	0.075	0.6610	0.011	31.27	0.28	513.43	4.04	71.82	1.32	0.00	0.0000
50	0.0007	0.279	1.4164	0.592	0.0005	6.831	0.0106	0.117	0.4034	0.017	30.32	0.30	499.78	4.27	72.63	0.84	0.00	0.0000
60	0.0007	0.345	1.2370	0.572	0.0005	7.180	0.0093	0.137	0.3652	0.015	30.15	0.32	497.40	4.60	69.53	0.73	0.00	0.0000

Step	36Ar [fA]	%1σ	37Ar [fA]	1%σ	38Ar [fA]	%1σ	39Ar [fA]	%1σ	40Ar [fA]	%1σ	40(r)/ 39(k)	± 2σ	Age (Ma)	± 2σ	40Ar(r) (%)	39Ar(k) (%)	K/Ca	± 2σ
09THD028 pyroxene (fine): J = 0.01050200 ± 0.00000578 (1σ) MDF = 0.994335 ± 0.00040 (1σ)																		
2.5	0.0009	0.283	0.0067	9.974	0.0002	17.386	0.0016	1.619	0.2783	0.116	15.08	1.19	265.75	19.44	8.38	0.64	0.12	0.0241
3	0.0104	0.171	0.0479	2.841	0.0022	1.726	0.0100	0.150	3.4182	0.010	30.80	1.25	506.80	17.91	8.96	4.12	0.11	0.0061
3.5	0.0210	0.162	0.1187	2.525	0.0045	0.917	0.0246	0.085	7.0366	0.005	31.44	0.98	515.88	13.96	10.94	10.16	0.11	0.0054
4	0.0040	0.177	0.0435	2.874	0.0009	4.294	0.0086	0.188	1.4774	0.022	32.04	0.59	524.51	8.33	18.69	3.57	0.10	0.0059
4.5	0.0020	0.210	0.0245	3.529	0.0005	7.919	0.0049	0.327	0.7414	0.044	33.14	0.61	540.07	8.66	21.67	2.01	0.10	0.0073
5	0.0068	0.180	0.0693	2.674	0.0016	2.431	0.0149	0.110	2.5172	0.014	32.46	0.57	530.39	8.07	19.19	6.17	0.11	0.0060
5.5	0.0077	0.184	0.0959	2.554	0.0019	1.902	0.0220	0.089	2.9960	0.011	32.23	0.44	527.16	6.27	23.64	9.11	0.12	0.0061
6	0.0021	0.220	0.0387	2.977	0.0006	7.178	0.0095	0.179	0.9298	0.035	32.37	0.35	529.08	4.92	32.99	3.93	0.13	0.0076
7	0.0029	0.199	0.0627	2.697	0.0008	4.273	0.0151	0.127	1.3318	0.025	32.29	0.27	528.03	3.82	36.43	6.23	0.12	0.0067
8	0.0025	0.184	0.0730	2.611	0.0009	4.266	0.0164	0.113	1.2592	0.026	31.61	0.21	518.32	2.99	41.01	6.77	0.12	0.0061
10	0.0032	0.189	0.1572	2.503	0.0011	3.336	0.0256	0.070	1.7335	0.019	30.67	0.17	504.84	2.46	45.09	10.57	0.08	0.0042
12	0.0019	0.196	0.2362	2.488	0.0007	5.894	0.0222	0.074	1.2011	0.027	29.84	0.13	492.96	1.90	54.85	9.15	0.05	0.0024
15	0.0017	0.260	0.6256	2.476	0.0007	6.149	0.0203	0.099	1.0310	0.032	29.16	0.20	483.04	2.98	56.29	8.25	0.02	0.0008
18	0.0018	0.243	1.0792	2.476	0.0006	5.338	0.0147	0.126	0.8461	0.039	28.32	0.40	470.75	5.80	46.64	5.78	0.01	0.0003
21	0.0020	0.198	1.2976	2.475	0.0006	8.083	0.0113	0.133	0.7795	0.041	27.29	0.60	455.70	8.82	36.30	4.30	0.00	0.0002
24	0.0015	0.250	1.0325	2.476	0.0004	10.218	0.0065	0.221	0.5146	0.063	26.65	0.88	446.16	13.13	29.73	2.38	0.00	0.0001
27	0.0016	0.249	1.0866	2.476	0.0004	10.512	0.0042	0.326	0.4901	0.066	24.35	1.54	411.78	23.32	17.29	1.44	0.00	0.0001
30	0.0015	0.218	0.9929	2.477	0.0003	14.665	0.0053	0.256	0.4890	0.066	27.32	1.04	456.13	15.40	25.80	1.91	0.00	0.0001
35	0.0013	0.236	0.9591	2.477	0.0003	12.927	0.0041	0.349	0.4092	0.079	26.06	1.37	437.37	20.43	21.59	1.41	0.00	0.0001
40	0.0009	0.286	0.7363	2.478	0.0002	23.519	0.0029	0.456	0.2789	0.116	25.77	1.54	433.04	23.04	21.93	0.98	0.00	0.0001
45	0.0006	0.443	0.6609	2.478	0.0001	24.273	0.0019	0.751	0.1526	0.211	25.55	2.39	429.78	35.77	23.39	0.58	0.00	0.0001
50	0.0002	0.657	0.2669	2.489	0.0001	61.972	0.0007	1.920	0.0663	0.486	23.80	3.24	403.39	49.25	19.57	0.23	0.00	0.0001
60	0.0003	0.642	0.3082	2.486	0.0001	57.517	0.0009	1.422	0.0910	0.355	23.21	2.78	394.43	42.42	18.69	0.30	0.00	0.0001

Step	36Ar [fA]	%1σ	37Ar [fA]	1%σ	38Ar [fA]	%1σ	39Ar [fA]	%1σ	40Ar [fA]	%1σ	40(r)/ 39(k)	± 2σ	Age (Ma)	± 2σ	40Ar(r) (%)	39Ar(k) (%)	K/Ca	± 2σ
09THD028 pyroxene (coarse): J = 0.01055000 ± 0.00000528 (1σ) MDF = 0.993399 ± 0.00040 (1σ)																		
2.5	0.0020	0.539	0.0327	4.721	0.0010	5.260	0.0082	1.514	0.7446	0.373	18.56	1.19	323.41	18.97	20.40	0.46	0.13	0.0129
3	0.0114	0.199	0.1170	3.447	0.0033	1.479	0.0416	0.169	4.8111	0.058	34.40	0.41	559.79	5.67	29.71	2.34	0.18	0.0127
3.5	0.0299	0.164	0.3012	3.287	0.0089	0.543	0.1253	0.070	13.127	0.021	33.75	0.28	550.70	3.97	32.17	7.04	0.22	0.0142
4	0.0097	0.198	0.1598	3.336	0.0036	1.483	0.0732	0.103	5.3389	0.052	33.45	0.20	546.58	2.89	45.79	4.11	0.24	0.0159
4.5	0.0059	0.251	0.1053	3.457	0.0022	2.383	0.0476	0.149	3.3325	0.083	33.34	0.25	544.92	3.55	47.55	2.67	0.23	0.0162
5	0.0218	0.178	0.2961	3.289	0.0076	0.704	0.1371	0.068	10.927	0.025	32.34	0.20	530.77	2.90	40.52	7.70	0.24	0.0158
5.5	0.0257	0.169	0.4123	3.284	0.0100	0.470	0.2004	0.054	14.023	0.020	31.87	0.16	524.11	2.25	45.48	11.26	0.25	0.0166
6	0.0087	0.206	0.2072	3.330	0.0042	1.397	0.1006	0.081	5.8092	0.048	32.01	0.14	526.05	2.02	55.34	5.65	0.25	0.0168
7	0.0121	0.185	0.2975	3.289	0.0062	0.962	0.1574	0.060	8.6168	0.032	32.07	0.11	526.94	1.57	58.49	8.84	0.27	0.0181
8	0.0093	0.204	0.3241	3.289	0.0062	0.891	0.1639	0.059	7.9714	0.035	31.86	0.09	523.91	1.33	65.41	9.21	0.26	0.0173
10	0.0086	0.205	0.5685	3.279	0.0085	0.598	0.2288	0.051	9.6636	0.029	31.33	0.07	516.31	0.95	74.04	12.85	0.21	0.0137
12	0.0037	0.315	0.5307	3.280	0.0047	1.078	0.1436	0.063	5.4134	0.051	30.30	0.08	501.61	1.12	80.15	8.06	0.14	0.0092
15	0.0025	0.444	0.8375	3.276	0.0038	1.364	0.1193	0.070	4.2199	0.066	29.70	0.09	492.78	1.36	83.57	6.68	0.07	0.0048
18	0.0019	0.562	1.0294	3.275	0.0019	2.558	0.0690	0.106	2.4668	0.112	28.99	0.16	482.56	2.37	80.31	3.84	0.03	0.0023
21	0.0031	0.383	1.5915	3.274	0.0017	3.252	0.0496	0.143	2.1434	0.130	28.02	0.27	468.23	4.02	63.34	2.73	0.02	0.0010
24	0.0041	0.318	1.6127	3.275	0.0015	3.279	0.0364	0.194	2.0581	0.135	27.43	0.39	459.58	5.78	46.96	1.98	0.01	0.0007
27	0.0046	0.276	1.6694	3.275	0.0014	3.903	0.0273	0.252	1.9564	0.142	27.50	0.53	460.62	7.87	36.72	1.47	0.01	0.0005
30	0.0052	0.271	1.6975	3.275	0.0014	3.608	0.0203	0.335	1.9290	0.144	26.76	0.76	449.63	11.26	26.56	1.08	0.01	0.0004
35	0.0055	0.253	1.7629	3.276	0.0013	4.037	0.0129	0.525	1.8080	0.153	25.62	1.26	432.59	18.87	16.54	0.66	0.00	0.0002
40	0.0056	0.260	1.4674	3.276	0.0012	3.844	0.0108	0.622	1.8130	0.153	25.47	1.42	430.27	21.41	13.73	0.55	0.00	0.0002
45	0.0033	0.375	0.9045	3.278	0.0008	6.702	0.0051	1.329	1.0255	0.271	23.77	2.50	404.67	38.09	10.35	0.25	0.00	0.0002
50	0.0025	0.474	0.7672	3.279	0.0005	8.905	0.0046	1.467	0.7881	0.352	24.07	2.59	409.15	39.47	12.44	0.23	0.00	0.0002
60	0.0051	0.262	1.5975	3.277	0.0010	5.445	0.0069	0.970	1.5374	0.180	24.59	2.38	417.02	36.06	9.26	0.33	0.00	0.0001

Step	36Ar [fA]	%1σ	37Ar [fA]	1%σ	38Ar [fA]	%1σ	39Ar [fA]	%1σ	40Ar [fA]	%1σ	40(r)/ 39(k)	± 2σ	Age (Ma)	± 2σ	40Ar(r) (%)	39Ar(k) (%)	K/Ca	± 2σ
09THD029 pyroxene (fine total): J = 0.01050200 ± 0.00000578 (1σ) MDF = 0.994335 ± 0.00040 (1σ)																		
2.5	0.0008	0.776	0.0094	18.426	0.0003	13.369	0.0030	1.661	0.2889	0.659	21.55	1.87	368.90	29.00	22.39	0.18	0.17	0.0615
3	0.0099	0.176	0.0641	3.667	0.0030	1.448	0.0323	0.162	3.9156	0.049	30.40	0.40	501.04	5.76	25.02	1.90	0.26	0.0192
3.5	0.0291	0.164	0.1952	2.637	0.0088	0.461	0.1089	0.064	12.097	0.016	31.60	0.31	518.12	4.44	28.42	6.41	0.29	0.0153
4	0.0063	0.197	0.0843	3.211	0.0026	1.370	0.0503	0.111	3.5460	0.054	32.99	0.20	537.84	2.78	46.74	2.96	0.31	0.0199
4.5	0.0036	0.253	0.0571	3.943	0.0016	3.033	0.0336	0.160	2.1949	0.087	33.18	0.24	540.63	3.31	50.72	1.97	0.31	0.0241
5	0.0118	0.177	0.1881	2.652	0.0052	0.795	0.1012	0.065	6.7944	0.028	32.57	0.15	532.00	2.16	48.44	5.95	0.28	0.0148
5.5	0.0130	0.177	0.2830	2.565	0.0075	0.624	0.1696	0.053	9.3609	0.021	32.47	0.10	530.48	1.45	58.75	9.97	0.31	0.0160
6	0.0038	0.217	0.1347	2.796	0.0030	1.401	0.0849	0.077	3.8993	0.049	32.61	0.09	532.55	1.32	70.93	4.99	0.33	0.0183
7	0.0056	0.199	0.2366	2.594	0.0053	0.834	0.1445	0.057	6.3388	0.030	32.49	0.07	530.76	0.98	73.98	8.50	0.32	0.0165
8	0.0049	0.208	0.2995	2.556	0.0060	0.779	0.1680	0.052	6.8439	0.028	32.20	0.06	526.77	0.82	78.94	9.88	0.29	0.0149
10	0.0054	0.204	0.5125	2.512	0.0084	0.489	0.2452	0.046	9.3160	0.021	31.64	0.05	518.81	0.65	83.16	14.41	0.25	0.0125
12	0.0032	0.252	0.6283	2.505	0.0062	0.607	0.1820	0.051	6.5131	0.030	30.94	0.05	508.74	0.71	86.24	10.69	0.15	0.0075
15	0.0027	0.299	0.9094	2.498	0.0046	0.989	0.1437	0.055	5.0572	0.038	30.21	0.06	498.20	0.89	85.47	8.42	0.08	0.0041
18	0.0026	0.303	1.3090	2.494	0.0034	1.379	0.1051	0.065	3.7608	0.051	29.70	0.09	490.95	1.29	82.32	6.14	0.04	0.0021
21	0.0017	0.405	1.1135	2.496	0.0017	2.930	0.0531	0.105	1.9347	0.098	29.23	0.15	484.02	2.24	78.98	3.08	0.02	0.0012
24	0.0015	0.445	1.0611	2.497	0.0009	4.386	0.0248	0.204	1.0435	0.183	28.78	0.32	477.52	4.67	66.39	1.42	0.01	0.0006
27	0.0013	0.481	0.9643	2.498	0.0007	6.229	0.0153	0.325	0.7239	0.263	28.60	0.50	474.95	7.31	57.87	0.86	0.01	0.0004
30	0.0012	0.485	0.9799	2.498	0.0006	6.623	0.0120	0.417	0.6150	0.309	28.44	0.65	472.56	9.44	52.47	0.67	0.01	0.0003
35	0.0013	0.455	0.9729	2.498	0.0005	8.136	0.0091	0.540	0.5571	0.342	27.48	0.87	458.46	12.75	41.58	0.50	0.00	0.0002
40	0.0010	0.614	0.6929	2.505	0.0004	11.933	0.0060	0.832	0.3862	0.493	27.47	1.19	458.24	17.58	39.45	0.33	0.00	0.0002
45	0.0007	0.835	0.4754	2.519	0.0002	19.863	0.0042	1.180	0.2706	0.703	26.81	1.59	448.58	23.60	38.13	0.23	0.00	0.0002
50	0.0014	0.452	1.0943	2.498	0.0004	10.459	0.0066	0.744	0.4877	0.390	26.92	1.31	450.23	19.36	32.22	0.34	0.00	0.0001
60	0.0009	0.638	0.6338	2.508	0.0003	12.026	0.0041	1.203	0.3260	0.584	25.70	1.75	432.06	26.10	29.13	0.22	0.00	0.0002

Step	36Ar [fA]	%1σ	37Ar [fA]	1%σ	38Ar [fA]	%1σ	39Ar [fA]	%1σ	40Ar [fA]	%1σ	40(r)/ 39(k)	± 2σ	Age (Ma)	± 2σ	40Ar(r) (%)	39Ar(k) (%)	K/Ca	± 2σ
09THD029 pyroxene (coarse): J = 0.01050200 ± 0.00000578 (1σ) MDF = 0.994335 ± 0.00040 (1σ)																		
0.5	0.00000	282.488	0.0004	223.500	0.0000	119.175	0.0000	312.47	0.0001	1,287	22.22	204.97	382.02	3177.0	470.28	0.00	0.01	0.0923
2.5	0.0015	0.853	0.0119	8.698	0.0004	11.462	0.0032	2.227	0.5014	0.933	21.39	3.93	366.48	60.87	13.42	0.17	0.14	0.0247
3	0.0256	0.170	0.0909	2.715	0.0064	0.860	0.0416	0.175	8.8592	0.053	29.15	0.77	482.88	11.18	13.67	2.25	0.24	0.0129
3.5	0.0464	0.162	0.2210	2.534	0.0130	0.366	0.1397	0.064	18.217	0.026	31.31	0.39	514.04	5.53	23.98	7.55	0.33	0.0166
4	0.0113	0.203	0.1039	2.661	0.0039	1.331	0.0703	0.108	5.6741	0.083	32.76	0.27	534.63	3.75	40.52	3.80	0.35	0.0187
4.5	0.0059	0.267	0.0712	2.831	0.0024	2.199	0.0475	0.151	3.3486	0.140	33.24	0.31	541.38	4.33	47.13	2.57	0.35	0.0197
5	0.0179	0.177	0.2025	2.544	0.0071	0.666	0.1328	0.069	9.6771	0.049	32.80	0.18	535.23	2.60	44.98	7.18	0.34	0.0173
5.5	0.0174	0.178	0.3284	2.513	0.0091	0.673	0.2137	0.054	12.194	0.039	32.90	0.11	536.55	1.62	57.58	11.55	0.34	0.0170
6	0.0045	0.331	0.1463	2.581	0.0036	1.465	0.1003	0.083	4.6267	0.101	32.85	0.14	535.95	2.01	71.18	5.42	0.36	0.0184
7	0.0069	0.243	0.2427	2.531	0.0060	0.793	0.1700	0.059	7.5966	0.062	32.75	0.09	534.45	1.31	73.22	9.19	0.36	0.0184
8	0.0050	0.297	0.2775	2.522	0.0060	0.842	0.1790	0.057	7.2900	0.064	32.51	0.08	531.05	1.18	79.74	9.68	0.34	0.0169
10	0.0055	0.283	0.5175	2.504	0.0084	0.600	0.2475	0.050	9.4432	0.050	31.78	0.06	520.81	0.91	83.20	13.37	0.25	0.0124
12	0.0029	0.468	0.5664	2.504	0.0054	0.952	0.1588	0.065	5.7040	0.082	30.81	0.09	506.93	1.29	85.55	8.57	0.15	0.0073
15	0.0029	0.446	0.8257	2.501	0.0040	1.249	0.1260	0.069	4.5772	0.102	30.05	0.11	495.96	1.59	82.36	6.79	0.08	0.0040
18	0.0036	0.383	1.1501	2.500	0.0026	1.898	0.0832	0.095	3.3834	0.138	29.11	0.17	482.27	2.53	70.89	4.46	0.04	0.0019
21	0.0034	0.393	1.1921	2.500	0.0019	2.932	0.0567	0.133	2.5448	0.184	28.98	0.25	480.38	3.70	63.60	3.02	0.02	0.0012
24	0.0020	0.630	0.9395	2.502	0.0010	4.823	0.0262	0.269	1.2455	0.376	28.01	0.52	466.18	7.67	57.50	1.38	0.01	0.0007
27	0.0019	0.670	0.9132	2.502	0.0008	6.018	0.0182	0.390	0.9907	0.472	27.69	0.76	461.61	11.21	49.12	0.95	0.01	0.0005
30	0.0013	0.962	0.6606	2.504	0.0005	11.477	0.0103	0.677	0.6040	0.775	27.68	1.30	461.45	19.16	45.27	0.53	0.01	0.0004
35	0.0014	0.884	0.7727	2.503	0.0005	10.035	0.0111	0.626	0.6502	0.720	27.67	1.24	461.27	18.17	44.80	0.57	0.01	0.0004
40	0.0015	0.862	0.7536	2.504	0.0005	11.064	0.0073	0.950	0.5612	0.834	27.15	1.92	453.67	28.30	32.89	0.37	0.00	0.0003
45	0.0008	1.575	0.4414	2.510	0.0003	16.583	0.0032	2.166	0.2710	1.726	26.22	4.35	439.78	64.74	27.89	0.16	0.00	0.0002
50	0.0008	1.444	0.4922	2.509	0.0004	13.336	0.0034	2.033	0.2922	1.601	26.25	4.11	440.22	61.19	27.46	0.17	0.00	0.0002
60	0.0022	0.587	1.0766	2.503	0.0007	7.260	0.0065	1.066	0.7045	0.664	24.40	2.34	412.49	35.32	19.87	0.31	0.00	0.0002

Step	36Ar [fA]	%1σ	37Ar [fA]	1%σ	38Ar [fA]	%1σ	39Ar [fA]	%1σ	40Ar [fA]	%1σ	40(r)/ 39(k)	± 2σ	Age (Ma)	± 2σ	40Ar(r) (%)	39Ar(k) (%)	K/Ca	± 2σ
09THD029 pyroxene (coarse total): J = 0.01055000 ± 0.00000528 (1σ) MDF = 0.980756 ± 0.00050 (1σ)																		
2.5	0.0009	0.730	0.0081	20.532	0.0004	11.022	0.0017	3.215	0.2717	0.873	9.88	3.71	179.28	64.04	6.04	0.08	0.11	0.0442
3	0.0108	0.211	0.0539	4.716	0.0026	1.493	0.0179	0.257	3.6988	0.064	27.46	0.89	460.04	13.22	13.24	0.90	0.17	0.0162
3.5	0.0373	0.202	0.1591	3.413	0.0093	0.399	0.0664	0.091	13.072	0.018	29.50	0.76	489.95	11.10	14.96	3.34	0.22	0.0148
4	0.0105	0.216	0.0806	3.864	0.0030	1.223	0.0362	0.134	4.2515	0.056	31.28	0.44	515.62	6.32	26.56	1.82	0.23	0.0180
4.5	0.0064	0.231	0.0575	4.490	0.0020	1.955	0.0262	0.178	2.7347	0.087	31.86	0.42	523.94	6.06	30.51	1.32	0.24	0.0213
5	0.0284	0.203	0.2055	3.352	0.0083	0.521	0.1053	0.070	11.771	0.020	31.49	0.37	518.60	5.29	28.13	5.30	0.27	0.0178
5.5	0.0308	0.204	0.3121	3.299	0.0101	0.354	0.1571	0.058	14.111	0.017	31.44	0.27	517.94	3.88	34.96	7.91	0.26	0.0172
6	0.0095	0.214	0.1731	3.398	0.0042	0.857	0.0917	0.074	5.7009	0.042	31.38	0.16	517.09	2.33	50.40	4.62	0.28	0.0187
7	0.0127	0.207	0.2687	3.312	0.0062	0.702	0.1449	0.061	8.2916	0.029	31.30	0.13	515.92	1.87	54.63	7.30	0.28	0.0186
8	0.0104	0.212	0.2857	3.302	0.0066	0.676	0.1779	0.057	8.6226	0.028	31.10	0.09	513.00	1.35	64.08	8.96	0.32	0.0214
10	0.0098	0.213	0.4430	3.275	0.0090	0.523	0.2775	0.054	11.335	0.021	30.42	0.06	503.23	0.91	74.37	13.97	0.33	0.0213
12	0.0065	0.226	0.5103	3.273	0.0076	0.565	0.2435	0.054	8.8920	0.027	28.73	0.06	478.68	0.81	78.54	12.26	0.25	0.0162
15	0.0051	0.237	0.7428	3.263	0.0064	0.735	0.2055	0.055	7.5283	0.032	29.65	0.06	492.16	0.85	80.72	10.33	0.14	0.0094
18	0.0051	0.238	1.0405	3.260	0.0046	0.952	0.1540	0.059	5.8952	0.040	29.09	0.08	483.97	1.14	75.66	7.73	0.08	0.0050
21	0.0065	0.245	1.7994	3.258	0.0040	0.987	0.1130	0.066	4.9371	0.048	28.09	0.14	469.28	2.04	63.60	5.64	0.03	0.0021
24	0.0046	0.251	1.6134	3.259	0.0022	1.666	0.0533	0.098	2.7065	0.088	27.74	0.25	464.08	3.62	53.47	2.63	0.02	0.0011
27	0.0035	0.283	1.2762	3.260	0.0014	3.402	0.0307	0.161	1.7708	0.134	27.78	0.36	464.75	5.38	46.70	1.50	0.01	0.0008
30	0.0033	0.276	1.2684	3.260	0.0013	3.554	0.0258	0.180	1.5591	0.152	27.58	0.42	461.76	6.21	44.02	1.25	0.01	0.0007
35	0.0029	0.307	1.4929	3.260	0.0011	3.887	0.0217	0.218	1.3318	0.178	27.76	0.55	464.40	8.08	43.04	1.04	0.01	0.0005
40	0.0037	0.265	1.9006	3.259	0.0012	3.266	0.0191	0.244	1.4425	0.165	27.89	0.75	466.36	11.02	34.29	0.89	0.00	0.0003
45	0.0009	0.685	0.5151	3.274	0.0003	12.691	0.0063	0.725	0.3924	0.604	25.62	1.21	432.59	18.10	38.71	0.30	0.01	0.0004
50	0.0012	0.521	0.7760	3.265	0.0004	9.712	0.0084	0.541	0.5291	0.448	27.96	1.00	467.42	14.77	41.66	0.40	0.01	0.0004
60	0.0012	0.563	0.6113	3.269	0.0005	10.167	0.0104	0.432	0.5912	0.401	28.26	0.76	471.88	11.14	47.56	0.50	0.01	0.0006